Transactions of the ASME®

Journal of Engineering for Gas Turbines and Power

Published Quarterly by The American Society of Mechanical Engineers

VOLUME 120 • NUMBER 3 • JULY 1998

TECHNICAL PAPERS

Gas Turbines: Aircraft Controls

Gas Turbines: Coal, Biomass, and Alternative Fuels

Gas Turbines: Combustion and Fuels

Gas Turbines: Controls and Diagnostics

(Contents continued on outside back cover)

This journal is printed on acid-free paper, which exceeds the ANSI Z39.48-1992 specification for permanence of paper and library materials.♾ ™

♲ **85% recycled content, including 10% post-consumer fibers.**

Technical Editor
H. L. JULIEN (1998)

Associate Technical Editors
Advanced Energy Systems
M. J. MORAN (1999)
Gas Turbine
D. COOKE (1999)
H. NELSON (1999)
J. PETERS (1999)
Internal Combustion Engines
D. ASSANIS (1999)
Nuclear
R. DUFFEY (2001)
Power
D. LOU (1998)

BOARD ON COMMUNICATIONS
Chairman and Vice President
R. K. SHAH

OFFICERS OF THE ASME
President, **W. M. PHILLIPS**

Executive Director, **D. L. BELDEN**

Treasurer, **J. A. MASON**

PUBLISHING STAFF
Managing Director, Engineering
CHARLES W. BEARDSLEY

Director, Technical Publishing
PHILIP DI VIETRO

Managing Editor, Technical Publishing
CYNTHIA B. CLARK

Managing Editor, Transactions
CORNELIA MONAHAN

Production Coordinator
COLIN MCATEER

Production Assistant
MARISOL ANDINO

Transactions of the ASME, Journal of Engineering for Gas Turbines and Power (ISSN 0742-4795) is published quarterly (Jan., April, July, Oct.) for $205.00 per year by The American Society of Mechanical Engineers, 345 East 47th Street, New York, NY 10017. Periodicals postage paid at New York, NY and additional mailing offices. POSTMASTER: Send address changes to Transactions of the ASME, Journal of Engineering for Gas Turbines and Power, c/o THE AMERICAN SOCIETY OF MECHANICAL ENGINEERS, 22 Law Drive, Box 2300, Fairfield, NJ 07007-2300.

CHANGES OF ADDRESS must be received at Society headquarters seven weeks before they are to be effective. Please send old label and new address.

PRICES: To members, $40.00, annually: to nonmembers, $205.00. Add $40.00 for postage to countries outside the United States and Canada.

STATEMENT from By-Laws. The Society shall not be responsible for statements or opinions advanced in papers or . . . printed in its publications (B7.1, par. 3).

COPYRIGHT © 1998 by The American Society of Mechanical Engineers. Authorization to photocopy material for internal or personal use under circumstances not falling within the fair use provisions of the Copyright Act is granted by ASME to libraries and other users registered with the Copyright Clearance Center (CCC) Transactional Reporting Service provided that the base fee of $3.00 per article is paid directly to CCC, Inc., 222 Rosewood Dr., Danvers, MA 01923. Request for special permission or bulk copying should be addressed to Reprints/Permission Department.

INDEXED by Applied Mechanics Reviews and Engineering Information, Inc. Canadian Goods & Services Tax Registration #126148048

Downloaded 03 Jun 2010 to 171.66.16.159. Redistribution subject to ASME license or copyright; see http://www.asme.org/terms/Terms_Use.cfm

(Contents continued)

Gas Turbines: Cycle Inovations

Gas Turbines: Heat Transfer

Gas Turbines: Manufacturing, Materials, and Metallurgy

Gas Turbines: Structures and Dynamics

Internal Combustion Engines: Diesel Engines

Internal Combustion Engines: SI Engines

(Contents continued on p. 668)

(Contents continued)

Internal Combustion Engines: Spark Ignition

ANNOUNCEMENTS

Transition of a Technology Base for Advanced Aircraft Gas Turbine Control Systems

M. E. McGlone
Pratt & Whitney,
A United Technologies Company,
M/S 726-03,
P. O. Box 109600,
West Palm Beach, FL 33410-9600

Technology assessments during the 1980s projected the development of advanced military fighter aircraft that would require propulsion systems that could accommodate multimission capability with super maneuverability. These propulsion systems would be required to provide significantly improved thrust to weight, reduced thrust specific fuel consumption, and up and away thrust vectoring capabilities. Digital electronic control systems with significantly expanded capabilities would be required to handle these multifunction control actuation systems, to integrate them with flight control systems, and to provide fail-operational capability. This paper will discuss the challenges that were presented to propulsion system control designers, the innovation of technology to address these challenges, and the transition of that technology to production readiness. Technology advancements will be discussed in the area of digital electronic control capability and packaging, advanced fuel management systems, high pressure fuel hydraulic actuation systems for multifunction nozzles, integrated flight propulsion controls, and higher-order language software development tools. Each of these areas provided unique opportunities where technology development programs and flight prototyping carried concepts to reality.

Overview

The preliminary design studies and configuration analysis conducted during the 1980s identified challenging objectives for propulsion system requirements for future aircraft. The propulsion systems would be required to provide increased levels of thrust at reduced system weight and improved propulsion efficiency for reduced thrust-specific fuel consumption. The ability to vector thrust and reverse thrust were projected to significantly improve overall aircraft maneuverability and capability (Tillman, 1990.)

Accomplishing these objectives would not only require significant improvements in turbomachinery, but also in the capability of the gas turbine engine control system to protect and operate the turbomachinery and the associated subsystems. The system would be required to gain maximum efficiency at steady-state operating conditions and provide smooth, rapid, stall-free transient response to throttle or flight control inputs.

The maneuverability of the aircraft could be enhanced by the ability to vector the engine thrust, especially for the upper left-hand corner of the flight envelope and during take-off and landing. The addition of a thrust vectoring nozzle to the engine significantly increases control system requirements. This system must coordinate the convergent and divergent sections of the nozzle to maintain control of engine pressure ratio during transients while simultaneously reacting to vectoring commands from the flight control. The addition of this capability not only places significant demands on the computer of the control system and adds additional control logic, but also requires a significant increase in overall horsepower available for actuation.

The effects on control system requirements were identified by an analysis conducted under studies such as the Air Force sponsored Full Authority Fault Tolerant Electronic Engine Control (FAFTEEC) program. This program projected a doubling of engine control loops and tripling of electronic control computing capability as compared to the then current systems. This projection seemed high at the time, but actually underestimated the requirement, as can be seen by comparing the F100-PW-220 engine in the F-15 aircraft to the Pratt & Whitney YF119 engine in the YF-22 flight prototype aircraft, shown in Fig. 1. The F100 engine requires six modulated loops, while the YF119 requires fourteen. The capability to functionally integrate the engine control and vectoring nozzle control with the flight control also introduces the requirement to communicate directly on the aircraft digital data bus. This significantly improves overall flight/propulsion control capability, and increases software complexity. The redundancy level built-in test and on-board engine diagnostics are significantly improved, and also increase software requirements. The overall effect is a significant growth in memory and computer throughput. Fortunately, the commercial demand for increased computation capability in workstations and personal computers has made this capability readily available through militarizing commercial electronic components. Computer capability has not been the issue. Interfacing this capability with the engine sensors and actuators and managing the development of logic and software have been the challenge.

Electronic Controls Hardware and Software

Hardware. The advent of digital computers that control gas turbine engines made marked improvement in overall engine performance, efficiency, and operability. The opportunities for further benefits seem endless, however, they result in increased complexity of the electronics and software. Figure 2 illustrates the growth in the computational capability of military and commercial gas turbine controls at Pratt & Whitney over the last 20 years. As discussed previously, the growth has been extensive since the late 1980s. The primary difference illustrated between military and commercial computer requirements lies in the additional logic required to operate the augmentor, variable nozzle area, and nozzle vectoring capability. The growth effect of increased thrust and efficiency is best evidenced by the commercial engines.

As noted earlier, the number of effectors on the military engines has more than doubled with the advent of the vectoring

---

Contributed by the International Gas Turbine Institute and presented at the 41st International Gas Turbine and Aeroengine Congress and Exhibition, Birmingham, United Kingdom, June 10–13, 1996. Manuscript received by the ASME Headquarters January 26, 1996. Paper No. 96-GT-107. Associate Technical Editor: J. N. Shinn.

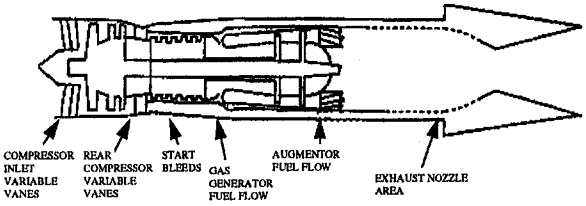

F100 DIGITAL ELECTRONIC ENGINE CONTROL

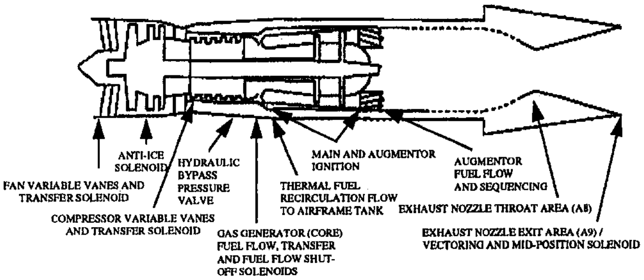

DIGITAL ELECTRONIC CONTROL

Fig. 1 Digital electronic control

nozzle. Initial prototype programs for vectoring and reversing nozzles utilized additional units for control of the dedicated nozzle functions. Figure 3 illustrates the architecture utilized by the F100-PW-229 vectoring nozzle engine flown during the STOL-maneuvering technology demonstration program in the modified F-15 aircraft. This, however, is not the optimum architecture due to minimal envelope on the engine and aircraft for additional components, additional complexity of the data bus system, and data delays in control loops caused by data transfer over the bus system.

Integration of these functions into the engine's full authority digital electronic control (FADEC) was the desired solution. Electronic component and circuit board packaging was the challenge. Technical approaches were available in the commercial world, but temperature and vibration environments were less demanding than on engine. Technology programs were funded to develop highly integrated electronic packages to accomplish integration of the additional analog interfacing circuits into small board areas using custom monolithic analog microcircuits and application-specific integrated circuits. Significant improvement in circuit board density was accomplished by utilizing surface mounted devices mounted on double sided circuit boards. A copper invar laminate was used between the boards to provide thermal matching, and an efficient heat transfer path was used to maintain acceptable component temperatures while on engine. These technical approaches were matured through engine testing in demonstrator engines and combined environment reliability testing. The accomplishment can be documented in Fig. 4 by comparing the YF119 FADEC unit to the F100 DEEC unit. The units are comparable in size and weight; however, the YF119 unit provided three times the improvement in capability in control functions and six times the improvement in computing power.

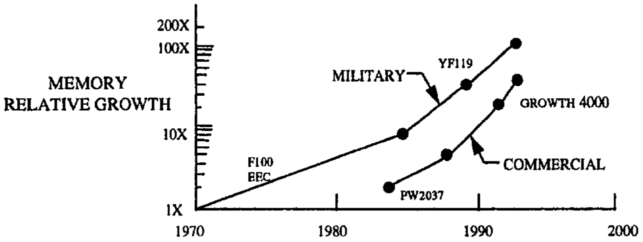

Engine Control Software Growth

Fig. 2 Engine control software growth

Logic and Software. The digital engine controls operating in today's fleet were implemented using custom microprocessors and control logic programmed into these units by a process that included defining the logic in flow diagrams, manually programming the diagram directly into assembly language code, and debugging the code through extensive code read, unit level tests, and module and system level testing. The quality of the resulting code was excellent; however, the labor was extensive.

Understanding what was then required to develop the software and the projections for engine control requirements of the future, it was imperative to automate the process. A technology program was established with a goal to evolve a computer automated process that significantly improved the productivity of the engine control logic designers and software developers, while continuing to provide a quality software product. The system envisioned and illustrated in Fig. 5 would allow the designer to define the logic in graphical format of data flow diagrams and control flow diagrams utilizing a computer workstation. These diagrams could then be combined into a set of control laws and schedules to be refined utilizing a simulation of the engine. After refinement, these diagrams are input directly into a higher-level source language. Ada was chosen as the language of choice to be compatible with the military standards. The system contains the capability for documentation compatible with MIL-STANDARD-2167, and also the capability to generate test cases to test the software modules along with expected test results. This was tested extensively with demonstrator engine programs, and it has generated the total software tool package used in the development of the Pratt & Whitney PT6-36B and F119-PW-100 engines. Productivity measurements on the system have demonstrated a 50 percent reduction in labor required to design and develop logic and software. The quality of the software produced exceeded the expectations by elimination of software errors and variability introduced by manual interpretation of the logic diagrams. The utilization of automated testing allowed standardization and documentation of regression testing. It also facilitated more comprehensive regression testing that, when combined with higher order system testing, can virtually eliminate errors introduced by inadvertent changes and logic complexity. The implementation and technology innovation of system simulator testing will be discussed later in the paper. A discussion of additional integration of aircraft and engine functions and their benefits and effects on

Nomenclature

DEEC = digital electronic engine control
DMICS = design methods for integrated control systems
FADEC = full authority digital electronic control
FAFTEEC = full authority fault tolerant electronic engine control
HIDEC = highly integrated digital electronic control
INTERFACE = integrated, reliable, fault-tolerant electronic engine control
SMTD = STOL maneuvering technology demonstrator
STOL = short take-off and landing
STOVL = short take-off and vertical landing

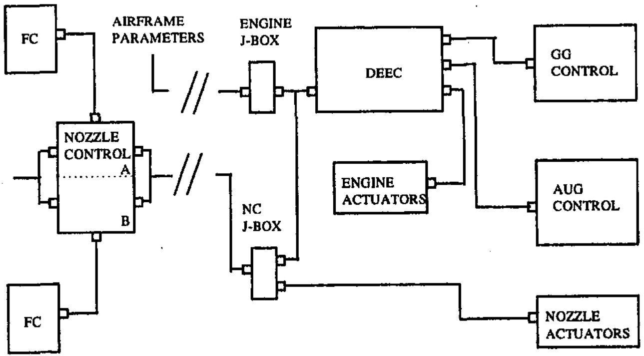

SMTD Engine Nozzle Control Architecture

Fig. 3 SMTD engine nozzle control architecture

system architecture may add a better appreciation of logic complexity and timing.

Fuel Management and Actuation Systems

The control system primary effectors coordinated by the FADEC on the advanced engines consist of fuel metering valves for the main combustor and augmentor and the hydraulic actuators that control variable geometry functions for the compression systems, air bleed, and cooling, and the exhaust nozzle system. As projected by early studies, the number of these effectors had a significant impact on the complexity of the FADEC and software. However, there were also significant challenges with other aspects of these systems. Technology to address these issues came in the form of system architecture as well as component technology and materials. The amount of hydraulic horsepower required to operate the vectoring nozzle was a significant increase over current systems. The thermal impact on fuel system heat load management, when combined with increased levels of aircraft system heat levels, required innovative system architecture changes. The nozzle actuator load, rate, temperature and fail-safe requirements, when combined with aggressive weight goals, required new materials and design features for the actuators.

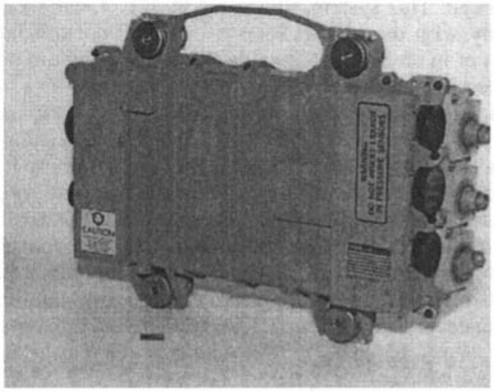

F100 - DEEC

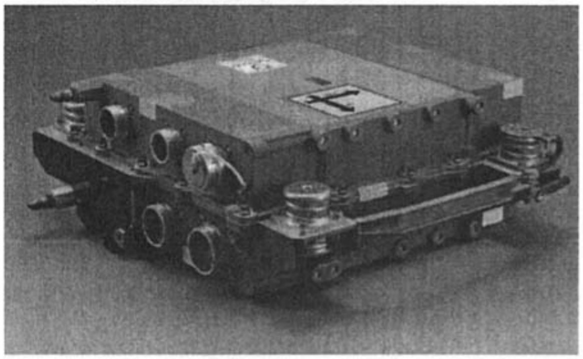

YF119 - FADEC

Fig. 4 F100 DEEC and YF119-FADEC

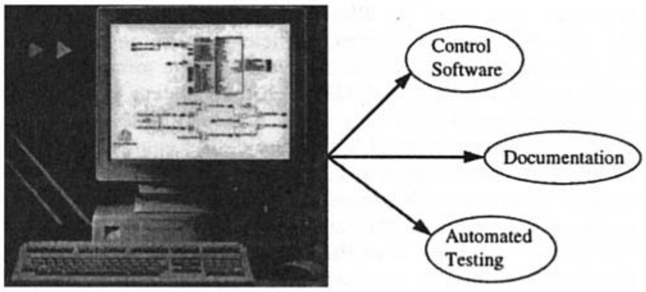

Fig. 5 Computer workstation

Thermal Management

The approach to thermal management for current engines was to isolate the engine fuel and oil system from the aircraft system. The specification was defined at the fuel delivery point to the engine, and the systems were managed independently. This was possible because the flow delivered to the engine was adequate to absorb the heat generated by the engine oil system and fuel pumping system inefficiencies and could be managed within the engine system. The same was true on the aircraft side of the fuel system. Advanced aircraft requirements for avionics and hydraulic power have significantly increased. Engine requirements for hydraulic power and oil system heat have increased. The capacity of the engine system to absorb and burn heat has decreased because engine cycle efficiencies have increased, thus decreasing burn flow at engine cruise points. Development programs have demonstrated that an integrated architecture can provide the benefit of flexibility to operate the aircraft and engine systems at best thermal efficiency over the majority of the mission. The schematic of the integrated approach is illustrated by Fig. 6. The addition of the fuel return path to the aircraft tank no longer restricts the heat sink available

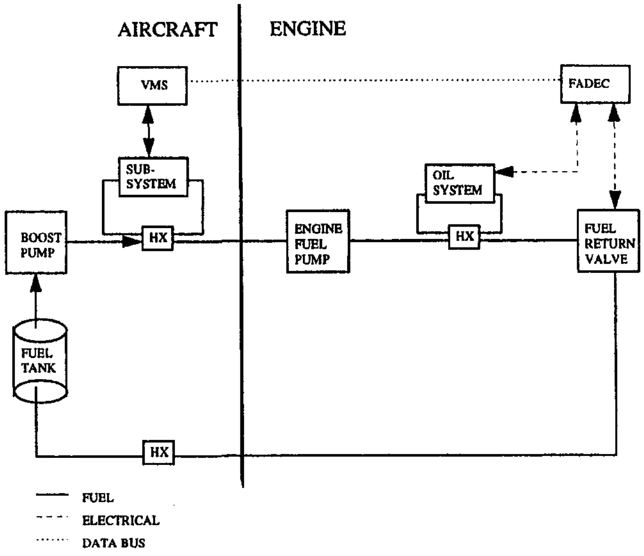

Fig. 6 Integrated architecture schematic

to engine burn flow, but allows the integrated system to flow the fuel necessary for thermal efficiency. The integration is accomplished across the data bus between the aircraft control systems and the engine FADEC. Either system can request changes that result in the best overall thermal efficiency through a set of integrated control laws. Essentially, engine burn flow temperature is maintained at a maximum allowable level to burn as much heat as possible through the engine combustors and to recirculate excess heat through heat exchangers that cool the fuel before returning it to the aircraft or the engine system. Recirculation flow is minimized by logic on the engine and aircraft.

Hydraulic Power and Actuators for Advanced Vectoring Nozzles

Thrust vectoring has been demonstrated on F-15, F-16, F-18, YF-22, YF-23, and other aircraft. Improvements have been demonstrated in overall aircraft performance and significant benefits have been projected for advanced aircraft, both conventional and STOVL. Mechanizing these multifunction nozzles is a challenge to the hydraulic power and actuation systems. Current engine nozzle systems are either hydraulically or pneumatically powered, usually with self-contained systems that require 20–25 horsepower. Thrust vectored nozzles can double or triple that requirement depending on functions and rate required.

Demonstrator programs have shown that maximum vectoring rate of the vectoring surface can occur simultaneously with a rapid thrust command that will require rapid engine exhaust nozzle area changes to hold desired engine pressure ratios. These maximum transient requirements, combined with the actuator loads, cause a significant increase for hydraulic power supply and electrohydraulic servovalve flow capacity. The increased hydraulic power capability is typically handled by adding a closed-loop hydraulic system to the engine dedicated to handle the nozzle with the primary power supply being provided by a variable displacement piston type pump. On most current engine configurations this adds the weight of a third pump, pulse damper, hydraulic reservoir, and heat exchanger, and introduces a third hydraulic medium for the engine maintenance requirements.

A unique system architecture has been demonstrated that can provide the hydraulic power required without the addition of a third power system. The system is a reconfiguration of current engine pumping technologies using a combination of gear and centrifugal pumps. The high flow centrifugal pump is used to boost the pressure for supplying fuel to the main combustor and augmentor. This pump provides additional boost pressure to the gear pump that is used for actuation pressure to the main engine and nozzle actuators. A FADEC controlled pressurizing valve can regulate the pressure rise required across the gear pump to minimize heat load by only providing high pressure during maximum nozzle demand periods. This architecture provides an open-loop type hydraulic supply utilizing engine fuel, thus eliminating the need for a hydraulic reservoir, and it requires no additional support equipment or air purging system after maintenance.

Component technology and material advances were required in the pumps and actuators to facilitate this system architecture. The centrifugal pump required features to allow operating the pump at higher turndown ratios than historically demonstrated, while minimizing heat rise and providing good low flow stability. Innovations in the gear pumps facilitated the capability to operate over a larger flow range at variable pressure and to pump at higher pressure rise and flow without a significant weight penalty. To minimize weight and handling of the high temperature at the aft end of the engines, titanium was used for the actuator manifolds and barrels. Several innovations in material coatings and seals were required to produce the reliability and durability required for piston and rod end seals that could tolerate the high temperature and piston velocity required. These innovations were matured over a period of four to five years and significant investment of resources.

These overall system architecture changes and component technology developments combined with the functional integration of the flight and propulsion control electronics have enabled the capability to implement significant performance enhancements with minimal impact on engine weight.

System Simulation and Test

As noted earlier, the advent of digital electronics for control of modern gas turbine engines has helped provide significant improvement in aircraft engine performance. A concern has always existed for the possibility of software/logic escapes that could cause the engine/nozzle to operate inappropriately. Field experience with current engines has shown the risk to be the highest for errors generated by logic that operates as intended when tested with the engines, but may operate differently when combined with pilot and aircraft interactions. The development approach for highly integrated systems such as the SMTD aircraft and the YF-22/23 was to test the entire vehicle management system electronic architecture with simulations of the aircraft and engines and to operate the total system before first flight and throughout the flight test program. This approach has proven to be highly effective; however, it is a complex test environment that is system focused. The test cost is expensive to focus on detail testing for engine/nozzle logic.

Pratt & Whitney has established a facility to provide a more comprehensive approach to testing of the FADEC and its logic before delivery of the logic to production or larger scale simulation facilities. Innovations in computer and aircraft engine simulation capability have made it feasible to affordably implement a facility where the engine electronics and software may be tested comprehensively with the aircraft simulation, data bus, and cockpit. This system, illustrated by Fig. 7, can be operated manually with pilot-in-the-loop with actual cockpit input and display, or in an automated mode that allows random operation of the aircraft around the flight envelope.

Both modes have proven to be effective. The manual mode allows the system to be operated by USAF test pilots to get important customer feedback early in the engine program that normally proceeds the aircraft program by several years. The automated mode allows comprehensive, cost effective testing, and is implemented with an auto pilot flying random missions and threat pursuits. Key engine performance parameters and all control and diagnostic flags are continuously monitored for exceedance or false alarms. The system has proven itself to

Automated Functional Test Flight Simulator

Fig. 7 Automated functional test flight simulator

be extremely effective at identifying problems that could have previously only been found at flight test or at total weapon system test facilities.

Conclusions

The preliminary design studies accomplished during the 1970s were accurate at identifying the challenges required in engine control system complexity and engine system simulation capability. The integrated control technology programs and flight demonstration accomplished during the 1980s such as DMICS, HIDEC, SMTD, and YF-22/23 established the role of the vehicle management system community in creating management techniques for establishment of requirements, communication, and resolution of integration issues, and for joint simulation and test facilities. These working relationships and experience have been invaluable at establishing a process for the development of highly integrated systems.

The implementation and flight test results of these development systems combined with the aggressive mission, weight, and cost goals of advanced systems generated technology demands, system architecture innovation, component and material technologies, and logic and software design/development tools that have challenged engine control system designers. The resulting technology base has been established to support development of advanced engine and nozzle systems for aircraft such as the Advanced Tactical Fighter and the Joint Strike Fighter.

References

Tillman, K. D., 1990, ''Integrated, Reliable, Fault-Tolerant Control for Large Engines,'' technical report, WRDC-TR-90-2040.

S. Consonni
Dipartimento di Energetica,
Politecnico di Milano,
20133 Milano, Italy

E. D. Larson[1]

T. G. Kreutz

Center for Energy and
Environmental Studies,
School of Engineering and Applied Science,
Princeton University,
Princeton, NJ 08544

N. Berglin

Department of Heat and Power Technology,
Chalmers University of Technology,
412 96 Göteborg, Sweden

Black Liquor Gasifier/Gas Turbine Cogeneration

The kraft process dominates pulp and paper production worldwide. Black liquor, a mixture of lignin and inorganic chemicals, is generated in this process as fiber is extracted from wood. At most kraft mills today, black liquor is burned in Tomlinson boilers to produce steam for on-site heat and power and to recover the inorganic chemicals for reuse in the process. Globally, the black liquor generation rate is about 85,000 MW_{fuel} (or 0.5 million tonnes of dry solids per day), with nearly 50 percent of this in North America. The majority of presently installed Tomlinson boilers will reach the end of their useful lives during the next 5 to 20 years. As a replacement for Tomlinson-based cogeneration, black liquor-gasifier/gas turbine cogeneration promises higher electrical efficiency, with prospective environmental, safety, and capital cost benefits for kraft mills. Several companies are pursuing commercialization of black liquor gasification for gas turbine applications. This paper presents results of detailed performance modeling of gasifier/gas turbine cogeneration systems using different black liquor gasifiers modeled on proposed commercial designs.

Introduction

Black liquor is the lignin-rich by-product of fiber extraction from wood in kraft pulp production. In 1994, the U.S. pulp and paper industry consumed 1.2 EJ (1.2×10^{18} J), or 38,000 MW, of black liquor. This exceeded the 1.0 EJ of fossil fuel used by the industry (AFPA, 1996). The industry burns black liquor today in Tomlinson recovery boilers that feed back-pressure steam turbines supplying process steam and electricity to mills. Tomlinson boilers also recover pulping chemicals (sodium and sulfur compounds) from the black liquor for reuse (Adams et al., 1997). Gasification technologies are under development to replace Tomlinson boilers. This paper assesses the prospective energy performance of black liquor gasifier/gas turbine technologies that are targeted for commercial application by early in the next decade. Black liquor gasifier development received considerable attention in the U.S. in the early 1980s following oil price shocks (Kelleher, 1985; Empie, 1991), but the prospects for commercializing technology appear considerably improved at present. In fact, the first commercial-scale demonstration of an integrated black-liquor gasifier/gas turbine system was announced in May 1997 and will take place at a Swedish pulp mill.

The work presented here is motivated by the current, renewed interest of the pulp and paper industry in black liquor gasification. Some 80 percent of all currently operating recovery boilers in the U.S. were built or rebuilt before 1980 (Fig. 1), so most of the recovery boilers in the U.S. (and Canada, as well) will need major attention or replacement over the next 5 to 20 years. As the most capital-intensive of U.S. manufacturing industries, the paper industry is interested in minimizing capital expenditures for replacements, but would like to do so while meeting increasingly stringent environmental regulations, improving energy performance, and reducing the risk of major recovery boiler explosions that occur periodically (Larson and Raymond, 1997; Larson et al., 1996; Industra, 1996). The need to replace Tomlinson boilers over the next two decades provides a once-in-thirty-years window of opportunity for the industry to make a major technology change (to gasification) to address these concerns.

Black liquor gasification technologies under development can be classified according to operating temperature, or equivalently, according to the physical state in which the majority of the inorganic content of the feed black liquor leaves the reactor. High-temperature gasifiers operate at 950°C or higher and produce a molten smelt of inorganic chemicals. Low-temperature gasifiers operate at 700°C or lower in order to insure that the inorganics leave as dry solids. Kvaerner and Noell are two companies developing high-temperature gasifiers for gas turbine applications. ABB and MTCI are developing low-temperature gasifiers for such applications. Pressurized operation (at about 25 bar) is being pursued for the high-temperature gasifiers. ABB has proposed a milder pressurization (perhaps up to 5 bar), and MTCI is an atmospheric-pressure design. Additional technology details are available elsewhere (Larson and Raymond, 1997; Larson et al., 1996; Larson et al., 1996a; Grace and Timmer, 1995; Stigsson and Hesseborn, 1995; Dahlquist and Jacobs, 1992; Aghamohammadi et al., 1995). Gasifier development by companies other than these four is at a much-reduced level of intensity (Industra, 1996).

Results are reported here of calculations of the full-load performance of gasifier/gas turbine systems incorporating three of the four gasifier designs under commercial development. Calculations based on the MTCI gasifier are reported elsewhere (Larson and Consonni, 1997).

Modeling Black-Liquor Cogeneration

General Approach. The starting point for the calculations is a computational model originally developed to predict the full-load, design-point performance of complex gas–steam power cycles (Consonni, 1992). The system of interest is defined as an ensemble of simulated components of twelve basic types: pump, compressor, combustor, gas turbine expander, heat exchanger, mixer, splitter, steam cycle (which includes HRSG, steam turbine, pumps, and all auxiliaries), air separation plant, shaft (which accounts for turbomachinery interconnections and electric losses), saturator, and chemical converter. Operating characteristics and mass and energy balances of each component are calculated sequentially and iteratively until the conditions

---

[1] Author to whom correspondence should be addressed.

Contributed by the International Gas Turbine Institute and presented at the 42nd International Gas Turbine and Aeroengine Congress and Exhibition, Orlando, Florida, June 2–5, 1997. Manuscript received at ASME Headquarters March 15, 1997. Paper No. 97-GT-273. Associate Technical Editor: H. A. Kidd.

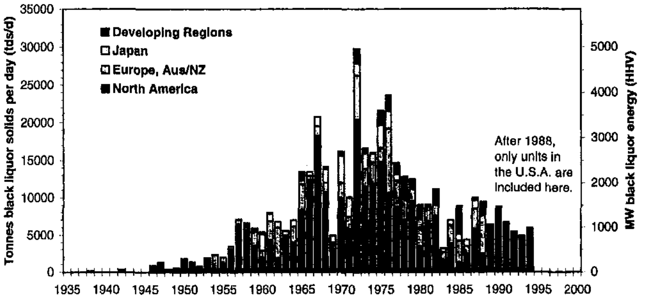

Fig. 1 Age and capacity of 540 operating recovery boilers (record is incomplete after 1988). Cumulative total black liquor processing capacity shown here is 390,000 tonnes of dry solids per day (tds/d), or 64,000 MW_{fuel}. *This total represents about 75 percent of total global capacity* in 1995.

(pressure, temperature, mass flow, etc.) at all interconnections converge toward stable values. The basic model is extensively described elsewhere (Consonni et al., 1991; Lozza, 1990; Lozza et al., 1993; Chiesa et al., 1993, 1995).

The model, using JANAF thermodynamic data (Stull and Prophet, 1971; Gardiner, 1984) in combination with SI steam tables (Schmidt, 1982), accurately simulates full-load performance of plant components that are crucial to the energy and mass balances (e.g., the gasifier, the gas turbine, the steam cycle, the heat exchanger network), but treats simplistically other components that, despite their technological relevance, have minor impacts on the plant mass and energy flows (e.g., H_2S scrubbing). The modeling work reported here ignores altogether the important impacts that gasification of black liquor might have on chemical recovery steps outside of a pulp mill's cogeneration plant, e.g., on the lime kiln (NUTEK, 1992; Industra, 1996; Larson et al., 1996). These impacts have little or no bearing on the heat and mass balances of the gasifier/gas turbine system, but would need to be considered at any actual mill.

Reference Black Liquor. Mass and energy balance calculations require only a correct estimate of the heating value, the dry solids content, and ultimate composition of the input fuel (Consonni and Larson, 1996; Larson et al., 1996). The dry solids content and ultimate composition determine the flux of atomic species into the power plant. The heating value allows closing the heat balances. Black liquor characteristics adopted for all calculations are shown in Table 1. Dry solids can include up to 1 percent chlorine (not shown in Table 1). Minor chlorine content has practical relevance, but a negligible impact on heat and mass balances, and so is neglected here.

Table 1 Reference black liquor and biomass used in calculations

	Ultimate Composition (dry weight %)							Heat Value (MJ/kg dry)	
	C	H	O	S	N	Na	K	Higher	Net
B.L.	37.2	3.6	34.4	3.7	0	18.6	2.5	14.363	12.409[a]
Bio.	50.0	6.1	42.5	0.06	0.6	ash = 0.8		20.000	16.222

(a) Net heating value (NHV) is commonly used for black liquor outside of North America. It accounts for unrecovered latent heat of water vapor and unrecovered heat tied up in reduced sulfur compounds leaving a reactor in practice. The NHV is calculated here using the formula of Adams, *et al.* (1997): NHV (MJ/kg) = HHV (MJ/kg) - 2.44x(18/2)xH - 12.9x(78/32)xSxη_s, where H and S are the mass fractions of hydrogen and sulfur in the original black liquor and η_s is the assumed efficiency of sulfur reduction. 100% sulfur reduction is assumed in this table.

Table 2 Equilibrium and vendor-reported gas compositions[a]

	Ar	CH_4	CO	CO_2	H_2	H_2O	H_2S	N_2
Equilibrium (mol %)	0.47	0.05	11.16	12.94	20.27	14.58	0.74	39.79
Vendor (mol %)[b]	---	2.5	10.5	13.5	19.4	14.6	1.4	38.1

(a) Values assume 72% dry solids black liquor with composition (weight % ds): C, 36.04; H 3.3; O, 34.23; S, 4.91; Na, 17.72; K, 3.8. Liquor feed at 115°C, air at 400°C, reactor temperature and pressure of 700°C and 1 bar, 99% C conversion, heat loss of 1.065% of feed HHV.

(b) Personal communication from D. Turek, ABB, Windsor, CT, Jan. 1996.

Gasification. The high sodium and potassium contents of black liquor help catalyze gasification reactions, so that even at relatively low temperatures, the composition of the product gas is close to equilibrium, except for methane and hydrogen sulfide (H_2S), e.g., see Table 2. This simplifies modeling the gasifiers for heat and mass balance purposes. Since discrepancies in H_2S are much smaller than those with CH_4, and the concentrations of H_2S are small regardless, ignoring the discrepancy in H_2S yields a negligible error in the overall heat and mass balance of the plant. Corrections for nonequilibrium methane content are made based on compositions reported by Berglin (1996) and Backman and Solmenoja (1994). While there is some uncertainty as to what the methane concentration would be in practice, sensitivity calculations confirmed that variations around the concentrations assumed here have little impact on overall plant heat and mass balances.

Gas Turbine. The accurate integrated modeling of actual commercial gas turbines is an important distinguishing feature of the present work relative to other studies that have examined black liquor gasifier/gas turbine applications in the kraft pulp and paper industry, e.g., Berglin (1996), Ihren (1994), and McKeough et al. (1995). For specificity, the Siemens KWU 64.3a is selected here for all calculations. The crucial parameters that determine turbomachinery efficiencies and cooling flows in the model are calibrated such that the model reproduces published performance of the actual commercial engine operating on natural gas fuel (Table 3). The good match with quoted performance provides a basis for confidence in the results for the gasification-based calculations.

The same gas turbine is selected here for all calculations to help illustrate intrinsic differences among alternative gasifier designs. The black liquor fuel requirements for a 64.3a turbine correspond (approximately) to the black liquor flow at typical modern kraft mills having production capacities ranging from 1100–1800 air-dry metric tonnes of final product per day. A perfect match between the quantity of gasified black liquor available at a mill and the fuel requirements of a specific gas turbine will be rare, because the fuel availability is largely determined by considerations related to pulp and paper production (and, possibly, the cost-effectiveness of generating excess power for external sale), while the size of the gas turbine is determined by the few models available on the market. A practical operating strategy at a mill (not considered here) might involve supplementing the available gasified black liquor with natural gas or gasified biomass to provide the full fuel requirement of a gas turbine.

While results are shown for only one gas turbine, the significance of the results is not restricted to this turbine alone. Very similar results would be obtained for turbines of other manufacturers that are of the same basic type (heavy-duty industrial),

Table 3 Calculated and vendor-quoted performance of the Siemens KWU 64.3a natural gas simple cycle gas turbine

	Predicted	Quoted
Input Assumptions		
Turbine inlet T,	1280	not avail.
Pressure ratio	16.6	16.6
Inlet air flow, kg/s	191.9	191.8
Calculated ouputs		
Exhaust flow,	196.3	194
Exhaust T, °C	563	565
Efficiency, %	36.4	36.8
Net Power, MW	70.1	70

same power output class, and same generation of technology. For example, the General Electric 6001FA is very similar to the Siemens KWU64.3a.

The use of gasified black liquor would require some adjustment in the operating parameters of an actual turbine. In particular, the fuel flow required to reach the design turbine inlet temperature will be higher than with natural gas, due to the lower volumetric energy density. All other factors constant, this larger fuel flow increases the flow through the turbine-expander, and thereby the required expander inlet pressure. Increasing the engine's compression ratio to achieve this may cause compressor stall. To avoid simulating unrealistic compressor operation, the engine's compression ratio is allowed to increase modestly (from 16.6 to 17), but further increase is limited by simulated closing of the compressor inlet guide vanes, which reduces air flow to the engine to avoid stall. Some hardware modifications may also be required, including enlarging the fuel nozzle flow area. The calculations assume that such hardware changes can be made without significantly affecting thermodynamic performance.

Product Gas Cleaning. For all plant configurations, cleaning of the syngas is assumed to be carried out by an isothermal scrubbing at 110°C. A variety of commercially proven processes are available for removing H_2S from syngas, but the practical feasibility of scrubbing gasified black liquor to meet turbine specifications and to recover sulfur for recycle to the pulp mill remains to be demonstrated. Within the model adopted here for the gasifier, only H_2S must be removed from the raw syngas—all sodium and potassium leave in the condensed phase. In practice, some CO_2 would also be removed when scrubbing H_2S. Given the much higher concentration of CO_2 than H_2S in the raw gas, we have assumed that 2 moles of CO_2 are removed for each mole of H_2S, which may overestimate the CO_2 removal that would result in practice (McKeough et al., 1995). The CO_2 removal rate has an important impact on causticizing requirements during recovery of the pulping chemicals (NUTEK, 1992), but has a negligible impact on cogeneration performance.

Heat Integration. For each plant configuration modeled here, an effort has been made to optimize the heat integration among components so as to maximize efficiency within practical cost (and material) constraints. The network of heat exchangers in each system has been designed following two guidelines. First, high-temperature gas streams transfer heat only to water or steam-water mixtures (evaporators); due to the high heat transfer coefficients achievable with water and two-phase mixtures, this arrangement guarantees acceptable heat exchanger metal temperatures. Second, to the extent that it would be possible in practice, heat is transferred across relatively small temperature differences and between flows having similar thermal capacities. This reduces heat transfer irreversibilities and increases overall system efficiency. In all cases, substantial quantities of low grade heat are rejected to the environment. No effort is made to find useful applications of this heat, e.g., as process hot water for the mill.

Tomlinson Boiler. To provide a consistent comparison between gasification-based systems and Tomlinson boiler cogeneration systems, the Tomlinson technology is modeled at a comparable level of detail. Table 4 compares model results with an industry-standard performance estimate. The difference in overall performance between the two is due primarily to the difference in assumed stack gas temperature and black liquor heating value (14.363 GJ/tds in this work and 13.950 GJ/tds in Adams et al.). In all calculations here, the Tomlinson steam pressure is set at 60 bar, a common level in practice to minimize corrosion in the furnace and superheater. Pressures of 80 bar or higher are found at a few mills worldwide. With pressures above 60 bar, power production efficiencies would be higher than calculated here, but the comparisons between calculated performance of Tomlinson-based systems and gasifier-based systems would not be qualitatively different.

Table 4 Tomlinson performance

	This work	Adams, 1997
INPUT ASSUMPTIONS		
Ambient air temp., °C	15.0	27.0
Feedwater temp., °C	89	110
Air preheat temp., °C	150	150
Smelt exit temp., °C	850	850
Carbon conv. to gas, %	99.00	98.48
Heat loss, % liquor HHV	2.0	2.5
Stack temp., °C	177	210
Flue O_2 (% dry vol.)	3.0	2.8
Soot blow steam, t/tds	0.18	0.18
Blowdown, t/tds	0.11	0.11
Steam pressure, bar	60	62
Steam temp., °C	450	482
CALCULATED		
Steam produced, t/tds	3.36	3.11
Heat to steam, %[a]	65.0	62.5

(a) Heat in steam delivered to turbine less heat in soot-blow steam, divided by input liquor HHV.

Process Steam Demands. The demand for process steam at a market-pulp or integrated pulp and paper mill sets the requirement for steam to be supplied by the cogeneration plant. Depending on many factors (end product, mill location and age, installed process equipment, etc.), mill steam demands can vary significantly (Fig. 2). Calculations are carried out here for a

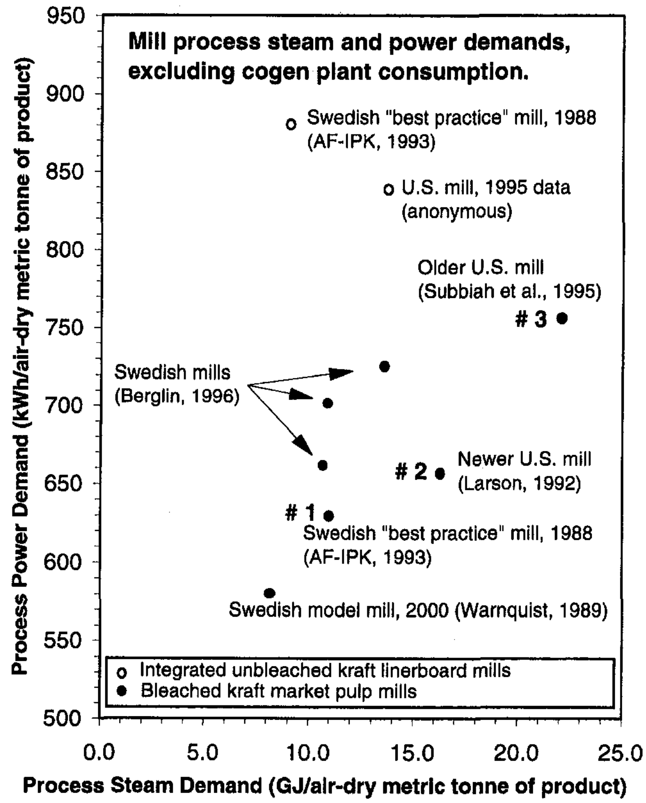

Fig. 2 Kraft-mill energy demands. "Swedish model mill" is an estimate of economically achievable level in a greenfield mill built in year 2000.

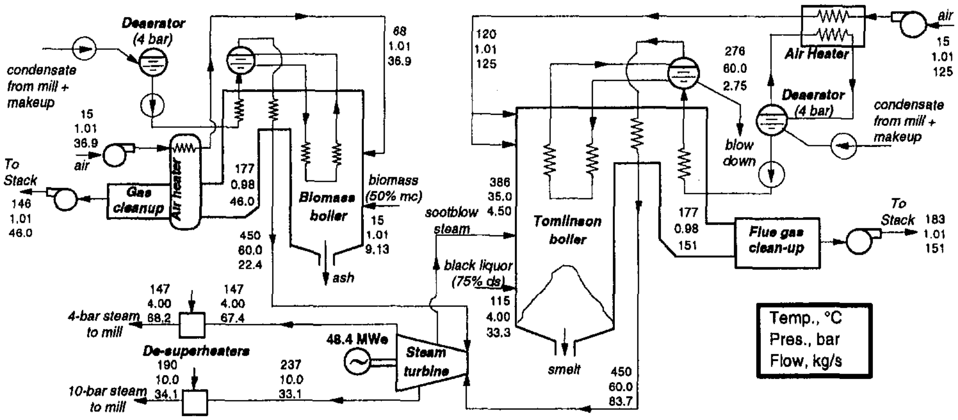

Fig. 3 Heat and mass balance for Tomlinson recovery boiler plus integrated biomass boiler meeting process steam demand of 16.3 GJ/admt. For additional details, see Table 7.

range of process steam demands. For steam demand levels that cannot be met using black liquor alone, supplemental consumption of biomass (Table 1) in a boiler is included.

Steam is generated at 90 bar in the HRSG from clean turbine exhaust and in the biomass boiler and fed to a steam turbine. Process steam is extracted from the turbine at 10 bar, with the balance of steam exhausting at 4 bar for process use. (One case without a steam turbine is considered, wherein process steam is generated directly at 10 and 4 bar.)

Process Flow Descriptions

Performance calculations are reported here for cogeneration systems based around Tomlinson boilers and three different gasifier designs: (*i*) pressurized, high-temperature, air-blown (based on Kvaerner's design), (*ii*) pressurized, high-temperature, oxygen-blown (based on Noell's design), and (*iii*) low-pressure, low-temperature, air-blown (based on ABB's design). Figures 3–6 show sample flow schematics.

High-Temperature Air-Blown Gasifier. The basic plant configuration with the pressurized, air-blown, high-temperature gasifier is shown in Fig. 4. Black liquor fed at 115°C is gasified at 25 bar in air bled from the gas turbine compressor. The product gas passes through an integral quench bath and is further

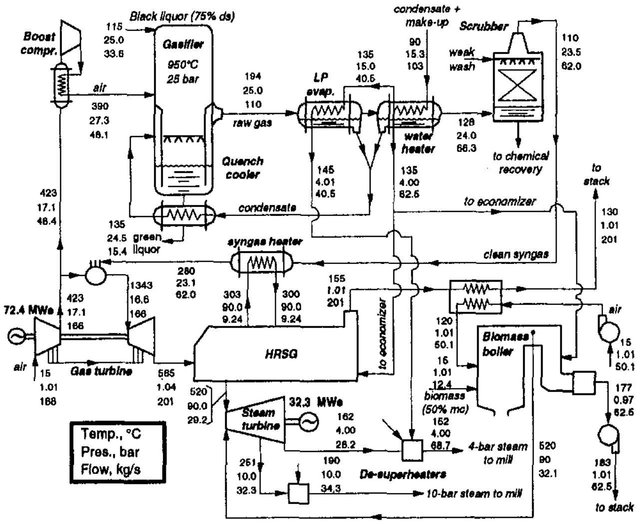

Fig. 4 Heat and mass balance for high-temperature, air-blown gasifier/combined cycle with integrated biomass boiler. Process steam demand of 16.3 GJ/admt is provided by the system. See Table 7 for additional details.

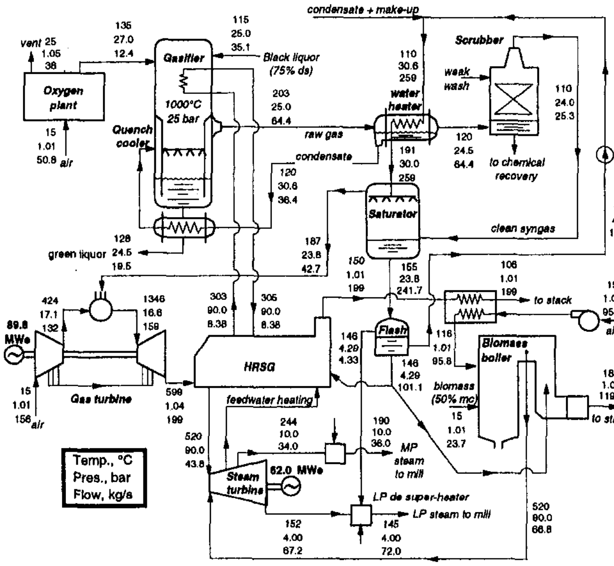

Fig. 5 Heat and mass balance for high-temperature, oxygen-blown gasifier (1000°C reactor temperature) in a combined cycle with an integrated biomass boiler. Process steam demand of 16.3 GJ/admt is provided by the system. See Table 7 for additional details.

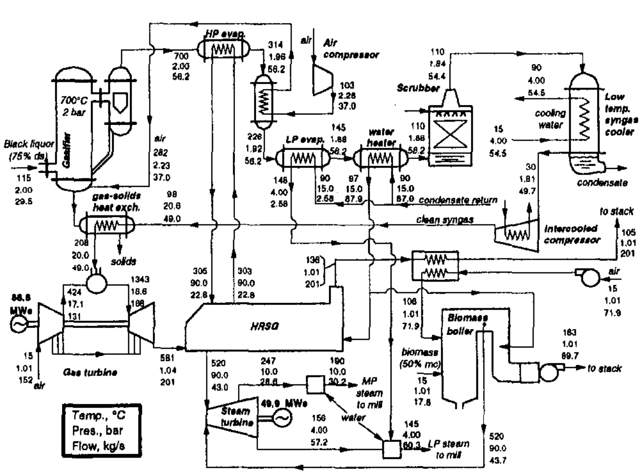

Fig. 6 Heat and mass balance for low-temperature, air-blown gasifiier in combined cycle with an integrated biomass boiler. Process steam demand of 16.3 GJ/admt is provided by the system. See Table 7 for additional details.

Table 5 Detailed assumptions used in models

Gasifier heat losses	0.5% of black liq. HHV
carbon conversion to gas	99%
gas & condensed phase compositions	equilibrium, except CH_4
Syngas coolers minimum ΔT	10°C
gas-side ΔP	2%
Heat exchangers minimum gas-liquid ΔT	10°C
minimum gas-gas ΔT	25°C
ΔP	2%, unless otherwise shown
heat losses	zero
HRSG minimum ΔT at pinch points	10°C
minimum ΔT at approach points	25°C
minimum subcooling ΔT at drum inlet	10°C
superheater ΔP	10%
economizer ΔP	25%
maximum steam superheat	520°C
gas-side ΔP	300 mm H_2O
heat losses	0.7% of heat released by gas
condensate return from mill	80% at 110°C
Steam cycle dearator pressure	2 to 4 bar
heat rejection parasitic power load	2% of rejected heat
pump efficiencies	*f* (volume flow)
steam turbine efficiencies	*f* (volume flow, Δh, rpm, etc.)
Electric generator efficiency	*f* (power output)
Biomass boiler flue oxygen	4% (dry volume)

cooled by raising low-pressure steam and preheating makeup and condensate return water. Water condenses from the product gas in this process and is recirculated to the quench bath. Recirculated condensate is preheated by the quench bath water as the latter carries away dissolved inorganics (green liquor). Weak wash (containing 30 g/L of NaOH) is used in the low-temperature scrubber to capture H_2S. The clean syngas is preheated before being fired in the gas turbine. Preheating does not appreciably improve cycle efficiency, but because of the low heating value of the fuel gas it is important in increasing combustion stability.

High-Temperature, Oxygen-Blown Gasifier. This plant configuration (Fig. 5) is similar to the previous one, except that oxygen is used in place of air. This permits higher gasifier temperatures (1000°C and 1400°C are considered) and the use of smaller-capacity equipment. Oxygen is produced from ambient air (rather than in integrated fashion from gas turbine compressor bleed air). Steam recovery from a gasifier cooling jacket is included in this case. Compared with the system in Fig. 4, the higher gasifier product heating value allows a saturator to be included upstream of the gas turbine to heat the syngas and increase its water vapor content. In effect, the saturator enables use of low-temperature heat in the combined cycle, rather than in the less efficient Rankine cycle alone, as in the case with the air-blown gasifier.

Low-Temperature, Air-Blown Gasifier. This plant configuration (Fig. 6) involves an air-blown fluidized-bed gasifier. A mild pressurization (2 bar) is considered, which offers some advantages over atmospheric pressure: (*i*) Scrubbing of the raw syngas can be done at elevated temperature (110°C, as in the other gasifier cases), which improves heat recovery, (*ii*) part of the compression work required for the fuel gas to be injected into the gas turbine combustor is accomplished by pumping black liquor feed, which is a small parasitic load relative to compressing a gas, and (*iii*) the volumetric flow along the syngas path is cut by about 50 percent, allowing the size of all components to be reduced. One notable feature included in this process configuration is the recovery of heat from the discharged bed solids. This heat is assumed to preheat clean fuel gas before it is fired in the gas turbine combustor. The practical feasibility of such a solid–gas heat exchanger requires examination.

Discussion of Results

Performance results are reported for cogeneration systems at kraft market pulp mills, where black liquor is assumed to be produced at a rate of 1.74 tonnes of dry solids per air-dry metric tonne of pulp (tds/admt). Black liquor feed rates for the gasifiers were set to the requirements of the gas turbine, as discussed above. The feed rate for the Tomlinson boiler (90 tds/hr) was selected to fall in the midrange of the gasifier feed rates. Table 5 shows key assumptions used in the calculations. Gasifier heat and mass balance results are reported in Table 6.

Figure 7 summarizes all of the heat and mass balance results, showing power production per air-dry metric tonne of pulp (kWh/admt) for each modeled system as a function of process steam produced. For reference, points marked Mill #1, #2, and #3 indicate process steam and power demands corresponding to those in Fig. 2. A shaded region is shown in Fig. 7 for each technology, the lower bound of which is the power output assuming that equal masses of medium-pressure (MP, 10-bar) and low-pressure (LP, 4-bar) process steam are generated. The upper bound is the power output when all process steam is LP steam. At the left edge of each region, the use of black liquor alone is sufficient to provide all process steam.

For higher levels of steam demand, biomass fuel is burned in a boiler whose steam production is integrated into the steam production from black liquor. The markers along each line in Fig. 7 indicate different levels of biomass fuel input. For comparison, the waste bark and hog fuel at a typical kraft mill converting logs into pulpable chips might amount to 0.25 dry tonnes of biomass per tonne of final pulp, or about 5 GJ/admt. Many mills may have access to much more biomass. One detailed study around a Weyerhaeuser mill in North Carolina iden-

Table 6 Calculated gasifier heat and mass balances. The gasifier feed in all cases is black liquor at 115°C containing 25 percent water and having the dry solids composition given in Table 1.

Reactor type →	Low P, T air-blown	High P, T air-blown	High P,T O_2-blown	High P,T O_2-blown
Assumptions				
Reactor temp., °C	700	950	1000	1400
Reactor pressure, bar	2	25	25	25
Air feed, t/tds	1.67	1.91	n.a.	n.a.
O_2 feed, t/tds	n.a.	n.a.	0.471	0.580
Oxidant temp., °C	268	390	135	135
Calculated Results				
Raw gas, t/tds	*2.543*	*2.784*	*1.344*	*1.477*
Ar (mol %)	0.498	0.555	0.870	1.062
CH_4	0.908	2.324	2.151	2.192
CO	11.619	10.532	23.059	21.894
CO_2	12.405	11.452	18.571	20.740
COS	0.019	0.028	0.051	0.021
H_2	19.083	10.307	22.371	12.503
H_2O	13.005	17.585	31.522	40.927
H_2S	0.637	0.594	1.081	0.264
NH_3	0.007	0.009	0.002	0.000
N_2	41.817	46.615	0.321	0.393
Condensed phase, t/tds	*0.463*	*0.461*	*0.460*	*0.436*
Smelt or dry solid	dry solid	smelt	smelt	smelt
Na_2SO_4 (weight %)	0.000	0.004	0.002	0.118
Na_2CO_3	81.873	79.945	79.525	62.206
Na_2S	7.668	8.005	7.901	17.398
NaOH	0.084	1.606	2.119	9.222
K_2CO_3	9.578	9.630	9.645	10.063
K_2SO_4	0.000	0.005	0.002	0.138
C	0.801	0.805	0.806	0.850

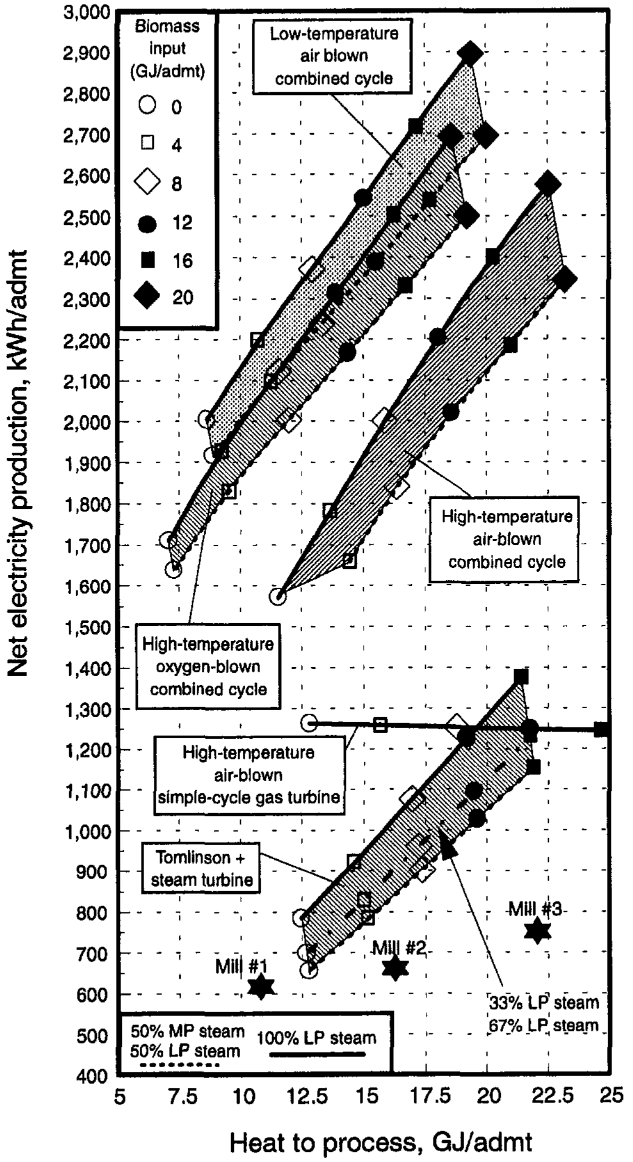

Fig. 7 Performance summary for alternative black liquor-based cogeneration systems. For reference, stars represent process steam and power demands for corresponding mill numbers in Fig. 2.

tified a sustainable supply of up to 3 dry tonnes of biomass per tonne of pulp (or 60 GJ/admt) at reasonable cost in the form of harvest residues and self- and externally generated mill residuals (Weyerhaeuser et al., 1995).

The curves for the gasification-based technologies in Fig. 7 are steeper than for the Tomlinson technology because of a higher biomass boiler pressure—the pressures are assumed to match those of the gas turbine HRSG (90 bar) and the Tomlinson boiler (60 bar). Also, as the biomass share of total energy input increases, differences in power output from one technology to the next diminish in most cases. (At the highest level of biomass input shown, the biomass energy input approaches the level of the black liquor energy input.)

The gasifier/gas turbine combined cycle systems produce more, or substantially more, kWh/admt than the Tomlinson-based system (Fig. 7). However, more supplemental biomass must be consumed with these systems to meet a given process steam demand. In all cases, including with the Tomlinson-based system, power production is in excess of a typical pulp mill's process power needs. In contrast, most North American pulp mills today use Tomlinson plus supplemental-fuel boilers with back-pressure steam turbines, but operate relatively inefficiently and so generate little or no excess power.

Several interesting comparisons among alternative gasifier-based systems are illuminated by a more detailed examination of the results in Fig. 7 for a fixed mill process steam demand. Table 7 summarizes performance calculations for alternative cogeneration systems that provide a level of process heat and power per admt that characterizes Mill #2. Figures 3–6 show heat balances for four of the cases in Table 7.

One interesting comparison is between a simple-cycle and a combined-cycle system with the same gasifier (high-temperature, air-blown). The simple cycle requires about half the biomass of the combined cycle to meet the same process steam demand. Note (from Fig. 7) that without supplemental firing of biomass, only about 20 percent of the power out of the combined cycle is provided by the steam turbine. The fraction is larger for the case in Table 7 (32 percent; see Fig. 4) because of supplemental biomass use. Correspondingly, the difference in power output between the simple and combined cycles meeting Mill #2's steam demand is larger than if supplemental firing were not required.

A second comparison is between two combined cycles using high-temperature gasifiers, one air-blown (operating at 950°C)

Table 7 Summary results for cogeneration with black liquor and biomass that meets steam demands per air-dry metric tonne of pulp (admt) corresponding to those for "Mill #2" in Fig. 2. Figures 3–6 show detailed flows for 4 of the 6 cases summarized here.

	Tomlin. + bio-boiler	Gasification + Biomass Boiler[a]				
		Low P,T Air-blwn CC	High Pres., Temp.			
			Air-blown		O_2-blown	
			CC	SC	1000	1400
Corresponding Figure #	**3**	**6**	**4**	--	**5**	--
Mill production, admt/day	1241	1098	1251	1312	1307	1751
Black liquor tds/admt	1.74	1.74	1.74	1.74	1.74	1.74
tds/hr	90	79.6	90.7	95.1	94.8	127
MW (HHV)	359	318	362	380	378	506
Biomass fuel dry t/admt	0.318	0.700	0.428	0.228	0.783	0.763
GJ/admt (HHV)	6.35	13.99	8.56	4.56	15.7	15.3
Fuel to turbine HHV, MJ/kg	n.a.	4.64	3.698	3.698	6.678	4.966
Flame T,[b] °C	n.a.	1770	1634	1587	1690	1458
Process steam,[c] total	16.3	16.3	16.3	16.3	16.3	16.3
GJ/admt,10-bar	5.5	5.5	5.5	5.5	5.5	5.5
GJ/admt, 4-bar	10.8	10.8	10.8	10.8	10.8	10.8
Gross Power Output, MW_e	48.4	136.7	104.7	72.8	151.8	180.0
Auxiliary consumption, MW_e	1.64	22.04	4.19	4.03	19.77	32.29
Net Power Output, MW_e	46.8	114.7	100.5	68.7	132.0	147.7
kWh/admt	904	2507	1928	1258	2425	2024
Net Excess Power, MW_e	12.8	84.7	66.3	32.9	96.3	99.8
kWh/admt	248	1851	1272	602	1769	1368
Fuel HHV to electricity	10.4	23.2	20.7	15.3	21.5	18.1
steam	52.0	41.8	48.6	55.1	40.2	40.6
Fuel NHV to electricity	12.2	27.4	24.3	17.9	25.5	21.5
steam	61.0	49.5	57.1	64.4	47.6	48.1
Total efficiency, HHV	62.4	65.0	69.2	70.4	61.7	58.7
NHV	73.1	76.9	81.4	82.3	73.1	69.5
Electricity/steam ratio	0.20	0.55	0.43	0.28	0.53	0.45
Incremental Fuel Chargeable to Power[d]						
MJ fuel (HHV) per kWh	---	4.8	2.2	-5.1	6.1	8.0
%	---	76	167	-71	59	45

(a) CC is combined cycle with back-pressure steam turbine. SC is simple cycle gas turbine. Results for 1000°C and 1400°C gasification temperature are shown for the cases with O_2-blown gasifiers.

(b) Maximum achievable temperature with fuel and oxidant temperatures and pressures shown in Figs. 3-6

(c) Assuming 80% condensate return at 110°C and fresh make-up at 15°C, the heat given to steam in the cogeneration plant is 2.315 GJ/tonne for 10-bar steam and 2.276 GJ/tonne for 4-bar steam.

(d) The numerator is the biomass fuel consumed in excess of that required to meet steam demand with the Tomlinson system. The denominator is the power produced in excess of that produced in the Tomlison case.

and the other oxygen-blown (operating at 1000°C). The O_2-blown system converts a smaller fraction of the input energy into steam, but a larger fraction into electricity (Table 7). A contributing factor is the use of the saturator with the O_2-gasifier in place of a low-pressure evaporator. This permits recovery of low-temperature heat into the combined cycle rather than into the Rankine cycle alone. An off-setting factor is the parasitic power consumed in producing oxygen. The net result is that to meet the same process steam demand, the O_2-blown system consumes considerably more biomass than the air-blown system, but electricity production per admt is much higher (Fig. 7).

A third comparison is between two O_2-blown systems operating with different gasification temperatures (Table 7). The fraction of fuel converted to steam in the system operating at 1400°C is comparable to that for the 1000°C system, but the fraction converted to electricity is considerably lower. This can be attributed primarily to the greater irreversibilities generated in the raw syngas quench step from 1400°C to 200°C, instead of 1000°C to 200°C. In the range 1000–1400°C, higher gasification temperature may provide benefits relating to chemical recovery due to the lower sodium carbonate levels in the smelt (Table 6) (Lorson et al., 1996b), but energy efficiency will suffer.

A fourth comparison is between combined cycles with high-temperature/high-pressure gasification and one using low-temperature/low-pressure gasification. The latter system provides the highest electrical efficiency of any system considered here (Fig. 7 and Table 7). This results primarily because with a lower gasifier outlet temperature, a larger fraction of the gasifier output enters the combined cycle rather than the Rankine cycle alone. (With higher gasifier outlet temperatures, a larger fraction of the gasifier output is recovered as steam, which can only be used in the Rankine cycle.) Also, the irreversibilities involved in cooling the gasifier product gas are smaller with the low-temperature design. Pressurization of the high-temperature gasifiers partly offsets the electric-efficiency advantage enjoyed by the low-temperature, low-pressure system.

A final observation is that adiabatic flame temperatures for the clean syngas streams fed to the gas turbine combustor in all cases (Table 7) are well above current turbine inlet temperature limits, so that future increases in firing temperatures can probably be achieved with gasified black liquor.

The final two rows in Table 7 are of interest in a situation where a mill is considering replacing an existing Tomlinson-based cogeneration system, a likely common situation over the next two decades (Fig. 1). A baseline alternative in this situation might be the installation of a new Tomlinson recovery boiler plus a supplemental-biomass boiler to augment steam delivery to a back-pressure steam turbine. If the mill has an opportunity to export power, then the incremental fuel chargeable to power (IFCP) shown in Table 7 provides a measure of the marginal fuel costs associated with the production of exported power using each of the gasification options shown in Table 7 in lieu of the Tomlinson baseline. The numerator of the IFCP is the biomass consumption required in excess of that in the Tomlinson case to meet the same process steam demand. The denominator of the IFCP is the amount of power generated in excess of the Tomlinson power production. The low IFCP heat rates (or, equivalently, high IFCP efficiencies) indicate that export power from any of the five systems (especially those based on air-blown gasification) would involve low (or negative) marginal fuel costs. Obviously capital investment and operating and maintenance costs would also be considered in any full evaluation of alternative cogeneration technology options.

Conclusions

Black liquor gasification systems offer the possibility for kraft-based market pulp or integrated pulp and paper mills to generate far more electricity than at present while still meeting process steam demands. Depending on the gasification technology and cycle design, power-to-steam ratios can vary widely, providing flexibility in meeting mill requirements. The present work has focused on better understanding the prospective energy benefits of black-liquor gasifier/gas turbine systems. Prospective benefits of gasification with regard to capital investment, environmental impact, flexibility in preparation of pulping chemicals, safety, and reliability have not been addressed.

Black liquor gasification for gas turbine applications is not yet proven commercially. However, the level of development of several gasification technologies appears advanced sufficiently that commercial-scale demonstrations could be launched toward full commercialization of gasifier/gas turbine systems (Larson and Raymond, 1997). The first such project was announced in May 1997. Key features that must be successfully demonstrated include gas cleanup to meet gas turbine specifications, stable gas turbine combustion of syngas, heat recovery from syngas streams and (in the case of the low-temperature gasification process) from solids, cost-effective recovery of pulping chemicals, and overall-plant thermal integration.

Acknowledgments

For helpful comments on a draft of this paper, the authors thank Terry Adams, Russ Andrews, Thore Berntsson, Craig Brown, Billy Davis, Patricia Hoffman, Ed Kelleher, Bob Kinstrey, George McDonald, Bill Nicholson, Del Raymond, Rolf Ryham, Al Streb, Gunnar Svedberg, and Björn Warnqvist. For assistance with artwork, we thank Roberto Biscuola and Ryan Hayward. For cost-sharing support of this research, we thank the Weyerhaeuser Company. For direct financial support, we thank the Office of Industrial Technologies of the U.S. Department of Energy. For additional support, S. Consonni thanks the Italian National Research Council, and N. Berglin thanks the Swedish Research Program for Sulfate Recovery/Black Liquor Gasification.

References

Adams, T. N., Frederick, W. J., Grace, T. M., Hupa, M., Iisa, K., Jones, A., and Tran, H., 1997, *Kraft Recovery Boilers*, Tappi Press, Atlanta, GA.

AF-IPK, 1993, "Energy Balances for 'Best Practice Mills' in Sweden: Bleached Market Kraft Pulp, Fine Paper, Linerboard, and Newsprint," consultant's report prepared for Weyerhaeuser Co., Tacoma, WA, Apr.

AFPA, 1996, "Fact Sheet on 1994 Energy Use in the U.S. Pulp and Paper Industry," American Forest & Paper Association, Wash., DC, Mar. 27.

Aghamohammadi, B., Mansour, M. N., Durai-Swamy, K., Steedman, W., Rockvam, L. N., Brown, C., and Smith, P., 1995, "Large Scale Pilot Testing of the MTCI/Thermochem Black Liquor Steam Reformer," *Proc. 1995 International Chemical Recovery Conference*, TAPPI Press, Atlanta, GA. pp. B297–B301.

Backman, R., and Solmenoja, K., 1994, "Equilibrium Behavior of Sodium, Sulfur, and Chlorine in Pressurized Black Liquor Gasification With Addition of Titanium Dioxide," *Paper and Timber*, Vol. 76(5), pp. 320–325.

Berglin, N., 1996, "Pulp Mill Energy Systems With Black Liquor Gasification—a Process Integration Study," Licentiate thesis, Department of Heat and Power Technology, Chalmers Univ. of Technology, Göteborg, Sweden.

Chiesa, P., Consonni, S., Lozza, G., and Macchi, E., 1993, "Predicting the Ultimate Performance of Advanced Power Cycles Based on Very High Temperature Gas Turbine Engines," ASME Paper No. 93-GT-223.

Chiesa, P., Lozza, G., Consonni, S., and Macchi, E., 1995, "An Assessment of the Thermodynamic Performance of Mixed Gas–Steam Cycles. Part B: Water-Injected and Hat Cycles," ASME JOURNAL OF ENGINEERING FOR GAS TURBINES AND POWER, Vol. 117, pp. 499–508.

Consonni, S., 1992, "Performance Prediction of Gas/Steam Cycles for Power Generation," Ph.D. Thesis No. 1893-T, Mechanical and Aerospace Engineering Dept., Princeton Univ., Princeton, NJ.

Consonni, S., Lozza, G., Macchi, E., Chiesa, P., and Bombarda, P., 1991, "Gas-Turbine Based Advanced Cycles for Power Generation, Part A: Calculation Model," *Proc. Yokohama International Gas Turbine Congress*, Gas Turbine Society of Japan, Tokyo, pp. III201–210.

Consonni, S., and Larson, E. D., 1996, "Biomass-Gasifier/Aeroderivative Gas Turbine Combined Cycles, Part A: Technologies and Performance Modeling, and Part B: Performance Calculations and Economic Assessment," ASME JOURNAL OF ENGINEERING FOR GAS TURBINES AND POWER, Vol. 118, pp. 507–525.

Dahlquist, E., and Jacobs, R., 1992, "Development of a Dry Black Liquor Gasification Process," *Proc. 1992 International Chemical Recovery Conference*, TAPPI Press, Atlanta, GA.

Empie, H. J., 1991, "Alternative Kraft Recovery Processes," *Tappi J.*, May, pp. 272–276.

Gardiner, W. C., ed., 1984, *Combustion Chemistry*, Springer-Verlag, New York.

Grace, T. M., and Timmer, W. M., "1995, A Comparison of Alternative Black Liquor Recovery Technologies," *Proc.1995 International Chemical Recovery Conference*, TAPPI Press, Atlanta, GA.

Ihren, N., 1994, "Optimisation of Black Liquor Gasification Cogeneration Systems," Licentiate thesis, Department of Chemical Engineering and Technology, Royal Institute of Technology, Stockholm, Sweden.

Industra Engineers & Consultants, Inc., 1996, *Black Liquor Recovery Alternate Study* (draft final report to U.S. Dept. of Energy), Seattle, WA, Sept. 30.

Kelleher, E. G., 1985, *Gasification of Kraft Black Liquor and Use of the Products in Combined Cycle Cogeneration, Phase II Final Report*, DOE/CS/40341-T5, prepared by Champion Int'l. Co. for U.S. Dept. of Energy, Washington, DC, July.

Larson, E. D., 1992, "Biomass Gasifier/Gas Turbine Cogeneration in the Pulp and Paper Industry," ASME JOURNAL OF ENGINEERING FOR GAS TURBINES AND POWER, Vol. 114, 1992.

Larson, E. D., Consonni, S., Berglin, N., and Kreutz, T., 1996, "Advanced Technologies for Biomass-Energy Utilization in the Pulp and Paper Industry," report to U.S. Dept. of Energy from Center for Energy and Environmental Studies, Princeton Univ., Princeton, NJ, Dec.

Larson, E. D., and Consonni, S., 1997, "Performance of Black Liquor Gasifier/Gas Turbine Combined Cycle Cogeneration in the Kraft Pulp and Paper Industry," *Proc. 3rd Biomass Conference of the Americas*, Elsevier Science, Oxford, United Kingdom.

Larson, E. D., and Raymond, D., 1997, *Report on the Workshop on Commercialization of Black Liquor and Biomass Gasification for Gas Turbine Applications in the Pulp and Paper Industry*, Center for Energy and Environmental Studies, Princeton University, Princeton, NJ, Mar.

Lorson, H., Schingnitz, M., White, V.F., and Dean, D. R., 1996a, "Black Liquor Recovery by Pressurized Oxygen-Blown Gasification," *Proc. 1996 Engineering Conference*, TAPPI Press, Atlanta, GA, pp. 557–565.

Lorson, H., Schingnitz, M., White, V. F., and Dean, D. R., 1996b, "Emerging Gasification Applications," presented at the 1996 Gasification Technologies Conference, Electric Power Research Institute, Palo Alto, CA, Oct.

Lozza, G., Chiesa, P., and Consonni, S., 1993, "Modelization of Integrated Coal Gasification Combined Cycles" 9811$$$$82 Italian, *Proc. VII Meeting on Combined Cycles: Technical and Economic Outlook (Milan, Oct. 1993)*, pp. 287–312, Pitagora publisher, Bologna, Italy.

Lozza, G., 1990, "Bottoming Steam Cycles for Combined Gas–Steam Power Plants: a Theoretical Estimation of Steam Turbine Performance and Cycle Analysis," *Proc. Cogen-Turbo Congress*, ASME, New York, pp. 83–92.

McKeough, P. J., Arpiainen, V., Makinen, T., and Solantausta, Y., 1995, "Black Liquor Gasification: Downstream Processes, Plant Performances and Costs," *Proc. 1995 International Chemical Recovery Conference*, TAPPI Press, Atlanta, GA, pp. B303–B310.

NUTEK, Swedish National Board for Industrial and Technical Development, 1992, *Black Liquor Gasification—Consequences for Pulping Process and Energy Balance*, R1992:8, Stockholm, Sweden.

Schmidt, E., 1982, *Properties of Water and Steam in SI units*, Springer-Verlag, Berlin.

Stigsson, L. L., and Hesseborn, B., 1995, "Gasification of Black Liquor," *Proc. 1995 International Chemical Recovery Conference*, TAPPI Press, Atlanta, GA, pp. B277–B295.

Stull, D. R., and Prophet, H., Project Directors, 1971, *JANAF Thermochemical Tables*, 2nd ed., U.S. National Bureau of Standards, Washington, DC.

Subbiah, A., Nilsson, L. J., and Larson, E. D., 1995, "Energy Analysis of a Kraft Pulp Mill: Potential for Energy Efficiency and Advanced Biomass Cogeneration," *Proc. 17th industrial Energy Technology Conf.*, Houston, TX, Apr.

Warnquist, B., 1989, *Pulp and Paper Production With Available Technology in the Year 2000 (Massa- och papperslinjer med tillganglig processteknik år 2000)*, Swedish Board for Industrial and Technology Development, Report 1989-10-24, Stockholm [in Swedish].

Weyerhaeuser Co., Stone & Webster, Amoco Oil, and Carolina Power & Light, 1995, *New Bern Biomass to Energy Project Phase I Feasibility Study*, published by National Renewable Energy Laboratory (Golden, CO) and Electric Power Research Institute (Palo Alto, CA).

R. A. Newby
Westinghouse Science &
Technology Center,
1310 Beulah Road,
Pittsburgh, PA 15235

R. L. Bannister
Westinghouse Electric Corporation,
Orlando, FL 32826-2399

A Direct Coal-Fired Combustion Turbine Power System Based on Slagging Gasification With In-Situ Gas Cleaning

Westinghouse began the development of a compact, entrained, slagging gasifier technology utilizing in-situ fuel gas cleaning for combustion turbine power cycles in 1986. The slagging gasifier is air-blown, and produces a hot, low-heating value fuel gas that can be combusted and quenched to combustion turbine inlet temperatures while maintaining low levels of NO_x emissions. The U.S. Department of Energy sponsored engineering studies and pilot testing during the period 1986 to 1992. This work has shown that the technology has promise, although performance improvements are required in some key areas. A major challenge has been the development of in-situ removal of sulfur, alkali vapor, and particulate to low enough levels to permit its use in combustion turbine power systems without additional, external gas cleaning. This paper reviews the Westinghouse slagging gasifier, direct coal-fired turbine power generation concept; the pilot test results; and the current development activities that Westinghouse is engaged in.

Overview of Direct Coal-Fired Turbine Development

Past experience with solid fuel firing in gas turbines has been reported for direct coal-fired turbine (DCFT) subscale development testing, and for pressurized fluidized bed combustion (PFBC). DCFT testing was conducted by the Locomotive Development Committee of Bituminous Coal Research Inc. during the period 1944 to 1959. The U.S. Bureau of Mines also conducted a DCFT program, and the Australian Aeronautical Research Laboratories tested DCFT from 1948 to 1970. This DCFT work has been reviewed extensively (EPRI, 1985; Stringer, 1985; Barkalow et al., 1979). In general, it was found that the high ash loadings in the expansion gas obtained with high-efficiency cyclone gas cleaning inevitably resulted in high rates of airfoil erosion and deposition, and further DCFT development was curtailed.

Commercial demonstrations of PFBC, a technology related to the DCFT with cyclone-based gas cleaning, have resulted in high ash loadings to "ruggedized" gas turbines. This commercial experience has shown moderate levels of turbine blade erosion and deposition at the low turbine inlet temperatures of PFBC (840–870°C) (Mudd and Reinhart, 1995). The ruggedized turbine maintenance intervals have been short, but acceptable, and plant availability has not been significantly reduced by turbine maintenance needs.

The U.S. Department of Energy (DOE), Morgantown Energy Technology Center, initiated another DCFT development program in the mid-1980s based on the premise that gas cleaning and coal beneficiation technologies had improved over the previous generation. Programs were conducted by Westinghouse, Solar, and Allison. Solar and Allison looked at industrial-scale turbines and applied micronized coal-slurry beneficiation and external gas cleaning techniques to produce coal-based fuels that minimized concerns for sulfur, particulate, and alkali content (Roberts et al., 1993; Rothrock et al., 1993). Westinghouse pursued development for heavy-duty, utility-scale combustion turbines firing utility-grade coals with minimal beneficiation. The Westinghouse approach required the developed of new in-situ gas cleaning technology.

Westinghouse teamed with AVCO/Textron and began the development of a direct coal-fired turbine system under DOE funding in 1986 (Thoman et al., 1987). The concept is based on a slagging, multiple-stage combustor previously conceptualized and tested at small capacity for MHD applications by AVCO. AVCO, subsequently becoming part of Textron Defense Systems, was subcontracted by Westinghouse to build a nominal 12.7 MkJ/hr. (12 MBtu/hr) slagging gasifier test system at their Haverhill, Massachusetts facility as part of the DOE program. Westinghouse and Textron tested the system, evaluated test data, and performed commercial plant conceptual designs. The test system was operated until mid-1992. Commercial design evaluations of the DCFT power generation system indicated the outstanding economic potential of this technology for lower cost of electricity than conventional coal-fired power generation techniques or natural gas-fired combustion turbines. The pilot testing, though, identified some technical hurtles that limited the feasibility of firing a combustion turbine directly with the fuel gas generated.

The DOE, DCFT Program ended in the mid-1990s with significant subscale pilot testing by all three contractors, and some demonstration testing by Allison and Solar. Westinghouse has subsequently pursued development and demonstration opportunities with electric utilities. In the early 1990s, Westinghouse began working with Northern States Power (NSP) on the commercialization of this power generation system as part of the development of a Clean Coal Technology (CCT) proposal (Jensen et al., 1992). Stone & Webster and Textron also participated in that effort, and additional engineering studies were conducted as well as slagging gasifier testing using NSP feedstocks (Bannister et al., 1992). The DCFT concept was modified, due to its fuel gas cleaning uncertainties, to include additional, external fuel gas cleaning. Eventually, due to changes in the NSP future capacity additions strategy, NSP ended their participation in the program.

The evolution of the DCFT technology has been slowed both by technical challenges and by the availability of cheap, clean

---

Contributed by the International Gas Turbine Institute and presented at the International Gas Turbine & Aeroengine Congress & Exhibition, Orlando, FL, June 2–5, 1997. Manuscript received by the ASME Headquarters February 17, 1997. Paper No. 97-GT-40. Associate Technical Editor: H. A. Kidd.

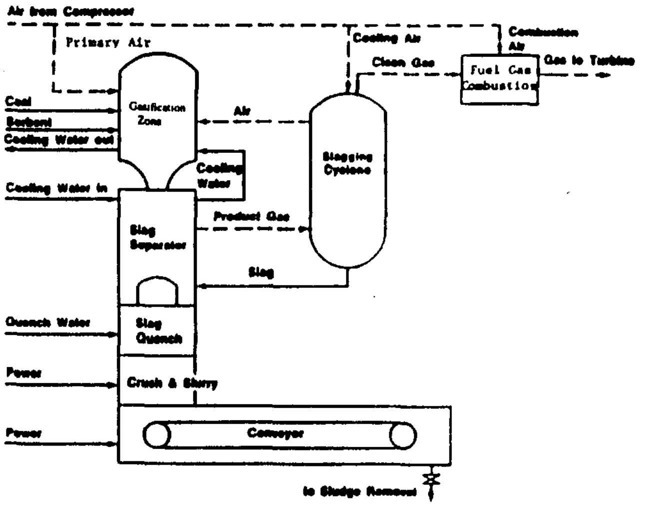

Fig. 1 Slagging combustor DCFT process flow diagram

natural gas for combustion turbine power generation. Westinghouse continues to pursue the development of the DCFT technology and is presently conducting small-scale testing and process design work, as well as planning development and demonstration efforts over the next four years.

Westinghouse DCFT Concept

The DCFT system uses closely coupled, compact coal gasifier modules that contain internal functions for simultaneous particulate removal and sulfur removal. The conceptual power plant flow diagram is shown in Fig. 1, identifying the following major plant components: the coal and sorbent preparation, handling, and feeding systems; the air compressor system; the slagging gasifier modules; the slag separator modules; the slagging cyclone modules; the slag quench and removal system; the fuel gas combustor modules; and the turbine combined cycle power island. The slagging gasifier, slag separator, and slagging cyclone modules are water and/or air-cooled vessels.

In the system, coal is dried and is pulverized to a size representative of pulverized coal (PC) boiler grade utility coal. The coal is pressurized and fed and distributed to several injection points around each gasifier module. Pneumatic feeding of the coal in dry form is the basis for the plant, although feeding coal as a water-paste has also been considered, with some potential advantages over the pneumatic system. Primary air, at an equivalence ratio of 1.4 or greater is boosted in pressure and coaxially injected with the coal. Sorbent particles for in-situ sulfur removal are also injected separately into the gasifier modules. The power plant design is modular in the gasification-combustion equipment. In a commercial power plant application, several of the slagging gasifier modules would be used to produce fuel gas for a single gas turbine, as shown in Fig. 2. Commercial slagging gasifier designs with capacities up to 73 Mw_t (250 MBtu/hr) have been previously projected. Each slagging gasifier would have one, or more slag separator vessels, one or more slagging cyclones, and would provide fuel gas to several fuel gas combustors located either external to the turbine cylinder or within the cylinder.

The gasifier vessel geometry, and the coal and air injection configurations are designed so that mixing is very intense, forming a stable toroidal vortex within the vessel, and the temperature is high enough (1650° to 1950°C) to efficiently gasify coal and to generate slag from the coal ash and sorbent. A slag layer deposits on the inner vessel walls, forming a protective layer for the water-cooled gasifier vessel (Bannister et al., 1990). Molten slag drains continuously downward along the wall and exits with the fuel gas through a nozzle that is directed onto an impact target in the slag separation vessel. The molten slag collected on the target drains to the bottom of the separator vessel, passing into a slag, water-quench vessel. The frozen slag is removed through a lock hopper system and directed to a slag disposal system.

The fuel gas passes out of the slag separator vessels and into slagging cyclone modules where the slag content is further reduced. The fuel gas enters the combustion modules where combustion of the fuel gas is completed and the gases are further diluted with air to achieve the desired turbine inlet temperature. The high-temperature gasifiers, slag separators, and slagging cyclone modules are water, steam, or air cooled, with the coolant streams being integrated into the plant power cycle. Figure 3 is a sketch of a slagging gasifier arrangement showing the close integration with the turbine that is potentially possible with this concept.

Sorbent particles injected into the gasifier stage may be calcium-based, iron-based, or others. The sorbent particles react quickly with the sulfur species (H_2S, COS, SO_2) within the gasifier fuel gas during their roughly 10 m/s residence, with the extent of removal of sulfur being very sensitive to the equivalence ratio used, the location of the sorbent feed, and the location of subsequent quenching and removal of the sorbent-slag particles. The sorbent is removed as part of the slag and the sulfur captured is incorporated into the slag. The system as shown has no provision for the control of alkali vapors in the fuel gas other than retention of alkali with the slag. Alkali sorbents may also be injected into the gasifier to improve alkali retention in the slag.

Many of the components and systems in the plant are commercial, while several items have a developmental status. The commercial systems needing to be integrated and optimized for the DCFT power plant are: the coal and sorbent systems, the air compressor system, the gas turbine and steam turbine systems, and the slag system (Pillsbury et al., 1989). The major developmental components are the slagging gasifier, the slag separator, and the slagging cyclone. The fuel gas combustor is an extrapolation of other Westinghouse low-heating value fuel gas combustors under development for low NO_x performance

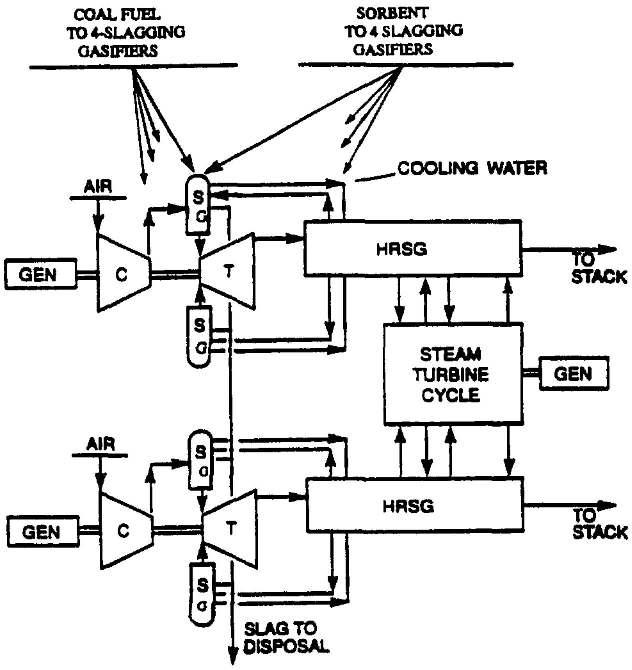

Fig. 2 DCFT power system arrangement

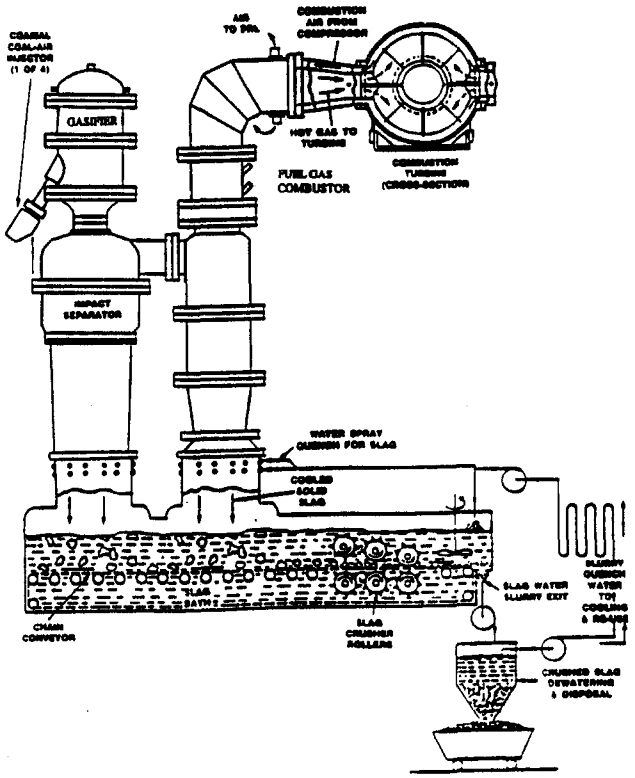

Fig. 3 Slagging gasifier—combustion turbine configuration

(Domeracki et al., 1995) and does not require specific development.

DCFT Comparison with IGCC

Commercial IGCC plants using cold gas cleaning have been successfully operated without significant turbine erosion, corrosion, or deposition (for example, the Texaco Cool Water plant, the Dow Chemical Plaguemine plant, and the Shell Demkolec plant). IGCC with hot fuel gas cleaning will be demonstrated for the first time in 1997 at the Sierra Pacific, Pinon Pine Power Project using fluidized bed gasification technology and ceramic filter fuel gas cleaning at about 540°C.

The Westinghouse slagging gasifier DCFT configuration has similarities with IGCC configurations, but differs from standard IGCC configurations in that

- the slagging gasifier fuel gas has a higher temperature and lower heating value than typical IGCC fuel gases generated in either oxygen-blown or air-blown gasifier;
- the slagging gasifier is modular, whereas IGCC systems tend to use a single, large gasifier vessel;
- the slagging gasifier has in-situ gas cleaning, whereas typical IGCC plants use complex fuel gas cleaning and cooling trains;
- the DCFT power plant strives to satisfy environmental and turbine protection requirements, while typical IGCC plants with cold gas cleaning are capable of achieving very stringent fuel gas cleaning levels; and,
- the slagging gasifier modules are closely coupled to the combustion turbine, whereas the typical IGCC configuration places the gasifier remote to the turbine, and require large plant area.

Slagging Gasifier Required Performance

The slagging gasifier system must satisfy pressure drop, carbon utilization, and gas cleaning requirements, although many other factors are also important and may constrain the system design with respect to space and layout, performance, operation, modularity of design, and cost. The requirements placed on fuel gas cleaning primarily relate to environmental emissions regulations for the power plant, and turbine protection standards.

Turbine protection standards have been developed by vendors from related field experience and from engineering models of performance (erosion, corrosion, and deposition) where no experience exists. The turbine protection standards relating to erosion and deposition damage are usually expressed in terms of allowable particle loading and size distribution carried in the turbine expansion gas (Newby and Bannister, 1994). Dependent on the specific turbine design, the acceptable turbine cleaning interval, and the acceptable blade replacement interval, the expansion gas particulate content that is allowable can vary significantly.

Table 1 lists an example of expansion gas particulate criteria for Westinghouse combustion turbines, with a 2500 h cleaning interval, and a 20,000 h blade replacement interval. The criteria is expressed as the particle loading in two key particle size ranges (<2 μm and 1–20 μm) that relate to both erosion damage and deposition damage. The range of particle loadings listed represent the various Westinghouse turbine expanders available, with larger machines being more tolerant to erosion, and higher inlet temperature machines being more sensitive to deposition. The erosion and deposition behavior of the flyash particles also depends upon the flyash particle erosivity and sticking coefficients, and these will differ with changes in slagging gasifier conditions and feedstocks. The corresponding particle limits for the fuel gas are less stringent by a factor of 2 to 4 that accounts for the dilution of the fuel gas by secondary combustion air. Economic studies by Westinghouse have shown that turbine rebidding intervals as short as 5000 h have little impact on the cost of electricity (Horazak et al., 1990).

Corrosion protection regulates the allowable concentrations of several contaminants in the turbine expansion gas (vanadium, lead, calcium, and primarily sodium and potassium vapor in coal-based systems) (Johnson, 1996). In the turbine expansion gas, the current Westinghouse standards call for total sodium (Na) plus potassium (K) vapor less than 50 ppbv, although these limits are not founded on coal-based fuel experience. Alkali vapor release resulting from particulate reaching the fuel gas combustor must also be included. In the fuel gas, the allowable alkali vapor content is higher by a factor that again accounts for the dilution of the fuel gas by secondary combustion air. The sulfur content of the fuel gas has little impact on turbine corrosion and is not limited by turbine protection standards, although downstream, heat recovery components will be influenced.

Current combustion turbine materials and airfoil designs are based largely on conventional, clean turbine fuels, and they do not consider particle erosion, deposition, and corrosion as major factors. Blade coatings and fuel additives have been developed to improve corrosion and deposition resistance to alkali vapors and other contaminants present in some petroleum-based liquid fuels. Some evaluations to understand the potential of limiting erosion and deposition damage by improved airfoil design has been conducted and may be a fruitful direction for development. (Wenglarz et al., 1995).

Table 1 Turbine inlet particulate specification example

Conditions: cleaning interval 2,500 hours; reblading interval 20,000 hours			
Particle loading limits in expansion gas (ppmw)			
Size Range:	2μm 2-3	1 - 20 μm 5-6	total loading 6-8

Emissions regulations vary significantly with plant locations throughout the world. IGCC plant emissions in the U.S. are regulated by New Source Performance Standards (NSPS) for sulfur oxides, nitrogen oxides, and particulate, and other pollutants, such as carbon monoxide, may also be regulated. Current NSPS for large, coal-fired power plants call for 70 to 90 percent sulfur removal, depending on the coal sulfur content. The recent amendments to the Clean Air Act set a cap on total sulfur emissions in the U.S., and this implies much more stringent sulfur emission control will be desirable for U.S. electric utilities.

For NO_x, the current NSPS for large, coal-fired power plants is 0.6 lb NO_2/MBtu for bituminous coals, and 0.5 lb/MBtu for subbituminous coals. The NO_x emissions are controlled primarily by the fuel gas combustor design and operation, and for most low heating value fuel gases, less than 0.3 lb/MBtu NO_2 should be achievable. Likewise, carbon monoxide emissions are primarily a function of the fuel gas combustor performance.

The current NSPS for coal-fired electric utility plant particulate emission is 0.03 lb/MBtu, equivalent to about 20–30 ppmw ash loading in the plant stack gas. The NSPS would allow particulate emissions from a coal-fueled turbine greater than those generally specified by the turbine manufacturer based on erosion and deposition.

In the U.S., the 1990 Clean Air Act Amendments require the consideration of standards for hazardous air pollutants (HAPs), including several metals, volatile organic compounds, HCl, dioxins and furans, and specifically include the consideration of particulate matter less than 10 microns in diameter (PM-10). Preliminary indications are that the HAPs regulations will not to have a great impact on solid fuel utility power plants, except possibly for HCl emissions, mercury, and PM-10. PM-10 legislation may make the emissions requirements for solid fuels more stringent than turbine protection requirements.

The plant solid waste must comply with National RCRA standards, as well as state and local regulations. This may mean that active sulfides and oxides in the solid waste streams need to be processed to render them inert and to provide a nonhazardous classification for the waste. Some entrained gasifier systems use flyash recycle to the gasifier to promote complete solid waste in the form of slag, considered to be relatively inert based on prior characterization studies.

Slagging Gasifier Pilot Testing

The slagging gasifier test facility was constructed at the Textron Defense Systems, Haverhill, MA site. It consists of a slagging gasifier unit, a slag removal vessel and slag quench hopper, a slagging cyclone, a fuel gas combustor, and a combustion product quench section and exhaust duct (Bannister, Newby, and Diehl, 1992). The facility had an air supply capable of about 3.2 kg/s (7 lb/s) total flow, and fed coal at rates of 320–450 kg/hr (700–1000 lb/hr). The gasifier operated at about 6 bar (87 psi) pressure in the tests, and primary air was supplied at a nominal rate of about 0.9 kg/s (2 lb/s), and was preheated to about 350°C. The facility was able to pneumatically distribute pulverized coal from a pressurized hopper to the gasifier, and a coal-water mixture feed system was also utilized in the testing. Sorbents were also pneumatically fed to the gasifier. Instrumentation, control, and analytical facilities also supported the test operation (Diehl et al., 1989).

In the testing, the gasifier temperature was maintained at a sufficient level for rapid partial-combustion of the coal, though not necessarily for slagging. The air injector velocities, with jet nozzle inner diameters changeable from about 2.5–3.2 cm (1.0 to 1.25 in.), were also maintained at sufficient levels (60–100 m/s) for effective vortex mixing. The "equivalence" ratio is defined as the operating fuel-to-air ratio over the stoichiometric fuel-to-air ratio, where the fuel-to-air quantities are based on ash and moisture-free coals. The gasifier was operated at equivalence ratios of 1.2 to 1.7.

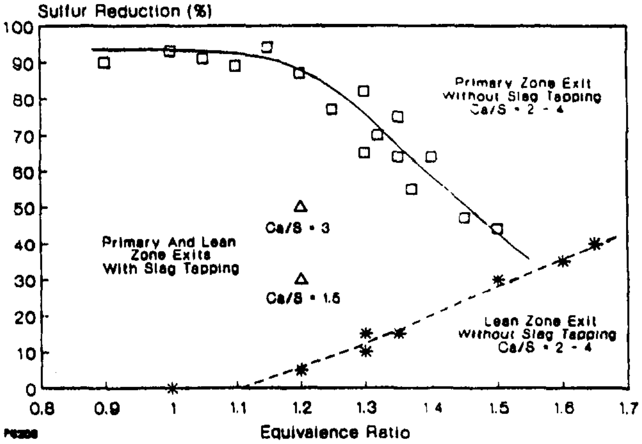

Fig. 4 Sulfur capture with Pittsburgh No. 8 Coal

Two limitations of the slagging gasifier pilot plant were its low design pressure of the vessels (about 8 bar (116 psi)) and the small capacity of slag withdrawal hoppers that limited run times to a maximum of about 2 h. While the vessel pressure and run-time capabilities were sufficient for preliminary testing of the slagging gasifier, longer run times are desirable to assess long-term phenomena. The limited operating pressure of the facility was acceptable, although higher pressures, similar to the probably commercial operating pressures (14–22 bar [203–319 psi]) would be desirable to reduce performance uncertainties.

Pilot testing addressed the following major parameters:

- alternative coals ranging from bituminous to subbituminous
- dry coal feed and coal-water feed
- air equivalence ratio 1.2 to 1.7
- alternative sorbent types: calcium based—limestone
  lime hydrate, calcium acetate
  iron based—hematite and
  magnetite
- sorbent feed rate: Ca/S 1.5 to 4.0
  Fe/S 1.5 to 4.0

Primary data was collected during testing with respect to the applicable design and operating parameters to assess, optimize and demonstrate performance:

- system pressure drop
- general operability
- carbon utilization
- NO_x emissions
- particle capture
- sulfur capture
- alkali vapor emission
- fuel gas combustibility

The slagging gasifier testing showed that several aspects of the slagging gasifier performance met or exceeded the program goals. These are, NO_x emission (<50 ppmv, dry, corrected to 15 percent 0_2), pressure drop, and carbon utilization (>98 percent). The operability of the gasifier was good, fuel gas combustion was efficient, stable, and reliable, and overall performance was slightly better for dry coal feeding than for coal-water feeding. All the coals tested were effectively handled and gasified.

Sulfur removal in the slagging gasifier was lower than the program goals, with a maximum of about 40 percent removal achieved at the gasifier exit. Figure 4 shows a plot of sulfur removal data at different points in the system. The top curve represents gas sampling results from within the gasifier vessel under conditions where the slag collected in the impact collection vessel was not removed from the vessel, but was allowed to accumulate during the testing. Sulfur removal as high as 95 percent was measured in this zone for equivalence ratios less than 1.2. The lower curve in Fig. 4 shows the sulfur removal measured at the fuel gas combustor exit, indicating that captured sulfur was released at points in the system following the primary gasification zone. The exhaust gas sulfur removal improved as the equivalence ratio was increased. The facility was later modified to include a large accumulation vessel for slag than would isolate and quench the collected slag from the gasifier. The two data points, shown for sulfur removal with the modified equipment, gave identical sulfur removal in both the primary gasifier zone and at the combustor exit, and also showed that the performance was improved substantially at the specific equivalence ratio considered in the test. The improved performance is attributed to the decomposition of accumulated slag and release of sulfur that occurred in the early testing. The results show further opportunity to improve sulfur removal performance.

The test data shows that slag capture achieved levels where, under some circumstances, the particulate emissions may satisfy current environmental standards, but the loading and size distribution would probably exceed turbine erosion/deposition criteria. The fuel gas sampling made by several techniques found that the alkali vapor content of the fuel gas might be close to current turbine requirements for coated blades, but these measurements were very uncertain in accuracy.

Current Activities and Plans

The major technical issues for the DCFT system are clearly

- in-situ sulfur removal performance
- slag capture efficiency
- alkali vapor control

These technical issues are the focus of the continuing Westinghouse development program. Technical enhancers are also being addressed. These require the application of known techniques to improve and/or establish performance capabilities in the following areas:

- NO_x emissions
- reliability
- maintainability
- integration with the turbine power island
- scaleup criteria
- use of fuels other than coals (biomass, heavy resids, black liquor, etc.)

These enhancers require testing and parallel engineering evaluations of equipment designs and power plant designs. Currently, laboratory testing and modeling is being performed in the areas of

- slag testing for sulfur and alkali capacity enhancement
- CFD analysis of gasifier for scaleup evaluation
- process modeling for optimization and cost estimation
- sulfur removal modeling for test program planning
- and alternative fuels evaluation and test planning

Westinghouse's future development plans include conducting additional pilot testing to improve the gasifier performance and to assess the feasibility of alternative fuels; performing engineering and test work on external hot gas cleaning configurations; and evaluating PCFT performance with low sulfur fuels.

References

Bannister, R. L., et al., 1992, "Development of a Direct Coal-Fired Combined Cycle for Commercial Application," ASME Paper 92-GT-25.

Bannister, R. L., Newby, R. A., and Diehl, R. C., 1992, "Developing a Direct Coal-Fired Combined Cycle," *Mechanical Engineering,* Vol. 114, No. 12, pp. 64–70.

Bannister, R. L., et al., 1990, "Recent Test Results in the Direct Coal-Fired 80MW Combustion Turbine Program," ASME Paper 90-GT-58.

Barkalow, R. H., et al., 1979, "Corrosion and Erosion of Materials in Coal Combustion Gas Turbines," *Proceedings of the Conference on Corrosion and Erosion on Coal Conversion System Materials,* Berkeley, CA, January.

Diehl, R. C., et al., 1989, "A Direct Coal-Fired 80MW Utility Combustion Turbine-Status Report," ASME Paper 89-GT-116.

Domeracki, W. F., et al., 1995, "Development of a Topping Combustor for Advanced Concept Pressurized Fluidized-Bed Combustion Systems," *Proceedings Advanced Coal-Fired Power Systems '95 Review Meeting,* DOE/METC-95/1018, p. 263.

EPRI, 1985, *Direct Coal-Fired Combustion Turbines,* workshop proceedings, EPRI AP-3939-SR, edited by COE Corp., April 1985.

Horazak, D. A., et al., 1990, "Economic Evaluation of Process Alternatives for Direct Coal-Fueled Combustion Turbine Combined Cycle," *Advances in Solid Fuels Technologies,* ASME FACT - Vol. 9, Book No. G00522, pp. 39–46.

Jensen, A. R., et al., 1992, "Development of a Direct Coal-Fired Advanced Combined Cycle Concept for Repowering and New Base Load Generation," ASME Paper 92-JPGC-GT-4.

Johnson, K. W., 1996, "Operations of Combustion Turbines on Alternate Fuel Oils," ASME Paper 96-GT-7.

Mudd, M. J., and Reinhart, W. P., 1995, "An Analysis of Four Years of Operation of the 70 MW Tidd PFBC Demonstration Plant," *Proceedings 13th Int. Conf. on Fluidized Bed Combustion,* ASME, NY, p. 925.

Newby, R. A., and Bannister, R. L., 1994, "Advanced Hot Gas Cleaning System for Coal Gasification Processes," ASME JOURNAL OF ENGINEERING FOR GAS TURBINES AND POWER, Vol. 116, pp. 338–344.

Pillsbury, P. W., et al., 1989, "Direct Coal Firing for Large Combustion Turbines: What Do Economic Projections and Subscale Combustor Tests Show," ASME Paper 89-JPGC/GT-4.

Roberts, P. B., et al., 1993, "Full-Scale and Bench-Scale Testing of a Coal-Fueled Gas turbine System," *Proceedings Joint Contractors Meeting,* DOE/METC-93/6132, DOE, p. 165.

Rothrock, J., et al., 1993, "Direct Coal-Fired Gas Turbines for Combined Cycle Plants," *Proceedings Joint Contractors Meeting,* DOE/METC-93/6132, DOE, pp. 178.

Stringer, J., 1995, "Erosion, Corrosion and Deposition in Coal-Fired Gas Turbines: The Experience Derived During the Past Decade," *Direct Coal-Fired Combustion Turbines,* workshop proceedings, EPRI AP-3939-SR, April.

Thoman, R. J., Horazak, D. A., and Hals, F. A., 1987, "Development of Coal-Fueled Gas Turbine Systems for Electric Utility Applications," ASME Paper 87-GT-271.

Wenglarz, R. A., et al., 1995, "Rugged ATS Turbines for Alternative Fuels," ASME Paper 95-GT-73.

Effect of Fuel Moisture Content on Biomass-IGCC Performance

W. E. M. Hughes

E. D. Larson

Center for Energy and
Environmental Studies,
School of Engineering and Applied Science,
Princeton University,
Princeton, NJ 08544

The moisture level in biomass fuels potentially impacts efficiency in conversion to power. This paper examines the efficiency and net power output of a fluidized bed gasifier-combined cycle with flue gas drying for a range of as-received raw biomass moisture contents and levels of pregasification drying. Due to the lack of empirical data available, a modeling approach is used to simulate the effect of varying moisture content in the gasifier feed biomass. For a specified as-received biomass moisture content, drying prior to gasification increases overall efficiency, but the gains in efficiency decrease with increasing levels of drying. For a specified post-dryer gasifier feed moisture content, cycle efficiency and power output increase with decreasing as-received biomass moisture down to 30 percent, below which the change in cycle performance is negligible.

Introduction

Typical moisture contents of freshly cut woody biomass are in the range of 30 to 60 percent. Many annual biomass crops, e.g., wheat straw, have a moisture content of 8 to 20 percent when harvested (Hall et al., 1993). In an integrated gasification combined cycle (IGCC), efficiency penalties and some operational challenges may arise when using wetter compared to drier fuels. During gasification, high moisture contents lead to lower raw product gas heating values, in part through the dilution of the product gas with additional water vapor. Partial oxidation gasifiers require a greater degree of combustion to provide heat for additional drying, increasing carbon dioxide levels. In air-blown gasifiers, the higher air requirement leads to increased dilution of the product gas with nitrogen. While tests by gas turbine manufacturers indicate that, with small modifications, some gas turbine combustors can be operated effectively on low heating value fuels (see below); low product gas heating values do pose technical challenges and potentially increased equipment costs.[1]

The objective of the work presented here is to examine, for a biomass pressurized fluidized bed gasifier combined cycle, the effect on cycle efficiency and power output of (1) fuel moisture content at the plant gate, and (2) level of drying prior to gasification. In this paper, "raw biomass" refers to the biomass at the plant gate and "feed biomass" refers to the biomass entering the gasifier after drying.

Due to the lack of empirical data, a modeling approach is necessary. The software used here for cycle modeling is able to accurately predict full-load design-point power and efficiency for cycles incorporating commercially available gas turbines. Details of the software are described elsewhere (Consonni et al., 1991; Consonni and Larson, 1996). Simulations were run for raw-biomass moisture contents of 50 percent, 40 percent, 30 percent and 20 percent. For each raw biomass moisture level, several feed-biomass moisture contents were considered ranging from no drying to complete drying. This paper focuses exclusively on the overall thermodynamic impacts of biomass moisture. Operational and cost challenges associated with drying and using wet feedstocks are not trivial, but are not addressed in this paper.[2]

System Design and Technological Considerations

Cycle Selection. The system modeled here is a combined cycle with a pressurized circulating fluidized bed gasifier,[3] hot product gas cleaning and flue gas drying (Fig. 1). Chipped raw biomass is dried, pressurized with nitrogen in a lock-hopper, and fed to the gasifier operating at 24 bar. Characteristics assumed for the bone-dry woody biomass are shown in Table 1. Gasification air is bled from the gas turbine compressor, cooled, and boosted to the required pressure. Product gas from the gasifier is cooled to 400°C before the filter. Heat from cooling the syngas is recovered as additional steam for the bottoming cycle. Ash is removed primarily at a downstream filter. The clean product gas is burned in the gas turbine combustor. Heat from the gas turbine exhaust is recovered in the heat recovery steam generator (HRSG), which feeds the steam turbine bottoming cycle. The exhaust gas from the HRSG is then used to directly dry the raw biomass before being vented at the stack.

Gas Turbine Options. The gas turbine in this analysis is modeled on the GE LM2500 aeroderivative gas turbine with a slightly increased pressure ratio (20.2 instead of 18.8)[4] that results from higher flow volumes typical of lower energy-content fuels. Closing the compressor inlet guide vanes was simulated in order to limit the pressure ratio to this value.

For large power plants, the lower pressure ratios and higher gas turbine outlet temperatures characteristic of heavy-duty industrial gas turbines (rather than aeroderivatives) are closer to the optimum parameters for maximum efficiency of natural gas-fired combined cycles (Macchi et al., 1995; Horlock, 1995; Corman, 1995). However, below 50 $\mathrm{MW_{el}}$ (a likely scale for many biomass applications), aero-engine-based combined cycles show higher efficiencies than industrial-based systems due to high topping cycle efficiencies, even at relatively small scales (Macchi et al., 1995). The LM2500 is especially appropriate for the scale considered here since the pressure ratio is toward

---

[1] Lower product gas heating values imply higher volumetric flow rates, and, hence, larger gasification and gas cleaning equipment.

Contributed by the International Gas Turbine Institute and presented at the International Gas Turbine & Aeroengine Congress and Exhibition, Orlando, FL, June 2–5, 1997. Manuscript received by the ASME Headquarters February 17, 1997. Paper No. 97-GT-4. Associate Technical Editor: H. A. Kidd.

[2] Operational challenges include the difficulty of maintaining at reasonable cost a constant biomass moisture level leaving a dryer as the incoming moisture level varies. (A consistent moisture level to the gasifier is needed to produce a consistent-quality gas.) Other challenges include handling especially wet feedstocks, prepyrolysis emissions during drying, dust control, and the risk of spontaneous combustion.

[3] Gasifier performance is based on that of a circulating fluid-bed design, as reported by Consonni and Larson (1996), but the overall system thermodynamic performance should be similar for a bubbling-bed design. Bioflow (a Scandinavian company) is developing a pressurized circulating fluidized bed gasifier. Also under development is the Institute of Gas Technology (U.S.A.) Renugas process—licensed to Carbona (a Finnish company)—based on bubbling fluidized bed gasification.

[4] This pressure ratio was selected based on discussion by Palmer et al. (1993) of the GE LM2500PE—a version of the LM2500 modified for steam injection.

the low end for large modern aeroderivative turbines, while efficiency is still high.

Combustion of Low Heating Value Fuel. A concern with using low-heating value fuels is insuring stable, complete combustion while achieving the desired temperature. In these simulations, the turbine inlet temperature was set at 1232°C. The oxygen concentration in the combustor outlet stream was used as an indicator of potential combustion stability problems (Larson and Hughes, 1996). If the heating value of the product gas resulted in an oxygen mole fraction of less than 5 percent, the turbine inlet temperature was reduced until 5 percent was achieved. This criterion ensures that a minimum requirement is met, i.e., that the specified flame temperature can theoretically be reached with the given fuel.

Ultimately, combustion stability and efficiency must be addressed empirically. Test results show that operation of gas turbine combustors on many low-heating value fuels is feasible. A GE LM2500 combustor has been tested under conditions simulating rated power operation, with fuels containing 5.6 to 8.4 MJ/m^3 (150 to 225 Btu/scf; approximately 5.7 to 9.1 MJ/kg on higher heating value (HHV) basis) (Sabla and Kutzko, 1985). Only two modifications were made: the fuel nozzle was enlarged and, in one set of tests, the swirl cup venturis were removed. Despite some adverse effects on the combustor exit temperature distribution, the researchers concluded that "operation of the engine at maximum power output with the current combustion system with appropriately sized gas nozzles appears completely viable." Flammability results showed that combustion could be maintained with fuel lower heating values (LHV) as low as 3.72 MJ/m^3 (100 Btu/Scf; 3.6 MJ/kg HHV) at a H_2:CO ratio of about 0.7 and as low as 2.88 MJ/m^3 (80 Btu/scf; 2.8 MJ/kg HHV) as the ratio approaches 1. Tests with a GE LM500 combustor showed stable combustion and acceptable combustion efficiency and exit temperature distribution with fuel heating values as low as 3.72 MJ/m^3 (100 Btu/scf) (Rahr et al., 1985). Fuels with heating values as low as 3.0 MJ/m^3 were successfully combusted in a one-fifth-scale model combustor of the ABB gas turbine type 11N2-LBtu (Liu and Schmidli, 1996).

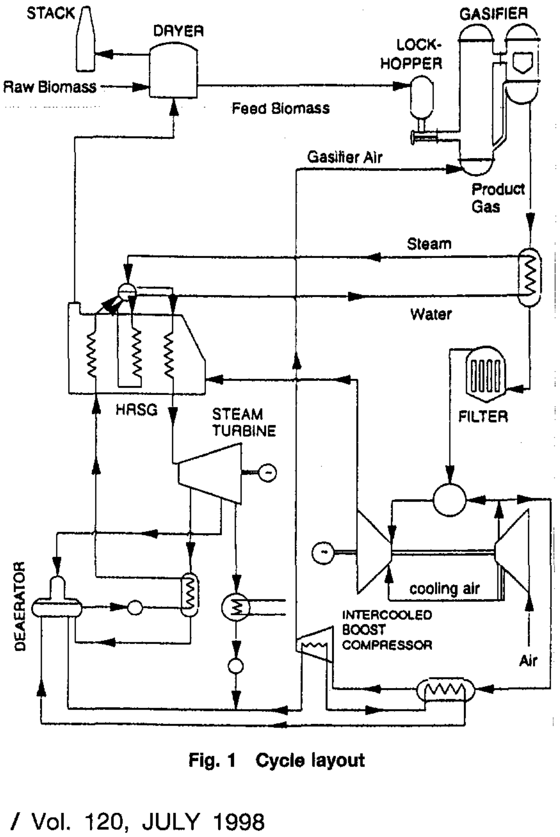

Fig. 1 Cycle layout

Table 1 Bone dry biomass composition (weight percent) and heating values

C	49.98
H	6.12
O	42.49
N	0.55
S	0.06
Ash	0.40
LHV (MJ/kg)	18.66
HHV (MJ/kg)	20.00

In this analysis, feed biomass with 30 percent moisture yields a product gas LHV of 3.7 MJ/Nm^3, which is within the range of some of the tests noted above. A feed moisture content of 50 percent gives a LHV of 1.7 MJ/Nm^3, requiring gas turbine inlet temperature derating by almost 200°C (to 1037°C). Combustion of such a fuel might require significant combustor modification and/or blending with a higher heat content fuel.

Gasification Modeling

Approach. Fluidized bed biomass gasifiers operate in a temperature range between 850°C and 1000°C. Since, at these temperatures (and for characteristic residence times), the product gas composition is far from equilibrium, the gasification modeling reported here relies on empirical data from gasifier developers. Currently, a consistent set of empirical data showing the effect of feed biomass moisture content on gasifier performance is not available from gasifier developers. This section describes the approach used in this analysis to estimate the performance of a gasifier for different feed biomass moisture levels.

The approach can be summarized in the following three steps: (1) a "base" cycle was designed using available empirical data for 15 percent moisture content feed biomass (Larson and Hughes, 1996); (2) all inputs to the gasifier were fixed at the base-case values, except for the feed moisture and the air/dry-biomass ratio (A/B)[5]; (3) the product gas composition was calculated so as to close the heat and mass balance for each set of feed moisture and A/B values.

Adjustments to the available empirical A/B (for 15 percent feed moisture content) were calculated based on the assumption that additional moisture to the gasifier requires additional combustion for a fixed gasifier temperature. Figure 2 shows the variation of the calculated A/B with feed moisture content and the resulting heating value of the product gas.

Justification for the Approach. Since the objective of this work is to estimate the effect of biomass moisture content on overall cycle efficiency and power output, the gasifier modeling focuses on the aspects most relevant to cycle efficiency and power output. For a fixed set of gasifier inputs and gasifier temperature, there is an important split between "sensible" and "chemical" energy production. The chemical energy leaving the gasifier is passed to the more efficient gas turbine-plus-steam turbine cycle. Most of the sensible heat in the product gas is recovered in the syngas cooler and passed to the steam cycle alone. The modeling approach taken here is focussed on accurately accounting for the relative quantities of sensible and chemical energy leaving the gasifier.

---

[5] The fixed inputs are biomass elemental composition and heating value; air temperature; gasifier heat loss; carbon conversion; and gasifier exit temperature.

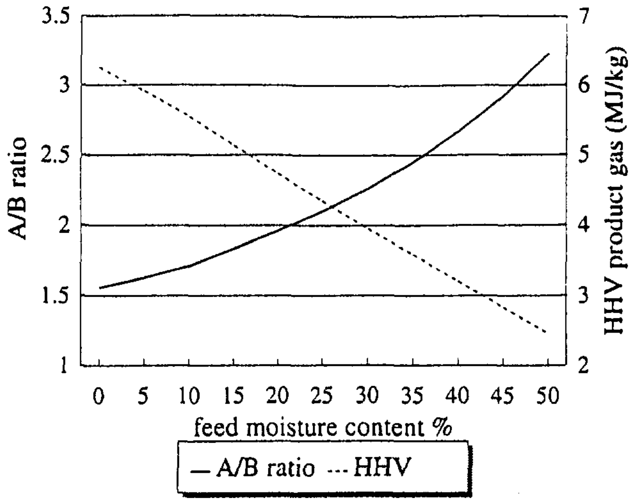

Fig. 2 Variation of combustor air-fuel ratio and product gas higher heating value

The choice of a fixed gasification temperature ensures that variations in cycle performance are due to changes in biomass moisture content rather than simply from a shift in the proportion of product gas energy from chemical to sensible heat. The selected temperature (953°C) is within the range specified by gasifier developers based on consideration of kinetic rates and avoiding ash agglomeration.

In an actual gasifier, for a fixed set of inputs and gasifier exit temperature, a unique gas composition is produced. Since no data are available for how the product gas composition actually varies with feed moisture content, the specific gas composition cannot be predicted by the modeling here. Instead, for fixed inputs and gasifier temperature, alternative gas compositions that close the gasifier mass and energy balance can be calculated. One of these alternative compositions may be close to what would be achieved in an actual gasifier, but the precise composition used in the model calculations turns out to have an essentially negligible impact on the overall cycle results, which can be explained as follows.

Table 2 Impact of gas composition on overall cycle efficiency. All inputs to the gasifier are fixed. Gasifier temperature is fixed at 953°C. Feed moisture content is 15 percent and *A/B* is fixed at the empirically reported value for this moisture content.

	Empirical	Alternative Calculated Compositions			
Composition					
Ar	0.481	0.471	0.473	0.479	0.491
CH_4	5.410	4.224	4.482	5.165	6.553
CO	16.237	9.465	10.93	14.85	22.74
CO_2	11.852	19.14	17.57	13.34	4.856
C_2H_4	0.121	0.094	0.100	0.115	0.146
H_2	10.167	20.70	18.42	12.33	0.041
H_2O	12.103	3.185	5.116	10.28	20.67
H_2S	0.015	0.015	0.015	0.015	0.015
NH_3	0.059	0.119	0.106	0.071	0
N_2	43.477	42.51	42.72	43.28	44.41
HHV (MJ/kg)	5.130	5.095	5.103	5.123	5.162
LHV (MJ/kg)	4.553	4.518	4.525	4.546	4.585
relative HHV CC efficiency	1	1.001	1.001	1.000	1.001

Table 3 Cycle characteristics held constant over all simulations

Gas turbine inlet temperature (°C)	1232 except where derating required[1]
Pressure ratio	20.2
Stack gas temperature (°C)	93
Temperature of gasifier air (°C)	100
Gasifier outlet temperature (°C)	953
Gasifier heat loss (% input biomass HHV)	0.5 - 1.0%[2]
Product gas temperature after cooling (°C)	400
Maximum steam temperature (°C)	450
Maximum steam pressure (bar)	67
Lockhopper power (kJ/kg)	114
HRSG pinch point ΔT (°C)	10
Syngas cooler pressure drop	5%
Other heat exchanger pressure drop	2%

[1] see text previous page.
[2] varies with feed moisture content: higher moisture content requires higher degree of heat release and therefore heat loss.

By specifying the input streams, the mass and energy entering the gasifier (and therefore the total enthalpy leaving the gasifier) are fixed. The input energy leaving the gasifier as sensible energy is determined by the gasifier outlet temperature and the specific heat capacity of the product gas. The latter is determined by the product gas composition. The remaining fraction of incoming energy is accounted for by the heat of formation of the product gas.[6]

For a fixed gasifier outlet temperature, varying the product gas composition results in a small change in the sensible energy—leaving the gasifier and a correspondingly small change in the enthalpy of formation. The product gas heating value is the difference between the enthalpy of formation of the reactants that combine to form the product gas (fixed in all cases) and the enthalpy of formation of the product gas, all at the same reference temperature. Thus, composition changes result in small variations in the product gas heating value for a fixed gasifier outlet temperature. An illustrative set of product gas heating values for a fixed set of inputs and fixed gasifier outlet temperature are shown in Table 2. Over a range of product gas compositions, overall cycle efficiency changes negligibly, compared to the calculation based on the original empirical gas composition.

Results and Discussion

Table 3 lists the cycle characteristics that were fixed for all simulations. Figures 3 and 4 show the variation of cycle effi-

---

[6] The energy equation for the gasifier is

$$m\cdot h_{\text{prod gas}} = \sum_{\text{prod gas}} (m_i\cdot h^0_{f,i}) + \sum_{\text{prod gas}} \left(m_i\cdot \int_{T0}^{T1} c_{p,i}dT\right) = m\cdot h_{\text{input}},$$

where m is the total mass, subscript i is for product gas constituents, h is the specific enthalpy (kJ/kg), h_f^0 is the enthalpy of formation at the reference temperature $T0$, $T1$ is the gasifier output temperature, and c_p is the specific heat capacity at constant pressure. The term containing the integral is defined here as the sensible energy of the product gas. By fixing $T1$, the range of possible gas compositions is constrained by the requirement that changes in the enthalpy of formation are balanced by changes in the specific heat capacity.

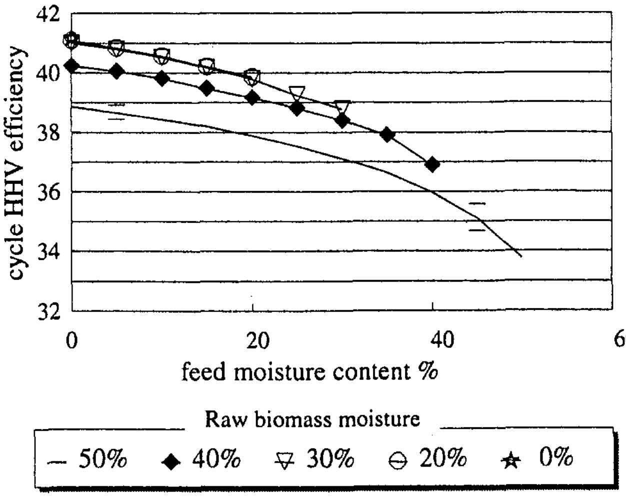

Fig. 3 Cycle HHV efficiency versus feed moisture content. The bars around the 50 percent raw-biomass line show the efficiencies calculated using A/B ratios of ±10 percent of the values shown in Fig. 2. The conclusions are not qualitatively different within this range of A/B ratio values. Note that for 15 percent feed-biomass moisture, the results are calculated directly from empirical data, and can be considered precise.

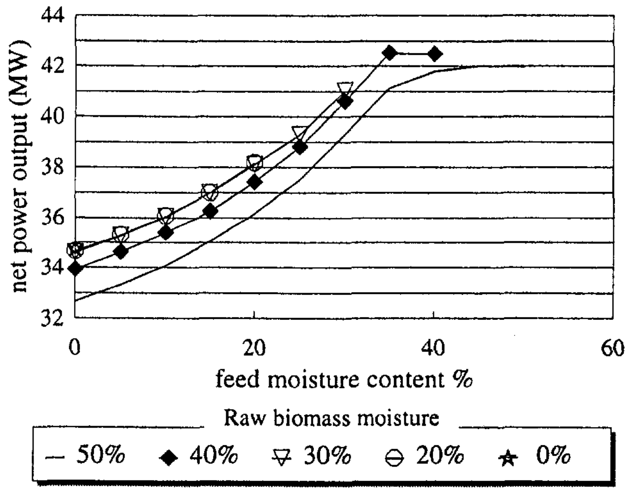

Fig. 4 Net cycle output versus feed moisture content

ciency and net power output with varying feed-moisture content. Curves are shown for raw-biomass moisture contents from 50 percent to 0 percent.

One important result shown in Fig. 3 is that for a given raw-biomass moisture content, reducing the feed-biomass moisture increases efficiency but at a decreasing rate. For example, for 50 percent raw biomass moisture content, reducing feed moisture content from 50 percent to 35 percent increases the efficiency by 2.5 percentage points; reducing from 15 percent to 0 percent changes the efficiency by less than 1 point. This suggests a trade-off between efficiency and additional dryer capacity/cost. If air-drying to 30 percent raw moisture content were achieved outside the cycle, the efficiency would be comparable to the baseline efficiency (drying from 50 percent to 15 percent moisture content) without any further drying. In this situation, it might be more cost-effective to eliminate the dryer entirely.

A second important result shown in Fig. 3 is the effect of the raw-biomass moisture content on efficiency, i.e., the vertical spacing of the curves. The "★" symbol on the vertical axis shows the efficiency that would be achieved if the raw biomass were bone-dry, so that no heat from the cycle is used for drying. Below 30 percent, the raw biomass moisture content has very little effect on overall efficiency: the curves for 0, 20, and 30 percent lie on top of each other. This occurs because excess low-grade heat exists that cannot be used anywhere in the cycle other than in drying, and, thus, its use for drying imposes no efficiency penalty.[7] Above 30 percent moisture content, the heat required for biomass drying exceeds the amount of available excess heat. In this case, drying reduces the heat that would be used in other parts of the system (such as in boiler water preheating), thereby imposing an efficiency penalty relative to a drier fuel. This result suggests significant increases in efficiency are possible if green biomass (50 percent moisture) can be air-dried to 30 percent moisture content before being used at a power plant. Results from a study conducted in Brazil indicate that 30 percent is a realistic target under appropriate climatic conditions (Gomes et al., 1996).

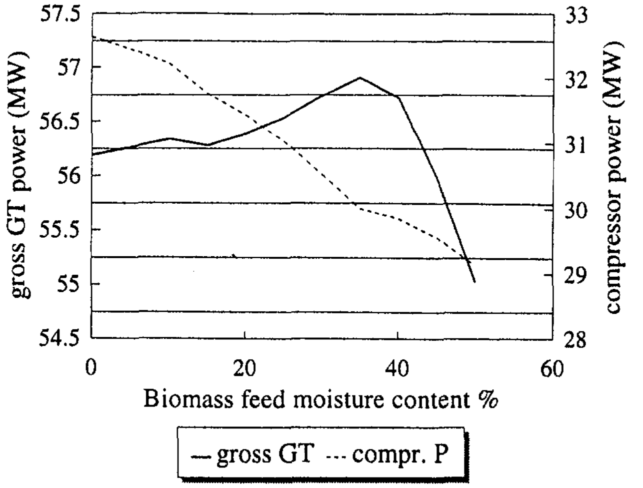

Fig. 5 Variation of gross gas turbine power and compressor power requirement

Figure 4 shows the effect of moisture content and drying on the net power generated. The general trend is that, for a given raw-biomass moisture content, increasing the feed moisture increases the net power output. As the heating value of the product gas falls with higher feed moisture content, the combustion occurring in the gas turbine moves from very lean toward stoichiometric, in order to reach the required turbine inlet temperature. This is achieved by increasing the fuel-air ratio in the gas turbine combustor. In the system modeled here, the compressor's air flow is reduced to maintain the appropriate fuel-air ratio. For higher fuel-air ratios, which accompany higher feed moisture content, greater proportions of the mixture entering the gas turbine combustor are brought to combustor pressure by compression of a solid (the biomass feed to the gasifier), thereby reducing air compression work (Fig. 5) and increasing net power output.

At high feed-biomass moisture (above about 35 percent), the rated turbine inlet temperature can no longer be reached with the low heating value fuels. Turbine inlet temperature must be reduced. Gross gas turbine power output falls sharply (Fig. 5) and net power output levels off (Fig. 4).

Suggestions for Future Work

For the biomass-IGCC system modeled here, drying prior to gasification increases overall efficiency regardless of initial moisture content, but the gains in efficiency decrease

---

[7] If a two-pressure level HRSG were assumed, more of the low grade heat could be used in the cycle, probably resulting in a slightly larger difference between the 30 percent and 20 percent curves in Fig. 3.

with increasing levels of drying. For a fixed moisture content into the gasifier, efficiency and power output are unaffected by the moisture content of the raw biomass into the dryer when this moisture level is 30 percent or less. Higher levels significantly reduce cycle efficiency. These results were developed for a cycle configuration that includes a pressurized circulating fluid-bed gasifier, hot gas cleanup, and a gas turbine with the characteristics of the LM2500. A number of alternative gasifier and gas cleanup technologies have been proposed for biomass-IGCC applications. The conclusions reached here may not hold for cycle configurations using other gasifier, gas cleanup, and/or gas turbine designs. Similar analyses for other cycle configurations, for example, using atmospheric, directly or indirectly heated gasification, would be of interest.

Flue gas drying has been assumed in the results reported here. It may be worthwhile to carry out similar analyses for other drying technologies that have been proposed. One technology that may be especially interesting is the IVOSDIG® dryer under development by Imatran Voima Oy (IVO), a Finnish electric utility. In the IVOSDIG® process, biomass is dried under pressure using steam, and the resulting steam evolved from water in the biomass is recovered and used downstream in the cycle. This process—direct pressurized drying with superheated steam—is reported to greatly reduce the efficiency penalty of drying compared to a flue gas drying system when starting with very high moisture content (>60 percent) fuels (Hulkkonen et al., 1991, 1993). (A trade-off may be greater capital cost and operational complexity for the IVOSDIG® system.) In a comparison of drying-system options with fuel dried from 62 percent to 15 percent moisture content, an increase in combined cycle higher-heating value efficiency of up to 3 percentage points, compared with flue gas drying, is reported by Hulkkonen et al. (1993). The possibility that the IVOSDIG® process might reduce the drying penalty associated with flue gas drying under a range of raw and feed biomass conditions deserves further consideration.

References

Consonni, S., and Larson, E. D., 1996, "Biomass-Gasifier/Aeroderivative Gas Turbine Combined Cycles, Part A: Technologies and Performance Modeling, and Part B: Performance Calculations and Economic Assessment," ASME JOURNAL OF ENGINEERING FOR GAS TURBINES AND POWER, Vol. 118, pp. 507–525.

Consonni, S., Lozza, G., Macchi, E., Chiesa, P., and Bombarda, P., 1991, "Gas-Turbine-Based Advanced Cycles for Power Generation. Part A: A Calculation Model," *Proceedings 1991 Yokohama International Gas Turbine Congress*, Gas Turbine Society of Japan, Tokyo, pp. 201–210.

Corman, J. C., 1995, "Gas Turbine Power Generation—Status and Environmental Considerations," *Proceedings, 1995 Cogen Turbo Power*, ASME, New York, NY.

Gomes, A., Alves, J., and Leite, H., 1996, "Teor de umidade da madeira em funcao do tempo de secagem," final report of Wood Drying Tests by COPENER for Companhia Hidro Electrica do Sao Francisco, Recife, Brazil.

Hall, D. O., Rosillo-Calle, F., Williams, R. H., and Woods, J., 1993, "Biomass for Energy: Supply Prospects," *Renewable Energy: Sources for Fuels and Electricity*, Johansson, Kelly, Reddy, and Williams, eds., Island Press, Washington D.C., pp. 595–651.

Horlock, J. H., 1995, "Combined Power Plants—Past, Present, and Future," *Transactions of the ASME*, Vol. 117, pp. 608–616.

Hulkkonen, S., Aijala, M., and Holappa, J., 1993, "Integration of a Fuel Dryer to a Gas Turbine Process," *ASME Cogen Turbo Power Book No. 100348*, IGTI-Vol. 8, pp. 61–67.

Hulkkonen, S., Raiko, M., and Ailala, M., 1991, "High Efficiency Power Plant Processes for Moist Fuels," *ASME Cogen-Turbo Book No. 100313*, IGTI-Vol. 6, pp. 429–433.

Larson, E. D., and Hughes, W. E. M., 1996, "Performance Modeling of Aeroderivative Steam-Injected Gas Turbines and Combined Cycles Fueled from Fixed or Fluid-Bed Biomass Gasifiers," Paper No. 96-GT-89, American Society of Mechanical Engineers, New York, NY.

Liu, Y., and Schmidli, J., 1996, "Experiments With a Gas Turbine Model Combustor Firing Blast Furnace Gas," Paper No. 96-GT-52, American Society of Mechanical Engineers, New York, NY.

Macchi, E., Consonni, S., Lozza, G., Chiesa, P., 1995, "An Assessment of the Thermodynamic Performance of Mixed Gas-Steam Cycles: Part A—Intercooled and Steam Injected Cycles," ASME JOURNAL OF ENGINEERING FOR GAS TURBINES AND POWER, Vol. 117, pp. 489–498.

Palmer, C. A., Erbes, M. R., and Pechtl, P. A., 1993, "Performance Prediction of the LM2500 Gas Turbine Using Low Heating Value Fuels," *Proceedings of Cogen-Turbo '93*, ASME, New York, NY.

Rahr, D. W., Sabla, P. E., Vinson, J. W., 1985, "Small Industrial Gas Turbine Combustor Performance With Low BTU Gas Fuels," Paper No. 85-GT-125, ASME, New York, NY.

Sabla, P. E., and Kutzko, G. G., 1985, "Combustion Characteristics of the GE LM2500 Combustor With Hydrogen-Carbon Monoxide-Based Low BTU Fuels," Paper No. 85-GT-179, ASME, New York, NY.

H. L. Relation

J. L. Battaglioli

General Electric Power Generation,
Schenectady, NY 12345

W. F. Ng

Department of Mechanical Engineering,
Virginia Polytechnic Institute and
State University,
Blacksburg, VA 24061-0238

Numerical Simulations of Nonreacting Flows for Industrial Gas Turbine Combustor Geometries

This study evaluates the application of the computational fluid dynamics (CFD) to calculate the flowfields in industrial combustors. Two-burner test cases, which contain the elemental flow characteristics of an industrial gas turbine combustor, are studied. Comparisons were made between the standard k-epsilon turbulence model and a modified version of the k-epsilon turbulence model. The modification was based on the work of Chen and Kim in which a second time scale was added to the turbulent dissipation equation. Results from the CFD calculations were compared to experimental data. For the two-burner test cases under study, the standard k-epsilon model diffuses the swirl and axial momentum, which results in the inconsistent prediction of the location of the recirculation zone for both burner test cases. However, the modified k-epsilon model shows an improved prediction of the location, shape, and size of the primary centerline recirculation zone for both cases. The large swirl and axial velocity gradients, which are diffused by the standard k-epsilon model, are preserved by the modified model, and good agreements were obtained between the calculated and measured axial and swirl velocities. The overprediction of turbulent eddy viscosity in regions of high shear, which is characteristic of the standard k-epsilon model, is controlled by the modified turbulence model.

Introduction

Designing the combustor for a gas turbine requires expensive testing and many iterations. Previously, the combustion engineer has relied primarily on experience, test results, and crude analyses based on empirical formulations to make final design decisions (Lefebvre, 1983). High temperatures, pressures, and flow rates in the combustor result in a flowfield where comprehensive experimental data are not easily obtained. Thus, computational fluid dynamics (CFD) is a particularly attractive design tool to the gas turbine industry since it has the potential to explain the flow physics inside the combustor. Numerical analysis can be used to reduce the number of design iterations by providing insight on the changes that a design parameter or geometrical feature will have on the characteristics of the flow in the combustor. This paper focuses on the problem of accurately predicting turbulent flow structures in complex industrial gas turbine combustor geometries. The accomplishment of this task is of significant importance to the combustor design engineer.

The accuracy of a turbulent flow calculation is dependent on the method of modeling the turbulence. Presently, the most widely used turbulence model in CFD codes is *k*-epsilon (Jones and Launder, 1972; Launder and Spalding, 1974). The *k*-epsilon model gives comprehensive results that are consistent with the experimental data for most turbulent flows. It is also computationally less time and memory intensive than Reynold's stress formulations, Large Eddy Simulations (LES), and direct numerical simulations (DNS). Time and memory are factors that are limited by a company's design deadlines and computer resources. Although widely used, the *k*-epsilon turbulence model underpredicts the large axial and tangential velocity gradients that are characteristic in a combustor. Numerous modifications have been made to the model that attempt to eliminate this problem. However, the applications of these improvements are limited to the narrow range of flow types for which they were developed (Moin, 1992). Geometries that are dominant in engineering industries involve a multitude of flow types, making these modifications inapplicable.

Y. S. Chen and S. W. Kim presented a modification to the *k*-epsilon turbulence model that was not flow specific, and could be applied to a broad range of flow configurations (Chen and Kim, 1987; Haroutinian and Engelman, 1993). Unlike previous modifications, the model was simple and took a more general approach to ascertaining a remedy to the problems associated with *k*-epsilon. Chen and Kim (referred to from here on as just Chen) applied their modification to a number of complex flow types, and demonstrated improved results for round and plane co-flowing jets, submerged jets, backward facing step flow, and a swirling flow case. In particular, the predictions of the backward facing step and swirling flow cases Chen had chosen demonstrated an improvement from the original standard *k*-epsilon model.

The purpose of this study is to evaluate the application of the Chen modification of the *k*-epsilon turbulence model to combustor geometries by applying the modification to two quarled burner test cases that contain the elemental flow characteristics of an industrial gas turbine combustor. The inlet boundary condition for Chen's swirling flow analysis is within the recirculation zone. Therefore, Chen merely tests his model's ability to maintain axial and tangential momentum within the recirculation zone. The inlet boundary condition chosen for the quarled burner cases, depicted in Figs. 1 and 2, is applied upstream of the expansion, before the recirculation zone becomes fully developed. These cases, therefore, provide a more accurate measure of the model's ability to predict the development of a recirculation zone induced by swirl. In addition, the quarled burner geometries include a ramp, which turns the flow before the expansion. This type of feature is common in industrial gas turbines.

Contributed by the Fuels and Combustion Technologies Division. Manuscript received by the ASME Headquarters September 28, 1994. Technical Editor: H. L. Julien.

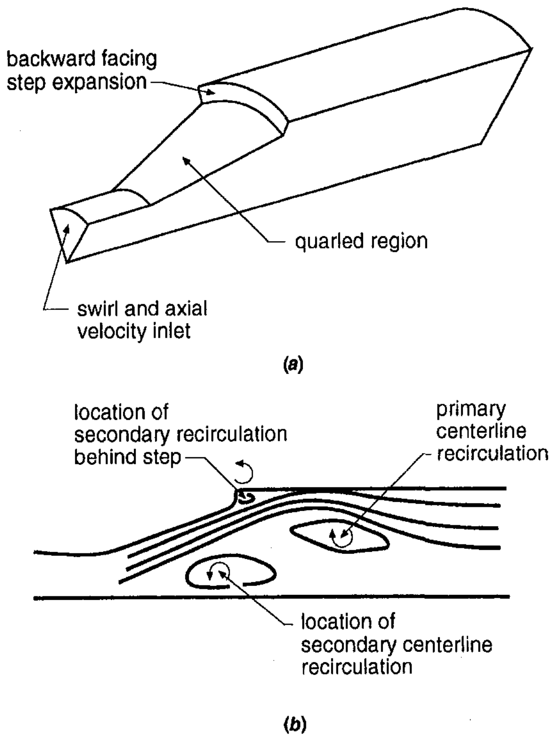

Fig. 1 Quarled burner case 1: (*a*) geometrical features; (*b*) flow features.

A description of the quarled burner test cases is included next. It contains a detailed description of the geometry, the flow characteristics, and experimental test locations of both burner cases. What follows is a description of the computational method and the turbulence models used for the test cases. Finally, the results of the computations performed with the original standard k-epsilon model and the Chen modification are presented, together with the experimental data.

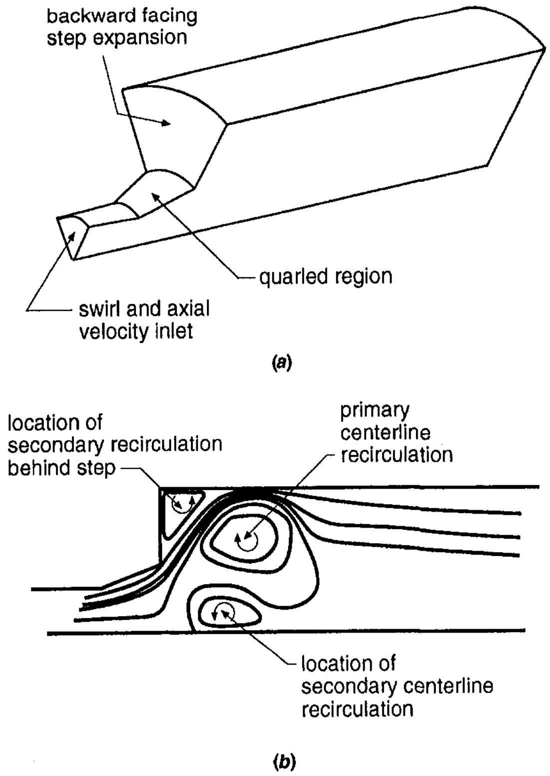

Fig. 2 Quarled burner case 2: (*a*) geometrical features; (*b*) flow features.

The Quarled Burner Test Cases. Flow in an industrial combustor is a combination of swirling, recirculating, and turning flows. The quarled burner geometry incorporates all three of these flow characteristics. Figures 1(*b*) and 2(*b*) show the flow features for quarled burner case 1 and case 2. Case 1, as seen in Fig. 1(*b*), characterizes axisymmetric swirling flow with a primary centerline recirculation zone, which is caused entirely by the tangential motion of the flow. The first quarled burner study also includes a small recirculation behind the expansion and a weak secondary centerline recirculation zone, which results in a stagnation region near the centerline. Case 2 demonstrates a combination of the effects of swirling flow, flow being turned through the quarl, and flow encountering a large expansion. As shown in Fig. 2(*b*), the second configuration is characterized by a primary centerline recirculation zone, similar to case 1, and a strong secondary recirculation behind the expansion. This geometry also contains a secondary centerline recirculation zone, which is larger than that of case 1 and is responsible for the positive axial velocity at the centerline. This configuration better represents the geometry and flow characteristics of an industrial combustor. It is this study that is of primary interest, and will best determine the applicability of the Chen modification to combustor geometries.

The function of the quarl, the ramped section prior to the expansion, is to produce a shorter but wider recirculation zone (Abou-Arab et al., 1991). Flow in these geometries is axisymmetric when the amount of rotation imparted on these flows is higher than that associated with the onset of vortex breakdown (Dellenback et al., 1987). The basic characteristics of a combustor, swirl, recirculating flow behind a step-like structure, and a slight expansion or quarl, are represented in the two-burner configurations evaluated.

The experimental data for these studies are taken from a report by Clarke et al. (1990). Both analyses are cold-flow experiments containing no combustion. In addition, the flows can be considered axisymmetric. The first quarled burner geometry consists of swirling flow that is expanded through a 21.4 E ramp (quarl) to a slight step. The length of the chamber is 4 meters. A diagram of the geometry is shown in Fig. 3(*a*). Experimental data is available at five axial locations, 0.17 m,

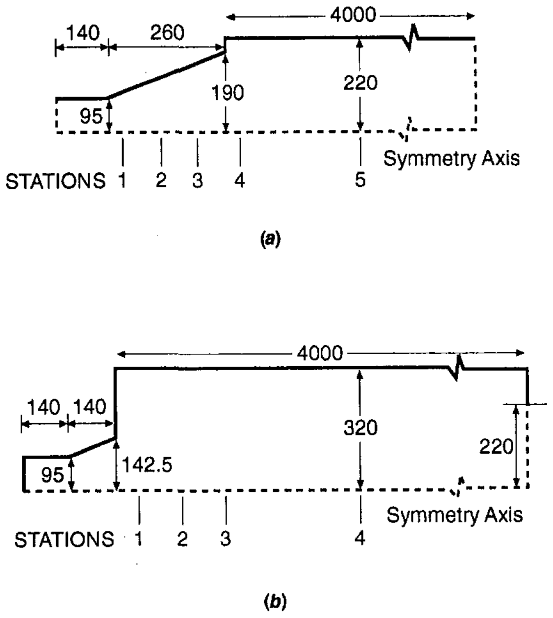

Fig. 3 (*a*) Quarled burner case 1, geometry; (*b*) quarled burner case 2, geometry.

0.25 m, 0.34 m, 0.45 m, and 0.75 m, downstream of the inlet. All but the last experimental station are located in the quarl. Both swirl and axial velocity data are given at each of the experimental locations.

The flow in the second case is turned through a 19.8 E quarl, and then expanded by a large step. The length of the chamber, which has an end contraction, is 4 meters. The geometry of case 2 is depicted in Fig. 3(*b*). Experimental data for this case is available at 0.32 m, 0.45 m, 0.58 m, and 0.905 m downstream of the inlet. None of the experimental locations are located in the quarl. Swirl and axial velocity measurements are available at each station.

The Computational Model

A three-dimensional commercial CFD code (STAR-CD) was used in this study. The implicit algorithm employed in the code is a pressure correction based scheme, a variant of the semi-implicit method for the pressure-linked equation algorithm of Patankar and Spalding (1980). The basic principle of the scheme is to predict the components of velocity by solving the momentum equations separately and then to introduce a correction based on the requirement of continuity (Raithby et al., 1979). All calculations presented in this paper were obtained by solving the full Navier-Stokes equations for turbulent flow.

Governing Equations. The behavior of the flow is governed by the incompressible form of the following time averaged, Navier-Stokes equations:

Conservation of Mass.

$$\frac{\partial}{\partial x_i}\langle \rho U_i\rangle = 0.$$

Conservation of Momentum.

$$\rho\frac{\partial\langle U_i\rangle}{\partial t} + \rho\langle U_j\rangle\frac{\partial\langle U_i\rangle}{\partial x_j} = -\frac{\partial\langle P\rangle}{\partial x_i} + \frac{\partial}{\partial x_j}\left[\mu\left(\frac{\partial\langle U_j\rangle}{\partial x_i} + \frac{\partial\langle U_i\rangle}{\partial x_j}\right)\right] - \frac{\partial}{\partial x_j}\rho\langle u_i u_j\rangle,$$

where $\langle\ \rangle$ indicates the mean, U is the average velocity, and u is the fluctuating velocity.

The Reynolds averaged momentum equation can be, for the most part, solved for the mean velocity and pressure. The equation is complicated by the last term on the right hand side $\rho\langle u_i u_j\rangle$ defined as the Reynolds turbulent stresses. This new term introduces six variables, greatly increasing the difficulty of solving the equation. Turbulence modeling is an attempt to simplify the computation of this term, and will be described later. The finite differencing method and the numerical accuracy are described in Relation (1993) and von Neumann and Raithby (1984). The calculation was two-dimensional axisymmetric. The solution was considered converged when the residual reached 1×10^{-5}.

Turbulence Modeling

The purpose of this section is to describe the modification made to the standard *k*-epsilon model based on the work of Chen (1987). For clarity, a brief description of the standard *k*-epsilon model is included.

The *k*-epsilon Turbulence Model. The turbulent viscosity can be modeled as follows:

$$\mu_t = \rho C_\mu \frac{k^2}{\epsilon}.$$

The turbulent kinetic energy, k, and dissipation, ϵ, can be found from the turbulent transport equations. The turbulent kinetic energy equation can be written as (Braaten, 1985)

$$\underbrace{\frac{\partial k}{\partial t} + \langle U_j\rangle\frac{\partial k}{\partial x_j}}_{1} = -\frac{\partial}{\partial x_j}\left(\underbrace{\frac{1}{\rho}\langle u_j p}_{2} + \underbrace{\frac{1}{2}\langle u u_i u_k\rangle}_{3} - \underbrace{2v\langle u_i s_{ij}\rangle}_{4}\right) \underbrace{- \langle u_i u_j\rangle S_{ij}}_{5} - \underbrace{2\nu\langle s_{ij} s_{ij}\rangle}_{6},$$

where

$$S_{ij} = \frac{1}{2}\left(\frac{\partial\langle U_i\rangle}{\partial x_j} + \frac{\partial\langle U_j\rangle}{\partial x_i}\right)$$

is the mean rate of strain, and

$$s_{ij} = \frac{1}{2}\left(\frac{\partial u_i}{\partial x_j} + \frac{\partial u_j}{\partial x_i}\right)$$

is the fluctuating rate of strain.

The six parts labeled on the turbulent kinetic energy equation correspond to the following: no. 1 is the rate of change of turbulent kinetic energy, no. 2 is the pressure gradient work, no. 3 is the transport by turbulent velocity, no. 4 is the transport by viscous stresses, no. 5 is the turbulent production, and no. 6 is the viscous dissipation.

The pressure strain term can be eliminated because $\partial u_j/\partial x_j = 0$ from the time dependent form of the continuity equation. The exact form of the turbulent kinetic energy equation is simplified to its final modeled form by the following assumptions:

- isotropic turbulence (valid at high Reynolds numbers)

$$\epsilon(\text{dissipation}) = \nu\left\langle\frac{\partial u_i}{\partial x_j}\frac{\partial u_i}{\partial x_j}\right\rangle$$

- application of eddy viscosity to the production term

$$-\langle u_i u_k\rangle = \frac{\mu_t}{\rho}\left(\frac{\partial\langle U_i\rangle}{\partial x_j}\frac{\partial\langle U_j\rangle}{\partial x_j}\right)$$

- simplification of the "turbulent" diffusion term by use of eddy diffusivity and the addition of the turbulent Prandtl number, σ_k.

$$-\langle u_i u_i u_k\rangle = \frac{\mu_t}{\sigma_k \rho}\frac{\partial k}{\partial x_j}$$

The final form of the turbulent kinetic energy equation that will be modeled is as follows:

$$\frac{\partial k}{\partial t} + \langle U_j\rangle\frac{\partial k}{\partial x_j} = \frac{\partial}{\partial x_j}\left[\left(\nu + \frac{\nu_t}{\sigma_k}\right)\frac{\partial k}{\partial x_j}\right] + P - \epsilon,$$

where, P (production) =

$$\nu_t\left(\frac{\partial\langle u_i\rangle}{\partial x_j} + \frac{\partial\langle u_j\rangle}{\partial x_i}\right)\left(\frac{\partial\langle u_i\rangle}{\partial x_k}\right)$$

and ν_t (turbulent kinematic viscosity) $\equiv \mu_t/\rho$.

The turbulent kinetic energy equation is solved in conjunction with the turbulent dissipation equation. The modeled equation for epsilon is given as

$$\underbrace{\frac{\partial \epsilon}{\partial t} + \langle u_k \rangle \frac{\partial \epsilon}{\partial x_k}}_{1} = \underbrace{\frac{\partial}{\partial x_k}\left[\left(\nu + \frac{\nu t}{\sigma_\epsilon}\right)\frac{\partial \epsilon}{\partial x_k}\right]}_{2} + \underbrace{C_1 \frac{\epsilon}{k} P - C_2 \frac{\epsilon^2}{k}}_{3}$$

where no. 1 is the rate of change of turbulent dissipation, no. 2 is the diffusion of the turbulent dissipation, and no. 3 is the sources of dissipation.

The model contains five empirical coefficients for which a reasonable range of values are determined by analysis of simple turbulent flows.

The turbulent kinetic energy and dissipation are solved for from their respective equations, and applied to the Boussinesq approximation to evaluate turbulent viscosity. The addition of the eddy viscosity to the molecular viscosity creates a greater dissipative effect in an attempt to simulate turbulent mixing. However, in areas of high shear, this model predicts the rate of production of turbulent kinetic energy to be much greater than that of dissipation, resulting in an overprediction of turbulent viscosity in these regions. The dissipative nature of the k-epsilon model results in inconsistent predictions, especially in swirling and recirculating flows where conservation of the momentum of the primary stream of flow is important. Because of the assumption of isotropic flow in the closure of the turbulent transport equations, the model also fails to give accurate predictions for flows that are highly anisotropic. The k-epsilon model proves to give qualitative results for many flows, however, it suffers from a few deficiencies which render it inapplicable to more complex flows.

The Chen Modification to the *k*-epsilon Turbulence Model. Chen attacks the most fundamental problem of the k-epsilon turbulence model, the overprediction of eddy viscosity in areas of high mean strain.

To correct this problem, Chen (1987) proposes the following additional source term be added to the dissipation equation:

$$\frac{\partial \epsilon}{\partial t} + \bar{u}_k \frac{\partial \epsilon}{\partial x_k} - \frac{\partial}{\partial x_k}\left[\left(\nu + \frac{\nu_t}{\sigma_\epsilon}\right)\frac{\partial \epsilon}{\partial x_k}\right] = C_1' \mathrm{Pr} \frac{\epsilon}{k} - C_2' \frac{\epsilon^2}{k} + C_3' \frac{P^2}{k}.$$

The last term on the right side of the equation is the proposed modification. The term adds a second time scale that allows the transfer of energy between the two transport equations to react more efficiently to mean strain. This time scale will allow the rates of production of turbulent kinetic energy and dissipation to converge. The result is a decrease of eddy viscosity where the velocity gradients are high, and an increase in μ_t where they are low.

The model constants CN_1, CN_2, and CN_3, as well as the turbulent Prandtl numbers are redetermined using the original stipulations imposed on the coefficients of the standard model. The coefficients were then numerically optimized resulting in the following final model values: $\sigma_k = 0.75$, $\sigma_\epsilon = 1.15$, $C_1' = 1.15$, $C_2' = 1.9$, and $C_3' = 0.25$.

Observing this final set of coefficients, it is noticed that in equilibrium flow (where production equals dissipation), dissipation can be substituted for production in the third term. The result is a source term identical to the first source term, Pr ϵ/k. The first and third coefficients, CN_1 and CN_3, respectively, can combine with the resulting coefficient being equal to C_1 of the original k-epsilon equation. So, in equilibrium flows, the Chen model reduces to the original k-epsilon model. In areas of high shear, however, production will not equal dissipation, and the first and third terms will not be identical in form. Rather, in areas of high production or shear, the third term will contribute to the production of dissipation more than the solitary term of the standard k.

Grids. The two-dimensional axisymmetric models used for the analysis of each case were determined to be grid independent by varying the mesh size and spacing. The grid for case 1 contains 287,400 cells all together (350 cells in the inlet, 700 cells in the quarl and 1824 cells to the exit, and 100 cells in the radial direction). The mesh is slightly packed towards the outer radius throughout the inlet, quarl, and portion of the expansion. This is done to better resolve the gradients, which are largest in this area of the flow. Case 2 is modeled using a grid containing 543,000 cells total (350 cells in the inlet, 350 cells in the quarl, 4730 cells in the expansion to the exit, and 100 cells in the radial direction). Similar to case 1, the grid is packed towards the outer radius in the inlet and quarl. In the expansion, the mesh is packed towards the outer radius and towards the center of the region. Again, this is done for better gradient resolution. Pictures of the grids are shown in Relation (1993).

Boundary Conditions. Inlet boundary conditions for both cases are given in Clarke et al. (1990) for tangential and axial velocity and turbulent kinetic energy and dissipation. The inlet axial velocity for the first case is specified as a constant value of 4.6 m/s, whereas the tangential velocity is linearly increasing from approximately zero at the centerline to 6.5 m/s at the outer radius. The turbulent kinetic energy and dissipation for case 1 are specified as 0.045 $\mathrm{m}^2/\mathrm{s}^2$ and 0.25 kg/m.s, respectively. The inlet axial velocity for case 2 is specified as 4.9 m/s, and the tangential velocity is linearly increasing from approximately zero at the centerline to 12 m/s at the outer radius. The turbulent kinetic energy and dissipation are given as 0.09 kg/m.s and 0.6 kg/m.s, respectively. At the outlet, the gradients of all variables normal to the exit plane are taken to be zero. Continuity need not be prescribed, as it is imposed on the flow by the solution method. A standard log law of the wall is applied to the walls and a cyclic boundary condition, which assures the tangential and axial components of velocity and scaler values are identical for the faces prescribed, is applied to the longitudinal faces of the model.

Results

The computational results of the quarled burner test cases, which are presented in this section, are compared with experimental velocity data to evaluate the improvement made by the model.

Case 1. Case 1 consists of a more elementary flow pattern than case 2, but its consideration enables the evaluation of the Chen modification's effect on the development of a centerline recirculation induced by swirl. Figures 4 and 5 show comparisons of numerical and experimental results for the swirl and axial velocities of case 1, respectively. Numerical results for both the standard k-epsilon model and the modified k-epsilon model are presented.

The improvement in the ability to accurately calculate the swirl velocity using the modified k-epsilon model is clearly illustrated in Fig. 4. The large gradients in swirl velocity are maintained throughout the quarl, giving the velocity profile a peaked appearance in this region. Predictions at stations 2 and 4 are greatly improved over those made with the standard k-epsilon model. At station 5, the modified k-epsilon model moves the profile of swirl velocity closer to the experimental result, but fails to completely resolve the characteristics of the flow.

The modified k-epsilon model also allows the flow's axial momentum to maintain a concentrated profile in regions of high shear. Figure 5 shows predictions of axial velocity, with the modification more closely matching the experimental data. The modification increases the velocity at the centerline, and predicts the peak in velocity at the outer radius. The comparison of the streamline patterns obtained from the experiment and the numerical simulations are presented in Fig. 6. As Figure 6 illus-

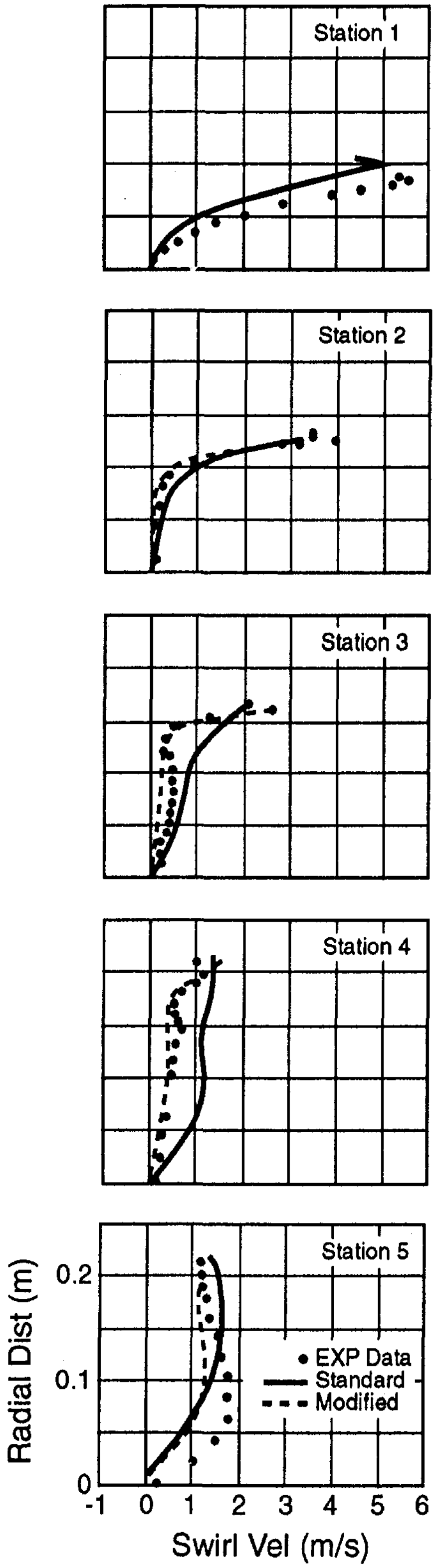

Fig. 4 Quarled burner case 1, swirl velocity predictions with the modified model

trates for the standard model, the center of primary recirculation is subsequently predicted to be closer to the axis of symmetry and further upstream than the experimental results dictate. The flow is characterized by a stream of high momentum fluid that moves along the outer radius of the quarl. This stream is indicated by the peaks seen in axial and swirl velocity as shown in Figs. 4 and 5. The standard *k*-epsilon model overpredicts eddy viscosity in this region, and allows the momentum of this stream to diffuse before it exits the quarl. As a result, the stream enters the expansion at a decreased angle, causing the low pressure region that forms below it to be predicted closer to the centerline than was determined experimentally. The unmodified standard

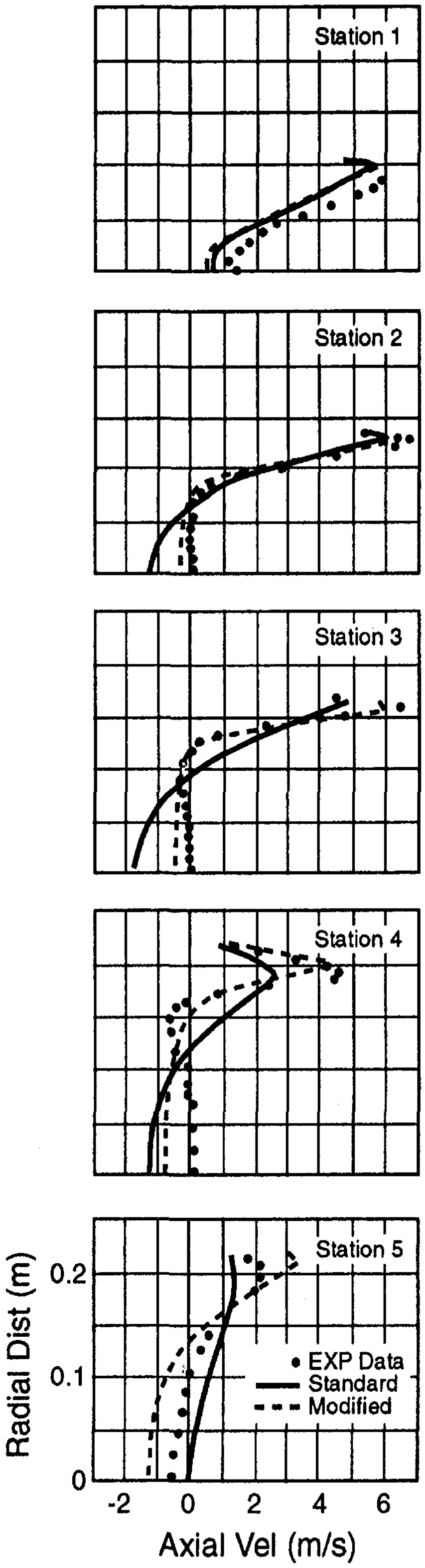

Fig. 5 Quarled burner case 1, axial velocity predictions with the modified model

Experimental Streamlines

(*a*)

Standard k-epsilon Model Streamlines

(*b*)

Modified k-epsilon Model Streamlines

(*c*)

Fig. 6 Quarled burner case 1: (*a*) experimental streamlines (Clarke et al., 1990); (*b*) k-epsilon model streamlines; and (*c*) modified *k*-epsilon model streamlines.

k-epsilon model predicts the center of primary recirculation to be further into the quarl and closer to the axis of symmetry (Fig. 6). Because the profiles of axial and swirl momentum are better preserved by the modified model, the high momentum stream of flow enters the expansion at an increased angle, allowing the low pressure region to form further away from the centerline. The result, as seen from Fig. 6, is that the location of the center of primary recirculation is more accurately predicted. The comparison of the experimental, standard *k*-epsilon, and modified *k*-epsilon streamline plots illustrates the ability of the modified model to predict the flow characteristics of this combustor geometry and, in contrast, the failure of the standard *k*-epsilon model to predict the placement of the recirculation zone.

Case 2. Case 2, like case 1, is characterized by a centerline primary recirculation (see Fig. 2). However, complicating the flow is the addition of a second recirculation zone behind the expansion (the backward facing step). The region of highest velocity gradients is at the outer radius of the quarl continuing on the same angle into the expansion. Significant gradients are also present near the walls behind the step and near the outer radius in the expansion.

Swirl and axial profiles of both experimental and computational results for case 2 are illustrated in Figs. 7 and 8, respectively. Because there exists a recirculation behind the step, the peak in swirl and axial velocities is not seen at the outer-radius, as in case 1, but at mid-radius. Again, it is apparent that the standard *k*-epsilon model does not predict the large swirl velocity gradients in the flow, and distributes the swirl momentum along the radial direction.

The modified *k*-epsilon model, because it decreases turbulent viscosity in regions with high velocity gradients, maintains the peaked nature of the swirl momentum of the flow in these regions. This is particularly evident from the predictions of swirl velocity at station 1 (Fig. 7). The standard *k*-epsilon model diffuses the momentum of the jet, whereas, the modified *k*-epsilon preserves its momentum, as indicated by the spike in the profile. The results of stations 2 and 4 show an improved agreement between the computational predictions and the experimental data.

The axial velocity results show similar improvements. As Fig. 8 illustrates, the modification also preserves the large gradients of axial velocity in the flow. At station 1, the appearance of the jet, which was pushed against the outside radius of the quarl by the momentum of the swirl and then dumped into the expansion, is also prevalent. Because the spiked nature of the swirl momentum is preserved, the structure of this jet will remain more dense, as compared to the more diffuse profile the standard *k*-epsilon model produces. As a result, the peak in the axial momentum of this jet is also preserved. The predictions made by the modified *k*-epsilon model at the remaining experimental stations also show the result of decreased eddy viscosity in this region, as the flow retains its structure.

By improving swirl and axial velocity predictions, the structure of the flow is also better predicted. The experimental, standard *k*-epsilon, and modified *k*-epsilon streamline plots (Fig. 9) clearly indicate that the modification is able to predict the correct placement of the centerline primary recirculation zone and the size of the secondary recirculation behind the step. The streamline plot of the standard *k*-epsilon predictions show the

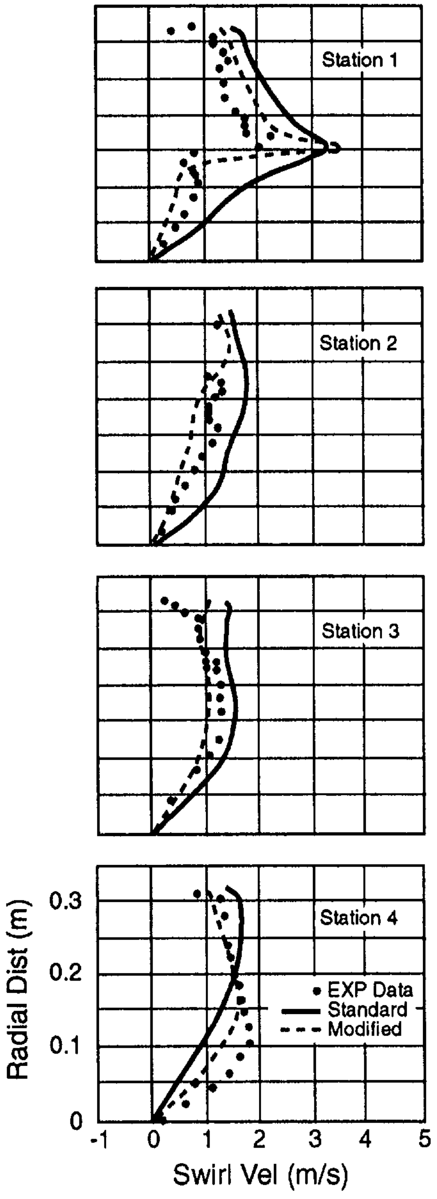

Fig. 7 Quarled burner case 2, swirl velocity predictions with the modified model

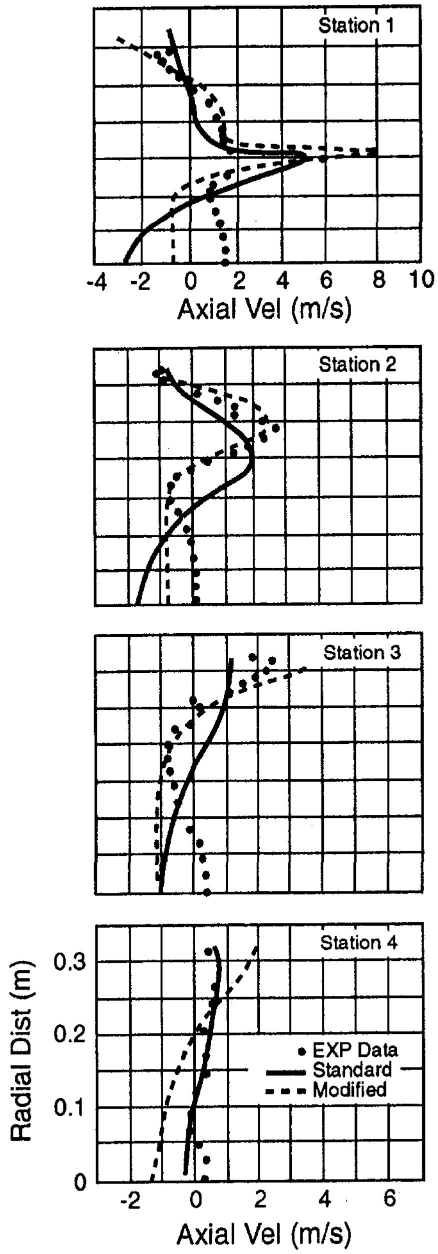

Fig. 8 Quarled burner case 2, axial velocity predictions with the modified model

stream that moves over the primary recirculation zone to be fatter than that predicted by the modified model, which indicates the failure of the standard *k*-epsilon model to predict the large gradients of swirl and axial velocity seen in this region of the flow. By maintaining the concentration of the jet momentum, the modified model is able, as in case 1, to accurately predict the location of the center of recirculation. As a result, the recirculation behind the step is also decreased.

Discussion

The improvements of the prediction of axial velocity can be attributed to the modified *k*-epsilon model's ability to control the overprediction of turbulent viscosity in regions of higher shear. Because the standard *k*-epsilon model overpredicts eddy viscosity in these regions, the momentum of the flow is diffused, resulting in the misrepresentation of the location and shape of flow features, such as the centerline recirculation zone characteristic of combustor geometries. The modified *k*-epsilon model controls this overprediction and allows the large gradients of axial and swirl velocity in regions of high shear to be preserved. Consequently, the locations and sizes of the primary flow features are better predicted.

For both test cases, in regions of greatest shear, the eddy viscosities calculated using the modified *k*-epsilon model were decreased by a factor of two, compared to the corresponding eddy viscosities calculated using the standard *k*-epsilon model. The effect this has on the calculated swirl and axial velocities is quite evident.

The changes made by the modified *k*-epsilon model improve the predictions of the major flow characteristics for the two-quarled-burner test cases. However, the improvement does not extend to making exact predictions throughout the flow. Figures 5 and 8 show that there are still inconsistencies in the axial velocity predictions between the experiments and the improved calculations. In particular, while the modified *k*-epsilon model makes great improvements in the axial velocity throughout the flow profile, it fails to predict the positive momentum measured experimentally at the centerline. One possible reason for the discrepancies in the predictions is the inability of *k*-epsilon to model highly anisotropic flows.

Studies of swirling flow entering an expansion show that the flow is highly anisotropic as it enters the expansion, with the axial velocity fluctuation dominating (Hallett and Günther, 1984). The anisotropy of the flow gives rise to a secondary centerline recirculation that opposes the primary zone flow. Because the *k*-epsilon model assumes isotropy, the modification is unable to capture this flow feature. It is noted that it is not the intention of the present model to attack *k*-epsilon inability to model anisotropy. The isotropic assumption is made in the derivation of the turbulent kinetic energy equation used in the *k*-epsilon model. Therefore, nothing can be done to remedy this problem, except to use a model that solves for the turbulent Reynolds stresses directly. These models do produce accurate results, but not without the cost of increased computational time and memory requirements. For the large and complex geometries that industrial combustion design engineers are interested

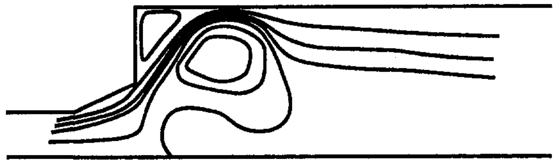

Experimental Streamlines

(*a*)

Standard k-epsilon Model Streamlines

(*b*)

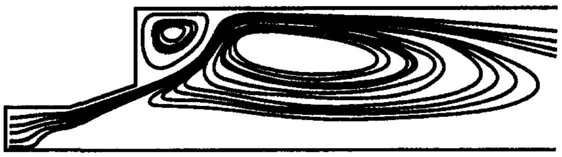

Modified k-epsilon Model Streamlines

(*c*)

Fig. 9 Quarled burner case 2: (*a*) experimental streamlines (Clarke et al., 1990); (*b*) k-epsilon model streamlines; and (*c*) modified *k*-epsilon model streamlines.

in modeling, such models are impractical. Speed and general consistency of results are of greatest importance in practical design applications. Therefore, the present modification proves to be a more acceptable option for modeling complex combustor geometries.

Conclusions

A numerical study was performed to calculate the nonreacting flows typical of industrial gas turbine combustor geometries, which contain a combination of swirling, turning, and recirculating flows. A comparison of the numerical results and experiments was made, with emphasis on investigating the effect of a modified *k*-epsilon turbulence model on the calculated flowfields. The modification added a second time scale term to the turbulent dissipation equation of the original *k*-epsilon model. This extra term will allow the turbulent energy transfer mechanism to react more effectively to mean strain. The resulting effect is a decrease in eddy viscosity in regions of high shear and an increase in regions of lower shear.

The modification improves results drastically. Comparisons of experimental and computational velocity profiles show the new model's ability to predict the peaks in swirl and axial momentum that the standard *k*-epsilon model fails to. This indicates that the modification preserves the gradients of the swirl and axial velocity, which *k*-epsilon has been shown to diffuse. The result is a significantly improved prediction of the location of the primary recirculation zone. The size of the primary recirculation zone, which was overpredicted by the standard *k*-epsilon model, is now correctly predicted by the modified model. The improvements are due to the control of the growth of eddy viscosity in regions of high shear. The standard *k*-epsilon model tends to overpredict eddy viscosity in these regions causing the diffusion of axial and swirl momentum. The modification is able to control this effect, which results in a decreased prediction of the eddy viscosity in regions of high shear.

The results presented in this paper indicate the modified *k*-epsilon model improves predictions over the standard *k*-epsilon model of turbulence. By improving velocity predictions, a more accurate representation of the locations of the characteristic recirculation zones is obtained. The prediction of the locations of recirculation zones is important to the combustion engineer, as these are the regions where flame is held. A flame front will be located at the edge of the recirculation zone. While this model has not yet been tested for reacting flows, the prediction of the location and size of recirculation regions allows the combustion engineer to predict the location of the flame, as well as hot spots, and to determine approximately how much fuel will be burned.

References

Abou-Arab, T. W., Richter, W., and Seeger, M., 1991, ''Experimental Investigation of Turbulent Isothermal Flow in a Two Dimensional Furnace Model,'' *International Journal of Engineering Fluid Mechanics*, Vol. 4, No. 1, pp. 111–126.

Braaten, M. E., 1985, ''An Introduction to Boundary Layer Theory and Turbulence Modeling,'' course notes: Power Generation Engineering, Fluid Mechanics Program, General Electric Research and Development Center, Schenectady NY.

Chen, Y. S., and Kim, S. W., 1987, ''Computation of Turbulent Flows Using an Extended k-ϵ Turbulence Closure Model,'' NASA CR-179204.

Clarke, D. S., Moore, J. R., and Wilkes, N. S., 1990, ''Prediction of Turbulent Swirling Flows Through Quarled Burners Using Reynolds Stress Turbulence Models,'' Harwell Laboratory Publication, AERE R 13726.

Dellenback, P. A., Metzger, D. E., and Neitzel, G. D., 1987, ''Heat Transfer to Turbulent Swirling Flow Through a Sudden Axisymmetric Expansion,'' *ASME Journal of Heat Transfer*, Vol. 109, pp. 613–620.

Hallett, W. L. H., and Günther, R., 1984, ''The Turbulent Structure of Swirling Flow in a Sudden Expansion,'' *Fourth Symposia on Turbulent Shear Flows*, pp. 19.25–19.28.

Haroutinian, V., and Engelman, M. S., 1993, ''Two-Equation Simulations of Turbulent Flows: A Commentary on Physical and Numerical Results,'' *Proceedings of the ASME 1993 Winter Annual Meeting*, ASME, New York.

Jones, W. P., and Launder, B. E., 1972, ''The Prediction of Laminarization with a Two-Equation Model of Turbulence,'' *International J. of Heat and Mass Transfer*, Vol. 15, pp. 301–314.

Korane, K. J., 1990, ''The Changing State of CFD,'' *Machine Design*, Vol. 62, No. 15, pp. 83–85.

Launder, B. E., and Spalding, D. B., 1974, ''Numerical Computation of Turbulent Flows,'' *Methods in Applied Mechanics and Engineering*, Vol. 3, pp. 269–289.

Lefebvre, A. H., 1983, *Gas Turbine Combustion*, Hemisphere, New York, pp. 107–151.

Moin, P., 1992, ''The Computation of Turbulence,'' *Aerospace America*, Vol. 30, No. 1, pp. 42–47.

von Neumann, J. P., and Raithby, G. D., 1984, ''Enhancement of the SIMPLE Method for Predicting Incompressible Fluid Flow,'' *Numerical Heat Transfer*, Vol. 7, pp. 147–163.

Patankar, S. V., 1980, *Numerical Heat Transfer and Fluid Flow*, Hemisphere, Washington, DC, pp. 121–133.

Raithby, G. D., and Schneider, G. E., 1979, ''Numerical Solution of Problems in Incompressible Fluid Flow: Treatment of the Velocity–Pressure Coupling,'' *Numerical Heat Transfer*, Vol. 2, pp. 417–440.

Relation, H. L., 1993, ''Application of a Modified *k*-Turbulence Model to Gas Turbine Combustor Geometries,'' MS thesis, Department of Mechanical Engineering, Virginia Tech, Blacksburg, VA.

White, F. M., 1991, *Viscous Fluid Flow*, McGraw-Hill, Inc., New York.

The Meaning of Activation Energy and Reaction Order in Autoaccelerating Systems

J. S. Ervin

S. P. Heneghan

University of Dayton Research Institute,
300 College Park,
Dayton, OH 45469-0140

Global reaction mechanisms and rate constants are commonly used in computational fluid dynamics models that incorporate chemical reactions to study aviation fuel thermal and oxidative thermal stability. Often these models are calibrated using one set of conditions, such as flow rate and temperature. New conditions are then calculated by extrapolation using the global expressions. A close inspection of the origin of global oxidation rate constants reveals that in systems that undergo autocatalysis or auto inhibition, a simple overall global activation energy and reaction order are not good descriptors of the reaction process. Furthermore, pseudo-detailed chemical kinetic modeling of a fuel that experiences autocatalysis shows that the observed reaction order for oxygen consumption varies with initial oxygen concentration, extent of reaction, and temperature. Thus, a simple global rate expression used to describe oxygen consumption in an autoaccelerating system is insufficient to allow extrapolation to different temperature or time regimes.

Introduction

Jet fuel is circulated in military aircraft for cooling. In the presence of heat and dissolved oxygen, jet fuel degrades, forming surface deposits and fouling close-tolerance valves. In time, accumulated surface deposits impair engine performance by disrupting the normal fuel flow within fuel system components (Hazlett, 1991). Moreover, the fouling of close-tolerance valves may lead to catastrophic failure of the aircraft. Since the chemical reactions in which dissolved oxygen is consumed are intimately tied to the chemical and physical processes of fouling, a fundamental understanding of dissolved oxygen consumption is imperative for proper aircraft design.

For over five decades, the thermal-oxidative stability of jet fuels generally has been studied by experiment and empirical models (Martel, 1987). However, these empirical models lack generality and offer little fundamental insight into fouling processes. Numerical solutions of the Navier-Stokes, energy, and species conservation equations are more general and can be used to predict oxygen consumption and surface deposition for different flow geometries, flow rates, and temperatures. Since fuel oxidation and deposition processes are extremely complex, global-chemistry kinetics have been used in computational simulations (Krazinski et al., 1992; Chin et al., 1994; Katta et al., 1995; Ervin et al., 1996). The global-chemistry mechanisms used in computational fluid dynamics simulations generally employ the single overall reaction

$$\text{Fuel} + O_2 \rightarrow \text{Products} \tag{1}$$

to represent fuel autoxidation. Although fuel autoxidation involves a complex series of reactions, the underlying assumption of Eq. (1) is that the overall reaction of a mixture of compounds can be represented by one rate equation. This rate equation is comprised of a rate constant multiplied by concentrations with simple order dependence, such as in Eq. (2):

$$\mathbf{RR} = -\frac{dO_2}{dt} = kO_2^N. \tag{2}$$

It is further assumed that the rate constant, k, is defined by the product of an Arrhenius A-factor (or pre-exponential) and an activation energy, as in Eq. (3):

$$k = Ae^{(-E_o/RT)}. \tag{3}$$

In previous studies that used global models to represent oxygen consumption as a single reaction, it was found that use beyond the temperature calibration regime resulted in very poor predictions of the measured mass of carbon deposits accumulated along the length of heated tubes. This was largely due to inadequate prediction of the complex process of oxygen consumption (Chin et al., 1994). Since nearly all current engineering computational fluid dynamics models of fuel oxidation and deposition use global chemistry, the underlying assumptions of the global mechanisms should be carefully considered. The objective of this paper is to demonstrate that the concepts of a single global activation energy and a single global reaction order are not well-defined in a chain branching process. It will be shown later, using simple low temperature oxidation of hydrocarbons with decomposition of the product peroxide molecules, that the global parameter E_o of Eq. (3) and the observed reaction order are functions of the initial conditions, time, and temperature.

Autoxidation Mechanism

The reaction mechanism for the oxidation of hydrocarbons has long been the discussion of numerous articles (Mayo, 1968). The intention of this paper is not to establish that one mechanism is correct, but rather to show that the global kinetic rate expression is nontrivial for a given mechanism. To accomplish this, a simple chain autoxidation mechanism that includes autocatalysis by means of a unimolecular peroxide decomposition reaction was selected. The autoxidation mechanism used in the analysis that follows is given in Table 1.

Theoretical Description

The general approach will be to first describe the rate law (**RR**) for autoxidation in terms of concentrations, temperature, and rate constant parameters, and then to apply the appropriate operators to extract activation energy and order from the rate law. The appropriate operators for activation energy, E, and oxygen reaction order, N, are given in Eqs. (4) and (5). Thus,

---

Contributed by the International Gas Turbine Institute and presented at the International Gas Turbine and Aeroengine Congress and Exhibition, Orlando, FL, June 2–5, 1997. Manuscript received by the ASME Headquarters March 7, 1997. Paper No. 97-GT-224. Associate Technical Editor: H. A. Kidd.

Table 1 Autoxidation mechanism used in present analysis

	Reaction	Reaction No.
initiation	initiation of $R^\bullet$	(1)
propagation	$R^\bullet + O_2 \rightarrow RO_2^\bullet$	(2)
	$RO_2^\bullet + RH \rightarrow RO_2H + R^\bullet$	(3)
chain-transfer/ termination reactions	$RO_2^\bullet + AH \rightarrow RO_2H + A^\bullet$	(3t)
autocatalysis	$RO_2H \rightarrow RO^\bullet + OH^\bullet$	(u)

E and N (Wylie and Barrett, 1982) applied to **RR** (Eq. (2)) yield E_o and N, respectively.

$$E = \frac{RT^2}{\mathbf{RR}} \frac{\partial}{\partial T} \tag{4}$$

$$N = \frac{O_2}{\mathbf{RR}} \frac{\partial}{\partial O_2} \tag{5}$$

Rate Law Derivation. Heneghan and Zabarnick (1994) have shown that in a strongly terminated oxidation system, such as described here, the rate of oxidation can be given by Eq. (6).

$$\mathbf{RR} = \frac{-dO_2}{dt} = \frac{k_3 \mathrm{RH} R_i}{k_{3t} \mathrm{AH}} + R_i \tag{6}$$

With the assumption of a long chain length,

$$\frac{k_3 \mathrm{RH}}{k_{3t} \mathrm{AH}} \gg 1 \tag{7}$$

the rate of oxidation can be given approximately as

$$\mathbf{RR} = \frac{-dO_2}{dt} \approx \frac{\mathrm{k_3 RH} R_i}{\mathrm{k_{3t} AH}} . \tag{8}$$

Zabarnick (1993) showed that a unimolecular decomposition reaction was adequate to show the curvature in oxygen consumption profiles observed in the experiments of Jones (1995). Thus, the rate of initiation can be given by Eq. (9).

$$R_i = k_u(O_{2(0)} - O_{2(t)}) + B \tag{9}$$

$$B = \mathrm{k_1} O^n_{2(t)} \tag{10}$$

In Eq. (9), R_i is the rate of formation of radicals, k_u is the unimolecular process associated with the decomposition of the oxidation products, and B is the baseline initiation rate given by Eq. (10). These initiation reactions have been the subject of much theorizing, but, to date, there has been no consensus on their form. In this analysis, a general reaction process is used that involves oxygen to an unknown power. It is important to note that if there is no autoacceleration ($k_u = 0$), global kinetic parameters provide an excellent description of the oxidation rates, and the activation energy is a valid parameter for extrapolation to new temperatures. In addition, it should be noted that k_1 and k_u exhibit Arrhenius behavior with regard to temperature.

Inserting R_i and B (Eqs. (9) and (10)) into the time derivative of oxygen concentration (Eq. (8)) leads to Eq. (11).

$$\mathbf{RR} = \mathrm{k}'(\mathrm{k}_u \Delta O_2 + \mathrm{k_1} O^n_{2(t)}), \tag{11}$$

where $\mathrm{k}' = (\mathrm{k_3 RH/k_{3t} AH})$, a unitless ratio, and ΔO_2 is $O_{2(0)} - O_{2(t)}$.

Activation Energy and Reaction Order. Applying the activation energy operator (Eq. (4)) to the global rate equation (Eq. (8)) yields the observed activation energy (E_o) in Eq. (12). This clearly shows that the activation energy is not a constant of the reaction process; it changes with dissolved oxygen concentration, and its rate of change varies with temperature.

$$E_o = E\mathbf{RR} = E_3 - E_{3t} + \frac{E_u k_u \Delta O_2 + E_1 k_1 O^n_{2(t)}}{k_u \Delta O_2 + k_1 O^n_{2(t)}} \tag{12}$$

The order operator can also be applied to the rate equation (Eq. (8)) to yield the observed order (N) of Eq. (13). The order of the reaction shows behavior similar to the activation energy in that it depends upon the progress of the reaction.

$$N = N\mathbf{RR} = \frac{-k_u O_{2(t)} + n k_1 O^n_{2(t)}}{k_u \Delta O_2 + k_1 O^n_{2(t)}} \tag{13}$$

Discussion

In general, the activation energy (Eq. (12)) for the process is the difference of the activation energy for propagation and termination plus the average of E_1 and E_u weighted by the corresponding rate of reaction (1) and reaction (u) of Table 1. At time zero ($O_{2(0)} = O_{2(t)}$), the acceleration reaction is not occurring, so that the average is E_1. As time progresses and O_2 decreases, ΔO_2 increases and the average approaches E_u. Therefore, the activation energy starts at $E_3 - E_{3t} + E_1$ and monotonically increases or decreases to $E_3 - E_{3t} + E_u$. (It is noted that if E_1 is equal to E_u, E_o remains constant.)

The order for the reaction is much more complicated. N is shown in Eq. (14) for time zero (also substituting B from Eq. (10)). This shows that the initial rate depends not only on the ratio of k_u, the acceleration rate, and baseline initiation rate B

Nomenclature

A = pre-exponential multiplier in rate constant expression
$A^\bullet$ = antioxidant radical
AH = antioxidant species
AO_2 = antioxidant peroxy radical
B = the baseline rate of radical formation
E = Arrhenius activation energy
E_o = observed activation energy
E = Arrhenius activation energy operator
I = initiator species
k = Arrhenius rate constant
M = molarity, moles/L
N = observed reaction order
n = oxygen reaction order of the initiation reactions
N = reaction order operator
$O_{2(t)}$ = dissolved oxygen concentration at time t
R = universal gas constant
$R^\bullet$ = alkyl radical species
R_i = rate of formation of radicals
RR = rate law for the loss of oxygen ($-dO_2/dt$)
RH = bulk hydrocarbon fuel
$RO^\bullet$ = alkoxy radical
$RO_2^\bullet$ = peroxy radical
RO_2H = hydroperoxide
R_{prime} = alkyl radical
SH = hydroperoxide decomposer
T = temperature
t = time
θ = the product 2.303RT

($k_1 O^n_{2(0)}$), but also on the initial value of the oxygen concentration $O_{2(0)}$. The ratio of k_u and B is evaluated using rates from Chin et al. (1994) in Eq. (15).

$$N = \frac{-k_u O_{2(0)}}{B} + n. \tag{14}$$

$$\log\left(\frac{k_u}{B}\right) = (14.8 - 40/\theta) - (11.3 - 35.8/\theta)$$

$$= 3.5 - 4.2/\theta \tag{15}$$

In Eq. (15), θ is defined as the product 2.303RT. Equations (14) and (15) show that N is -0.1 for n equal to zero at a normal air saturation concentration of oxygen ($O_{2(0)} = 1.8 \times 10^{-3}$ M, where M is molarity in moles/L) and at a temperature of 185°C. However, N approaches zero with decreasing temperature.

To support the previous analysis and to further demonstrate that the concept of a simple overall global reaction order is unclear for an autoaccelerating system, pseudo-detailed chemical kinetic modeling was performed using the mechanism of Table 2. The model is pseudo-detailed in the sense that the chemical kinetics of oxygen consumption are described using several reactions that represent the dominant chemistry, rather than hundreds of reactions as might be found in a detailed model. All rate parameters given in Table 2 are taken from Zabarnick (1996), who used this mechanism to successfully reproduce the chain mechanism that is responsible for oxygen consumption in hydrocarbon fuels. The initiation step (reaction 1 of Table 2) is assumed to occur by unimolecular decomposition of an initiating species, I. This is a simple representation of an inadequately understood initiation process, but it is used to begin the chain with a low production rate of $R^\bullet$ radicals (Zabarnick, 1993, 1996) that becomes negligible once the autoxidation chain begins. Thus, for reaction 1, a small Arrhenius A-factor of 0.001 s^{-1} was chosen along with an activation energy of zero. Using the parameters of Table 2, Zabarnick (1996) predicted oxygen concentrations that compared favorably with the near-isothermal experiments of Jones (1996) and with experiments in which the antioxidant concentration was varied (Zabarnick, 1996). In addition, a similar mechanism was used to predict dissolved oxygen consumption and hydroperoxide production in the nonisothermal flow studies of Ervin et al. (1997). The salient feature of the mechanism of Table 2 is that it permits alkyl hydroperoxide decomposition, and, thus, can be used to simulate autocatalysis.

Table 2 Reaction mechanism used for pseudo-detailed kinetic modeling (Zabarnick, 1996)

Reaction	Arrhenius A-factor (mol, L, and S)	Activation Energy (kcal/mol)	Reaction No.
$I \rightarrow R^\bullet$	0.001	0	(1)
$R^\bullet + O_2 \rightarrow RO_2^\bullet$	3 x 10^9	0	(2)
$RO_2^\bullet + RH \rightarrow R\,O_2H + R^\bullet$	3 x 10^9	12	(3)
$RO_2^\bullet + RO_2^\bullet \rightarrow$ termination	3 x 10^9	0	(4)
$RO_2^\bullet + AH \rightarrow R\,O_2H + A^\bullet$	3 x 10^9	5	(5)
$AO_2^\bullet + RH \rightarrow AO_2H + R^\bullet$	3 x 10^5	10	(6)
$A^\bullet + O_2 \rightarrow AO_2^\bullet$	3 x 10^9	0	(7)
$AO_2^\bullet + AH \rightarrow A\,O_2H + A^\bullet$	3 x 10^9	6	(8)
$AO_2^\bullet + AO_2^\bullet \rightarrow$ products	3 x 10^9	0	(9)
$R^\bullet + R^\bullet \rightarrow R_2$	3 x 10^9	0	(10)
$RO_2H \rightarrow RO^\bullet + {}^\bullet OH$	1 x 10^{15}	42	(11)
$RO^\bullet + RH \rightarrow ROH + R^\bullet$	3 x 10^9	10	(12)
$RO^\bullet \rightarrow R_{prime}^\bullet$ + carbonyl	1 x 10^{16}	15	(13)
${}^\bullet OH + RH \rightarrow H_2O + R^\bullet$	3 x 10^9	10	(14)
$RO^\bullet + RO^\bullet \rightarrow$ termination	3 x 10^9	0	(15)
$R_{prime}^\bullet + RH \rightarrow$ alkane $+ R^\bullet$	3 x 10^9	10	(16)
$RO_2H + SH \rightarrow$ products	3 x 10^9	0	(17)

With the assumption of an isothermal reacting system, the time-varying species concentrations were found numerically by a finite difference solution of the coupled ordinary differential equations that arise from the mechanism of Table 2. The following were input to the numerical code: the activation energies and pre-exponential multipliers of Table 2, concentrations (O_2, AH, RH, SH, and I) for each species at time zero, reaction temperature and time, and the grid resolution. Three different fractions (10, 50, and 100 percent) of the normal air saturation concentration (1.8×10^{-3} M at 25°C) estimated from tabulated jet fuel properties (Coordinating Research Council, 1983) were used as initial oxygen concentrations for each temperature of interest. The RH concentration was estimated from the molarity of liquid jet fuel (average molecular weight of 170 amu and a density of 0.684 g/cm^3 at 185°C, for example) in this temperature range (Coordinating Research Council, 1983), and a small I concentration (1.0×10^{-7} M) was used to initiate the chain. The temperatures chosen for the simulations were 185°C and 215°C. It is expected from the value of the activation energy associated with reaction 11 of Table 2 that the production rate of radicals by hydroperoxide decomposition will be much more significant at 215°C than at 185°C. Thus, the effects of autoacceleration are expected to be more substantial at the higher temperature. The computational grid was uniformly spaced in time using a maximum of 400 nodes, and the equations were solved sequentially in an iterative manner. More refined computational grids resulted in negligible changes in the computed values. The solution was considered to be converged when the computed residuals for the species decreased by six orders of magnitude. Using the rate parameters given in Zabarnick (1996), it was found that the numerical procedure described here could reproduce the oxygen profiles computed by Zabarnick (1996), who used an entirely different solution technique.

For completeness, two kinds of computations were performed: those for an inhibited system and those for a completely noninhibited system. For the inhibited system, the initial AH concentration was 2.3×10^{-4} M, which is a representative value for jet fuels (Zabarnick, 1993; Heneghan and Zabarnick, 1994). For the completely uninhibited case, which could represent autoxidation in a severely hydrotreated fuel, the AH concentration was set equal to 0 M. For simplicity, SH, the hydroperoxide decomposer, was assumed to be zero in all computations. Such simulations have been found to represent autoxidation well in a fuel that is low in heteroatomic species (Ervin et al., 1997). In the figures that follow, three different fractions (10, 50, and 100 percent) of the normal air saturation

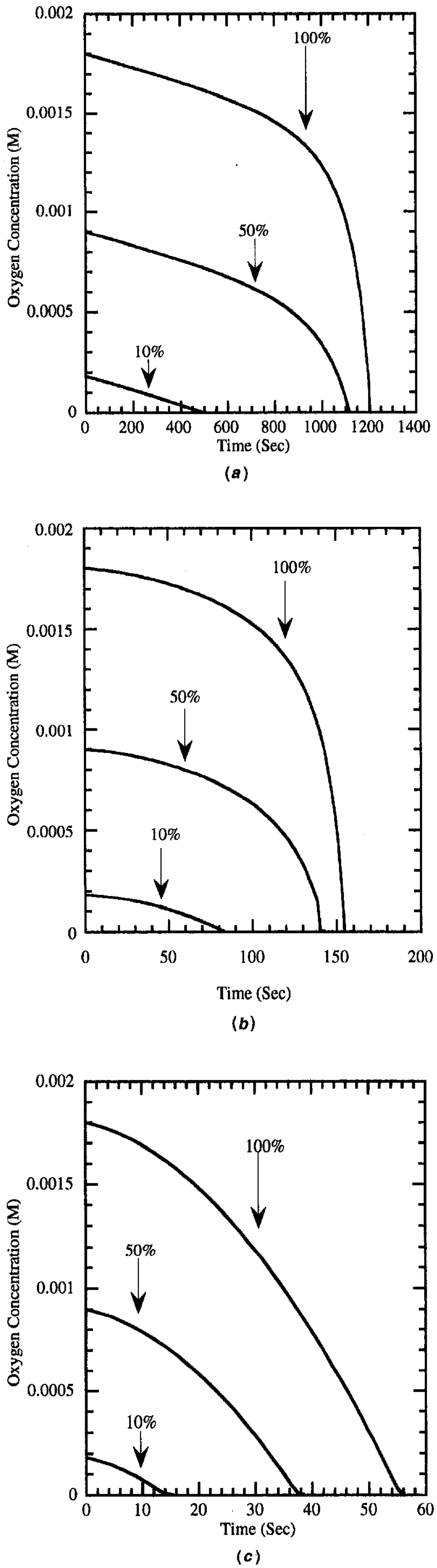

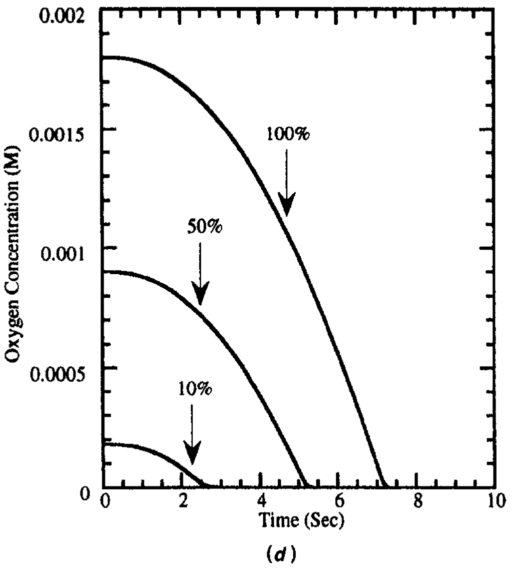

Fig. 1(*a*) Decay of oxygen concentration with time for different initial oxygen concentrations at 185°C & antioxidant concentration of 2.3 × 10^{-4} M; (*b*) decay of oxygen concentration with time for different initial oxygen concentrations at 215°C and antioxidant concentration of 2.3 × 10^{-4} M; (*c*) Decay of oxygen concentration with time for different initial oxygen concentrations at 185°C and antioxidant concentration of 0 M; and (*d*) decay of oxygen concentration with time for different initial oxygen concentrations at 215°C and antioxidant concentration of 0 M.

concentration are given as initial oxygen concentrations. Figures 1(*a*) through (*d*) show the computed decay profiles of dissolved oxygen concentration.

Figures 1(*a*) and 1(*b*) show the computed decay profiles of dissolved oxygen concentration for fuel with an initial antioxidant concentration of 2.3 × 10^{-4} M. As expected, as the temperature is increased from 185°C (Fig. 1(*a*)) to 215°C (Fig. 1(*b*)), the time required for complete depletion of the dissolved oxygen for each initial oxygen concentration decreases. The enhanced oxygen consumption rate with increasing temperature is primarily due to the temperature dependence of reactions 3 and 11 of Table 2. In this temperature range, the alkyl hydroperoxides produced in reaction 3 of Table 2 decompose, generating radi-

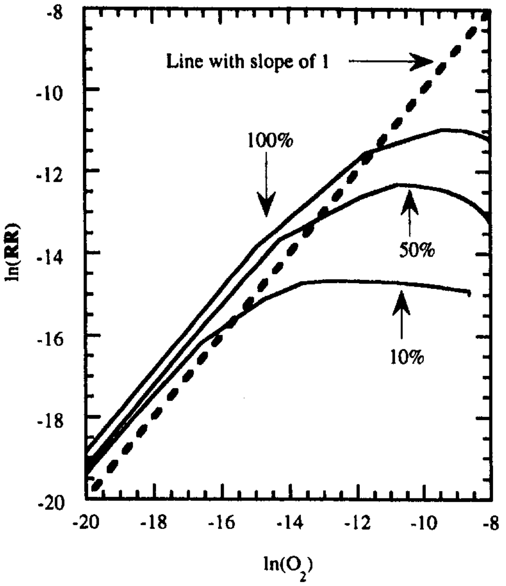

Fig. 2 Observed order plot for different initial oxygen concentrations. 185°C and antioxidant concentration of 2.3 × 10^{-4}M.

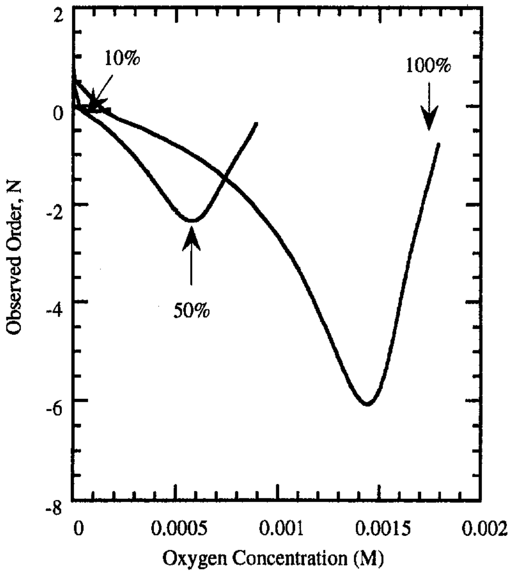

(*a*)

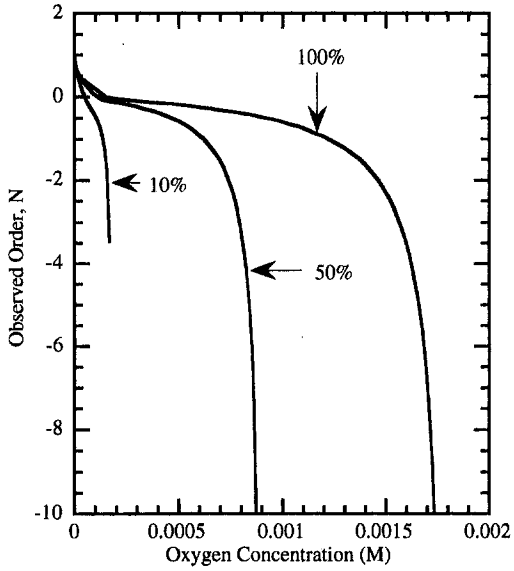

(*c*)

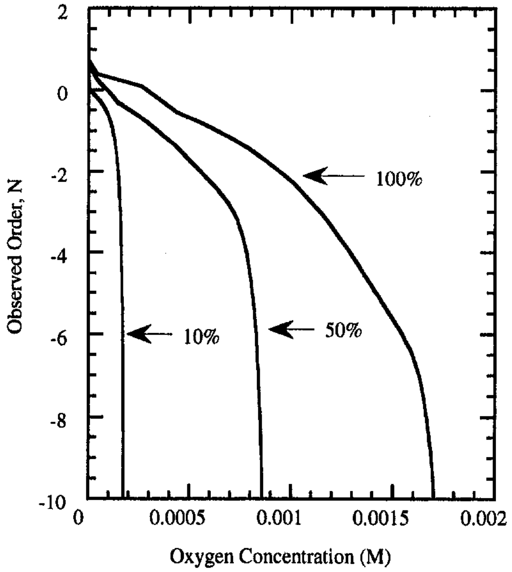

(*b*)

Fig. 3(*a*) Variation of *N* with oxygen consumption for different initial oxygen concentrations. 185°C and antioxidant concentration of 2.3 × 10^{-4} M; (*b*) Variation of *N* with oxygen consumption for different initial oxygen concentrations. 215°C and antioxidant concentration of 2.3 × 10^{-4} M; and (*c*) variation of *N* with oxygen consumption for different initial oxygen concentrations. 185°C and antioxidant concentration of 0 M.

cals (reaction 11) that greatly increase the rate of oxygen removal.

Figures 1(*c*) and 1(*d*) (fuel temperatures of 185°C and 215°C, respectively) show dissolved oxygen decay profiles resulting from a zero AH concentration. Given the same temperature and initial dissolved oxygen concentration, the dissolved oxygen is reacted at a significantly greater rate with the noninhibited system than with the presence of AH (Figures 1(*a*) and 1(*b*)). The decrease in oxygen decay rate associated with the fuel containing the antioxidant occurs because AH acts to interfere with the chain propagation. Again, as in Figures 1(*a*) and 1(*b*), as the temperature is increased from 185°C to 215°C, the time period required for complete oxygen removal decreases because the rate of alkyl hydroperoxide decomposition significantly increases as the temperature is increased. As observed by Zabarnick (1993) in numerical simulations and by Jones et al. (1995) in nearly isothermal flowing experiments, autocatalysis is characterized by curvature of the oxygen decay profile. Thus, at 185°C, the oxygen profile is nearly linear, and the nonlinearity increases at 215°C as the rate of alkyl hydroperoxide decomposition rises. Similarly, for the fuel containing antioxidants, the oxygen decay profile is nearly linear for much of the period before oxygen depletion at 185°C (Fig. 1(*a*)), and the nonlinearity increases at 215°C (Fig. 1(*b*)).

If an initial oxygen concentration is established and then followed in time by either experiment or computational simulation, a functional relationship between O_2 and time for a given set of conditions can be established. The rate (**RR**) can be calculated from the time derivative of the computed oxygen concentration, and the observed order can be found from the plot of ln (**RR**) versus ln (O_2). Values of ln (**RR**) for three different initial oxygen concentrations at a temperature of 185°C and AH concentration of 2.3 × 10^{-4} M are given in Fig. 2. Figure 2 shows that d ln (**RR**)/d ln (O_2), the observed order, changes continuously for each O_2 curve until the dissolved oxygen is significantly diminished. As the three curves converge, they are more linear with a slope that approaches unity. Thus, Fig. 2 shows that the observed order depends on both the initial and remaining dissolved oxygen concentrations.

More explicitly for the three different initial oxygen concentrations at 185°C, Fig. 3(*a*) gives values of *N* resulting from the calculation of d ln (**RR**)/d ln (O_2) as part of the finite difference computations. (These values of *N* may also be derived from Fig. 2 by taking tangents to the curves shown.) Figure 3(*a*) shows that *N* changes in a complicated manner with O_2 concentration which also decreases with time: *N* is a small negative number at time zero, and then approaches unity as the oxygen nears depletion. Thus, Fig. 3(*a*) reveals that a constant overall reaction order cannot represent the observed behavior of this autoaccelerating system. (In practice, the overall reaction order is some *N* selected at an arbitrary time that is often near time zero). Furthermore, Fig. 3(*a*) shows that *N* varies with the initial oxygen concentration. Figure 3(*b*) at a temperature of 215°C shows that *N* again is different for different initial oxygen concentrations and varies with the concentration of unreacted dissolved oxygen. At 215°C, where the hydroperoxide decomposition reactions become more important, *N* is initially a negative number and remains negative over much of the oxygen consumption history. For small oxygen concentrations, *N* becomes equal to unity. Thus, the behavior of *N* is very different from that observed at 185°C. Figures 3(*a*) and (*b*) show that the observed reaction order depends strongly on temperature, initial oxygen concentration, and the extent of reaction.

Figure 3(*c*) shows that *N* changes with initial O_2 concentration and the extent of O_2 consumption for conditions in which the initial AH concentration is zero at a reaction temperature of 185°C. In Fig. 3(*c*), *N* is negative near time zero but approaches unity for dissolved oxygen concentrations that fall below 0.0001 M. For conditions of zero antioxidant and a temperature of 215°C (not shown), the computed *N* values were negative near time zero but approached unity for small dissolved oxygen concentrations in a manner similar to that observed at the lower temperature in Fig. 3(*c*). Figures 3(*a*), (*b*), and (*c*) show that the value for the overall reaction order is dependent on how the order is measured. Thus, to determine the order of the initiation reactions, it is insufficient to follow the rate and the oxygen concentration in time and extrapolate the observed *N* back to time zero.

For simplicity, some engineering computational fluid dynamics codes that use global chemistry assume an overall reaction order for oxygen consumption of unity (Krazinski et al., 1992). Others (Chin et al., 1994; Ervin et al., 1996) permit a step change in the global order. These models ignore the initiation region of the observed order curve (Fig. 3(*c*), for example) and assume that the overall reaction order is 0 until the O_2 is reduced to some arbitrary critical concentration. At this low concentration, the order is set equal to unity. For initial dissolved O_2 concentrations of 100 percent and 50 percent of normal air saturation, Fig. 3(*c*) (with zero initial AH) demonstrates that an overall zero order reaction over much of the oxygen profile at 185°C, with a change to an overall first order reaction, is a reasonable first approximation to the more detailed modeling. As the temperature is increased, the rate of peroxide decomposition will also increase, and the effects of autoacceleration on *N* are more significant. In addition, Fig. 3(*c*) shows that for small initial dissolved oxygen concentrations (here, on the order of 0.0001 M) that very little of the oxygen decay profile is characterized by an *N* of zero. Furthermore, with the nonzero antioxidant concentration for both temperatures (Figs. 3(*a*) and (*b*)), it is obvious that assuming either an overall constant first order reaction or a zero order reaction that then switches to a first order reaction will be different from the *N* given by the pseudo-detailed kinetic modeling. Thus, as the fuel is heated to greater temperatures, or if antioxidants are used, the explicit form for the global order will not be simple. Moreover, Figs. 3(*a*) through (*c*) suggest that the error in using a simple overall global expression for oxygen consumption may be large.

Conclusions

Analysis and numerical simulation of low temperature oxidation of a hydrocarbon fuel have been used to show that a single overall activation energy and observed order are functions of the initial conditions, time, and temperature. The activation energy and the reaction order both depend on the initial concentration of dissolved oxygen and the concentration remaining. Applying the operator for activation energy and reaction order to the rate law for a complicated (autoaccelerating) rate does not necessarily yield a simple activation energy or reaction order, as might be expected from a global reaction rate law. Consequently, the activation energy or the reaction order of such a reaction process are not well defined concepts, and referring to them in the classical manner is incorrect. Furthermore, using these concepts to extrapolate data in time or temperature will likely yield erroneous results. These findings have important implications for the use of simple global parameters in engineering computational fluid dynamics models that simulate autoaccelerating systems. Pseudo-detailed kinetic mechanisms for oxygen consumption (as in Table 2) have been found in previous works to predict reasonably well oxygen consumption measurements. As a practical consequence, pseudo-detailed global models may be used to represent autoxidation instead of a single, simplistic reaction that may fail to represent a complex series of reactions.

Acknowledgments

This work was supported by the US Air Force, Fuels and Lubrication Division, Aero Propulsion and Power Directorate, Wright Laboratory, WPAFB, under Contract No. F33615-92-C-2207 (Technical Monitor: C. W. Frayne). The authors acknowledge the many beneficial discussions with Dr. S. Zabarnick of the University of Dayton Research Institute.

References

Chin, L. P., Katta, V. R., and Heneghan, S. P., 1994, "Numerical Modeling of Jet Fuel Autoxidation in Flowing Systems," *ACS Preprints, Div. of Petroleum Chemistry,* Vol. 39, p. 19.

Coordinating Research Council, 1983, *Handbook of Aviation Fuel Properties,* Coordinating Research Council, Atlanta, GA.

Ervin, J. S., Williams, T. F., and Katta, V. R., 1996, "Global Kinetic Modeling of Aviation Fuel Fouling in Cooled Regions in a Flowing System," *Ind. Eng. Chem. Res.,* Vol. 35, p. 4028.

Ervin, J. S., Zabarnick, S., and Williams, T. F., 1997, "Modeling of Jet Fuel Oxidation at Low Temperatures," AIAA 97-0272, AIAA 35th Aerospace Sciences Meeting, Reno, NV, Jan. 1997.

Hazlett, R. N., 1991, *Thermal Oxidative Stability of Aviation Turbine Fuels,* ASTM, Philadelphia, PA.

Heneghan, S. P., and Zabarnick, S., 1994, "Oxidation of Jet Fuels and Formation of Deposits," *Fuel,* Vol. 73, p. 35.

Katta, V. R., Blust, J., Williams, T. F., and Martel, C. R., 1995, "Role of Buoyancy in Fuel-Thermal Stability Studies," *J. of Thermophysics and Heat Transfer,* Vol. 9, p. 159.

Krazinski, J. L., Vanka, S. P., Pearce, J. A., and Roquemore, W. M., 1992, "A Computational Fluid Dynamics Model for Jet Fuel Thermal Stability," ASME JOURNAL OF ENGINEERING FOR GAS TURBINE AND POWER, Vol. 114, p. 104.

Jones, E. G., Balster, W. J., and Post, M. E., 1995, "Thermal Degradation of Jet-A Fuel in a Single Pass Heat Exchanger," ASME JOURNAL OF ENGINEERING FOR GAS TURBINE AND POWER, Vol. 117, p. 125.

Jones, E. G., Balster, W. J., and Rubey, W. A., 1995, "Fouling of Stainless Steel and Silcosteel Surfaces During Aviation-Fuel Autoxidation," *ACS Preprints, Div. of Petroleum Chemistry,* Vol. 40, p. 660.

Jones, E. G., Balster, L. M., and Balster, W. J., 1996, "Thermal Stability of Jet A Fuel Blends," *Energy and Fuels,* Vol. 10, p. 509.

Martel, C. R., 1987, "Military Jet Fuels, 1944–1987," Air Force Wright Aeronautical Laboratory Technical Report AFWAL-TR-87-2062, Wright-Patterson Air Force Base, OH.

Mayo, F. R., 1968, "Free-Radical Autoxidations of Hydrocarbons," *Acc. Chem. Res.,* Vol. 1, p. 193.

Wylie, C., and Barrett, L., 1982, *Advanced Engineering Mathematics,* McGraw-Hill, New York.

Zabarnick, S., 1993, "Chemical Kinetic Modeling of Jet Fuel Autoxidation and Antioxidant Chemistry," *Ind. Eng. Chem. Res.,* Vol. 32, p. 1012.

Zabarnick, S., 1998, "Chemical Kinetic Modeling of Jet Fuel Autoxidation and Antioxidant Chemistry," *Energy and Fuels,* Vol. 12, p. 547.

T. Nakata
Fulbright Scholar.
Lawrence Livermore National Laboratory,
P. O. Box 808, L-644,
Livermore, CA 94550

M. Sato

T. Hasegawa

Central Research Institute of
Electric Power Industry,
Yokosuka 24001,
Japan

Reaction of Fuel NO_x Formation for Gas Turbine Conditions

Ammonia contained in coal-gasified fuel is converted to nitrogen oxides (NO_x) in the combustion process of a gas turbine in integrated coal gasification combined cycle (IGCC) system. Research data on fuel-NO_x formation are insufficient, and there still remains a wide explored domain. The present research aims at obtaining fundamental knowledge of fuel-NO_x formation characteristics by applying reaction kinetics to gas turbine conditions. An instantaneous mixing condition was assumed in the cross section of a gas turbine combustor and both gradual mixing condition and instantaneous mixing condition were assumed at secondary air inlet section. The results may be summarized as follows: (1) in the primary combustion zone under fuel rich condition, HCN and other intermediate products are formed as ammonia contained in the fuel decomposes; (2) formation characteristics of fuel-NO_x are affected by the condition of secondary air mixing; and (3) the conversion ratio from ammonia to NO_x declines as the pressure inside the combustor rises under the condition of gradual mixing at the secondary air inlet. These results obtained agreed approximately with the experimentation.

Introduction

Coal, our most abundant fossil fuel resource, is coming of age in gas turbine power generation with the presently perceived abundance of natural gas, technologies that use coal as a fuel for gas turbines are being vigorously pursued. Integrated coal gasification combined cycle (IGCC) is a system in which coal is partially oxidized in air or oxygen to produce a mixture of CO and H_2, called synthesis gas, that is used as fuel for a gas turbine. Reduction of NO_x emissions and increasing the inlet temperature of gas turbines are the most significant issues in the gas turbine development.

The coal gasified fuel, which is produced in a coal gasifier of air-blown entrained flow-type has a calorific value as low as $\frac{1}{10}$ of that of natural gas. Furthermore, the fuel contains ammonia when a gas cleaning system is a hot type, and ammonia will be converted to nitrogen oxides (NO_x) in the combustion process of a gas turbine. Since the flame temperature is low, only a small amount of thermal NO_x is produced. However, a large amount of fuel NO_x will be produced (Sato et al., 1990a).

Sato et al. (1990b) have conducted experimental research on the effect of fuel composition and equivalence ratio on the fuel NO_x emission characteristics using a small-scale diffusion burner. Yamauchi et al. (1991) studied the effect of hydrocarbon components contained in the fuel on fuel-NO_x formation characteristics by considering the reaction kinetics.

Moreover, models for predicting NO_x emission in a gas turbine combustor have been proposed by many researchers including Fletcher and Heywood (1971) and Mizutani and Katsuki (1976). Since fuels with low fuel-compound nitrogen are generally used in gas turbine combustors, reaction term of fuel NO_x formation is not taken into account in those models.

The present research aims at obtaining more fundamental knowledge by applying the elementary reaction kinetics to gas turbine conditions. Furthermore, since the mixing conditions of secondary air inlet are expected to have a significant effect on fuel NO_x formation characteristics, four different models in which mixing time is changed are introduced. Additionally, the effect of combustion conditions, methane concentration in the fuel and pressure inside the combustor on fuel NO_x formation are examined. The kinetics results are compared with those obtained in the combustion test conducted on a 1300°C-class gas turbine combustor for use in IGCC.

Calculation Models

Reaction Model and Kinetics Calculation. The standard composition of a low calorific coal gasified fuel is shown in Table 1. Main combustible components are CO and H_2. The fuel also contains a small amount of methane and ammonia.

The scheme of the elementary reaction equations and the reaction rate coefficients describing fuel NO_x formation are those proposed by Miller and Bowman (1989). We have ascertained the performance of these reaction rate data through extensive investigation. The scheme is composed of 234 elementary reaction equations. A total of 50 chemical species are considered: CH_4, CH_3, CH_3O, CH_2OH, CH_2O, CH_2, CH, CO, CO_2, C, H_2, H, O, OH, O_2, H_2O, HO_2, H_2O_2, N_2, N, NO, NO_2, N_2O, HCN, CN, H_2CN, NH_3, NH_2, NH, NNH, HNO, HCNO, HOCN, HNCO, NCO, C_2N_2, HCO, CH_2CO, C_2H, C_2H_2, C_2H_3, C_2H_4, C_2H_5, C_2H_6, HCCO, HCCOH, C_3H_2, C_3H_3, C_4H_2 and C_4H_3. Thermodynamic data are taken from the JANAF Thermochemical Tables (Chase et al., 1985). Some specific data such as intermediate properties not shown in the above tables are calculated by applying the CHEMKIN Thermodynamic Data Base (Kee et al., 1992).

In the kinetics calculation, the GEAR is used as an ordinary differential equation system solver (Hindmarch, 1974). The GEAR, an implicit multistage solution, is known to be an extremely effective numerical solver in particularly stiffness problems.

Gas Turbine Combustor Modeling. Inside the gas turbine combustor, uneven combustion occurs with a complicated, high-speed swirling flow. Thus, in making a reaction model of a gas turbine combustor, it is necessary to take into account such factors as flow, diffusion, and radiant heat transfer of the flame. However, we introduce the simplified mixing model since studying the fundamental characteristics of fuel NO_x formation is the main objective in this study. This report does not take into account either the effect of diffusion or of heat transfer.

Figure 1 shows the typical outline of the 1300°C-class gas turbine combustor designed by Mandai et al. (1991) for use

---

Contributed by the International Gas Turbine Institute and presented at the 4th ASME/JSME Thermal Engineering Joint Conference, 1995 ASME/JSME/JSES International Solar Energy Conference, Maui, HI, March 19–24, 1995. Manuscript received by the ASME Headquarters September 20, 1997. Technical Editor: H. L. Julien.

Table 1 Standard composition of the coal gasified fuel

Composition	CO	18.3 %
	H_2	6.9 %
	CH_4	2.5 %
	CO_2	15.9 %
	N_2	56.3 %
	NH_3	1000 ppm
	HHV	4190 kJ/m^3N
	LHV	3950 kJ/m^3N

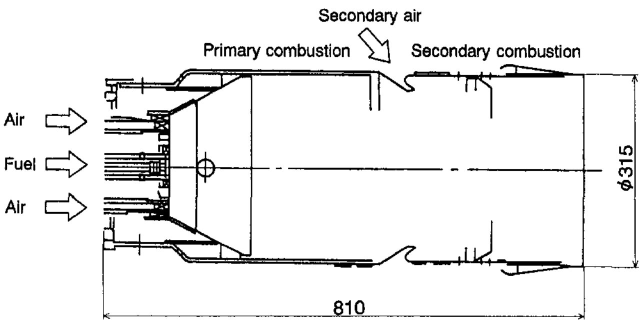

Fig. 1 Gas turbine combustor for this study

in IGCC system. This combustor is designed to produce low emissions of NO_x, a class of pollutant that is increasingly restricted in many countries. This combustor, 810 mm in total length and 315 mm in inside diameter, corresponds to one can of multican-type combustor of a 150 MW-class gas turbine. To achieve flame stabilization firing low calorific gas, fuel and air are fed at swirling angles of 45 deg and 40 deg, respectively. Also, to restrain the formation of fuel NO_x, two-stage combustion is designed under which the equivalence ratio of the primary combustion zone is set at a fuel-rich condition of 1.6. Combusting mixed fuel and air under fuel rich condition keeps the primary chamber in deoxidization atmosphere, reducing NO_x formation. The primary combustion chamber is thermal barrier coated and convection cooled. The combustion load rate is about 320 $W/(m^3 \cdot Pa)$. Inlet air temperature is set at 643 K and the pressure is set at 0.1 MPa.

The air distribution of the combustor is shown in Fig. 2. It is calculated by considering the opening area of each air hole and the coefficient of discharge.

The air bypass valve shown in Fig. 3 is installed at the transition piece of the combustion system. The amount of air that flows into the front stage of the combustor is adjusted by opening the bypass valve. It is possible to alter the equivalence ratio in combustion chamber continuously. About half of the air flows directly into the transition piece when the bypass valve is open.

The reaction time is ascertained by using the adiabatic flame temperature as the mixing gas temperature on the assumption that the air that flows through each air hole is mixed instantaneously with the main flow at each cross section. In this way, the relationship between the resident time of the air-fuel mixture and the equivalence ratio is obtained (Fig. 4(*a*)). This indicates that the equivalence ratio shifts from fuel-rich to fuel-lean condition with a resident time of about 8 ms in between. With this characteristic in mind, the present research considers the following calculation models:

- the combustor, which consists of a primary combustion zone and a secondary zone, can be expressed by modular model where each zone means a stirred reactor (Pratt et al., 1971);
- the total reaction time is 20 ms; 10 ms for the primary combustion zone and the same for the secondary zone;
- the equivalence ratio in the primary combustion zone is fixed, while the equivalence ratio at the outlet of the combustor is set at 0.5, which corresponds to the adiabatic flame temperature of 1573 K (1300°C);
- The reaction temperature in the primary zone is regarded as the adiabatic flame temperature corresponding to the designed equivalence ratio. At the same time, irrespective of the mixing conditions of secondary air, the reaction temperature in the secondary combustion zone is set at 1573 K.

According to the rapid mixing of secondary air, intermediate products such as NHi and HCN formed in the primary combustion zone are expected to be converted to NO (Takagi et al., 1978). The following four cases are thus assumed for the distribution of equivalence ratios in the secondary combustion zone—from case a where the mixing takes place instantaneously to cases *b*, *c* and *d*, where, given the delay in mixing of secondary air, the mixing takes place in stages:

- case *a*: where the secondary air mixes instantaneously;
- case *b*: where the secondary air mixes in five steps within a span of 2 ms, from 10 ms to 12 ms;
- case *c*: where the secondary air mixes in five steps within a span of 10 ms, from 10 ms to 20 ms;
- case *d*: where the secondary air mixes in ten steps within a span of 10 ms, from 10 ms to 20 ms.

Figure 4(*b*) shows the equivalence ratio distribution for each case when the primary equivalence ratio ϕ is set at 1.6.

Calculation Results and Discussion

Basic Characteristics of Fuel NO_x Formation. Shown here are the basic characteristics of fuel NO_x formation obtained by kinetics calculations using 248 elementary reaction equations (Nakata, 1993). Figure 5 shows the behavior over time of typical chemical species under 1500 K temperature and stoichiometric condition. The vertical axis represents the mole fraction of each species when the initial fraction of the fuel is set at 1

Nomenclature

C.R. = conversion ratio from ammonia to NO_x
HHV = higher heating value of the fuel kJ/m^3
LHV = lower heating value of the fuel kJ/m^3
P = pressure inside the combustor MPa
T = reaction temperature K
Tadia = adiabatic flame temperature K
TFN = total fixed nitrogen (=NO + NH_3 + HCN)
t = reaction time ms
ϕ = equivalence ratio

Subscripts

1 = primary combustion zone
2 = secondary combustion zone
ex = combustor exit

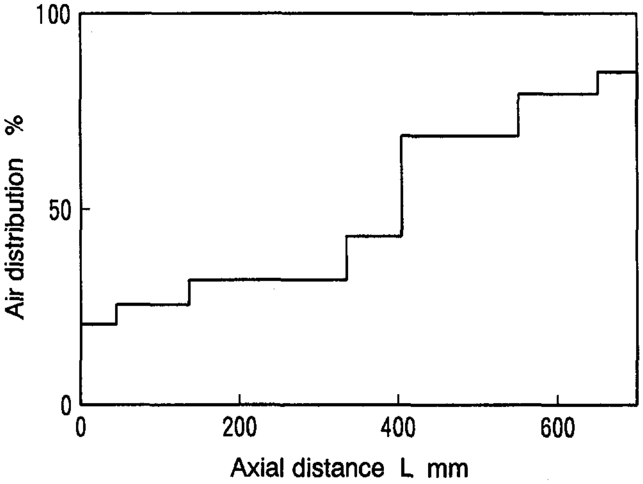

Fig. 2 Air distribution of the combustor

mole. The decomposition of ammonia advances rapidly from about 0.01 ms after the commencement of the reaction, and most of it is converted to NO within about 0.1 ms. Before the decomposition of ammonia, radical chemical species O, H, and OH are formed rapidly, followed by the formation of NH_2 and NH. Thus, the ammonia in the fuel is believed to react with OH and other radical species and decompose to NHi, then convert to NO. Following the decomposition of methane and ammonia, the intermediate product HCN begins to increase after an interval of about 0.01 ms. It decreases together with the formation of NO after that. CO and H_2 begin to react more slowly than methane.

Figure 6 illustrates the characteristics of NO formation when the temperature is altered. It shows that the NO formation rate increases at the higher reaction temperature. Especially, at 2000 K and higher, fuel NO is formed rapidly, followed by the formation of Zeldovich NO. Conversely, when the reaction temperature falls to 800 K, the decomposition reaction of ammonia becomes stagnant, resulting in little NO formation.

Formation Behavior of NH_3, NO_x, and HCN in the Primary Combustion Zone. Shown here are the calculation results of the formation behavior of intermediate products such as NH_3, NO, and HCN, when the reaction time is 10 ms and the primary combustion zone is assumed. The mole fraction of fuel NO is obtained by subtracting the thermal NO calculated when ammonia is not added to the fuel from the total amount of NO.

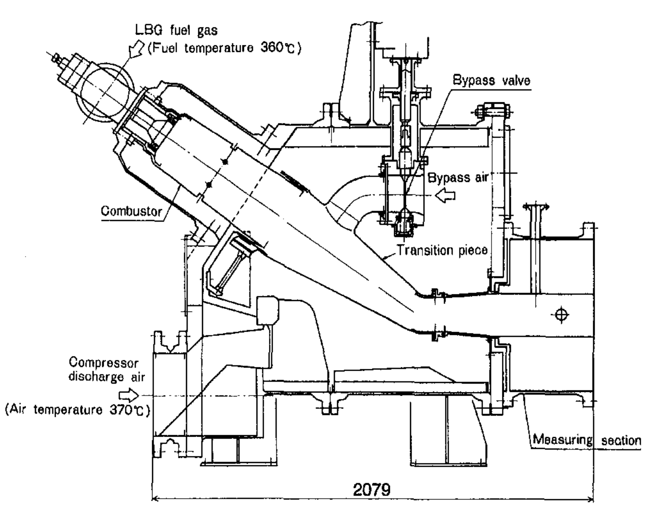

Fig. 3 Sectional drawing of the combustor test section

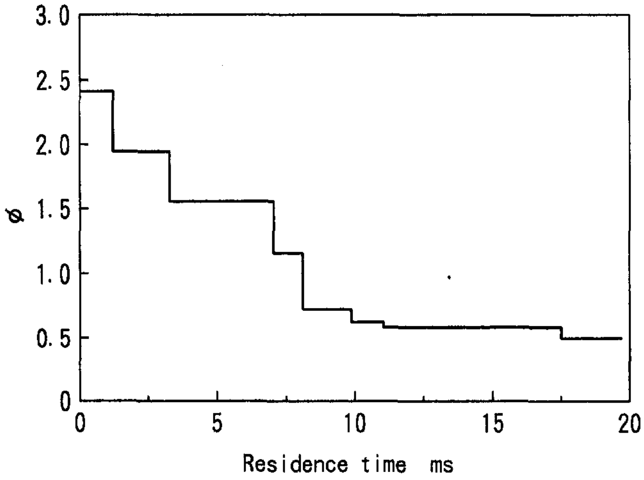

Fig. 4(a) Relation between residence time and equivalence ratio (tested combustor)

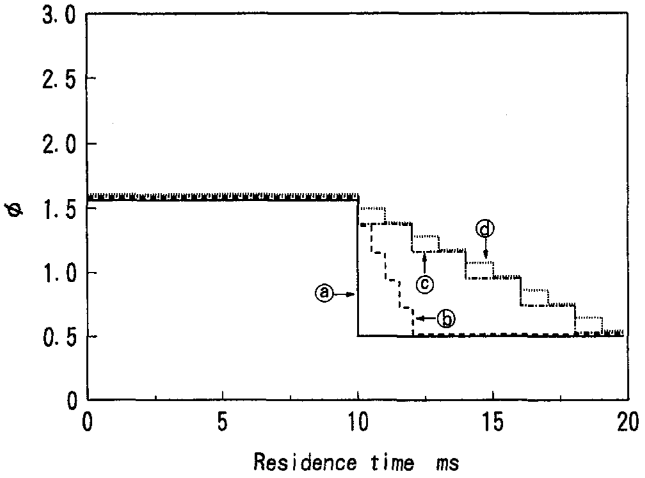

Fig. 4(b) Relation between residence time and equivalence ratio (modeling)

Figure 7 shows the case when the reaction temperature is altered with the equivalence ratio set at 2.0. NO increases with the increase in reaction temperature, but HCN decreases. However, since hardly any HCN is formed when the fuel does not contain methane, it can be surmised that the difference in this

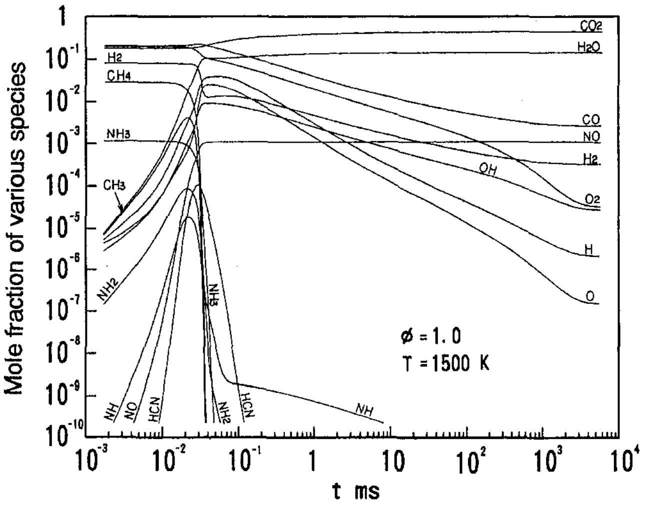

Fig. 5 Calculated mole ratio of typical chemical species

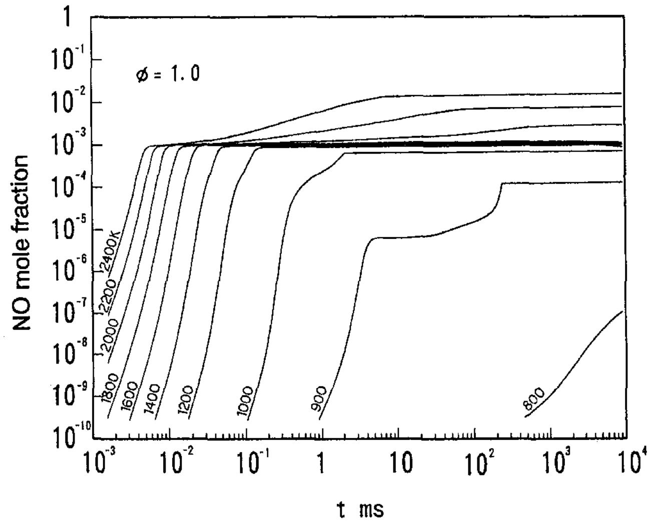

Fig. 6 Effect of reaction temperature on NO formation

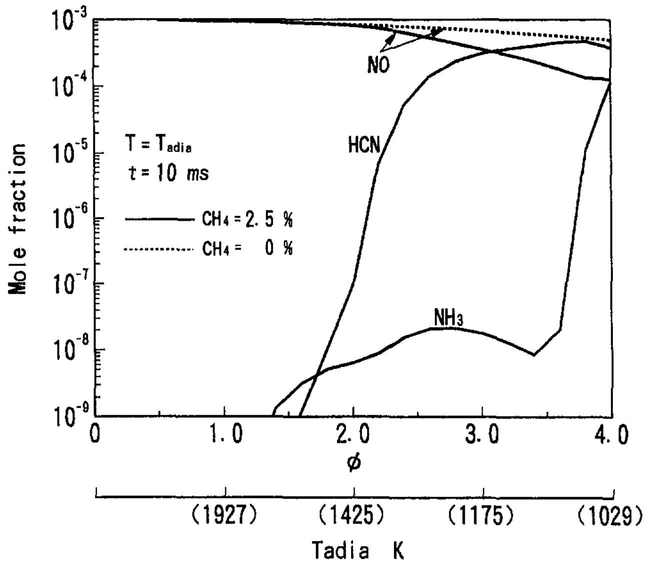

Fig. 8 Effect of equivalence ratio on NO, HCN, and NH_3 formation in primary combustion zone

characteristic has an effect on fuel NO_x formation characteristics, which will be discussed later.

Figure 8 shows the effect of the equivalence ratio on the formation of intermediate products. The richer the equivalence ratio, the less the amount of NO formed. When methane is contained in the fuel, the formation of HCN becomes conspicuous.

Figure 9 indicates the rate of ammonia conversion to NO, HCN, and other intermediate products concerning the standard fuel composition that includes methane. In addition, the figure indicates the sum of NO, HCN, and NH_3 as the total fixed nitrogen (TFN). When the equivalence ratio in the primary combustion region is expended up to 2.0, TFN decreases in the same way that NO decreases. However, when the equivalence ratio exceeds 2.0, and a quite rich condition is obtained, the amount of HCN formed increases, which offsets the amount of NO reduced, with the result that TFN remains practically unchanged.

Effect of Secondary-Air Mixing Conditions. In Figure 10, the symbol of a triangle shows the result of the atmospheric combustion test conducted on the combustor indicated in Fig. 1. In the experiment, the fuel flow is fixed and a bypass valve is used to change the equivalence ratio in the combustor. The tested combustor is characterized by the fact that it strives to slow down the mixing of secondary air by installing secondary-air slits.

Furthermore, the symbol of open circle shows the experimental result of a combustor in which a scoop is installed to facilitate the mixing of the secondary air (Nakata et al., 1990). In either case, until the primary equivalence ratio is about 2, the conversion ratio falls in tandem with the increase in the equivalence ratio. When the primary equivalence ratio reaches around 2 and even higher, the conversion ratio increases gradually in the combustor designed to facilitate the mixing of the secondary air. In the tested combustor, as the mixing of the secondary air is slow, it is believed that the NO formation in the secondary combustion zone is restrained even when HCN and NH_3 formed in the primary zone are increased.

Figure 11 shows the calculation results of the conversion ratio for cases a through *d*. In case *a*, where instantaneous mixing is assumed, the rate of ammonia conversion to NO remains virtually unchanged after the primary equivalence ration ϕ_1 declines from about 1 to 2.5. Since the conversion ratio is the same as the TFN in the primary combustion zone shown in Fig. 9, HCN and other intermediate products can all be con-

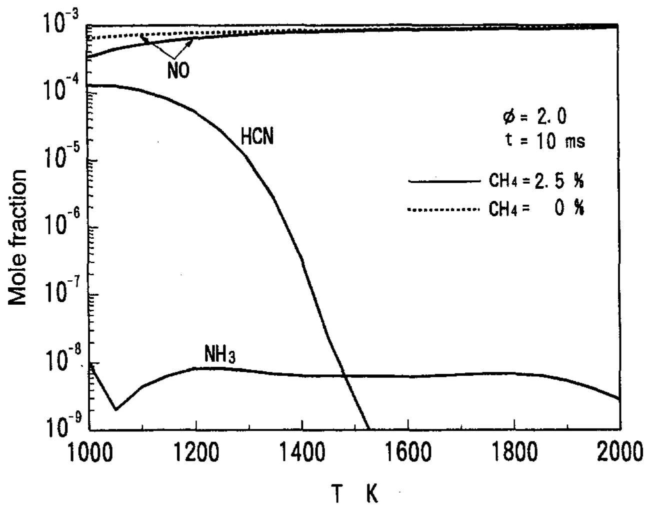

Fig. 7 Effect of reaction temperature on NO, HCN, and NH_3 formation in primary combustion zone

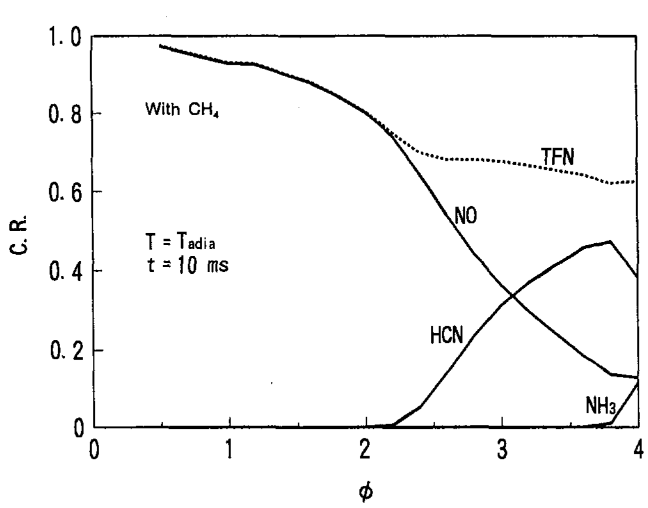

Fig. 9 Effect of equivalence ratio on conversion ratio in primary combustion zone

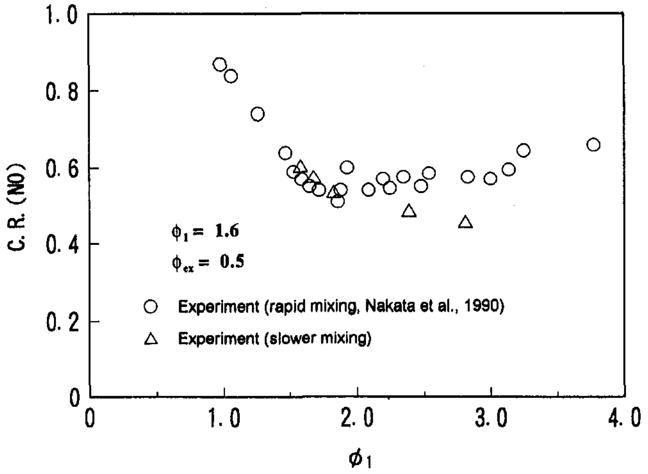

Fig. 10 NO emission characteristics of the tested combustor

sidered to be converted to NO in the secondary combustion zone.

Next, where secondary-air mixing is performed in stages, it is found that the slower the mixing the lower the conversion ratio. For instance, when the primary equivalence ratio is 4, the conversion ratio gradually declines from 0.63 in case *a* to 0.42 in case *d*. The NO formed in the primary combustion zone is believed to be discharged from the fuel-lean secondary zone without being decomposed. This kind of difference in conversion ratio is, therefore, believed to spring from the ease with which HCN and NH_3 formed in the primary combustion zone is converted to NO in the secondary zone. Another calculation for a case where the fuel does not contain any methane reveals no difference in the conversion ratio, even when the secondary-air mixing conditions are changed.

The calculations for the present research and the experimental values shown in Fig. 10 reveal that the calculated values are higher if the primary equivalence ratio is the same. Moreover, the experimental value of the primary equivalence ratio is about 1.8 when the conversion ratio is about 0.5, but the calculated value is about 4. In other words, the primary equivalence ratio in the experiments tilts to the fuel-rich side.

One reason is that since the diffusion flame is assumed in the combustor, there is a reaction zone where the fuel is richer than the average equivalence ratio used for the calculation. As a result, the ammonia in the fuel decomposes in the richer side of the flame, and the reaction of the intermediate products is accelerated mainly under this condition.

The time histories of typical chemical species formation are shown in Fig. 12(*a*) for case *a* and in Fig. 12(*b*) for case *c*. In either case, the results are obtained when the primary equivalence ratio is 4.0. In case *a*, radical chemical species such as OH, O, and H are rapidly formed as secondary air is instantaneously introduced 10 ms after the reaction begins. Furthermore, virtually at the same time that methane decomposes, intermediate products such as HCN and NHi that are formed in the primary combustion zone are converted to NO in a very short time. Meanwhile, as the secondary air is mixed in several steps in case *c*, ammonia decomposes after the methane decomposes. It is followed by the advancement in the decomposition of HCN. Radical species are consumed in the decomposition reaction of methane. Thus, the conversion from such intermediate products as NHi and HCN to NO occurs in an atmosphere containing relatively small amounts of radical species. From this it can be argued that the rate of ammonia conversion to NO declines when the secondary-air mixing is slow because the conversion from HCN and other intermediate products to NO in the secondary combustion zone is restrained.

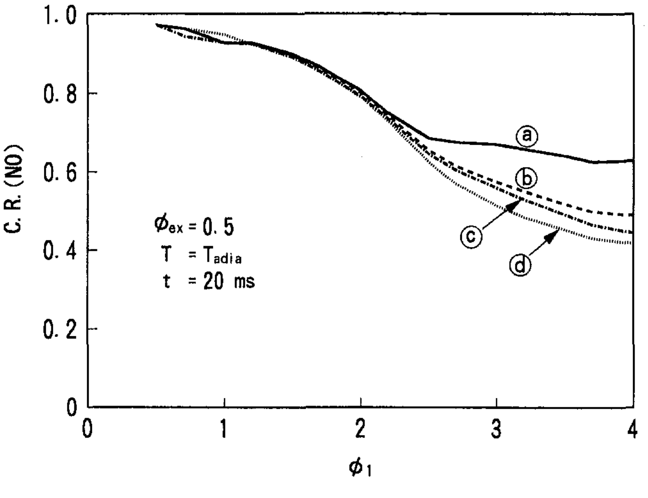

Fig. 11 Effect of primary equivalence ratio on conversion ratio in two stage combustion

Effect of Methane in the Fuel. Figure 13 shows the effect of methane content in the fuel on intermediate products such as HCN formed in the primary combustion zone. The calculation was performed with the primary equivalence ratio at 4 and

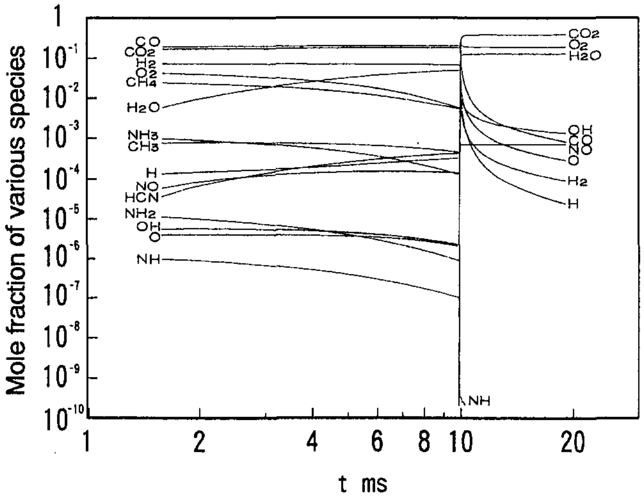

Fig. 12(*a*) Calculated mole ratio of typical chemical species (case *a*)

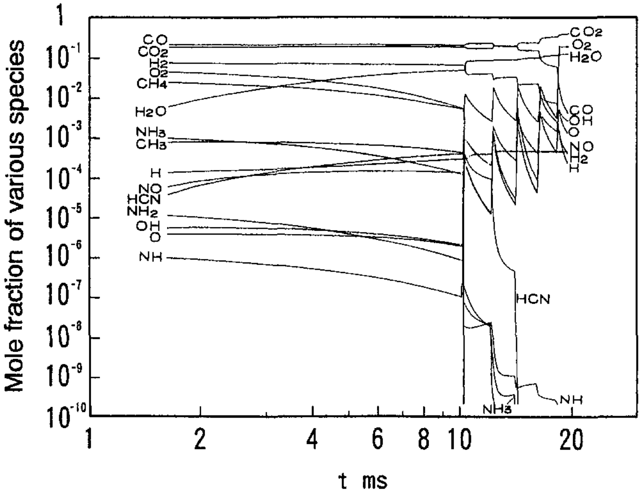

Fig. 12(*b*) Calculated mole ratio of typical chemical species (case *c*)

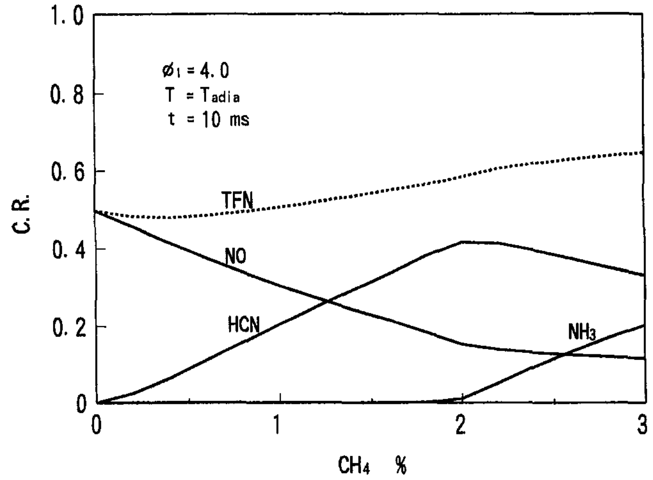

Fig. 13 Effect of CH_4 content on conversion ratio in primary combustion zone

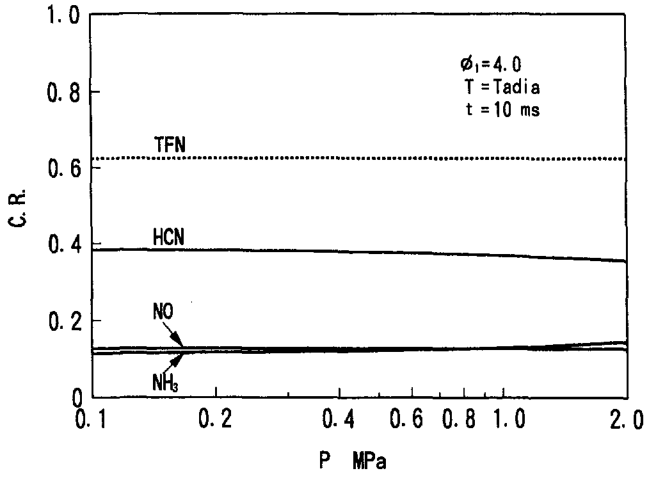

Fig. 15 Effect of pressure inside the combustor on conversion ratio in primary combustion zone

the reaction time at 10 ms. NO decreases are associated with the increase in methane concentration, but since HCN is formed, the TFN tends to increase.

Next, Figure 14 shows the conversion ratio to NO at two stage combustion. In case *a*, as the TFN indicated in Fig. 13, all intermediate products such as HCN formed in the primary combustion zone are converted to NO in the secondary zone. Also, in case *c*, the conversion ratio does not rise but remains virtually fixed, even when the methane concentration increases. The result shows that the higher the methane content is, the more conspicuous the effect of slow secondary air mixing on the reduction of NO.

The symbol of the open circle shows the result of atmospheric combustion test of a combustor that aims at achieving rapid secondary-air mixing (Sato et al., 1991). The primary equivalence ratio is set at 1.7. The conversion ratio rises as the methane concentration increases, and this tendency is virtually the same as the computed results obtained in case *a*.

Effect of Pressure Inside the Combustor. Results of kinetic calculations focusing propane (Ogasawara et al., 1973) and low calorific fuels (Nakata et al., 1992) have been reported (investigating the effects of pressure on thermal NO_x formation). The tendency observed in all these results is for the NO emission to be higher when the pressure is high, which is generally consistent with the experimental results (Ainger et al., 1990). Ainger showed a very strong dependency of the NO_x on pressure, which is not seen in much of the subsequent literature on lean-premixed combustion for gas turbine engines. Concerning fuel NO_x, while experimental results (Inada et al., 1983) have been reported on the lowering of NO emission as pressure rises, there are no reports of investigations on the effect of pressure based on kinetics calculations.

Figure 15 shows the effect of pressure on intermediate products formed in the primary combustion zone with the primary equivalence ratio set at 4.0 and the reaction time at 10 ms. NO does not change even when the pressure rises, but HCN does change slightly, and NH_3 increases a small degree. The TFN is virtually fixed and the effect of pressure is not significant.

Next, the conversion ratio to NO at two-stage combustion is shown in Fig. 16. In case *a*, the conversion ratio does not change even when pressure rises, and it is the same as the conversion ratio indicated in Fig. 15. In case *c*, the effect of pressure is significant, that is, the higher the pressure, the more the conversion ratio declines. For example, when pressure is 2.0 MPa, the conversion ratio in case *c* is 0.36, or about 60 percent of 0.62 in case *a*.

The time histories of the mole fraction of various chemical species are shown in Fig. 17 for case *c* when the pressure is high at 2.0 MPa. The reaction of CO and H_2 in the secondary combustion zone is faster, and radical chemical species such as OH and O decrease considerably when the pressure is at 2.0

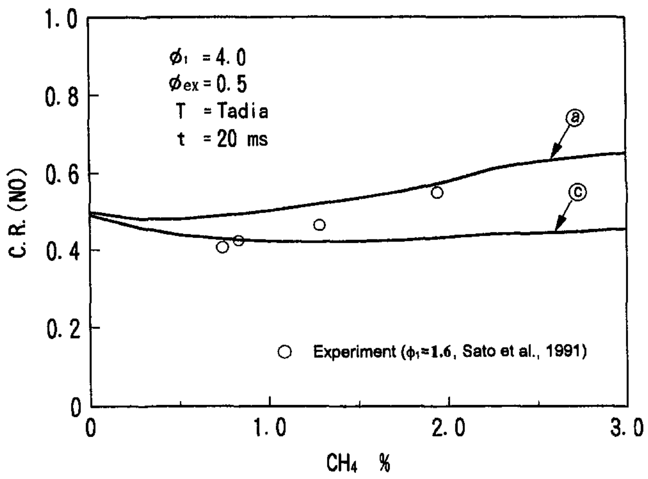

Fig. 14 Effect of CH_4 content on conversion ratio in two stage combustion

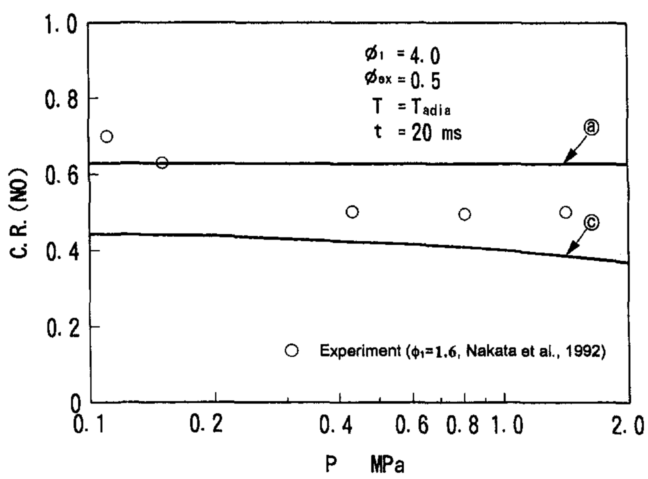

Fig. 16 Effect of pressure inside the combustor on conversion ratio in two stage combustion

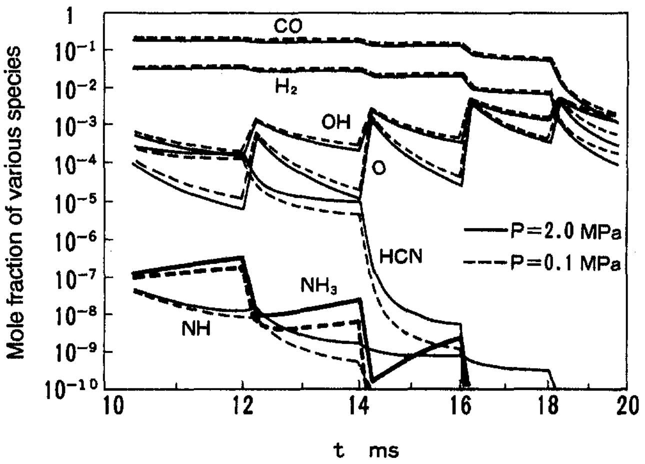

Fig. 17 Calculated mole ratio of typical chemical species (case c, p = 2.0 MPa)

MPa than when it is at 0.1 MPa. Likewise, the decomposition of both NHi and HCN is slower when the pressure is high. Thus, if the pressure is high, the conversion of intermediate products to NO advances in the secondary zone when the atmosphere contains a relatively small amount of radical species. Therefore, the formation of NO is restrained.

The symbol of open circle shown in Fig. 16 is the result of a pressurized combustion test (Nakata et al., 1992). When the pressure rises from 0.1 MPa to 0.4 MPa, the conversion ratio falls from 0.7 to 0.5, and when the pressure is 0.4 MPa and higher, the conversion ratio is virtually fixed at 0.5. The tested combustor is designed to promote secondary-air mixing, but when the pressure is below 0.4 MPa, the amount of NO formed tends to decrease. Conversely, when the pressure is high, it remains unchanged, as in case *a*. This, together with the transformation in combustion and burning velocity, is believed to have an effect on the flame structure, including flame stabilization near the burner. The result of the combustion test reveals that as the pressure in the combustor rises from 0.1 MPa to 0.4 MPa, the combustibility in the fuel-rich primary combustion zone improves, and the temperature of the combustor wall rises significantly. Consequently, it seems that the rise in pressure triggers a change in the flow and the combustion state in the primary combustion zone and exerts influence on the secondary-air mixing conditions.

Conclusion

The following points were observed: in the primary combustion zone under fuel rich condition, HCN and other intermediate reactants are produced accompanying the decomposition of ammonia contained in the fuel; fuel NO formation characteristics in the secondary combustion zone are significantly affected by secondary-air mixing conditions; since radical species such as O and OH are formed rapidly when secondary air mixes instantaneously with gas, intermediate products such as HCN formed in the primary combustion zone are all converted to NO, thus raising the concentration of NO emission; when secondary air mixes gradually with combustion gas, it restrains the formation of radical species, thus lowering the conversion ratio to NO. The effect of pressure inside a combustor on fuel NO formation is observed when the mixing of secondary air is gradual: the conversion ratio to NO declines as the pressure rises.

Acknowledgment

Thanks are due to our many colleagues with whom we have discussed this concept. In addition, we used the large-capacity computer of the Central Research Institute of Electric Power Industry to calculate the numerical values in this study.

References

Ainger, M., Mayer, A., and Schiessel, P., 1990, "Second-Generation Low-Emission Combustors for ABB Gas Turbines: Tests Under Full-Engine Conditions," ASME Paper No. 90-GT-308.

Chase, Jr., M. W., Davies, C. A., Downey, Jr., J. R., Frurip, D. J., McDonald, R. A., and Syverud, A. N., 1985, "JANAF Thermochemical Tables Third Edition," *Journal of Physical and Chemical Reference Data*, Vol. 14.

Fletcher, R. S., and Heywood, J. B., 1971, "A Model for Nitric Oxide Emissions from Aircraft Gas Turbine Engines," AIAA Paper No. 71-123.

Hindmarsh, A. C., 1974, *GEAR: Ordinary Differential Equation System Solver*, computer documentation, UCID-30001, Rev. 3, Lawrence Livermore National Laboratory, Livermore, CA.

Inada, M., Mandai, S., and Nakahara, T., 1983, "Research on Low-BTU Gas Combustion," *Proceedings of the 21st Japanese Combustion Symposium*, pp. 46–48.

Kee, R. J., Rupley, J. A., and Miller, J. A., 1992, "The Chemkin Thermodynamic Data Base," *Sandia Report*, No. SAND 87-8215B. UC-4.

Mandai, S., Sato, N., Sato, M., Ninomiya, T., and Nakata, T., 1991, "Experimental Evaluation of a Low NO_x LBG Combustor with Air Bypass System," *Proceedings of the Yokohama International Gas Turbine Congress*, Vol. 3, pp. 73–78.

Miller, J. M., and Bowman, C. T., 1989, "Mechanism and Modeling of Nitrogen Chemistry in Combustion," *Prog. Energy Combust. Sci.*, Vol. 15, pp. 287–338.

Mizutani, Y., and Katsuki, S., 1976, "Emission Composition of Gas Turbine Combustor," *Trans. Jpn. Soc. Mech. Eng.*, Vol. 42, No. 355, pp. 943–953.

Nakata, T., Sato, M., Ninomiya, T., Abe, T., Mandai, S., and Sato, N., 1990, "Experimental Evaluation of a Low NO_x LBG Combustor Using Bypass Air," ASME Paper No. 90-GT-380.

Nakata, T., Sato, M., Ninomiya, T., Yoshine, T., and Yamada, M., 1992, "Development of a 1300oC-Class Gas Turbine Combustor Burning Coal-Derived Low-BTU Gaseous Fuels, Fourth Report," *Trans. Jpn. Soc. Mech. Eng.*, Vol. 58, No. 553, pp. 2890–2897.

Nakata, T., 1993, "Research on NO_x formation mechanism and Low NO_x Combustion Engineering in LBG-Fueled Gas Turbine Combustor," Ph.D. thesis, Tohoku University, Japan.

Ogasawara, M., Takagi, T., and Fujii, K., 1973, "Fundamental Study on NO and CO Formation in Combustion Gases and its Reduction, Second Report," *Trans. Jpn. Soc. Mech. Eng.*, Vol. 39, No. 327, pp. 3427–3433.

Pratt, D. T., Bowman, B. R., and Crowe, C. T., 1971, "Prediction of Nitric Oxide Formation in Turbojet Engines by PSR Analysis," AIAA Paper No. 71-713.

Sato, M., Nakata, T., Yoshine, T., and Yamada, M., 1990a, "Development of a 1300oC-Class Gas Turbine Combustor Burning Coal-Derived Low-BTU Gaseous Fuels," *Trans. Jpn. Soc. Mech. Eng.*, Vol. 56, No. 530, pp. 3147–3154.

Sato, M., Nakata, T., and Yamauchi, K., 1990b, "NO_x Emission Characteristics of Coal-Derived Low BTU Gas Fuel," *Journal of the Fuel Society of Japan*, Vol. 69, No. 10, pp. 952–959.

Sato, M., Ninomiya, T., Nakata, T., Ishikawa, H., Yoshine, T., and Yamada, M., 1991, "Development of a 1300oC-Class Gas Turbine Combustor Burning Coal-Derived Low BTU Gaseous Fuels," *Trans. Jpn. Soc. Mech. Eng.*, Vol. 57, No. 535, pp. 803–810.

Takagi, T., Tatsumi, T., Ogasawara, M., and Tatsumi, K., 1978, "Fundamental Study on NO and CO Formation in Combustion Gases and Its Reduction, Fifth Report," *Trans. Jpn. Soc. Mech. Eng.*, Vol. 44, No. 388, pp. 4282–4291.

Yamauchi, K., Sato, M., and Nakata, T., 1991, "The Effects of CH4 Contained in Coal Gas Fuel on NO_x Formation," *Trans. Jpn. Soc. Mech. Eng.*, Vol. 57, No. 535, pp. 811–818.

Effect of Pressure on Emission Characteristics in LBG-Fueled 1500°C-Class Gas Turbine

T. Hasegawa

M. Sato

T. Ninomiya

Central Research Institute
of Electric Power Industry,
2-6-1 Nagasaka, Yokosuka-Shi,
Kanagawa-ken,
Japan

Developing integrated coal gasification combined cycle (IGCC) systems ensures cost-effective and environmentally sound options for supplying future power generation needs. In order to enhance thermal efficiency of IGCC and to reduce NO_x emission, a 1500°C-class gas turbine combustor for IGCC was designed, tested, and the performance of the combustor was evaluated under pressurized conditions. The designed combustor had the following three characteristics: (1) in order to assure the stable combustion burning low-Btu gas (LBG), an auxiliary combustion chamber was installed at the entrance of the combustor; (2) to reduce fuel NO_x emission that was produced from the ammonia (NH3) in the fuel, the rich-lean combustion method was introduced; and (3) to compensate for the declined cooling-air associated with the higher temperature of the gas turbine, the tested combustor was equipped with a dual-structure transition piece so that the cooling air in the transition piece can be recycled to cool down the combustor liner wall. As a result of combustor tests, it is confirmed that CO emission is less than 20 ppm, the conversion rate of NH3 which contains about 1000 ppm in the coal gasified fuel to NO_x shows 40 percent or below, and the liner wall temperature remained below almost 850°C under high pressure (1.4 MPa), rated load condition.

Introduction

IGCC is considered one of the most important systems in the future coal utilization technology in power generation systems and is being promoted by Japan, the United States, and Europe. In Japan, the government and electric power companies have been undertaking experimental research for a 200T/D pilot plant program since 1986 to 1996. The Central Research Institute of Electric Power Industry (CRIEPI) has developed the air-blown pressurized two-stage entrained-bed coal gasifier, hot gas cleaning system, and gas turbine combustor technology.

The reduction of NO_x emission and increasing the combustor-outlet gas temperature are the most significant issues in gas turbine development in IGCC. In our laboratory, we are developing a 150 MW, 1500°C-class gas turbine combustor for IGCC both to enhance thermal efficiency and to reduce NO_x emission from the plant. The standard composition of the coal gasified fuel produced in an air-blown entrained-bed coal gasifier is shown in Table 1. The coal gas has CO and H_2 as the main combustible components, and a small amount of CH_4. Its calorific value is as low as 4.2 MJ/m^3, one tenth of natural gas. Furthermore, the coal gaseous fuel contains ammonia (NH_3), about 1000 ppm, when a gas cleaning system is a hot/dry type, and ammonia will be converted to nitrogen oxides in the combustion process of a gas turbine. The reduction technology of NO_x emission and stable combustion technology are the most significant issues in gas turbine combustion technology in IGCC.

In the previous study [1], the rich-lean combustion technology of coal gasified fuel was applied as a method for reducing fuel NO_x emission that is produced from the NH_3 in the fuel. The 150 MW, 1500°C-class gas turbine combustor (CGT7001) was designed and tested under atmospheric pressure condition. From the test results, it was confirmed that the tested combustor had the excellent performance, except emitting CO about 2000 ppm under atmospheric pressure rated load condition. It will be necessary to evaluate its performance of the designed combustor under pressurized condition as a machine actually in operation.

In this study a 1500°C-class gas turbine combustor (CGT8001) for IGCC is designed based on the previous atmospheric combustion tests (CGT7001), tested and evaluated under pressurized conditions. This paper will propose the low-NO_x combustion technology for coal gasified fuel and provide useful engineering guidelines for the research and development of the gas-turbine combustor.

Test Facilities and Test Method

Test Facilities. The schematic diagram of the test facilities is shown in Fig. 1. The raw fuel obtained by mixing CO_2 and steam with gaseous propane is resolved to CO and H_2 inside the fuel reforming device. A hydrogen separation membrane is used to adjust the CO/H_2 molar ratio. Then, N_2 is added to adjust the fuel-calorific value to the given calorie, at the same time NH_3 is injected, then coal derived simulated gases are produced. The air provided to the combustor is pressurized to 2.0 MPa by using a four-stage centrifugal compressor. Both fuel and air are supplied to the gas turbine combustor after being heated separately to the given temperature with a preheater.

The combustion testing area has two test rigs, each of which is capable of performing full-scale atmospheric pressure combustion tests as well as half-scale high-pressure combustion tests. Figure 2 shows a cross-sectional view of the combustor test rig under pressurized conditions. After passing through the transition piece, the exhaust gas from the combustor is introduced into the measuring section where gas components and temperature are measured. The components of the combustion gas are analyzed by an automatic gas analyzer and each gas component, such as NO, NO_2, CO, CO_2, O_2 and THC, is continuously recorded and analyzed. After that, the gas temperature is lowered through a quenching pot using an injection system of water spray.

Measurement System. Samples are taken from the exit of the combustor through a water-cooled stainless steel probe located on the center-line of the measuring duct. The sample

---

Contributed by the International Gas Turbine Institute and presented at the International Gas Turbine & Aeroengine Congress & Exhibition, Orlando, FL, June 2–5, 1997. Manuscript received by the ASME Headquarters March 15, 1997. Paper No. 97-GT-277. Associate Technical Editor: H. A. Kidd.

Table 1 Standard composition of the air-blown, entrained-bed coal gasified fuel

Composition	CO	22.9 %
	H_2	8.6 %
	CH_4	0.5 %
	CO_2	12.9 %
	H_2O	2.0 %
	N_2	53.1 %
	NH_3	1000 ppm
HHV	4.2 MJ/m^3 (1000 kcal/m^3)	
LHV	3.7 MJ/m^3 (950 kcal/m^3)	

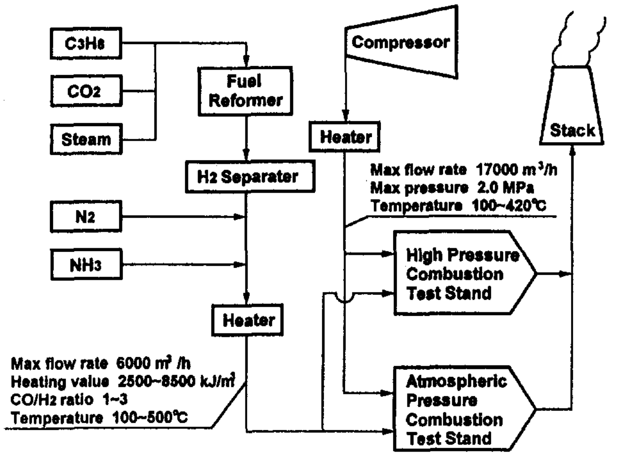

Fig. 1 Schematic diagram of the experimental facility

lines of stainless steel are thermally insulated with heat tape to maintain the sampling system above the dew point of the exhaust gas. The continuous gas samples are introduced into an emission console that measures CO and CO_2 by infrared analysis, NO and NO_x by chemiluminescence analyses, O_2 by paramagnetic analysis, and hydrocarbons by flame ionization. LBG are sampled from the fuel gas supply line at the inlet of combustor and CO, H_2, CH_4, H_2O, CO_2, and N_2 are determined by gas chromatography. Heating values of LBG are monitored by a calorimeter and calculated from analytical data of gas components obtained from gas chromatography.

The temperatures of the combustor liner wall are measured by 40 sheathed type-K thermocouples with a diameter of 1 mm welded on the liner wall. The temperature distributions of the combustor exit gas were measured by traversing an array of five type-R thermocouples.

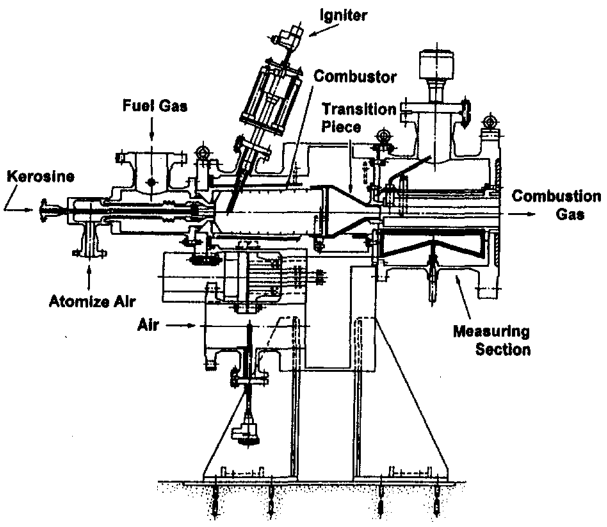

Fig. 2 Combustion test rig

Testing Method. From the examination of the thermal efficiency and the specific power output, it was concluded that the pressure ratio of 18 was the most adequate condition. However, due to restrictions imposed on the test facilities, the combustion test had to be done under 1.4 MPa. Therefore, the mass balance of the 1500°C-class gas turbine was examined to find the overall amount of air flow which is converted to an amount for a single combustor. In the high-pressure combustion test, effects of the pressure on the combustion characteristics were examined by adjusting the conditions so that the cross-sectional average gas velocity in the combustor can be constant.

As for fuel conditions, HHV was set at 4.2 MJ/m^3, the ammonia concentration was fixed at 1000 ppm, and the standard molar ratio of $(CO + CH_4)/H_2$ was set at 2.7.

In combustion tests, the combustor was ignited under atmospheric pressure condition with a lower amount of fuel flux, and then combustion pressure is increased by increasing Qa and Qf with sectional flow velocity kept constant.

Testing Combustor

Design Concept of the Combustor. Figure 3 shows the relation between the combustor outlet gas temperature and the air distribution in the gas turbine combustor using low-calorific coal-gasified fuel. To calculate air distribution, the overall amount of air is assumed to be 100 percent. The amount of air for combustion is first calculated at 1.2 times of a theoretical air ($\phi = 0.83$), 30 percent of the total air is considered as the cooling air for the combustor liner wall, and the remaining air is considered as diluting air. According to this figure, as the gas turbine temperature rises as high as 1500°C, the ratio of

Nomenclature

C.R. = conversion rate of ammonia to NO_x, %
HHV = higher heating value of the fuel, MJ/m^3
LHV = lower heating value of the fuel, MJ/m^3
NHi = one or more of NH_2, NH, and N
P = pressure in the combustor, MPa
Qa = air flow rate, m^3/h
Qf = fuel flow rate, m^3/h
TFN = total fixed nitrogen
Ta = air inlet temperature, °C
Tf = fuel inlet temperature, °C
Tex = combustor exit gas temperature, °C
Tr = reaction temperature, °C
Tadia = adiabatic flame temperature, °C
t = reaction time, ms
u = mean sectional flow velocity at 0°C, m/s
η = combustion efficiency, %
ϕ = equivalence ratio
ϕ_{ex} = equivalence ratio at combustor exit
ϕ_p = equivalence ratio in the primary combustion zone
CGT7001 = 1500°C-class gas turbine combustor
CGT8001 = 1500°C-class gas turbine combustor for this study (half size for high pressurized tests)

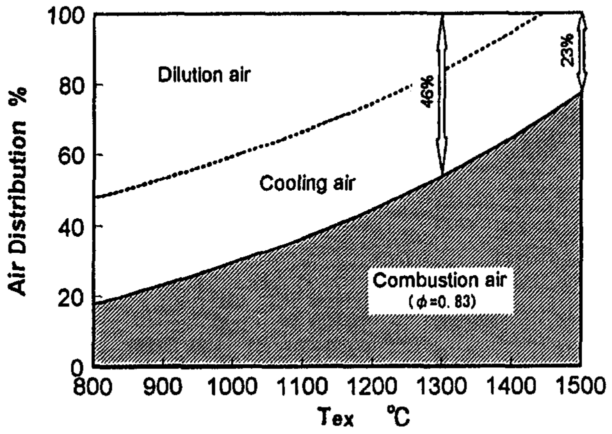

Fig. 3 Air distribution design of a gas turbine combustor which burns low-Btu coal gasified fuel

cooling air and diluting air decreases significantly, and the flexibility of the combustor design is minimized. To summarize these characteristics, it can be said that the design concept of the gas-turbine combustor utilizing low-calorific fuel should consider the following issues when the gas-turbine temperature rises:

1 *Combustion Stability*-it is necessary to stabilize the flame of low-calorific fuel.

2 *Low NO_x-Emission Technology*-to restrain the production of fuel NO_x from NH_3 in the fuel.

3 *Cooling Structure*-to efficiently cool the combustor wall with less amount of air.

Figure 4 presents characteristics of the designed and tested 1500°C-class combustor named CGT8001 compared with full-size combustor [1] named CGT7001. Figure 5 illustrates the external view of the combustor. The CGT7001 combustor corresponds to the operating size of a multi-can, 150 MW-class gas turbine combustor. The CGT8001 combustor has been developed by using the CGT7001 as a basis and halving it in dimension because of the limited capacity of fuel supply of the high pressure test facilities. The main design concept of the CGT8001 combustor was to secure stable combustion of a low-calorific fuel in a wide range of turn-down operation, low NO_x emission, and enough cooling-air for the combustor liner. The combustor is designed for advanced rich-lean combustion that is effective in decreasing fuel NO_x emission resulting from fuel-bound nitrogen in the fuel. Combustion tests are conducted on a half-scale combustor under pressurized condition.

Assurance of Flame Stabilization. In order to assure flame stability of low-calorific fuel, an auxiliary combustion chamber is installed at the entrance of the combustor. The ratio of the fuel allocated to the auxiliary combustion chamber is 15 percent of the total amount of fuel. The fuel and the combustion air are injected into the chamber through a sub-swirler with a swirling angle of 30 deg. By setting the equivalence ratio in this chamber at 1.0 under rated-load conditions, a stable flame can be maintained. As indicated in the following section, this flame is especially effective for maintaining flames in the fuel-rich combustion zone. The rest of the fuel is introduced into the main-combustion zone from the surrounding of the exit of the auxiliary combustion chamber.

Fuel-NO_x Reduction. To restrict the production of fuel NO_x that is attributable to NH_3 contained in the fuel, a two-stage combustion method (rich-lean combustion method) is introduced. The tested combustor has a two-chamber structure which separates the primary combustion zone from the secondary combustion zone. In addition, the combustor has the following three main design characteristics for reducing fuel NO_x.

1 *Design of the Air to Fuel Ratio in the Primary Combustor.* The equivalence ratio of the primary combustor is determined based on the combustion tests previously conducted using a small diffusion burner [2]. Figure 6 presents an example of the test results that indicate the influence of the equivalence ratio of the primary-combustion zone to the conversion rate of NH_3 to NO_x at the exit of the secondary-combustion zone. It also indicates the influence of CH_4 concentration in the fuel. From the test results, it is known that the conversion rate of NH_3 to NO_x is affected by both the equivalence ratio in the primary-combustion zone using the two-staged combustion method and CH_4 concentration in the fuel. When the fuel contains CH_4, HCN produced in the primary-combustion zone is easily con-

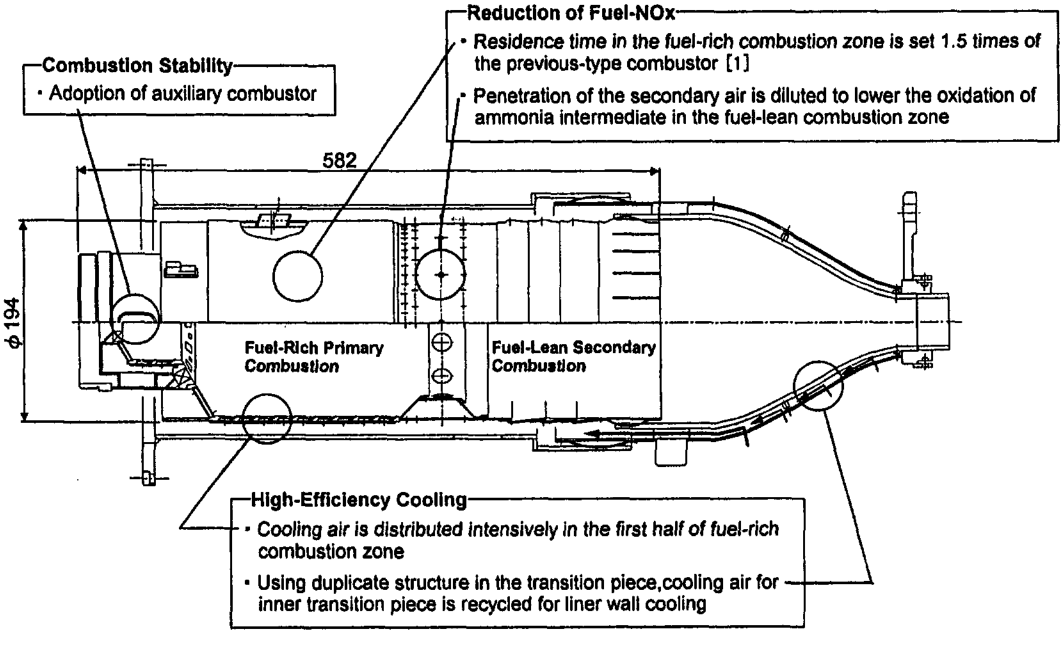

Reduction of Fuel-NOx
- Residence time in the fuel-rich combustion zone is set 1.5 times of the previous-type combustor [1]
- Penetration of the secondary air is diluted to lower the oxidation of ammonia intermediate in the fuel-lean combustion zone

Combustion Stability
- Adoption of auxiliary combustor

High-Efficiency Cooling
- Cooling air is distributed intensively in the first half of fuel-rich combustion zone
- Using duplicate structure in the transition piece,cooling air for inner transition piece is recycled for liner wall cooling

Fig. 4 Design concept of a 1500°C-class gas turbine combustor (CGT8001)

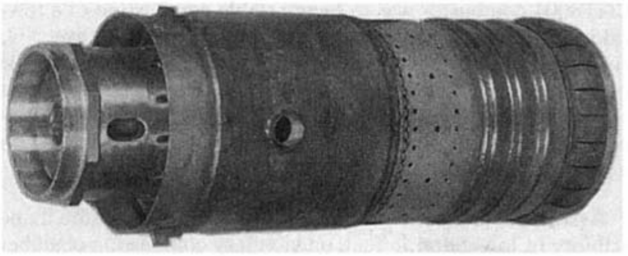

Fig. 5 Tested combustor liner (CGT8001)

verted to NO_x in the secondary-combustion zone along with the decomposition of NH_3. Therefore, there is a particular equivalence ratio which minimizes the NO_x conversion rate. Based on the fact that low-calorific fuel provided for the test contained approximately 0.5 percent of CH_4, the equivalence ratio in the primary-combustion zone was set at 1.6. The fuel and the combustion air are injected into the chamber through the main swirler, which has 30 deg swirl angle and 15 deg introvert angle, to make these gases premixed.

2 *Residence Time in the Primary Combustor.* Residence time in the primary-combustion chamber was increased 1.5 times of the 1300°C-class combustor [3], which we developed before. It has been observed in the 1300°C-class combustor tests that part of the air that flowed through the secondary-air inlet flowed backwards into the primary-combustion zone and as a result the fuel in the primary-combustion zone was more diluted than designed, and the planned rich-lean combustion could not be realized [4]. Based on this experience, the overall length of the primary-combustion zone was extended by about 60 mm, compared to the 1300°C-class combustor. By doing so, the residence time in the primary-combustor was extended from about 7 ms to 11 ms.

3 *Introduction Method of Secondary Air.* An innovative idea was applied for secondary-air introduction. With the decomposition of fuel N, a large portion of the total fixed nitrogen (TFN) produced in the primary-combustion zone, including NO, HCN, and NHi, is converted to NO_x in the secondary-combustion zone. The influence of secondary air-mixing conditions on the NO_x production was examined from the viewpoint of reaction kinetics. Figure 7 [5] shows the equivalence ratio distribution models in the combustor when the primary equivalence ratio ϕp is set at 1.6. The following two cases are thus assumed for the distribution of equivalence ratios in the secondary-combustion zone: one presents the case where the secondary air is mixed instantaneously with the main flow, the other is where the secondary air is mixed in ten steps. The combustor can be expressed by a modular model, where each combustion zone means a perfect stirred reactor; neither the effect of diffusion, nor that of radiant heat transfer of the flame are taken into account. The reaction temperature in the primary zone is regarded as the adiabatic flame temperature corresponding to the designed equivalence ratio and the reaction time is set at 10 ms. At the same time, irrespective of the mixing conditions of secondary air, the reaction temperature in the secondary combustion zone is set at 1300°C, which corresponds to the equivalence ratio of 0.5, and the reaction time is set at 10 ms. As a result, it was found that the slower mixing of the secondary air made the NO_x conversion rate decline further (Fig. 8)[5]. The calculation results shown in Fig. 8, and the combustor test results mentioned later in Fig. 12, reveal that the calculated value is higher than the experimental value. One reason for this is that since the diffusion flame is assumed in the combustor, there is a reaction zone where the fuel is richer than the average equivalence ratio used for the calculation. Based on this result, an exterior wall was installed at the secondary air-inlet section in the tested combustor to make an intermediate pressure zone of the dual structure. By providing this dual structure, the flow speed of the secondary air introduced to the secondary-combustor decreased to 70 m/s, compared to 120 m/s without an exterior wall, thus the secondary air mixing was weakened.

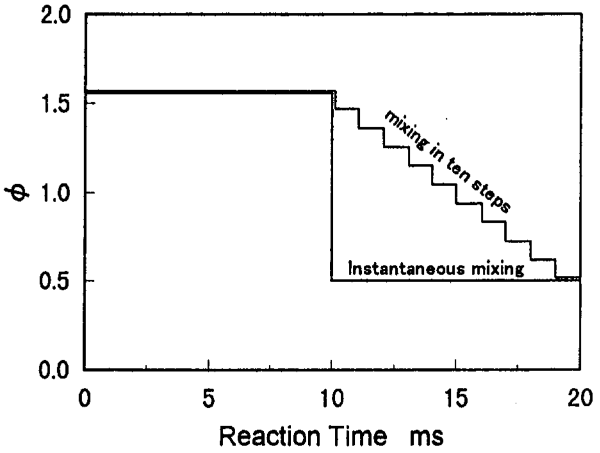

Fig. 7 Relation between the reaction time and the equivalence ratio distribution, using in the analysis [5]

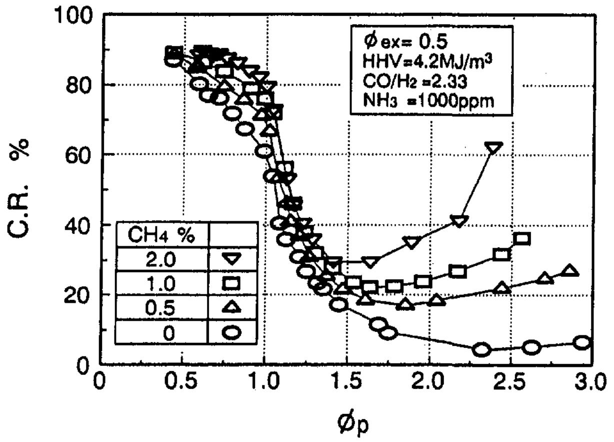

Fig. 6 Effect of methane content on conversion rate of ammonia in the fuel to NO_x, defining by the experiments using a small diffusion burner [2]

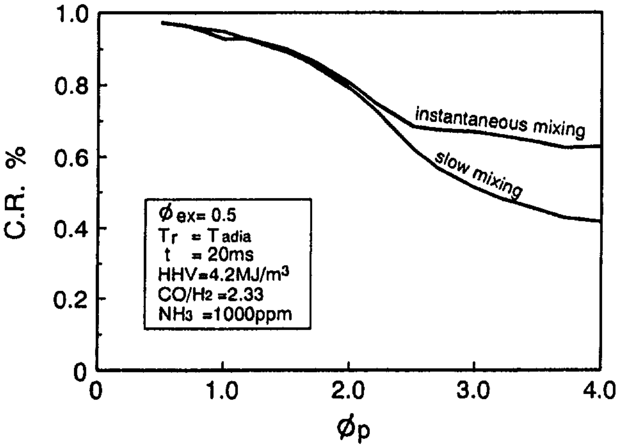

Fig. 8 Relation between equivalence ratio in primary combustion zone and conversion rate of ammonia in the fuel to NO_x, defining by the calculation [5]

Table 2 Standard test condition

Ta : 427 ℃
Tf : 360 ℃
Tex : 1500 ℃
u : 16 m/s
P : 1.4 MPa
ϕ_{ex} : 0.62
NH_3 : 1000 ppm
Loading rate in combustor
8.0 × 10^4 MJ/(m^3·h·atm)

Cooling of the Combustor Liner Wall. In order to compensate for the declined cooling-air ratio associated with the higher temperature of the gas turbine, the tested combustor is equipped with a dual-structure transition piece so that the cooling air in the transition piece can be recycled to cool down the combustor liner wall. The cooling air that flowed into the transition piece from the exterior wall cools the interior wall with an impingement method, and moves to the combustor liner at the upper stream side. This methods makes it possible for about 6 percent of the cooling air, which is traditionally used only for cooling the transition piece, to be reused for cooling the combustor liner wall.

For the auxiliary combustor and the primary-combustion zone of which temperatures are expected to be especially high, the layer-built cooling structure that combined impingement cooling and film-cooling was employed. For the secondary-combustion zone, the film-cooling method was used.

In addition to the above design characteristics, the primary-air inlet hole is removed in order to maintain the given fuel-rich conditions in the primary-combustion zone. Also, the overall length of the tested combustor was kept equal to that of the 1300°C-class combustor. The length of the secondary combustion zone was reduced to compensate for the extension of the primary-combustion zone.

The overall length of the combustor, including the auxiliary chamber, is 582 mm (this is $\frac{1}{2}$ the length for CGT7001), and the inside diameter is 194 mm (this is $\frac{1}{2}$ the diameter for CGT7001). The standard conditions in the combustion tests are summarized in Table 2. The loading rate in the combustion chamber at the design point is 8.0×10^4 MJ/(m^3·h·atm).

Test Results and Discussion

Thermal Characteristics of the Combustor Liner Wall. Figure 9 shows the temperature distribution of the combustor liner wall when the pressure inside the combustor changes. Based on the overall temperature, we can see that the temperature increased to an adequate level, and a stable flame was maintained in both the auxiliary-combustion chamber and the primary combustion chamber. At any of the pressures inside the combustor, the overall liner-wall temperature almost remained under 850°C, the allowable heat resistant temperature. This indicates that, while the amount of heat transferred in the process of flame radiation increases with the rise in pressure, the convection cooling on the combustor wall also tends to increase. And emissivity of coal-gas burning flame is lower than that of the conventional flame when hydrocarbon fuel, such as natural gas, is burned. (As a result of the above reasons, there was no noticeable effect of the pressure on the wall temperature, because emissivity of the flame burned with CO and H_2 which are the main combustible components in the coal gasified fuel, is lower than that of hydrocarbon flame.)

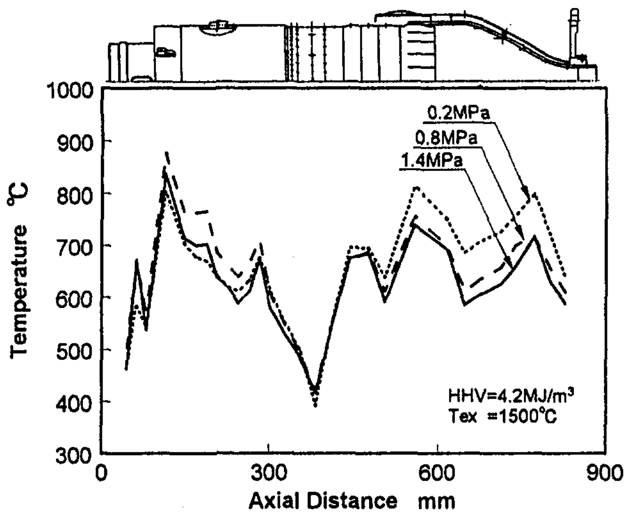

Fig. 9 Liner wall temperature distribution

CO Emission Characteristics. When the combustor-outlet gas temperature rises, CO emission tends to increase and combustion efficiency declines. CO emission is also affected by pressure. We observed the emission characteristics of CO when the pressure in the combustor changed. Under conditions such as when the combustor-outlet gas temperature was set at a constant value of 1500°C, effects of pressure on both CO emission and the combustion efficiency using fuel calorific value as a parameter are shown in Fig. 10. In each fuel calorific value, CO emission tends to decline significantly as the pressure in the combustor increases. When the fuel calorific value was 4.2 MJ/m^3, although 700 ppm of CO was emitted under atmospheric pressure, CO emission declined sharply as the pressure increased, and CO emission was 20 ppm or lower when the pressure rised to 0.8 MPa or above. Thus, the combustion efficiency was nearly 100 percent under rated load conditions. This is because that reaction rates increase and oxidation reactions of CO are enhanced when the pressure in the combustor increases. Under conditions of 0.8 MPa or below, where the pressure is relatively low, there was a noticeable effect of fuel calorific value on CO emission. That is, as the equivalence ratio which made the combustor-outlet gas temperature 1500°C was raised as the fuel calorific value decreased, the CO emission increased. The combustor is designed for standard testing fuel composition with HHV of 4.2 MJ/m^3.

NO_x Formation Characteristics. Figure 11 shows the relation between the pressure in the combustor and the NO_x emission characteristics of coal gasified fuel when its coal gaseous

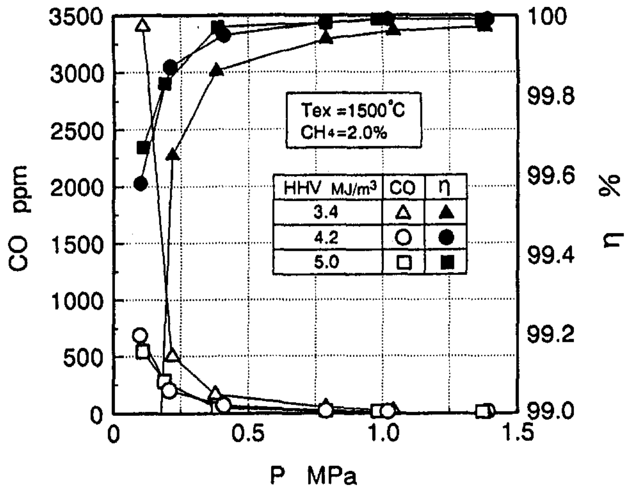

Fig. 10 CO emission characteristics

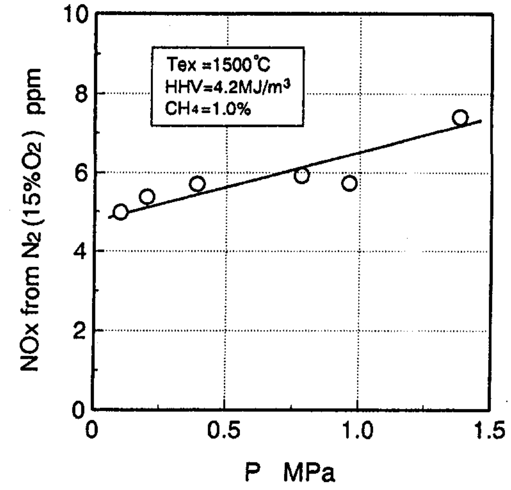

Fig. 11 NO_x emission characteristics from N_2 fixation

fuel does not contain NH_3. The vertical axis represents the NO_x emission that is produced from the N_2 fixation with the correction of 15 percent O_2. The equivalence ratio of the combustor-outlet is set at 0.62, so that the temperature of combustion gas at the combustor outlet would be equivalent to the rated load temperature of 1500°C. The NO_x emission increased gradually from 5 ppm under atmospheric pressure with the rise in pressure, reaching 7 ppm under operational conditions of 1.4 MPa. This result agrees with the NO_x emission characteristics from the N_2 fixation of 1300°C-class combustor that the authors previously developed [3].

As an example of the effect that pressure exerts on the level of the NO_x emission from the N_2 fixation in the gas turbine combustor, it is known that the pressure to the power of 1.5 is nearly proportional to the speed at which the Zeldovich NO is produced (i.e., $d[\mathrm{NO}]/dt \propto P^{1.5}$) and that the NO_x emission mole fraction is proportional to the pressure to the power of 0.5 [6]. In the case of the combustor used coal gaseous fuel under consideration, the NO_x emission from N_2 fixation increased in accordance with about the power of 0.2 of the pressure. Thus, the pressure had a smaller effect on NO_x formation from N_2 fixation with the coal gaseous fuel when compared to that of conventional fuels such as natural gas.

From the view point of the NO_x formation, it is known that the NO_x emission is affected by the super-equilibrium O-atom, and prompt NO is produced in large quantities. However, the effect of the super-equilibrium O-atom on the NO_x formation is believed to be small, because the tested combustor has adapted the rich-lean combustion methods that make the primary region the fuel-rich condition, and the flame temperature of coal gaseous fuel hardly rises if the pressure increases. The prompt NO formation is not also necessary to be taken into account in our study because the coal gaseous fuel contains only a small amount of CH_4, about 1 percent. Also, in the case of the coal-gasified low-calorific fuel, the flame temperature is about 500°C lower than that of the hydrocarbon flame, so NO_x from N_2 fixation is emitted on a low level. (In addition to that, since the tested combustor has adapted the rich-lean combustion methods and is designed to slow secondary-air mixing, the effect of pressure on NO_x emission from N_2 fixation is believed to be small, while the NO_x emission mole fraction originated from Zeldvich NO production is proportional to the pressure to the power of 0.5, as is mentioned above.)

As the methane (CH_4) content and the fuel calorific value of the coal gaseous fuel will be changed with the type of the coal gasifier and operation conditions for gasification, it is very important to evaluate the effects of both the methane content in the fuel and the fuel calorific value on the NO_x emission characteristics. Figure 12 shows the relation between the pressure in the combustor and the conversion rate of NH_3 in the fuel to NO_x under the conditions where the combustor outlet gas temperature was 1500°C. The NH_3 concentration in the fuel was fixed at 1000 ppm. And, as a parameter, the CH_4 concentration in the fuel was changed within the range of 1.0 percent to 2.7 percent. When the CH_4 concentration is changed, CO/H_2 molar ratio is set constant, and the fuel calorific value is adjusted with N_2. In each concentration of CH_4 in the fuel, the conversion rates of NH_3 to NO_x will slightly decrease with increases in the pressure. Furthermore, the conversion rate of NH_3 to NO_x is affected by the pressure in the combustor, and it rises with an increase in the concentration of CH_4 in the fuel. In case of the fuel containing 1.0 percent of CH_4, the conversion rate of NH_3 to NO_x decreases to 40 percent or below when the pressure is 0.4 MPa and higher.

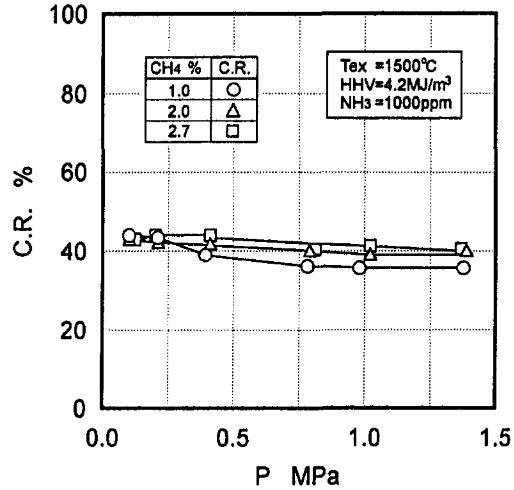

Fig. 12 Effect of methane content on conversion rate of ammonia in the fuel to NO_x

Figure 13 indicates the effect of the pressure on the conversion rate of NH_3 to NO_x using CH_4 concentration as a parameter through the numerical analysis in diffusion combustion taking into account reaction kinetics and multicomponent diffusion [7]. In each concentration of CH_4, the conversion rate of NH_3 to NO_x declines as the pressure in the combustion chamber rises. The concentration of each radical, such as OH, O radical, which promotes the NO_x formation, decreases as the pressure

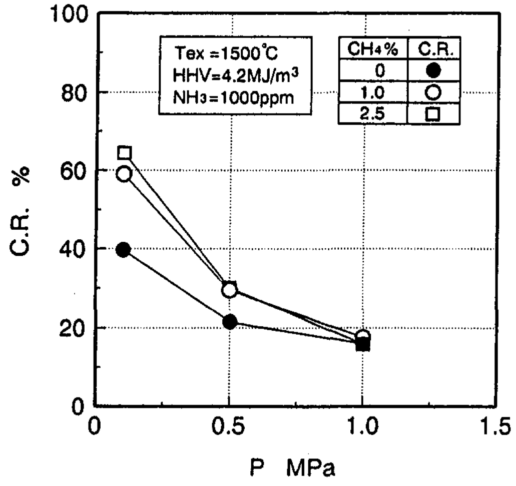

Fig. 13 Effect of methane content on conversion rate of ammonia in the fuel to NO_x, defining by the calculation [7]

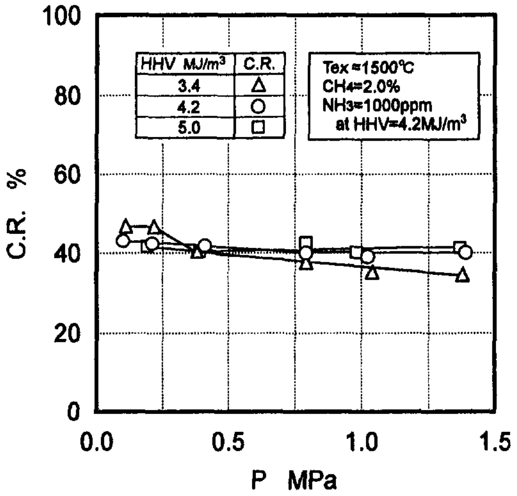

Fig. 14 Effect of fuel calorific value on conversion rate of ammonia in the fuel to NO_x

increases. Furthermore, the conversion rate of NH_3 to NO_x rises as the CH_4 concentration in the fuel increases. CH_4 contained in the fuel induces the production of HCN from NH_3, which is easily converted to NO_x. As the CH_4 concentration increased, NO_x formation through HCN increased. These analytical results indicate the same tendency as the combustion tests using the developed combustor. According to the effect of pressure on the conversion rate of NH_3 to NO_x, the calculation results were more sensitive than the experiments in the present study. One reason is that the combustion in the actual combustor is a complicated phenomenon with a complex flow, compared with the laminar diffusion flame assumed for the calculation. That is, together with the increase of the pressure in the combustor, the combustibility in the fuel-rich primary combustion zone improves, and the recirculation in the primary combustion zone is intensified; it also promotes that the secondary-air is caught up in the primary-combustion zone. Consequently, the primary-equivalence ratio is decreased with increasing the pressure, and the effect of pressure on the conversion rate of NH_3 to NO_x is restrained.

Figure 14 shows the relation between the pressure in the combustor and the conversion rate of NH_3 in the fuel to NO_x using the fuel calorific value as a parameter, under the conditions where the combustor outlet gas temperature was 1500°C. The NH_3 concentration in the fuel was set to be proportional to the fuel calorific values. Figure 14 reveals that the conversion rate of NH_3 to NO_x has a tendency to decrease slightly with decreases in the fuel calorific value under high pressurized conditions, which is 0.4 MPa or more. (This tendency increases as the pressure increases.)

Conclusion

The results are summarized as follows:

1 The tested combustor shows excellent combustion stability under the rated load condition. Judging by that matter, the auxiliary combustion chamber has the desired effect on flame holding for fuel-rich combustion.

2 NO_x emission from N_2 fixation is exhausted about 7 ppm or below (corrected at 15 percent O_2), even under the rated load conditions.

3 It is confirmed that the fuel NO_x emission hardly depends on the pressure in the combustor, methane content in the fuel, and fuel calorific value, and its conversion rate is reduced to 40 percent (70 ppm corrected at 15 percent O_2), even under the pressurized, rated load conditions.

4 The combustor performance, such as the combustion efficiency and the liner wall temperature, are satisfactory for 1500°C-class gas turbine combustor under the pressurized, rated load conditions.

Acknowledgment

The authors wish to express their appreciation to many people who have contributed in this investigation. In designing this equipment we received kind suggestions and advice from Mr. Toshiyuki Yosine, Mr. Masahiko Yamada and Mr. Akihiro Onoda of Toshiba Corporation.

References

1 Nakata, T., Sato, M., Ninomiya, T., and Hasegawa, T., 1994, "A Study on low NO_x combustion in LBG-Fueled 1500°C-class Gas Turbine," ASME Paper No. 94-GT-218.

2 Sato, M., Nakata, T., and Yamauchi, K., 1990, "NO_x Emission Characteristics of Coal-Derived Low BTU Gas Fuel," *Journal of the Fuel Society of Japan*, Vol. 69, No. 10, pp. 952–959.

3 Nakata, T., Sato, M., Ninomiya, T., Yoshine, T., and Yamada, M., 1993, "Effect of Pressure on Combustion Characteristics in LBG-Fueled 1300°C-class Gas Turbine," ASME Paper No. 93-GT-121.

4 Ninomiya, T., Nakata, T., Hasegawa, T., and Sato, M., 1993, "Development of 1500°C-class Gas Turbine Combustor for Use in IGCC-2nd Report," *CRIEPI REPORT*, EW93004, Central Research Institute of Electric Power Industry, Yokosuka, Japan.

5 Nakata, T., Sato, M., and Hasegawa, T., 1995, "Reaction Kinetics of Fuel NO_x Formation for Gas Turbine Conditions," *Proc. 4th ASME/JSME Thermal Engineering Joint Conference*, Vol. 3, ASME, NY, pp. 227–234.

6 *JSME Data Book*, 1980, "Formation Mechanisms and Controls of Pollutants in Combustion System," p. 285.

7 Xu, Z., Sato, M., Hasegawa, T., and Takagi, T., 1996, "Numerical Analysis in Diffusion Combustion of Coal Gasified Fuel," Transactions of the Japan Society of Mechanical Engineers, Vol. 62, No. 602, pp. 3689–3695.

A. K. Gupta

M. J. Lewis

S. Qi

The Combustion Laboratory,
University of Maryland,
Department of Mechanical Engineering,
College Park, MD 20742

Effect of Swirl on Combustion Characteristics in Premixed Flames

A double concentric premixed swirl burner is used to examine the structure of two different methane-air premixed flames. Direct flame photography together with local temperature data provides an opportunity to investigate the effects of swirl number distribution in each annulus on the global and local flame structure, flame stability and local distribution of thermal signatures. An R-type thermocouple compensated for high-frequency response is used to measure the local distribution of thermal signatures in two different flames, each of which represents a different combination of swirl number in the swirl burner. In order to improve the accuracy of the temperature data at high-frequency conditions, information on the thermocouple time constant are also obtained under prevailing conditions of local temperature and velocity by compensating the heat loss from the thermocouple sensor bead. These results assist in quantifying the degree of thermal nonuniformities in the flame signatures as affected by the distribution of swirl and to develop strategies for achieving uniform distribution of temperatures in flames.

Introduction

Swirl flows have been widely investigated for several decades because of their extensive use in all kinds of practical systems, including gas turbine combustion. Numerous experiments in swirl flows have been carried out extending from very fundamental isothermal flows as well as reacting flows to those formed in very complex swirl combustor geometries. Experimental results have established the general characteristics of swirl flows and revealed important effects of swirl on promoting flame stability, increasing combustion efficiency, and controlling emission of pollutants from combustion [1]. Leuckel and Fricker [2] conducted a variety of measurements using a nonpremixed single swirl burner consisting of an annular swirling air jet and a centrally located nonswirling fuel jet. Chen and Driscoll [3] have provided an understanding of the physical processes that occur within the nonpremixed flames by examining the enhanced mixing characteristics in swirl flows resulting from the formation of a central toroidal recirculation zone. A thermal-inertia compensated thermocouple technique that produces a linear response of the thermocouple at higher frequencies was used by Gupta et al. [4] to investigate turbulent temperature characteristics of swirling nonpremixed flames. By achieving a linear response of the thermocouple to higher frequencies, important information on the structure of turbulent flames can be obtained that could not be ordinarily observed. Accurate measurements of the rms temperature fluctuations are possible when the output of the thermocouple is compensated to higher frequencies [4]. Although the frequency compensation can be carried out to several kHz, there are practical limitations (e.g., electronic noise) associated with the thermocouple compensation technique.

Most previous studies have been conducted on single swirl burners instead of the double concentric swirl burners that are playing an ever-increasing role in practical combustor desigh. The double concentric burner allows for variation of the radial distribution swirl via control over the axial and angular momentum of the jets in the two annuli of the burner. As such, at a fixed overall swirl number, the detailed flow distribution can be significantly different under various operational conditions of the burner. By introducing the swirling flow through concentric annuli, it is possible to control the radial distribution of flow and swirl for achieving significantly different flame stability limits, levels of turbulence, volumetric heat release rates, and combustion characteristics in general.

Significantly different combustion and emission characteristics have been obtained by altering the relative proportions of the swirling flow in various annuli [5]. Marshall and Gupta [6] investigated thermal characteristics of diffusion flames obtained through various combinations of swirl and axial inlet momentum distributions in a double concentric swirl burner. Fluctuating temperature measurements were obtained in the flames, including the recirculation zone and the shear layer and post-combustion regions. By maintaining a constant equivalence ratio, a comparison of the magnitude and distributions of temperatures for different flames were obtained. These results provided the important role of radial distribution of swirl and jet axial momentum on the flame thermal characteristics.

The use of lean premixed combustion in gas turbine combustors has been preferred over nonpremixed combustion by the gas turbine manufacturers for achieving low NO_x emission. Although the use of lean premixed combustion is attractive for pollution reduction, it may provide a penalty in system complexity, acoustic instabilities, and increased size and weight. Although disadvantages may prohibit the use of lean premixed combustion in certain applications, it still offers advantages over the other types of combustors used in gas turbine applications. The use of lean premixed combustion reduces the peak flame temperatures obtained near the fuel-air interface in the traditional diffusion flame type of combustors. The degree of premixing determines the thermal field uniformity of the flame. In all premixed combustor configurations the fuel-air mixture is premixed upstream of the swirler, which is used for the stabilization of the flame at all power conditions. The use of swirl assists in the stabilization of the flame by transporting hot and chemically active species from the downstream region of the flame to the root of the flame, which therefore alters the transport of gases within the combustor and creates a thermal nonuniformity.

The extent of thermal nonuniformity in premixed flames is not known and can be expected to depend upon the combustor

---

Contributed by the International Gas Turbine Institute and presented at the International Gas Turbine & Aeroengine Congress & Exhibition, Orlando, FL, June 2–5, 1997. Manuscript received by the ASME Headquarters March 15, 1997. Paper No. 97-GT-276. Associate Technical Editor: H. A. Kidd.

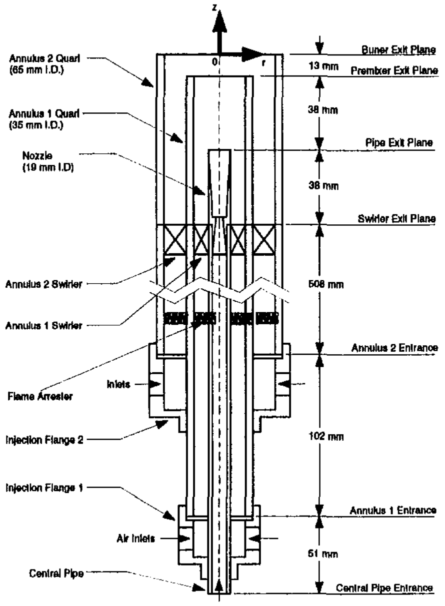

Fig. 1 A Schematic of the premixed swirl burner

configuration, the degree and distribution of swirl in the combustor, and other input and operational parameters of the combustor. The nonuniformity in the thermal field can, in turn, have an influence on the performance of the combustor in addition to the emission levels, including NO_x.

In order to examine the effect of fuel-air premixing on the resulting thermal field, an experimental premixed swirl burner facility was developed. The facility is very similar to the one described in [6], except for the well-mixed fuel-air mixture in each annuli, including the central pipe, and the presence of a flame quench trap upstream of the swirler in each annuli. Results obtained on the mean and fluctuating temperature measurements are aimed at providing the effect of swirl on the thermal characteristics of premixed co-swirling flames.

Experiment Facility

A schematic diagram of the experimental burner is given in Fig. 1. The burner has a double concentric swirl arrangement in which the radial distribution of swirl and momentum distribution of the flow in the two annuli and the central pipe can be independently controlled. The facility consists of a burner, a test section, a flow control system, and a two-dimensional traverse mechanism. The premixed burner is similar to the diffusion flame burner facility discussed in [6], except that it has the necessary flame arrestor in each annuli, which is used to prevent flashback and can mix the reactants well prior to their arrival over the swirler. At the top of the burner is the flame stabilization section, which includes two glass tubes for the two nozzles in the burner (having inner diameters of 65 mm and 35 mm), a centrally located premixed fuel-air nozzle, and two swirlers for the annulus 1 and annulus 2 jets. The swirl strength in the central nozzle and annulus 1 and 2 can be changed to any desired value. A backward facing step is placed inside the central nozzle in order to make the methane-air mixture completely turbulent. The divergence in this central nozzle permits smooth interaction between the central flow and the surrounding outer annulus 1 nozzle flows. The two swirlers generate the tangential momentum to form a central toroidal recirculation zone for flame stabilization. Each swirler consists of eighteen straight vanes fixed in place by thin inner and outer rings. The inside and outside swirlers can be fixed independently, and this allows the variation of the radial distribution of swirl combination in the burner. Therefore, the facility permits examination of the flames formed with strong swirl in the central region and weak swirl on the outside, or vice versa. It is also possible to form flames having co-swirl and/or counter-swirl in the annuli.

In the present study, only the co-swirling flames are examined, with varying radial distribution of swirl in the burner for a fixed stoichiometry of 0.625 in each annuli. A two-dimensional traverse assembly is used to move the thermocouple with respect to the fixed burner with a spatial accuracy of 0.0254 mm. The test section is situated above the burner and is formed from an open-ended cube enclosure around the burner exit. This arrangement provides isolation of the flame from external ambient disturbances. The flow control system for the burner consists of a series of rotameters, pressure gauges, and control valves to measure and regulate the air and methane flow rates prior to their entry into the premixer and subsequently into the two annuli and the central nozzle of the burner.

Experimental Conditions and Diagnostics

Two premixed flames have been examined here. These flames were produced with changes in swirl strength distribution between the two annuli. Previous work has presented results designated flames 1 and 2 [7]. For flame 3, the swirl vane angle was 30 deg and 55 deg in annulus 1 and 2, respectively. However, for flame 4, the swirl vane angle was 45 deg and 55 deg in annulus 1 and 2, respectively. The experimental conditions for the examined flames are given in Table 1.

High frequency temperature measurements have been taken with an R-type microthermocouple probe. The probe utilizes a *Pt*/*Pt*-13% Rh thermocouple with a wire diameter of 50 μm. This wire diameter is small enough not to cause any significant intrusion in the flame while maintaining structural rigidity of the thermocouple. No measurable disturbance to the flame was observed when the thermocouple was inserted in the flame. The signal of the thermocouple is amplified and digitized at 10 kHz for a total of 300,000 samples at every probe location in the flame. The thermocouple output is compensated to high frequencies so that high sampling frequency provides resolution to the small time scale turbulence that may occur in flames. The large number of samples provides the flow thermal statistics. The resulting long sampling time of 30 s allows for averaging over the low-frequency temperature fluctuations and ensures good statistical information of the thermal field. The mean value at a location is the arithmetic mean temperature of the samples.

Measurements are taken at different points in the flame region by moving the thermocouple with respect to the burner. Great care was taken to obtain a symmetrical flame with respect to the burner vertical axis. Subsequent measurements carried out on the flames validated their axisymmetric behavior. Half-plane measurements were then sufficient to characterize the complete

Table 1 Experimental test matrix

	Axial Momentum Distribution		Swirl Vane Angles	
	Flame 3	Flame 4	Flame 3	Flame 4
Central Pipe	M_{cp} = 300 lbm ft/min^2		No Swirl	
Annulus 1	M_{an1} = 1500 lbm ft/min^2		30°	45°
Annulus 2	M_{an2} = 2163 lbm ft/min^2		55°	

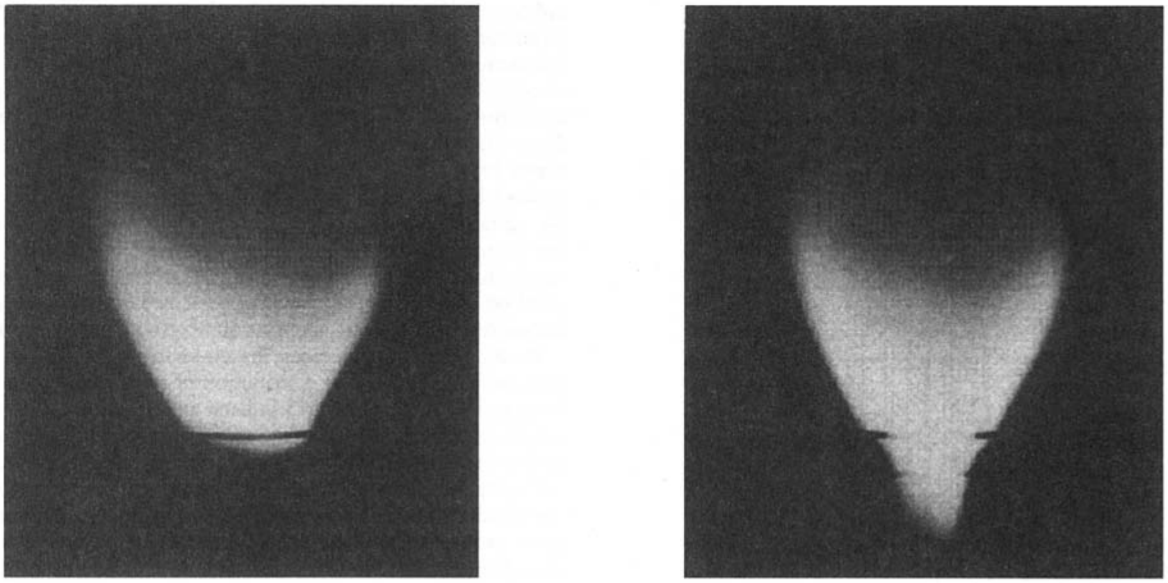

Fig. 2 Direct photograph of flame 3 (left) and flame 4 (right)

flame because of the observed axisymmetry. The half plane consists of 12 radial positions at 9 axial elevations for a total of 108 probing locations. The horizontal spacing of the grid is 6.35 mm, while for the vertical it is 19.05 mm. It is situated directly above the burner orifice with the location of the home coordinates in the center of the burner exit plane.

The response time of the thermocouple probe is insufficient to accurately resolve temperature fluctuations faster than about 50 Hz, even with the very small thermocouple bead formed with 50 μm diameter wires—though temperature fluctuations up to several kHz can occur in strongly swirling flames [1]. Therefore, the time constants were measured to compensate the raw temperature data for thermal inertia effects of the utilized thermocouple. In order to determine the time constant of the thermocouple, the wire is heated by a DC power supply and cooled down in the flame periodically. In this manner, a series of heating and cooling pulses are obtained, and the value of the time constant, τ, is calculated from the resulting decay times of the thermocouple signature. In each flame, the time constant is measured at 30 locations (at every other measurement point in both the axial and radial direction). Due to the fluctuation of temperatures in the flame, the process is repeated up to 300 times at each measurement location. The resulting temperature decay curves are averaged to produce a smooth decay curve from which the time constant, τ, is determined as the value at which the overheat ΔT, has decreased by a factor of l/e.

Results and Discussion

The test conditions are given in Table 1. Global flame features are described first, followed by the quantitative data on mean and fluctuating temperatures, probability density distribution of temperatures, power spectra, and integral and micro-scale of temperature time scales.

Flame Photographs. Figure 2 shows a direct comparison of flame 3 and flame 4. It is interesting to note from the direct flame photographs that the flame length is longer for flame 4 (with 45 deg swirl in annulus 1) than for flame 3 (with 30 deg swirl), while the other flow conditions are kept constant.

It is generally believed that the swirl number has an important effect in characterizing the combustion process and that in-

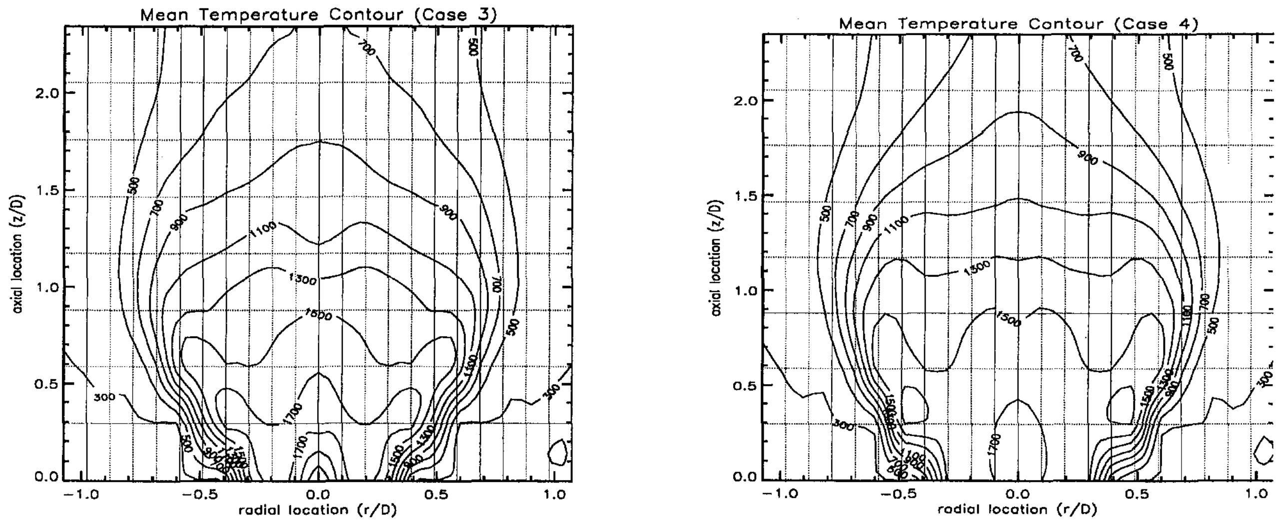

Fig. 3 Compensated flame temperature contour for flames 3 (left) and 4 (right)

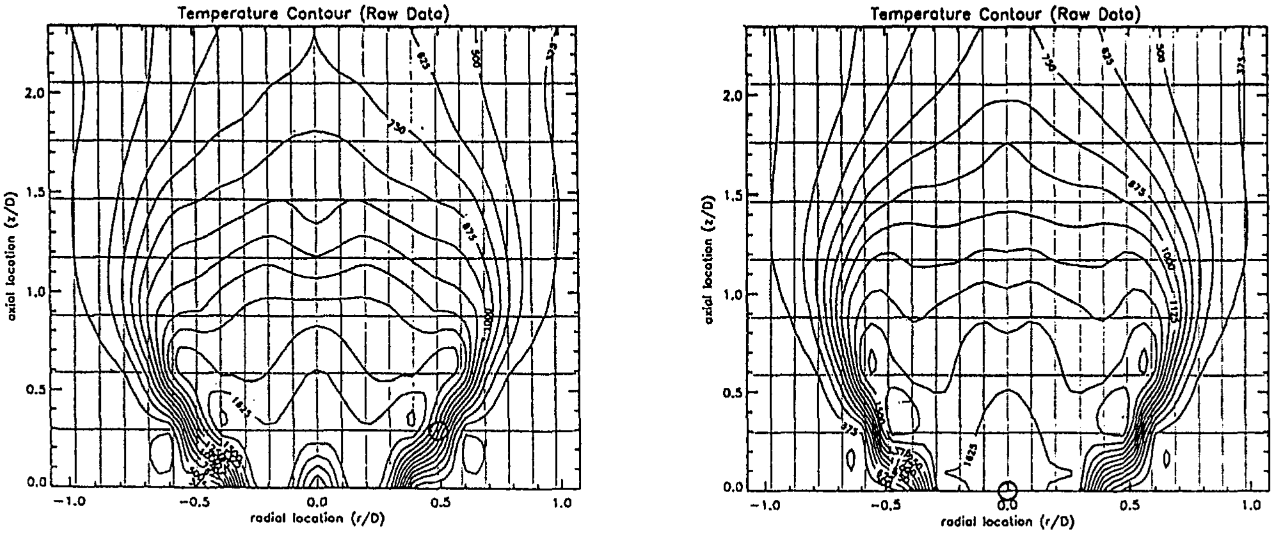

Fig. 4 Uncompensated flame temperature contour for flames 3 (left) and 4 (right)

creased swirl number produces enhanced tangential momentum, which provides a better mixing between the incoming hot chemical reactants and the fresh fuel-air mixture. This rapid mixing decreases the flame length. However, high swirl is also expected to produce excess turbulence that results in large tangential velocity gradients and a negative flame stretch. The presence of negative stretch [8] through the tangential velocity gradient at the flame (also quantified by the Karlovitz number, $K = (1/A)(dA/dt)$, where A is the flame surface area and t is the time)) decreases the flame surface area, and, therefore, the volumetric burning rate. Because the flame length depends on reaction rate of combustion, it is therefore reasonable that the flame becomes longer from flame 3 to 4.

Mean and Fluctuating Temperature Data. Two kinds of temperature maps are provided to obtain insight on the local and global thermal structure of the strongly swirling premixed turbulent flames. The raw temperature data is compensated for thermal inertia effects of the thermocouple and for radiative losses. Characteristic temperature probability density function data is also provided both with and without thermal inertia compensation. This will be used to examine the local turbulent thermal structure of the flames.

The mean and fluctuating temperature data are presented as temperature contour maps (see Figs. 3, 4, and 5). The lines displayed represent the isothermal contours in the flame. A grid representing the probe locations is superimposed with the isothermal maps to facilitate the discussion and to refer to certain areas and points within the flowfield.

Mean Compensated Temperature Data. The results presented in Fig. 3 and Fig. 4 for flames 3 and 4 show the direct effect of thermal inertia compensation of the thermocouple on flame temperatures. The results of compensated mean temperature contours account for not only the thermal inertia effects of the thermocouple but also the radiative losses from the thermocouple. A comparison of the mean temperature data between the uncompensated and compensated data reveals that the calculated temperature difference can be as large as 300 K at the same location in the flame. Therefore, the importance of the compensation technique for mean and fluctuating temperature measurement can be recognized when it is desired to determine NO_x emission levels from the temperature data. The importance of accurate temperature data can also be recognized for estimating other pollutant emissions and heat transfer characteristics of the flame.

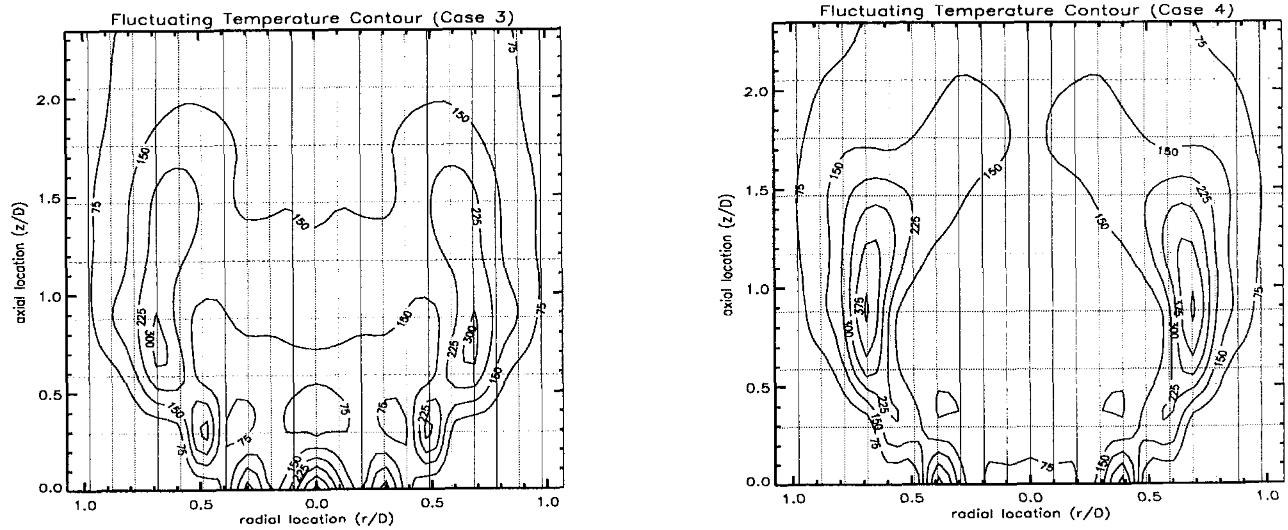

Fig. 5 Fluctuating temperature contour for flames 3 (left) and 4 (right)

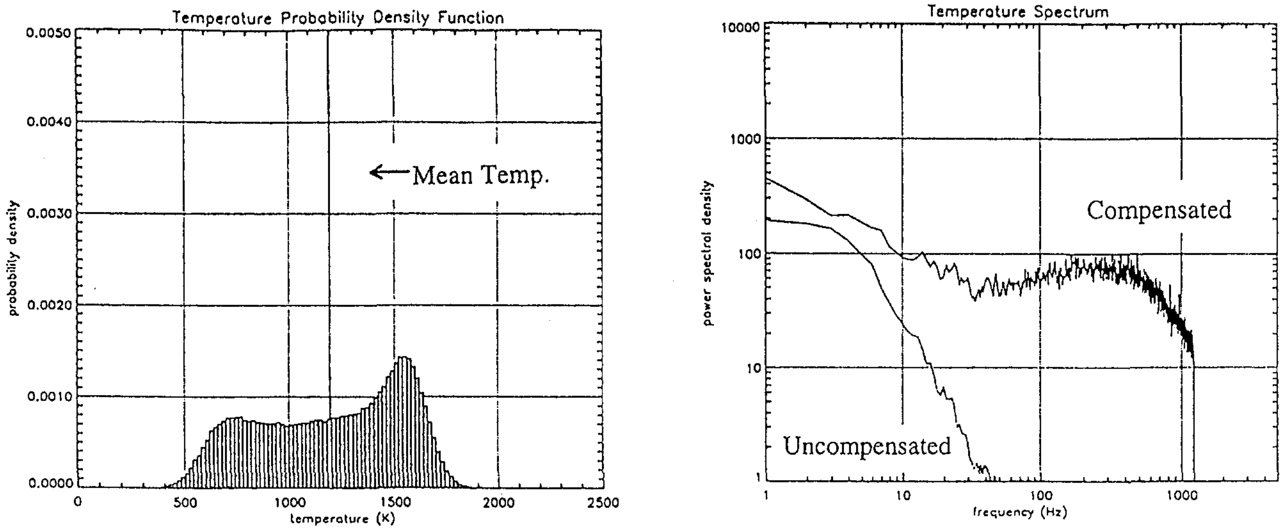

Fig. 6 Temperature spectrum and probability density function at probe location of $r/D = 0.49$, $x/D = 0.29$ in flame 3

From the compensated mean temperature data shown in Fig. 3, one can see that for flame 3 there is a very large reaction region where the mean temperature is 1700 K. However for flame 4, the mean temperature reaches 1700 K near to the burner exit. Due to the presence of very strong turbulence at the burner exit in flame 4, the transportation rate of species increases dramatically, which is expected to increase the flame speed. In order to obtain a very stable premixed flame, the flame speed must match the incoming reactant flow speed. In flame 4, the flame speed is expected to be very high and combustion is steady near the burner exit region. This suggests that the mixture must have burned earlier and the high temperature region occurs at an early stage in flame 4.

The overall temperature in flame 4 is lower than that for flame 3. This is attributed to the increased recirculation of external air in flame 4 compared to flame 3. In addition, the distribution of temperature at downstream positions suggests that in flame 4 the combustion process extends further downstream than in flame 3. In flame 4, the higher swirl number produces large turbulence at the exit of the burner and improves the small scale mixing between the reactants (methane-air mixture) and the hot chemical species. Thus, the fuel-air mixture begins to react very fast and produces a high temperature reaction region. The strong turbulence also assists in mixing in the larger internal recirculation zone. The entrained mixture reduces the local equivalence ratio and increases the heat loss from the flame, which subsequently decreases the flame temperature and extends the spatial evolution of combustion process. The strong turbulence in the flame can cause local extinction, which results from the discrepancy between the mass diffusivity and the thermal diffusivity. In this case, the mass diffusivity is larger than the thermal diffusivity so that the transport of heat can not keep pace with the transport of mass. From this, one can infer that increasing the swirl number will not necessarily improve the overall combustion process. An important task here has been to determine the effect of radial distribution of swirl in a co-annular swirl burner on the global flame development and the subsequent combustion behavior. The mean temperature data showed a bimodal probability density distribution at certain locations of the flame. In the shear layer region, the temperature distribution is bimodal, having two distinct well-defined temperature peaks corresponding to the unburned and recirculated (partially burned) gas mixture, respectively.

Fluctuating Temperature Data. The distributions of fluctuating temperatures for flames 3 and 4 are shown in Fig. 5. This data supports the observed expansion of the flame length

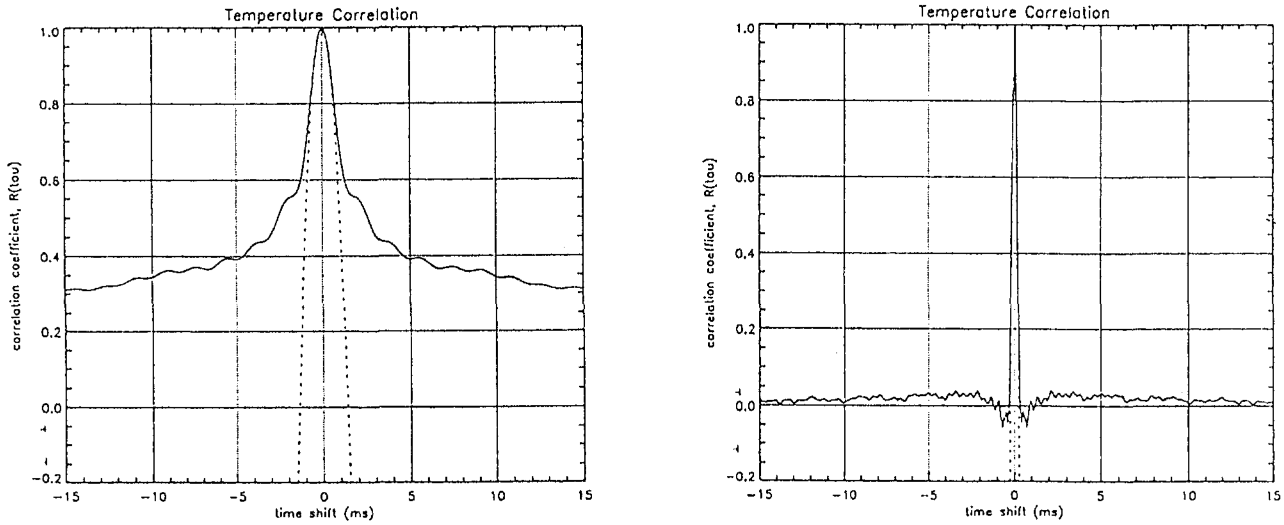

Fig. 7 Micro and integral-time scales at two locations (left diagram: $r/D = 0$, $z/D = 2.34$; right diagram: $r/D = 0.49$, $z/D = 0.29$) in flame 3

Table 2 The temperature distribution and the corresponding time scales at four probe locations in flame 3

Location Parameter	r=0 z=0	r=0 z=0.29 D	r=0.49 D z=0.29 D	r=0 z=2.34 D
Mean Compensated Temperature	1113.3 K	1778.7 K	1193.2 K	749.6 K
Fluctuating Temperature	481.8 K	62.7 K	344.1 K	98.4 K
Thermal Microscale Time	0.41 ms	0.75 ms	0.24 ms	1.37 ms
Thermal Integral Time	2.16 ms	5.79 ms	0.79 ms	12.5 ms

(compare flame lengths and mean temperature data) when the momentum in annulus 2 is maintained constant while the swirl strength in annulus 1 is changed. All flames stabilized with the 45 deg swirler in annulus 1, and are longer and somewhat narrower than those with a weaker swirl of 30 deg in annulus 1, when other parameters are constant. The displayed contour line for the 150 deg temperature fluctuations shows the fluctuating temperature region for flame 3 is much wider than in flame 4. The central core region of the flame was also found to have higher fluctuations for flame 3 than flame 4. A high level of temperature fluctuations is indicative of the strong heat and mass transport phenomenon. In this region, many high-temperature, chemically active species are being mixed with the fresh unburned fuel-air mixture prior to combustion. Combining the fluctuating temperature data with the mean temperature data, one can see that the reaction rate in the recirculation region is very fast. The fluctuating temperatures in flame 4 are much lower than those obtained in flame 3. This is attributed to the stronger turbulence that enhances the mixing, resulting in a far more uniform flowfield.

In both flames, the values of the fluctuating temperatures are much higher than those expected in premixed flames. We attribute this to the swirlers used in the burner for flame stabilization. The large fluctuations in temperature show that the subsequent thermal signatures are far from being uniform. This shows the swirlers' effect on the flow field in premixed flames.

Temperature, Power, Spectra, and Probability, Density Distribution. Temperature power spectra as well as probability density distribution of temperatures at various spatial locations in each flame were obtained to determined both with and without the thermal inertia compensation of the thermocouple. Sample results are shown in Fig. 6 for flame 3, and corresponds to a spatial location of 0.49 burner diameters away from the flame center and 0.29 diameters downstream the burner exit plane. The results show a significant effect of thermal inertia compensation on the thermocouple signature even at very low frequencies. At higher frequencies the difference between the compensated and uncompensated signals becomes much larger. The results obtained at other locations and in other flames revealed similar findings.

The temperature probability density function shown in Fig. 6 shows the occurrence of temperatures between 400 K and 1850 K at this location in the flame. The bimodal temperature distribution has two peaks, one at a temperature of about 780 K and the other at about 1550 K. The peak near 780 K indicates the presence of unburned fuel-air mixture and hot gases in the flame. The peak at the higher temperature is caused by hot recirculated combustion products. The presence of both the unburned fuel-air mixture and hot combustion products is a good indicator of strong turbulence and large amounts of entrained air in this region.

The impact of the compensation can be seen very clearly in the temperature power spectra shown in Fig. 6. This compensation effect is responsible for the significantly higher power spectral density at frequencies larger than about 10 Hz. Reasonable information about the local turbulent flame structure can therefore be obtained only after a proper thermal inertia compensation is made to the thermocouple data. The characteristic thermal time scales associated with the premixed flames are important, as they provide information on the large and small-scale mixing in the flames. Information on the integral and micro-scale of thermal signatures was obtained from the auto-correlation of the fluctuating temperature data. Sample results at two distinctly different locations for flame 3 are shown in Fig. 7. The two curves represent the shear layer region and the post flame region. At the shear layer region the micro and integral-time scales were found to be 0.24 and 0.79 ms, respectively. These time scales changed with position in the flame as well as the flame swirl used for the two flames, as shown in Table 2 and 3. The data clearly show the extent of thermal signature variation in the premixed flames.

Summary

In this study we have obtained quantitative data on mean and fluctuating temperatures in two turbulent premixed swirling flames using fine wire thermometry. A digital compensation technique was used to decrease the effective response time of the probes.

The direct flame photographs proved to be a good overall diagnostic tool to document the flame shapes, global behavior, and dimensions. Most preliminary results were first observed by comparing the flame photographs obtained under different operational conditions.

The mean and fluctuating temperature measurements provided insight into the local thermal turbulent structure of the premixed flames, and they are found to be higher after accounting for the radiative heat loss. Thermal inertia compensation provided significant improvements in determining the flame thermal signatures. The fluctuating values of the measured temperatures are significantly increased after corrections are made for the attenuation in the thermocouple signal at the higher frequencies. Examined premixed flames did not provide uniform thermal field characteristics despite the well-mixed, fuel-air mixture preparation upstream of the combustor prior to its

Table 3 The temperature distribution and the corresponding time scales at four probe locations in flame 4

Location Parameter	r=0 z=0	r=0 z=0.29 D	r=0.49 D z=0.29 D	r=0 z=2.34 D
Mean Compensated Temperature	1736.9 K	1746.4 K	1647.4 K	785.6 K
Fluctuating Temperature	70.3 K	84.3 K	178.3 K	100.8 K
Thermal Microscale Time	0.45 ms	2.34 ms	0.25 ms	1.08 ms
Thermal Integral Time	4.32 ms	14.4 ms	2.80 ms	7.59 ms

introduction into the combustor. The use of swirl in turbulent flames therefore significantly modifies the thermal characteristic of the flames. The role of swirl in premixed flames is important from the point of view of flame stability and combustion and emission characteristics.

The flow thermal characteristics of the flames changed significantly when the annulus 1 swirl was changed. Different flow structures can be created by varying this parameter. Further work in this area will assist in providing guidelines for better design and use of swirlers in combustors.

Acknowledgments

This research was supported by the South Carolina Energy Research and Development Center, Clemson University, Dr. Dan Fant. Program Manager Assistance provided by Dr. Andre Marshall during various stages of experimentation and diagnostics as well as the development of frequency compensated thermocouple diagnostics is greatly appreciated. The help of Armin Wellhoffer and Harald Kafitz with data acquisition and data analysis is much appreciated.

References

1 Gupta, A. K., Lilley, D. G., and Syred, N., 1984, *Swirl Flows,* Abacus Press, Tunbridge Wells, England.

2 Leuckel, I. W., and Fricker, N., 1976, ''The Characteristics of Swirl-Stabilized Natural Gas Flames,'' *J. Inst. Fuel,* Vol. 49, June 1976, pp. 103.

3 Chen, R. H., and Driscoll, J. F., 1988, ''The Role of Recirculation Vortex in Improving Fuel-Air Mixing Within Swirling Flames,'' *22nd Symposium (International) on Combustion,* The Combustion Institute, Pittsburgh, PA, pp. 531–540.

4 Gupta, A. K., Syred, N., and Beer, J. M., 1975, ''Fluctuating Temperature and Pressure Effects on the Noise Output of Swirl Burners,'' *Proc., 15th Symposium (International) on Combustion,* The Combustion Institute, Pittsburgh, PA, pp. 1367–1377.

5 Gupta, A. K., Beer, J. M., and Swithenbank, J., 1976, ''Concentric Multi-Annular Swirl Burners: Stability Limits and Emission Characteristics,'' *Sixteenth Symposium (International) on Combustion,* The Combustion Institute, Pittsburgh, PA, pp. 79–91.

6 Marshall, A. W., and Gupta, A. K., 1996, ''Effects of Jet Momentum Distribution on Thermal Characteristics of Co-Swirling Flames,'' Paper No. 96-0404. 34th AIAA Aerospace Sciences Meeting, AIAA, Reston, VA.

7 Qi, S., Gupta, A. K., and Lewis, M. J., 1997, ''Effect of Swirl on Temperature Distribution in Premixed Flames,'' Paper No. 97-0373 AIAA, Reston, VA, 35th AIAA Aerospace Sciences Meeting & Exhibit.

8 Law, C. K., 1988, ''Dynamics of Streched Flames,'' 22nd Symposium (International) on Combustion, The Combustion Institute, Pittsburgh, PA, pp. 1381–1402.

A Semi-Analytical Finite Rate Two-Reactor Model for Gas Turbine Combustors

J. H. Tonouchi
Analytic and Computational Research, Inc.
Cincinnati, OH

T. J. Held

H. C. Mongia

General Electric Aircraft Engines Company
Combustion Center of Excellence
Cincinnati, OH

A gas turbine combustor is modeled using a two-reactor, finite-rate mixing and chemistry gas particle approach. The first reactor, used to simulate combustion in the primary zone, permits independent definition of the rates of macromixing and micromixing within the reactor, and the amount of premixing of fuel and air entering the reactor. Finite-rate macromixing is simulated by consideration of the fluid particle residence time distribution frequency function and the ages of the particles in the reactor. Finite-rate micromixing is simulated using a modified Coalescence-Dispersion (C-D) model. The second reactor model simulates combustion in the dilution zone of the combustor, and is modeled as a plug flow reactor with cross-flowing jets of dilution air and co-flowing streams of cooling film air. The primary zone reactor model predicts physically reasonable trends in mean temperature, and CO and NO_X emissions as the macromixing and micromixing parameters are varied with respect to the perfectly stirred reactor limit. The model also has shown to predict the correct trends in modeling NO_X and CO emissions from aircraft engine gas turbine combustors.

Introduction

A numerical model of a gas turbine combustor that incorporates finite-rate mixing and chemical processes is presented in this study. This model is based on the population balance chemical reactor modeling approach (Pratt, 1975). Population balance modeling defines the steady-state flow through the combustor as a stream of particles which are born as they enter the combustor, age as they reside in the combustor, and die as they exit. The time that a particle spends in the combustor is its residence time (Danckwerts, 1957; Zweitering, 1959).

Mixing of the fluid particles is defined in terms of "macromixing" and "micromixing." Macromixing is the gross convective recirculation or back mixing in the combustor that brings thermally hot fluid particles into physical proximity with the unignited cold fluid particles. Micromixing is the molecular diffusion among particles that allows the hot particles to ignite the cold particles through the diffusion of heat and mass. Typically, reactor network simulations of gas turbine combustors have utilized perfectly stirred reactor (PSR) models, which neglect both these effects. In addition, PSR models cannot account for the imperfect premixing of fuel and air before entering the combustor. In the present model, finite-rate macro and micromixing and variable premixedness of the fuel and air are considered.

This model is similar to a finite-rate macromixing and micromixing model that was used to model lean-premixed combustion of CH_4/Air within a high-intensity jet-stirred reactor (Tonouchi and Pratt, 1995). Finite-rate macromixing was varied by the flow of fluid particles among the control volumes based on an assumed entrainment model for the jet. Finite-rate micromixing was applied using Curl's Coalescence-Dispersion (C-D) model (Curl, 1963).

Model Description

Most gas turbine combustors have a primary zone characterized by a high rate of back mixing followed by intermediate and dilution zones where the burned and partially burned gases mix with crossflowing jets of air (Lefebvre, 1983). Figure 1 shows a schematic drawing of the flow within these zones. The gases in the primary zone recirculate axially inward due to the high swirl component of the flow. The gases in the intermediate and dilution zones, which will be referred to collectively as the dilution zone, are essentially in plug flow with crossflows of air jets. Because their flowfields are fundamentally different, the modeling approach uses separate reactors to simulate combustion in these two zones. Both reactor models assume adiabatic conditions.

Primary Zone Reactor. The primary zone reactor model is a variation of the work by Kattan and Adler (1972). Finite-rate macromixing is described in terms of the residence time distribution of particles flowing through the reactor and the ages of the particles in the reactor. Finite-rate micromixing is incorporated using a modified C-D model.

Finite-Rate Macromixing. For an ensemble of particles which flow through the reactor, the distribution of particle residence times can be described by the residence time distribution (RTD) frequency function, $f(t)$. The RTD frequency function is defined such that $f(t)dt$ represents the fraction of particles which exit the reactor during a certain residence time interval of t to $t + dt$. The function $f(t)dt$ can also be viewed as the probability that a particle, upon reaching an age between t and $t + dt$, will exit the reactor (Pratt, 1975). Thus $f(t)$ describes the flow within the combustor volume in terms of particles moving in "age space."

One of the two extremes of macromixing include infinitely effective back mixing, such as in a perfectly stirred reactor (PSR). The RTD frequency function for a PSR is a decaying exponential, Eq. (1) (Pratt, 1975),

$$f(t)|_{\text{PSR}} = \frac{1}{t_{\text{PSR}}} \exp\left(\frac{-t}{t_{\text{PSR}}}\right), \qquad (1)$$

where t_{PSR} is the mean residence time of the PSR. Equation (1) is derived by considering a step input of a tracer fluid in the PSR. By performing a mass balance of the tracer fluid in the PSR, an expression is obtained for the concentration of the

---

Contributed by the International Gas Turbine Institute and presented at the International Gas Turbine & Aeroengine Congress & Exhibition, Orlando, FL, June 2–5, 1997. Manuscript received by the ASME Headquarters March 1, 1997. Paper No. 97-GT-126. Associate Technical Editor: H. A. Kidd.

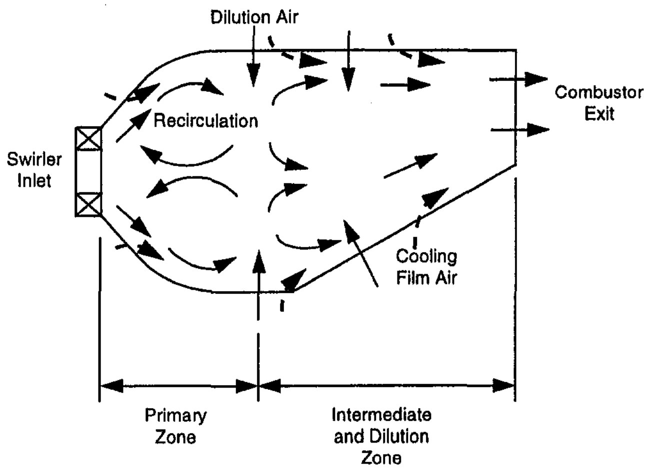

Fig. 1 Schematic drawing of flow within a gas turbine combustor

tracer fluid as a function of time at the reactor exit. The derivative of this expression gives Eq. (1) (Levenspiel, 1972).

The other macromixing extreme is zero back mixing, as in the case of a plug flow reactor (PFR). In a PFR, particles which enter together at time $t = 0$, will exit together at time t_{PFR}. The PFR has an RTD frequency function of a Dirac delta function centered at t_{PFR},

$$f(t)|_{\text{PFR}} = \delta(t - t_{\text{PFR}}). \tag{2}$$

Finite-rate macromixing within the primary zone reactor is modeled by defining the RTD frequency function $f(t)$ for fluid particles entering from each reactor inlet. These inlets include fuel/air particles from the swirlers and air particles from dilution and cooling holes. For this work, it is assumed that $f(t)$ for particles entering from the swirler inlet has a shape which approaches the form of Eq. (1) as the rate of macromixing is increased to the infinite macromixing PSR limit and the form of Eq. (2) as the macromixing rate is decreased to the zero macromixing PFR limit. More specifically, $f(t)$ is assumed to have the form of a PSR in series with a PFR,

$$f(t) = \frac{H(t - t_0)}{t_s - t_0} \exp\left(-\frac{t - t_0}{t_s - t_0}\right), \tag{3}$$

where t_0 is the time the fluid particles reside in the PFR, t_s is the mean residence time for the PSR/PFR arrangement, and $H(t - t_0)$ is the Heaviside unit function. The derivation of Eq. (3) is similar to the derivation of Eq. (1), with the exception that the time variation of the tracer concentration at the PSR/PFR exit is delayed by the PFR time, t_0 (Levenspiel, 1972).

For the primary zone modeled as a PFR in series with a PSR, the minimum time that a fluid particle resides in this reactor arrangement is t_0, the PFR time, since the minimum time that a fluid particle spends in a PSR is zero. In applying Eq. (3) to the primary zone reactor, t_0 is associated with the minimum time a fluid particle spends in the combustor primary zone. This time is one-half the fluid particle cycle time, or one-half the time a fluid particle takes to make one round trip in the primary zone of the combustor (see Fig. 1). As t_0 approaches zero, implying a high rate of recirculation, Eq. (3) approaches the form of Eq. (1). For t_0 approaching the mean residence time t_s, implying little backmixing, Eq. (3) approaches the form of Eq. (2). For the primary zone reactor model, t_{cycle} is defined as the characteristic macromixing time for fuel/air particles entering the reactor from the swirler inlet, and can be estimated as V_{swirler}/L, where V_{swirler} is the velocity of the swirler inlet gases and L is the length of the primary zone.

Air from the dilution hole inlets is typically used to promote recirculation of the fuel and air from the swirlers (see Fig. 1). Although most of this air flows into the dilution zone, some is entrained into the recirculation zone. For air particles entering from the dilution hole inlets, the RTD frequency function is assumed to have the following form:

$$f(t) = \frac{H(t - t_{tr})e^1}{t_{tr}} \exp\left(-\frac{t}{t_{tr}}\right), \tag{4}$$

where t_{tr} is defined as the transit time or the minimum time that a fluid particle spends in the primary zone and $H(t - t_{tr})$ is the Heaviside function. The factor of e is a normalization constant. The fundamental basis for Eq. (4) is derived from consideration of contact times between the air jet and the edge of the recirculation zone.

With RTD frequency functions defined for particles flowing from each inlet, the $f(t)$ for particles which exit the primary zone is assumed to be a mass average of the frequency functions for each inlet,

$$f(t)|_{\text{primary zone}} = \frac{\sum_i^{\text{inlets}} \dot{m}_i f_i(t)}{\dot{m}_{\text{total}}}, \tag{5}$$

where $\dot{m}_{\text{total}}$ is the total mass flow rate through the reactor. Equation (5) is used to prescribe the amount of macromixing in the primary zone by serving as a weighting function for particles to exit the reactor. In earlier formulations of particle models (Butler and Pratt, 1986; Correa, 1995; Chen, 1997;

Nomenclature

a, b = β-PDF coefficients
c_β = constant of proportionality relating the C-D mixing frequency to ϵ and k
$f, \bar{f}$ = mixture fraction, mean mixture fraction
$f(t)$ = residence time distribution frequency function
I_m = number of C-D mixing events per feed (particle entering reactor) event
k = turbulent kinetic energy
L = length of the primary zone
m = total mass in the reactor
$\dot{m}_{\text{total}}$ = total mass flow rate through reactor
N = total number of particles in the reactor
$P(f)$ = inlet mixture fraction probability density function
P_{bulk} = probability for a bulk flow particle to be selected for a C-D event
P_{dil} = probability for a dilution air particle to be selected for a C-D event
PV = inlet mixture fraction variance parameter
t = time
t_0 = residence time in the plug flow reactor component of a PSR/PFR
t_{cycle} = cycle time
t_{PFR} = residence time in plug flow reactor
t_{PSR} = residence time in perfectly stirred reactor
t_s = mean residence time
t_{tr} = dilution air hole transit time
V_{swirler} = velocity of the gases exiting from the swirler inlet
x_{dil} = mixing bias factor for the C-D mixing probability of a dilution air particle
β = C-D mixing frequency
Δt = timestep
ϵ = turbulent dissipation rate

Chen, 1993) the reactor volume was assumed to have infinite macromixing rates or to have an RTD frequency function resembling Eq. (1). Thus, particles of any age were randomly selected from the ensemble to exit the reactor. In this model, since finite-rate macromixing is assumed, Eq. (5) is used to specify that only particles close to an age of t may be randomly selected to exit.

Finite-Rate Micromixing. Variable-rate micromixing is simulated using a modified form of the C-D model, where micromixing is simulated by randomly pairing particles and allowing them to mix (coalesce) before being dispersed and allowed to react as individual batch, or closed system, reactors. In this work, the C-D model is modified in two ways. First, unlike the original Curl model, which assumes that the reactor is infinitely macromixed and thus any two particles can be paired, only particle pairs that are likely to be physically near each other are randomly selected to mix. This model does not track the location of each particle in the reactor, but assumes that two particles are likely to be near each other if their ages are nearly the same or their ages differ by a multiple of the fluid particle cycle time.

The second modification to the Curl model is the way in which two paired particles mix. In the original approach, the extensive properties (enthalpy and chemical species masses) of the particles are averaged, and each particle assumes the averaged properties. In the present model, a randomly selected fraction of their extensive properties are exchanged (Dopazo, 1979; Janika et al., 1978).

After mixing, each of the particles undergoes batch reaction until it is selected again for a mixing event or exits the reactor. The number of C-D events is prescribed by the micromixing parameter I_m, which is defined as the number of C-D events per feed (particle entering reactor) event, or as the ratio of the C-D mixing frequency β to the reciprocal mean residence time $1/t_s$. The mixing frequency is typically estimated as

$$\beta = c_\beta \frac{\epsilon}{k}, \qquad (6)$$

where ϵ is the turbulent dissipation rate, k is the turbulent kinetic energy, and c_β is a proportionality constant (Pratt, 1975). For this work, an averaged ϵ/k was determined for the entire reactor from CFD calculations. The proportionality constant c_β is set to a value of 5, obtained by "tuning" the model's predictions for a given combustor condition. The same value of c_β is used for all the results presented in this paper. The micromixing parameter I_m has the limits of zero, representing no micromixing among the fluid particles, and infinity, representing molecular homogeneity within the reactor.

Numerical Approach. Initially, the primary zone reactor consists of a user-defined number of equal-mass fluid particles. Each of these particles is assigned the temperature and composition of a PSR with the same volume and inlet conditions as the primary zone.

At each timestep, discrete fluid particles enter the reactor from the swirler inlet and dilution holes. The rate of particles entering from an inlet i is $N_i = m_i N/m$, where m_i is the mass flow rate of inlet i, N is the total number of particles in the reactor, and m is the total mass in the reactor. Particles entering from the swirler inlet have a composition and temperature representative of the inlet stream of fuel and air. The composition of each entering particle is randomly weighted from an assumed beta-PDF of the mixture fraction ($P(f)$) and a user-defined mixture fraction variance (PV), as defined by the following equations:

$$P(f) = f^{a-1}(1-f)^{b-1}\frac{\Gamma(a+b)}{\Gamma(a)\Gamma(b)}$$

$$a = \frac{\bar{f}}{PV} - \bar{f}, \quad b = \frac{1-\bar{f}}{PV} + (\bar{f} - 1). \qquad (7)$$

The limit of $PV = 0$ corresponds to a perfectly premixed inlet, while $PV = 1$ gives completely non-premixed inlet particles. Particles entering from dilution and cooling inlets are assigned the composition and temperature of the inlet air stream.

Since the flow through the reactor is steady, the rate of particles exiting the reactor is equal to the rate of particles entering the reactor. Because finite-rate macromixing is assumed, the selection of particles to exit the reactor is random but weighted by Eq. (5). Thus, finite-rate macromixing is implicitly applied in the selection of particles to exit the reactor.

After the flow of particles into and out of the reactor, micromixing is simulated by applying the C-D model to the ensemble of particles. The number of C-D events per timestep, defined as the time between a feed (particle entering from the swirler inlet) event, is given by the mixing parameter I_m. It is assumed that I_m is an averaged value for the entire primary zone. As explained earlier, the probability that a given particle pair will mix is weighted by their relative ages. The batch kinetics of the particles are calculated using a modified form of the SENKIN package in Chemkin-II (Kee et al., 1989). The chemical kinetic mechanism used is the semi-empirical n-heptane oxidation scheme of Held et al. (1996), which consists of 255 reactions among 41 species. The formation mechanism for NO_X is taken from GRI-Mech 2.11 (Bowman et al., 1996), and accounts for an additional 97 reactions and 17 species.

The process of inflow, outflow, and micromixing is repeated until a stationary state in the temperature and species concentrations is achieved, usually in 5 mean residence times. Typically, the convergence rate is limited by the NO mass fraction. Runtimes using 500 particles for the conditions examined in this work required 20 to 25 hours on a Pentium Pro 200 computer.

Dilution Zone Reactor. The combustor primary zone is characterized by a significant amount of back mixing; downstream in the dilution zone the gas is essentially in plug flow with cross streams of dilution air and co-flowing streams of combustor wall cooling film air. The dilution zone reactor simulates the plug flow of particles that have exited the primary zone reactor. It is assumed that there is no back mixing in the dilution zone; thus, the mixing of particles in the axial direction is not permitted. Without back mixing, a Lagrangian approach can be used for this reactor model, where a plug of fluid particles is followed as it flows through the dilution zone. Dilution and cooling air particles are introduced as the plug passes the axial location of these inlets. The number of air particles entering the plug depends on the inlet's mass flow rate relative to the mass flow rate entering the dilution flow reactor.

For each user-defined timestep Δt, the C-D model is applied to the ensemble of particles. The number of C-D events per timestep is prescribed by I_m for the dilution flow reactor model. Particles selected to undergo C-D events are chosen at random, but each particle probability of selection is weighted by an empirical biasing factor related to its cross-flowing momentum. A nominal mixing frequency is assigned to the main inlet (the primary zone reactor exit), which is related to the bulk turbulence properties as described in Eq. (6). Cooling film particles are assumed to have the same mixing frequency since these particles are co-flowing within the dilution flow reactor. An entering dilution air particle, because it is cross-flowing and has a higher momentum than the bulk flow, is assumed to have a higher mixing frequency (i.e., probability of selection for a mixing event) since it has greater opportunity to interact with the other particles in the plug. The probability for a dilution air particle to be selected for a C-D event, P_{dil}, is given as follows:

$$P_{\text{dil}} = x_{\text{dil}} P_{\text{bulk}}, \qquad (8)$$

where P_{bulk} is the probability for a bulk flow particle to be selected for a C-D event, and x_{dil} is defined as the mixing bias factor. The mixing bias factor is assumed to be proportional to the ratio of the dilution air jet momentum to the bulk flow momentum. For the purposes of this work, x_{dil} was set to 10, based on order-of-magnitude estimates of the relative dilution jet and bulk flow momenta. As the dilution air particle mixes with other particles, it transfers its momentum to those particles, thus eventually approaching a uniform mixing bias with the bulk flow. In other words, the dilution air particle's probability for a C-D event decreases to that of the co-flowing particles. To simulate this effect, a C-D encounter also exchanges momentum (and hence, probability for micromixing) between two particles. The momentum transfer between paired particles is assumed to be proportional to their mass exchange.

The plug of particles that exits the reactor gives the properties of the fluid for one combination of inlet particles and random mixing processes. In order to achieve a statistical sample of particles, it is necessary to pass a number of particle groups through the reactor. For the results presented in this work, 2 or 3 passes of 500 particles were used, limited due to computer runtime considerations. Further investigation is needed to assess the number of passes required and the number of particles per pass to achieve a stationary state for a range of operating conditions.

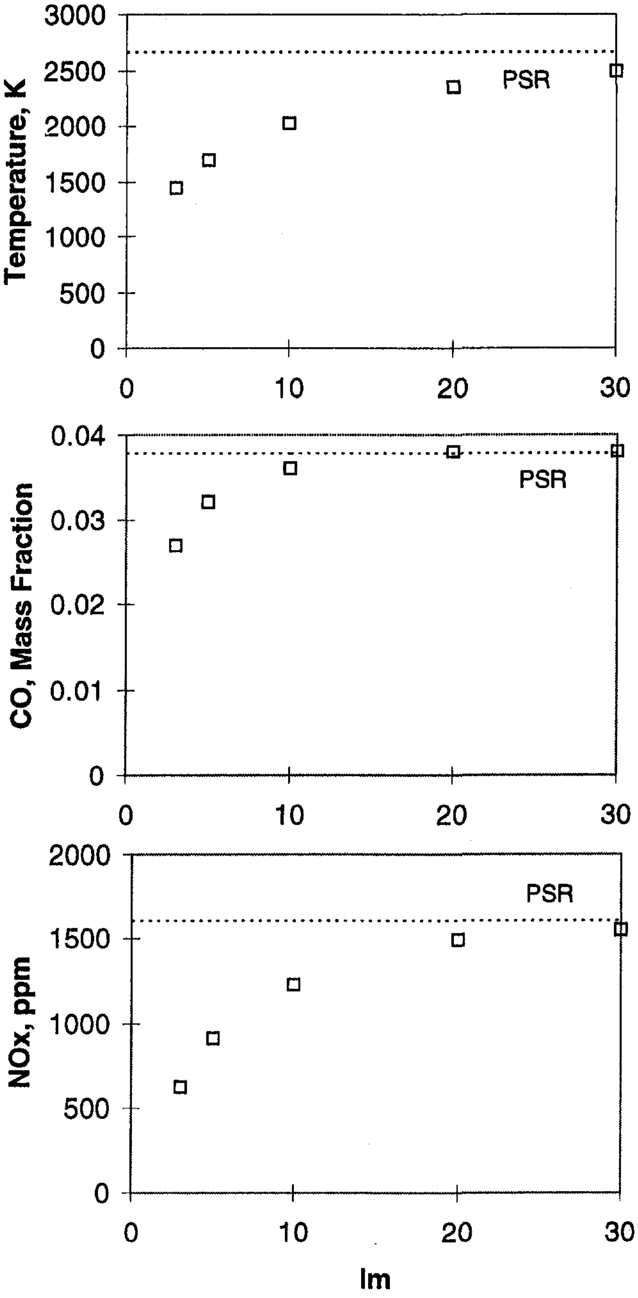

Fig. 2 Temperature, CO, and NO_X predictions versus the micromixing parameter I_m using the primary zone reactor. The dashed lines represent the $I_m = \infty$ PSR limit, assuming the entire primary zone is a perfectly stirred reactor.

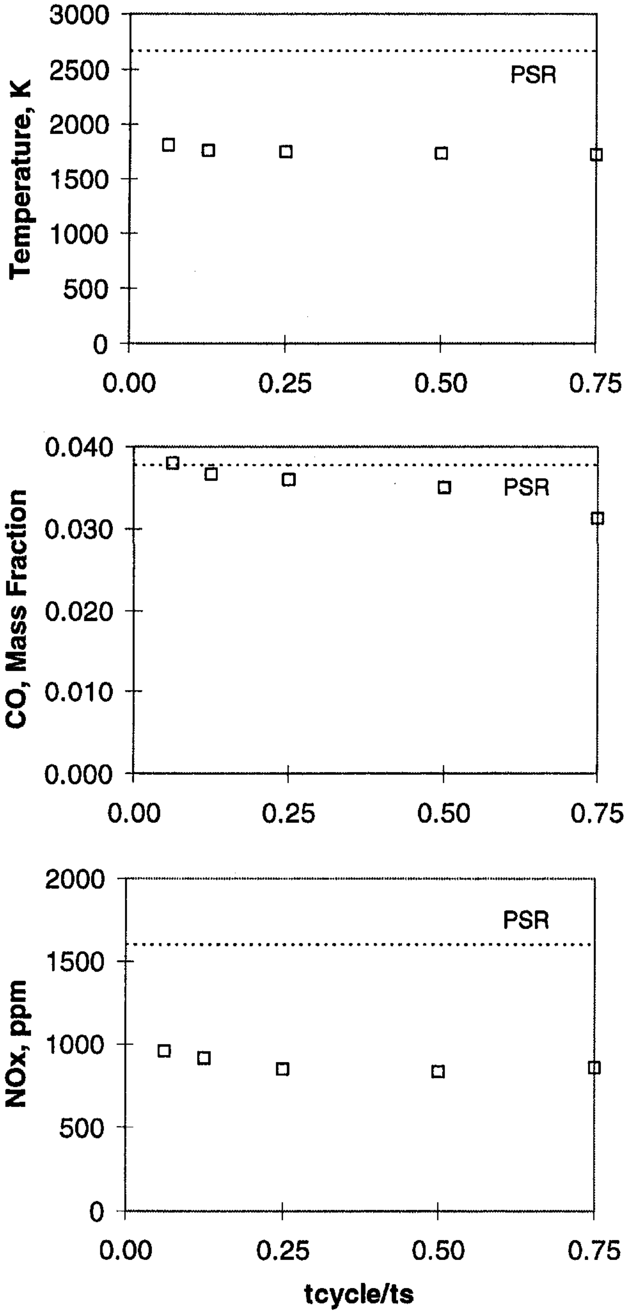

Fig. 3 Temperature, CO, and NO_X predictions versus the ratio of the fluid particle cycle time to the mean residence time using the primary zone reactor. The dashed lines represent the PSR limit, assuming the primary zone reactor is a PSR.

Variation of Primary Zone Reactor Model Parameters

There are four mixing parameters in the primary zone reactor model. The fluid particle cycle time and the transit time of dilution air particles, t_{cycle} and t_{tr} respectively, determine the rate of macromixing. The rate of micromixing is specified by I_m. The fourth parameter is the mixture fraction variance, which specifies the premixedness of the fuel and air before it enters the reactor. A parametric study was performed to verify that the primary zone reactor predicts the correct trends with respect to the PSR limit and to investigate the sensitivities of the model parameters.

The primary zone modeled was for a combustor with a swirler inlet and three dilution holes. The nominal conditions modeled were heptane fuel, an overall mass fuel/air ratio of 0.0301, at 30.4 atm. The fuel and air entering from the swirler are assumed to be perfectly premixed and enter at a temperature of 855 K; the mass fuel/air ratio for this stream was 0.07 (corresponding to an equivalence ratio of 1.1). The volume of the primary zone was estimated at 7500 cm^3, and the mean residence time about 1.3 ms.

The macromixing times were estimated from the geometry of the combustor and the mass flow rates through the swirler and dilution holes. For the baseline condition, the cycle time was estimated to be one-fourth the mean residence time. The transit times for the air particles entering from the dilution holes were estimated from estimates of the particles' trajectories from the holes to the primary zone exit. The dilution hole transit times were fixed for all the conditions examined in this study. The micromixing parameter I_m was determined from Eq. (6) to be about 6. About 500 to 600 particles were used in this study.

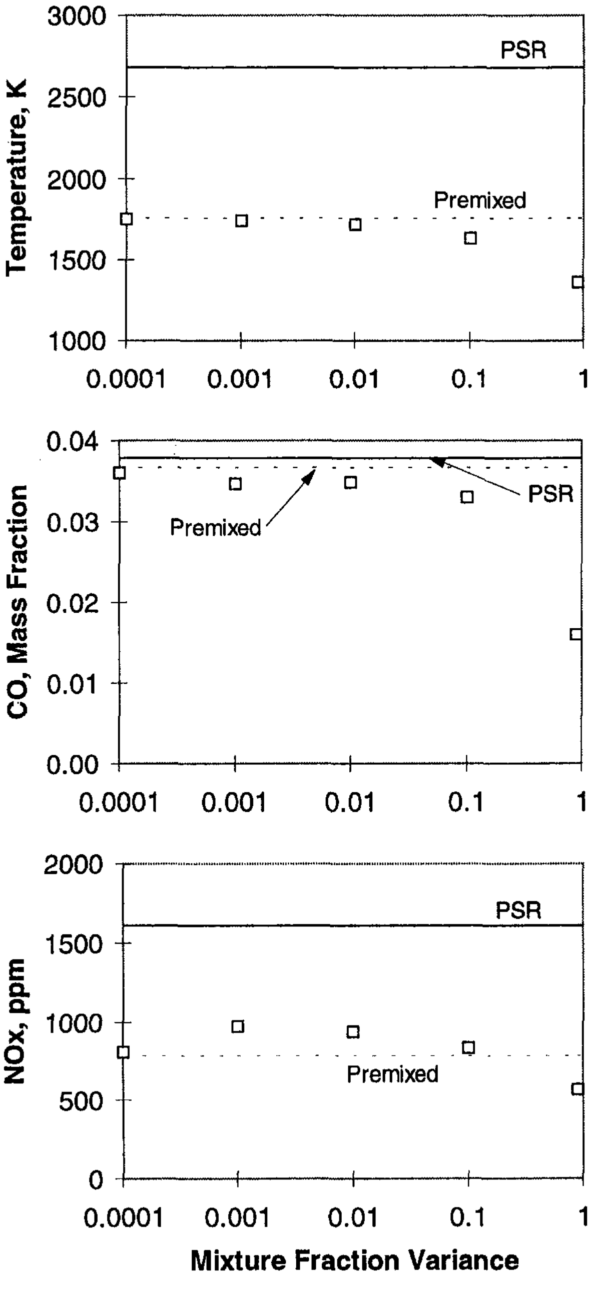

Fig. 4 Temperature, CO, and NO_X predictions versus mixture fraction variance (Eq. (6)). The dashed lines represent the results for premixed (zero mixture fraction variance) conditions. The solid lines represent the PSR results, assuming the primary zone reactor is a PSR.

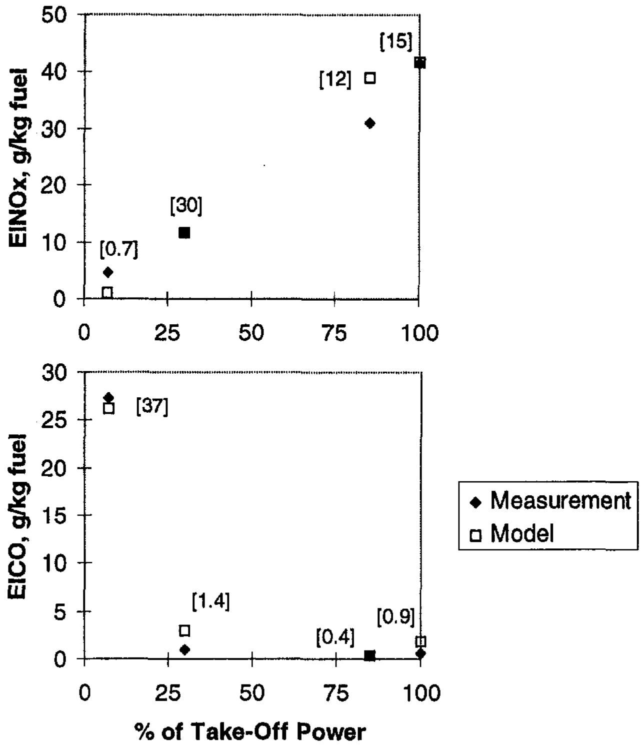

Fig. 5 Comparison of the modeled results with the measured data for combustor 1. The measured data are taken from the combustor 1 outlet. The modeled results are the ensemble particle mean properties which exit the dilution flow reactor. The data in the brackets are the root mean square of the particle properties. For the points modeled above, the micromixing frequency β is assumed to be 4000 Hz for the primary zone reactor, and 5000 Hz for the dilution flow reactor.

Figure 2 shows the results of varying only the mixing parameter I_m from the conditions given above. The points plotted represent the mean properties of the particle ensemble. The figure shows that as the micromixing rate parameter I_m is increased, the predicted temperature, CO, and NO_X approach the PSR limit, calculated independently using the PSR code of Glarborg et al. (1986). Increasing I_m gives the hot particles more opportunities to mix and ignite the cold particles. This leads to an overall increase in the reactor temperature, CO, and NO_X because of the greater number of burned and partially burned particles relative to the number of unignited cold particles, which have an inlet temperature of 855 K and zero concentrations of CO and NO_X.

For an I_m of 2, combustion could not be sustained in the reactor. The rate of micromixing among the particles is too low, thus allowing little opportunity for the hot particles to ignite the inflowing cold particles. Because the conditions preclude the possibility of autoignition, a minimum amount of micromixing is required for sustained combustion within the reactor.

Figure 3 presents the results of varying the fluid particle cycle time, t_{cycle}, with the other model parameters held fixed at the conditions specified earlier. The results indicate that the cycle time does not significantly influence the ensemble mean temperature, CO, or NO_X, despite a variation of t_{cycle} from a condition of high recirculation (small cycle time) to a macromixing condition approaching plug flow (large cycle time). It appears that for the conditions chosen for this parametric study, the micromixing effects (variation of I_m) are more significant than macromixing effects. Further study is required to examine under what conditions the macromixing parameters of cycle time and dilution hole transit times, which were fixed for this study, would play a more significant role.

The results of varying the initial mixing state of the fuel and air are shown in Fig. 4. Increasingly poor premixing (increasing variance) results in a lower ensemble mean temperature and lower CO, as an increasing number of unreacted fuel particles exit the reactor. For a relatively small amount of non-premixedness ($PV = 0.001$), NO_X emissions increase by 24 percent over the perfectly premixed inlet case, even though the mean temperature has slightly decreased. Under perfectly premixed conditions, the maximum possible temperature is the equilibrium temperature of the mixture (i.e., all the fluid particles have the same mixture fraction). With imperfect premixing, some particles achieve a mixture fraction closer to stoichiometric than the mean, which has the effect of adding a high-temperature "tail" to the particle temperature distribution. Because of the high sensitivity of NO_X formation rate to temperature, this change has the effect of increasing NO_X emission levels. As the variance increases, the lower mean temperature eventually causes the observed decrease in NO_X emissions.

Modeling Gas Turbine Combustor Data

Three combustors, referred to as combustors 1, 3, and 4 (numbering identical to Danis et al. (1996)), are modeled for this study, at four operating conditions varying from idle to sea level takeoff power. The combustors are all production single-annular, rich dome designs, and the emissions data are from certification tests. To limit the number of free input parameters to the two-reactor approach, several assumptions are made in modeling the data.

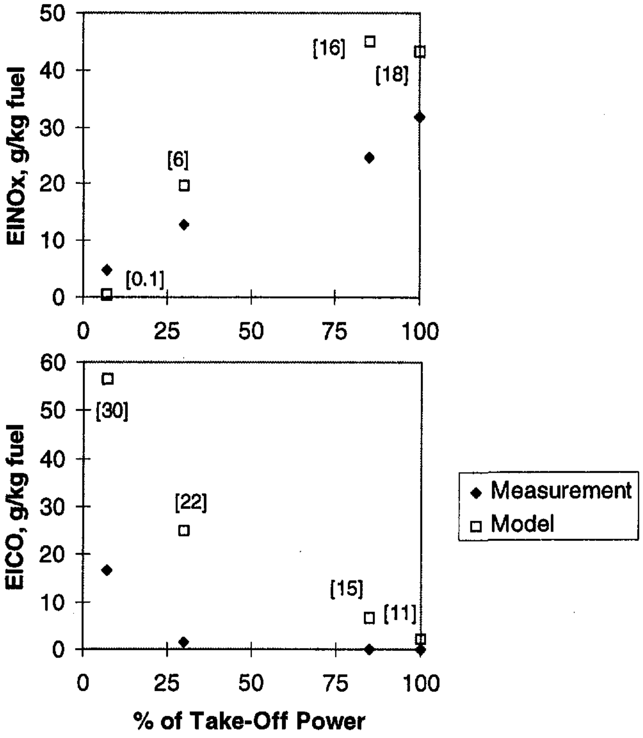

Fig. 7 Comparison of the modeled results with the measured data for combustor 4. The measured data are taken from the combustor 4 outlet. The modeled results are the ensemble particle mean properties which exit the dilution flow reactor. The data in the brackets are the root mean square of the particle properties. For the points modeled above, the micromixing frequency β is assumed to be 3000 Hz for the primary zone reactor, and 4000 Hz for the dilution flow reactor.

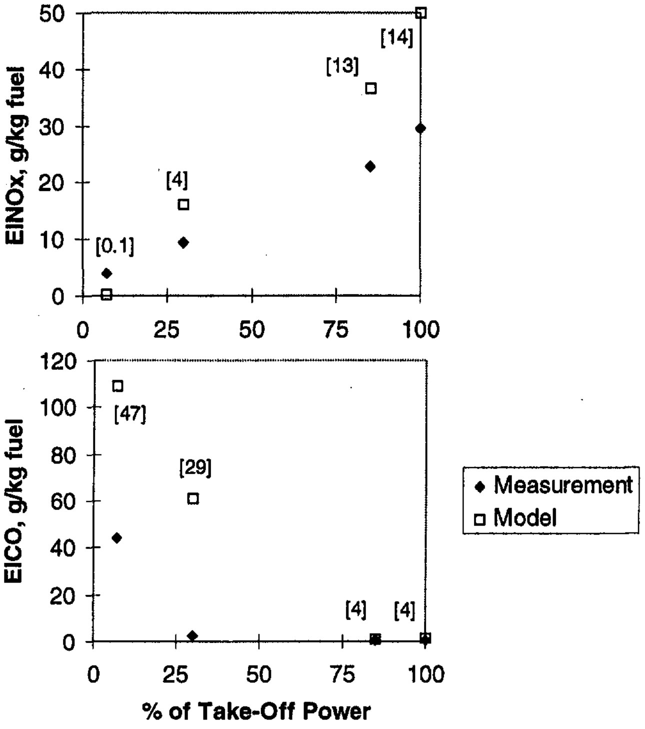

Fig. 6 Comparison of the modeled results with the measured data for combustor 3. The measured data are taken from the combustor 3 outlet. The modeled results are the ensemble particle mean properties which exit the dilution flow reactor. The data in the brackets are the root mean square of the particle properties. For the points modeled above, the micromixing frequency β is assumed to be 3000 Hz for the primary zone reactor, and 4000 Hz for the dilution flow reactor.

- For a given combustor, the volumes of the primary and dilution zones, as well as the flow splits of fuel and air flows through inlets, dilution holes, and cooling film are held fixed for the range of power conditions modeled.
- The micromixing frequency β is assumed to be independent of operating condition. The micromixing frequency is estimated from Eq. (6) to be from 3000 to 5000 Hz, corresponding to an I_m of about 5 to 10.
- The fluid particle cycle time in the primary zone is assumed to be one-fourth the mean residence time. The transit times for the dilution particles introduced into the primary zone reactor are estimated from the location of these holes.
- The fuel and air entering from the swirler inlet are assumed to be premixed (zero mixture fraction variance).
- The fuel (heptane) mass flow rate is adjusted to match the equivalence ratio of the Jet-A data.
- About 500 to 600 particles are used in the primary zone reactor; the number of particles exiting the dilution flow reactor after one pass is about 1000 to 1300. The results given in the modeling are for one pass.

Figures 5 through 7 present the calculated and measured CO and NO_X emissions from the three combustors. The modeled results are the particle ensemble mean properties exiting the dilution flow reactor. The data in brackets next to the modeled results are the root mean square (rms) of the particle properties exiting the dilution flow reactor.

The two-reactor model gives the correct trends for all three combustors over the modeled conditions. The agreement with the measured data is reasonable, considering the assumptions and lack of optimization used in modeling these data. The comparisons with combustor 1 are good, while for combustors 3 and 4, the model tends to overpredict NO at higher power conditions and overpredict CO at low power conditions. Better agreement with the measurements can be expected by considering the variation of the primary model parameters, particularly I_m, which is probably not constant over the range of power conditions examined.

Two general observations can be made based on informal variation of the modeling parameters. The first is that the NO_X emissions level primarily depends on conditions in the primary zone reactor, consistent with the high temperature dependence of the thermal NO_X formation rate. The particle ensemble NO_X does continue to increase in the dilution flow reactor; however, varying I_m in the dilution reactor does not significantly influence the NO_X production rate. The second observation is that the dilution flow reactor plays a predominant role in determining the CO emissions level. The micromixing parameter I_m significantly affects the CO oxidation rate in the dilution zone.

Further study is required to understand the sensitivities of the two-reactor model parameters. Additional work is required to determine the minimum number of particles to achieve a "particle number independent" solution. Similar work must be performed to assess the number of particles and passes through the dilution zone reactor.

Conclusions

A two-reactor model incorporating finite-rate chemistry and mixing has been described, and early parametric studies and comparisons to emissions data reported. Qualitative success has been obtained by varying only the micromixing parameters in the primary zone reactor and dilution flow reactor. Further investigation is required to assess the relative sensitivities and interactions of the model parameters, particularly the effects of inlet mixture fraction variance. From the parametric studies and data modeled to this point, the micromixing parameter I_m appears to play a more significant role in determining CO and NO_X emissions than the macromixing parameters.

References

Butler, G. W., and Pratt, D. T., 1986, "Coalescence/Dispersion Modeling of Turbulent Combustion in a Jet-Stirred Reactor," *AIAA Journal*, Vol. 24, pp. 1817–1821.

Bowman, C. T., et al., 1996, *GRI-MECH Version 2.11*, University of California, Berkeley, Berkeley, CA, http://www.me.berkeley.edu/gri_mech.

Chen, J.-Y., 1997, "Stochastic Modeling of Partially Stirred Reactors," *Combustion Science and Technology*, Vol. 122, p. 63.

Chen, J.-Y., 1993, "Stochastic Modeling of Partially Stirred Reactors," Paper No. 93-071, Fall Meeting, Western States Section/The Combustion Institute, Menlo Park, CA.

Correa, S. M., 1993, "Turbulence-Chemistry Interactions in the Intermediate Regime of Premixed Combustion," *Combustion and Flame*, Vol. 93, pp. 41–60.

Curl, R. L., 1963, "Dispersed Phase Mixing: I. Theory and Effects in Simple Reactors," *AIChE Journal*, Vol. 9, pp. 175–181.

Danckwerts, P. V., 1957, "The Effect of Incomplete Mixing on Homogeneous Reactions," *Chemical Reaction Engineering*, 12th Meeting European Federation Chemical Engineering, Amsterdam, Pergamon, New York, pp. 93–102.

Danis, A. M., Pritchard, B. M., and Mongia, H. C., 1996, "Empirical and Semi-Empirical Correlation of Emissions Data from Modern Turbopropulsion Gas Turbine Engines," ASME Paper No. 96-GT-86.

Dopazo, C., 1979, "Relaxation of Initial Probability Density Functions in the Turbulent Convection of Scalar Fields," *Physics of Fluids*, Vol. 22, pp. 20–30.

Glarborg, P., Kee, R. J., Grcar, J. F., and Miller, J. A., 1986, *PSR: A Fortran Program for Modeling Well-Stirred Reactors*, Sandia Report, SAND86-8209, Sandia, Livermore, CA.

Held, T. J., Marchese, A. J., and Dryer, F. L., 1997, "A Semi-Empirical Reaction Mechanism for n-Heptane Oxidation and Pyrolysis," *Combustion Science and Technology*, Vol. 123, pp. 107–147.

Janika, J., Kolbe, W., and Kollman, W., 1978, "The Solution of a P.D.F. Transport Equation for Turbulent Diffusion Flames," *Proceedings 1978 Heat Transfer and Fluid Mechanics Inst.*, C. T. Crowe and W. L. Grosshandler, eds., Stanford University Press, Stanford, CA, pp. 296–312.

Kattan, A., and Adler, R. J., 1972, "A Conceptual Framework for Mixing in Continuous Chemical Reactors," *Chemical Engineering Science*, Vol. 27, pp. 1013–1028.

Kee, R. J., Rupley, F. M., and Miller, J. A., 1989, *Chemkin II: A Fortran Chemical Kinetics Package for the Analysis of Gas-Phase Chemical Kinetics*, Sandia Report SAND89-8009, Sandia, Livermore, CA.

Lefebvre, A. H., 1983, *Gas Turbine Combustion*, Hemisphere Publishing, New York.

Levenspiel, O., 1972, *Chemical Reaction Engineering*, John Wiley & Sons, Inc., New York.

Pratt, D. T., 1975, "Mixing and Chemical Reaction in Continuous Combustion," *Progress in Energy and Combustion Science*, Vol. 1, pp. 75–88.

Tonouchi, J. H., and Pratt, D. T., 1995, "A Finite-Rate Macromixing, Finite-Rate Micromixing Model for Premixed Combustion," Paper No. 95F-167, Western States Section/The Combustion Institute, Stanford, CA.

Zweitering, T. N., 1959, "The Degree of Mixing in Continuous Flow Systems," *Chemical Engineering Science*, Vol. 11, pp. 1–15.

The GE Rich-Quench-Lean Gas Turbine Combustor

A. S. Feitelberg

M. A. Lacey

GE Corporate Research and Development,
One Research Circle,
Niskayuna, NY 12309

The General Electric Company has developed and successfully tested a full-scale, F-class (2550°F combustor exit temperature), rich-quench-lean (RQL) gas turbine combustor, designated RQL2, for low heating value (LHV) fuel and integrated gasification combined cycle applications. Although the primary objective of this effort was to develop an RQL combustor with lower conversion of fuel bound nitrogen to NO_x than a conventional gas turbine combustor, the RQL2 design can be readily adapted to natural gas and liquid fuel combustion. RQL2 is the culmination of a 5 year research and development effort that began with natural gas tests of a 2" diameter perforated plate combustor and included LHV fuel tests of RQL1, a reduced scale (6" diameter) gas turbine combustor. The RQL2 combustor includes a 14" diameter converging rich stage liner, an impingement cooled 7" diameter radially-stratified-quench stage, and a backward facing step at the entrance to a 10" diameter film cooled lean stage. The rich stage combustor liner has a novel double-walled structure with narrow circumferential cooling channels to maintain metal wall temperatures within design limits. Provisions were made to allow independent control of the air supplied to the rich and quench/lean stages. RQL2 has been fired for almost 100 hours with LHV fuel supplied by a pilot scale coal gasification and high temperature desulfurization system. At the optimum rich stage equivalence ratio NO_x emissions were about 50 ppmv (on a dry, 15 percent O_2 basis), more than a factor of 3 lower than expected from a conventional diffusion flame combustor burning the same fuel. With 4600 ppmv NH_3 in the LHV fuel, this corresponds to a conversion of NH_3 to NO_x of about 5 percent. As conditions were shifted away from the optimum, RQL2 NO_x emissions gradually increased until they were comparable to a standard combustor. A chemical kinetic model of RQL2, constructed from a series of ideal chemical reactors, matched the measured NO_x emissions fairly well. The CO emissions were between 5 and 30 ppmv (on a dry, 15 percent O_2 basis) under all conditions.

Introduction

The General Electric Company is developing gas turbines and a high temperature desulfurization system for use in integrated gasification combined cycle (IGCC) power plants. High temperature desulfurization, or hot gas cleanup (HGCU), offers many advantages over conventional low temperature desulfurization processes, but does not reduce the relatively high concentrations of fuel bound nitrogen (FBN) that are typically found in low heating value (LHV) fuel. When fuels containing bound nitrogen are burned in conventional gas turbine combustors, a significant portion of the FBN is converted to NO_x. For this reason, methods of reducing the NO_x emissions from IGCC power plants equipped with HGCU are needed. Rich-quench-lean (RQL) combustion can decrease the conversion of FBN to NO_x because a large fraction of the FBN is converted into non-reactive N_2 in a fuel rich stage. Additional air, required for complete combustion, is added in a quench stage. A lean stage provides sufficient residence time for complete combustion.

The objective of the RQL2 program has been to develop a gas turbine combustor that has a lower conversion of FBN to NO_x than a conventional LHV fuel combustor and is suitable for use in a GE heavy duty gas turbine. Such a combustor must be of appropriate size and scale, configuration (can-annular), and capable of reaching F-class firing conditions (combustor exit temperature = 2550°F).

RQL2 Development

The development of RQL2, a full scale (14" rich stage diameter, 20 lb/s total flow), rich-quench-lean gas turbine combustor is the culmination of a five year research and development effort. This program began with testing of a small (2" diameter) perforated plate burner, using natural gas and natural gas/ammonia mixtures for fuel (Goebel and Feitelberg, 1992). The promising perforated plate burner tests were followed by the development of RQL1, a reduced scale (6" rich stage diameter, 0.75 lb/s total flow), rich-quench-lean combustor. RQL1 was tested using high temperature LHV fuel produced by the pilot scale coal gasification and HGCU facility located at GE Corporate Research and Development (Bowen et al., 1995). At the optimum operating conditions the conversion of NH_3 to NO_x in RQL1 was about 15 percent, significantly lower than expected from a conventional gas turbine combustor burning the same fuel. A detailed discussion of the RQL1 design and test results can be found in Bowen et al. (1995).

The approach taken to design RQL2 combustor was to build upon the prior RQL and LHV fuel combustor designs that were developed and tested at GE Corporate Research and Development (Bowen et al., 1995). Several design features from the RQL1 combustor such as a converging rich stage geometry, a radially stratified quench section, and a backward facing step, were incorporated into the RQL2 design. Design features from conventional LHV fuel combustors were also used in the RQL2 design. The RQL2 combustor uses a fuel nozzle that was developed for conventional swirl stabilized diffusion flame LHV fuel combustors (Battista et al., 1996) as well as a filmed cooled lean stage liner which is similar to the liners used in conventional LHV fuel combustors. In addition, the RQL2 combustor takes advantage of new gas turbine technology; for example,

---

Contributed by the International Gas Turbine Institute and presented at the International Gas Turbine & Aeroengine Congress & Exhibition, Orlando, FL, June 2–5, 1997. Manuscript received by the ASME Headquarters March 1, 1997. Paper No. 97-GT-127. Associate Technical Editor: H. A. Kidd.

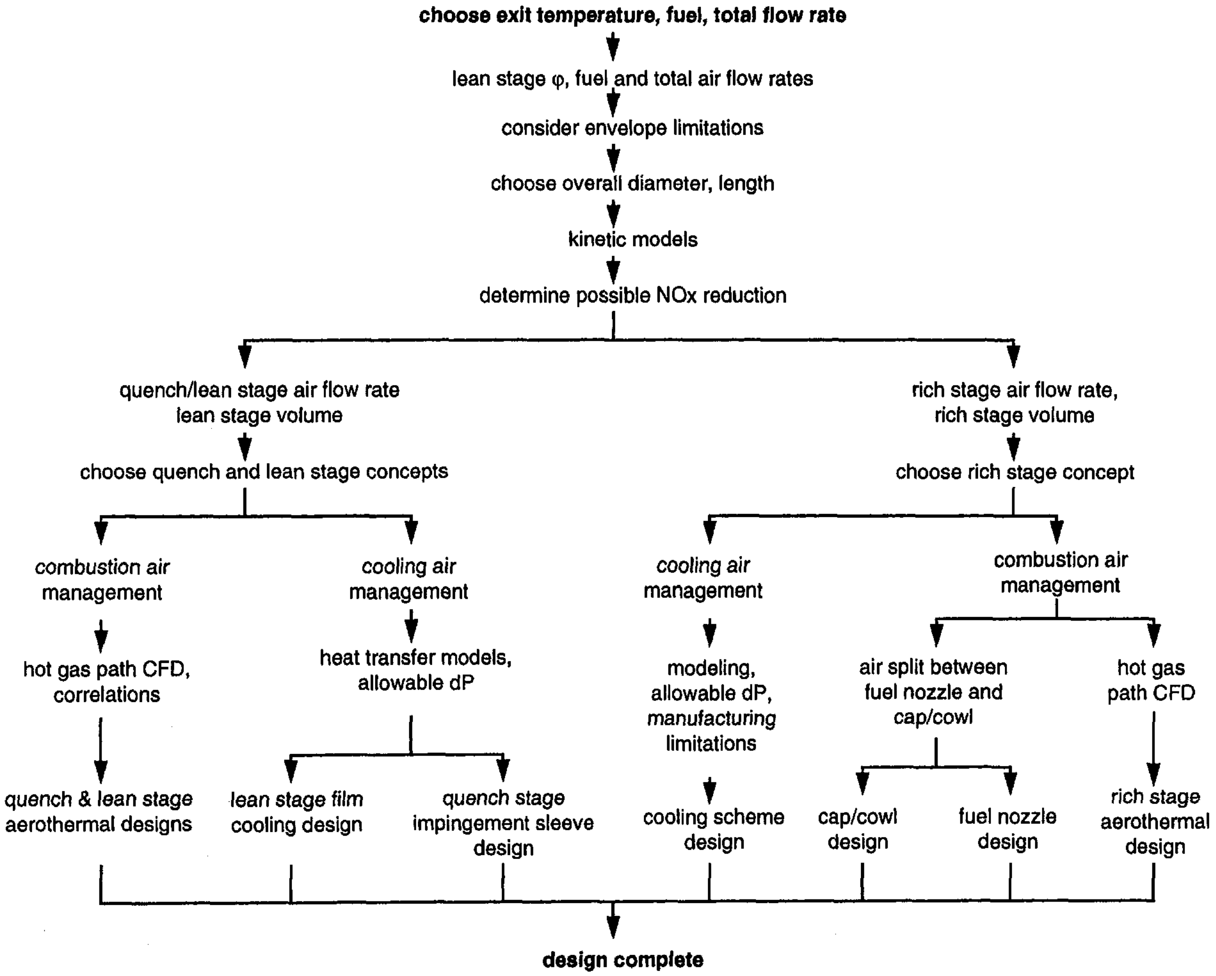

Fig. 1 RQL2 design methodology

the RQL2 rich stage liner uses a new cooling scheme developed at GE Corporate Research and Development (Jackson et al., 1996).

The separation of the air supplies for the rich stage and quench/lean stage is another design feature first used in RQL1. Dividing the total combustion air into two separate, independently controlled streams is important from a research perspective, because this capability allows us to search for the optimum rich stage operating conditions. In addition, overall air management (e.g., air pressure drop) is simplified, because the rich stage cooling scheme can be designed almost independently of the quench/lean stage cooling scheme. This allowed much of the detailed design and modeling work for the rich stage to proceed independently of the quench/lean stage design.

The general methodology used to design RQL2 is shown in Fig. 1. The overall fuel/air ratio was determined by selecting the maximum combustor exit temperature, and by the decision to use pilot plant LHV gas as the fuel (see Table 1). The goal of designing a combustor suitable for use in GE heavy duty gas turbines dictated the configuration (can-annular) and overall dimensions of the RQL2 combustor. This constraint also made some RQL combustor concepts, such as the multi-annular swirl burner, unsuitable (Domeracki, 1994). The distribution of the total available volume between the rich, quench, and lean stages was determined by combining: (1) a computational fluid dynamics (CFD) analysis, which predicted the overall flow field and the size and shape of the recirculation zones, and (2) chemical kinetic models, which related the rich stage residence time and temperature to the conversion of NH_3 to NO_x.

Table 1 Typical pilot plant low Btu fuel composition

Species	Mole Percent
CO	8.6
H_2	17.3
CH_4	2.7
N_2	30.1
CO_2	12.6
H_2O	28.0
Ar	0.3
NH_3	0.4
TOTAL	100.0

Higher Heating Value = 110 Btu/SCF
(4370 kJ/kg)

RQL2 Design

A schematic of the RQL2 combustor and test stand can be found in Fig. 2. The 24″ diameter pressure vessel containing the RQL2 combustor is divided into two separate chambers that are fed by independently controlled air supplies. The hot combustion gases flow through the RQL2 combustor liner, an impingement cooled transition piece, a sector from the film cooled first stage nozzle of a GE LM6000 gas turbine, and then

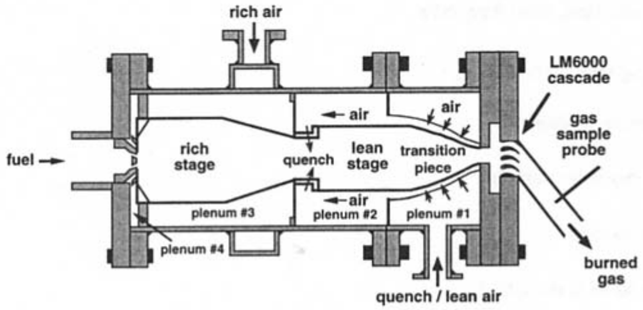

Fig. 2 RQL2 combustor and test stand

exit into a water cooled exhaust duct. The burned gas is sampled with a water cooled probe located downstream of the LM6000 nozzle sector. The transition piece and all downstream components were used in previous LHV fuel combustion tests (Bowen et al., 1995).

A single LHV gas fuel nozzle produces the swirl stabilized rich stage diffusion flame. This fuel nozzle, referred to as the N7B fuel nozzle, was originally designed for use in conventional LHV fuel gas turbine combustors. Details of the development and testing of this fuel nozzle may be found elsewhere (Battista et al., 1996; Bowen et al., 1995).

The rich stage combustor liner consists of a 14″ diameter cylindrical section followed by a conical section which reduces the diameter of the flow path from 14″ to 7″. Both the cylindrical and conical sections are approximately 13.5″ long. Flow visualization tests and computational fluid dynamics (CFD) analyses have shown that the converging section is necessary to prevent the low pressure core of the swirling flow from drawing lean stage gases back upstream into the rich section. The converging section also provides a convenient method of reducing the flow area to a reasonable size for proper quenching.

Developing an adequate cooling scheme for the rich stage liner presented special challenges. The rich stage liner is relatively large, but relatively little air is available for cooling. Film cooling, one of the most effective methods of combustor liner cooling, is not desirable on the rich stage if NO_x emissions are to be minimized. Ceramic components like those used in other RQL combustors (e.g., Lew et al., 1981) were rejected because of durability concerns. For these reasons, the RQL2 rich stage combustor liner was fabricated with a novel double-walled structure. Internal cooling passages with narrow dimensions conduct cooling air circumferentially around the liner (see Fig. 3(*a*)). Air enters each rectangular cooling channel through an inlet hole and exits each channel through a slot which discharges into one of eight longitudinal collection tubes. The collection tubes, in turn, discharge into a plenum that supplies the air for the fuel nozzle and cap/cowl. The final design shown in Fig. 3(*a*) was selected only after a detailed heat transfer analysis which used published correlations for convective heat transfer, a finite element analysis code, and custom software tools. Haynes 230 was selected as the material for construction because of its superior properties at high temperatures.

The rich stage cooling structure was formed by first rolling the conical and cylindrical inner shells and then machining the shallow cooling channels into these shells. Bosses were welded longitudinally along the shells to provide enough material to weld the collection tubes and outer skin segments to the inner shell. The skin segments, with predrilled inlet air holes, were then welded to the bosses. The inner shells and cooling channels are shown in Fig. 3(*b*), prior to the attachment of the bosses and outer skin segments. The outer skin segments were bonded to the ribs of the inner shell using a laser spot welding technique. Figure 3(*c*) shows the rich stage liner just prior to laser spot welding. Finally, the cylindrical and conical sections were welded together and the collection tubes were welded in place using manual gas tungsten arc welds. Additional details of the manufacturing methods can be found in Jackson et al. (1996).

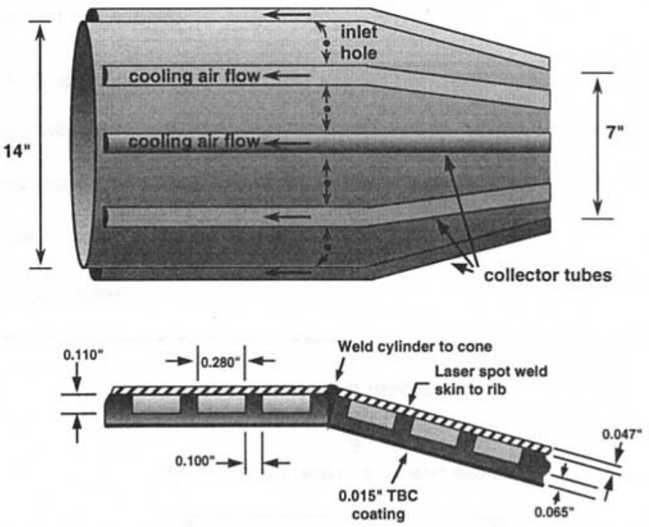

Fig. 3(*a*) Double walled rich stage combustor liner. Top: general arrangement of inlet cooling holes and collector tubes with the direction of air flow within the double-walled structure indicated. For clarity, inlet holes are shown for only one circumferential cooling channel. Bottom: liner wall cross section in the region of the junction between the cylindrical and conical sections showing the dimensions of the internal cooling channels.

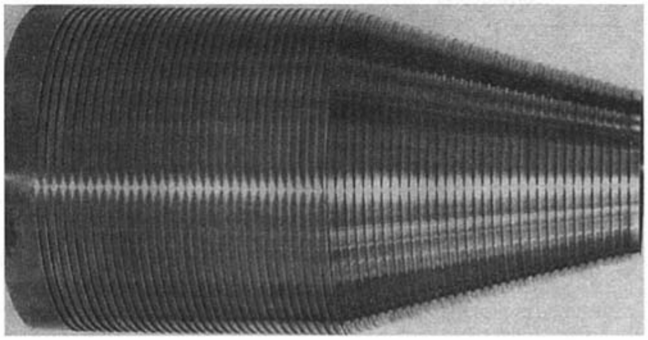

Fig. 3(*b*) Inner shell of rich stage combustor liner prior to attachment of longitudinal bosses and outer skin

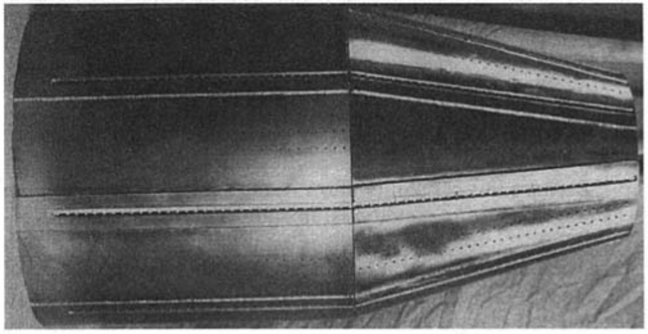

Fig. 3(*c*) Rich stage combustor liner just prior to laser spot welding of outer skin segments to inner shell

The quench section consists of a 7″ diameter cylindrical section, approximately 4.3″ long, and a backward facing step at the entrance to the lean section. The quench/lean stage air enters the combustor through quench air holes located at the downstream end of the cylindrical section. Rapid quenching is achieved with quench air holes of different sizes, referred to here as a ''radially stratified quench''. Larger holes create larger jets with greater momentum and which penetrate further into the hot gas flow. Smaller holes create smaller jets which do not penetrate to the centerline of the combustor. The quench/lean

Table 2 RQL2 test conditions. Combustion chamber pressure = 10 atm ± 10 percent for all air splits.

	Rich Stage/Lean Stage Air Flow Rate Ratio		
	20/80	30/70	40/60
LHV Fuel Temperature	680 °F	680°F	640°F
LHV Fuel Flow Rate	0.8 – 1.5 lb/s	0.7 – 1.3 lb/s	0.5 – 1.3 lb/s
Rich Stage Air Temperature	680°F	690°F	700°F
Rich Stage Air Flow Rate	0.85 lb/s	1.1 lb/s	1.4 lb/s
Lean Stage Air Temperature	740°F	740°F	710°F
Lean Stage Air Flow Rate	3.3 lb/s	2.6 lb/s	2.1 lb/s

air entering through the smaller holes mixes with the flow closest to the wall, while the quench/lean air entering through the larger holes mixes primarily with the flow near the centerline of the combustor. The quench holes were sized using standard correlations for jets penetrating into a cross flow (Lefebvre, 1983). Both the cylindrical section and backward facing step are impingement cooled.

The lean section was fabricated from the aft portion of a modified MS6000 liner, and is approximately 10.5″ in diameter and 14.5″ long. The MS6000 film cooling holes were reduced in diameter and all of the mixing and dilution air holes were eliminated. The design goal was for 70 percent of the quench/lean air to enter the combustor through the quench holes, with the remaining 30 percent entering through the lean stage film cooling holes. To reduce cooling air leakage, a modified MS6000 combustor hula seal is used to seal the interface between the lean section and the transition piece.

Using flow sleeves, baffles, and seals, the region inside of the pressure vessels was divided into four plenums (see Fig. 2). The quench/lean stage air is fed into plenum #1, and from this plenum the air flows through an impingement sleeve to cool the transition piece. After cooling the transition piece all of the air from this plenum flows into plenum #2, which feeds the quench holes and the lean stage liner film cooling holes. Similarly, the air for the rich stage is fed into plenum #3, flows through the double-walled rich stage combustor liner and into plenum #4, which supplies air to the fuel nozzle and cap/cowl.

The RQL2 pressure vessel is divided into separate chambers to allow independent variation of the rich and lean air flow rates. This arrangement was chosen to simplify the design process and to allow for examination of RQL2 performance at off-design air flow rates. However, at the design air split between the rich and lean stages, there is little difference in pressure between plenum #2 and plenum #3. In other words, the separate plenums are not required at design conditions. RQL2 can be considered the prototype for a practical, full scale gas turbine combustor.

Results and Discussion

The first pilot plant test of RQL2 (designated as Test 9 for programmatic reasons) was conducted during March 1996. RQL2 test conditions are listed in Table 2. Due to limitations of the HGCU system, the LHV fuel flow rate was limited to 1.5 lb/s, rather than the gasifier capacity of 2.2 lb/s. Although the HGCU system accepts LHV gas at about 1000°F, the relatively low fuel flow rates and heat losses from the piping combined to produce relatively low fuel temperatures at the combustor inlet (see Table 2). The reduction in fuel flow rate and temperature necessitated corresponding reductions in the air flow rate to achieve the target combustor exit temperature.

RQL2 was fired for more than 96 hours during Test 9. During this time several series of tests were conducted with the total combustion air divided into varying fractions between the rich and quench/lean stages. In a typical series, both the total air flow rate and the fractional distribution of the combustion air between the rich and quench/lean stages were held constant. The fuel flow rate was then adjusted in steps to vary the combustor exit temperature from about 1600°F to more than 2550°F. During this process, which typically required several hours to complete, continuous measurements were made of NO_x, CO, CO_2, and O_2 concentrations in the exhaust gas. An analyzer failure early in Test 9 prevented measurements of unburned hydrocarbon emissions. The ability to maintain combustor exit temperatures characteristic of F-class gas turbines was a major achievement for RQL2, and represents a significant improvement over other RQL combustors (Domeracki et al., 1994).

Figure 4 shows NO_x emissions measured during Test 9 with 20 percent of the combustion air sent to the rich stage and 80 percent of the combustion air sent to the lean stage. Figures 5 and 6 show measured NO_x emissions with air splits of 30 percent rich/70 percent lean and 40 percent rich/60 percent lean, respectively. The conversion of NH_3 to NO_x is also shown in Figs. 4 through 6. Conversion was calculated using the measured fuel NH_3 concentration of 4600 ppmv, and by assuming non-FBN NO_x formation (e.g., thermal NO_x) was negligible. This is a reasonable assumption for the very low heating value pilot plant fuel (higher heating value = 110 Btu/SCF).

As expected from models and previous RQL1 results, NO_x emissions were a strong function of the air split between the rich and lean stages, as well as the rich stage equivalence ratio and the combustor exit temperature. With the air split held constant, a distinct minimum in NO_x emissions was observed

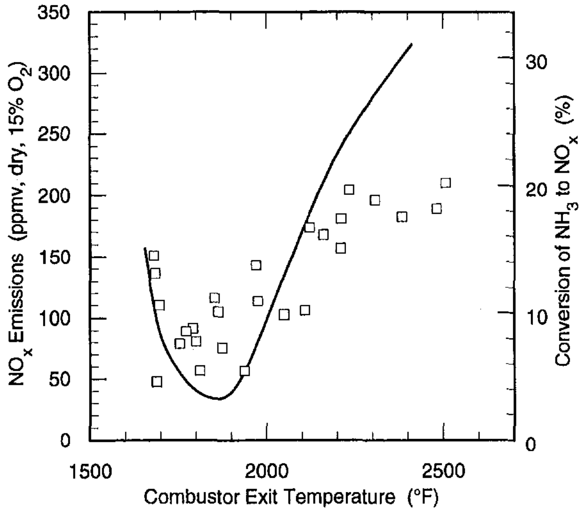

Fig. 4 RQL2 NO_x emissions at a 20/80 rich/lean air split. The solid line represents SLICER model predictions.

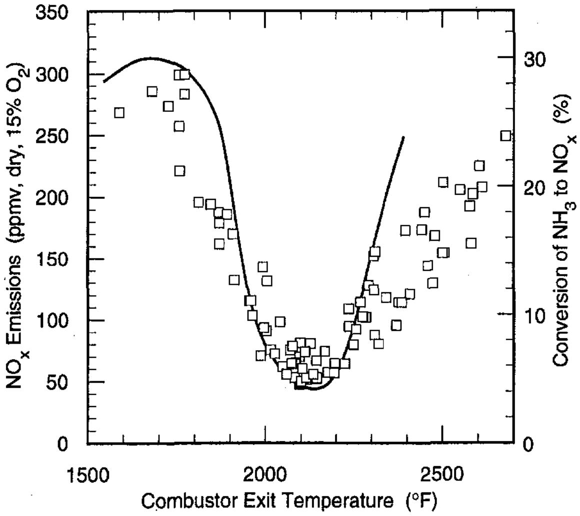

Fig. 5 RQL2 NO_x emissions at a 30/70 rich/lean air split. The solid line represents SLICER model predictions.

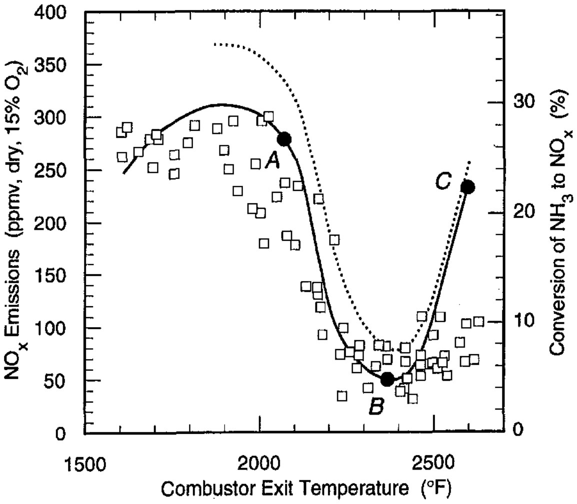

Fig. 6 RQL2 NO_x emissions at a 40/60 rich/lean air split. The solid line represents the SLICER model predictions at the experimental conditions and 3.5 lb/s of combustion air. The dashed line is an extrapolation of the SLICER model to full flow. Model points labeled *A*, *B*, and *C* correspond to rich stage equivalence ratios of 0.9, 1.25, and 1.6, respectively.

at the optimum rich stage equivalence ratio. With an air split of 40 percent rich/60 percent lean, the minimum in NO_x emissions occurred at a combustor exit temperature of about 2400°F. With a 30/70 rich/lean air split, the minimum in NO_x occurred at a combustor exit temperature of about 2100°F. With a 20/80 air split, the minimum in NO_x occurred at about 1800°F. For all three air splits, the minimum occurred at a rich stage equivalence ratio of about $\varphi_{\text{rich}} = 1.25$.

At the optimum rich stage equivalence ratio, NO_x emissions were about 50 ppmv (on a dry, 15 percent O_2 basis). With 4600 ppmv NH_3 in the fuel, this corresponds to a conversion of NH_3 to NO_x of about 5 percent. At the optimum conditions, RQL2 NO_x emissions were more than a factor of 3 lower than expected from a conventional diffusion flame combustor burning the same fuel. For example, in previous pilot plant tests using a GE MS6001B combustor, the conversion of NH_3 to NO_x ranged from 20 to 80 percent, depending upon the combustor exit temperature (Battista et al., 1996). As conditions were shifted away from the optimum, RQL2 NO_x emissions gradually increased until they were comparable to a standard combustor.

RQL2 NO_x emissions measured during Test 9 were modeled with sequentially linked ideal chemical reactor (SLICER) networks, a set of custom software modules. SLICER models are assembled from these custom software modules and the Chemkin II package of programs and subroutines (Glarborg et al., 1986; Lutz et al., 1988; Kee et al., 1989). In the SLICER model of RQL2, the rich stage was represented as an equivolume perfectly stirred reactor (PSR) and a plug flow reactor (PFR) in series. The SLICER model combines the flow exiting the rich stage PFR with the quench/lean stage air in a second PSR, which feeds a second PFR. Inputs to the SLICER model include the measured combustion chamber pressure, rich and quench/lean air flow rates, air temperature, fuel composition, fuel flow rate, and fuel temperature. The chemical kinetic mechanism included more than 50 species and 250 elementary reaction steps (Michaud et al., 1992).

Results from the SLICER modeling, using experimental conditions as inputs to the model, are indicated by the solid lines in Figures 4, 5, and 6. The SLICER representation of RQL2 both qualitatively and quantitatively matches the NO_x emissions measurements. The SLICER predictions are insensitive to the relative sizes of the rich stage PSR and PFR. At high rich stage equivalence ratios the SLICER NO_x emissions are slightly sensitive to the relative size of the quench/lean PSR and PFR. Increasing the quench PSR volume tends to decrease model NO_x emissions at high φ_{rich}.

Several prior studies (e.g., Heap et al., 1977) have shown that the rich stage gas residence time has a significant impact on the overall conversion of FBN to NO_x in an RQL combustor, with longer rich stage residence times yielding lower conversions. Unfortunately, RQL2 could not be tested at the full air flow rate of 20 lb/s, because of the limited availability of LHV fuel (Table 2 shows the maximum total combustion air flow rate was 4.2 lb/s). However, the SLICER model can be used to extrapolate the performance of RQL2 to full flow conditions, and therefore, the shorter rich stage residence times characteristic of full flow. The dashed line in Fig. 6 shows the predicted NO_x emissions from RQL2 at a total combustion air flow rate of 20 lb/s. All other model parameters, including the rich/lean air flow rate ratio, were unchanged. The model predicts that the conversion of FBN to NO_x at the optimum conditions will increase from about 5 percent at reduced flow to about 8 percent at full flow, still well below the ~30 percent conversion expected at base load from a standard LHV fuel gas turbine combustor.

The key chemical reactions that govern NH_3 destruction and NO_x formation in RQL2 can be identified using the SLICER model and by performing a reaction path analysis (RPA) on individual reactors. For example, consider the chemical reactions within the rich stage PSR at a 40/60 air split. Near the optimal rich stage equivalence ratio (designated by point *B* in Fig. 6), a major route for NH_3 destruction is

$$NH_3 \rightarrow NH_2 \rightarrow NH \rightarrow N \rightarrow N_2,$$

where reaction partners have been omitted for brevity. Key reactions in this NH_3 destruction pathway are

$$NH + H \rightarrow N + H_2 \qquad (R1)$$

and

$$N + NO \rightarrow N_2 + O. \qquad (R2)$$

R1 is a simple abstraction reaction, while R2 is the reverse of one of the well-known thermal NO_x formation reactions. Comparing reaction rates at point *A* ($\varphi_{\text{rich}} = 0.9$) to point *B* ($\varphi_{\text{rich}} = 1.25$) shows that when the rich stage PSR is too lean, the molar flux of *N* atoms through the forward direction of R1 slows down by a factor of four, mainly due to a nine-fold reduction in the *H* atom concentration. This reduces *N* atom concentrations by a factor of twelve. As a consequence, N_2

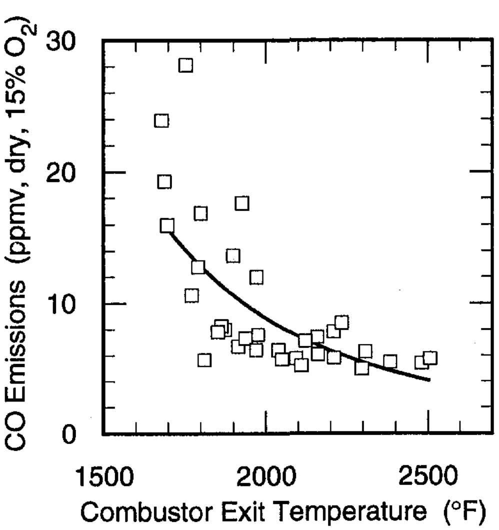

Fig. 7 RQL2 CO emissions at a 20/80 rich/lean air split. The solid line shown in Figs. 7 through 9 is a best-fit through the measurements, not a model prediction.

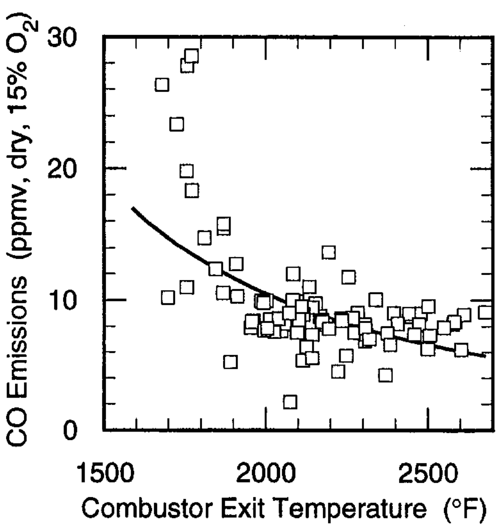

Fig. 8 RQL2 CO emissions at a 30/70 rich/lean air split

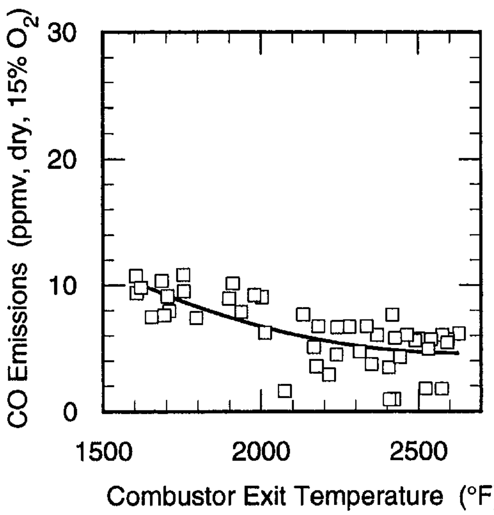

Fig. 9 RQL2 CO emissions at a 40/60 rich/lean air split

formation (and NO destruction) through R2 slows down at point *A* relative to point *B*. The gas leaving the rich stage PSR at point *B* contains only 55 ppmv NO_x (on a dry, 15 percent O_2 basis), and some of this NO_x will be destroyed in the rich stage PFR. In contrast, the gas leaving the rich stage PSR at point *A* contains 278 ppm NO_x (on a dry, 15 percent O_2 basis), and none of this NO_x will be destroyed in the rich stage PFR.

When the rich stage PSR is too fuel rich (point *C* in Fig. 6, $\varphi_{\text{rich}} = 1.6$), a different reaction becomes important. Reaction R3

$$NH_3 + H \rightarrow NH_2 + H_2 \qquad \text{(R3)}$$

is a source of NH_2 at point *B*, but is an NH_2 sink at point *C*. The rich stage PSR NH_2 concentration at point *C* is more than 5 times the NH_2 concentration at point *B*, causing R3 to proceed in the reverse direction and make NH_3 rather than destroy NH_3. The NH_3 concentration in the rich stage PSR at point *C* is 39 times greater than at point *B*. With NH_3 destruction dramatically slowed in the rich stage, a relatively large amount of NH_3 survives until the quench stage, where a significant fraction is converted into NO_x.

A similar modeling and reaction path analysis effort was completed for the reduced scale RQL1 combustor (Bowen et al., 1995). The key reactions and conclusions drawn from both analyses are nearly identical. However, the RQL1 combustor was tested on a low heating value fuel containing only 1650 ppmv NH_3, while RQL2 was tested with a fuel containing 4600 ppmv NH_3. This suggests the reaction path analysis presented here is applicable over a wide range of fuel NH_3 concentrations.

Sato et al. (1990) and others have suggested that the fuel hydrocarbon content has a significant influence on the overall conversion of NH_3 to NO_x in a rich-lean combustor, with the conversion increasing as the fuel hydrocarbon content increases. Reactions involving HCN have generally been attributed as the cause for this increased conversion (Heap et al., 1990; Takagi et al., 1979). However, the SLICER model of RQL2 and subsequent reaction path analysis suggest that under the conditions of this study, the fuel methane content has no effect on the overall conversion of NH_3 to NO_x. The role of fuel methane content in determining NO_x emissions from RQL2 is a suitable subject for additional experimental and theoretical investigations.

Measured CO emissions are shown in Figs. 7, 8, and 9 for the same air splits shown in Figs. 4, 5, and 6, respectively. CO emissions were between 5 and 30 ppmv (dry, 15 percent O_2) under all conditions, indicating the quench stage design provided adequate mixing, and the short lean stage provided sufficient residence time to complete combustion. Overall, CO emissions were lowest when the air split was closest to the design value (the 40/60 air split) and tended to increase as the air split was adjusted away from the design value (the 30/70 and 20/80 air splits).

Conclusions

The RQL2 combustor has demonstrated the potential for low NO_x emissions from IGCC power plants equipped with HGCU. At full flow, F-class gas turbine conditions, and with 4600 ppmv NH_3 in the fuel, the overall conversion of NH_3 to NO_x in RQL2 is projected to be 8 percent, versus about 30 percent in a standard LHV gas turbine combustor. RQL2 is also a significant improvement over previous RQL combustor designs, which have not achieved the same conversion and firing temperature targets. In addition, RQL2 uses no ceramic components, and can be considered the prototype for a practical, full scale RQL gas turbine combustor.

Because combustor modifications (such as RQL2) are almost always a less expensive method of NO_x reduction than flue gas treatment, the adoption of rich-lean combustion technology will increase the environmental and economic attractiveness of IGCC power generation using HGCU. The concepts generated in the design and development of RQL2, as well as the improved understanding of rich-lean combustion, may be applied in future LHV fueled gas turbines. RQL2 concepts may also be incorporated into low NO_x combustors for natural gas and liquid fuel turbines.

The excellent agreement between the SLICER model and the RQL2 test results over a wide range of combustor exit temperatures and air splits suggests that the modeling approach is reasonable and can provide valuable insights into the factors which govern the performance of a rich-lean combustor. The reaction path analysis identified the elementary chemical reactions which are most important in the conversion of NH_3 to NO_x, and suggested that HCN does not play a significant role in the overall conversion of NH_3 to NO_x. In addition, the SLICER model suggests the fuel methane concentration should have little impact on the overall performance of RQL2.

Acknowledgments

This work was supported by the U.S. Department of Energy, Morgantown Energy Technology Center, under contract number DE-AC21-87MC23170, with GE Environmental Systems. The support of METC project managers Abbie Weigand-Layne and Edward L. Parsons, Jr. is gratefully acknowledged.

References

Battista, R. A., Feitelberg, A. S., and Lacey, M. A., 1996, "Design and Performance of Low Heating Value Fuel Gas Turbine Combustors," ASME Paper No. 96-GT-531.

Bowen, J. H., Feitelberg, A. S., Hung, S. L., Lacey, M. A., and Manning, K. S., 1995, "Performance of Low Btu Fuel Gas Turbine Combustors," in *Proceedings of the Advanced Coal-Fired Power Systems '95 Review Meeting,* DOE/METC-95/1018, pp. 250–262.

Domeracki, W. F., Dowdy, T. E., and Bachovchin, D., 1994, "Development of Topping Combustor for Advanced Concept Pressurized Fluidized Bed Combustion," in *Proceedings of the Coal-Fired Power Systems 94 - Advances in IGCC and PFBC Review Meeting,* DOE/METC-94/1008, pp. 265–279.

Glarborg, P., Kee, R. J., Grcar, J. F., and Miller, J. A., 1986, "PSR: A FORTRAN Program for Modeling Well-Stirred Reactors," Sandia National Laboratories Report SAND86-8209.

Goebel, S. G. and Feitelberg, A. S., 1992, "Experimental and Theoretical Study of Low Emissions Rich-Quench-Lean Combustion," a poster paper presented at the 24th Symposium (International) on Combustion, July 5–10, Sydney, Australia.

Heap, M. P., Tyson, T. J., Cichanowicz, J. E., Gershman, R., Kau, C. J., Martin, G. B., and Lanier, W. S., 1977, "Environmental Aspect of Low Btu Gas Combustion," *Sixteenth Symposium (International) on Combustion,* The Combustion Institute, Pittsburgh, PA, pp. 535–542.

Jackson, M. R., Ritter, A. M., Abuaf, N., Lacey, M. A., Feitelberg, A. S., and Lang, P., 1996, "Joining of Wrought Ni-Base Combustor Alloys," ASME Paper No. 96-GT-219.

Kee, R. J., Rupley, F. M., and Miller, J. A., 1989, "Chemkin-II: A Fortran Chemical Kinetics Package for the Analysis of Gas-Phase Chemical Kinetics," Sandia National Laboratories Report SAND89-8009.

Lefebvre, A. H., 1983, *Gas Turbine Combustion,* Hemisphere, New York, NY.

Lew, H. G., DeCorso, S. M., Vermes, G., Notardonato, Jr., D. C., and Schwab, J., 1981, "Low NO_x and Fuel Flexible Gas Turbine Combustors," ASME Paper No. 81-GT-99.

Lutz, A. E., Kee, R. J., and Miller, J. A., 1988, "SENKIN: A Fortran Program for Predicting Homogeneous Gas Phase Chemical Kinetics With Sensitivity Analysis," Sandia National Laboratories Report SAND 87-8248.

Michaud, M. G., Westmoreland, P. R., and Feitelberg, A. S., 1992, "Chemical Mechanisms of NO_x Formation for Gas Turbine Conditions," *Twenty-Fourth Symposium (International) on Combustion,* The Combustion Institute, Pittsburgh, PA, pp. 879–887.

Sato, M., Ninomiya, T., Nakata, T., Yoshine, T., Yamada, M., and Hisa, S., 1990, "Coal Gaseous Fueled, Low Fuel-NO_x Gas Turbine Combustor," ASME Paper No. 90-GT-381.

Takagi, T., Tatsumi, T., and Ogasawara, M., 1979, "Nitric Oxide Formation From Fuel Nitrogen in Staged Combustion: Roles of HCN and NH_i," *Combustion and Flame,* Vol. 35, pp. 17–25.

High Pressure Test Results of a Catalytic Combustor for Gas Turbine

T. Fujii

Y. Ozawa

S. Kikumoto

M. Sato

Central Research Institute
of Electric Power Industry,
Yokosuka, Kanagawa, Japan

Y. Yuasa

H. Inoue

Kansai Electric Power Company, Inc.,
Amagasaki, Hyogo, Japan

Recently, the use of gas turbine systems, such as combined cycle and cogeneration systems, has gradually increased in the world. But even when a clean fuel such as LNG (liquefied natural gas) is used, thermal NO_X is generated in the high temperature gas turbine combustion process. The NO_X emission from gas turbines is controlled through selective catalytic reduction processes (SCR) in the Japanese electric industry. If catalytic combustion could be applied to the combustor of the gas turbine, it is expected to lower NO_X emission more economically. Under such high temperature and high pressure conditions, as in the gas turbine, however, the durability of the catalyst is still insufficient. So it prevents the realization of a high temperature catalytic combustor. To overcome this difficulty, a catalytic combustor combined with premixed combustion for a 1300°C class gas turbine was developed. In this method, catalyst temperature is kept below 1000°C, and a lean premixed gas is injected into the catalytic combustion gas. As a result, the load on the catalyst is reduced and it is possible to prevent the catalyst deactivation. After a preliminary atmospheric test, the design of the combustor was modified and a high pressure combustion test was conducted. As a result, it was confirmed that NO_X emission was below 10 ppm (at 16 percent O_2) at a combustor outlet gas temperature of 1300°C and that the combustion efficiency was almost 100 percent. This paper presents the design features and test results of the combustor.

Introduction

Selective catalytic reduction (SCR) is used for the denitrification equipment in Japanese thermal power plants, but it requires large building and operating costs. Because environmental pollution such as acid rain is caused by nitrogen oxides, with more gas turbines used for combined cycle and cogeneration systems, deNO_X is more keenly required.

In the use of LNG, thermal NO_X, which is formed from the nitrogen in the air in high temperature combustion zones, is generated. In this state, the catalytic combustion method, which is expected to lower the thermal NO_X emission, attracts attention.

In this method, a lean and homogeneous premixture is supplied to the catalyst, which is preheated to its active temperature and combustion, is completed by the catalytic and thermal reaction within the catalyst bed. For this reason, there is no local high temperature region and low NO_X combustion can be realized.

In 1970s the development of catalytic combustors was actively pursued in the USA and Japan [1–5]. In case of these combustors, the catalyst temperature rose over the combustor outlet gas temperature, for example 1100°C or 1300°C. Also, the deactivity of catalyst, caused by high temperature and the burnout caused by a nonhomogeneous premixture, happened; it revealed that the durability of the catalyst at high temperatures was still insufficient and that a homogeneous premixture was needed, thus preventing the realization of a high temperature catalytic combustor. To overcome these difficulties, a joint R & D projected by CRIEPI (Central Research Institute of Electric Power Industry) and KEPCO (Kansai Electric Power Co., Inc.) was started in 1988 that was aimed at the realization of a catalytic combustor for the gas turbine. Table 1 shows the targeted goals. In this work, a catalytic combustor combined with premixed combustion was designed, and an atmospheric combustion test was completed in 1993. The results were 2 ppm (at 16 percent O_2) in NO_X emission, almost 100 percent in combustion efficiency, 3 percent in overall combustor pressure loss, and 14 percent in pattern factor [6, 7]. A catalytic combustor for high pressures was designed based on the design of the atmospheric combustor and a high pressure test was conducted.

Concept of the Combustor

Figure 1 shows the concept of the catalytic combustor combined with premixed combustion. The burner system is composed of catalyst segments and premixing nozzles. To keep the mechanical and thermal reliability of the catalyst, the catalyst is divided into small pieces and mounted in each of the catalytic combustor segments. Catalytic combustion temperature is controlled below 1000°C. The lean premixed gas from the premixing nozzles is injected into the catalytic combustion exhaust gas and burned to achieve a combustion gas temperature of 1300°C. By combining with lean premixed combustion, less NO_X is expected, and it is possible to reduce the load on the catalyst and to keep the catalyst temperature below 1000°C. As a result, the durability of the catalyst is improved. Furthermore, the injected premixed gas is heated by the catalytic combustion gas, to stabilize the premixed combustion.

At first, on the basis of the above concept, an outer catalyst type combustor (OCT type) and a center catalyst type combustor (CCT type) were designed and tested at atmospheric pressure. Figure 2 shows the OCT type and CCT type combustors. In case of the OCT combustor, because mixing of the catalytic combustion gas with the injected premixed gas was insufficient, combustion stability and uniformity of gas temperature at the combustor outlet were insufficient. The CCT combustor could not achieve stable combustion without a mixing device of a ceramic baffle plate after the catalyst, and it caused a growth of pressure loss [6]. From these results, an advanced catalytic

---

Contributed by the International Gas Turbine Institute and presented at the 41st International Gas Turbine and Aeroengine Congress and Exhibition, Birmingham, United Kingdom, June 10–13, 1996. Manuscript received by the ASME Headquarters January 13, 1996. Paper No. 96-GT-382. Associate Technical Editor: J. N. Shinn.

Table 1 Performance goal of catalytic combustor

COMBUSTOR OUTLET GAS TEMPERATURE	1300°C
NOx EMISSION (converted at 16% O_2)	<10ppm
COMBUSTION EFFICIENCY	>99.9%(at rated load)
DIFFERENCIAL PRESSURE	<5%
PATTERN FACTOR	<15%

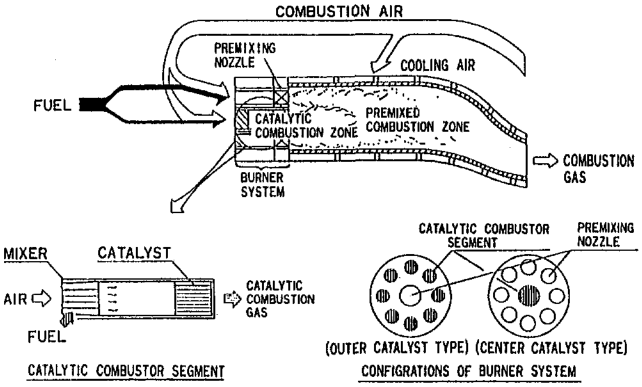

Fig. 1 Concept of catalytic combustor

combustor (ACC1000 type), which was superior in reducing pressure loss and realizing stable combustion, was designed and tested at atmospheric pressure. Figure 3 shows the ACC1000 type combustor.

The high pressure combustor was designed on the basis of the ACC type combustor.

Test Conditions

Figure 4 is a schematic diagram of the test facility for a gas turbine combustor. This facility can test one combustor for a 20 MW class multican type gas turbine in a pressure range from 3 to 13.5 ata and in an air flow rate range from 3000 to 13500 m_N^3/h.

The air from a compressor is heated to 370°C by an air heater and fed through a flow control valve to a pressure vessel in one line. The air in the pressure vessel is partially used to cool the liner and transition piece of the combustor, and the remaining air is used for combustion. The combustion air introduced into the burner section can be heated by a preburner (to 400°C) and fed into a catalytic combustion section and a premixed combustion section; fuel is injected and mixed in these sections. Subsequently, the lean premixed gas is provided to the catalyst segments and premixing nozzles. The catalytic combustion temperature is controlled at about 800°C. The exhaust gas is mixed with the lean premixed gas that is injected from the premixing nozzles, and the lean premixed combustion is conducted in the liner. As a result, the combustor outlet gas temperature becomes 1300°C.

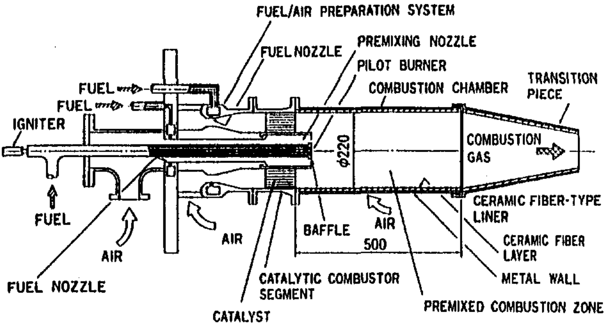

OCT type

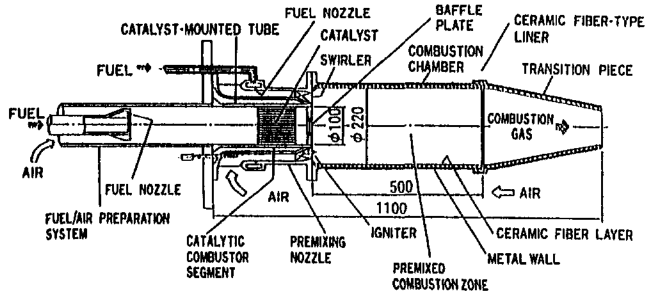

CCT type

Fig. 2 OCT and CCT type combustor

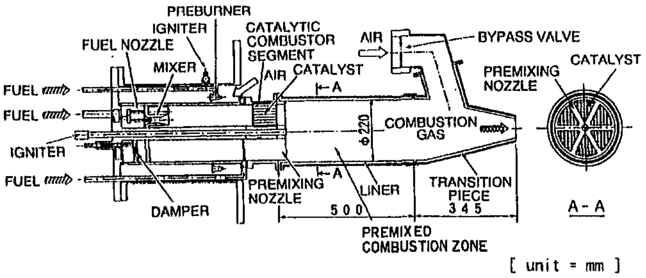

Fig. 3 ACC1000 combustor

Figure 5 shows the ACC2000 type combustor for high pressure and Fig. 6 shows the actual hardware. The design of the high pressure combustor is basically the same as that of the atmospheric combustor (ACC1000 type) but because the load on the catalyst increases at high pressures, the number of catalyst stages is increased and the catalyst cell pitch is smaller—increase the surface area. In the ACC1000 type combustor, there was an air bypass valve at the transition piece for partial load. At first, however, the bypass valve is not installed in the

Nomenclature

CO = carbon monoxide emission, ppm
F = fuel fraction, percent
NO_X = nitrogen oxides emission, ppm
P = pressure, ata
T = temperature, °C
UHC = unburned hydrocarbon emission, ppm
ΔP = pressure loss, percent
η = combustion efficiency, percent
λ = excess air ratio,

Subscript

c = catalyst inlet
g = combustor outlet
in = combustor inlet

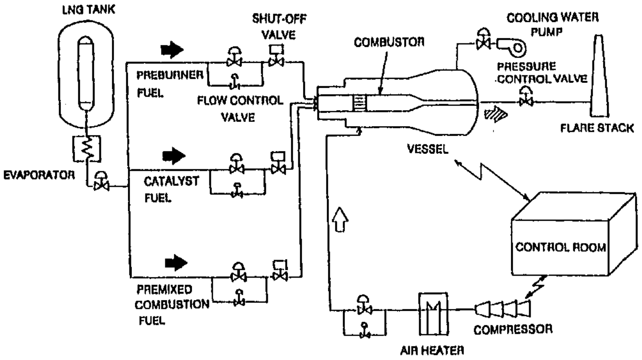

Fig. 4 Schematic diagram of test facility

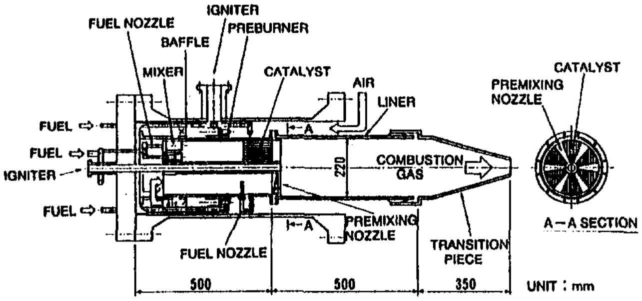

Fig. 5 High pressure combustor (ACC2000)

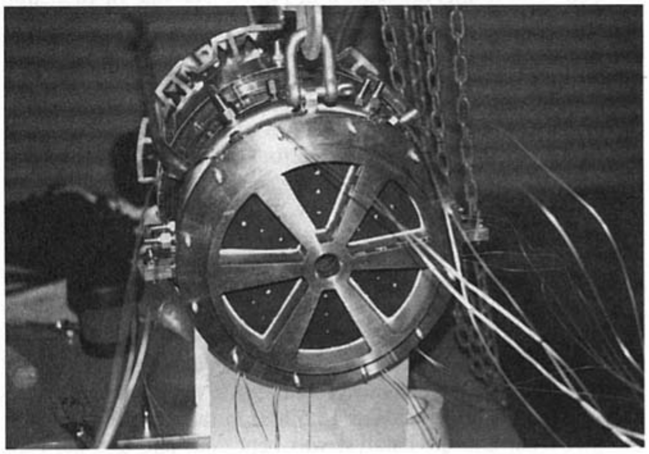

Fig. 6 Catalytic combustor

ACC2000 type combustor in order to confirm the performance at full load.

For the structures of respective parts of the combustor, the preburner is an annular type, and to be able to meet a wider load range, diffusion combustion is selected. When the preburner is ignited, an igniter is inserted in it. If ignition is confirmed, the igniter is pulled out. The burner system consists of catalyst segments and premixing nozzles. Six fan-shaped catalyst segments and six premixing nozzles are arranged alternately to form a circle. The shape of the premixing nozzle is constructed to inject the premixed gas into the catalytic combustion gas at a 90 deg angle. For smooth ignition of the premixed gas, the igniter is inserted in the premixed combustion section. In the measurement duct, which is behind the combustor outlet, combustion gas temperature and emission are always measured by thermocouples and gas sampling.

Table 2 Fuel components

CH_4	87.65%
C_2H_6	4.64%
C_3H_8	4.23%
i-C_4H_{10}	1.55%
n-C_4H_{10}	1.75%
i-C_5H_{12}	0.15%
n-C_5H_{12}	0.00%
N_2	0.03%

Table 3 Measurement instruments

ITEMS	MESUREMENT INSTRUMENTS
NO_x	CHEMI-LUMINESCENCE
CO	NON-DISPERSIVE INFRARED
CO_2	NON-DISPERSIVE INFRARED
O_2	PARAMAGNETIC
UHC	FLAME IONIZATION

Table 4 Standard test conditions

PRESSURE	13.5ata
TOTAL AIR FLOW RATE	13500m^{3}N/h
CATALYST INLET GAS TEMP.	370°C
CATALYST TEMP.	<1000°C
COMBUSTOR OUTLET GAS TEMP.	1300°C

Table 2 shows the fuel components. Fuel is fed into 3 lines of preburner, catalyst, and premixing nozzles, so that the loads of the respective combustion sections can be controlled by the fuel flow rates to the respective sections.

The catalyst has been designed by CRIEPI and manufactured by a catalyst company. Its major active ingredient is palladium, which is supported on a stabilized alumina washcoat on a honeycomb type monolith made of cordierite. The catalyst used is 25 mm in length and 1.8 mm in cell pitch. It is provided as six fan-shaped segments formed by dividing a ring 40 mm in inner diameter and 200 mm in outer diameter and arranging it in two stages. In this combustor, the fraction of fuel to the catalyst is restricted by the catalyst temperature limitation, and the remaining fuel is distributed to the premixing nozzles. In order to raise the combustor outlet gas temperature to 1300°C, the fuel concentration of the mixture from the nozzles is higher than that for the catalyst. Also, the thick mixture caused NO_X formation. In order to increase the fraction of fuel to the catalyst to reduce NO_X emission, the fuel conversion in the catalyst bed must be reduced adequately; therefore, the catalytic activity was controlled, and the catalyst length and the cell pitch were selected. The catalyst surface temperatures are measured by thermocouples that are inserted and cemented in catalyst cells, and the catalyst fuel is controlled to keep the temperatures at about 800°C.

There are four gas sampling points: preburner outlet, catalyst inlet, premixing nozzle interior, and combustor outlet. By measuring the emission values of NO_X, UHC, O_2, CO, and CO_2, the combustion efficiencies of individual sections and mixture flow rates are calculated. The measuring methods are shown in Table 3.

Table 4 shows the conditions of a full load. At the full load, the preburner was not ignited, but a small amount of fuel was injected from the preburner, which was used like a fuel nozzle

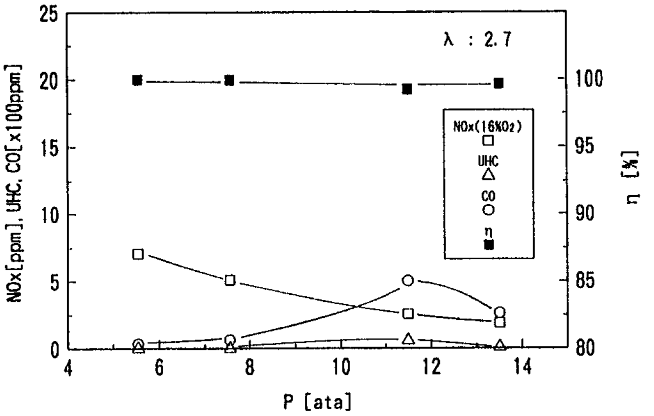

Fig. 7 Effect of pressure

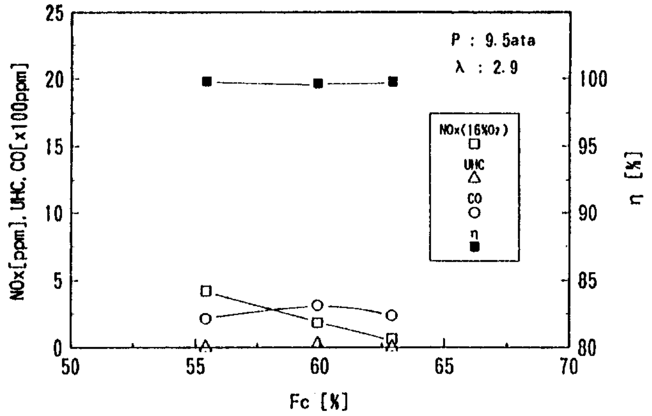

Fig. 9 Effect of fuel distribution

for the purpose of promoting the mixing of fuel with air. In the experiment, catalyst and premixed gas were ignited under conditions of 3 ata and 3000 m_N^3/h of air. When ignition had been completed, the pressure, air flow rate, and fuel rate were gradually increased to the full load.

Test Results

Effect of Pressure. To examine the effect of pressure on the combustion characteristics, a preliminary test was conducted. In this test, the preburner was not ignited, but instead, used as a fuel nozzle. The pressure was increased from a low pressure, with the combustor outlet gas temperature kept at 1200°C. At this time, the air flow rate was increased in proportion to the pressure, and the catalyst inlet gas temperature and the catalyst temperature were controlled at 370°C and about 800°C, respectively.

Figure 7 shows the test results. Combustion efficiency was almost 100 percent to show stable combustion between 3.5 ata and 13.5 ata. The maximum NO_X emission was below 7 ppm converted at 16 percent O_2.

Figure 8 shows the fuel flow rates of preburner, catalyst segments, and premixing nozzles, respectively. Because the fuel conversion in the catalyst bed was decreasing with increasing pressure, the increase of fuel for the catalyst was made greater than the increase of pressure in order to keep the catalyst temperature at about 800°C. Accordingly, the fraction of fuel to the catalyst was increased, and the fraction of fuel to the premixing nozzles was decreased with increasing pressure. However, NO_X is not formed in the catalyst bed, but in the premixed combustion zone. Since the fuel concentration of the premixture injected from the premixing nozzles is thicker than that for the catalyst, as the fuel concentration from the premixing nozzles decreases, the high temperature zone, in which NO_X is formed, decreases in the premixed combustion zone. For these reasons, NO_X emission is surmised to have been decreased with the rise of pressure.

Effect of Fuel Distribution. To see the effect of the fuel distribution to the catalyst and the premixing nozzles on NO_X emission, the fuel distribution to the catalyst and the premixing nozzles were changed at a medium pressure with the total fuel rate kept constant while the fuel supply to the preburner was stopped. The results are shown in Fig. 9. The rate of fuel supplied to the catalyst to the total fuel is chosen as the abscissa. According to the increase of the fuel rate to the catalyst, NO_X emission tended to be lower. The reason is that the premixture from the premixing nozzles is higher in fuel concentration than the premixture for the catalyst that was diluted. The combustion efficiency was not affected by the fuel rate to the catalyst, and it remained almost constant. The reason is surmised to be that when the fuel rate to the catalyst was low, the premixture from the premixing nozzles was high in concentration in order to stabilize combustion; when the fuel rate to the catalyst was high, the catalytic combustion gas temperature rose to stabilize combustion.

Combustion Characteristics at Full Pressure. Figure 10 shows the effect of combustor outlet gas temperature on the combustion characteristics at 13.5 ata. In this test, the fuel for the preburner and the catalyst was kept constant, and the fuel

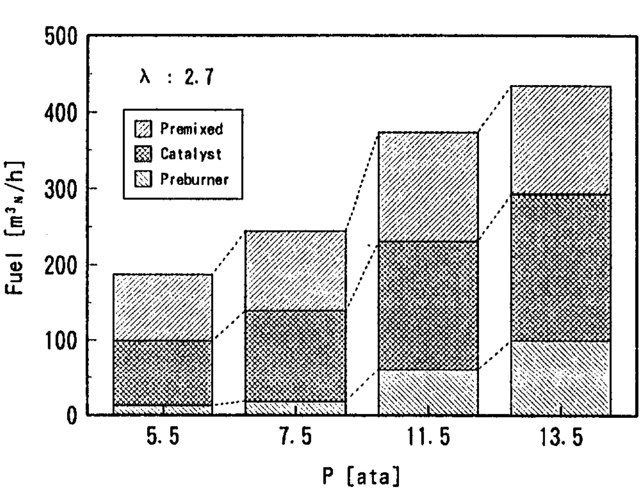

Fig. 8 Fuel flow rates (T_g = 1200°C)

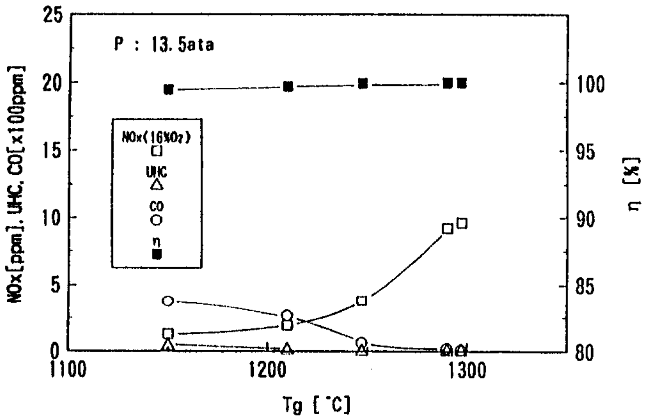

Fig. 10 Effect of combustion temperature

for the premixing nozzles was increased gradually from 1150°C of combustor outlet gas temperature to 1300°C.

NO_X emission was increased with the rise of combustor outlet gas temperature, but was kept below 10 ppm (at 16 percent O_2) at a combustor outlet gas temperature of 1300°C. Combustion efficiency was increased with increasing combustor outlet gas temperature—over 99.9 percent at 1250°C.

Distribution of Liner and Transition Piece Temperatures. Figure 11 shows the distributions of liner and transition piece temperatures at respective pressures. There was a high temperature area in the transition piece inlet at a high pressure, but the temperatures are lower than the limit operation temperature of the liner and transition piece.

Pressure Loss. Figure 12 shows the effect of pressure on the pressure loss of each section. Pressure loss was almost constant at any pressure. The maximum overall combustor pressure loss was about 2.5 percent, lower than the targeted level of 5 percent.

Discussion

Published NO_X emission levels of 1300°C class dry low NO_X combustors using the premixed combustion method are about 21 ppm (at 16 percent O_2) [8, 9]. The catalytic combustor reported in this paper can lower NO_X emission to less than half—to suggest that the use of a catalytic combustion in a gas turbine combustor is significant.

Recently, test results are published on a combustor in which all the fuel is supplied to a catalyst for partial combustion in the catalyst to control the catalyst temperature. The unburned gas is burned in the gaseous phase combustion zone behind the catalyst [10]. It is reported that this method produces little NO_X in the gas phase combustion zone since there is no NO_X-producing high temperature area because of a less temperature distribution. However, this method has an operating window that can achieve both a low enough catalyst temperature to provide long term reactor operation, and a high enough catalyst temperature to promote gas phase combustion after the catalyst.

In the combustor reported in this paper in which a premixed gas is additionally injected into the catalytic combustion gas for gas phase combustion (because of the temperature distribution caused in the gas phase combustion zone), NO_X emission is higher than in the above method. By the way, this combustor also has an operating window, but since the catalyst temperature and the combustor outlet gas temperature can be controlled independently, the operating window is wide.

In the atmospheric pressure combustion test of an ACC1000 combustor using a ceramic fiber-type liner and transition piece, respectively [11], NO_X emission could be kept at 2 ppm (at 16 percent O_2) [7]. When using the ceramic fiber type liner and transition piece, the quantity of cooling air for the liner and transition piece can be decreased to about 10 percent. The air for the premixing nozzles can also be increased by that to lower the fuel concentration in the premixing nozzles. As a result, it can be considered that NO_X emission can be decreased.

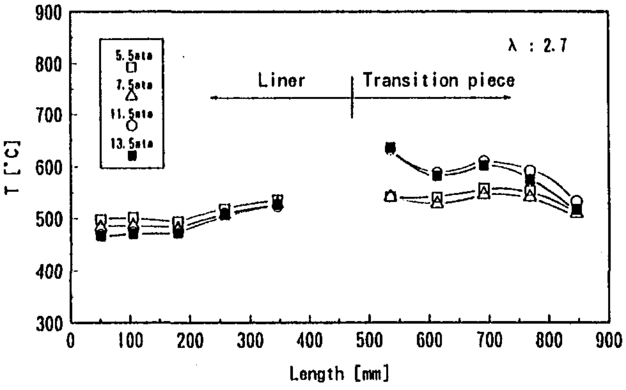

Fig. 11 Temperature distribution of liner and transition piece

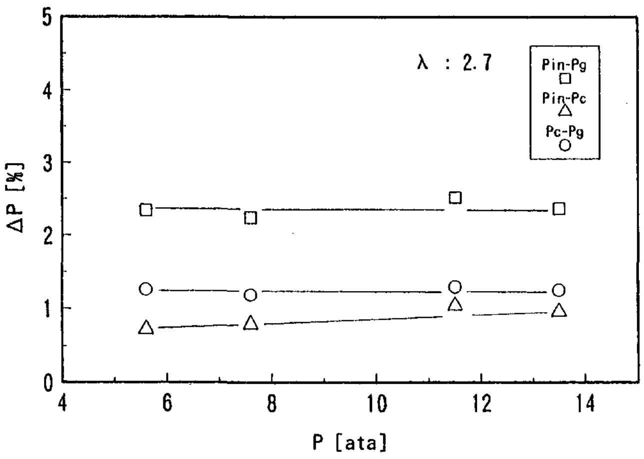

Fig. 12 Pressure loss

So, the characteristics of the ACC combustor using a ceramic liner at high pressures is also planned to be examined in future.

Conclusion

A catalytic combustor combined with premixed combustion was tested at high pressures. As a result, NO_X emission was below 10 ppm at a combustor outlet gas temperature of 1300°C. It may be possible to lower NO_X emission by increasing the combustion air and by decreasing the cooling air. In the future, it will be necessary to estimate the long term performance of catalyst and combustor.

Acknowledgments

Our deepest gratitude goes to Z. Hotta, T. Yamanaka, J. Hirano of KEPCO, T. Abe and T. Hisamatsu of CRIEPI, who helped us in promoting this research project, H. Fukuzawa, who helped us in the preparation of the catalysts, Y. Tochihara of CRIEPI who helped us in the performance of this test, S. Mandai of Mitsubishi Heavy Industry, who helped us to design the metal liner.

References

1 Pfefferle, W. C., Carrubba, R. V., et al., 1975, "Cata Thermal Combustion: A New Process for Low-Emissions Fuel Conversion," ASME Paper No. 75-WA/FU-1.

2 Pfefferle, W. C., and Pfefferle, L. D., 1986, "Catalytically Stabilized Combustion," *Prog. Energy Combust. Sci.,* Vol. 12, pp. 25–41.

3 Blazowski, W. S., and Walsh, D. E., 1975, "Catalytic Combustion: An Important Consideration for Future Application," *Combustion Science and Technology,* Vol. 10, No. 5/6.

4 Krill, W. V., Kesselring, J. P. et al., 1979, "Catalytic Combustion for Gas Turbine Applications," ASME Paper No. 79-GT-188.

5 Fukuzawa, H., and Ishihara, Y., 1980, "Catalytic Combustion for Gas Turbine," *Proceedings of a 4th Workshop on Catalytic Combustion,* EPA-600/9-80-035, pp. 349–346.

6 Ozawa, Y., Saiga, M. et al., 1991, "Design and Testing of Low NO_X Catalytic Combustor for Gas Turbine," 91-YOKOHAMA-IGTC-107.

7 Ozawa, Y., Saiga, M. et al., 1993, "Test Result of Low NO_X Catalytic Combustor for Gas Turbine," ASME Paper No. 93-GT-344.

8 Davis, L. B., 1995, "Dry Low NO_X Combustion Systems for GE Heavy-Duty Gas Turbines," 95-YOKOHAMA-IGTC-139.

9 Althaus, R., and Imwinkelried, B., 1995, "ABB's Advanced Gas Turbines GT24/GT26: Testing and Validation Program," 95-YOKOHAMA-IGTC-144.

10 Beebe, K. W., Cutrone, M. B. et al., 1995, "Development of a Catalytic Combustor for a Heavy-Duty Utility Gas Turbine," 95-YOKOHAMA-IGTC-141.

11 Hisamatu, T., and Abe, T., 1989, "Development of Ceramic Fiber Combustion of Gas Turbines," CRIEPI Report No. EW88004.

M. Hilton
m.hilton@reading.ac.uk

A. H. Lettington

J. J. Thomson Physical Laboratory,
University of Reading,
Whiteknights, P. O. Box 220,
Reading, RG6 6AF,
United Kingdom

C. W. Wilson
Defence Research Agency, Pyestock,
Farnborough, GU14 OLS,
United Kingdom

Gas Turbine Exhaust Emissions Monitoring Using Nonintrusive Infrared Spectroscopy

Infrared (IR) spectra of the exhaust emissions from a static gas turbine engine have been studied using Fourier Transform (FT) spectroscopic techniques. Passive detection of the infrared emission from remote (range ~ 3 m) hot exhaust gases was obtained nonintrusively using a high spectral resolution (0.25 cm^{-1}) FTIR spectrometer. Remote gas temperatures were determined from their emission spectra using the total radiant flux method or by analysis of rotational line structure. The HITRAN database of atmospheric species was used to model the emission from gas mixtures at the relevant temperatures. The spatial distribution of molecular species across a section transverse to the exhaust plume ~10 cm downstream of the jet pipe nozzle was studied using a tomographic reconstruction procedure. Spectra of the infrared emission from the plume were taken along a number of transverse lines of sight from the centerline of the engine outwards. A mathematical matrix inversion technique was applied to reconstruct the molecular concentrations of CO and CO_2 in concentric regions about the centerline. Quantitative measurement of the molecular species concentrations determined nonintrusively were compared with results from conventional extractive sampling techniques.

Introduction

Current awareness of environmental issues has prompted an increase in academic research on novel techniques for atmospheric pollution monitoring. Gas turbine engine manufacturers and end users have an interest in monitoring the emissions from combustion systems both to meet regulatory requirements and to improve combustion efficiency.

Conventional extractive sampling gas analysis techniques in current use have a number of disadvantages. They require expensive probe systems which must be traversed from point to point. Residual chemistry can occur in transporting the sample to the gas analysis equipment.

Optical nonintrusive techniques have potential to offer real time multicomponent gas analysis and in flight continuous monitoring of species concentrations. FTIR spectroscopy, costing an order of magnitude less than extractive probe systems is one of the techniques being studied for exhaust gas monitoring.

FTIR spectroscopic techniques have been used in a variety of configurations to study gases. Many atmospheric species have IR activity and can be monitored simultaneously and with high sensitivity. Extractive gas samples can be analyzed in an FTIR spectrometer using a long path cell (Herget and Lowry, 1991). The cell contains mirrors to generate multiple reflections, and increase the path length over which absorption can occur. This active technique probes the target gas with a beam of modulated I.R. radiation, and then measures the spectral absorption.

However, there are a number of applications where FTIR spectroscopic techniques have been useful in studying gases remotely rather than by obtaining samples. Industrial sites and landfill tips can be continuously monitored for gaseous pollutants using active long path systems (Herget, 1982; Partridge, 1991; Reid et al., 1993; Russwurm et al., 1991). Active double-ended techniques require a source of modulated radiation to probe the target gas on the far side of which is an I.R. detector or retroreflector to return the beam to the detector in the spectrometer.

Passive single-ended techniques involve the measurement of I.R. emission and are generally less sensitive than active (probe beam) systems by 1 or 2 orders of magnitude. However, there are some remote monitoring applications where positioning a double ended system would be impractical, e.g., effluent plumes from tall smoke stacks and refinery flares. Passive I.R. radiation measurements have been used to retrieve the concentrations of CO, N_2O, NO, SO_2, and HCl in addition to CO_2 and H_2O vapour from the smoke stack effluent of thermal power plants and municipal incinerators (Wormhoudt et al., 1985; Prengle et al., 1973; Carlson et al., 1988). The threshold detection limit of each species improves with increasing stack gas temperature.

Passive remote emissions monitoring systems have recently been used to study jet engine exhaust plumes in Holland and Germany (Schleijpen et al., 1993; Lindemeir, 1994). Heland et al. (1994) have measured H_2O, CO_2, CO, and NO levels in the exhaust plumes of JT8 and CFM56-3 gas turbine engines. Hilton and Lettington (1996) have previously described nonintrusive FTIR spectroscopic studies of CO and CO_2 concentrations in the exhaust gases of a Rolls Royce Avon gas turbine engine.

This paper describes the use of single-ended passive techniques to obtain nonintrusive measurements of gas temperature and concentration distributions in the exhaust plume of a Rolls Royce Spey gas turbine engine.

Infrared Activity of Gas Molecules

From quantum theory, gases that are infrared active absorb or emit radiation as their molecules undergo spontaneous or induced transitions between different energy levels. Photons are emitted or absorbed at characteristic wavelengths determined by the structure of the molecules. A molecular species may be identified from the observed intensity at these wavelengths. The relative population of the energy levels is determined by the temperature-dependent Boltzmann distribution. The intensity of the absorption or emission is therefore determined by both the gas temperature and the number of molecules present. The net radiance detected by an FTIR spectrometer system depends on

---

Contributed by the International Gas Turbine Institute and presented at the International Gas Turbine and Aeroengine Congress and Exhibition, Orlando, FL, June 2–5, 1997. Manuscript received by the ASME Headquarters March 7, 1997. Paper No. 97-GT-180. Associate Technical Editor: H. A. Kidd.

the relative temperatures of all the molecules in the field of view (FOV). The spectrometer observes emission lines when the gas temperature is higher than that of the background, or absorption lines when this temperature differential is reversed.

The instrument response function, its FOV, and interferent species all affect the observed radiance of the target gas. In particular, the CO_2 and water vapour content of the atmosphere along the path absorbs extensive regions of the emission spectrum. Concentration measurements made at long range (~ 100 m) are usually quoted in the form of concentration × path length (ppm m) since the spectrometer detects the total contribution from all the molecules along the path from the detector to the gas plume. The temperature of the plume gases can be determined using techniques based on rotational line intensity distribution (Spellicy and Persky, 1985; Wang et al., 1990). When this temperature is known, the concentration × path length product can be obtained by matching the observed emission spectrum with modelled spectra (Haus et al., 1993; Schäfer et al., 1993). Where the spatial extent of the plume is well defined, as with the Spey exhaust, the relative path lengths in air and the plume can be determined and molecular concentrations in the plume calculated.

Spatial Distributions of the Molecular Species

FTIR spectroscopy has been used to nonintrusively study the change in molecular distributions across sections through laboratory hydrocarbon flames. The FOV of the spectrometer is traversed across the flame and spectra recorded along different lines of sight. The molecular distribution across the section is then reconstructed using a tomographic matrix inversion technique (Hilton, 1995; Hilton et al., 1995). The mathematical inversion procedure assumes that the flame is axially symmetric.

Along each line of sight, the molecules in one region of the flame may absorb the radiation emitted by those in another region; therefore, a self absorption correction must be applied before quantitative measurements may be made. Best et al. (1991) and Solomon et al. (1992) have measured both the absorption and emission of flames to obtain the spatial distributions of temperatures and species concentrations. This work, however, describes the use of purely passive nonintrusive FTIR spectroscopy to determine thermodynamic gas temperatures and relative molecular concentrations of CO and CO_2 in a gas turbine exhaust plume.

Passive Remote FTIR Spectroscopy

The FTIR spectrometer is based on a Michelson interferometer. In passive remote monitoring mode, I.R. radiation from a external source (in this case the thermal emission from the Spey engine exhaust gases) enters the spectrometer via an NaCl window. The parallel beam of input radiation is split by a KBr beamsplitter into two beams, one of which is reflected back to the beamsplitter by a static retroreflector, and the other by a moving retroreflector. The moving retroreflector introduces an optical path difference between the two beams recombining at the beamsplitter. As the optical path difference between the beams changes with the movement of one retroreflector, the intensity of the output beam is modulated by constructive and destructive interference.

The intensity of modulated output is recorded by a liquid nitrogen cooled Mercury Cadmium Telluride detector. A Fast Fourier Transform chip inside the spectrometer converts the variation in intensity with optical path difference to produce a spectrum of the variation in intensity with spectral frequency. Data are collected over a time period of ~ 30 s, in which time 20 or so scans of the moving mirror have occurred. Increasing the number of scans improves the signal to noise ratio (SNR) at the expense of time taken. Spectral data are downloaded from the spectrometer via a serial data port to a laptop computer.

Thermodynamic Gas Temperature. While the wavelength of infrared spectral lines is determined by the molecular structure of each species, the relative intensity of the spectral lines changes with the temperature of the molecules. Carbon monoxide has strong spectral lines that are widely spaced in a region of the spectrum that is relatively free from interference by other molecules. The relative intensity distribution of these spectral lines can be used to calculate thermodynamic gas temperatures. The gas temperature is found by determining the temperature-dependent slope of a function of the CO line radiance plotted against line quantum number.

Concentrations. Molecular concentrations are determined from the observed emission spectra by comparison with modelled spectral lines. The HITRAN (Rothman et al., 1992) database contains line-by-line information about 32 naturally occurring atmospheric species. From this database, the temperature-sensitive absolute line intensities can be calculated for individual spectral lines. The effect of atmospheric absorption by CO_2 or H_2O present in the path to the exhaust plume can be included in the model. Once the FTIR spectrometer has been calibrated for radiance measurements, the number of molecules of each species can be obtained by comparing the observed line intensity with the modelled absolute line intensity.

Tomographic Reconstructions. Emission spectra are taken with the spectrometer sighted horizontally on consecutive positions from the centreline down to the outer edge of the exhaust plume, transverse to the gas flow. At each of these positions, the radiance detected by the spectrometer is the sum of all the contributions from each volume element along the path.

Assuming the plume has axial symmetry, then the spectral data measured along these linear paths may be expressed simply as a sum of the contributions from a number of concentric regions about the axis of the plume. In this way, a set of simultaneous equations is built up summing the contribution from each element to the total emission detected along each linear path. These equations are solved to determine the spectral contribution from each of the volume elements.

Spectra obtained near the centre of the flame will contain contributions from the largest number of elements, those near the boundaries the least. The central element will be well defined spatially. Computational analysis using a matrix inversion, which is valid for systems with axial symmetry, is used to reconstruct the distribution of different molecular species within the traversed section of the plume.

The algorithms were originally derived for axially symmetric flames, and it should be noted that the exhaust plume does not in practice possess perfect symmetry. However, it is a reasonable approximation in the region of the exit plane.

Engine Instrumentation

The Spey engine studied at DRA Pyestock has been used for a number of experimental projects and the temperature and molecular species distribution in its exhaust gases monitored extensively using conventional probe systems.

Extractive gas samples were obtained using a single-point, multiposition probe positioned in a plane transverse to the exhaust gas flow 10 cm behind the jet pipe nozzle. The probe can be sited at any radial distance from the centreline or circumferential angle of the plume. A stainless-steel gas sampling tube heated to 150 ± 5°C transferred the combustion products to gas analysis equipment mounted in a mobile laboratory outside the test bed. Intrusive temperature measurements were made at the extractive sampling positions using a radiation shielded thermocouple. It was necessary that the line of sight of the spectrometer was clear during the nonintrusive measurements. Therefore, extractive samples and thermocouple measurements were taken during engine runs preceding and subsequent to the nonintrusive

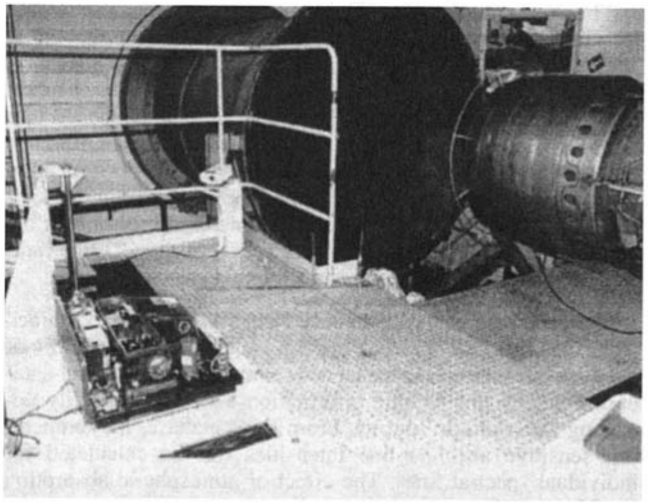

Fig. 1 FTIR spectrometer and traverse optics with Spey engine on Glen test bed

studies, but with the engine operating at identical idle and max continuous conditions. Previous experience has shown that reproducible gas analysis results can be obtained by restoring the same engine conditions on different occasions.

Figure 1 shows the unprotected FTIR spectrometer mounted with vibration isolators onto the metalwork of the test bed. The vertical pole supported by the triangular stanchion on the far side of the instrument is part of the remotely controlled motorized traversable mirror system. This allows spectra to be taken along different lines of sight from the centerline of the engine down to the lower regions of the jet pipe nozzle approximately 300 mm below. Underneath the moving mirror, a compensating mirror arrangement maintains a constant optical pathlength for each line of sight.

The FTIR spectrometer was aligned with the transfer optics using a compact solid state red laser. The stepper motor was positioned so that the optical axis of the system was directed 10 cm aft of the jet pipe nozzle, and, initially, along the engine axis (centreline). The stepper motor control computer and the spectrometer were operated remotely from the test bed control room.

Prior to engine running, the spectrometer was topped up with liquid nitrogen, firmly mounted, and encased with substantial acoustic padding. Calibration spectra were obtained using a high emissivity, black body IR source at temperatures up to 670 K.

Test Results

The engine was allowed to soak at both idle and max continuous before IR spectra were obtained at seven traverse mirror points, starting with the line of sight along the centerline and stepping 50 mm down between points.

Figure 2 shows typical CO emission bands in spectra taken along the centerline at the two engine conditions. The vertical scale is a measure of the radiance in arbitrary instrument units. The horizontal scale is reciprocal wavelengths or cm^{-1}. The regularly spaced spectral lines separated by 4 cm^{-1} are characteristic of CO, while those more irregularly and widely spaced are characteristic of H_2O.

At idle, CO lines can readily be observed in the whole family of spectra obtained as the line of sight was moved down from the centerline position. However, at max continuous, the engine runs very efficiently, typically generating CO levels of <20 ppm. CO emission line intensities at these concentrations are small compared with the noise levels of the observed spectra; therefore, no quantitative information could be obtained for CO levels at max continuous.

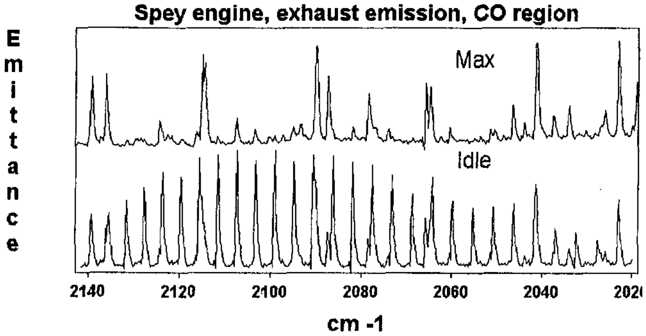

Fig. 2 Passive emission spectra

The CO_2 band emits strongly, and in some regions becomes saturated, i.e., the gas becomes opaque.

Thermodynamic gas temperatures were determined by comparing the band intensity in the saturated region with calibration spectra. At idle, there was sufficient CO band intensity for an analysis of rotational line intensities to compare with the CO_2 temperature measurements. These showed agreement to ±1 percent.

Figure 3 shows the temperature distribution across the plane through the exhaust gases, as typically measured by thermocouples and as calculated from the saturated CO_2 band. For the IR spectra analysis, the temperature and molecular concentration distribution across the plume have been assumed to be symmetrical about the centreline of the engine.

There is good agreement between the two types of temperature measurements at idle, but the nonintrusive measurements are lower than the thermocouple measurements at max continuous (particularly near the centre of the plume). The observed IR spectra are the net result of absorption and emission contributions from all molecules along the line of sight. High intensity lines emitted by CO_2 near the center of the plume can be absorbed by cooler CO_2 molecules in the outer regions of the plume. This effect is called self absorption and could cause apparently low line intensities to be observed.

Also, while the thermocouple is measuring the temperature at a single point in space, the nonintrusive measurements are made by gathering the radiation emitted from a horizontal column of finite cross-sectional area (aperture ~50 mm, beam divergence 2 mrad). The nonintrusive temperature measurements are, effectively, an average over the FOV of the instru-

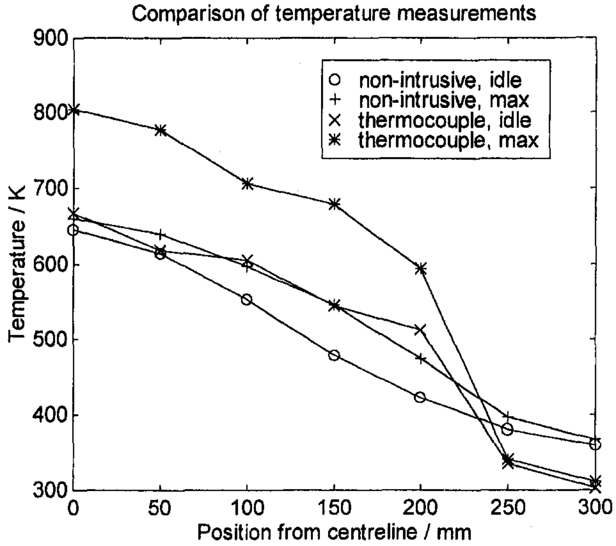

Fig. 3 Radial temperature distribution

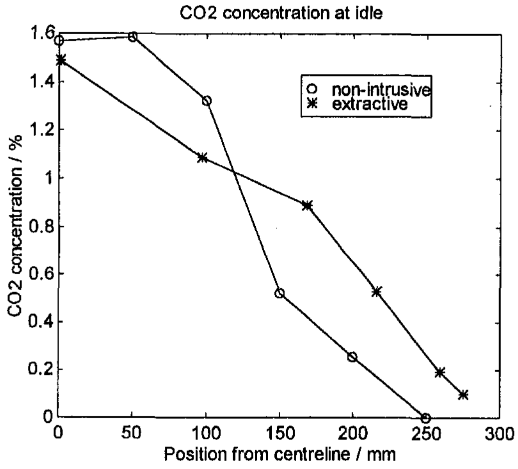

Fig. 4 Radial CO_2 distribution (idle)

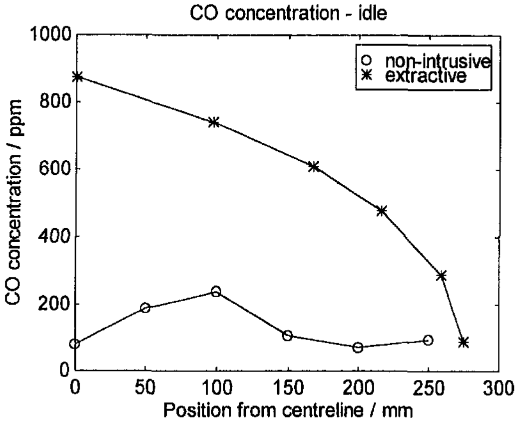

Fig. 5 Radial CO distribution (idle)

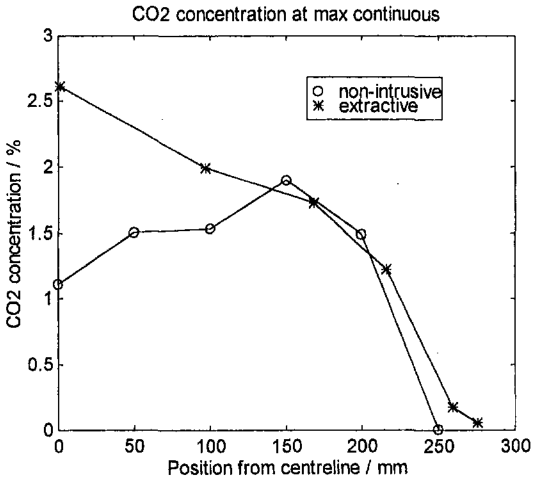

Fig. 6 Radial CO_2 distribution (max)

ment. This results in a smoothing out of the radiation intensity from highly localized regions of high or low gas temperature.

Figures 4, 5, and 6 show the results of the mathematical inversion procedure to calculate the CO_2 and CO concentrations in six concentric regions of the plume from 6 line of sight traverse points. Thermocouple measurements of plume temperature distribution were used in the inversion model rather than the apparent temperatures obtained from the CO_2 band intensities. Only 6 of the 7 traverse points were used in the inversion because the seventh point looking horizontally through the section of the plume 300 mm down from the centreline had very low spectral line intensities comparable with the noise levels of the FTIR spectrometer.

The figures plot the calculated and extractive concentration distributions from the center of the plume out horizontally. The nonintrusive results shown are the calculated concentrations of CO and CO_2 within the six concentric annular regions about the center of the plume predicted by the mathematical inversion.

The agreement between the extractive gas analysis results and the nonintrusive measurements is best for CO_2 at idle and, in the outer regions of the plume at max continuous. The CO concentrations determined nonintrusively were consistently low. There are a number of factors that have contributed to these discrepancies. As discussed previously, the nonintrusive measurements are made over a finite FOV. The nonintrusive data points are plotted assuming an even distribution within six bands across the plume. Extractive measurements taken at a single point can not be expected to match exactly with concentrations averaged over a wider area. The proposed addition of front end optics to reduce the FOV of the spectrometer should improve the correspondence between the nonintrusive and extractive measurements.

The current inversion model is unsophisticated and relies on a small number of line-of-sight projections on which to base the reconstruction. More projections would improve the reconstruction by reducing the significance of noise in the small number of line intensity measurements.

Self absorption can reduce the apparent intensity of the spectral lines emitted near the center of the plume, results in the region of low CO_2 concentrations observed in Fig. 5. This is likely to be more significant at max continuous than at idle because of the increased temperature gradients present. The self absorption correction used in the model is being revised.

Observed CO line intensities are an order of magnitude lower than those of CO_2 because of the smaller quantities emitting. This results in a lower SNR for CO compared with CO_2. The sensitivity to detector noise and nonlinearity, instrument line shape function, self absorption effects, baseline drift, errors in temperature measurements, etc. will be heightened where the SNR is low. Improvements to the model by which the CO concentration is calculated are under consideration. However, the results have shown that some agreement can be obtained between extractive gas analysis measurements and those obtained nonintrusively.

Conclusions

FTIR spectroscopy has been shown to provide useful information by nonintrusively monitoring the exhaust gas flow. In this instance, the molecular species CO and CO_2 have been studied since their distinctive strong spectral lines can be easily identified and intensities measured. However, there are other species which could be detected from their I.R. spectra including H_2O, NO, NO_2, and unburnt hydrocarbons. The quantitative analysis of these compounds from their I.R. spectra is more difficult because of the complexity and/or weakness of the lines. Increasing the instrument sensitivity by using an Indium Antimonide detector and modifications to the modelling would improve the ability of the system to study low concentration species.

Thermodynamic gas temperatures have been calculated from saturated CO_2 band intensities, with results that agree well with thermocouple measurements, except in regions of very high temperature gradients.

The radiance calibration, instrument response factors of the FTIR spectrometer and limitations of the current inversion reduce the efficiency of the molecular concentration distribution reconstruction. A number of methods to improve the technique are currently under investigation.

The mathematical inversion procedure has reconstructed the molecular concentration distribution within 6 concentric regions of the plume. The reconstruction works best when the plume temperatures are lower than 650 K and molecular concentrations are high. The current inversion assumes axial plume symmetry and could be improved by accounting for the true geometry and increasing the number of linear projections (line of sight measurements) used in the model. However, this work has demonstrated that FTIR spectroscopy can make useful nonintrusive measurements of gas turbine exhaust emissions. While the accuracy of nonintrusive measurements is not that of probe systems, the technique has a number of advantages over extractive exhaust gas monitoring. One instrument can monitor a number of species simultaneously; the exhaust gas flow is not perturbed by intrusions; the response is rapid and unlike probe systems it could, in the future, be used for in flight monitoring.

Acknowledgments

This work has been supported by the Defence Research Agency, U.K. Ian Thomas and Nick Davies of the Physics Department of Reading University and the Glen Test Bed crew at DRA Pyestock provided technical assistance.

References

Best, P. E., Chien, P. L., Carangelo, R. M., Solomon, P. R., Danchak, M., and Ilovici, I., 1991, ''Tomographic Reconstruction of FT-IR Emission and Transmission Spectra in a Sooting Laminar Diffusion Flame: Species Concentrations and Temperatures,'' *Combustion and Flame,* Vol. 85, pp. 309–318.

Carlson, R. G., Hayden, A. F., and Telfair, W. B., 1988, ''Remote Observations of Effluents From Small Building Smokestacks Using FTIR Spectroscopy,'' *Applied Optics,* Vol. 27, No. 23, pp. 4952–4959.

Haus, R., Schäfer, K., Mosebach, H., and Heland, J., 1993, ''FTIS in Environmental Research: Mobile Remote Sensing of Air Pollution,'' *Proceedings 9th International Conference on Fourier Transform Spectroscopy,* Vol. 2089, J. E. Bertie and H. Wieser, eds., Society of Photo-Optical Instrumentation Engineers, Bellingham, WA, pp. 319–319.

Heland, J., Haus, R., and Schäfer, K., 1994, ''Remote Sensing and Analysis of Trace Gases From Hot Aircraft Engine Plumes Using FTIR-Emission Spectroscopy,'' *Science of the Total Environment,* Elsevier, Vol. 158, pp. 85–91.

Herget, W. F., 1982, ''Analysis of Gaseous Air Pollutants Using a Mobile FTIR System,'' *American Laboratory,* Vol. 14, No. 12, pp. 72–78.

Herget, W. F., and Lowry, S. R., 1991, ''Auto Exhaust Gas Analysis by FTIR Spectroscopy,'' *Measurement of Atmospheric Gases,* Vol. 1433, H. I. Schiff, ed., Society of Photo-Optical Instrumentation Engineers, Bellingham, WA, pp. 275–289.

Hilton, M., 1995, ''Passive Emission Monitoring of Remote Combustion Gases Using Fourier Transform Infrared Spectroscopy,'' PhD. thesis, Reading University, U.K.

Hilton, M., Lettington, A. H., and Mills, I. M., 1995, ''Quantitative Analysis of Remote Gas Temperatures and Concentrations From Their Infrared Emission Spectra,'' *Journal of Measurement Science and Technology,* Vol. 6, pp. 1236–1241.

Hilton, M., and Lettington, A. H., 1996, ''Industrial Gas Turbine Exhaust Emission Monitoring Using Nonintrusive FTIR Spectroscopy,'' *Proceedings of Applied Optics Divisional Conference of the Institute of Physics,* K. T. V. Grattan, ed., Institute of Physics Publishing, Bristol, UK and Philadelphia, PA, pp. 337–342.

Lindemeir, E., 1994, ''Evaluation of Infrared Emission Spectra of Aircraft Exhaust With the FitFas Software,'' *Annales Geophysicae,* Vol. 12, pp. 417–421.

Partridge, R., 1991, ''Long-Path Monitoring of Atmospheric Pollution,'' *Measurement & Control,* Vol. 23, pp. 293–298.

Prengle, H. W., Morgan, C. A., Fang, C. S., Huang, L. K., Campani, P., and Wu, W. W., 1973, ''Infrared Remote Sensing and Determination of Pollutants in Gas Plumes,'' *Environment Science and Technology,* Vol. 7, No. 5, pp. 417–423.

Reid, S. A., Hughes, J. I. L., Roberts, P. T., Archibald, I., and Gregory, K., 1993, ''Development of Open Path Systems for Emission Rate Measurements,'' *Proceedings of Optical Sensing for Environmental Monitoring,* Vol. SP-89, Air and Waste Management Association, Pittsburgh, PA, pp. 305–321.

Rothman, L. S., Gamache, R. R., Tipping, R. H., Rinsland, C. P., Smith, M. A. H., Benner, D. C., Devi, V. M., Flaud, J-M., Camy-Peyret, C., Perrin, A., Goldman, A., Massie, S. T., Brown, L. R., and Toth, R. A., 1992, ''The HITRAN Database: Editions of 1991 and 1992,'' *Journal Quantitative Spectroscopy and Radiative Transfer,* Vol. 48, pp. 469–507.

Russwurm, G. M., Kagann, R. H., Simpson, O. A., McClenny, W. A., and Herget, W. F., 1991, ''Long-Path FTIR Measurements of Volatile Organic Compounds in an Industrial Setting,'' *Journal of Air & Waste Management Association,* Vol. 41, pp. 1062–1066.

Schäfer, K., Haus, R., and Heland, J., 1993, ''Measurement of Gaseous Compounds From Emissions Sources and in Ambient Air by Fourier Transform Infrared Spectroscopy: Method and Results of FTIS-MAPS,'' *Proceedings of Optical Sensing for Environmental Monitoring,* Vol. SP-89, Air & Waste Management Association, Pittsburgh, PA, pp. 455–465.

Schleijpen, H. M. A., Crajé, M. W. J., and Eisses, S. M., 1993, ''High Resolution Spectroscopy in the Field,'' *Proceedings of the Infrared Technology XIX Conference,* Vol. 2020, B. F. Andresen and F. D. Shepherd, eds., Society of Photo-Optical Instrumentation Engineers, Bellingham, WA, pp. 225–233.

Solomon, P. R., Morrison, Jr., P. W., Serio, M. A., Carangelo, R. M., Markham, J. R., Bates, S. C., and Cosgrove, J. E., 1992, ''Fourier Transform Infrared Spectroscopy for Process Monitoring and Control,'' *Industrial, Municipal, and Medical Waste Incineration Diagnostics and Control,* Vol. 1717, J. J. Santoleri, ed., Society of Photo-Optical Instrumentation Engineers, Bellingham, WA, pp. 104–115.

Spellicy, R. L., and Persky, M. J., 1985, ''Flare Efficiency Monitoring by Remote Infrared Sensing,'' Infrared Methods for Gaseous Measurements, J. Wormhoudt, ed., Marcel Dekker, NY.

Wang, J., Wang, X., Li, H., and Gu, X., 1990, ''Flame Temperature Remote Measurement From Infrared Emission Line Intensities of Rotation-Vibration Band of Molecules,'' *Spectroscopy Letters,* Vol. 23, No. 4, pp. 515–526.

Wormhoudt, J., Conant, J. A., and Herget, W. F., 1985, ''High Resolution Infrared Emission From Gaseous Sources,'' Infrared Methods For Gaseous Measurements, Wormhoudt, J., Ed., Marcel Dekker, New York.

Aspects of Jet Fuel Oxidation

S. Zabarnick

S. D. Whitacre

University of Dayton Research Institute,
Aerospace Mechanics Division,
300 College Park/KL 463,
Dayton, OH 45469-0140

A quartz crystal microbalance (QCM)/Parr bomb system with a headspace oxygen sensor is used to measure oxidation and deposition during thermal oxidative stressing of jet fuel. The advantages of the oxygen sensor technique in monitoring fuel oxidation is demonstrated. Simultaneous measurement of deposition using the QCM shows a strong correlation between oxidation and deposition in jet fuels. Studies performed over the temperature range 140 to 180°C show that surface deposition peaks at an intermediate temperature, while bulk deposition increases with temperature. In studies of jet fuel antioxidants, we find that rapid increases in oxidation rate occur upon consumption of the antioxidant. The antioxidant appears to be consumed by reaction with alkylperoxy radicals. In studies of metal deactivator (MDA) additives, we find that MDA is consumed during thermal stressing, and this consumption results in large increases in the oxidation rate of metal containing fuels. Mechanisms of MDA consumption are hypothesized.

Introduction

Jet fuel undergoes oxidative chemistry upon being heated in the fuel systems of advanced military aircraft. Besides being heated by heat transfer from the hot turbine compressor air (or in the afterburner by combustor exhaust), the fuel is also heated while being used as a coolant for various engine and airframe components (Hazlett, 1991). It has been predicted that this coolant usage will become even more important in future advanced aircraft (Heneghan et al., 1996). Air saturated fuel typically contains ≈60 ppm (w/w) or 1.8×10^{-3} M of oxygen. This very small amount of oxygen can result in the formation of gums and deposits which are capable of impairing proper performance of the fuel system and grounding of the aircraft. In a flowing fuel system, the mass of deposits formed per volume of fuel is small, on the order of 1 μg/mL (≈1.2 ppm w/w) for complete oxygen consumption (Edwards, 1996); but, the volumes of fuel used in military aircraft are extremely large over the lifetime of an aircraft. Thus, the small amounts of deposits that form can build up over time, ultimately resulting in filter plugging, fouling of close tolerance valves, valve hysteresis, and other problems.

The amount of deposits which form on fuel systems components is a function of the bulk temperature history of the fuel, the fuel system surface temperatures, and the flow rates encountered. These parameters will vary continuously during a typical mission. The temperature history of the fuel will determine the extent of oxygen consumption. Also, each fuel sample will have quite different oxidative and deposit forming characteristics. Additional complications in understanding oxidation and deposition occur when safety systems are employed that attempt to lower the oxygen concentration of the fuel tank ullage, such as the on-board inert gas generating system (OBIGGS). It is believed that in present military aircraft fuel systems only a relatively small percentage (<10 percent) of the dissolved oxygen is consumed as the fuel flows from the tank to the fuel nozzle. Despite this fact, most jet fuel tests employed to date have used conditions where the dissolved oxygen is completely consumed to maximize these difficult to quantify deposits.

As military aircraft fuel system conditions are so complex, all test devices are simplifications of these real systems. Also, as thousands of hours of run time with many thousands of gallons of fuel are typical of the conditions to which real engine components are subjected, most test devices are operated in an accelerated mode. That is, one or more test parameters are adjusted to increase the deposition rate, and, therefore, decrease the test time and/or reduce the volume of fuel required. Accelerated conditions can entail higher temperatures or higher oxygen availabilities, or a combination of the two. Most flowing tests employ higher temperatures to yield measurable deposits in a reasonable time, while static (batch) tests usually employ higher oxygen availabilities. It is important to consider the difference in conditions between the laboratory test and the aircraft when evaluating the relevance of the tests. Thus, it is important to understand the effect that changes in these parameters have on oxidation and deposition. An understanding of the effect of changes in temperature and oxygen availability on oxidation and deposition is crucial. As the US Air Force and its contract researchers are presently involved in development of jet fuel additives to increase fuel thermal stability and allow increased aircraft fuel system temperatures (the JP-8 + 100 program), it is important to evaluate the effect of oxygen availability and temperature on additive behavior and effectiveness. To address these issues we utilize a test device which can simultaneously monitor both deposition and oxidation during the thermal stressing of a jet fuel. This device is a static reactor which uses a quartz crystal microbalance (QCM) for the in-situ measurement of deposition, and a polarographic oxygen sensor that is situated in the reactor headspace to monitor oxidation. Previously, we have demonstrated the usefulness of the quartz crystal microbalance (QCM) with a pressure monitoring technique for studying the deposition and oxidation of jet fuels (Zabarnick, 1994). The addition of the polarographic oxygen sensor allows more meaningful oxidation information, as it directly monitors the headspace oxygen concentration.

Experimental

The QCM/Parr bomb system has been previously described in detail, and will only be outlined briefly here (Zabarnick, 1994; Zabarnick and Grinstead, 1994). The Parr bomb is a 100 mL stainless-steel reactor. It is heated with a clamp-on band heater, and its temperature is controlled by a PID controller through a thermocouple immersed in the fuel. The reactor contains an *rf* feedthrough, through which the connection for the quartz crystal resonator is attached. The crystals are 2.54 cm in diameter, 0.33 mm thick, and have a nominal resonant frequency of 5 MHz. The crystals were acquired from Maxtek Inc. and are available in crystal electrode surfaces of gold, silver, platinum, and aluminum. For the studies reported here, gold crystal electrodes were used. The QCM measures deposition (i.e., an increase in mass) that occurs on overlapping sections of the two sided electrodes. Thus, the device responds to deposi-

---

Contributed by the International Gas Turbine Institute and presented at the International Gas Turbine and Aeroengine Congress and Exhibition, Orlando, FL, June 2–5, 1997. Manuscript received by the ASME Headquarters March 7, 1997. Paper No. 97-GT-219. Associate Technical Editor: H. A. Kidd.

Table 1 Properties of fuels studied

Fuel Number and Type	Total Sulfur (ppm)	Copper (ppb)
F-2827 (Jet A)	763	<5
F-2747 (Jet A-1)	37	<5
F-3119 (Jet A)	1000	7
F-3145 (JP-5)	not determined	285
F-3139 (Jet A)	not determined	not determined
Exxsol D-110 (solvent)	3	not determined

tion that occurs on the metal surface, and does not respond to deposition on the exposed quartz.

The device is also equipped with a pressure transducer (Sensotec) to measure the absolute headspace pressure and a polarographic oxygen sensor (Ingold) to measure the headspace oxygen concentration. Previous studies have demonstrated the value of determining the oxidation characteristics of fuels and fuels with additives. A personal computer is used to acquire data at one-minute intervals during the experimental run. The following data are recorded during a run: temperature, crystal frequency, headspace pressure, headspace oxygen concentration, and crystal damping voltage.

The reactor is charged with 60 mL of fuel, which is sparged with the appropriate gas for one hour before each test. The reactor is then sealed, and the heater is started. All runs in this study were performed at 140°C; heat-up time to this temperature is 40 ± 5 minutes. Most runs are conducted for 15 hours, after which the heater is turned off and the reactor allowed to cool. Surface mass measurements can only be determined during the constant temperature (±0.2°C) portion of an experimental run. The crystal frequency is converted to a surface mass measurement using the process described below.

For the temperature effect studies, a slightly different method was used to prevent significant oxygen consumption and deposition during the heat-up period. For these runs, the fuel is sparged with nitrogen for one hour to purge the fuel of dissolved oxygen. The reactor is then sealed and heated to temperature. Once the fuel has reached temperature, air or oxygen is added through the gas inlet line, and the headspace pressure is monitored to determine the amount added. This technique prevents significant oxidation from occurring during the heat-up period for higher temperature runs.

The theory that relates the measured frequency changes to surface mass has been presented in detail elsewhere (Martin et al., 1991). The frequency change of a crystal immersed in a liquid fuel can be due to two effects: the first results from changes in the surface mass density, and the second is due to changes in the liquid density and viscosity. At constant temperature and relatively small extents of chemical conversion, the liquid properties remain constant, and the frequency change can be related to surface deposition via the equation

$$\rho_s = -(2.21 \times 10^5 \text{ g}/(\text{cm}^2 s)) \frac{\Delta f}{f_0^2}, \qquad (1)$$

where f_0 is the unperturbed resonant frequency, Δf is the change in resonant frequency, and ρ_s is the surface mass density (mass/area). The reproducibility of the mass deposition measurements on fuels is limited to ±20 percent for the QCM technique. The fuels studied and some of their properties are listed in Table 1. The fuels were acquired from the Fuels and Lubricants Division of Wright Laboratory, Wright-Patterson AFB, Ohio, and are referred to by the Wright Lab assigned accession number.

Bulk fuel insolubles were measured gravimetrically. The cooled, post-test fuel was filtered with a pre-weighed 1 μm microfiber glass filter. The reactor was rinsed twice with 5 mL portions of hexane which were subsequently filtered. The filter was dried in a laboratory oven at 100°C for two hours to remove residual fuel. The hot filter was cooled in a desiccate chamber and then weighed to determine the bulk deposit mass.

BHT (2,6 di-tert-butyl-4-methylphenol) was quantified by gas chromatography-mass spectrometry (GC-MS). 500 μL fuel samples were withdrawn from the reactor through a GC septum and extracted with 500 μL of methanol. 2 μL samples of the methanol solution were injected into a Hewlett-Packard GC-MS operating in single-ion monitoring (SIM) mode. The mass spectrometer was set to follow the intensity of the 205 amu fragment ion and the 220 amu parent ion of BHT. Calibration curves were obtained by injecting standard solutions of BHT in methanol.

MDA was quantified by a procedure developed by Streibich (Streibich, 1996). 10 mL of fuel is passed through a silica gel solid phase extraction cartridge. The polar components, including MDA, are retained on the cartridge and subsequently eluted with methanol. The methanol is evaporated and the remaining condensate is dissolved in 200 μL of toluene. This toluene solution is injected into a GC/MS operated with base deactivated injector liner and column. Single ion monitoring of the 161 amu fragment ion and the 282 amu parent ion were used for quantitation.

Results and Discussion

Correlation Between Oxidation and Deposition—Oxygen Sensor Measurements. Previously we demonstrated the ability of the Parr bomb/QCM device to simultaneously measure deposition and oxidation (Zabarnick, 1994). This study used a pressure transducer to monitor the headspace pressure during the test. As oxygen is consumed in the fuel, the headspace oxygen diffuses into the fuel, resulting in a pressure drop in the headspace. While the pressure transducer technique is valuable for providing an indirect measure of oxidation, it has limitations. In particular, any changes in the volatility of the fuel during stressing will result in headspace pressure changes that cannot be separated from changes due to oxygen consumption. Thus, it was demonstrated that in a slow oxidizing fuel (F-2827) the production of volatiles was able to completely mask the pressure drop due to oxygen removal. Another disadvantage of the pressure technique is that the pressure at which oxygen is completely consumed is not known. Thus, the leveling off of the pressure is usually taken to indicate complete consumption, an assumption that is not always true. To provide a more quantitative measure of the oxidation process in the Parr bomb/QCM system we have modified the device to accept a polarographic oxygen sensor. While this sensor provides a headspace oxygen measurement only, it responds to the gaseous oxygen concentration and not to pressure changes due to volatiles, and has an easily calibrated zero oxygen level to allow determination of the point of complete oxygen consumption.

The advantages of the oxygen probe over the pressure transducer are demonstrated for two fuels in Fig. 1. Figure 1(*a*) shows the limitations of the pressure monitoring technique. Fuel F-2827 displays a flat pressure profile during the entire run despite generating a relatively large deposition of ≈4 μg/cm^2 during the 15 hour run. The oxygen sensor results in Fig. 1(*b*) show that oxygen is indeed consumed in the fuel, dropping from 33 to 24 percent during the run. Thus, ≈28 percent of the original oxygen is consumed. Figure 1(*b*) also demonstrates the correspondence between oxidation and deposition for this fuel. Both oxidation and deposition are relatively slow during the first three hours, increasing significantly at longer times. The deposition process continues for this fuel throughout the run, and the oxygen sensor profile shows that this is due to the presence of oxygen throughout the run. The different levels of noise in the deposition plots in the two F-2827 runs are due to experimental variations; the QCM is very sensitive to electromagnetic noise in the laboratory. Also shown in these plots are the deposition and oxidation profiles for fuel F-2747. The

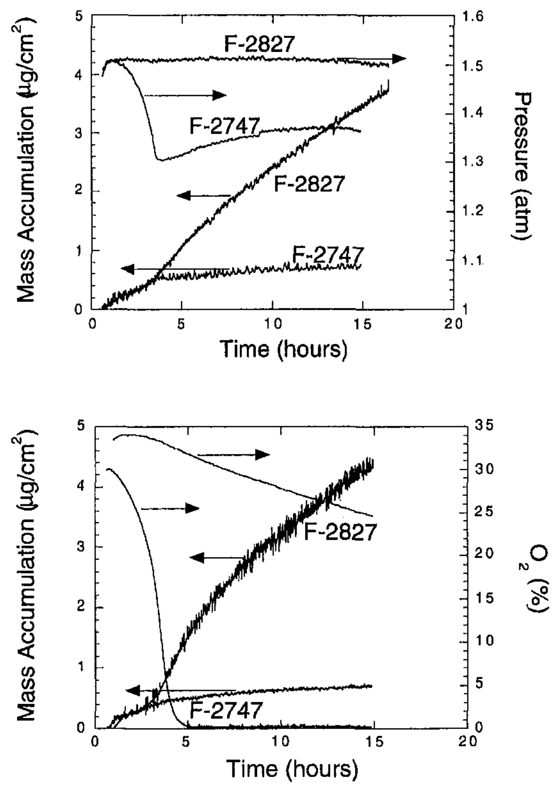

Fig. 1 Plots of mass accumulation and pressure (*a*, top) and percent oxygen (*b*, bottom) for fuel F-2827 and F-2747 at 140°C

pressure sensor profile in Fig. 1(*a*) shows a rapid decrease in pressure over the first 4 hours, with a slow rise in pressure at longer times. Previously, this slow rise in pressure was attributed to the production of volatiles during thermal stressing of the fuel (Zabarnick, 1994). Figure 1(*b*) shows that oxygen rapidly decays to zero over the first five hours of the run. The oxygen sensor measurements are not affected by the formation of volatile products. Most of the deposition of this fuel occurs during the oxygen decay, with only a slight rise in deposition at longer times. It is apparent that the oxygen sensor is able to provide quantitative information on the oxidation process without the limitations of the pressure monitoring technique.

This quantitative measure of the oxidation process allows a direct comparison of the deposit forming efficiency of the two fuels. After normalizing by the amount of oxygen consumed, we calculate that F-2827 is 22 times more efficient at producing deposition than fuel F-2747. Obviously, the quantitative information provided by the oxygen sensor overcomes the limitations of the pressure measurement technique, and yields crucial information for the interpretation of jet fuel thermal stability studies. Even more valuable information would result from in-situ measurement of the oxygen concentration in the liquid fuel. Unfortunately, the oxygen sensor is limited to temperatures below 60°C and is not able to handle the high temperatures encountered during the stressing of jet fuel. The oxygen sensor is also valuable for studies of jet fuel additives as demonstrated in the following studies.

The observed strong correspondence between oxidation and deposition has been observed in this system for a large variety of fuels and fuel/additive combinations. In general, it is found for a given fuel that deposition and oxidation occur concurrently. This is illustrated graphically in Fig. 2 for fuel F-3145 with 3.0 mg/L MDA added. Also shown in the figure is the very good agreement between the oxygen sensor and pressure measurements. The pressure measurement maximum and minimum have been normalized to the oxygen sensor measurements to allow comparison. The actual pressure varied over the range 1.2 to 1.4 atm. The figure shows that the fuel begins to deposit near six hours, and deposition levels off at 5.1 $\mu g/cm^2$ after 11 to 12 hours. Correspondingly, oxygen removal begins near six hours and is complete near 11 hours.

It is important to differentiate between the correspondence between oxidation and deposition for a given fuel as reported here, and the inverse relationship between oxidation rate and deposition over a range of fuels previously reported (Heneghan and Zabarnick, 1994). The present data shows that the oxidation process is responsible for deposition; for a given fuel, if we slow or delay oxidation by the addition of additives, we will slow or delay deposition. But, when one looks at a range of fuels with widely different oxidation rates, one finds that, in general, the fast oxidizing fuels are lower depositors than the slow oxidizing fuels. It was hypothesized that this is due to the presence of naturally occurring antioxidants in the slow oxidizing fuels; these naturally occurring antioxidants slow oxidation and increase deposition (Heneghan and Zabarnick, 1994).

Studies of the Temperature Dependence of Oxidation and Deposit Formation. Previously, we reported on the temperature dependence of jet fuel deposition and oxidation in the QCM system over the range 140 to 180°C (Zabarnick et al., 1996). We found that although the oxidation rate increases with temperature, final surface deposition displays a more complex temperature dependence. The two fuels studied showed a maximum efficiency for producing surface deposits near 150 to 160°C. Reduced deposition was noted at both higher and lower temperatures. These results contrasted sharply with most previous measurements, which report increasing deposition with temperature for the regime below 400°C (Hazlett, 1991). We hypothesized that the different temperature dependence of deposition was due to a difference in the regime of oxygen availability in these tests. Most previous work was performed on either static tests with unlimited oxygen availability or flowing heated tube tests with partial oxygen consumption. Both of these systems will have temperature dependencies of deposition that are controlled by the temperature dependence of the oxidation rate. Due to the unlimited oxygen availability conditions of the bubbling air/oxygen static flask tests, the increase in oxidation rate with temperature will result in an increase in deposition with temperature. In the case of the flowing heated tube tests, it is less obvious that the deposition rate will be controlled by the oxidation rate. These tests use relatively high temperatures and short residence times, which result in incomplete oxygen consumption. This relatively short reaction time along with possible laminar flow conditions results in oxygen consumption occurring near the tube wall surface, while the bulk fuel may

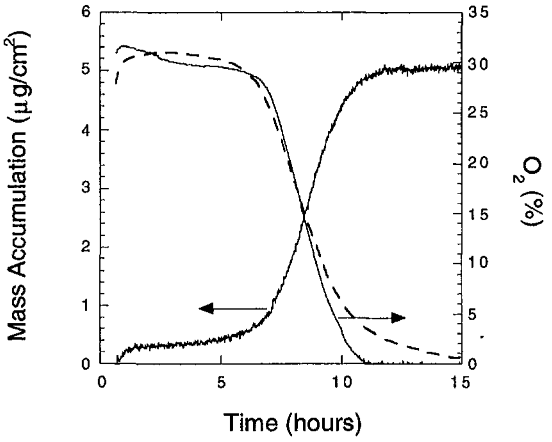

Fig. 2 Plots of mass accumulation, oxygen percent, and relative pressure (- - -) for fuel F-3145 with 3.0 mg/L MDA

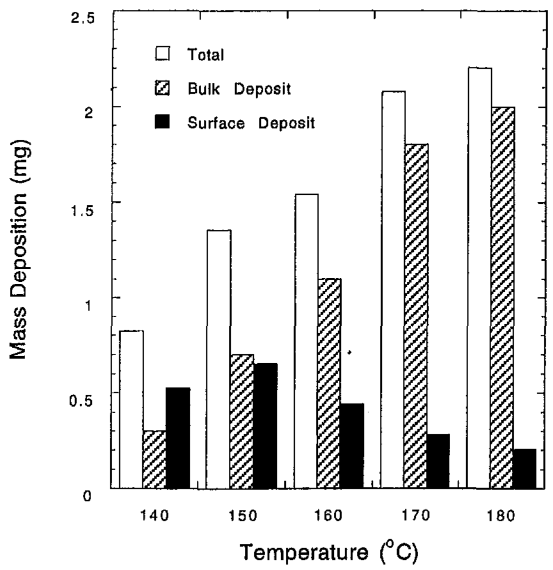

Fig. 3 Histogram of bulk, surface, and total insoluble mass versus temperature for fuel F-3119

not show significant oxygen consumption. Thus, the bulk fuel appears to be an unlimited supply of oxygen to the surface. Thus, the deposition rate at the surface reflects this nonvarying oxygen concentration in the bulk, and results in a similar temperature dependence of deposition as the bubbling static tests.

Recently, in agreement with our measurements, other workers have observed a decrease in surface deposition versus temperature over the range 155 to 225°C in a flowing heated tube (Jones and Balster, 1994). These experiments were conducted under very slow flow conditions, where complete oxygen consumption occurs within the tube. Thus, these experiments with limited oxygen and complete oxygen consumption more closely mimic the oxygen regime of our QCM experiments. The oxygen limited and complete or near-complete oxygen consumption conditions for most fuels tested in the QCM results in a final surface deposition amount that is independent of the oxidation rate. Rather, the final surface deposition is a measure of the efficiency of deposit production for a given amount of oxygen. Our previous study shows that near 150 to 160°C the efficiency of surface deposition is at a maximum, with less efficient production of surface deposits at both higher and lower temperatures.

To better understand the temperature dependence of deposit formation, we have developed a technique to measure the amount of bulk deposits, i.e., insoluble deposits that stay in the liquid fuel, but do not adhere to the reactor surfaces. These were measured gravimetrically by a technique described in the experimental section. Final surface and bulk deposit measurements were performed on fuel F-3119 with 125 mg/L of Betz 8Q406, a detergent/dispersant additive being considered for the US Air Force JP-8 + 100 program, over the temperature range 140 to 180°C. The results are shown in Fig. 3. To compare the final bulk deposit mass with the surface deposition, the areal mass density (the measured mass accumulation over the active surface area of the QCM electrode) was converted to total mass by multiplying by the calculated total surface area exposed to liquid fuel in the reactor. This surface area includes the inside of the reactor surface, the thermocouple, gas inlet tube, QCM crystal surface, and the QCM adapter. We calculate an estimated total surface area of 68 cm^2 for the reactor. The calculation of the total surface deposit uses the assumption that the areal mass density remains constant over the entire wetted surface of the reactor. This assumption is an oversimplification as we routinely observe greater deposition near the liquid/headspace interface in this reactor, but it allows a semiquantitative comparison of the bulk and surface deposits. The figure demonstrates that the surface deposition is a maximum at 150°C, decreasing at both higher and lower temperatures, in agreement with the previous observations on other fuels. Oxygen consumption was complete at all temperatures studied. The bulk deposition increases with temperature throughout the temperature range. As the bulk deposition is larger than the surface deposition at all temperatures but 140°C, the total deposition also increases with increasing temperature.

The data of Fig. 3 show that there appears to be a partitioning of deposits from the surface to the bulk with increasing temperature, although the increase in bulk deposit mass is much larger than the decrease in estimated surface deposit mass. As oxygen is completely consumed at all temperatures studied, these changes in bulk and surface deposition are due to changes in the chemistry of deposit formation with temperature. It is also possible that solubility differences with temperature can play a role in this partitioning. Jones and Balster (1994) measured bulk and surface deposition over the temperature range 155 to 225°C in a flowing rig with complete oxygen consumption. They reported a decrease in surface deposition with temperature, but noted no change in bulk deposition with temperature. It is important to note that Jones and Balster measured bulk deposits from particles collected on an in-line 0.45 μm filter downstream of the heated section. In the present work, the fuel remains at temperature for 15 hours, is allowed to cool for many hours, and is then subsequently filtered through a 1 μm filter. The technique used in the present study gives much more time for insoluble material to precipitate. These differences in methodology may account for the differences observed in the temperature dependence of the bulk deposits.

Studies of Peroxy Radical Intercepting Antioxidants. Peroxy radical intercepting antioxidants are widely used in the petroleum industry to slow the oxidation of petroleum distillates. Military jet fuels which are hydrotreated require the addition of antioxidants to prevent the formation of gums and peroxides during storage and handling. In addition, the US Air Force is considering the use of an antioxidant additive in the JP-8 + 100 thermal stability additive package. We have noted, in rapidly oxidizing fuels stressed at 140°C in the QCM system (Zabarnick and Grinstead, 1994), that the addition of an antioxidant additive can significantly delay oxidation and deposition. But, in such fast oxidizing fuels, the oxygen removal process will begin after some time.

This behavior is illustrated in Fig. 4 for a hydrocarbon solvent, Exxsol D-110. Exxsol D-110 is a dearomatized, narrow-cut aliphatic solvent with <1 percent aromatics and 3 ppm sulfur. As it is highly refined, it contains few naturally occurring antioxidants, and, therefore, oxidizes quite rapidly. The figure shows that complete oxygen consumption occurs in two hours at 140°C. As it contains few naturally occurring antioxidants, Exxsol D-110 is an ideal model fuel in which to study antioxidants. We have added the antioxidant BHT over the concentration range 4.2 to 50 mg/L, and measured the headspace oxygen concentration. Deposition is not reported as it is quite low for this solvent. The figure shows that as the concentration of added BHT is increased, the oxidation process is delayed. But, after the delay period, oxidation occurs at a very similar rate to the neat fuel. Chemical kinetic schemes can reproduce this delay in oxidation (Zabarnick, 1993); but, it is not clear why the oxidation rate increases at longer times. One possible explanation is that the antioxidant molecule is consumed during the slow oxidation time until it is reduced below some critical level, then the oxidation process can proceed. This explanation is supported by the concentration dependence of the oxygen curves of Fig. 4. The more antioxidant that is present the longer is the delay before rapid oxidation occurs. A second explanation is that oxidation products build up slowly during the slow oxida-

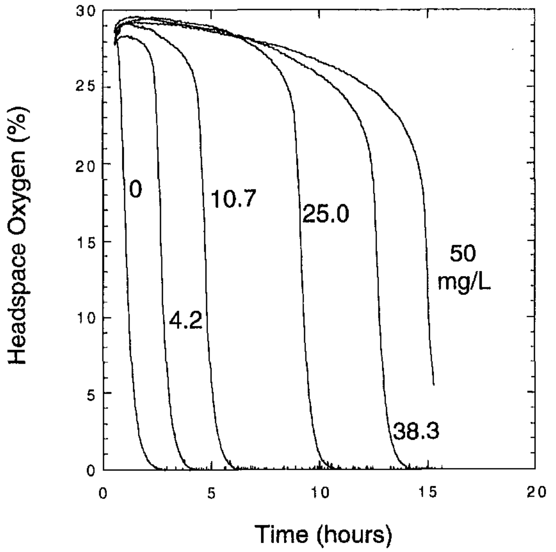

Fig. 4 Plots of headspace oxygen concentrations versus time for Exxsol D-110 at various concentrations of added BHT at 140°C

tion, and reach a critical level at which point they can help initiate faster oxidation.

To test the first theory, we have measured the concentration of BHT during a run by withdrawing 500 μL samples and performing the GC-MS analysis for BHT described in the experimental section. These experiments were performed in fuel F-3139, a fast oxidizing Jet A fuel. The results are shown in Fig. 5. The neat fuel consumes all of the headspace oxygen in three hours, and the addition of 25 mg/L of BHT delays the time of complete oxygen consumption out to seven hours. The figure shows that the BHT concentration decreases to near zero over the first 5 hours of the run. The oxidation rate increases when the BHT concentration begins to get quite low (<5 mg/L). Unfortunately, not enough data were taken during the 3 to 6 hour range to better determine the critical BHT concentration below which the oxidation rate increases. We believe that these BHT concentration measurements support the first explanation hypothesized above. Recently performed chemical kinetic modeling also supports the supposition that the consumption of the antioxidant will precipitate rapid oxidation (Zabarnick, 1998).

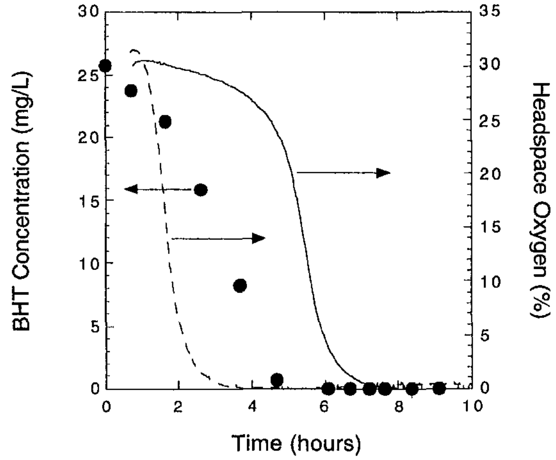

Fig. 5 Plots of BHT (●) and headspace oxygen concentrations versus time for fuel F-3139 neat (dashed line) and with 25 mg/L BHT (solid line) at 140°C

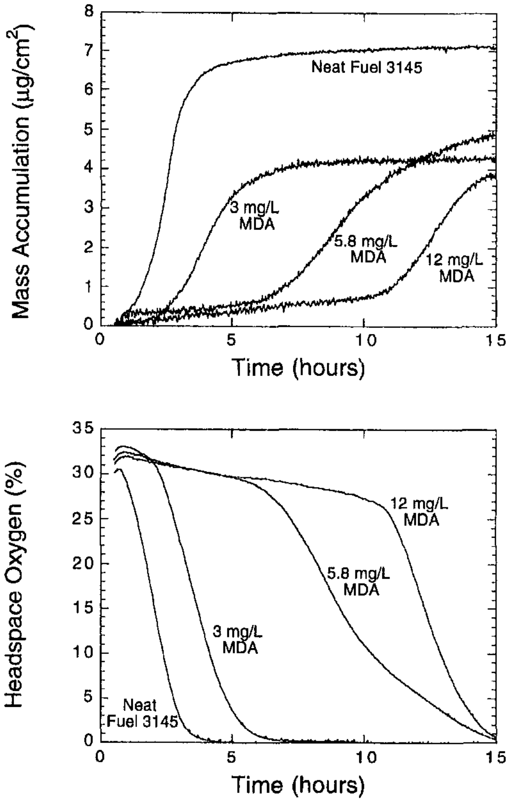

Fig. 6 Plots of mass accumulation (*a*, top) and percent oxygen (*b*, bottom) for fuel F-3145 at various concentrations of added MDA at 140°C

Presumably the antioxidant is being consumed by reaction with peroxy radicals in its role as a peroxy radical inhibitor.

Studies of Metal Deactivator Additives. Metal deactivator species have been used for many years in the petroleum industry to inhibit the catalytic effect of metals in petroleum distillates (Downing et al., 1939). These metals, and copper in particular, act to catalyze the autoxidation chemistry, thereby greatly increasing oxidation and deposition rates. This catalytic effect occurs at the part per billion level of dissolved metal. It was realized early on that the presence of these metals in petroleum distillates had the effect of greatly reducing the antioxidant capabilities of peroxy radical inhibiting antioxidant species. Thus, metal deactivator additives were developed as an inexpensive solution to suppressing the catalytic activity of the metals without removing them from the system. The metal deactivators, N,N′-disalicylidene-1,2-propanediamine and N,N′-disalicylidene-1,2-cyclohexanediamine, are optional additives in the JP-8 military specification (MIL-T-83133D). In the jet fuel community, the use of metal deactivators is controversial due to their possible over response in the JFTOT thermal stability fuel specification test (Clark, 1988).

Although originally designed to chelate metal ions in solution, it has been proposed that these metal deactivators may also act by surface passivation of exposed metal surfaces and as antioxidants by radical inhibition (Clark et al., 1990). To further explore the nature of metal deactivators as thermal stability additives we have performed a series of experiments in the QCM system. In these studies we use fuel F-3145, which has been doped with 285 ppb copper, and the metal deactivator, N,N′-disalicylidene-1,2-propanediamine, hereafter referred to simply as MDA. In Figs. 6(*a*) and 6(*b*) are shown plots of deposition and headspace oxygen at 140°C for fuel F-3145 neat and with 3.0, 5.8, and 12.0 mg/L added MDA. The neat fuel

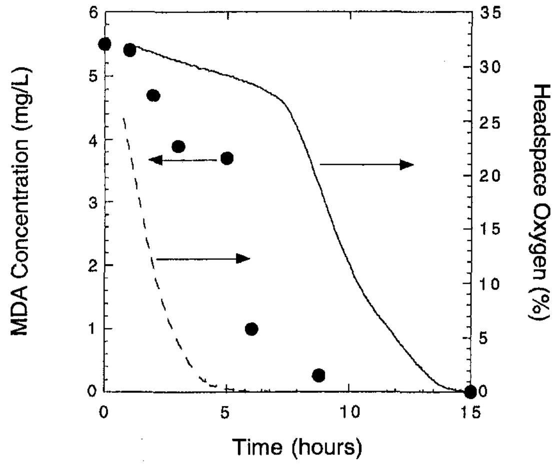

Fig. 7 Plots of MDA (●) and headspace oxygen (line) concentrations versus time for fuel F-3145 with 5.8 mg/L MDA at 140°C. Dashed line is oxygen profile for fuel F-3145 neat

produces deposition during the first four hours, after which the deposition levels. The oxygen sensor data show that oxidation occurs during this initial four hour period, and oxygen is completely consumed at five hours. The addition of MDA delays both the oxidation and deposition processes. Increasing amounts of MDA allow longer delays in oxidation and deposition. With 3 mg/L added MDA, these processes are delayed for one hour, with 5.8 mg/L the delay is five hours, and with 12 mg/L the delay is 10 hours. The final deposit amounts for all of the MDA concentrations are near 4 $\mu g/cm^2$, reduced from the 7 $\mu g/cm^2$ produced by the neat fuel.

As fuel F-3145 contains 285 ppb copper, a delay in the oxidation and deposition process is fully expected. Clark (1988) reported a chelation ratio for MDA:Cu of 1.1:1 mol/mol or 5:1 w/w. Thus, all of the copper can be complexed by the addition of approximately 1.1 mg/L MDA. Therefore, even the smallest amount of added MDA shown in Fig. 6, 3 mg/L, is enough to completely complex all of the copper in the fuel. If MDA acted only as a simple complexing agent of copper and was not depleted during the test, we would expect the oxidation and deposition results to be identical for these three concentrations of MDA, because addition of excess MDA (>1.1 mg/L) should have no effect on oxidation or deposition. Instead, we see that the oxidation delay is a function of the concentration of MDA.

The two previously reported secondary behaviors of MDA, surface passivation, and free radical inhibition may be able to yield the observed behavior. In addition, if MDA is consumed by chemical reaction, the observed behavior would be expected. To date, we are not aware of any previous reports of MDA consumption during thermal stressing of a fuel. To test this third mechanism we have measured the concentration of MDA present during an experimental run, and the results are shown in Fig. 7. A separate experimental run was used for each MDA concentration point shown in the figure, as the analysis required 10 mL of fuel. The figure shows that the MDA concentration drops during the entire run, resulting in an MDA concentration below the detection limit at 15 hours. The figure also shows that oxygen consumption is moderately slow until seven hours, after which the oxidation rate increases substantially. The time of rapid increase in the oxidation rate occurs when the MDA concentration drops below approximately 1 mg/L. This is close to the predicted concentration requirement (1.1 mg/L) for chelation of all of the copper as determined by the binding ratio. It would appear that when the MDA concentration falls below this level, unchelated copper becomes available to catalyze the initiation reactions, and, thereby, accelerates the oxidation process. These results clearly show that the consumption of MDA controls the time delays observed from MDA addition to fuel.

However, the mechanism by which MDA is depleted is uncertain. We are not aware of any MDA consumption reactions reported in the literature. Presumably, MDA could be removed by chemical reaction, complexation with reaction products, or adsorption to the reactor walls. MDA contains phenolic hydrogen atoms that may be amenable to attack by peroxy radicals. Complexation of acidic reaction products is also a possible pathway for MDA consumption.

Conclusions

This study has utilized the QCM/Parr bomb system with a headspace oxygen sensor to simultaneously measure oxidation and deposition during thermal oxidative stressing of jet fuel. We have demonstrated the advantages of the oxygen sensor over the pressure monitoring technique for following the oxidation process. In particular, the simultaneous in-situ measurements of headspace oxygen concentration and QCM deposition show the strong correlation between oxidation and deposition in jet fuels. In a given fuel, the slowing or delaying of oxidation will slow or delay deposition. We have shown that, over the temperature range 140 to 180°C, surface deposition peaks at an intermediate temperature, but bulk deposition increases with temperature. We conclude that the temperature dependence of deposition is a function of the oxygen availability of the system and the extent of oxygen conversion. We find that rapid increases in oxidation will occur upon consumption of an added antioxidant to a fast oxidizing fuel. The antioxidant appears to be consumed by reaction, presumably with alkylperoxy radicals. We find that MDA is consumed during thermal oxidative stressing, and this consumption results in large increases in the oxidation rate in metal containing fuel. Mechanisms for MDA consumption have been hypothesized. The consumption of antioxidants and MDA have important implications in the design of jet fuel thermal stability improving additive packages, particularly in the additive concentration optimization process.

Acknowledgments

This work was supported by the US Air Force, Propulsion Directorate, Air Force Research Laboratory, WPAFB under Contract Nos. F33615-92-C-2207 and F33615-97-C-2719 with Mr. Charles Frayne as technical monitor. We would like to thank Mr. Rich Streibich and Ms. Becky Grinstead for developing the BHT and MDA analysis techniques.

References

Clark, R. H., 1988, "The Role of a Metal Deactivator in Improving the Thermal Stability of Aviation Kerosenes," presented at the 3rd International Conference on the Stability and Handling of Liquid Fuels, London, UK.

Clark, R. H., Delargy, K. M., and Heins, R. J., 1990, "The Role of Metal Deactivator Additive in Improving the Thermal Stability of Aviation Kerosines: Additive Adsorption Studies," *Prepr.-Am. Chem. Soc., Div. Fuel Chem.*, Vol. 35, pp. 1223–1230.

Downing, F. B., Clark, R. G., and Pedersen, C. J., 1939, "Suppression of Metal Catalysts in Gasoline Gum Formation," *Oil & Gas J.*, Vol. 38, pp. 97–101.

Edwards, T., 1996, "Recent Research Results in Advanced Fuels," *Prepr.-Am. Chem. Soc., Div Pet. Chem.*, Vol. 41, pp. 481–487.

Hazlett, R. N., 1991, *Thermal Oxidation Stability of Aviation Turbine Fuels*, ASTM, Philadelphia, PA.

Heneghan, S. P., and Zabarnick, S., 1994, "Oxidation of Jet Fuels and the Formation of Deposits," *Fuel*, Vol. 73, pp. 35–43.

Heneghan, S. P., Zabarnick, S., Ballal, D. R., and Harrison, W. E., 1996, "JP-8+100: The Development of High Thermal Stability Jet Fuel," presented at the 34th Aerospace Sciences Meeting and Exhibit, Reno, NV.

Jones, E. G., and Balster, W. J., 1994, "Formation of Insolubles in a Jet-A Fuel: Temperature Effects," *Prepr.-Am. Chem. Soc., Div Pet. Chem.*, Vol. 39, pp. 78–81.

Martin, S. J., Granstaff, V. E., and Frye, G. C., 1991, ''Characterization of a Quartz Crystal Microbalance with Simultaneous Mass and Liquid Loading,'' *Anal. Chem.*, Vol. 63, pp. 2272–2281.

Streibich, R., 1996, unpublished results, University of Dayton Research Institute, Dayton, OH.

Zabarnick, S., 1993, ''Chemical Kinetic Modeling of Jet Fuel Autoxidation and Antioxidant Chemistry,'' *Ind. Eng. Chem. Res.*, Vol. 32, pp. 1012–1017.

Zabarnick, S., 1994, ''Studies of Jet Fuel Thermal Stability and Oxidation Using a Quartz Crystal Microbalance and Pressure Measurements,'' *Ind. Eng. Chem. Res.*, Vol. 33, pp. 1348–1354.

Zabarnick, S., 1998, ''Chemical Kinetic Modeling of Antioxidant Chemistry for Jet Fuel Applications,'' *Energy & Fuel*, in press.

Zabarnick, S., and Grinstead, R. R., 1994, ''Studies of Jet Fuel Additives Using the Quartz Crystal Microbalance and Pressure Monitoring at 140 C,'' *Ind. Eng. Chem. Res.*, Vol. 33, pp. 2771–2777.

Zabarnick, S., Zelesnik, P., and Grinstead, R. R., 1996, ''Jet Fuel Deposition and Oxidation: Dilution, Materials, Oxygen, and Temperature Effects,'' ASME JOURNAL OF ENGINEERING FOR GAS TURBINES AND POWER, Vol. 118, pp. 271–277.

An Efficient Computational Model for Premixed Turbulent Combustion at High Reynolds Numbers Based on a Turbulent Flame Speed Closure

V. Zimont
CRS 4, via Nazario Sauro 10,
09123 Cagliari, Italy

W. Polifke

M. Bettelini

W. Weisenstein

ABB Corporate Research,
Baden-Dättwil, Switzerland

Theoretical background, details of implementation, and validation results for a computational model for turbulent premixed gaseous combustion at high turbulent Reynolds numbers are presented. The model describes the combustion process in terms of a single transport equation for a progress variable; turbulent closure of the progress variable's source term is based on a model for the turbulent flame speed. The latter is identified as a parameter of prime significance in premixed turbulent combustion and determined from theoretical considerations and scaling arguments, taking into account physico-chemical properties and local turbulent parameters of the combustible mixture. Specifically, phenomena like thickening, wrinkling, and straining of the flame front by the turbulent velocity field are considered, yielding a closed form expression for the turbulent flame speed that involves, e.g., speed, thickness, and critical gradient of a laminar flame, local turbulent length scale, and fluctuation intensity. This closure approach is very efficient and elegant, as it requires only one transport equation more than the nonreacting flow case, and there is no need for costly evaluation of chemical source terms or integration over probability density functions. The model was implemented in a finite-volume-based computational fluid dynamics code and validated against detailed experimental data taken from a large-scale atmospheric gas turbine burner test stand. The predictions of the model compare well with the available experimental results. It has been observed that the model is significantly more robust and computationally efficient than other combustion models. This attribute makes the model particularly interesting for applications to large three-dimensional problems in complicated geometries.

Introduction

The quantitatively correct numerical simulation of turbulent reacting gas flows is currently one of the most challenging problems in many branches of industry; in particular, in connection with low-emission combustion. A key difficulty is the elaboration of a physico-chemical model for the average heat release intensity and the mean rate of products creation, particularly if certain simplifying assumptions (e.g., the "fast chemistry" limit) are not applicable.

In this report, theoretical background, implementation, and validation of a turbulent combustion model suitable for lean-premixed gas turbine applications with high Reynolds numbers and moderately fast chemistry are described. The model is formulated in terms of a single transport equation for a progress variable, which can (in its basic form) be used for numerical modeling of the average rates of heat release and products creation. The closure for the progress variable's source term is based on a model for the turbulent flame speed, which is considered to be the main hydrodynamic and physico-chemical parameter of premixed turbulent combustion. The following physico-chemical phenomena are considered in the determination of this velocity:

- influence of fuel concentration, fuel composition, and pressure on the combustion process
- thickening and distortion of the flame front by small-scale and large-scale turbulence at high turbulent Reynolds number Re and moderate Damköhler number Da
- quenching by turbulent straining ("stretch effect")
- changes of local composition in regions of high turbulent strain due to the different molecular diffusivities of heavy and light species ("preferential diffusion effect")

Theoretical considerations, scaling arguments, numerical simulations of laminar flames and experimental data are combined to eventually yield analytical, "closed-form" expressions for the diffusion and source terms in the transport equation for the progress variable. We emphasize that the popular "fast chemistry" assumption, which is arguably not adequate for lean-premixed combustion at gas turbine conditions, is not invoked.

In previous publications [1–4] the model was validated against standard experimental data on turbulent flame speeds and against propagation speeds of spherical combustion waves in stirred bombs for different fuels, stoichiometric ratios, and turbulent velocities. In this work, the model was implemented in a three-dimensional computational fluid dynamics code and validated against detailed experiments from a large scale atmospheric gas turbine burner test stand.

The paper is organized as follows: the transport equation for the progress variable and its closure are described in the next section; then, a model for the turbulent flame speed to complete the closure and the "stretch effect" extension of the model, which is needed at high turbulent intensities, are introduced and discussed

---

Contributed by the International Gas Turbine Institute and presented at the International Gas Turbine and Aeroengine Congress and Exhibition, Orlando, FL, June 2–5, 1997. Manuscript received by the ASME Headquarters March 20, 1997. Paper No. 97-GT-395. Associate Technical Editor: H. A. Kidd.

in some detail; the final sections describe the experimental setup, the numerical implementation, and the results of three-dimensional validation computations.

Turbulent Flame Speed Closure

In engineering calculations of premixed turbulent combustion, the chemical processes resulting in products creation and heat release can, in many cases, be described adequately with a single progress variable c. It is defined here as a normalized mass fraction of products ($c = 0$ in the unburnt mixture and $c = 1$ in the products). The (unclosed) transport equation for c has the following form [5]:

$$\frac{\partial}{\partial t}(\bar{\rho}\tilde{c}) + \frac{\partial}{\partial x_k}(\bar{\rho}\tilde{u}_k\tilde{c}) = \frac{\partial}{\partial x_k}\left(\bar{\rho}\,\frac{\nu_t}{\mathrm{Sc}_c}\frac{\partial\tilde{c}}{\partial x_k}\right) + \overline{\dot{w}_c}. \tag{1}$$

Both Reynolds averages $(\overline{\ldots})$ and Favre averages $(\widetilde{\ldots})$ are used with

$$\bar{\rho}\cdot\tilde{c} = \overline{\rho c}, \tag{2}$$

$$c'' = (c - \tilde{c}). \tag{3}$$

The transport Eq. (1) for c is closed by substituting

$$\overline{\dot{w}_c} = \rho_u U_t |\nabla\tilde{c}| \tag{4}$$

for the source term, where $U_t(>0!)$ is a velocity scale dependent upon the physico-chemical characteristics of the combustible mixture and the local turbulence parameters. This turbulent flame speed closure (TFC) for the source term was proposed by Zimont [6]. It is related to the so-called G-equation,[1] first proposed by Markstein [7] for laminar flames and further developed by Peters and others (see [8]) in the context of turbulence premixed combustion.

Some aspects of the closure ansatz (4) shall be illustrated briefly by considering the one-dimensional case. Assuming, for the moment, stagnating medium ($u_k = 0$), fixed turbulence parameters, and density (in this case U_t = const. and ν_t = const.), the transport equation for c can be written as

$$\frac{\partial\tilde{c}}{\partial t} = \frac{\nu_t}{\mathrm{Sc}_c}\frac{\partial^2\tilde{c}}{\partial x^2} + U_t\frac{\partial\tilde{c}}{\partial x}. \tag{5}$$

Clearly, Eq. (5) describes a "combustion" wave moving with velocity U_t from right to left. Furthermore, the width of the wave is growing due to turbulent diffusion.[2]

Note that (4) contains the unburnt mixture density ρ_u because only then do Eqs. (1) and (4) result in the correct reactant flow rate, which is equal to $\rho_u U_t$ for constant U_t (this can be rigorously proved). Then, integration of (5) between $x = -\infty$ to $x = +\infty$ (in a coordinate system moving with velocity U_t) leads to the mass conservation equation

$$\rho_b(\tilde{u}_b + U_t) = \rho_u U_t. \tag{6}$$

Temperature can be computed directly from the reaction progress variable c as

$$T(c) = (1 - c)T_u + cT_b, \tag{7}$$

where the indexes u and b denote the unburnt and burnt values. Density ρ is then easily found using the gas law, assuming constant pressure and constant mean molecular weight.

A Model for U_t

Obviously, a model for the turbulent flame speed U_t is needed in order to make the closure (4) complete. In a first step, the model developed by Zimont [6] (see also Borghi [9]) for wrinkled and thickened flamelets[3] is used to express U_t in terms of turbulence parameters and physico-chemical characteristics of the combustible mixture.

We will now present a short overview of this model. The core idea is that small-scale turbulent structures intensify the transfer processes inside the flamelets and determine their thickness δ_{nt} and propagation velocity U_{nt}, while large-scale turbulent vortices wrinkle the "thickened" flamelets and control the width of the averaged turbulent combustion zone. The total flamelet area depends on the entire spectrum of turbulence and is determined by its integral characteristics and by the parameters of the thickened flamelets. This mechanism of turbulent combustion is only possible if there is a physical mechanism able to limit the expansion of the thickened flamelets. It has been shown [6, 9, 12] that larger and larger vortices are engulfed by the thickened flamelets until an equilibrium is established between convection, heat conduction, and chemical reaction processes. The following relations,

$$U_{nt} \sim u'\mathrm{Da}^{-1/2} > U_l \tag{8}$$

and

$$\delta_{nt} \sim l_t\mathrm{Da}^{-3/4} > \delta_l,$$

have been derived using dimensional analysis[4] and Kolmogorv scaling for small-scale turbulence.

The average turbulent flame velocity U_t is larger than the velocity of the "thickened" front U_{nt} by a factor that depends on the ratio between the area δS of a flame surface element and the projection δS_0 of this element normal to the direction of average flame front propagation:

$$U_t \sim U_{nt}\overline{\left(\frac{\delta S}{\delta S_0}\right)} \sim U_{nt}\frac{\Sigma}{\Lambda}, \tag{9}$$

where $\Sigma^2 = \overline{(z - \bar{z})^2}$ is the variance in flame position due to turbulent convection ($z = z(x, y)$ is the local position of the

---

[1] Not to be confused with the the "stretch factor" G, see below.

[2] This is apparent if the one-dimensional transport Equation (5) for $\tilde{c}$ is expressed in a coordinate system $x' = x + U_t t$ moving with the front; Eq. (5) then reduces to the standard diffusion equation.

[3] It is generally agreed that wrinkled and thickened flame structures are characteristic for lean-premixed gas turbine combustion, due to the high turbulent intensities and relatively long chemical times prevalent at these conditions, see, e.g., Polifke et al. [10] and Sattelmayer et al. [11].

[4] Recall that Da $\sim \tau_t/\tau_c$; $\tau_t \sim l_t/u'$; $\tau_c \sim \chi_u/U_l^2$.

Nomenclature

ρ = density
T = temperature
c = progress variable
a = rate of strain
g_{cr} = critical gradient
G = stretch Factor
U_l, δ_l = laminar flame speed and thickness
U_{nt}, δ_{nt} = thickened flame speed and thickness
k = turbulent kinetic energy
ϵ = turbulent dissipation rate
u' = turbulent velocity
l_t = turbulent integral length scale
τ_t = turbulent turnover time
τ_c = chemical heat release time
Re = turbulent Reynolds number
Da = Damköhler number
Sc = Schmidt number
ν, ν_t = dynamic, turbulent viscosity
χ_l = molecular heat transfer coefficient
λ = excess air ratio

flamelet element), and Λ denotes the microscale of the random flame front surface.

For the purpose of estimating Σ, and provided that $U_{nt} \ll u'$, the combustion front can be considered to consist approximately of the same fluid particles. Consequently, Σ^2 is subject to the customary turbulent diffusion relationship

$$\Sigma^2 \sim D_t t \sim u' l_t t, \tag{10}$$

where D_t is a constant turbulent diffusion coefficient (see Zimont [9] for more details)

$$\tau_t \le t \ll \frac{l_t}{U_{nt}} \sim \tau_t \mathrm{Da}^{1/2}. \tag{11}$$

In a statistically stationary situation,

$$\Lambda \sim (u' \delta_{nt} t)^{1/2} \tag{12}$$

follows from the requirement that U_t be constant and dimensional considerations. Combining (8), (10), and (12), we obtain

$$\overline{\left(\frac{\delta S}{\delta S_0}\right)} \sim \left(\frac{l_t}{\delta_{nt}}\right)^{1/2} \sim \mathrm{Da}^{3/4}, \tag{13}$$

which finally yields, combined with (8) and (9), the following expression for the turbulent combustion velocity:

$$U_t = \mathrm{A} u'^{3/4} U_l^{1/2} \chi_u^{-1/4} l_t^{1/4}. \tag{14}$$

The molecular heat transfer coefficient of the unburnt mixture χ_u can be found in standard references, or determined with suitable computer programs. Similarly, laminar flame speeds U_l for many fuels and operating conditions of interest can be found in the literature or can be determined in experiments or with computations of one-dimensional laminar flames with a detailed chemical mechanism. Note that changes in pressure, fuel concentration, etc. will affect parameters χ_u and U_l and thereby influence the value of U_t in a well-defined and physically meaningful way.

Assuming that a standard $k - \epsilon$ turbulence model is used, turbulent intensity u' and length scale l_t are determined from turbulent kinetic energy k and dissipation ϵ. The prefactor A has been determined by evaluation of a large experimental database of stirred bomb experiments in [2, 3]. The value $A = 0.52$ experimentally reproduces found turbulent flame speeds for a wide range of fuels and operating conditions with good accuracy. Herewith, complete closure for the progress variable's source term has been achieved. Note that all parameters appearing on the l.h.s of (14) are either (*a*) overall numerical constants, (*b*) constants describing physico-chemical properties of the combustible mixture, or (*c*) readily derived from a standard two-equation turbulence model.

It is worth emphasizing that (14) has been rigorously derived from the underlying physical model and dimensional analysis, and does not contain empirical information with the exception of the constant A (which should be of order unity). This "rigid" theoretical construction allows to reduce to a minimum the number of empirical parameters (used for "tuning" the combustion model), and assures fixed dependence on controlling factors.

The relations (8) and (14) are valid if

$$\mathrm{Re}^{3/4}\mathrm{Da}^{-3/2} \ge 1 > \mathrm{Da}^{-1/2}. \tag{15}$$

It can be shown from this relation that the combustion model applies when vortices of minimal scale (Kolmogorov length) are smaller than the width of the laminar flame. For insufficiently large Re, the flamelets will be laminar, for large τ_c (small Da) U_{nt} will be of the order of u', and wrinkling of flamelets will not occur.

The various powers in (14), which express the dependence of U_t on the physico-chemical and turbulent properties of the combustible mixture, are in good agreement with experimental results; the interested reader is referred to [1–4].

Equation (14) does not take into account two physical effects that are significant under certain circumstances: preferential diffusion and turbulent "strain". The latter effect provides an explanation for the experimentally observed reduction in turbulent combustion intensity at very high turbulent velocities, and is connected with the straining of flamelets by small-scale turbulent eddies. This "stretch effect" is of importance for low-emission gas turbines, and, indeed, should be incorporated in any combustion model designed for high turbulent Reynolds numbers—in particular if combustion near lean blow-off is considered (see the next section).

Preferential diffusion, on the other hand, causes local composition changes in the distorted and strained flamelets due to different molecular diffusion coefficients of fuel and oxidizer. Consequently, maximum turbulent combustion rates are achieved with slightly lean mixtures for light fuels (like hydrogen and methane) and slightly rich mixtures for heavy fuels (like propane and vaporized oil), respectively. This effect has also been introduced in the model. However, as it is of only minor importance if methane or natural gas is used as fuel, no details are given in this report and the interested reader is referred to [2, 3].

In concluding this section, we want to point out that the model for turbulent flame speed just presented is particularly suitable for the case of lean-premixed combustion in gas turbines. Specifically, the extremely high turbulent Reynolds *Re* numbers prevalent in gas turbines, and the relatively large chemical time scales typical of fuel lean combustion ensure that relations (15), which govern the applicability of the model (14) for turbulent flames speeds, are satisfied. We emphasize again that changes in operating pressure, inlet temperature, fuel concentration, and fuel composition[5] affect the predicted value of turbulent flame speed U_t in a well-defined and physically meaningful way.

The Stretch Effect

As mentioned above, for industrial low-emission combustors operated near lean blow-off the effect of strain or "stretch" must have a considerable impact on the mean turbulent heat release intensity. To expand the range in which the proposed closure may be used, we have combined it with the model of flamelets quenching through stretching suggested by Bray [13]. Differently strained flamelets are reduced to either unstrained ones (no quenching) if the absolute value g of the velocity gradient is less than some critical value g_{cr}, or to highly strained flamelets (with negligible contribution to the reaction progress) for $g > g_{cr}$.

To take the stretch effect into acount, the source term (4) of the progress variable equation is multiplied by a stretch factor G (the probability of unquenched flamelets) that is obtained by integrating the log-normal distribution[6] of the turbulent dissipation rate ϵ:

$$G = \frac{1}{2}\,\mathrm{erfc}\left\{-\sqrt{\frac{1}{2\sigma}}\left(\ln\frac{\epsilon_{cr}}{\tilde{\epsilon}} + \frac{\sigma}{2}\right)\right\}, \tag{16}$$

where erfc denotes the complementary error function, and $\sigma = \mu_{str} \ln (L/\eta)$ is the standard deviation of the distribution of ϵ, with μ_{str} a constant measured to be 0.26 and $\epsilon_{cr} = 15\nu g_{cr}^2$.

For steady laminar flows, the critical velocity gradient g_{cr} for flame quenching may be obtained numerically, see, for example,

---

[5] This is particularly important for combustion of, e.g., MBTU fuels containing large amounts of H_2 and CO.

[6] Valid at high turbulent Reynolds numbers.

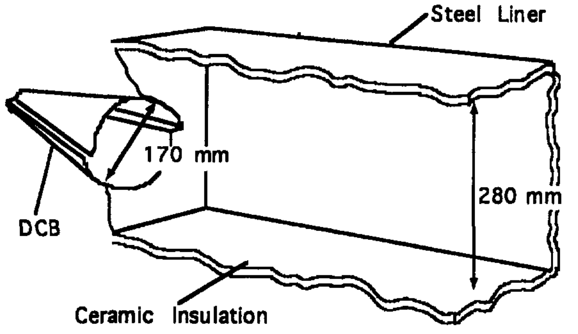

Fig. 1 Sketch of the test rig with double cone burner (not to scale)

[14]. However, difficulties emerge in using these results for the present purpose. Different stationary model problems (single-flame or twin-flame configuration) give large variations in the predicted variations of g_{cr}. Additionally, in turbulent flows, g_{cr} must be larger than in the stationary cases, as the smallest turbulent eddies (resulting in the largest strain rates) do not persist long enough to quench a flame front locally. For these reasons, the values of g_{cr}, to be used in industrial simulations, have to be tuned and theory or numerical modeling can only suggest a range of physically plausible values. Indeed, g_{cr} is the only significant parameter for "tuning" the TFC model to the DCB experimental data.

Model Validation

Previous model validation has been focused on (*a*) a comparison of the expression (14) for the turbulent flame velocity with experimental data on premixed turbulent combustion [2, 3, 4], and (*b*) a comparison of the calculated consumption rate in spherical premixed turbulent flames using (1) and (4) with direct experimental measurements in stirred bombs [2] using different fuels (CH_4, C_2H_6, C_3H_8, H_2) and different air excess ratios (typically in the range 0.6–1.6).

In general, good agreement between the TFC model and experimental data has been observed. As already mentioned above, it was found that $A = 0.52$ is the optimum value for the hydrocarbon fuels investigated and $A = 0.61$ for hydrogen (though the results obtained using $A = 0.52$ were quite satisfactory also for hydrogen).

In the present work, the TFC model has been validated against detailed experimental data from an ABB double cone burner (DCB) with 0.17 m nominal diameter mounted in an atmospheric test rig. A DCB comprises two halves of a cone that are shifted with respect to each other in the radial direction such that two inlet slits of constant width are formed. A strong tangential component is imparted to the gas entering the burner through these slits. The degree of swirl is chosen such that, at the burner outlet, the flow undergoes a vortex breakdown resulting in a zone of recirculation that acts as an aerodynamic flame holder. This type of flame stabilization in free space is the characteristic property of the DCB. Fuel gas is injected through a number of small holes along the burner's inlet slit, providing a high degree of fuel-air premixing and making flame flash back into regions upstream of the burner impossible. More details have been given by Sattelmayer et al. [15].

The burner used in the experiments fires into a ceramically insulated combustion chamber of square cross section with 0.28 m side length, see Fig. (1). For the experiments reported here, the burner is operated with a mass flow rate of about 0.3 kg/s. Using natural gas as fuel at an excess ratio $\lambda = 2$ and preheating the combustion air with an electrical heater such that the inlet temperature of the combustible mixture $T_i = 650$ K, an adiabatic temperature $T_{ad} \approx 1755$ K is reached. The stability of the operation point during the experiments is maintained by controlling the global excess ratio calculated from an exhaust gas sample taken at the far end of the combustion chamber. The variations in λ do not exceed ± 0.01.

With an estimated turbulent length scale $l_t \approx 0.005$ m and turbulent intensities of order $u' \approx 10$ m/s (as observed in experiment), the DCB's turbulent Reynolds number is of order 1000, which is certainly higher than typically reached in laboratory-scale experiments. At the lean conditions considered here, chemical time scales are quite large, and one may estimate the Damköhler number Da ≈ 3. This suggests quite significant flamelet thickening through turbulent transport; the relation (15), which determines the applicability of the TFC model, is just barely fulfilled.[7] Indeed, (8) yields $\delta_{nt} \approx 0.5 l_t$.

Diagnostic access is provided such that measurements of temperature, chemical species, and velocities can be performed in the streamwise horizontal and vertical planes as well as in the axis-normal plane at various downstream positions with up to several hundred positions-per-measurement plane. An uncoated *Pt* − *PtRh* thermocouple, mounted on an uncooled ceramic probe, is used to measure temperature. No corrections for radiation loss are made as too many of the relevant parameters needed for an exact radiation correction are not known. The maximum errors in temperature measurement are estimated to less than 70 K. Mean and fluctuating values of the axial component of velocity were determined with laser-Doppler anemometry (LDA). Note that the measurement results shown in the following figures represent temporal mean values, averaged over 10 s per data point.

Numerical Implementation

The geometry of the DCB, the combustion chamber, and the upstream plenum were represented by a boundary-fitted, structured, single-block computational grid with approximately 230,000 computational cells. This resolution is not enough to resolve fuel injection along the slits with sufficient accuracy; therefore, in the computations, homogeneous fuel-air mixture enters the inlet section of the computational domain, i.e., the upstream side of the plenum.

Implementation of the basic TFC model (see Eqs. (1) and (4)) in a finite volume based fluid dynamics code, which relies on the well-known $k - \epsilon$ model [16] for the computation of turbulent flows, has proven to be straightforward, as the transport equation for c is in standard form. The heat release submodel couples with the flow field only via the density ρ, which can be computed from the progress variable c as follows:

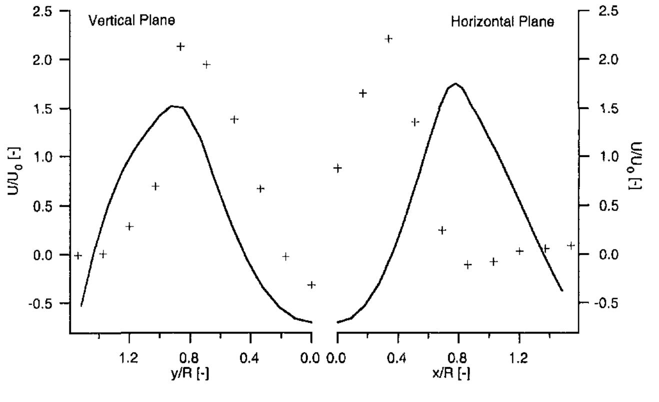

Fig. 2 Computed (——) versus measured (+) profiles of axial velocities at downstream position *z/D* = 0.25 in the vertical (left half) and the horizontal planes (right half), respectively, of the combustor.

---

[7] Of course, the appication of flamelet models which assume Da → ∞ seems entirely inappropriate under the present circumstances.

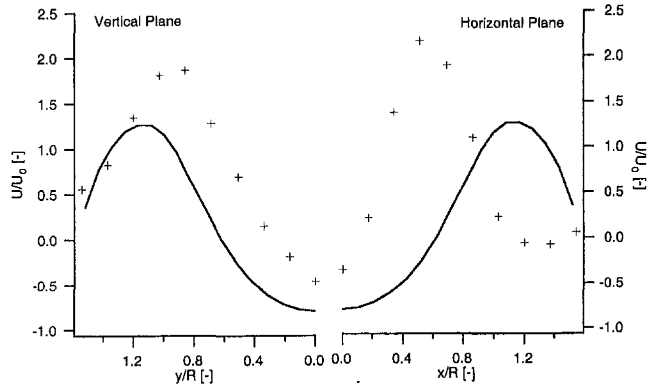

Fig. 3 Computed (——) versus measured (+) profiles of axial velocities at downstream position $z/D = 0.4$

$$\frac{1}{\rho(c)} = \frac{1-c}{\rho_u} + \frac{c}{\rho_b}, \tag{17}$$

assuming constant pressure and mean molecular weight, and invoking the standard definition of the progress variable. Again the indexes u and b refer to the unburnt and burnt state, respectively.

The turbulent intensity u' and length l_t were computed from turbulent kinetic k and dissipation ϵ using the standard constants of the $k-\epsilon$ model, as given in [16].

Some difficulties occured with the computation of the source term $\overline{\dot{w}}_c$, which requires knowledge of the gradient of the progress variable (see Eq. (4)). Using a standard second order central difference scheme to compute the gradient of c from its cell center values, it was found that in regions where the computational grid is highly skewed and nonuniform, the gradient shows slight fluctuations that do not correspond to the c-field. It was investigated whether the use of higher order schemes or a scheme that relies on a version of Gauss' law would bring improvement in this respect. However, this was not the case, and the conclusion was that the TFC model should only be used on computational grids of good quality. Fortunately, these irregularities of the source term did not adversely affect the convergence behavior of the model, presumably due to the "smearing" effect of the diffusive term in the transport equation of the progress variable c. In general, we have found that the TFC model is numerically benign[8] and efficient.

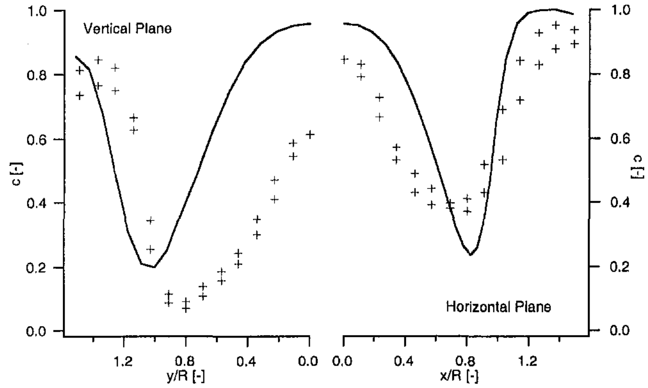

Fig. 4 Computed (——) versus measured (+) profiles of the progress variable c at downstream position $z/D = 0.25$. Note that experimental data points from the left and right halves of the horizontal and the top and bottom halves of the vertical plane, respectively, have been overlayed in these graphs.

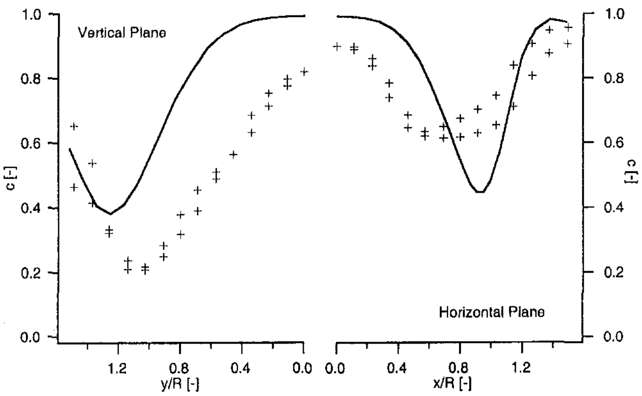

Fig. 5 Computed (——) versus measured (+) profiles of the progress variable c at downstream position $z/D = 0.4$

Comparing the computational requirements of the TFC model against those of an extended Magnussen Model with two-step chemistry as used in [10] and a flamelet model ([17]) involving integrations of probability density functions for reaction progress and turbulent strain, we observe that the extended Magnussen model requires about two times and the flamelet model and about four times as much CPU time per iteration as the TFC model. Also, we have experienced that the TFC model achieves convergence even if started from a very poor "initial guess," while the extended Magnussen model requires careful preparation of the initial flow, temperature, and species concentration distributions if divergence of the iterative solution process is to be avoided.

Results

An analysis of temperature and velocity distributions obtained with the TFC model shows that the qualitative features of the computed turbulent reacting flow field agree with design expectations [15], previous two-dimensional results [10] and the measurements. Most prominent is a central recirculation zone containing hot combustion products downstream of the burner exit, which acts as a hydrodynamic flame holder. Surrounding the central recirculation zone is an annular stream of fresh mixture displaying rather large axial velocities of more than twice the nominal burner exit velocity. In the corner formed by the front panel and combustor liner, there is an outer recirculation zone of smaller strength. The shear layers that separate the recirculation zones and the annular stream of fresh mixture provide intense turbulent mixing, and heat release is highest in these regions.

A more careful comparison of experimental and computational results displays significant discrepancies between computation and experiment with respect to the size and location of the central recirculation zone, which is much too wide and long in the computation. Also, the strength of the recirculation is significantly overpredicted. Profiles of axial velocity illustrating this observation are shown in Figs. 2 and 3.

In the experiment, and to a lesser extent also in the computation, an asymmetry between the horizontal and the vertical planes of measurement was found due to the imperfect axial symmetry of the burner (the burner's inlet slit are in the horizontal plane). Therefore, data from both planes of measurement are displayed in Figs. 2–5. Note that in Fig. 2 and 5, the experimentally determined profiles of velocity in the two planes of measurement do not match at the intersection of the two planes, i.e., the centerline of the combustion chamber. This mismatch, which may help to roughly assess the accuracy of the experimental results, is (in our opinion) due to inaccuracies in probe positioning and alignment relative to the burner and in the control of the operating point.

---

[8] This is reportedly not so for the G-equation, where the absence of the diffusive term in the transport equation leads to numerical difficulties.

The deficiencies found are not necessarily a shortcoming of the TFC ansatz (strongly swirling flows are notoriously difficult to predict with $k - \epsilon$, and even Reynolds stress models). Indeed, a comparison of various turbulent combustion models carried out by Bettelini et al. [17] showed that the size and strength of the central recirculation zone was inadequately predicted with all combustion models considered. Clearly, the modeling of the turbulent exchange of momentum needs to be improved. Furthermore, although the grid employed in these simulations is certainly quite large, there is some evidence that the solutions obtained are not grid-independent, e.g., switching to higher-order discretization schemes does have a noticeable influence on velocity and temperature fields.[9] It is unfortunate that the interior of the burner is not accessible to measurements, as the details of the flow field inside the double cone would certainly provide valuable further insight into the intricacies of the flow field.

Profiles of the progress variable c, which is essentially a normalized temperature, experiment and computation with the TFC model are compared in Figs. 4 and 5. Near the centerline computed temperature profiles are significantly higher than measured ones, clearly a consequence of the overpredicted convective transport of combustion products within the recirculation zone.

It is apparent that in the experiment, temperature distributions in the horizontal and vertical plane differ significantly from each other.[10] Clearly, the present computation on the three-dimensional grid reproduces this asymmetry between vertical and horizontal planes only to some extent, resulting in elevated minimum values of the progress variable c in the vertical plane, and delayed reaction in the horizontal plane. The overpredicted width and strength of the central recirculation zone, which is axisymmetric, is certainly, to some extent responsible for the observed discrepancies in temperature distribution.

A value of $g_{cr} = 8000\ \mathrm{s}^{-1}$ has been used for the computation presented here. Note that with a somewhat lower value (e.g., $g_{cr} = 6000\ \mathrm{s}^{-1}$) the temperature increase at the axis occurs a bit further downstream (yielding better agreement with the experiment in this respect), but then the off-axis regions of lower temperature extend too far downstream (not shown in the figures). These values for the critical gradient g_{cr} correspond well with computations of quasi-one dimensional strained laminar flames with detailed chemistry [14]: using the symmetrical (twin-flame) fresh-to-fresh configuration, extinction occurs at a strain rate $a \approx 3000\ \mathrm{s}^{-1}$, while for the asymmetrical fresh-to-burnt flame, an extinction strain rate[11] $a \approx 8000\ \mathrm{s}^{-1}$ has been determined.

In the present context, two "internal parameters" of the TFC model are of interest and plotted in Fig. 6: the stretch factor G (see Eq. (16)) and the turbulent flame speed U_t (see Eq. (14)). It is observed that in the shear layers surrounding the recirculation zone, $G \approx 0.4$, i.e, turbulent straining reduces combustion intensity by more than 50 percent in this region of the combustor. Also, near the combustor walls, the effect of the stretch factor is quite pronounced. The computed turbulent flame speed is quite nonuniform (reflecting the structure of the fields of turbulent kinetic energy k and dissipation ϵ), and peaks with 12 m/s at a value that is more than 20 times as large as the laminar flame speed for the conditions considered.

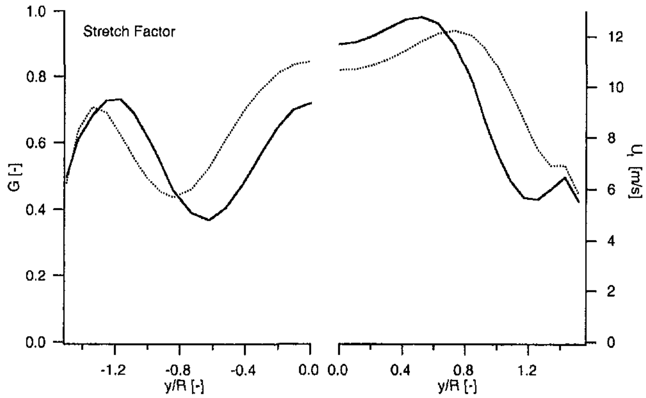

Fig. 6 Profiles of stretch factor (left half) and turbulent flame velocity (right half) in the vertical plane at downstream positions *x/D* = 0.25 (——) 0.4 (· · ·)

Summary and Conclusion

A model for premixed combustion at high Reynolds numbers that is based on a turbulent flame speed closure (TFC) has been implemented and validated with three-dimensional computations against detailed experimental data from a gas turbine burner test stand. The TFC model has performed very satisfactory; qualitative features of the reacting flow have been well reproduced, and the model is computationally robust and very efficient. The latter fact is obviously of particular importance to industrial applications.

The TFC ansatz is in some sense quite similar to many combustion models that are currently in use in industry or investigated at a research level. In all these models, certain assumptions about the structure of the turbulent combustion process (e.g., the flamelet assumption) are made, and detailed submodels are constructed to achieve closure for a particular equation. The rational behind this approach is clearly that a combustion model will reproduce the correct dependence of the turbulent heat release rates or the width of the combustion front, etc., on the physico-chemical parameters if all the submodels involved describe the details of the turbulent combustion process with sufficient accuracy. Frequently the submodels are then solved numerically as part of the overall computation process, involving, e.g., integration over probability density functions and/or reduced chemical mechanisms, etc. Here is where the TFC model differs radically from its competitors, as established theoretical and experimental facts are introduced a priori in analytical form in the formulation of the model. This approach is not only computationally very efficient, as integration over probability density functions, but determination of chemical reaction rates, etc., are not required; it also has the promise of reproducing "automatically" the experimentally observed influence of the main controlling factors on heat release intensity and temperature distributions. Whether the TFC model will fulfill this promise cannot be decided before parametric validation studies are carried out, covering, e.g., a range of equivalence ratios, preheat temperatures, Reynolds and Damköhler numbers, etc.

The TFC ansatz can be extended to the cases of partially premixed (see [18]) or nonadiabatic combustion. This work is in progress and shall be reported elsewhere. Also, exploiting the peculiarities of NO_x formation in lean-premixed combustion (as they are summarized, e.g., in [10, 11, 19]) it is relatively straightforward to construct a NO_x post-processor for the TFC model. This has already been done, and good agreement with the experiment has been achieved. Details shall be published elsewhere. Whether it is also possible to construct a "post-

---

[9] The computational results shown were obtained with a second-order upwind scheme and a $k - \epsilon$ model with standard values for all model constants.

[10] Again, the experimentally determined profiles do not match up exactly at the centerline.

[11] Obviously, temperature cannot be used as an indicator of extinction for fresh-to-burnt flames, as the maximum temperature is always equal to the adiabatic temperature in this configuration. Also, the convergence behavior of the one-dimensional laminar model does not indicate "extinction." In our experience, a converged solution can be obtained at all strain rates if one restarts from a previous solution with somewhat lower strain. We therefore define "extinction strain rate" for an fresh-to-burnt flame as the value a, where the OH concentration does not increase markedly above its equilibrium value throughout the computational domain. This criterion is physico-chemically well-motivated, and works well for lean to moderately rich flames at atmospheric pressure.

processor" for CO and unburnt hydrocarbons, or whether the TFC model can be extended to predict these emissions in some other way, shall be the subject of future work.

Acknowledgments

We are indebted to Bernhard Rogg and Weigang Wang for making the RUN-1DL program available.

References

1 Zimont, V. L., and Lipatnikov, A. N., 1993, "A Numerical Closure of Averaged Heat Release Rate in Premixed Turbulent Flows," pp. 340–343.

2 Karpov, V. P., Lipatnikov, A. N., and Zimont, V. L., 1994, "A Model of Premixed Turbulent Combustion and its Validation," *Archivum Combustionis,* Vol. 14, No. 3–4, pp. 125–141.

3 Zimont, V. L., and Lipatnikov, A. N., 1995, "A Numerical Model of Premixed Turbulent Combustion of Gases," *Chem. Phys. Report,* Vol. 14, No. 7, pp. 993–1025.

4 Zimont, V. L., Karpov, V. P., and Lipatnikov, A. N., 1995, eds., *Influence of molecular heat and mass transfer processes on premixed turbulent combustion,* The 8th International Symposium on Transfer Phenomen in Premixed Turbulent Combustion, San Francisco, July 1995.

5 Bray, K. N. C., 1980, "Turbulent Flow With Premixed Reactants," *Turbulent Reacting Flows,* P. A. Libby and F. A. Williams, eds., Springer Verlag, New York.

6 Zimont, V. L., 1979, "Theory of Turbulent Combustion of a Homogeneous Fuel Mixture at High Reynolds Numbers," *Combust. Expl. and Shock Waves,* Vol. 15, pp. 305–311.

7 Markstein, G. H., 1964, *Non-Steady Flame Propagation,* Pergamon Press, Tarrytown, New York.

8 Peters, N., 1992, "A Spectral Closure for Premixed Turbulent Combustion in the Flamelet Regime," *J. Fluid Mech.,* Vol. 242, pp. 611–629.

9 Borghi, R., 1988, "Turbulent Combustion Modelling," *Prog. in Energy and Combust. Science,* Vol. 14, No. 1.

10 Polifke, W., Döbbeling, K., Sattelmayer, T., Nicol, D. G., and Malte, P. C., 1995, eds:, *A NO_x Prediction Scheme for Lean-Premixed Gas Turbine Combustion Based on Detailed Chemical Kinetics,* Vol. 93-GT-342, ASME, New York.

11 Sattelmayer, T., Polifke, W., Winkler, D., and Döbbeling, K., 1996, "NO_x Abatement Potential of Lean-Premixed GT-Combustors," presented at the ASME Turbo Asia 96, Jakarta, Indonesia, Nov. 5–7, 1996.

12 Peters, N., 1991, *Length Scales in Laminar and Turbulent Flames,* pp. 155–182, Chapter 6.

13 Bray, K. N. C., 1987, Complex Chemical Reaction Systems, Mathematical Modeling and Simulation, Springer Verlag New York Inc., New York, p. 356.

14 Rogg, B., 1988, "Response and Flamelet Structure of Stretched Premixed Methane-Air Flames," *Combust. and Flame,* Vol. 73, pp. 45–65.

15 Sattelmayer, T., Felchlin, M. P., Haumann, J., Hellat, J., and Styner, D., 1992, "Second-Generation Low-Emission Combustors for ABB Gas Turbines: Burner Development and Test at Atmospheric Pressure," ASME JOURNAL OF ENGINEERING FOR GAS TURBINES AND POWER, Vol. 114, pp. 118–125.

16 Launder, B. E., and Spalding, D. B., 1974, "The Numerical Computation of Turbulent Flows," *Comp. Meth. in Appl. Mech. and Eng.,* Vol. 3, pp. 269–289.

17 Bettelini, M., Polifke, W., Geng, W., Müller, U. C., Weisenstein, W., Döbbeling, K., 1997, "Comparison of Combustion Models for Lean Premixed Gas Turbine Combustion," presented at the 4th Int. Conference on Technologies and Combustion for a Clean Environment, July 7–10, Lisbon.

18 Zimont, V. L., 1977, *On Calculation of Partially Premixed Gases Combustion, Combustion of Heterogeneous and Gas Systems,* USSR Academy of Science, Russia.

19 Polifke, W., 1995, "Fundamental and Practical Limitations of NO_x Reduction in Lean-Premixed Combustion, presented at Euroconference—Premixed Turbulent Combustion: Introduction to the State of the Art, Aachen.

T. A. Healy

L. J. Kerr

L. J. Larkin

Pratt & Whitney,
Propulsion Systems Analysis,
MS 731-95,
P.O. Box 109600,
West Palm Beach, FL 33410-4669

Model Based Fuzzy Logic Sensor Fault Accommodation

Sensor in-range fault accommodation is a fundamental challenge of dual channel control systems in modern aircraft gas turbine engines. An on-board, real-time engine model can be used to provide an analytical third sensor channel that may be used to detect and isolate sensor faults. A fuzzy-logic-based accommodation approach is proposed that enhances the effectiveness of the analytical third channel in the control system's fault isolation and accommodation scheme. Simulation studies show the fuzzy accommodation scheme to be superior to current accommodation techniques.

Introduction

Modern aircraft gas turbine engines are often equipped with dual channel (duplex) control systems. This differs greatly from flight control systems that are typically either triplex or quadruplex. There are a number of reasons for this disparity, including:

- Inherent reliability of the engine system is limited by the failure rate of the rotating machinery—driving the control system to zero failures has limited benefits. Duplex provides sufficient fault coverage (typically 95 percent to 99+ percent) to balance the control system failure rate with that of the other engine subsystems.
- Cost, weight, and space requirements are all significantly less for a duplex system than a triplex or quadruplex system.
- Engine control system failures do not often result in loss of vehicle control, which is often the case for most flight control failures. In single engine aircraft, engine shutdowns can cause loss of the vehicle, but usually not the pilot. In dual engine aircraft, engine shutdowns usually result in loss of mission capability.

With the exception of certain "prime reliable" components, such as fuel pumps and actuator pistons that have negligible failure rates, the duplex system provides sufficient redundancy such that no single failure can cause loss of system functionality. In order to provide fault coverage, however, the control system must detect and isolate the fault, then perform the appropriate accommodation. For the large majority of faults, detection and isolation are one and the same. Processors can fail memory, check-sum, or timer checks. Servo valves can show shorts or opens via current checks. Sensors can fail rate or range checks or have shorts or opens.

One category of faults that provides a significant fault isolation challenge in duplex systems is in-range sensor faults. If both channel's sensors pass range and rate checks, but disagree, the question of which value to use poses a dilemma. If both channels agree within the tolerance of the sensing system's accuracy, then the two sensors can be averaged to get a "good" value. Once the disagreement becomes gross, however, one value must be considered "good", and the other discarded.

One approach for selecting the "good" sensor is to look at failure modes. A thermocouple that is inserted into the engine's hot section will read a much cooler temperature if a short occurs in the wires leading to the probe. Failure modes that will cause the thermocouple to read high are rare. Therefore, selecting the high channel for this type of sensor would be a reasonable approach. Since many types of sensors do not have a "most likely" failure direction, another approach is to select "safe". A speed sensor, which counts magnetic pulses, can fail either high if a chafed cable generates spurious pulses, or low if a short-circuit eliminates some of the pulses. The consequences of picking an erroneously low speed signal may include catastrophically overspeeding the engine. The consequences of picking an erroneously high signal are usually limited to a performance loss that results from unnecessarily limiting engine speed. By this logic, the obvious choice for a select "safe" strategy is to choose the high signal. This strategy falls apart, however, if the speed error is high enough, since this error drives the engine to shutdown—a highly undesirable result for a single engine aircraft.

Recent advances in the technology of modeling gas turbine engines has produced accurate, real-time engine models that are suitable for incorporation in the engine control system's embedded software (Kerr, 1992). The real-time models are constructed using a simplified analytical model of the engine to minimize on-board computing requirements, and allow for real-time execution. In order to provide accurate predictions, a state observer is employed that causes the model to "track" the sensors, and thereby provide more accurate predictions for synthesized engine variables.

An on-board model provides an alternative approach to the in-range sensor fault isolation problem, since it can effectively provide an analytical third channel of a sensor. This third channel can referee the disputes between the duplex channels and greatly improve the chances of selecting the sensor that is providing the most correct value to the control system. The state observer feature of the model complicates the implementation of the third channel approach, since the model tends to "track" the voted sensor value, and can thereby lose its ability to provide a discriminator between the two sensors.

Triplex Redundancy Management. Several viable options exist for handling triplex sensors. Either the mean of the three channels or the median value can be used by the control system as the "voted" value. Using the mean has the advantage that it is statistically the closest approximation to the "true" value of the sensed parameter when all three sensors are functioning properly. The mean, however, is corrupted when a sensor is faulty, but has not yet been detected and isolated. The median is normally quite close to the mean and has the advantage that it is not corrupted when one sensor drifts or provides erratic readings. Figure 1 illustrates these two approaches.

Fault detection and isolation is usually accomplished by a parity space approach (Patton, 1992). Parity is examined by comparing the relative errors between each of the three sensors. If two of the errors become large relative to the third, then the parity vector becomes large and points to the erroneous sensor. Figure 2 illustrates this approach. These approaches assume that

---

Contributed by the International Gas Turbine Institute and presented at the International Gas Turbine and Aeroengine Congress and Exhibition, Orlando, FL, June 2–5, 1997. Manuscript received by the ASME Headquarters March 7, 1997. Paper No. 97-GT-222. Associate Technical Editor: H. A. Kidd.

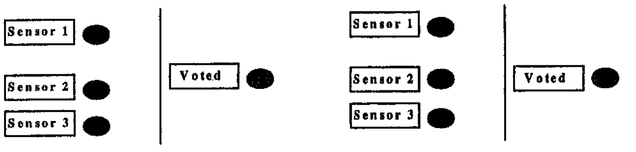

Figure 1 a - Mean Value Voting

Figure 1 b - Median Value Voting

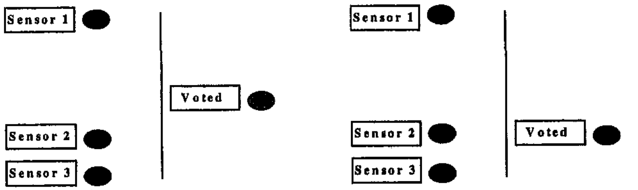

Figure 1 c - Mean Value Voting-Faulted Case

Figure 1 d - Median Value Voting-Faulted Case

Fig. 1 Median versus mean value voting

the three sensors are essentially identical and that their values should all be given equal weight in "voting" the value to be used by the control system. With an analytical third channel, the model value may need to be considered differently than the values given by the sensors.

For most sensors, the sensed value would be given precedence over the model predictions. Under this scenario, the voted value could be the average of the two sensors, providing they agree with each other. If a disagreement occurs, the model would be consulted to pick the correct sensor (the one which agrees most closely to the model), and the voted value would then become that sensor. The disadvantage of this approach is that the control system must abide the corrupted average until the faulted sensor exceeds a tolerance limit that must be sufficiently wide to preclude false alarms.

This paper will offer a simple, fuzzy logic based approach that weights the sensor average based on the sensors agreement with the other channel and the model. This approach attempts to use the relative agreement of the three inputs to provide a robust dual channel/analytical triplex voting scheme.

Application of Fuzzy Logic to Redundant Sensor Selection

The problem of redundant sensor selection is particularly suited to the calculus of fuzzy if/then rules as described by Zadeh (1992) for several reasons. First, the fuzzy if/then paradigm, along with the concept of linguistic variables (a variable whose values are linguistic terms rather than numbers) (Zadeh, 1973), provides a structure with which to capture human intuition and experience in the form of if/then rules. As we (humans) look at the data of various redundant sensor failure scenarios, it is very easy for us to choose an appropriate voted value at any time during and after the failure. It is this ability we wish to capture in the sensor selection algorithm. Second, the use of fuzzy sets to represent our input/output variables (through fuzzification/defuzzification) provides precision at the set level that allows us to write fuzzy rules at a very high level of abstraction. This makes populating the fuzzy rulebase a very simple and straight forward process. Third, the structure of the fuzzy system allows for any number of antecedents in each of the rules that make up the fuzzy rulebase. This allows us to simply generate multidimensional nonlinear relationships between inputs and output(s). These relationships make up a response surface referred to as a fuzzy associative memory or FAM (Kosko, 1992), which would otherwise be very difficult to visualize or create.

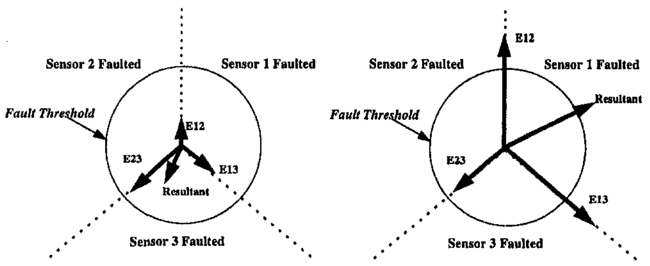

Fig. 2 Parity space approach: (*a*) normal case; and (*b*) sensor 1 faulted

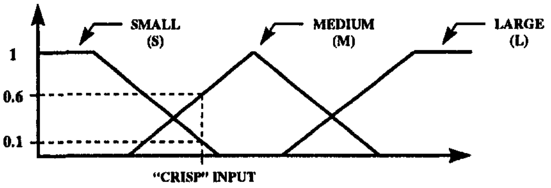

Fig. 3 Typical membership functions

The operation of any fuzzy logic if/then system can be broken down into three primary functions as follows.

- fuzzification of inputs: conversion of the "crisp" (or real) inputs into fuzzy variables
- fuzzy inferencing: evaluation of the fuzzy if/then rules
- defuzzification: conversion of the output fuzzy variable(s) into "crisp" output(s)

The specifics of a fuzzy system for redundant sensor selection are detailed in the sections that follow.

Fuzzification (Fuzzy Membership Functions). Our fuzzy system will be based on a series of if/then rules in which the antecedent and consequent parts are linguistic variables that are fuzzy rather than crisp. The meaning of these linguistic variables is defined by their membership functions. As mentioned previously, we have chosen to use a parity space approach in which the "crisp" inputs to our system will be the relative errors between each of the following three sensors:

$$E12 = ABS(S1 - S2)$$

$$E1M = ABS(S1 - SM)$$

$$E2M = ABS(S2 - SM)$$

where $S1$ is the value from sensor no. 1, $S2$ is the value from sensor no. 2, and SM is the model predicted value. A conscious decision was made to consider the absolute values of these errors since the goal of the fault detection and accommodation (FDA) system is to isolate the faulted sensor, not determine if it is faulted high or low. The inclusion of the sign of the error adds complexity to the algorithm, with no benefit to its effectiveness. Figure 3 shows a typical triangular membership function that could be used to fuzzify the crisp inputs. The scale of the abscissa axis is dependent upon the particular sensor in question and is influenced by experience/knowledge of that sensor's most likely failure mode. A logical choice for a scale factor is the expected variability of the sensor. The granularity of the linguistic variables was chosen, as shown, to be three (small, medium, large).

In this example, the crisp input shown is considered "small" to the degree 0.1 and "medium" to the degree 0.6. For the fuzzy sensor selection system, each of the sensor errors ($E12$, $E1M$, $E2M$) are fuzzified using the same set of membership functions. Some investigation was done into the effect of using differently shaped membership functions (such as sinusoidal) with no discernible effect on the outcome. The overlap of the membership functions can be used to tune the overall input/output response surface, while the granularity or number of membership functions can be used to provide more flexibility in the accommodation of particular combinations of sensor values.

E12 = L	E2M S	E2M M	E2M L
E1M S	M	A1M	A1M
E1M M	A2M	M	A1M
E1M L	A2M	A2M	M

E12 = M	E2M S	E2M M	E2M L
E1M S	A12	A12M	A1M
E1M M	A12M	A12M	A12M
E1M L	A2M	A12M	A12

E12 = S	E2M S	E2M M	E2M L
E1M S	A12	A12	A12
E1M M	A12	A12	A12
E1M L	A12	A12	A12

Fig. 4 Sample fuzzy if/then rulebase

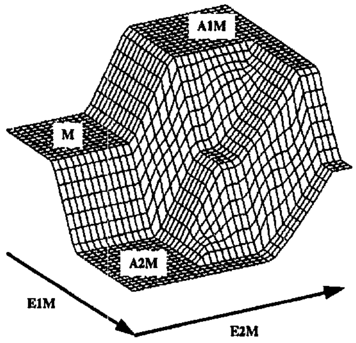

Fig. 5 A portion of the response surface

Fuzzy Inferencing (Fuzzy Rulebase). Once the inputs are fuzzified, they can be used to evaluate the fuzzy if/then rulebase. Again, it is the precision of the fuzzy membership function that defines the linguistic variable that allows the use of highly abstract if/then rules. Since the order of our input (n) is three, and the granularity of our membership functions (m) was chosen to be three, there are exactly $n^m = (3)^3 = 27$ possible combinations of inputs that make up the fuzzy "possibility space" (Kang, 1993). Therefore, we must come up with n^m rules to completely fill the fuzzy if/then rulebase. It should be recognized that depending upon the membership functions, not all of these combinations are physically possible, and, therefore, require no rule to be generated, yet are included for completeness. Figure 4 shows a sample fuzzy if/then rulebase for the redundant sensor selection system. The antecedent portions of the rules depicted in Fig. 4 are the fuzzy representations of the three input sensor errors.

The consequent portion of the rules are any of a number of sensor/model average values $\{A12 = AVE(S1, S2), A1M = AVE(S1, SM), A2M = AVE(S2, SM), A12M = AVE(S1, S2, SM)\}$. In this example, we have chosen to ignore the model predicted value when the two sensor inputs agree ($E12$ small). As the error between sensor no. 1 and no. 2 increases ($E12$ medium), we begin to use the model-predicted value to influence the selected value. And, as the error grows even larger ($E12$ large), we use the model-predicted value and our knowledge of the relative errors to choose an appropriate average. For example, one of the rules states the following:

IF ($E12$ is medium) AND ($E1M$ is small)

AND ($E2M$ is large) THEN use $A1M$.

The rule selection allows incorporation of experimental knowledge of the particular sensor and its typical failure modes. The rulebase may vary significantly depending on the expected accuracy of the particular model estimated parameter (the most likely failure mode of the sensor) or the relative consequences of an erroneously selected value.

Each antecedent of each rule in the rulebase is evaluated using the fuzzified inputs, and will result in a degree of fulfillment between 0.0 and 1.0. The antecedents are then combined using the logical product or minimum function (the fuzzy equivalent to the logical AND) (Schwartz, 1994) to produce a resultant degree of fulfillment for each rule. Consider the previously mentioned rule and suppose the values of the errors are such that $E12$ is considered medium to the degree 0.7, $E1M$ is considered small to the degree 0.3, and $E2M$ is considered large to the degree 0.4. The resultant degree of fulfillment of this rule will be MIN(0.7, 0.3, 0.4) = 0.3.

Defuzzification. Once the degree of fulfillment of each rule in the rulebase has been determined all that remains is to defuzzify the output value. The result of the rulebase evaluation is a fuzzy set that must be converted into an appropriate crisp value (a voted sensor value). A simple defuzzification method is to use the degree of fulfillment weighted average of the rulebase consequent blocks. We define

$$\text{Voted value} = (\sum c_i^* \text{dof}_i)/\sum \text{dof}_i,$$

where c_i is the consequent part of the ith rule, and dof_i is the degree of fulfillment of the ith rule. This method of defuzzification is equivalent to the "mean of maxima" method summarized by Filev (1991), with the consequent part of the ith rule corresponding to the maxima of a fuzzy membership function. The boundedness of this defuzzification method (and most methods) is guaranteed since the output can only be weighted averages of the inputs.

Response Surface. The overall relationship between inputs and output(s) can be mapped as an "$n + 1$" dimensional response surface referred to as a fuzzy associative memory or FAM. For the fuzzy sensor selection system this four-dimensional surface can only be visualized in part. Figure 5 represents a portion of this surface that was generated by holding $E12$ constant and large while varying $E1M$ and $E2M$ over their respective ranges of possibility and holding the consequent averages constant. The ultimate implementation of the fuzzy sensor selection system would be in the form of a trivariate look-up table representing the entire response surface.

Experimental Results

The fuzzy logic approach to redundant sensor selection was demonstrated using the simulation of an advanced gas turbine

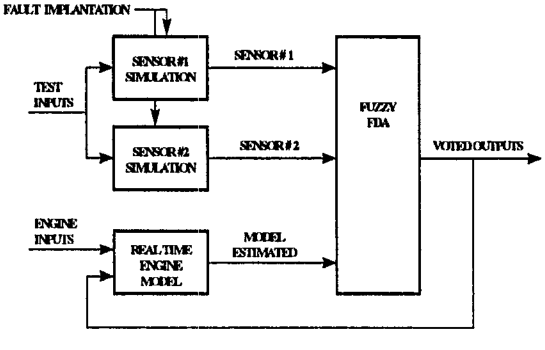

Fig. 6 Fuzzy FDA test configuration

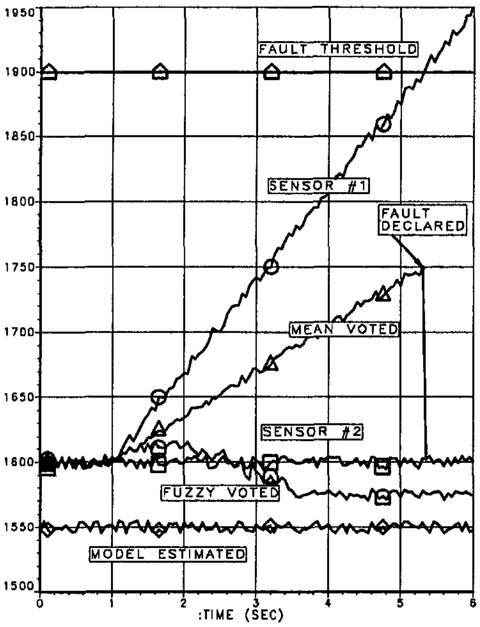

Fig. 7 Fuzzy versus mean value voting

engine control system. This control system features an on-board, real-time engine model that is utilized for parameter synthesis as well as FDA.

Figure 6 shows the test configuration for this study. For convenience, the model and FDA logic were implemented as a piece of software separate from the rest of the control system. This allowed for easy fault implementation, and minimized the computing time required to conduct the tests.

Simulated faults were implanted into engine temperature, pressure, and rotor speed sensors. The faults were implemented as either slow drifts (no fault to threshold in 5 *s*) or sudden shifts (no fault to threshold in 0.15 *s*). The sudden shift time was chosen to implement the fault in a small number of algorithm compute cycles, which minimized the ability of the model to track the faulted input. The slow drift allows ample time for the model to track the signal. The faults were implanted singly and in combinations of sensors. Each test case was started with the values from each of the two simulated sensors being set equal. One channel's value was drifted beyond the in-range threshold value. The test cases were presented to both the baseline FDA scheme and the fuzzy FDA scheme.

Figure 7 shows a representative test case in which one of the sensor values is forced to drift out of range (high). It can be seen that with the baseline FDA approach, the "voted" sensor value follows the average of the two sensors until the fault threshold is reached. At this level, the sensor in closest agreement with the model is selected, and the "voted" value becomes that sensor's output. The disadvantage of this approach is evident in the large error that the system must tolerate prior to failure declaration and the rapid transient that occurs when the fault declaration is declared. By comparison, the fuzzy logic based FDA approach minimizes the error and gently returns the voted value to its final level.

Twenty-two (22) fault cases were tested. In cases where the faults were implanted into pressure or temperature signals, the fuzzy approach reduced the error of the voted signal by up to 5 percent. In all cases, the performance of the fuzzy FDA was superior to the baseline approach. When faults were implanted into rotor speed signals, there was no difference between the fuzzy FDA and baseline FDA scheme. Analysis showed that the real-time engine model's filter tunes so closely to the low rotor speed and high rotor speed sensors that the model does not generate an "independent" value for these parameters. Expected "sensor noise" values for the speed signals used in designing the Kalman Filter gains for the state observer were extremely low. As a result, the model output tracks the voted sensor value extremely well, and the model does not provide an independent estimate. Experience has shown that tight tracking of the rotor speed signals has a beneficial effect on model accuracy, and, therefore, this problem is inherent in this type of model.

Conclusion

This paper has presented a simple and robust fuzzy logic based approach for redundant sensor selection. The methodology enhances the capability of self-tuning, on-board, real-time engine models to provide an analytical third channel for dual channel electronic control systems.

The simulation test results show that the technique minimizes sensor fault effects when compared to a conventional approach based on averaging the dual sensor values until a fault is declared. The reduction in corruption of the voted value enhances the effectiveness of the FDA system, since the model has less tendency to track the faulted sensor. Reduced errors in the voted sensor values has obvious benefits to the control system.

One area where the fuzzy approach showed no improvement over the baseline was in accommodating speed sensor faults. This resulted from the tight tracking of the state observer to the speed signal. One possible approach for overcoming this problem could be to have an "untuned" version of the model running which would be dedicated to providing inputs to the FDA.

References

Filev, D. P., and Yager, R. R., 1991, "A Generalized Defuzzification Via BAD Distributions," *Int. J. Intell. Syst.*, Vol. 6, pp. 687–697.

Kang, H., and Vachtsevanos, G., 1993, "Fuzzy Hypercubes: Linguistic Learning/Reasoning Systems for Intelligent Control and Identification," *Journal of Intelligent and Robotic Systems*, Vol. 7, pp. 215–232.

Kerr, L. J., Nemec, T. S., and Gallops, G. W., 1992, "Real-Time Estimation of Gas Turbine Engine Damage Using a Control Based Kalman Filter Algorithm," *Journal of Engineering for Gas Turbines and Power*, Vol. 114, No. 2, pp. 187–195.

Kosko, B., 1992, *Neural Networks and Fuzzy Systems, A Dynamical Systems Approach to Machine Intelligence*, Prentice Hall, Englewood Cliffs, New Jersey, pp. 299–338.

Patton, R. J., and Chen, J., 1992, "Review Of Parity Space Approaches to Fault Diagnosis Applicable to Aerospace Systems," *Proc. AIAA Guidance, Navigation and Control Conference*, AIAA-92-4538.

Schwartz, D. G., Klir, G. J., and Ezawa, Y., 1994, "Applications of Fuzzy Sets and Approximate Reasoning," *Proceedings of the IEEE*, Vol. 82, No. 4.

Zadeh, L. A., 1973, "Outline of a New Approach to the Analysis of Complex Systems and Decision Processes," *IEEE Trans. Syst. Man. Cybern.*, Vol. SMC-3, No. 1, pp. 28–44.

Zadeh, L. A., 1992, "The Calculus of Fuzzy If/Then Rules," *AI Expert*, March, pp. 23–27.

Thickness Measurement of MCrAlY High-Temperature Coatings by Frequency Scanning Eddy Current Technique

G. Antonelli

M. Ruzzier

CISE SpA,
via Reggio Emilia 39,
20090 Segrate Mi,
Italy

F. Necci

ENEL SpA DCO Roma,
Roma, Italy

Nondestructive characterization of nonserviced, high-temperature coatings can be considered one of the important factors to achieve a higher level of structural integrity of advanced gas turbines. The present paper describes an innovative eddy current technique especially developed for measuring the thickness of metallic (MCrAlY) coatings applied by vacuum plasma spray on Ni-base superalloys. Conventional eddy current techniques, well established for quality control of coating thickness, are not applicable in this case because of the low difference of electrical conductivities of coating and base materials, which is a consequence of their quite similar physical and chemical properties. The new technique employs fast frequency scanning of the electromagnetic field in the range 100 kHz–10 MHz, corresponding to probing depths from 1 mm to 0.1 mm. Dedicated hardware has been developed featuring high sensitivity, stability, and harmonic rejection. Analysis of the measured data (i.e., probe impedance versus frequency), in order to estimate the relevant diagnostic parameters (coating thickness, coating, and base metal electrical conductivities), is carried out on the basis of a theoretical model of interaction between a plane electromagnetic wave and test piece. The results of tests performed on a nonserviced first stage blade are reported and compared with reference destructive data. Reliability, accuracy and practical applicability of the method meets the requirements for in-shop quality control.

1 Introduction

From the early nineties, ENEL (the Italian National Electric Power Authority) has started a program for the installation of large heavy duty gas turbines for electricity production that operate in simple or combined cycle—this latter being mainly related with the repowering of existing power plants.

As the settling of these plants proceeded, growing attention was paid to the problem of quality control during acceptance of the many hundreds of coated blades. It is, in fact, the high-temperature oxidation/corrosion behavior of the coating that determines the need of blade refurbishment. Therefore, 100 percent nondestructive acceptance test was considered a key issue to assure that the expected service life of the coating could be reached. The problem was more relevant for MCrA1Y coatings applied by plasma spray, for which a qualification of the spraying process was available only on the basis of a very limited number of destructive measurements.

In order to approach this problem, ENEL and CISE started a research program with the aim of selecting a proper NDT technique for the measurement of the thickness of new MCrA1Y coatings. Both ultrasound and electromagnetic techniques were investigated. This paper presents the results obtained by using a frequency scanning eddy current technique.

2 Analysis of the Problem

To deal with the problem of a quantitative nondestructive evaluation of the coating thickness on MCrA1Y-Ni superalloys turbine blades, the following analysis steps have been considered:

1 As MCrA1Y coatings are applied with plasma-spray techniques, and are not diffusive, they present quite sharp interfaces with the base metal; the interdiffusion layer is thin ($\sim 10\ \mu m$) as compared to the coating thickness ($>100\ \mu m$).

2 The coating is applied to these turbine blades by a series of computer-controlled passes in the tip-to-root direction; for each pass, the targeted zone of the blade is positioned orthogonally to the coating stream in order to guarantee an optimized deposition. When coating the leading and trailing edges, the concave side of the blade may collect some coating with the wrong incidence angle, which, therefore, is less compact. Such a poor-quality coating should not be adjacent to the substrate, so the two edges need to be coated after the rest of the blade; this procedure causes some noncompacted coating to cover the compacted one on the concave side (Fig. 1).

3 MCrA1Y coatings possess physical and chemical properties quite similar to those of the Ni superalloys; one of the possibly discriminating properties is the electrical conductivity, which shows slight differences (3–10 percent) between the two materials.

4 Electrical conductivity may be inspected by conventional eddy-current techniques, which provide well established methods for coating thickness measurements in the case of high conductivity differences (>30 percent) between the coating and the base metal. Eddy-current methods may also give qualitative information for small conductivity differences, but in this case they are no longer able to give reliable quantitative information due to the scatter in the conductivity values relative to different lots of material.

5 Eddy current measurements are affected by the blade curvature.

According to the above analysis, it turns out that the outlined problem can be summarized as follows: given a layered conductor, it is required to determine the conductivity and thickness

---

Contributed by the International Gas Turbine Institute and presented at the International Gas Turbine & Aeroengine Congress & Exhibition, Orlando, FL, June 2–5, 1997. Manuscript received by the ASME Headquarters February 17, 1997. Paper No. 97-GT-1. Associate Technical Editor: H. A. Kidd.

of each layer, in particular, the MCrAlY coated blades can be considered as two-layer conductors on the convex side, and three-layer conductors on the concave side.

The experimental approach can rely on eddy-current measurements; a multi-frequency technique is required, as it is necessary to test the material at different depths. The collected data need to be interpreted through a physical model for the interaction between the electromagnetic field and the material, as a simple calibration-based procedure is not expected to give reliable quantitative results. Moreover, the blade curvature must be taken into account by providing a suitable correction procedure.

3 The Frequency Scanning Eddy-Current Technique

3.1 Hardware. A PC-based, eddy-current instrument has been designed and produced in order to meet the requirements of the measurement in terms of precision and reproducibility.

The instrument is composed of an electronic module performing the main functions typical of an eddy-current instrument. It provides excitation to the probe, performs amplification, balancing, and syncronous demodulation of the voltage signal from the probe, and it furnishes to the PC (via RS232) the inphase and quadrature components of the demodulated signal with 12-bit resolution. Setting up and control of the electronic module in order to perform frequency scanning of probe excitation as well as signal presentation and analysis is carried out by the PC.

Special care was given in the design to ensure high stability of probe excitation and balancing (to minimize harmonic distorsion of the excitation signal and to maintain linearity of the syncronous demodulation and A/D conversion in the whole frequency range from 100 kHz to 10 MHz).

3.2 Probe. The probe is a transmit-receive, differential and auto-balanced eddy-current probe; these characteristics are needed in order to exploit the high-sensitivity and high-stability properties of the hardware. The geometry of the probe is cylindrical; the diameter of the coil (about 5 mm) has been established as a compromise between high spatial resolution required by measurement and low skin depth/diameter ratio required to approach a plane wave behavior of the sensing electromagnetic field.

3.3 Measured Quantity. As it happens for conventional eddy current equipments, the frequency scanning eddy current instrument measures the probe impedance for each frequency up to a rotation, a gain, and an offset in the impedance plane; these transformations depend only on the instrument characteristics and not on the physical properties of the material under inspection. Modelling such an instrument-dependent quantity is not an easy task, and this suggests to introduce some data manipulation capable of eliminating it.

Moreover, eddy-current measurements are affected by the so-called "lift-off effect", which depends on the distance between the probe and the sample; as the distance undergoes little variations, the probe impedance describes a straight segment in the impedance plane that defines the "lift-off direction," which for small conductivity variations may be considered sample-independent. It is very difficult to keep the distance between the probe and the sample constant, so the lift-off effect has to be cancelled by retaining only the impedance component which is orthogonal to the lift-off direction.

To take into account the above considerations, the following measurement procedure has been developed: (1) two reference samples, A and B, are chosen with homogeneous conductivities σ_A, σ_B different from each other but similar to the conductivity values of the sample S to be inspected: (2) two reference frequency-scanning measurements, Z_{A0} and Z_{A1}, are performed on sample A, at two different lift-off values λ_0, λ_1: these two measurements determine the lift-off direction on A which, as the conductivity values of A, B, and S are similar, is also the lift-off direction on B and S; (3) a third reference frequency-scanning measurement, Z_B, is performed on sample B at a lift-off value as near as possible to λ_0; and (4) a frequency-scanning measurement, Z_S, is performed on sample S at a lift-off as near as possible to λ_0. The (complex) quantity $Z_{A1} - Z_{A0}$ determines the lift-off direction; the direction orthogonal to it is therefore lift-off free.

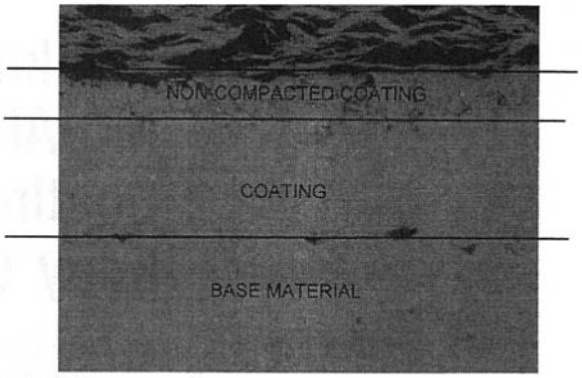

Fig. 1 Concave side coating structure

Let Q_A, Q_B, and Q_S denote the measured impedances obtained from the frequency scannings on samples A, B, and S at lift-off λ_0, after projection over the lift-off free direction. The quantity

$$R_S \equiv \frac{Q_S - Q_A}{Q_B - Q_A} \tag{1}$$

is called normalized impedance; it is clearly lift-off free, and, moreover, it may be easily verified that it is also instrument-independent; therefore, it is a more physical quantity than the raw eddy-current measurement.

4 Direct Model

The information about the physical parameters is contained in the probe impedance via the interaction between the sample and the electromagnetic field produced by the probe. Apart from the blade curvature (to be discussed in the next paragraph), the material may be modelled as a plane N-layered conductor bounded only on the upper side ($z = 0$) with a piecewise constant conductivity distribution in the depth; let σ_n be the conductivity of the nth layer, and L_n the z-coordinate of the interface between the $(n - 1)$th and the nth layer: in the following, the complete set of conductivity values and interface coordinates will be indicated with the symbol p. The simplest model for an electromagnetic field interacting with such a material is that of a plane wave parallel to the sample's surface (Fig. 2).

In this geometry, and for the reference system shown in Fig. 2, the only nonvanishing components of the fields are the x component of the magnetic field H_x, and the y component of the electric field E_x. Both of them depend only on the coordinate z and on the time t. So for a monochromatic wave with angular frequency ω, they may be written as

$$H(x, t) = H_x(z)e^{i\omega t}n_x$$
$$E(x, t) = E_y(z)e^{i\omega t}n_y, \tag{2}$$

where n_x and n_y are unit vectors in the x and y-direction, respectively. In this situation, the four Maxwell equations reduce to two, as Gauss' law and the absence of magnetic monopoles law are identically satisfied; Ampere's and Faraday-Neumann-Lenz' laws become, respectively, (MKS)

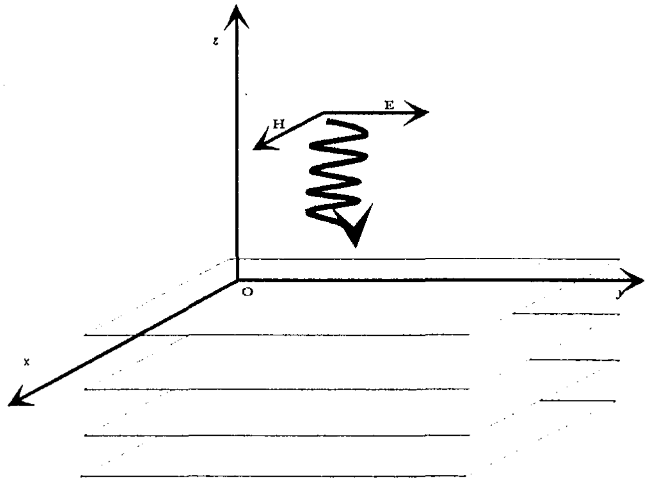

Fig. 2 Plane wave on a multilayered conductor

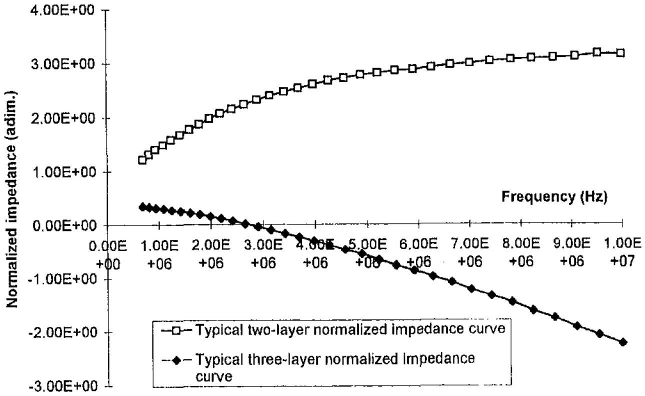

Fig. 3 Sample normalized impedance curves

$$\partial_z H(z) = [\sigma(z) + i\omega\epsilon]E(z)$$
$$\partial_z E(z) = i\omega\mu H(z), \tag{3}$$

where $\sigma(z)$ is the electrical conductivity distribution, μ is the vacuum permeability, ϵ is the vacuum permettivity, i is the imaginary unit, and the subscripts x and y have been dropped. If in (3) the second equation is derived with respect to z, and then the first is used to eliminate H, a second-order differential equation is obtained for $E(z)$. Within the nth layer this takes the form

$$\partial_z^2 E_n(z) = i\omega\mu\sigma_n E_n(z), \tag{4}$$

where $E_n(z)$ is the electric field within the nth layer; the displacement current term $i\omega\epsilon$ has been discarded because, for the frequency range of interest, it is negligible as compared to the conductivity value. The general solution of (4) is

$$E_n(z) = C_n^{(+)}(\omega)e^{\xi_n(\omega)(z-L_n)} + C_n^{(-)}(\omega)e^{-\xi_n(\omega)(z-L_n)}, \tag{5}$$

and, from the second of (3),

$$H_n(z) = \frac{\xi_n(\omega)}{i\omega\mu}\{C_n^{(+)}(\omega)e^{\xi_n(\omega)(z-L_n)} - C_n^{(-)}(\omega)e^{-\xi_n(\omega)(z-L_n)}\}, \tag{6}$$

where

$$\xi_n(\omega) \equiv (1+i)\sqrt{\frac{\omega\mu\sigma_n}{2}}, \tag{7}$$

and $C_n^{(+)}(\omega)$, $C_n^{(-)}(\omega)$ are coefficients to be determined with the boundary conditions on E_n and H_n. These are as follows:

$$\left.\begin{aligned} H_n(L_{n+1}) &= H_{n+1}(L_{n+1}) \\ E_n(L_{n+1}) &= E_{n+1}(L_{n+1}), \end{aligned}\right. \quad n = 1, 2, \ldots (N-1)$$
$$H_1(0) = H_0$$
$$\lim_{z\to-\infty} E_N(z) = 0, \tag{8}$$

where H_0 is the value of the magnetic field at the surface of the sample.

Equations (8) provide $2N$ linear equations in the $2N$ coefficients $C_n^{(+)}(\omega)$, $C_n^{(-)}(\omega)$; the only nonhomogeneous equation is the third, so the value assumed by H_0 contributes only with an overall constant factor to the value of the fields.

Solution of (8) gives the coefficients $C_n^{(+)}(\omega)$ and $C_n^{(-)}(\omega)$ that, using (5) and (6), give the electric and magnetic field distribution in the material; above the material, Eqs. (3) become

$$\partial_z H(z) = i\omega\epsilon E(z)$$
$$\partial_z E(z) = i\omega\mu H(z) \tag{9}$$

and Eq. (4) becomes the wave equation

$$\partial_z^2 E_a(z) = -\frac{\omega^2}{c^2}E_a(z), \tag{10}$$

where c is the speed of light in the vacuum, and the subscript a indicates that (10) refers to the air above the material.

The ratio

$$Z_\lambda(\omega) \equiv \frac{E_\omega(\lambda)}{H_\omega(\lambda)}, \quad \lambda \geq 0, \tag{11}$$

where the subscript ω is used to explicitate the frequency dependence of the fields, is called plane wave impedance (Kaufmann and Keller, 1981) relative to the lift-off λ; as it is a ratio between two field quantities, it does not depend on the value assigned to H_0. Using (9) and (10) it may be shown that, for small values of λ,

$$Z_\lambda(\omega) \cong Z_0(\omega) + i\omega\mu\lambda. \tag{12}$$

The lift-off free component of the plane wave impedance is, therefore, its real part; furthermore, it is equal to the real part of the plane wave impedance $Z_0(\omega)$ evaluated on the sample's surface.

If $Q_A(\omega)$ and $Q_B(\omega)$ are the real parts of the plane wave impedances relative to two single-layer conductors A and B with different conductivities and $Q_S(\omega)$ is the real part of the plane wave impedance relative to an arbitrary multilayer conductor, the normalized plane wave impedance relative to S is defined as

$$R_S(\omega) \equiv \frac{Q_S(\omega) - Q_A(\omega)}{Q_B(\omega) - Q_A(\omega)}. \tag{13}$$

It may easily be verified that $R_S(\omega)$ reduces to a constant if S is a single-layer sample.

Interpretation of the frequency-scanning normalized impedance data is performed on the basis of the model for the normalized real part of the plane wave impedance (Fig. 3).

Curvature Correction. As pointed out in section 2, a correction procedure is needed to account for the blade curvature. Let k be a set of curvature parameters describing the curvature at a given point of the blade and p a set of parameters characterizing the layer structure in the same point. Furthermore, let k_0 be the value of the curvature parameters relative to a flat sample and p_0 the value of the layer parameters relative to a single-layer structure. To the first order in $(k - k_0)$ and $(p - p_0)$, an hypothetical "curvature" plane wave model for the normalized impedance would be related to the "flat" plane wave model by the relation

$$R(\omega; k, p) = R(\omega; k_0, p) + R(\omega; k, p_0) - R(\omega; k_0, p_0). \quad (14)$$

The last term on the right is relative to a flat single-layer sample; therefore, it is a constant. Moreover, it may be made to vanish by choosing the reference sample A similar enough to the sample described by the parameter p_0. Reordering of the other three terms gives

$$R(\omega; k_0, p) = R(\omega; k, p) - R(\omega; k, p_0). \quad (15)$$

Equation (15) means that the difference between the normalized impedance relative to a coated blade and the normalized impedance relative to a noncoated blade with the same geometry can be modelled with the plane wave model described above.

In the following, this correction procedure will always be understood so that the variable k may be dropped everywhere.

5 Inverse Model

The model described in section 4 may be used to predict the plane wave normalized impedance relative to a multi-layered conductor described by the set of parameters p. For a given set of frequencies $\{\omega_i\}$, $i = 1, 2, \ldots, N_f$, the normalized impedances will be indicated with the symbol $R(\omega_i, p)$; the calculation of these quantities is referred to as the direct problem.

Given a set of experimental normalized impedance data R_i, $i = 1, 2, \ldots, N_f$, relative to a set of frequencies $\{\omega_i\}$, the problem of determining a set of parameters p for which the relation

$$R_i = R(\omega_i, p), \quad i = 1, 2, \ldots, N_f \quad (16)$$

holds (up to experimental errors) is called the inverse problem.

In general, inverse problems are ill-posed problems (Tikhonov and Goncharsky, 1987), in the sense that they may not possess a unique and/or a stable solution. To reduce this uncertainty, some a priori knowledge must be considered. In the case of MCrAlY coatings, the number of layers is known (c. section 2). For the convex side of the blade, three parameters have to be determined, namely, the conductivity values of the coating and of the base metal and the interface position. For the concave side of the blade, five parameters have to be determined, namely, the conductivity values of the surface coating, the good coating and the base metal, and two interface positions.

Regardless of the number of layers, providing that this number is known, a parameter estimate may be obtained by applying a least-squares procedure to the sum of square errors

$$S[p, \{\omega_i\}_{i=1}^{N_f}] \equiv \sum_{i=1}^{N_f} [R(\omega_i, p) - R_i]^2. \quad (17)$$

An iterative minimization procedure for the solution of inverse problems like (17) is provided by the conjugate gradient method (Ortega and Rheinbolt, 1970). This method is largely used for the inversion of impedance experimental data in magnetotelluries problems (Norton and Bowler, 1993). It has also been proposed for electromagnetic nondestructive controls (Bowler and Norton, 1992). Once the estimates of the parameters p have been obtained, it is possible to obtain their confidence intervals by applying standard methods in statistical analysis.

6 Experimental Setup

The experimental setup used for the frequency-scanning eddy-current measurements is composed of the following elements: (1) transportable PC (486 DX2 66 MHz); (2) acquisition software; (3) software implementation of the inverse plane wave model; (4) frequency-scanning eddy-current equipment; (5) transmit-receive, auto-balanced differential eddy-current probe; and (6) transportable mechanical handler.

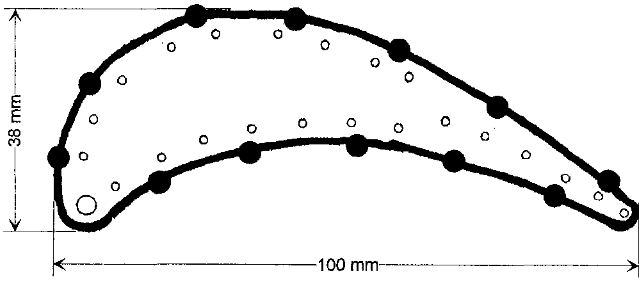

Fig. 4 Eddy current measurement locations (black circles): first section at about 40 mm from the tip; second section at about 90 mm from the tip.

The PC drives the frequency-scanning eddy-current equipment. The acquisition and the inversion software, which appear under the same interface, are installed on the PC and run as a MATLAB application. The probe, reference samples, and blade are supported by the mechanical handler, which also lodges the frequency-scanning equipment.

The experimental measurements are taken following the procedure outlined in section 3.3. The curvature correction is performed using pre-registered normalized impedance curves that are taken in advance on selected points of a noncoated blade with the same geometry of the blades to be inspected.

A single frequency-scanning measurement (about 30–40 different frequency values) is performed in about 5 s; a complete single-point measurement (i.e., comprised blade positioning and reference measurements) takes between 2 and 5 min, depending mainly on the difficulties in blade positioning.

7 Coating Thickness Evaluation on AMDRY995-UDIMET520 Turbine Blades

A couple of nonserviced first stage turbine blades has been made available by ENEL SpA CRAM Milano for nondestructive measurements and for partial reference destructive measurements. The base metal is UDIMET520 for both blades. One of them has been coated with AMDRY995, while the other has been left uncoated for curvature correction measurements.

Frequency-scanning eddy-current data have been collected on both sides of the blades at the points shown in Figs. 4–9. Figures 5–9 also show the destructive measurement locations near the tip. For each point shown in the figures, a frequency-scanning eddy-current measurement in the range 0.7 MHz–10 MHz has been performed (for the material inspected, these

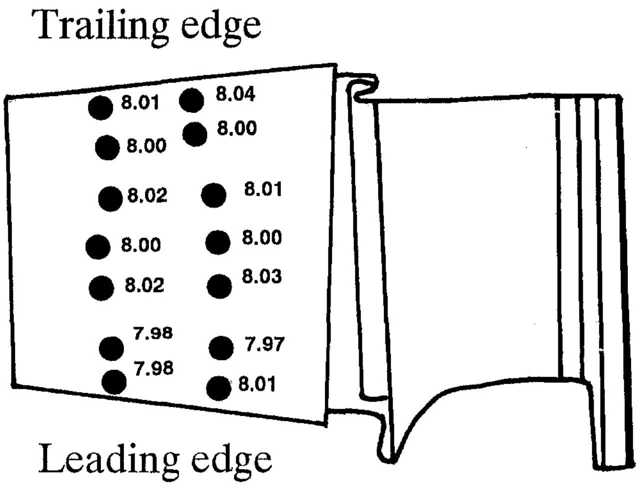

Fig. 5 Nondestructive evaluation of base metal conductivity (convex side); values in S/m × 10^6, 90 percend conf. interval ± 0.02 × 10^6 S/m

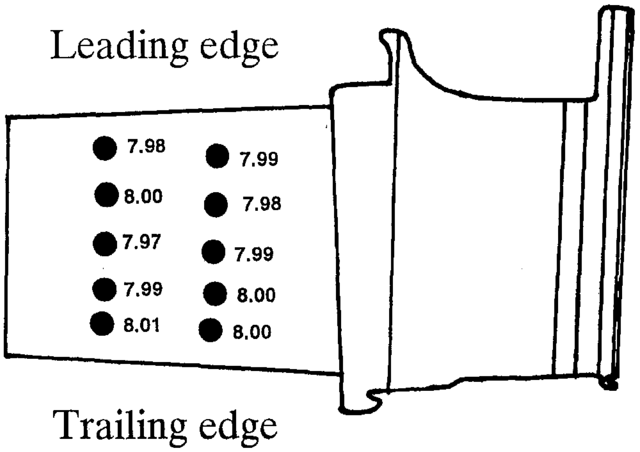

Fig. 6 Nondestructive evaluation of base metal conductivity (concave side); values in S/m × 10^5, 90 percend conf. interval ± 0.03 × 10^5 S/m

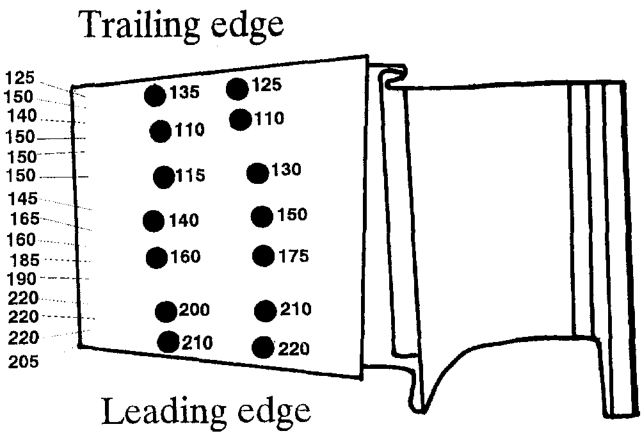

Fig. 7 Reference and nondestructive evaluation of coating thickness (convex side); values in μm, 90 percend conf. interval less than ± 10 μm

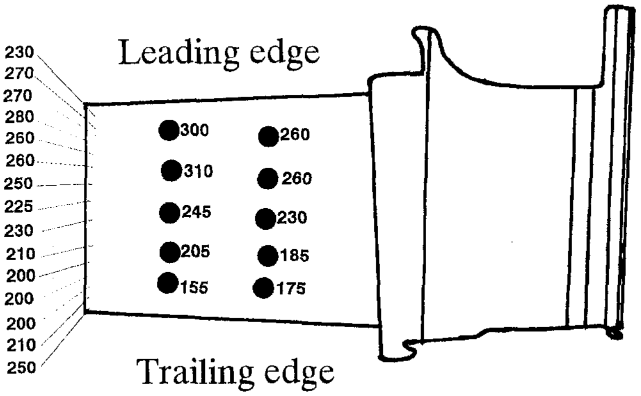

Fig. 8 Reference and nondestructive evaluation of coating thickness (concave side); values in μm, 90 percend conf. interval less than ± 25 μm

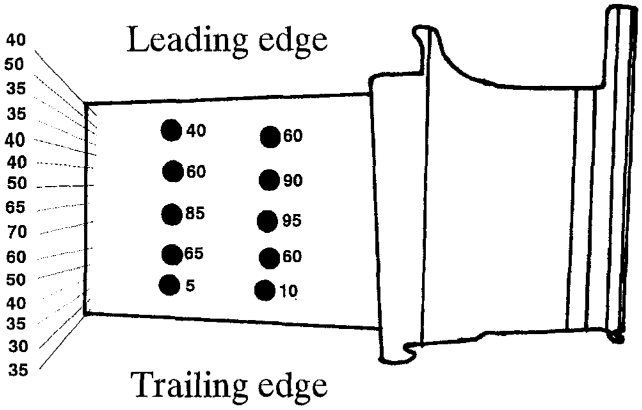

Fig. 9 Reference and nondestructive evaluation of noncompacted coating thickness (concave side); values in μm, 90 percend conf. interval ± 20 μm

frequencies correspond to skin depths between 150 and 500 μm), along with the necessary reference measurements on two flat UDIMET 520 samples with uniform conductivities (7.90 × 10^5 S/m and 8.16 × 10^5 S/m). Curvature correction has been applied according to the method described above using frequency-scanning measurements performed on the noncoated blade. Normalized and curvature-corrected data are shown in Fig. 3.

While the curves on the convex side of the blade agree with a two-layer structure, the curves on the concave side cannot be interpreted in the same way. A third low-conductivity surface layer needs to be added in order to get normalized impedance curves as those found on the concave side. This layer can be identified with the noncompacted coating described in section 1. According to the different layer structures found on the two sides of the blade, two different models have been used to estimate the conductivity and thickness of each layer; data relative to the convex side have been inverted with a two-layer model, while for data relative to the concave side a three-layer model has been used. In principle, a three-layer model could be used also when a two-layer model is applicable; some tests showed that no differencies in the parameter estimates arise due to the choice of the model.

Data inversion results, together with the destructive reference data, are reported in Figs. 5–9. Both conductivity and thickness values show reliable features, and the latter are also in good agreement with the reference destructive data. In detail, the following may be observed:

1 Conductivity values of the base metal are uniform on both sides of the blade within the confidence intervals (±0.03 × 10^5 S/m at 90 percent confidence level), as it is expected for high quality materials such as Ni-based superalloys.
2 The coating thickness on the convex side grows from the trailing to the leading edge (90 percent confidence interval: ±10 μm); the trend and the thickness values are in good agreement with the reference data. Moreover, the thickness is constantly moving from the tip to the root, which agrees with the quality control data obtained by the manufacturer on blades of the same kind.
3 The noncompacted coating thickness on the concave side (90 percent confidence interval: ±20 μm) is more or less constant from the tip to the root, and it shows a maximum in correspondence of the maximum blade curvature, decreasing toward the edges, with the lowest values next to the trailing edge. This trend is well-explained by considering the coating procedure (Section 1, b) and the fact that the more the surface is curved, the more it can collect extra coating when the edges are plasma sprayed. Reference data confirm the overall behavior of this parameter, quantitative discrepancies being due to the fact that such low thicknesses would require higher testing frequencies;
4 The total (i.e., normal + noncompacted) coating thickness on the concave side (90 percent confidence interval: ±25 μm) shows the same trend as observed for the convex side. The

quantitative agreement with reference data is less good for the same reason as above.

8 Conclusion

A frequency scanning eddy current technique has been developed and applied to measure the thickness of new MCrAlY coating applied by vacuum plasma spray on Ni-base blades.

It relies on high performance proprietary hardware and model-based inversion of eddy current data and enables thickness measurements, even in the case of very small conductivity difference between coating and base materials. Moreover the measurement is not dependent on small conductivity variations of both materials to be traced to different lots.

At present, extensive validation of the technique is being performed on first and second stage blades in order to verify applicability to in-shop quality control. In addition, applications of the same technique to different problems like nondestructive characterization of the evolution of serviced RT22 coatings and thickness measurement of very thin alluminum layers applied on Al alloys are currently under investigation.

In principle, the eddy-current, frequency-scanning method is applicable to every conductive (nonferromagnetic) material—limits being dictated by the geometry of the component and by the frequency range required (provided that a suitable curvature correction procedure can be defined and no a priori obstacle exists for an application to components, such as aerospace turbine blades or other small and high-curvature components).

Acknowledgment

The authors are grateful to F. Cernuschi and ENEL SpA CRAM Milano for supporting a preliminary stage of the research and for supplying the blades used in the experimental measurements.

References

Kaufmann, A. A., and Keller, G. V., 1981, "The Magnetotelluric Sounding Method," *Methods in Geochemistry and Geophysics*, Elsevier, NY.

Tikhonov, A. N., and Goucharsky, A. V., 1987, "Ill-Posed Problems in the Natural Sciences," MIR Publishers, Moscow, USSR.

Ortega, J. M., and Rheinboldt, W. C., 1970, "Iterative Solution of Nonlinear Equations in Several Variables," Academic Press, San Diego, CA.

Norton, S. J., and Bowler, J. R., 1993, "Theory of Eddy-Current Inversion," J. Appl. Phys., Vol. 73, Vol. 2, p. 501.

Bowler, J. R., and Norton, S. J., 1992, "Eddy-Current Inversion for Layered Conductors," *Res. Nondestr. Eval.*, Vol. 4, p. 205.

Blade Fault Recognition Based on Signal Processing and Adaptive Fluid Dynamic Modeling

A. Stamatis

N. Aretakis

K. Mathioudakis

National Technical University of Athens,
Mechanical Engineering Department,
Iroon Polytechniou 9, Zografou,
Athens, 15710
Greece

An approach for identification of faults in blades of a gas turbine, based on physical modelling, is presented. A measured quantity is used as an input, and the deformed blading configuration is produced as an output. This is achieved without using any kind of "signature," as is customary in diagnostic procedures for this kind of faults. A fluid dynamic model is used in a manner similar to what is known as "inverse design methods": the solid boundaries that produce a certain flow field are calculated by prescribing this flow field. In the present case, a signal, corresponding to the pressure variation on the blade-to-blade plane, is measured. The blade cascade geometry that has produced this signal is then produced by the method. In the paper, the method is described, and applications to test cases are presented. The test cases include theoretically produced faults as well as experimental cases where actual measurement data are shown to produce the geometrical deformations that existed in the test engine.

1 Introduction

Techniques for the identification of faults of blades in gas turbines have significantly advanced in recent years. The interest in blade faults, in particular, stems from the fact that they account for a substantial percentage of gas turbine failures, as reported by Meher-Homji (1995), who has provided a thorough review on all aspects of blade failures in gas turbines.

Various techniques exist today for the identification of blade faults in gas turbines. The research group of the authors has contributed to this area by developing relevant diagnostic techniques (Mathioudakis et al., 1991; Dedoussis et al., 1994). The usual procedure for identifying a fault is by associating it with a "signature" (see, for example, Cempel, 1991; Mathioudakis, 1995). Signatures are derived by processing measurement data, and reducing them to a form appropriate for fault identification. An a priori knowledge of the correspondence of faults to signatures gives the possibility to conclude about the presence of a fault, when its signature is obtained. Personal judgement or artificial intelligence techniques, as the trend is today, are used in order to take a decision about the presence of a fault once a signature is available.

In the present paper, a novel approach is introduced. Instead of processing measurement data for deriving signatures, the processing provides, as a result, a direct geometrical picture of the fault. Therefore, it is not necessary to go through the derivation of signatures and application of relevant classification techniques in order to identify a fault. It could be said that the procedure is the equivalent to recognizing a person from their picture rather than from their signature.

As it will become obvious from the description of the proposed technique and the discussion that follows, it possesses various advantages over the usually employed diagnostic processes. To the authors' knowledge it is the first time that a technique of this kind is developed in the field of gas turbine diagnostics.

In the following paragraphs we first give a brief reference to the ideas behind the technique which is then followed by a description of the technique itself. Application cases are then presented, and, finally, features of the technique are discussed.

2 Interrelation of Cause and Effect: Fault Identification

Before presenting the principles of the method proposed, it is useful to give some basic notions about the principles underlying a procedure for the diagnosis of faults. For the vast majority of cases, a fault manifests itself as a change of geometrical characteristics of parts of a machine (typical examples are parts broken or deformed). In order to establish the possibility of diagnosing a machine condition, a correspondence of this condition to the values of the measured quantities should be known. This correspondence is intrinsically established through the physical laws governing the operation of the machine. The behavior of any relevant physical quantity is linked through these laws to the detailed geometry of the machine and the kind of phenomena taking place in it.

If we consider a machine using a fluid as a working medium, as is the case for turbomachines, the variation of the flow quantities at one particular location in the machine is determined, via the laws of fluid mechanics, from the geometry of the solid boundaries and the physical properties of the fluid. A change in geometry will then reflect on the values of the flow quantities and can be calculated by application of the relevant physical laws.

We see that if suitable quantities are measured, they reflect changes in geometry, and can, therefore, be used to indicate the presence of a fault. If the possibility to calculate the flow field for the different geometries exists, then the change in the measurement quantities can be evaluated. If the change represents a fault, its signature is obtained by calculation. In this way, a library of signatures can be built so that when an experimental signature becomes available, the corresponding fault can be recognized by comparison to the signatures of this library.

An approach of this type will be termed a "direct" approach in the following. (Direct in the sense that a fault signature is calculated from the geometry changes corresponding to a fault.)

Contributed by the International Gas Turbine Institute and presented at the International Gas Turbine and Aeroengine Congress and Exhibition, Orlando, FL, June 2–5, 1997. Manuscript received by the ASME Headquarters March 7, 1997. Paper No. 97-GT-197. Associate Technical Editor: H. A. Kidd.

The group of the present authors has demonstrated that rotor blade fault signatures can be successfully simulated (Dedoussis et al., 1994). The basic idea was that by calculation of the flow field over a blade cascade, time signals of unsteady wall pressure are reconstructed. Producing such signals for healthy and faulty cascades gives the possibility to produce fault signatures, as the difference between the power spectra of faulty and healthy signals.

The problem that is examined now is the inverse of the previous one. We want to examine if we can calculate the geometry changes from the changes they produced in fluid dynamic quantities. This kind of problem is known as an "inverse" problem in fluid mechanics. A typical such problem is the derivation of the coordinates of an airfoil from a prescribed distribution of pressure we want to be developed on its suction and pressure surfaces. Inverse design methods are widely used today for designing blades and passages of turbomachines (see, for example, Van den Braembusche, 1994).

The method we introduce here achieves a solution to such a problem for faults in blade cascades. We will use the method of simulating pressure signals from healthy and faulty blade rows, introduced by Dedoussis et al. (1994) as the starting point. The presentation that follows is given in a generalized way, as it is applicable to different diagnostic applications, which can involve different measured quantities or faults. The way it is applied to the particular cases examined is also presented together with specific examples in order to make the presentation as clear as possible.

3 Adaptive Fluid Dynamic Modelling and Geometry Alteration Identification

We define a vector **g** whose elements g_i are geometric parameters that fully define a blade row

$$\mathbf{g} = [g_1, \ldots, g_L].$$

A set of values of these parameters completely specifies the geometry of a blade row. For example, g_i may be the stagger angle of each individual blade of a compressor blade row ($L = N_b$). For rows of blades with a particular airfoil shape and blade spacing, **g** completely defines the geometry of the blade row ($L = 2N_b$). If we want to have a more general case, **g** should also include elements for blade spacing, chord, profile, etc.

For a particular blade row defined by **g**, application of a fluid dynamic simulator F_f produces a calculated signal S_c, corresponding to the following particular geometry:

$$S_c = F_f(\mathbf{g}). \tag{3.1}$$

We use an operator, termed D to denote the processing applied to a signal in order to derive a fault signature. For example, it consists of the calculation of power spectra, averaging, and taking differences in the methods reported by Mathioudakis et al., 1991. Application of the diagnostic processing then produces the fault parameter vector $\mathbf{d}_c$ (fault signature) corresponding to the following particular geometry:

$$\mathbf{d}_c = D(S_c) = D(F_f(\mathbf{g})). \tag{3.2}$$

So, for any given geometry, we can produce a fault parameter. The problem is now to define the geometry that has produced a measured fault parameter $\mathbf{d}_m$. This means that we are looking for means to invert relation (3.2) so that we obtain **g** from $\mathbf{d}_m$. Although it is not directly evident how such an inversion may take place, we may obtain this target by incorporating the direct approach into an iterative solver of nonlinear equations. The way to do it is as follows.

Firstly, we assign a condition identity vector **f** with elements defined by the relations

$$f_i = g_i / g_{i,0},$$

where $g_{i,0}$ is the geometry parameter of Blade i in its initial healthy condition, and g_i is the geometry parameter of Blade i in unknown condition. The elements of **f** represent the deviation of the actual geometry from the initial intact geometry. Therefore, if the values of parameters f_i are determined, it is possible to calculate the actual geometry by the relations

$$g_i = f_i \cdot g_{i,0}.$$

For these values of g_i using the direct simulation approach, we obtain the fault signature

$$\mathbf{d} = D(F_f(\mathbf{g})).$$

The deviation between fault signatures of the simulated and measured signals is expressed by the following error terms:

$$\mathbf{e} = \mathbf{d}_c - \mathbf{d}_m = D(F_f(\mathbf{g})) - \mathbf{d}_m \tag{3.3}$$

These errors reflect the wrong initial estimate for the condition identity vector **f**. Through this formulation, the inverse problem solution is the solution of the nonlinear equations

$$\mathbf{e}(\mathbf{f}) = 0, \tag{3.4}$$

i.e., we are seeking the **f** that is rendering a simulated fault signature identical to the corresponding measured one. A numerical technique can be used for this purpose. For example, the Newton-Rampson procedure can be used based in the following updating scheme:

$$\mathbf{f}^{n+1} = \mathbf{f}^n + \mathbf{J}^{-1}\mathbf{e}^n, \tag{3.5}$$

(where **J** is the Jacobean of the linearized system 3.2) until the error $\mathbf{e}^n$ becomes smaller than a given tolerance.

Since a signature $\mathbf{d}_m$ evaluated from measured signals contain noise, another way of formulating the problem is to seek those **f** that minimize a norm of vector **e**:

Nomenclature

ah, af = correlation coefficients for healthy and faulty condition, respectively (Eq. 4.1)
d = fault parameter
D = processing operator
Da, **Dp** = fault signature vectors (Eqs. 4.3, 4.4)
e = error terms
f = condition identity vector
F_f = dynamic simulator
$f(t)$ = faulty signal for one rotor revolution
g = geometry vector
$h(t)$ = healthy signal for one rotor revolution
J = Jacobean
M = number of points in time signal corresponding to one blade-to-blade passage
N = number of points in time signal for one rotor revolution
N_b = number of blades
Ph, Pf = passage maximum pressure coefficients for healthy and faulty condition, respectively
Sc = calculated signal
$w(t)$ = the portion of a healthy signal corresponding to one blade-to-blade passage

Sub and Superscripts

i, k = blade index
n = iteration number
o = initial intact condition

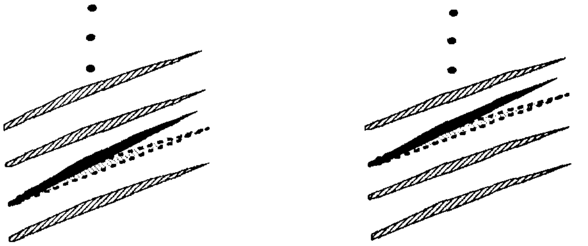

Fig. 1 Cascades with a twisted blade at a different circumferential location. They both produce identical fault signatures.

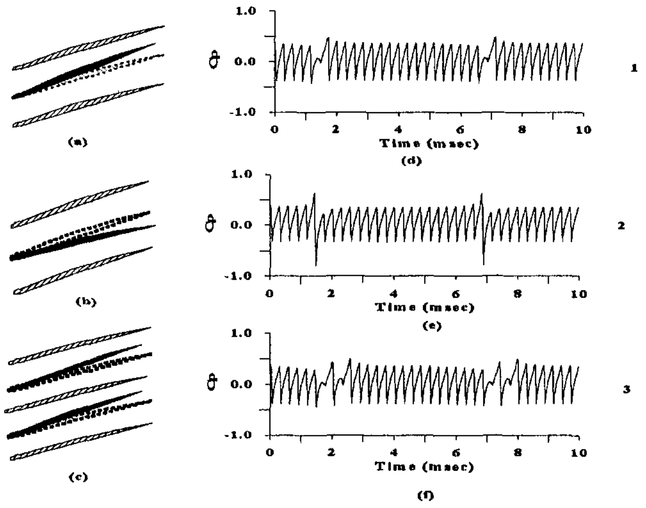

Fig. 2 Three different cases of blade faults (*a*), (*b*), (*c*), and the corresponding unsteady pressure signals (*d*), (*e*), (*f*).

$$\mathbf{f} : \|\mathbf{e}(\mathbf{f})\| \text{ is minimum.}$$

Because the algorithm is structured in this way (namely, we modify the solid boundaries of our fluid dynamic solver to adapt the experimental signals), we named the procedure "Adaptive Fluid Dynamic Modelling."

4 Establishing Signatures for One-To-One Correspondence

The mathematics of the procedure described above gives some requirements for the fault parameters **d**—if a good fault identification capability is desired. A first requirement, in order to have a unique solution to the inversion of Eq. 3.2, is that a one-to-one correspondence between **g** and **d** exists. This requirement expresses what is intuitively known, that for identification of a fault, this fault must have a unique fault signature. Equivalently, every different fault must have a different signature. A second requirement is related to the level of detail desired in fault identification. The more detailed the diagnosis, the more geometrical properties should be reflected in the fault parameters. For example, when dealing with blade faults it is desirable to know not only that a blade is faulty but also what is the location of this blade and what is the kind and severity of the fault.

In order to make these points clearer, we use a counter example. Spectral differences have been found to be good fault signatures for identifying the existence and kind of blade faults, as documented by Mathioudakis et al. (1991). These signatures cannot, however, provide enough detail as to the location of a faulty blade, while they can confuse some cases of different faults. For example, two cascades containing one blade twisted by the same angle but at different locations, as is shown in Fig. 1.

These two geometries produce the same spectral difference pattern since phase information is lost in the power spectra. Also consider two cascades with one blade twisted by opposite angles, as shown in Fig. 2. These two cascade geometries produce different time signals, as is shown in Fig. 2, but the two spectral difference patterns are almost the same as presented in Fig. 3. In Fig. 2, a third cascade geometry and the corresponding time signal are presented, which produces a significantly different pattern from the two other cascade geometries, as is shown in Fig. 3.

These inadequacies became apparent at an initial stage of the present work when spectral differences were used as fault parameters **d**. In order to overcome them, new fault parameters were introduced. The following requirements were set for these parameters: (*a*) they should contain information sufficient for defining the geometry of every individual blade of a blade row; and (*b*) a fault parameter reflecting the condition of a blade should be sensitive to small changes in this blade geometry, but relatively insensitive to changes in neighbouring blades.

We confined ourselves to the faults linked to change in spacing and the setting angle of blades. So, the geometry of every blade is defined by two geometric parameters, its stagger angle, and its position with respect to a reference position. This implies that a fault parameter vector for a rotor with N_b blades should contain $2N_b$ elements in order to have sufficient information for defining the $2N_b$ geometric parameters of this blade row.

Two fault parameters have been defined, and they are presented below. The definition is based on the observation that the geometry of the individual blades of a turbomachine blade row has a direct influence on blade-to-blade pressure distribution. Departure from periodicity gives local differentiations of the pressure signal. An index of the repeatability of the blade-to-blade pressure distribution can be established by comparing the signal under examination to a signal from a blade passage of an intact, periodic cascade.

Correlation Coefficients for Blade-To-Blade Pressure Distribution. A first parameter is derived by correlating each one of the faulty blade-to-blade pressure distributions with one corresponding to a healthy passage. We denote by $h(t)$ and $f(t)$ time signals from one rotor revolution of a healthy and a faulty cascade, respectively, and by $w(t)$ the portion of a healthy signal corresponding to one blade-to-blade passage, as shown in Fig. 4. The corresponding discretized signals are denoted by $H(i)$, $F(i)$, and $W(i)$, respectively. These signals are normalized using the minimum and maximum values both of the signals in order to obtain values between 0 and 1.

Next, we define the correlation coefficients ah_k, and af_k between healthy, faulty time signals, and the average healthy blade-to-blade distribution according to the following relations:

$$\alpha h_k = \frac{\overline{h(t)\cdot W(t)}}{\overline{W(t)^2}} \tag{4.1a}$$

$$\alpha f_k = \frac{\overline{f(t)\cdot W(t)}}{\overline{W(t)^2}} . \tag{4.1b}$$

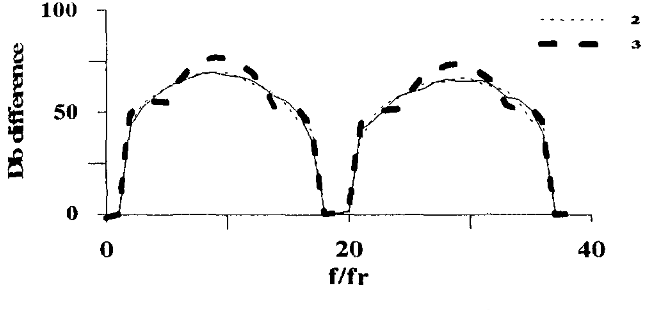

Fig. 3 Spectral differences (used as fault signatures) for the cases of faults of Fig. 2

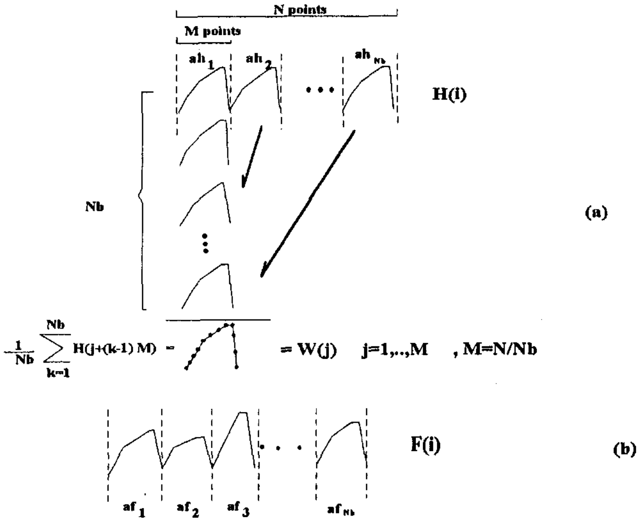

Fig. 4 Healthy and faulty time signal for one rotor revolution. Derivation of the average passage pressure signal.

The averaging in these relations extends over one blade passage. When the signals are available as discrete time signals (sampled by a digital data acquisition system), then these relations are expressed in a discretized form. For example, relation 4.1*b* becomes

$$af_k = \frac{\sum_{j=(k-1)\cdot M+1}^{k\cdot M} F(j)\cdot W(j-(k-1)\cdot M)}{\sum_{j=1}^{M} W(j)^2},$$

$$k = 1, \ldots, Nb. \quad (4.2)$$

The fault signature is defined as the vector **Da** with elements:

$$Da_k = \frac{af_k - ah_k}{ah_k}\cdot 100, \quad k = 1, \ldots, Nb. \quad (4.3)$$

Passage Maximum Pressure Coefficients. The second parameter is based on maximum pressure coefficient of each blade-to-blade portion of the signal denoted by Ph_k for healthy and Pf_k for faulty time signals over one rotor revolution, as shown in Fig. 5.

$$Ph_k = \max_{t_{k-1}\le t\le t_k} [h(t)]$$

$$Pf_k = \max_{t_{k-1}\le t\le t_k} [f(t)],$$

which, in descretized form, become

$$Ph_k = \max\nolimits_{i=1}^{M} [H(i + (k-1)\cdot M]$$

$$Pf_k = \max\nolimits_{i=1}^{M} [F(i + (k-1)\cdot M] \quad k = 1, \ldots, Nb.$$

The fault signature **Dp** defined as a vector with elements

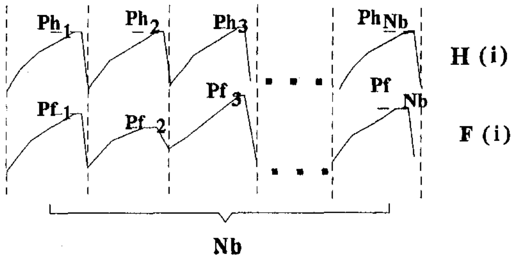

Fig. 5 Blade-to-blade maximum pressure coefficients

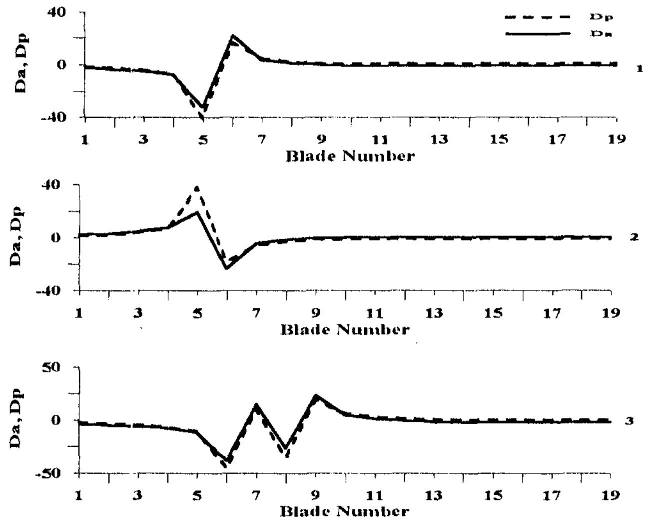

Fig. 6 Fault signatures in terms of *Da* and *Dp* for the faults of Fig. 2

$$Dp_k = \frac{pf_k - ph_k}{ph_k}\cdot 100 \quad k = 1, \ldots, Nb. \quad (4.4)$$

For the derivation of both of the above parameters the knowledge of a healthy signal for a period of at least one revolution is necessary. Healthy signals can be produced by simulation. In this case, the signal consists of N_b identical segments, one for each blade passage. $W(t)$ is one of these segments. If the healthy signal comes from measurement, then phase averaging over one period provides the healthy signal $h(t)$, while further phase averaging over one passage provides $w(t)$.

5 Application Test Cases

In order to illustrate the features of the described procedure, application examples are now presented. The test case chosen corresponds to blading of the compressor of an industrial gas turbine for which experimental data are available (see Mathioudakis, et al., 1991). It is thus possible to check the reliability of the proposed method by applying to known test case, and comparing with previously existing methods. Of course, checking of the mathematics was first done by applying the inverse technique to simulated data, and it was verified that it performs successfully.

We will first examine some properties of fault signatures in terms of the parameters **Da** and **Dp** introduced above. Signatures for the cases of Fig. 2 have been calculated and are shown in Fig. 6.

From this figure we can make the following observations:

- each fault produces a distinctly different pattern for both parameters
- the new parameters do not exhibit the disadvantages of spectral differences, which gave the same signatures for the first two signals.
- both parameters seem to provide the same kind of information for these signals

We now proceed to application of the fault recognition method to data obtained from measurements on an industrial gas turbine into which two different blade fault cases were introduced. The two faults were a twisted compressor rotor blade—once by increasing and once by decreasing its stagger angle. The procedure described above has been applied to the measured time signals, and the corresponding geometries were calculated. The results are illustrated in Figs. 7 and 8. On the same figures, the input measured signals are shown, as well as the estimated signal once adaptation was achieved. Correspond-

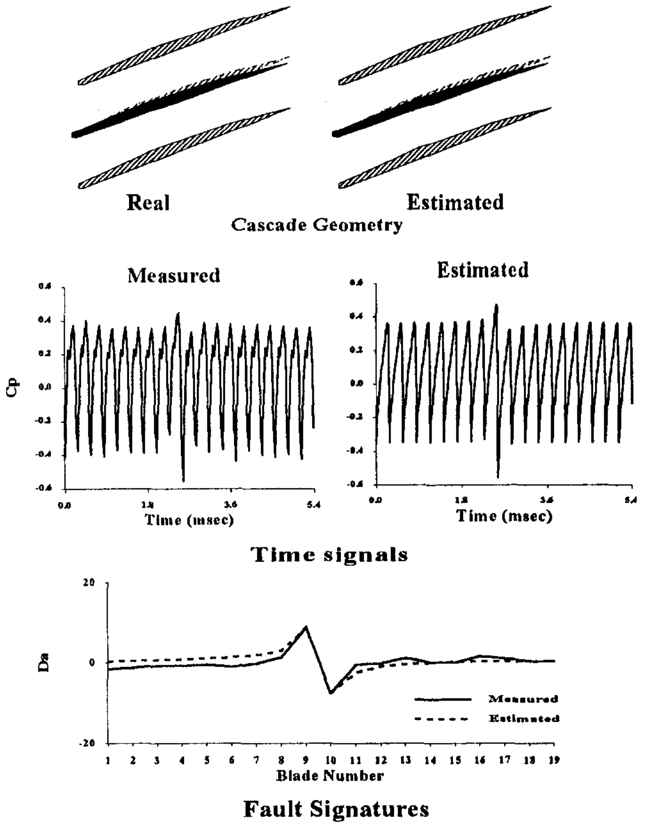

Fig. 7 Experimental and estimated time signals (duration of one period) and the corresponding fault signatures for one blade twisted (small positive twist)

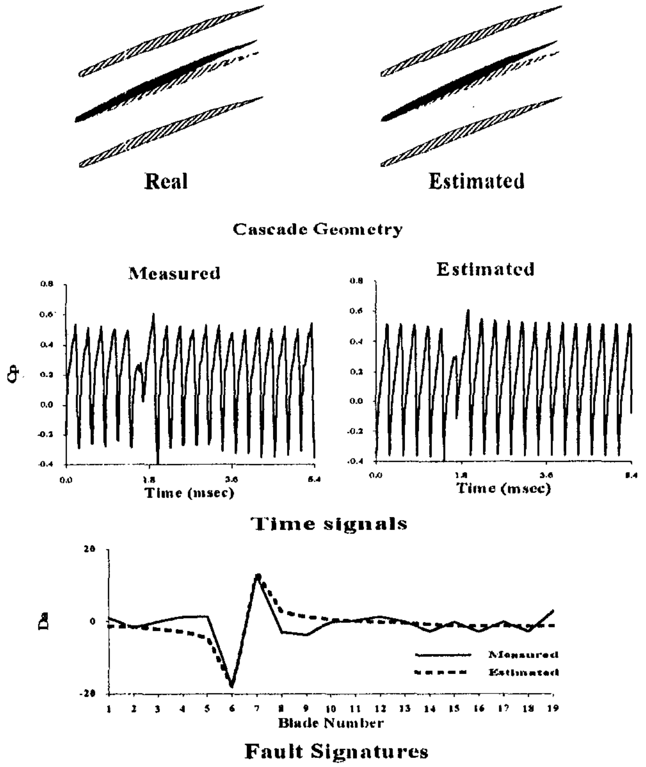

Fig. 8 Experimental and estimated time signals (duration of one period), and the corresponding fault signatures for one blade twisted (large negative twist)

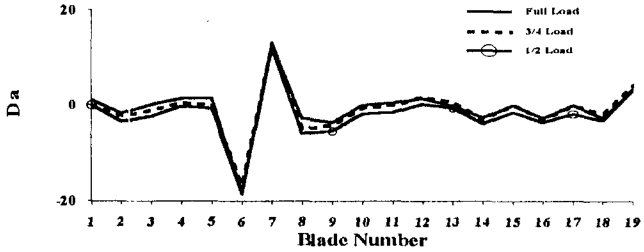

Fig. 9 Fault signatures for one blade twisted (large negative twist) for different operating conditions

ing fault signatures through which the solution was achieved are also shown in the figures.

A first observation from both figures is that the reproduced fault is identical to the actual one (small differences in the twist angle are not visible). The measured signals show remarkable similarity to the corresponding estimated ones for the two examined cases, as is shown in these figures. It should be noticed that although the experimental signals contain random noise, which is not present in the simulated ones, the presence of the twisted blade in both cases is correctly represented. This feature is also observed in the corresponding fault signatures (evaluated from test data and simulated signals) in both cases. It is remarkable to notice that the method has correctly identified the twist of the blades, which was in different directions and of different magnitudes in the two cases.

Finally, it was also verified that the twisted blade fault was identified from data at different operating conditions of the gas turbine. The fault signatures, which lead to the fault, are shown in Fig. 9. From this figure it is shown that the signatures remain the same for different operating conditions.

Further cases of application to different blade faults are illustrated in Figs. 10, 11, and 12. In these figures, the geometry of different faults (the pressure signals produced by the simulator and the corresponding signatures) are presented. It is interesting to remark that while **Da** and **Dp** are equivalent in most cases, they may provide quite different signatures in others, as shown in Fig. 12. Figure 10 indicates that the twisted blade fault is identifiable even if different twist angles exist. In Fig. 11, cases of groups of blades twisted are considered; in Fig. 12(*a*), a combination of twisted and misplaced blades is considered.

6 Discussion

We are now going to discuss some aspects of application of the proposed method. In particular, we want to put in perspective the possibilities, but also the limitations, of the proposed method.

As a first point, it must be said that the possibilities of the method rely on the reliability of the signature simulation model. The model we have used has proven to be sufficiently reliable for fault signature prediction, although it is based on a rather simple fluid dynamic solver, as discussed in more detail by Dedoussis et al. (1994). Of course, the fluid dynamic solver can be substituted by a more sophisticated one, but the advantages expected are marginal in view of a high penalty in computation time.

Implementation of the method presented above has become realistic only through the advances in development of digital computers. Performing direct simulations is achieved in a few minutes for a rotor with a realistic number of blades, on a personal computer. Solution of the inverse problem can be much lengthier on a PC, since it involves a number of ''direct'' passes. It can be much faster, however, if implemented in a parallel computer environment. The nature of the solution algorithm is such that parallelization can be effectively implemented. The authors have undertaken such an application, and performances can be characterized as ''quasi-real-time.''

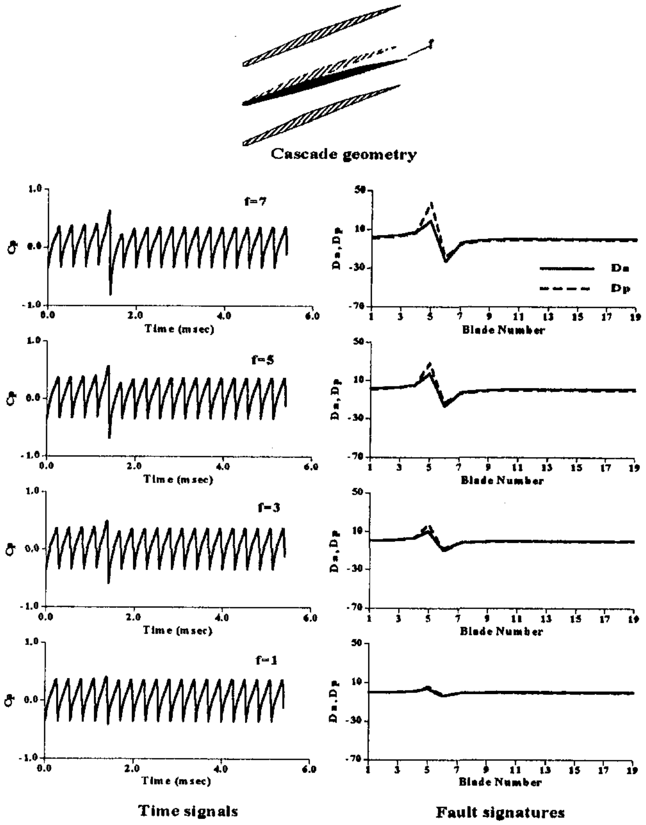

Fig. 10 Time signals and corresponding fault signatures for one blade twisted by different angles (positive twist)

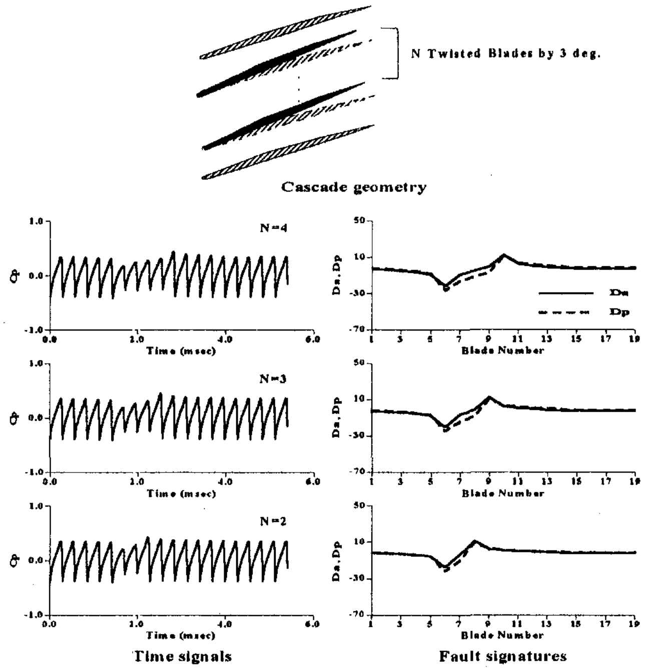

Fig. 11 Time signals and corresponding fault signatures for two, three, and four adjacent blades twisted by the same angle

The authors have actually implemented the method on a PC in a user-friendly environment. An example of one screen display is given in Fig. 13. On this figure we can see that, apart from the signals, a direct picture of a fault is obtained, together with the geometric details characterizing the fault.

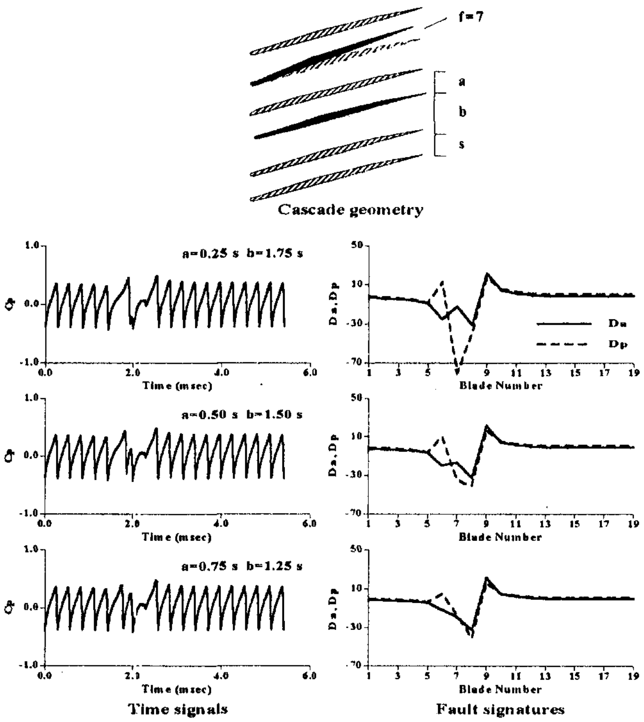

Fig. 12 Time signals and corresponding fault signatures for one twisted and one misplaced blade separated by one healthy blade (different percentages of misplacement)

The presentation of the method given above is in a generalized form so that it does not rely on a particular type of simulator or fault signature. Other kinds of fault signatures can be employed, provided they satisfy the requirements set in section 4. One additional point that has to be mentioned here is that suitability for incorporation in the inverse approach is also related to the solution algorithm of the nonlinear system.

One particular desirable property of fault parameters, in this respect, is that they must change smoothly with the parameters characterizing the faults. Nonsmooth changes may induce problems to the iteration scheme. On the other hand, it is useful to examine how the fault parameters behave in function of the fault geometric parameters. Such a study can reveal if one-valued dependence exists, or if there are ranges of variables where multivalued solutions may be possible. This is a part of

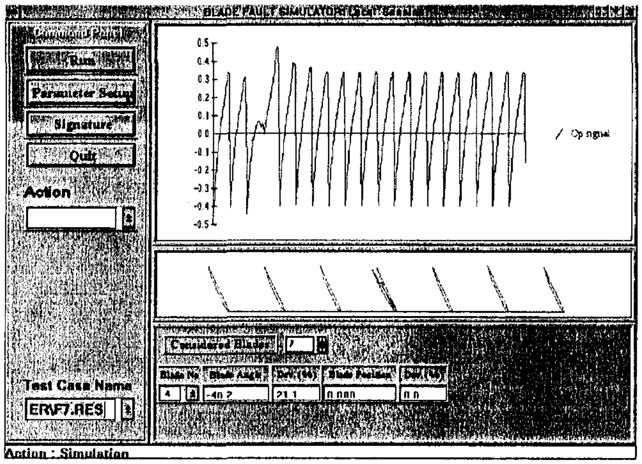

Considered Blades: 7

Blade No	Blade Angle	Dev.(%)	Blade Position	Dev.(%)
4	-40.2	21.1	0.000	0.0

Test Case Name: ERVF7.RES

Action : Simulation

Fig. 13 A Typical screen from the interactive environment materializing the present method a study when the method is being set up. A study of this type is reported by Stamatis et al. (1996).

It may be useful here to point out some of the advantages offered by the present approach with respect to approaches based on fault signatures. Of course, the first obvious advantage is the form in which the result is offered, which needs no interpretation. Another significant advantage, however, is the elimination of the need for a fault signature database. On top of that, the methods provides information that would have needed very extensive databases if the signature approach were followed. For example, this method gives a possibility for estimating the twist angle in a continuous manner. Fault signatures for many values of the twist angle would have to be stored in order to have the same possibility for the signature approach.

Finally, it should be mentioned that the faults covered in this work are essentially limited to those for which a good simulation capability exists. The steps of the procedure apply, however, to any case for which the modeling possibility exists independently of nature of measured quantities or kind of faults. In this respect, more types of faults could be covered. For example, if the airfoil shape is handled through parametric expressions, faults altering this shape could be covered (e.g., namely, blade deterioration). On the other hand, extension to data of a different nature is, in principle, possible. If, for example, a reliable model for casing vibration response to faults becomes available, then it is possible that this procedure can be implemented to casing vibration data.

7 Conclusions

A new method for direct identification of faults in blades of gas turbine components has been presented. The method provides a direct geometrical picture of blade faults, and does not rely on fault signatures and related procedures. Its capability to successfully identify faults was demonstrated by application to experimentally available data.

Although specific algorithms and fault parameter definitions have been employed in the test cases examined, the method is presented in a generalized formulation. Techniques materializing particular aspects, as, for example, the fluid dynamic simulator or the fault signature definition, could be substituted by different ones. In this way, the method, as presented here, offers the basis for an extension to other diagnostic applications covering data or faults of a nature different from the ones examined here.

References

Cempel, C., 1991, *Vibroacoustic Condition Monitoring*, Ellis Horwood Ltd., London.

Dedoussis, V., Mathioudakis, K., and Papailiou, K., 1994, "Numerical Simulation of Blade Fault Signatures from Unsteady Wall Pressure Signals," ASME paper No. 94-GT-289.

Loukis, E., Wetta, P., Mathioudakis, K., Papathanasiou, A., and Papailiou, K. D., 1991, "Combination of Different Unsteady Quantity Measurements for Gas Turbine Blade Fault Diagnosis," ASME paper no. 91-GT-201.

Loukis, E., Mathioudakis, K., and Papailiou, K. D., 1993, "A Methodology for the Design of Automated Gas Turbine Diagnostic Systems," ASME paper no. 93-GT-47.

Mathioudakis, K., Loukis, E., and Papailiou, K. D., 1990, "Casing Vibration and Gas Turbine Operating Conditions," ASME JOURNAL OF ENGINEERING FOR GAS TURBINES AND POWER, Vol. 112, No. 4, pp. 478–485.

Mathioudakis, K., Papathanasiou, A., Loukis, E., and Papailiou, K. D., 1991, "Fast Response Wall Pressure Measurement as a Means of Gas Turbine Blade Fault Identification," ASME JOURNAL OF ENGINEERING FOR GAS TURBINES AND POWER, Vol. 113, No. 2, pp. 269–275.

Mathioudakis, K., 1995, Diagnostic Techniques Based on Fast Response Measurements, *Measurement Techniques*, Von Karman Institute Lectures Series 1995-01.

Meher-Homji, C. B., 1995, "Blading Vibration and Failures in Gas Turbines: Part C—Detection and Troubleshooting," ASME paper no. 95-GT-420.

Stamatis, A., Aretakis, N., Mathioudakis, K., Papailiou, K., 1996, "Using HPC for Early Fault Diagnosis in Gas Turbines," Hipercosme CS2.D3 Report, ESPRIT 20059 RTD Project.

Van den Braembusche, R. A., 1994, Inverse Design Methods for Axial and Radial Turbomachines, *Numerical Methods for Flow Calculation in Turbomachines*, Von Karman Institute Lecture series 1994-06.

Heavy-Duty Gas Turbine Plant Aerothermodynamic Simulation Using Simulink

G. Crosa

F. Pittaluga

A. Trucco

Universita' di Genova,
Istituto di Macchine e Sistemi Energetici,
Italia

F. Beltrami

A. Torelli

F. Traverso

Ansaldo Energia, Genova, Italia

This paper presents a physical simulator for predicting the off-design and dynamic behavior of a single shaft heavy-duty gas turbine plant, suitable for gas-steam combined cycles. The mathematical model, which is nonlinear and based on the lumped parameter approach, is described by a set of first-order differential and algebraic equations. The plant components are described adding to their steady-state characteristics the dynamic equations of mass, momentum, and energy balances. The state variables are mass flow rates, static pressures, static temperatures of the fluid, wall temperatures, and shaft rotational speed. The analysis has been applied to a 65 MW heavy-duty gas turbine plant with two off-board, silo-type combustion chambers. To model the compressor, equipped with variable inlet guide vanes, a subdivision into five partial compressors is adopted, in serial arrangement, separated by dynamic blocks. The turbine is described using a one-dimensional, row-by-row mathematical model, that takes into account both the air bleed cooling effect and the mass storage among the stages. The simulation model considers also the air bleed transformations from the compressor down to the turbine. Both combustion chambers have been modeled utilizing a sequence of several sub-volumes, to simulate primary and secondary zones in presence of three hybrid burners. A code has been created in Simulink environment. Some dynamic responses of the simulated plant, equipped with a proportional-integral speed regulator, are presented.

Introduction

Efficiency and reliability of heavy-duty gas turbine plants have been considerably improved over the past two decades, with the result that these units have gained a significant fraction of the electric-power market all over the world. This fact and the interest addressed in recent years to the gas-steam combined plants are also responsible for a significant impulse toward development of numerical simulation tools for detailed analyses of off-design performance and dynamic behavior of gas plants. Since gas-turbine units are often required to rapidly follow frequent changes in power demand, the prediction of their dynamic behavior is very important both to help the design of plant components and control devices, and to assess optimal operational procedures, e.g., proper actions suitable to counter performance deterioration in service.

Several dynamic simulation models for heavy-duty gas power-plants are described in literature: some of them in the frequency domain (Rowen, 1983, 1992; Hannet, 1993), others in the time domain (Bolfo, 1990; Watts, 1992; Saravanamuttoo, 1992; Cohen, 1987; Schobeiri, 1994).

The present authors have developed some experience on modeling gas power plants, and, in previous papers (Pitto et al., 1993; Crosa, 1995a, b) have presented dynamic-behavior analyses of noncontrolled and controlled heavy-duty plants. In these simulations, mathematical models assume as state variables density, velocity, and static pressure of the fluid in addition to wall temperature and rotational speed. In consequence of this choice, the simulation proved to be accurate and satisfactory, but the differential equations, describing plant components that resulted were rather complex. Moreover, the code, written in FORTRAN, using a set of Nag routines as a mathematical solver, is powerful but not easy to use by others, especially from industry.

With the aim of simplifying dynamic equations by introducing state variables technically more significant, a new mathematical model has been studied with mass flow rate, static pressure, and static temperature as state variables, in addition, of course, to wall temperature and rotational speed.

The new code, developed in collaboration between IMSE, University of Genoa, and Ansaldo Energia, operates within the Simulink environment (Mathworks software) and can be implemented on personal computers. The program is readily understandable by performance analysts as well as development and management engineers, usually not specialists in simulation. It also allows a more precise simulation of the plant components by introducing FORTRAN modules describing individual components or parts of them into Simulink blocks. In the power plant case presented here there are three 32-bit FORTRAN 77 modules, each regarding: the row-by-row analysis of the turbine that accounts for the blades' geometry and the combustion chamber split in sub-volumes according to the local processes and the bleed cooling system.

The calculations discussed here have been performed in relation to a typical heavy-duty gas plant, but the components' description can be easily updated, modified, or rearranged within the same computer program structure without difficulty.

Mathematical Model of the Gas-Plant

The gas-turbine plant taken as an example in this paper has the following performance data: power output 65 MW; rotational speed 5400 rpm; maximum pressure 16 bar. The plant is characterized by elevated turbine-inlet temperatures that require intensive turbine blade cooling. The number of stages is 17 for the compressor and 4 for the turbine. There are two offboard silo-type combustion chambers: in the case of premixed operation, flame temperatures are kept low to counter NO_x formation; in the case of the diffusion-flame regime, which is the case here discussed, water or steam can be injected into the primary zone.

Contributed by the International Gas Turbine Institute and presented at Turbo Asia '96, November 5–7, 1996, Jakarta, Indonsia. Manuscript received by the ASME Headquarters January 31, 1996. Paper No. 96-TA-22. Associate Technical Editor: J. N. Shinn.

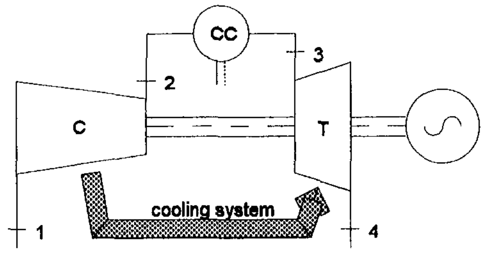

Fig. 1 Plant fluid flow diagram

The plant, in mathematical modelling terms, is a multivariable, highly nonlinear stiff process and consists of a set of algebraic and time dependent ordinary differential equations. The evolving fluid has been considered subject to mass, momentum, energy storage, and also exposed to heat transfer from the wall, taking into account the metal-stored energy. The fluid is assumed to be a mixture of perfect gases with temperature dependent specific heats and variable chemical composition in the different plant stations.

Simulation follows the "intercomponent volume" method that assumes every block to be as described by the steady-state component, followed by a fictitious volume where mass, momentum, and energy storage takes place. The method was improved so that no explicit reference to a "physical volume" exists (Crosa, 1995a, b).

The model in the time domain is shortly given as

$$\dot{x} = f(x, y, u) \quad (1)$$

$$0 = h(x, y, u), \quad (2)$$

where x, y, u are, respectively, the state vector, the output vector, and the input vector, and f and h are the function vectors. To solve the nonlinear stiff equation set, one of the implicit methods provided by Simulink mathematical software was used (gear method).

For the whole noncontrolled plant, the input variables are the atmospheric pressure and temperature, the VIGV angle, the fuel mass flow rate, and the load power.

In Fig. 1 and Fig. 2, the fluid flow and the steady-state information diagrams of the gas turbine unit are shown: the block R, downstream of the turbine T, represents the heat recovery steam generator, in case it is present. Figure 3 shows the main layout of Simulink plant dynamic model.

In the dynamic analysis, every block, represented in Fig. 2 a single component, is split into three or more blocks, described by a first-order differential equation in a function of time.

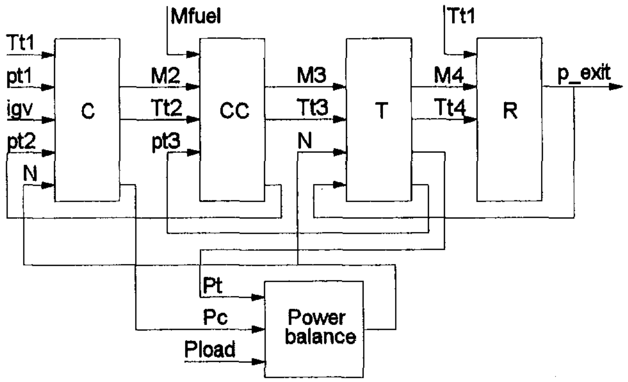

Fig. 2 Steady-state plant information diagram

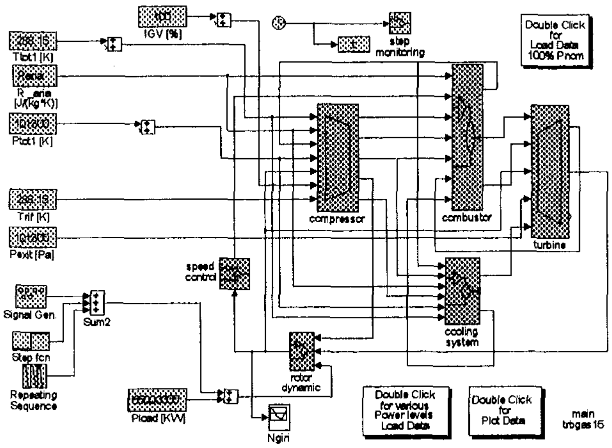

Fig. 3 Simulink main layout of plant model

Compressor. In the present case, the 17-stage transonic compressor has variable inlet guide vanes (VIGV) and 2 rows of adjustable-pitch stationary vanes. The drawn-off pressures of the 5 air bleeds optimize the supply of cooling air to the turbine bladings.

The off-design, steady-state behavior is described (in the form of tabular data) by the total pressure ratio and efficiency characteristic maps, given in terms of "corrected quantities" evaluated at the inlet conditions. In the plant model the compressor has the following five independent variables: the inlet total

Nomenclature

a_1, a_2 = compressor inlet and outlet sound speed
c_1, c_2 = compressor inlet and outlet flow speed
C_C = compressor thermal capacity
c_p = specific heat capacity at constant pressure
c_v = specific heat capacity at constant volume
$K_{\mathrm{Cint}}, K_{\mathrm{Cext}}$ = internal and external compressor thermal exchange coefficient
L_C = compressor fluid inductance
$\dot{m}_1, \dot{m}_2$ = compressor inlet and outlet mass flow
M_{a1}, M_{a2} = compressor inlet and outlet Mach number
N = rotational speed
p_1, p_2 = compressor inlet and outlet static pressure
P_C = compressor absorbed power
p_{t1}, p_{t2} = compressor inlet and outlet total pressure
R_{aria} = relative air constant
T_1, T_2 = compressor inlet and outlet static temperature
T_{pC} = compressor wall static temperature
T_{t1}, T_{t2} = compressor inlet and outlet total temperature
S_C = compressor surface
T_{rif} = reference temperature
V_C = compressor volume

Greeks

β = compression ratio
ρ_1, ρ_2 = compressor inlet and outlet density
Φ_C = compressor wall thermal flow
Ω_1, Ω_2 = compressor inlet and outlet flow area

Superscripts

$*$ = "star" quantities

pressure and temperature, the outlet total pressure, the rotational speed, and the VIGV angle.

The equations set of the dynamic mathematical model is presented in the Appendix. For sake of simplicity, the equations set is relative to the compressor as a single block, whilst, in the simulation, the compressor can be represented by either a characteristic map of the entire machine or by the five characteristics of the serial of five partial compressors, interlinked by dynamic volumes in which only the mass storage is taken into account.

The partial-compressor characteristics have been derived using a row by row one-dimensional Ansaldo code, and the results are transferred to Simulink code in form of tabular data. This latter feature yields improved values for the pressures and temperatures of air cooling bleeds at the inlet of the pipe cooling system and upstream of the blow-off valves for surge protection.

The compressor Simulink implementation, as an ensemble of five stage-groups, is presented in Fig. 4, whilst the Fig. 5 is obtained by expanding the former. The steady-state values are calculated by linear interpolation (performed by appropriate Simulink blocks, named "Look-Up-2D tables") of data tables that are charged in the Matlab workspace through proper input files; the model can run with different characteristic maps by changing these files.

Combustion Chamber Module. In order to predict, with a certain detail level, the operative behavior of the combustion chamber, both from a thermo-chemical and a pollutant emission point of view, while maintaining an adequate numerical efficiency, an extended correlative approach has been set up, which, in connection with a proper zonal subdivision of the combustor module, would capture, for each specific zone, the main effects of the locally "prevailing" processes. The selection, the cross comparison, and the calibration of the correlations adopted were basically guided by a rather accurate check of their respective outcome, both in values and in trends, in relation to the field data available for the heavy-duty typology of gas turbine plants here under investigation. It is important to remark how effective the technique has turned out, toward a successful correlation assessment, of carefully checking predictions versus specifications of the physical variables (like the local residence times, temperatures, etc.), rather than versus adjustment of numerical coefficients. This helped particularly in the phase of discarding many correlation "structures" wherein acceptable overall predictions could be achieved only through specifications of the said variables that appeared to be clearly wrong for heavy-duty applications.

The combustor operational conditions to be modeled are extremely wide and diversified: they encompass both the diffusion and premixed regimes for gaseous fuel as well as the liquid-fuel diffusion flames with and without water or steam injection. In addition, for each regime, the entire power range from idle to full load is to be predicted. The specific application here under study refers to a natural-gas diffusion-flame operation (dry), and this will be now discussed. The complete models' structure is reported in detail, together with extensive parametric analyses of results, final choices' motivations, and relevant validating comparisons, in Trucco (1996).

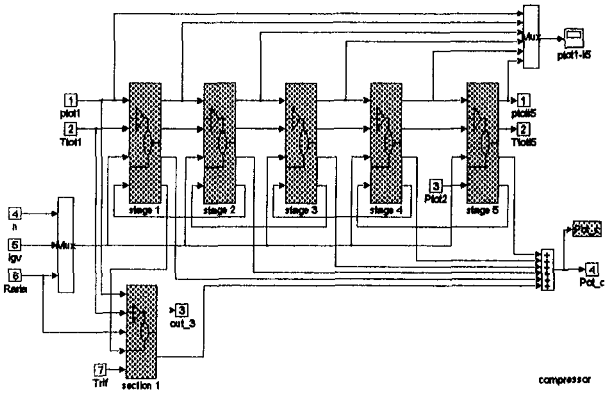

Fig. 4 Multistage compressor Simulink layout

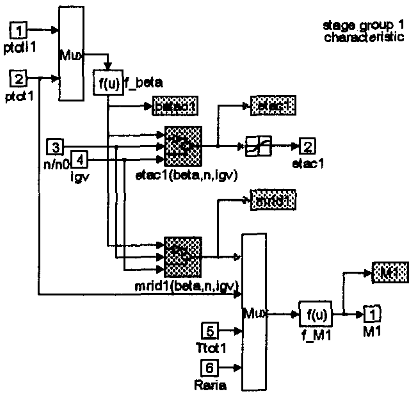

Fig. 5 Further Simulink sub-scheme of compressor

Combustors' geometries are of the silo-like typology, with three burners, 120 deg apart from each other. The modelization has maintained this angular partition, superimposing a longitudinal zonal subdivision in line with the locally prevailing processes, assumed to take place from inlet to combustor outlet. In dependence of the operational regime, the "sub-volumes' framework" is different for each regime-specific module.

The preliminary step to be performed, common to all regimes, is that of providing the adiabatic flame temperature as a function of chamber pressure, fuel H/C composition, equivalence ratio, and reactants' inlet conditions. To this aim, resort has been made to the functional expression given in Gulder (1986a) as Eq. (1), yielding flame temperature behavior as derived from the extended application of a detailed chemical equilibrium code. Though valid for jet fuels composition, the same parametric dependence on H/C ratio has been retained also for methane, after checking its substantial validity, at least within the approximation levels here required. By adopting the same approach, also the specific heats, the mean molecular weights and the densities of combustion gases can be evaluated, together with the partial pressures of CO_2 and H_2O. The expressions that have been set in the program are taken from Gulder (1986b) and Gulder (1988).

For the methane diffusion-flame operation, the combustor, in addition to the three angular partitions (each with $\frac{1}{3}$ of total mass flow in normal conditions), is sub-divided lengthwise into three successive zones, named primary, secondary, and mixed-out. Primary sub-volumes are the conceptual (more than geometrical) regions where the near-stoichiometric primary flames are located. Due to their turbulent characteristics and high spatial irregularity, they should be interpreted only in a global "effective" sense. After detailed checks and comparisons (Trucco, 1996), the typical assumptions for the locally prevailing equivalence ratio φ have turned out around 0.97 at full power, linearly decreasing with load (more precisely, decreasing with the overall φ) down to about 0.93 at idle condition. These values seem quite acceptable, if one just thinks that, to yield a more physically correct local temperature, the "primary-effective" φ-level should also take care of the increasing heat losses from flame front as the load is decreased.

The primary zone NO_x emissions' predictions are based on the following functional expression, given as Eq. (8) in Rizk and Mongia (1993):

$$NO_x = 10^{13} \times (p/1.4 \times 10^6)^{aa} \exp(-71442/T) \times A, \quad (3)$$

where p and T are pressure and local temperature, and

$$aa = 11.95 \times \exp(-\varphi/7.56) - 10.0$$

$$A = (7.56 \times \varphi^{-7.2} - 1.6) \times \tau^{0.64}.$$

Primary zone temperatures are evaluated by utilizing the just discussed φ-values, whilst the local residence times τ are assumed in the range 1 to 3 m/s. This latter assumption is roughly derived by using experimental thicknesses for methane diffusion flames (taken, e.g., from Andrews, 1972) divided by the local flow velocities. Anyhow, the approximation is balanced by observing that specification of τ is obviously important, but not most critical, for the correlation outcome.

Secondary sub-volumes are conceived to be those where, still keeping a kind of individual-burner dependence, the flame reaches about its nominal φ, by mixing with secondary air. In these ''effective'' zones, NO_x formation is predicted by adopting the parametric expression given as Eq. (11) in Rizk and Mongia (1993):

$$NO_x = 10^{13} \times (p/1.4 \times 10^6)^{aa} \exp(-71442/T) \times B, \quad (4)$$

where aa is the same as above, and

$$B = (1.172 \times \varphi^{-4.56} - 0.6) \times \tau^{0.876}.$$

Here, to compute temperatures, φ-values are assumed to be already near the nominal ones, since the additional dilution air fed through the combustor walls, for cooling purposes, is minimal. This air mass-flow will be taken care of in the mixed-out sub-volume. To give some values, if the full-power overall φ-levels are 0.45, those in secondary zones, ahead of cooling-air mixing, are taken about 0.48. Residence times in secondary sub-volumes are conceptually associated with those in the swirl-induced recirculating zones, whose spatial extensions and in/out mass flow diffusion are assumed on mostly empirical bases, but supported by in-house flow visualizations and theoretical three-dimensional combustive Navier-Stokes analyses, in addition to available published data (Trucco et al., 1996; Beltrami et al., 1996a, b). Typical residence times result in the order of 20 m/s. The implied approximation is here balanced by observing the small net-addition of NO_x in secondary zones, due to the already strongly lowered temperatures.

No further NO_x formation is assumed in the (single) mixed-out sub-volume, corresponding to the aft part of the combustor, wherein no angular variation of variables is considered to be present any longer. From simple bulk flow analyses, it turns out, on a first approximation, that transit times in this sub-volume result of the same order of residence times in secondary zones, e.g., at full mass-flow, transit times in this volume are about 23–25 m/s, so that the overall combustor residence time could be set at 45 m/s. This value is important for evaluating emissions of other pollutants.

Particularly in connection with CO emissions, an observation must be made. In Rizk and Mongia (1993), in addition to NO_x, CO emission correlations are also given, which, in the case under discussion here (a heavy-duty situation versus the airborne combustors of said reference), have proved to yield inconsistent results (see Trucco et al. (1996) for details). Since a main variance between airborne and heavy-duty combustors is the large difference in available volumes and residence times related to post-flame processes, the above inconsistencies are most probably due to the critical influence played by the recombination processes in final CO-levels assessment, whilst their influence on NO_x was minimal. After careful checks and comparisons, also on the base of combustor manufacturer's direct operational outcome, the best choice of a functional expression for CO prediction turned out to be that given as Eq. (28) in Lefebvre (1995):

$$CO = 0.18 \times 10^9 \exp(7800/T_l)/[p^2\tau(\Delta p/p)^{0.5}], \quad (5)$$

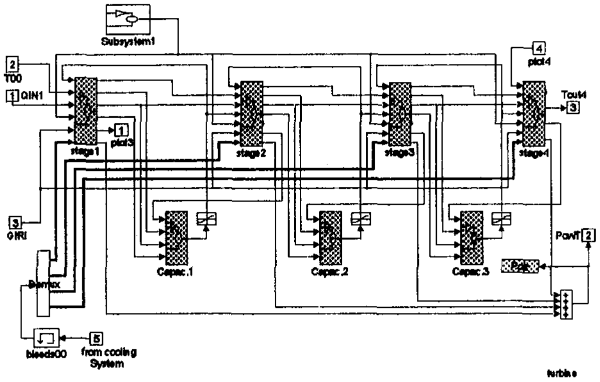

Fig. 6 Four-stage turbine Simulink layout

where T_l is primary-zone temperature, τ is overall residence time, and $\Delta p/p$ is the nondimensional pressure drop, governing the fuel/air mixing process.

Finally, for UHC assessment, Eq. (7) of Rizk and Morgia (1993) is adopted, namely,

$$UHC = 0.755 \times 10^{11} \exp(9756/T_l)/[p^{2.3}\tau^{0.1}(\Delta p/p)^{0.6}] \quad (6)$$

with the same meaning of parameters in Eq. (5). Again, validation of (6) for the present situation is discussed in Trucco (1996).

The simulation program of the combustion chamber has been written using 32-bit FORTRAN 77 instructions that is inserted into a Simulink block and properly linked to other component blocks. Thermochemical and emission data are thus obtained together with the information essential for plant modeling and component matching, like combustion efficiency, pressure loss and stability limits.

In view of the large volume of the combustion space available in industrial gas turbine, mass, momentum, and energy storage is to be taken into account in transient response simulation. The dynamic behavior is then computed, adding three differential equations to the steady-state equation set, and introducing a simple lag-time block for the combustion delay.

Turbine. The 4-stage turbine is described by a one-dimensional row by row Ansaldo mathematical model, suitable to predict the off-design turbine behavior quantifying every source of inefficiency. The cooling effects of the air-bleeds in each blade row is taken into account, with thermodynamic cooling loss evaluation. The cooling flows in a high temperature turbine are typically about 30 percent of compressor inlet airflow, thus playing an important role in cycle and in every component efficiency prevision. Their accurate modeling flow is necessary for a reliable performance analysis. The input variables of the turbine block are mass flow rate and total temperature upstream of the turbine, exhaust static pressure, rotational speed, and temperature and pressure of cooling bleeds. The code is written in FORTRAN 77 and consists of a series ''sequential calculations'' moving upward from the last stage to the first. The output information of one stage allows to calculate the next stage and so on, with successive substitution of the guessed variables, by a ''trial and error'' method, up to convergence. Since the equations set, in the turbine calculation section, is solved sequentially not simultaneously, this makes its use difficult in the Simulink environment, producing a long calculation time.

The problem has been solved splitting the turbine into four partial mono-stage turbines. This is possible because in dynamic situations the mass storage effect among the stages is to be taken into account; therefore, the turbine is modeled with interconnecting 4-blocks of mono-stage turbine (incorporated in Simulink as 4 mex-files) with three inter-volumes with mass storage place. The Simulink scheme is presented in Fig. 6. In this situation the ''trial and error'' code is applied four times. This procedure saves computing time.

Cooling System. Thermodynamic parameters of the four air bleeds along the way from the compressor to the turbine blades are evaluated, solving an algebraic equation set regarding the path-net externally and internally to the group. The air bleeds follow different ways. The turbine first rows of stator blading is supplied with precooled air that passes through a heat exchanger and is boosted by a blower. The rotor disks and blades are cooled by air passing through the hollow shaft.

A FORTRAN code describes and solves the cooling system equation set. The air-bleed pressures and temperatures at the inlet of the turbine are determined so that row by row the energy balance in the mixing process with the main flow can be computed.

Computer Program

The gas turbine code runs in a Simulink package on a personal computer. Simulink graphically facilitates the model definition using block diagram windows. The model is created by connecting, with graphical lines, a succession of blocks that can be simple blocks (available in library as integrator, derivative, sum, or product etc.) or more complex blocks, built by the user with Matlab language.

To reduce the model complexity some plant component is described in Matlab program or in FORTRAN code. The 32-bit MicroWay FORTRAN 77 compiler was used as recommended by the Mathworks Inc.. During the compilation of every FORTRAN block, two appropriate interface routines have been linked to the main routine to translate the FORTRAN into the Simulink environment that is settled in C language.

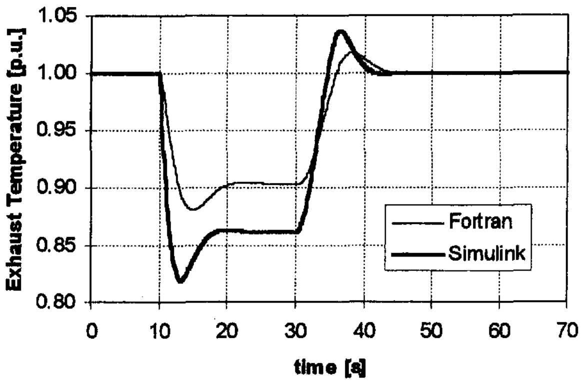

Fig. 9 Exhaust temperature comparison

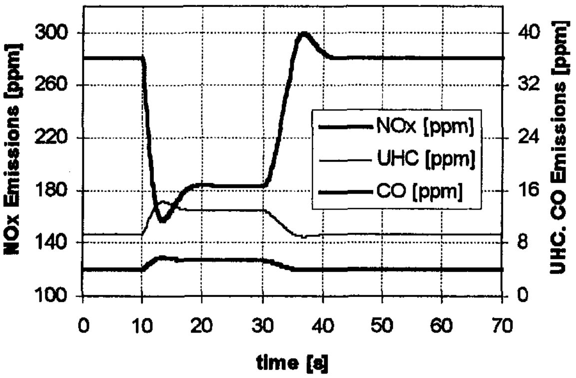

Fig. 10 NO_x, UHC, and CO emissions

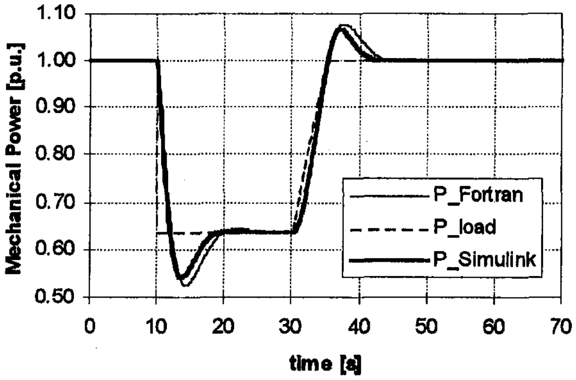

Fig. 7 Mechanical powers comparison

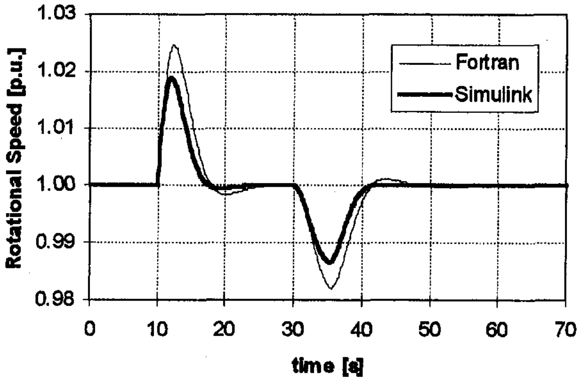

Fig. 8 Rotational speed comparison

Results and Discussion

The nonlinear, time dependent model is able to simulate wide load variations. In Figs. 7, 8, 9, and 10 the transient plots of important variables of the plant as functions of time are shown, connected with a request load schedule. Starting from a steady-state condition at 90 percent of rated load a step of −36 percent of initial value is imposed, followed by a stabilising interval of 20 seconds and by a load ramp of +36 percent in 5 *s* (the plotted values are in per unit of initial value). The VIGV angle is kept constant at 100 percent, the fuel mass flow is governed by a PI speed controller, and the methane combustion takes place as a diffusion flame, without steam injection.

The first three figures display the transient response comparison of the new Simulink model with the results obtained using a previous FORTRAN code (Crosa, 1995a, b).

Though the codes are rather different in both state variables and component description, the curves for power and rotational speed are rather similar. The the exhaust temperature time histories are in disagreement, mainly owing to the different control systems and very different turbine models.

In Fig. 10, the CO, UHC, and NO_x emissions during the transient, estimated with the current model, are shown. The code allows simulating strong transients, but the run times are not short. The analysis of the dynamic behavior of the plant for a step reduction of the request load of 50 percent from nominal conditions requires about 25 min on a Pentium 90 PC for 50 *s* of simulation time.

The accuracy of the result depends above all on the validity of the models used to represent the off-design component behavior. To study strong transients, the characteristic maps of turbomachineries have to be effective in a large range of operation, and this task is not easy to obtain. However, there is a separation between the regime range where accuracy is very important and regimes where calculations can only show the general behavior of similar power plants.

For instance, during the starting procedure of a gas plant, the compressor can pass through the rotating stall region and the mass flow rate in the cooling system can even be inverted. It is necessary to change the stagger of the blades, to blow off some air at different stages, and to close some valves in the cooling system. These procedures can be analyzed. The stall and surge characteristics of the compressor are generally not well known, but the simulation can give important indications for a safe design of gas turbine plants.

Conclusion

A dynamic gas turbine simulation program has been developed and implemented on a personal computer using Simulink. The code is not simple, in spite of the effort of excluding superfluous information. The compression and expansion simulation takes into account the air bleeds and the cooling effect; the combustion chamber is complex and considers different combustion processes, with different fuels, with or without steam, and can determine the CO, UHC, and NO_x emissions. Some external apparatuses are modeled, as the bleed system with blower and heat exchanger, considering the actual pipe geometry, and also the electrical generator.

The code accurately reflects the steady-state performance of the actual plant. As experimental data in transient conditions are by now not available, in order to test the capability of the program to simulate the dynamic plant behavior, a comparison between a previous FORTRAN code and the new Simulink model was carried out. The comparison provided quite satisfactory results concerning power, rotational speed, and thermo-fluo-dynamic variables, but not exhaust emissions because the were not calculated in the old code.

The new modeling technique presented here yields results as accurate as previous methods, but, in addition, allows a more detailed description of the plant, reducing the development time using the built-in analysis tools of Matlab.

The code is modular and the component models can be easily replaced by others more simple or complex (provided, for instance, by FORTRAN programs), preserving, of course, the same input and output variables. Different power and architecture can be analyzed without problems.

The implemented model will be improved by both extending the range of turbomachinery characteristic validity in order to simulate start-up and shut-down transients and by adding the control system simulation that, using Simulink tools, can be introduced without difficulties.

References

Andrews, G. E., and Bradley, D., 1972, "The Burning Velocity of Methane-Air Mixtures," *Combustion and Flame,* Vol. 19, pp. 275–288.

Beltrami, F., Torelli, A., Fattori, M., and Pittaluga, F., 1996a, "Theoretical Predictions of Thermo-Chemical Performances and Pollutant Emissions of Heavy-Duty Gas Turbine Combustors by Means of Extended-Parameterization Modeling," Proc. Workshop Turbomachinery '96, IMSE, University of Genoa, Italy.

Beltrami, F., Mennucci, M., Luccoli, R., Traverso, S., and Pittaluga, F., 1996b, "Lagrangian-Eulerian 3D Navier-Stokes Simulation of Combustion Processes Inside a Gas Turbine Combustor for Power Generation," Proc. Workshop Turbomachinery '96, IMSE, Univ. of Genoa.

Bolfo, S., Berta, G. L., Cori, R., Del Re, S., Durelli, E., and Pini Prato, A., 1990, "Modello per l'analisi dinamica di turbine a gas," ATI Sezione Toscana—Sezione Emilia Romagna, Atti del IV Convegno Nazionale Gruppi Combinati Prospettive Tecniche ed Economiche, Firenze, 31 Maggio.

Cohen, H., Rogers, G. F. C., and Saravanamuttoo, H. I. H., 1987, *Gas Turbine Theory,* 3RD ed., Longman's, London, England.

Crosa, G., Ferrari, G., and Trucco, A., 1995a, "Modelling and Decoupling the Control Loops in a Heavy-Duty Gas Turbine Plant," ASME Paper No. 95-GT-61, International Gas Turbine and Aeroengine Congress and Exposition, Houston, Texas, June 5–8.

Crosa, G., Ferrari, G., Torelli, A., and Troilo, M., 1995b, "Nonlinear an linearized model of a heavy-duty gas turbine plant," ASME Paper No. 95-CTP-88, Cogen-Turbo Power Conference, Vienna-Austria, Aug. 23–25.

Gulder, O. L., 1986a, "Flame Temperature Estimation of Conventional and Future Jet Fuels," ASME JOURNAL OF ENGINEERING FOR GAS TURBINES AND POWER, Vol. 108, pp. 376–380.

Gulder, O. L., 1986b, "Combustion Gas Properties: Part II . . . ," ASME JOURNAL OF ENGINEERING FOR GAS TURBINES AND POWER, Vol. 108, pp. 455–459.

Gulder, O. L., 1988, "Combustion Gas Properties: Part III . . . ," ASME JOURNAL OF ENGINEERING FOR GAS TURBINES AND POWER, Vol. 110, pp. 94–99.

Hannet, L. N., Afzal, K., 1993, "Combustion Turbine Dynamic Model Validation From Tests," *IEEE Trans. of Power Systems,* Vol. 8, No. 1, Feb., pp. 152–158.

Lefebvre, A. H., 1995, "The Role of Fuel Preparation in Low Emissions Combustion," ASME Paper No. 95-GT-465.

Pitto, P., Troilo, M., Trucco, A., 1993, "A Model of the Dynamics of an Heavy-Duty Gas Turbine Plant," ANIPLA International Meeting, Milano, 23–25 November.

Rizk, N. K., and Mongia, H. C., 1993, "Semianalytical Correlations for NO_x, CO, and UHC Emissions," ASME JOURNAL OF ENGINEERING FOR GAS TURBINES AND POWER, Vol. 115, pp. 612–619.

Rowen, W. J., and Van Housen, R. L., 1983, "Gas Turbines Airflow Control for Optimum Heat Recovery," *Trans. of the ASME,* Vol. 105, Jan., pp. 72–79.

Rowen, W. J., 1983, "Simplified Mathematical Representations of Heavy-Duty Gas Turbines," ASME *Journal of Engineering for Power,* Oct. Vol. 105, pp. 865–869.

Rowen, W. J., 1992, "Simplified Mathematical Representations of Single Shaft Gas Turbines in Mechanical Drive Service," *Turbomachinery International,* July/Aug., pp. 26–32.

Saravanamuttoo, H. I. H., 1992, "Component Performance Requirements," AGARD Lecture Series 183: Steady and Transient Performance Prediction of Gas Turbine Engines, May.

Shinskey, F. G., *Process Control Systems,* McGraw-Hill International Editions, New York.

Shobeiri, M. T., Attia, M., and Lippke, C., 1994, "GETRAN: A Generic Modularli Structured Computer Code for Simulation of Dynamic Behaviour of Aero and Power Generation Gas Turbines Engines," ASME JOURNAL OF ENGINEERING FOR TURBINES AND POWER, Vol. 116, pp. 483–494.

Trucco, A., Troilo, M., and Pittaluga, F., 1996, "Modeling the Ansaldo Gas Turbine Plant," IMSE Report 1037 on Research Contract No. C.223.94, University of Genoa, Apr.

Yonghong, W., 1991, "A New Method of Predicting the Performance of Gas Turbine Engines," ASME JOURNAL OF ENGINEERING FOR GAS TURBINE AND POWER, Jan. Vol. 113, pp. 106–111.

APPENDIX 1

The whole equation set for the compressor is described by the following equations (here the compressor is presented as a unique block for simplicity sake). The "star quantities" are used to evaluate the variables related to the component characteristic maps.

From the continuity equation,

$$\frac{\partial T_2^*}{\partial t} = \frac{T_2^*}{p_2^*} \cdot \left[\frac{\partial p_2^*}{\partial t} - \frac{R T_2^*}{V_C} \cdot (\dot{M}_1 - \dot{M}_2) \right]. \tag{7}$$

From the momentum (fictitious) equation,

$$\frac{\partial \dot{M}_2}{\partial t} = \frac{1}{L} \cdot (p_{t2}^* - p_{t2}). \tag{8}$$

From the energy equation:

$$\frac{\partial p_2^*}{\partial t} = \frac{R_{\text{aria}}}{c_{v_2 *}} \cdot \left\{ \frac{1}{V_C} [\dot{M}_1 c_{p1} (T_{t1} - T_{rif}) - \dot{M}_2 c_{p2_*} (T_{t2}^* - T_{rif}) \right.$$
$$+ \Phi - P_C] + + \left[\left(\frac{c_2^{*2}}{2} + c_{v_{2*}} T_{rif} \right) \frac{(\dot{M}_1 - \dot{M}_2)}{V_C} \right.$$
$$\left. \left. - \frac{c_2^*}{\Omega_2} \frac{\partial \dot{M}_2}{\partial t} \right] \right\} \tag{9}$$

From the heat transfer through the walls equation,

$$\frac{\partial T_{pC}}{\partial t} = \frac{1}{C_C} \cdot [K_{C\_pi} S_C (T_2 - T_{pC}) - K_{C\_pe} S_C (T_{pC} - T_{t1})]. \tag{10}$$

The algebraic equations are

$$\rho_1 = \frac{p_1}{R_{\text{aria}} T_1} \tag{11}$$

$$c_1 = \frac{\dot{M}_1}{\Omega_1 \rho_1} \tag{12}$$

$$a_1 = \sqrt{k_1 R_{\text{aria}} T_1} \quad \text{where} \quad k_1 = c_{p1}/c_{v1} \tag{13}$$

$$\text{Ma}_1 = \frac{c_1}{a_1} \tag{14}$$

$$T_1 = \frac{T_{t1}}{\left(1 + \frac{k_1 - 1}{2} \text{Ma}_1^2\right)} \tag{15}$$

$$p_1 = \frac{p_{t1}}{\left(1 + \frac{k_1 - 1}{2} \text{Ma}_1^2\right)^{k_1/k_1 - 1}} \tag{16}$$

$$\frac{\dot{M}_1 \sqrt{T_{t1}}}{p_{t1}} = f_{M_1}\left(IGV, \frac{p_{t2}^*}{p_{t1}}, \frac{n}{\sqrt{T_{t1}}}\right) \tag{17}$$

$$\eta_C = f_{\eta_C}\left(IGV, \frac{p_{t2}^*}{p_{t1}}, \frac{n}{\sqrt{T_{t1}}}\right) \tag{18}$$

$$P_C = \dot{M}_2 c_{p2} (T_{t2} - T_{rif}) - \dot{M}_1 c_{p1} (T_{t1} - T_{rif}) \tag{19}$$

$$\rho_2^* = \frac{p_2^*}{R_{\text{aria}} T_2^*} \tag{20}$$

$$c_2^* = \frac{\dot{M}_2}{\Omega_2 \rho_2^*} \tag{21}$$

$$a_2^* = \sqrt{k_2^* R_{\text{aria}} T_2^*} \quad \text{where} \quad k_2^* = c_{p2_*}/c_{v2_*} \tag{22}$$

$$\text{Ma}_2^* = \frac{c_2^*}{a_2^*} \tag{23}$$

$$T_{t2} = T_2 \cdot \left(1 + \frac{k_2 - 1}{2} \text{Ma}_2^2\right) \tag{24}$$

$$p_{t2}^* = p_2 \cdot \left(1 + \frac{k_{2_*} - 1}{2} \text{Ma}_2^{*2}\right)^{k_{2_*}/k_{2_*} - 1} \tag{25}$$

$$\rho_2 = \frac{p_2}{R_{\text{aria}} T_2} \tag{26}$$

$$c_2 = \frac{\dot{M}_2}{\Omega_2 \rho_2} \tag{27}$$

$$a_2 = \sqrt{k_2 R_{\text{aria}} T_2} \quad \text{where} \quad k_2 = c_{p2}/c_{v2} \tag{28}$$

$$\text{Ma}_2 = \frac{c_2}{a_2} \tag{29}$$

$$T_2 = \frac{T_{t2}}{\left(1 + \frac{k_2 - 1}{2} \text{Ma}_2^2\right)} \tag{30}$$

$$p_2 = \frac{p_{t2}}{\left(1 + \frac{k_2 - 1}{2} \text{Ma}_2^2\right)^{k_2/k_2 - 1}} . \tag{31}$$

A. Agazzani

A. F. Massardo
Mem. ASME.

University of Genova,
Istituto di Macchine e Sistemi Energetici,
via Montallegro 1,
16145 Genova, Italy

C. A. Frangopoulos
National Technical University of Athens,
Department of Naval Architecture and
Marine Engineering,
157 10 Zografou, Greece

Environmental Influence on the Thermoeconomic Optimization of a Combined Plant With NO_x Abatement

Methods to analyze, improve, and optimize thermal energy systems have to take into account not only energy (exergy) consumption and economic resources, but also pollution and degradation of the environment. The term "environomics" implies a method that takes thermodynamic, economic, and environmental aspects systematically into consideration for the analysis and optimization of energy systems. For optimization of energy systems, the environmental aspects are quantified and introduced into the objective function. In this particular work, the environomic approach is followed for the analysis and optimal design of a combined-cycle plant. In addition to the basic configuration, two alternatives for NO_x abatement are studied: Selective Catalytic Reduction (SCR) and steam injection. The optimization problem is solved for each configuration, and the results are compared with each other. The effect of the unit pollution penalties and of the limits imposed by regulations is studied. Some general conclusions are drawn.

Introduction

The thermal-energy systems consume not only fuel and economic resources, but they have also an harmful effect on the environment. Pollutant emissions from combustion have become of great concern due to their impact on human health and nature. Restrictions in specific pollution components are introduced in several countries. Emission taxes are also introduced to restrict air pollution.

Therefore, methods and techniques utilized for the optimization of thermal-energy systems have to deal not only with energy consumption and economics, but also with the pollution and degradation of the environment.

Environomics was introduced by Frangopoulos (1991, 1992) as an extension of thermoeconomics, in order to include environmental aspects in the thermoeconomic analysis and optimization of energy systems. In addition to flows of energy, exergy, and costs, flows of other consumed resources as well as flows of pollutants are considered; degradation of the environment is taken into consideration by treating the environment as a consumed resource.

The objective of this work is to analyze and prove the potential of environomics by means of application examples. With the introduction of environmental costs due to pollution, which depend on essential parameters such as unit pollution penalties (i.e., costs imposed by society or governmental institutions) and limits imposed by regulations, several scenarios can be analyzed for the same plant. As application examples, two NO_x abatement systems for a combined-cycle plant have been selected: steam injection and SCR.

The steam injection is a method frequently utilized for the NO_x abatement since it is easily feasible and suitable for traditional existing combustors. Water or steam injection decreases the flame temperature and lowers the NO_x emissions, but involves several remarkable adverse effects: it produces an increase in carbon monoxide (CO) and unburned hydrocarbon (UHC) emissions and causes some losses of thermal efficiency; water consumption, if considerable, causes supplying problems in certain localities and an increase of the plant and management costs because water must be treated and demineralized carefully; and the combustor useful life decreases because of fouling and scaling. Furthermore, in locations where the ambient concentration of NO_x exceeds the standards, emission regulations may become too stringent to be met by modification of the combustion process with the steam injection. Therefore, since emission with steam injection normally reaches values of around 40–60 ppmvd, this situation could require different treatment of the exhaust gas to remove NO_x.

Selective catalytic reduction (SCR) is now commonly used to control NO_x emissions from combustion sources in countries with strict emission regulations, even if its capital cost is greater than a system with steam injection. For gas turbines, NO_x emission reduction to as low as 10 ppmvd is sometimes required by the authorities, and is generally easily achieved by the SCR systems.

Several of these aspects have been taken into consideration here from an environomic point of view: comparison among systems with and without NO_x abatement is carried out and the influence of the two aforementioned essential parameters is analyzed and discussed in depth.

Brief Presentation of the Environomic Approach

In the environomic analysis and optimization of energy systems, the effect of the system construction and operation on the environment is taken into consideration. In order to do so, the effect is quantified, and a penalty is imposed. To cope with the penalty, pollution abatement equipment and techniques can be introduced, the performance of which is measured by the degree of abatement:

$$\delta = \frac{\dot{p}_i - \dot{p}}{\dot{p}_i},$$

where p_i is the initial pollution, before abatement, and p is the pollution after abatement. A discussion on appropriate measures of pollution, $\dot{p}$, can be found in the literature (Frangopoulos, 1991b, 1992; Frangopoulos and von Spakovsky, 1993).

Contributed by the International Gas Turbine Institute and presented at the International Gas Turbine and Aeroengine Congress and Exhibition, Orlando, FL, June 2–5, 1997. Manuscript received by the ASME Headquarters March 15, 1997. Paper No. 97-GT-286. Associate Technical Editor: H. A. Kidd.

The sensitivity of the particular environment to a certain pollutant is taken into consideration by the pollution penalty factor, as it will be explained in one of the following sections.

The optimization problem in environomics, considered under steady-state conditions, is mathematically stated as follows:

$$\min_{x} F = \sum_{i=1}^{n_{\text{unit}}} \dot{Z}_i^{\$} + \sum_{i=1}^{n_{\text{resources}}} (\dot{\Gamma}^{\$}_{\text{resource}})_i + \sum_{i=1}^{n_{\text{pollutant}}} (\dot{\Gamma}^{\$}_{\text{pollutant}})_i - \sum_{i=1}^{n_{\text{revenue}}} (\dot{\Gamma}^{\$}_{\text{revenue}})_i \quad (1)$$

subjected to

$h_j(\mathbf{x}, \mathbf{y}) = 0 \quad j = 1, \ldots,$ number of equality constraints

$g_k(\mathbf{x}, \mathbf{y}) \leq 0 \quad k = 1, \ldots,$ number of inequality constraints

where

$\mathbf{x} = \{x_i\} \quad i = 1, \ldots,$ number of independent variables

$\mathbf{y} = \{y_i\} \quad i = 1, \ldots,$ number of dependent variables

$$\dot{Z}^{\$} = Z^{\$}(\mathbf{x}, \mathbf{y})$$

$$\dot{\Gamma}^{\$}_{\text{pollution}} = \Gamma_{\text{pollution}}(\mathbf{x}, \mathbf{y})$$

$$\dot{\Gamma}^{\$}_{\text{revenue}} = \Gamma_{\text{revenue}}(\mathbf{x}, \mathbf{y})$$

The first term in the objective function, Eq. (1), represents the capital costs of the system components (including investment, depreciation, maintenance, etc.), the second term is the cost of resources bought by the system, the third term is the cost due to pollution of the environment resulting from the operation of the energy system (Frangopoulos and von Spakövsky, 1993). If the revenues of all the system products are included (fourth term), then F is the negative of the system profit.

System Analysis and Simulation

A modular simulator tool for thermoeconomic analysis of thermal-energy systems has been utilized here; the code, called thermoeconomic modular program (TEMP) has been presented in detail by Agazzani and Massardo (1996). The tool has been aimed at the following targets: thermodynamic and exergy analysis, thermoeconomic analysis, and optimization.

The thermoeconomic technique utilized is similar to the T.F.A. (thermoeconomic functional analysis) developed by Frangopoulos (1983, 1991) and the E.F.A. (engineering functional analysis) developed by von Spakovsky (1993). By means of a functional productive analysis in which each component has several inputs and one output (product), the code allows the functional exergy flows (i.e., the productive relationships, in addition to the physical exergy flows, expressed by the extensive variable exergy) among the components to be calculated. Besides, marginal and average unit costs of each functional exergy flow are determined, and, therefore, the global thermoeconomic performances of the components (internal economy) are defined. The calculation of the marginal and average unit costs is carried out only at the end of the optimization procedure, corresponding to the optimum point (Agazzani et al., 1995).

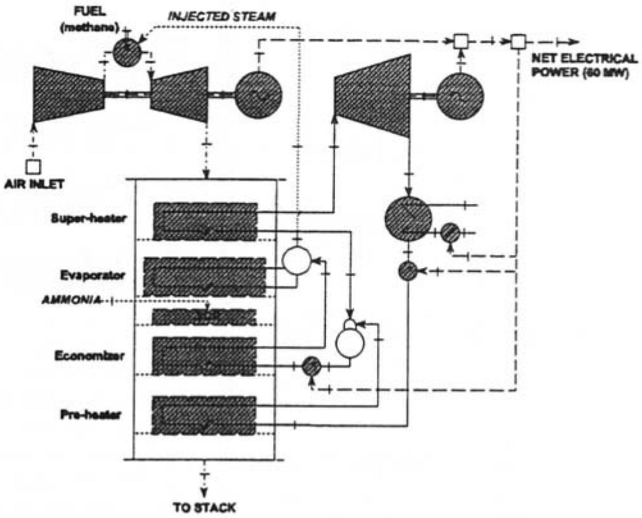

Fig. 1 Combined plant with an SCR abatement unit inside the HRSG or steam injection for removing NO_x; the grey-filled units represent components with a capital cost.

The code has been expanded by means of the introduction of a new module (the SCR), the modification of the combustor module in order to insert the injected steam and the pollutant emissions estimation and the introduction of an apt module for the make-up water. Furthermore, damage costs due to the pollutant emissions have been enclosed.

The modularity of the code allows the study of several configurations of multipressure combined plants (Agazzani and Massardo, 1996). However, since the aim of this work is to present and clarify the methodology, a relatively simple plant has been selected: it is a combined-cycle plant of a single-pressure heat recovery steam generator equipped with an SCR abatement unit inside the HRSG or with steam injection inside the combustor chamber of the gas turbine for removing NO_x (Fig. 1).

Emissions Estimation. In this work, a gas turbine with a typical diffusion flame combustor, and, therefore, with high NO_x emissions, has been considered. The formation of NO_x and CO emissions has been established employing correlations.

Nomenclature

c = unit cost (\$/kJ) or unit pollution penalty (\$/kg)
$C^{\$}$ = purchased cost (\$)
F = objective function
f_p = pollution penalty factor (harmfulness factor)
g = inequality constraint function
h = equality constraint function
k = constant related with the specific properties of a selected SCR catalyst (h^{-1})
M = molecular weight
$\dot{m}$ = mass flow rate (kg/s)
$\dot{p}$ = measure of pollution
p = pressure (Pa)
SV = SCR space velocity (h^{-1})
t = primary zone residence time (s)
T = temperature (K)
V = volume (m^3)
$\dot{V}$ = volumetric flow rate (m^3/s)
x_i = independent decision variable
$\mathbf{x}$ = set of independent variables
y_i = dependent variable
$\mathbf{y}$ = set of dependent variables
$Z^{\$}$ = annualized capital cost (including investment, depreciation, maintenance, etc.) (\$/s)
α = intensive property of the pollutant
α_o = intensive property of the pollutant in the environment
$\bar{\alpha}$ = critical limit of the intensive property (harmfulness limit)
β = pressure ratio
δ = degree of abatement of the pollutant
$\dot{\Gamma}^{\$}$ = rate of costs (\$/s)

Subscripts

g = flue gas
w = water

Since the emissions from a combustor depends on the type and the geometry, in order to not complicate a lot the thermoeconomic study, some parameters have been fixed for all the calculations; in particular, the primary zone residence time (which depends on the geometry) and the excess air in the same zone (which has influence on the primary zone combustion temperature) have been fixed.

The following correlations have been employed for the NO_x and CO emissions estimation (Rizk and Mongia, 1993):

$$NO_x = 5.10 \cdot 10^{14} \cdot (t - 0.5 \cdot t_e)^{0.5} \cdot \exp\left(-\frac{71100}{T_{st}}\right) \times p^{-0.05} \cdot \left(\frac{\Delta p}{p}\right)^{-0.5} \quad (2)$$

$$CO = 0.18 \cdot 10^9 \cdot \exp\left(-\frac{71100}{T_{pz}}\right) \Big/ \left[p^2 \cdot (t - 0.4 \cdot t_e) \cdot \left(\frac{\Delta p}{p}\right)^{0.5}\right], \quad (3)$$

where the emissions are in g/kg fuel; t_e is the fuel evaporation time (for a gaseous fuel this is fixed equal to zero); T_{st} is the stoichiometric flame temperature in degrees Kelvin; p the combustion pressure in Pa; $\Delta p/p$ the nondimensional linear pressure drop; t is the primary-zone residence time in seconds, and has been fixed equal to $2 \cdot 10^{-3}$ s; and T_{pz} is the primary zone combustion temperature in degrees Kelvin (in order to calculate the temperature T_{pz}, an air excess of about 3 percent has been assumed in the primary zone).

The unit of the emissions is "g/kg fuel", and, therefore, the mass flow rate of fuel that is burnt must be known. The combustor model considered here is a diffusion-flame model, and almost all of the fuel is burnt into the primary zone. Therefore, the mass flow rate of NO_x and CO at the exit of the combustor has been roughly calculated by means of the product between the value obtained with the correlation and the mass flow rate of fuel utilized by the gas turbine.

Steam Injection Model. In the model of steam injection utilized for the NO_x emissions abatement, the steam has been considered a perfect gas and injected inside the combustor (into the primary zone) in order to decrease the combustion temperature. In such a case, in accordance with the correlations above mentioned, the NO_x emissions decrease but the CO emissions increase (see the opposite influence of the temperature into the two correlations). The values of NO_x and CO emissions are determined by calculating the new value of the stoichiometric combustion temperature (T_{st}) or the primary zone combustion temperature (T_{pz}), and then utilizing the same correlations mentioned above. A cost of 0.5 $/m^3 has been set for the demineralized make-up water into the steam plant (its mass flow rate is equal to the steam mass flow rate injected into the gas turbine).

SCR Model. Selective catalytic reduction with ammonia is one of the most effective techniques for removing NO_x from combustion gases. The ammonia, injected into the exhaust gas upstream from a catalytic reactor, is applied as a suitable reduction medium on a technical scale.

The catalyst bed is situated in the heat recovery steam generator (Fig. 1) at the appropriate location to provide the optimum reaction temperature. Ammonia reacts with NO and NO_2 as follows:

$$6\,NO_2 + 8\,NH_3 \rightarrow 12\,H_2O + 7\,N_2$$

$$6\,NO + 4\,NH_3 \rightarrow 6\,H_2O + 5\,N_2$$

When oxygen is present, the corresponding reactions are

$$2\,NO_2 + 4\,NH_3 + O_2 \rightarrow 6\,H_2O + 3\,N_2$$

$$4\,NO + 4\,NH_3 + O_2 \rightarrow 6\,H_2O + 4\,N_2$$

Since oxygen is usually present in combustion gas and practically all of the NO_x is present as NO, the NH_3/NO_x stoichiometric ratio is 1.0, i.e., one mole of NH_3 is required for removing one mole of NO_x. The homogeneous reactions occur in a narrow temperature range at about 800°C, and are accompanied by undesirable side reactions; besides, it is difficult to achieve a high level of NO_x removal with a process based on homogeneous reduction. Utilizing a catalyst, the operating temperature can be reduced to the range of 220–420°C (the temperature depends upon the type of catalyst), but with an increase in capital cost.

The NO_x removal is called selective because the reduction chemicals should react exclusively with the pollutant.

In the presence of oxygen, the NO reduction by ammonia over ceramic catalyst is in many cases in accordance with an Eley-Rideal mechanism (Weber et al., 1991). Due to this reaction mechanism, the NO conversion is independent of the initial NO concentration. Considering the catalytic reactor as an ideal flow tube, the NO reduction for a given type of catalyst must be written as

$$\ln(1 - \delta_{NO_x}) = -k/SV, \quad (4)$$

where δ_{NO_x} is the NO_x degree of abatement and SV is the space velocity [h^{-1}]. SV is given by the ratio of the volume flow rate to the catalyst volume, and is thus proportional to the reciprocal of the mean residence time of the gas in the catalyst. The rate constant k is related with the specific properties of a selected catalyst and usually shows an exponential dependence according to the Arrhenius equation. On the other hand, it has to be taken into account that with increasing temperatures, the oxidation of NH_3 into NO may be enhanced as well. Taking into consideration these two opposite aspects, the degree of NO conversion reaches maximum values near temperatures of 250–300°C. This allows the SCR to be inserted between the evaporator and the economizer inside the HRSG.

The constant k of industrially applied catalyst is about 7500 h^{-1} at optimum reaction temperature (above 300°C).

The amount of ammonia to be injected into the flue gas stream is usually controlled by the flow rate of the flue gases and the inlet gas NO concentration. In order to avoid significant clean gas concentration, the molar NH_3/NO_x ratio is usually selected lower than 1 (about 0.9–0.95). Therefore, the ammonia mass flow rate is given by

$$\dot{m}_{NH_3} = \delta_{NO_x} \cdot \dot{m}_{NO_{x_{inlet}}} \frac{M_{NH_3}}{M_{NO}} \cdot r, \quad (5)$$

where

M_{NH_3} = 17.030 = ammonia molecular weight
M_{NO} = 30.0061 = NO molecular weight
r = molar NH_3/NO_x ratio
$\dot{m}_{NO_{x_{inlet}}}$ = NO mass flow rate at the SCR inlet (kg/s)

The pressure drop of an industrial ceramic catalyst that has been designed to remove more than 90 percent of NO_x is in the range of about 500 to 900 Pa. On the basis of this data, the pressure loss of an SCR can be estimated as follows:

$$\Delta p = -\frac{k \cdot 700}{SV \cdot \ln(1 - 0.9)}. \quad (6)$$

The catalyst cost is estimated by means of its volume. This last is given by

$$V_{cat} = -3600 \cdot \dot{V}_g \cdot \frac{\ln(1 - \delta)}{k}, \quad (7)$$

where $\dot{V}_g$ is the flue gas volumetric flow rate. The catalyst cost

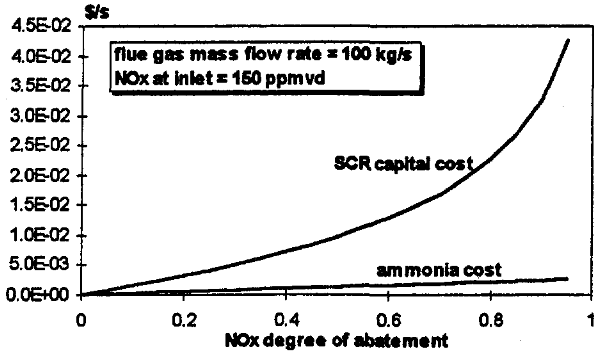

Fig. 2 Influence of δ_{NO_x} on the SCR capital cost

$C^{\$}_{cat}$ depends on its composition (base metal or noble metal); since the catalyst cost is about 70 percent of the SCR total cost (Eskinazi et al., 1989), the SCR cost can be estimated (for a noble metal catalyst) as follows:

$$C^{\$}_{SCR} = C^{\$}_{cat}/0.7 = c_1 \cdot V_{cat}/0.7, \qquad (8)$$

where $c_1 = 16245$ \$/m^3 (Frey et al., 1991).

The ammonia unit cost c_{NH_3} is 0.230 \$/kg (Rosenberg et al., 1992).

As an example of a SCR system cost, Fig. 2 shows the influence of the NO degree of abatement for a unit with a flue gas mass flow rate of 100 kg/s and 150 ppmv (15% O$_2$, dry) of NO at the inlet.

Optimization. The goal of the optimization for both analyzed plants is to minimize the rate of the total cost (including construction and operation) of the system:

$$\min \dot{\Gamma}^{\$}_{tot}(\mathbf{x}, \mathbf{y}) = \sum \dot{Z}^{\$}_i + \dot{\Gamma}^{\$}_{fuel} + \dot{\Gamma}^{\$}_{resource} + \dot{\Gamma}^{\$}_{NO} + \dot{\Gamma}^{\$}_{CO}, \qquad (9)$$

where

$$\dot{\Gamma}^{\$}_{fuel} = c_{fuel} \dot{m}_{fuel} LHV_{fuel}$$

$$\dot{\Gamma}^{\$}_{resource} = c_w \dot{m}_w \quad \text{or} \quad \dot{\Gamma}^{\$}_{resource} = c_{NH_3} \dot{m}_{NH_3}.$$

$\mathbf{x}$ is the set of decision variables, and $\mathbf{y}$ is the set of all functional exergy flows. Equation (9) is derived from the Eq. (1), in which the revenue term has not been considered since the only system product, the electrical power, has been fixed in this work (there is no need to include it since addition of a constant does not change the optimum point).

The total cost includes the annualized capital costs $\dot{Z}^{\$}_i$ of the plant units, including investment, depreciation, maintenance, etc. (see the appendix), the fuel cost, the costs of auxiliary resources $\dot{\Gamma}^{\$}_{resource}$ (i.e., ammonia cost for the plant with the SCR or make-up water cost for the plant with steam injection), and the costs due to the pollution of the environment resulting from the NO and CO emissions ($\dot{\Gamma}^{\$}_{NO}$, $\dot{\Gamma}^{\$}_{CO}$).

The selected independent decision variables are (see Table 1) pressure ratio and maximum temperature of the gas turbine, pressure of the produced steam, NO$_x$ degree of abatement (for the plant with the SCR), and mass flow rate ratio between steam injected and fuel (for the plant with steam injection). It would be useful to introduce a degree of abatement also for the steam injection system; however, the mass flow rate ratio between steam injected and fuel is a variable often utilized in literature.

Table 1 Decision variables

Decision variables	Optimization range
max. gas temperature [°C]	1100-1400
pressure ratio	10-30
steam pressure [MPa]	6-14
NOx degree of abatement (for the plant with the SCR)	0-0.95
mass flow rate ratio between steam injected and fuel (for the plant with steam injection)	0-2

Table 2 Nominal values of main parameters

min. ΔT between gas and evaporating steam (pinch point) [°C]	10	ΔT between inlet evaporator and outlet economizer [°C]	10
ΔT between gas and superheated steam or water [°C]	25	ΔT between condensing steam and cooling water [°C]	5
gas-turbine expander isentropic eff.	0.88	turbine mechanical efficiency	0.995
deaerator pressure [MPa]	0.14	pump isentropic efficiency	0.83
condenser pressure [MPa]	0.005	net electrical power [MW]	60
compressor isentropic efficiency	0.86	steam turbine isentropic eff.	0.85
alternator efficiency	0.985	environment temperature [°C]	15
maximum steam temperature [°C]	≤565	pump electrical/mechanical eff.	0.90
fuel LHV (methane) [kJ/kg]	50030	annual fixed charge rate	18.7%
number of operating hours per year	8000	c_{NO_x} [\$/kg NO$_x$]	7.5
unit energy fuel cost c_{fuel} [\$/kJ]	$4.0 \cdot 10^{6}$	c_{CO} [\$/kg CO]	1.014
outlet turbine steam quality	>0.86	stack gas temperature [°C]	>100

Table 2 reports the quantities considered known and fixed once and for all at the beginning of calculation; other hypotheses done for the calculation are reported in Agazzani and Massardo (1996). The net electrical power has been fixed equal to 60 MWe. The maximum allowable steam temperature has been set equal to 565°C. Two inequality constraints have been taken into consideration during the optimization: outlet turbine steam quality (>0.86) and stack gas temperature (>100°C).

The equality constraints, imposed by the physical and economic model of the system, consist of mathematical relations describing the thermodynamic performances as well as the costs of components and other economic parameters as functions of the independent variable set x. A nonlinear algorithm of optimization described in depth by Massardo et al. (1990), is directly applied to the objective function. Therefore, the physical and cost models are used to describe the objective function of the system, while the mathematical formulation of the T.F.A.–E.F.A. is not requested here to find the optimum design conditions. In this way, the introduction of many dependent variables related to the internal economy of the system is not necessary to locate the minimum, and, therefore, it can be avoided with a strong reduction in computation time (Agazzani and Massardo, 1996). However, the calculation of the internal economy (marginal and average unit costs) is performed at the optimum conditions.

The last two terms of Eq. (9) are the pollution costs due to the NO$_x$ and CO emissions from the gas turbine exhaust to the environment. These are damage cost terms and can be written as (von Spakovsky and Frangopoulos, 1994):

$$\dot{\Gamma}^{\$}_{NO_x} = c_{NO_x} f_{pNO_x} \dot{m}_{NO_x}, \quad \dot{\Gamma}^{\$}_{CO} = c_{CO} f_{pCO} \dot{m}_{CO} \qquad (10)$$

in which the mass flow rates of NO$_x$ and CO to the environment have been selected as the pollution measure. c_{NO_x} and c_{CO} (Table 2) are the unit pollution penalties that are taken equal to the damage caused to the environment per unit mass of a pollutant (Goswami, 1993). These represent costs imposed by society, governmental institutions, international organizations, etc., on the systems as a result of the damage caused by the emissions in the environment.

Several suggestions have been made for the pollution penalty factors f_p that appear in Eqs. (10) (Frangopoulos and von Spakovsky, 1993); the harmfulness factor has been used here as follows:

$$f_{p_i} = \frac{\alpha_i - \alpha_{0_i}}{\bar{\alpha}_i - \alpha_{0_i}}, \qquad (11)$$

where α_i is the intensive property of the ith pollutant, α_{0_i} is the intensive property of the ith pollutant in the environment, and

$\bar{\alpha}_i$ is the harmfulness limit of the intensive property of the ith pollutant (if it is exceeded, the pollution may become particularly harmful).

The concentration has been selected as the intensive property for the pollutants in this example. In such a case, if the value of the standard air quality limit concentration is selected as the intensive property of the pollutant in the environment (α_{0i}) and emissions limit concentration from a power plant is selected as the harmfulness limit ($\bar{\alpha}_i$) of the intensive property, then the value of α_{0i} can be neglected in comparison to the values of $\bar{\alpha}_i$. As an example, according to the values imposed by Italian decrees on pollutant emissions, for the NO pollutant, the value of α_0 is about 0.130 mg/m^3 (~0.200 mg/m^3 as NO_2), while the value of $\bar{\alpha}$ is about 200 mg/m^3. Then, $\alpha_{0i} \ll \bar{\alpha}_i$, and, therefore, the pollution penalty factor f_p, becomes

$$f_{p_i} \cong \frac{\alpha_i}{\bar{\alpha}_i} . \qquad (12)$$

In accordance with the emission limits imposed by the EU, the selected harmfulness limits for NO and CO are

NO_x = 50 ppm volume dry, 15% O_2 as NO (about 75 ppmvd as NO_2)
CO = 80 ppm volume dry, 15% O_2

The above value for NO_x has been changed during the calculations in order to analyze the influence of the harmfulness limit.

What does happen if f_p is greater than one? A plant should not operate at all if its emissions are higher than limits set by regulations. Consequently, there would be no condition for imposing the penalty, except if the meaning of the regulations is changed: instead of setting limits that can not be violated, limits which can be violated are set; but, since such a change would have a negative effect on the environment, a new greater penalty is imposed.

In conclusion, a penalty (i.e., $c_{NO_x} \dot{m}_{NO_x}$, or $c_{CO} \dot{m}_{CO}$) is imposed for every kilogram of a pollutant emitted by a plant, no matter if the concentration is higher or lower than a limit set by regulations. Then, the introduction of the factor f_p increases or decreases this penalty according to the relationship between the real concentration and the one set by regulations.

Several scenarios can be analyzed in order to establish how f_p must be considered when it reaches values between 0 and 1; three decision cases have been set here when $f_p \leq 1$:

- case (a): f_p retains its value, as it results from the calculations
- case (b): f_p is set equal to 1
- case (c): f_p is set equal to 0

In case (a), a pollution penalty is still considered, but less than the one of case (b). In case (c), if the concentration of the pollutant is lower than a limit imposed by regulations, then there is no pollution penalty.

The introduction of these pollution costs, corrected by the factor f_p, is different from the direct utilization of inequality constraints that may be imposed by safety considerations for each pollutant; with this procedure, the optimization also takes into account those configurations that have emissions greater than the limits imposed by regulations. However, only case (c) could be considered very similar to an inequality constraint since a penalty takes part in the objective function only if emission is greater than the limits imposed by regulations. It will be shown how case (c) forces the decision variables towards values that allow the analyzed plant to have emissions just equal to the limits imposed by regulations (harmfulness limits).

Optimization Results and Comments

Table 3 reports the results of the combined plant optimization, without NO_x abatement systems and without taking into consideration the pollution penalty costs due to the NO_x and CO emissions (baseline plant). It is interesting to observe how the high maximum gas temperature involves a high NO_x emission (about 150 ppm). The plant draws near to the optimum efficiency conditions; this occurs in order to limit the fuel consumption whose cost is about four times greater than the total capital costs.

Table 3 Optimal results without pollution penalty costs (baseline combined plant)

Decision variables (optimal values)				
max. gas temperature pressure ratio	1400 °C 16.22	steam pressure	14.0 MPa	
capital costs	10.63 c\$/s	fuel cost	44.59 c\$/s	
Objective function (total cost)	55.22 c\$/s	thermal efficiency = 53.82%		
	g/kg gas	mg/Nm^3 gas	g/kg fuel	ppmvd 15% O_2
NO	0.2052	195.76	8.163	146.2
CO	0.142	135.6	5.654	108.5
CO_2	68.97	65793	2744	33507

Instead, in Table 4, the results of the plant including the pollution penalty costs are reported. In comparison with the previous case, the NO_x emission is lower (89 ppm), but the CO emission increases considerably (230 ppm). This is due to the strong difference between the two unit pollution penalties c_{NO_x} and c_{CO} (7.5 \$/kg against 1.014 \$/kg). The high influence of the NO pollution cost has brought the decision variables towards values that decrease the NO emission: in particular, the maximum gas temperature and the pressure ratio are decreased. In the table, the selected cases ($a \div c$) for the pollution penalty factor are not distinguished since f_{pNO_x} and f_{pCO} do not reach values less than 1 (i.e., both the emissions are greater than the emission limits imposed by the EU, 50 ppm for NO and 80 ppm for CO).

The next step regards the study of the optimum plant with SCR or steam injection in the three decision cases (a), (b), and (c) set for the pollution penalty factor f_p.

Table 5 (case (a)) and Table 6 (case (b)) report the main results of the analyzed plants (independent decision variables, costs, emissions, etc.). The second case involves greater values for the NO degree of abatement and the steam/fuel mass flow rate ratio: this is caused by the higher penalty policy obtained setting $f_p = 1$ when it is less than one.

Unlike the previous case (Table 4), the introduction of NO_x abatement techniques results in an increase of the optimum value of the maximum gas temperature and drives the optimal design towards the optimum efficiency conditions again. Therefore, during the calculations, the maximum gas temperature and the steam pressure have reached optimal values near to their upper limits (1400°C and 14 MPa respectively), probably for the following reasons: (i) in order to respect the inequality constraint on the flue gas stack temperature (>100°C) and (ii) in order to increase the thermal efficiency of the systems, and, therefore, decrease both the fuel consumption and the mass flow rate of the NO and CO emissions.

Obviously, the SCR capital cost has a great influence on the total capital costs (around 15–20 percent), and the system with

Table 4 Optimal results with pollution penalty costs (baseline combined plant)

Decision variables (optimal values)				
max. gas temperature pressure ratio	1291.5 °C 11.47	steam pressure	14 MPa	
capital costs	10.032 c\$/s	fuel cost	46.31 c\$/s	
NO poll. cost (fp_{NOx}=1.78)	15.36 c\$/s	CO poll. cost (fp_{CO}=2.88)	8.10 c\$/s	
Objective function (total cost)	79.81 c\$/s	thermal efficiency = 51.83%		
	g/kg gas	mg/Nm^3 gas	g/kg fuel	ppmvd 15% O_2
NO	0.118	119.24	4.973	89.07
CO	0.286	287.8	12.00	230.3
CO_2	65.39	65793	2744	33507

Table 5 Optimal results for case (*a*): (*a*) plant with SCR; (*b*) plant with steam injection.

Decision variables (optimal values)			
max. gas temperature	1400 °C	steam pressure	13.99 MPa
pressure ratio	16.69	NO degree of abatement	0.872
gas turbine	4.173 c$/s	steam turbine	3.257 c$/s
HRSG	1.133 c$/s	condenser	0.589 c$/s
SCR	2.792 c$/s	GT alternator	0.9625 c$/s
pumps	0.076 c$/s	steam plant alternator	0.555 c$/s
Fuel cost	44.63 c$/s	NO poll. cost (fp_{NO}=0.39)	0.7054 c$/s
Ammonia cost	0.216 c$/s	CO poll. cost (fp_{CO}=1.27)	1.533 c$/s
Objective function (total cost)	60.62 c$/s	thermal efficiency = 53.77	

Emissions	g/kg gas	mg/Nm^3 gas	g/kg fuel	ppmvd
NO	0.02714	26.025	1.085	19.4
CO	0.133	127.52	5.32	102
CO_2	68.61	65793	2744	33507
NO before abatement = 0.213 g/kg gas				

Decision variables (optimal values)			
max. gas temperature	1399.8 °C	steam pressure	14 MPa
pressure ratio	20.87	steam/fuel mass flow rate ratio	1.726
gas turbine	5.042 c$/s	condenser	0.480 c$/s
HRSG	1.143 c$/s	GT alternator	1.061 c$/s
pumps	0.077 c$/s	steam plant alternator	0.453 c$/s
steam turbine	2.829 c$/s		
Fuel cost	45.59 c$/s	NO poll.cost (fp_{NOx}=1)	0.484 c$/s
Water cost	0.1967 c$/s	CO poll.cost (fp_{CO}=1.174)	1.328 c$/s
Obj. function (total cost)	58.69 c$/s	thermal efficiency = 52.64	

Emissions	g/kg gas	mg/Nm^3 gas	g/kg fuel	ppmvd
NO	0.0073	6.80	0.284	5.1
CO	0.127	117.4	4.90	94
CO_2	70.95	65793	2744	33507

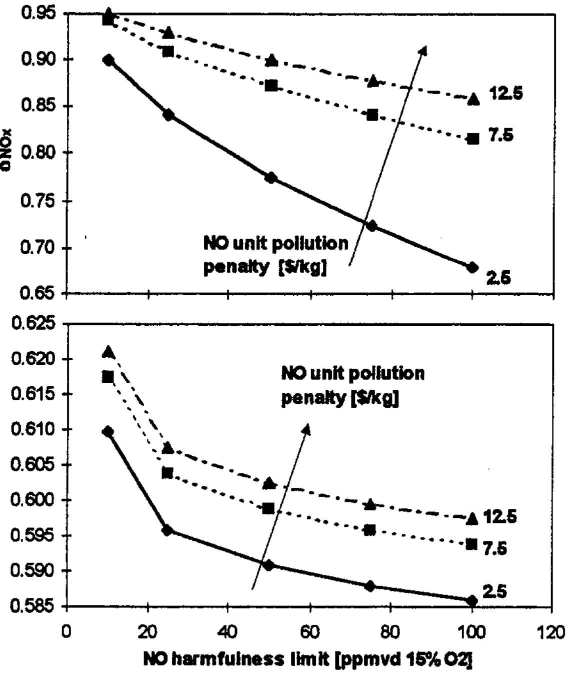

Fig. 3 Influence of c_{NO_x} and $\bar{\alpha}_{NO_x}$ on the plant with SCR—case (*a*): f_p keeps its value when less than 1.

SCR has a total cost greater than the system with steam injection; however, the difference between the plant with SCR and the plant with steam injection is not so great. This is due to the following considerations:

1 The steam injection inside the combustor chamber causes an increase of the fuel consumption (whose energy cost has been fixed equal to $4.0 \cdot 10^6$ \$/kJ) and a decrease of the thermal efficiency even if the power of the gas turbine increases. It must be remembered that the steam is not easily available in nature: it must be produced downstream of the gas turbine with a process of thermal recovery. Therefore, the steam injection improves both the power and the efficiency of a gas turbine (STIG plant), but for a combined plant, the injected steam must be considered removed from the expansion into the steam turbine. In this case, the following points occur: the gas turbine power increases while the steam turbine power decreases, although not in proportion to the removed steam because the HRSG operates with a greater flue gas mass flow rate (generating more steam); and the combined effect is that the combined cycle efficiency decreases. On the contrary, the introduction of the SCR inside the HRSG does not change the efficiency of the plant (if a pressure loss is taken into consideration, the efficiency decrease is very small).

Table 6 Optimal results for case (*b*) ($f_p = 1$ when less than 1): (*a*) plant with SCR; (*b*) plant with steam injection.

Decision variables (optimal values)			
max. gas temperature	1400 °C	steam pressure	14.0 MPa
pressure ratio	16.6	NO degree of abatement	0.901
gas turbine	4.143 c$/s	steam turbine	3.263 c$/s
HRSG	1.137 c$/s	condenser	0.591 c$/s
SCR	3.129 c$/s	GT alternator	0.961 c$/s
pumps	0.076 c$/s	steam plant alternator	0.557 c$/s
Fuel cost	44.63 c$/s	NO poll. cost (fp_{NO}=1)	1.396 c$/s
Ammonia cost	0.221 c$/s	CO poll. cost (fp_{CO}=1.3)	1.577 c$/s
Objective function (total cost)	61.68 c$/s	thermal efficiency = 53.77	

Emissions	g/kg gas	mg/Nm^3 gas	g/kg fuel	ppmvd
NO	0.0209	20.02	0.835	15
CO	0.135	129.34	5.39	103.5
CO_2	68.7	65793	2744	33507
NO before abatement = 0.211 g/kg gas				

Decision variables (optimal values)			
max. gas temperature	1400 °C	steam pressure	14 MPa
pressure ratio	20	steam/fuel mass flow rate ratio	1.287
gas turbine	4.897 c$/s	condenser	0.505 c$/s
HRSG	1.135 c$/s	GT alternator	1.038 c$/s
pumps	0.077 c$/s	steam plant alternator	0.476 c$/s
steam turbine	2.931 c$/s		
Fuel cost	45.33 c$/s	NO poll. cost (fp_{NOx}=0.24)	0.2707 c$/s
Water cost	0.146 c$/s	CO poll. cost (fp_{CO}=1.166)	1.302 c$/s
Obj, function (total cost)	58.111 c$/s	thermal efficiency = 52.94	

Emissions	g/kg gas	mg/Nm^3 gas	g/kg fuel	ppmvd
NO	0.01705	15.996	0.667	11.95
CO	0.124	116.6	4.86	93.3
CO_2	70.11	65793	2744	33507

2 The water consumption, if considerable, causes supplying problems in certain localities; water must be treated and demineralized carefully, with an increase of the plant and management costs. A cost of 0.5 \$/m^3 has been set here for the demineralized make-up water but, by changing this value, different results can be obtained.

3 The steam injection causes an increase of CO emissions; in order to keep these last at a low level, the combustor chamber pressure must be increased (see Eqs. 2 and 3); therefore, in order to avoid a strong CO emission increase, the optimal values of the pressure ratio for the plants with steam injection are slightly greater than those for the plants with SCR (see Table 6); this causes an increase of the capital cost, in particular, of the compressor (Agazzani and Massardo, 1996).

Figures 3, 4, 5, and 6 show the influence of the unit pollution penalty c_{NO_x} and the harmfulness limit $\bar{\alpha}_{NO_x}$ on the two plants. The NO abatement should increase with the NO harmfulness limit reduction (and the NO unit pollution penalty increase) causing higher total costs, particularly for low $\bar{\alpha}_{NO_x}$ values. This happens in particular for case (*a*) (Figs. 3 and 4), while a different behavior is obtained for case (*b*). In this case, the plant with steam injection does not seem to depend on the NO limits (see Fig. 6). Evidently, very low NO emissions (less than 10 ppm) are reached, also with high limits (i.e., 100 ppm); therefore, $f_{p_{NO_x}}$ is always set equal to one. Instead, for the plant with SCR, the same behavior is found only for high c_{NO_x} and $\bar{\alpha}_{NO_x}$ values, while for low c_{NO_x} and $\bar{\alpha}_{NO_x}$ values the degree of

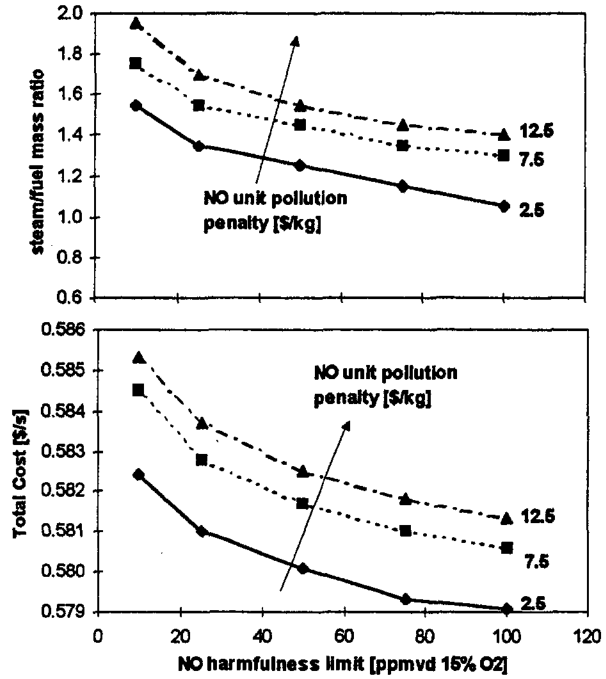

Fig. 4 Influence of c_{NO_x} and $\bar{a}_{\mathrm{NO}_x}$ on the plant with steam injection—case (*a*): f_p keeps its value when less than 1.

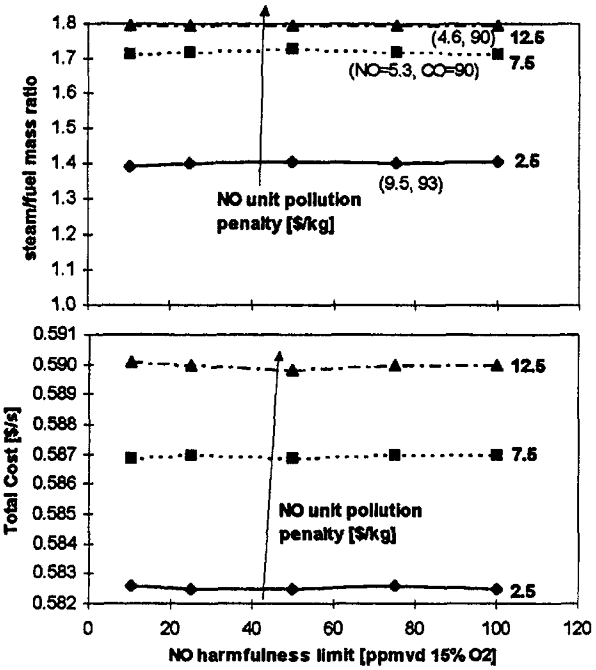

Fig. 6 Influence of c_{NO_x} and $\bar{a}_{\mathrm{NO}_x}$ on the plant with steam injection—case (*b*): f_p = 1 when less than 1.

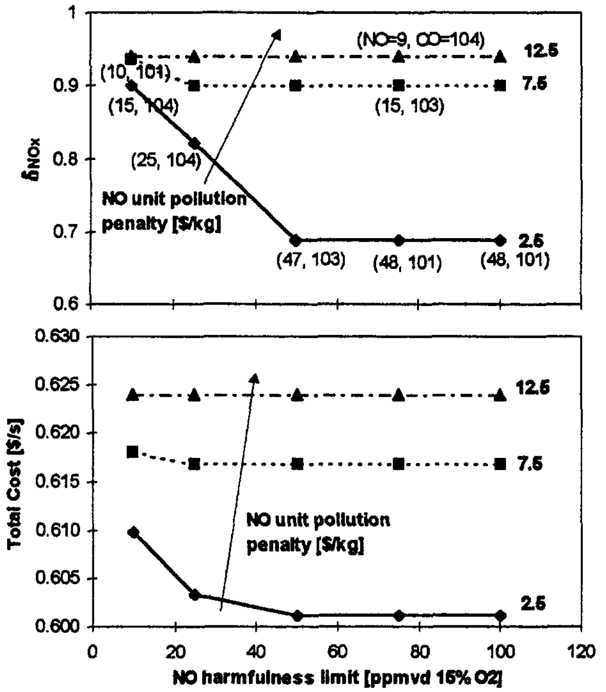

Fig. 5 Influence of c_{NO_x} and $\bar{a}_{\mathrm{NO}_x}$ on the plant with SCR—case (*b*): f_p = 1 when less than 1.

abatement increases in order to limit the NO pollution penalty costs. The numbers between brackets, near the points of Figs. 5 and 6, indicate the NO and CO emissions, respectively (in ppm).

By increasing the NO unit pollution penalty or reducing its harmfulness limit, the steam injected (and therefore the water consumption) increases a lot (see Figs. 4 and 6). This would cause a further increase of CO production, and, so, the optimum pressure ratio would increase some more. Therefore, if a greater penalty is imposed for the CO (i.e., increasing the pollution penalty or decreasing the harmfulness limit), the plant with steam injection could not achieve the imposed harmfulness limit, with a strong increase of the CO damage cost term. In this case, joined also with an increase of the make-up water cost and the unit fuel cost, the cost difference between the plant with SCR and the plant with steam injection could become lower.

Up to this point, results show that CO emissions are always higher than the limit of 80 ppm: the cause is that the value selected for the CO unit pollution penalty (1.014 $/kg) is too low in comparison with c_{NO}. Therefore, a parametric study has been carried out for the case (*b*), by increasing the c_{CO} value (see Fig. 7) and keeping always $\bar{a}_{\mathrm{CO}} = 80$ ppm (the values of c_{NO_x} and $\bar{a}_{\mathrm{NO}_x}$ are set equal to 7.5 $/kg and 50 ppm, respectively). In such a case, the CO emissions decreases below the harmfulness limit of 80 ppm, causing greater values of the pressure ratio (see the value of β near the points of Fig. 7). On the contrary, the increase of this last case also involves a short increase of the NO pollution abatement.

In case (*c*), in which the pollution penalty is similar to an inequality constraint, the optimization code brings the decision variables, and in particular the NO_x degree of abatement and the mass flow rate ratio between injected steam and fuel, towards values that allow the harmfulness limits to be respected (see Table 7). Their values, and so the total costs, are considerably lower than those obtained in the two previous cases, in particular for high NO limits. The values of δ_{NO_x}, steam/fuel mass ratio and total cost (see Fig. 8) do not depend on the NO unit pollution penalty, since the optimum plant achieves NO emission values always lower than the limits imposed by regulations (i.e., the harmfulness limit $\bar{a}_{\mathrm{NO}_x}$).

Conclusions

Combined plants with SCR or steam injection as NO abatement techniques have been analyzed from an environomic point of view. CO and NO_x emissions have been taken into consideration; in particular, the influence of the unit pollution penalty

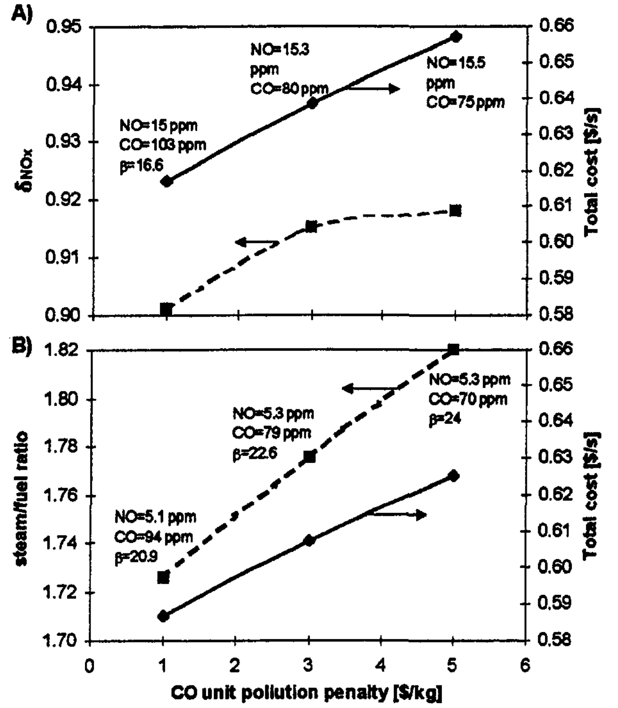

Fig. 7 Influence of c_{CO} ($\bar{a}_{CO}$ = 80 ppm, $\bar{a}_{NO_x}$ = 50 ppm, $c_{NO_x} = 7.5\ \$/\mathrm{kg}$): (*a*) plant with SCR; (*b*) plant with steam injection.

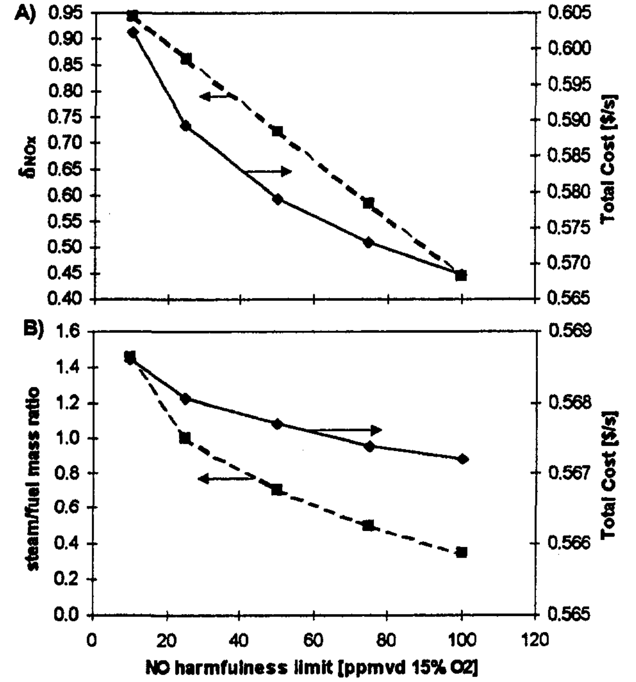

Fig. 8 Influence of c_{NO_x} and $\bar{a}_{NO_x}$—case (*c*): f = 0 when less than 1. (*a*) Plant with SCR; (*b*) plant with steam injection.

and of the limit imposed by regulations on the system has been revealed.

With the introduction of the environomic approach, several scenarios can be analyzed for the same plant.

The results obtained here must be considered not as an absolute solution. They are valid under the economic assumptions made in this work with no claim to general applicability. Furthermore, the emissions are strongly influenced by the assumptions done for the combustor chamber. However, the numerical examples presented here serve to clarify the methodology and can be interpreted as a starting point for an environomic comparison of different plants.

Also, the effect of the variations of the unit pollution penalty and the imposed limit for the CO emission could prove to be interesting. A further development of the model can be carried out with the introduction of the unburned hydrocarbons emission (UHC). These last two points will be analyzed in the near future.

Table 7 Optimal results for case (*c*) (f_p = 0 when less than 1): (*a*) plant with SCR; (*b*) plant with steam injection.

Decision variables (optimal values)				
max. gas temperature	1400 °C	steam pressure	13.98 MPa	
pressure ratio	18.66	NO degree of abatement	0.722	
capital costs	12.991 c$/s	NO pollution cost (fp$_{NO}$=0)	0	
Fuel cost	44.70 c$/s	CO pollution cost (fp$_{CO}$=0)	0	
Ammonia cost	0.212 c$/s	Objective function (total cost)	57.903 c$/s	
thermal efficiency = 53.69				
Emissions	g/kg gas	mg/Nm^3 gas	g/kg fuel	ppmvd
NO	0.06831	66.914	2.79	50
CO	0.102	99.97	4.169	80
CO$_2$	68.61	65793	2744	33507
NO before abatement = 0.246 g/kg gas				

Decision variables (optimal values)				
max. gas temperature	1399.7 °C	steam pressure	14 MPa	
pressure ratio	20	steam/fuel mass flow rate ratio	0.625	
capital costs	11.32 c$/s	NO pollution cost (fp$_{NOx}$=0)	0	
Fuel cost	45.04 c$/s	CO pollution cost (fp$_{CO}$=0)	0	
Water cost	0.0704 c$/s	Objective function (total cost)	56.43 c$/s	
thermal efficiency = 53.28				
Emissions	g/kg gas	mg/Nm^3 gas	g/kg fuel	ppmvd
NO	0.0689	66.66	2.78	50
CO	0.103	99.96	4.166	80
CO$_2$	68.05	65793	2744	33507

Acknowledgment

The authors wish to acknowledge the funding from the National Research Council of Italy (CNR), under contract n° 94.00038.CT07.

References

Agazzani, A., Massardo, A., and Satta, A., 1995, "Thermoeconomic Analysis of Complex Steam Plants," ASME Cogen Turbo Power, Wien, 95-CTP-38.

Agazzani, A., and Massardo, A., 1997, "A Tool for Thermoeconomic Analysis and Optimization of Gas, Steam and Combined Plants," ASME TRANSACTIONS, JOURNAL OF ENGINEERING FOR GAS TURBINE AND POWER, October, Vol. 119, pp. 885–892.

Agazzani, A., 1996, "Thermoeconomic Analysis of Energy Systems," Ph.D. thesis, University of Pisa, Italy.

Boehm, R. F., 1987, *Design Analysis of Thermal Systems,* John Wiley and Sons, New York.

Eskinazi, D., Cichanowicz, J. E., Linak, W. P., and Hall, R. E., 1989, "Stationary Combustion NOx Control—A Summary of the 1989 Symposium," *The Journal of Air Waste Management Association,* Vol. 39, No. 8, Aug., pp. 1131–1139.

Frangopoulos, C. A., 1991a, "Comparison of Thermoeconomic and Thermodynamic Optimal Designs of a Combined-Cycle Plant," *Proceedings of Analysis of Thermal and Energy Systems,* ATHENS '91, Athens, Greece, June 3–6, pp. 305–318.

Frangopoulos, C. A., 1991b, "Introduction to Environomics," *Second Law Analysis—Industrial and Environmental Applications,* G. M. Reistad et al., eds., AES-Vol. 25/HTD-Vol. 191, ASME, N.Y., pp. 49–54.

Frangopoulos, C. A., 1992, "An Introduction to Environomic Analysis and Optimization of Energy-Intensive Systems," in *International Symposium on Efficiency, Costs, Optimization and Simulation of Energy Systems,* ECOS '92, Zaragoza, Spain, 15–18 June, ASME, New York, pp. 231–239.

Frangopoulos, C. A., and von Spakovsky, M. R., 1993, "The Environomic Analysis and Optimization of Energy Systems (Part I and II)," *Proceedings of the International Conference on Energy Systems and Ecology: ENSEC '93,* Cracow, Poland, July, Vol. I, ASME, New York, pp. 123–144.

Frey, H. C., and Rubin, E. S., 1991, "Probabilistic Evaluation of Advanced SO$_2$/NOx Control Technology," *The Journal of Air Waste Management Association,* Vol. 41, No. 12, Dec., pp. 1585–1593.

Goswami, D. Y., 1993, "Solar Energy and the Environment," presented at the International Conference on Energy Systems and Ecology: ENSEC '93, J. Szargut and G. Tsatsaronis eds., Cracow, Poland, July, ASME, New York.

Lazzaretto, A., and Macor, A., 1994, "Marginal and Average Costs in Engineering Functional Analysis," presented at Florence World Energy Research Symposium, FLOWERS '94, Florence, July 6–8.

Massardo, A., Satta, A., and Marini, M., 1990, "Axial Flow Compressor Design Optimization," ASME *Journal of Turbomachinery,* Vol. 112, pp. 399–410.

Rizk, N. K., and Mongia, H. C., 1993, "Semianalytical Correlations for NOx, CO, and UHC Emissions," ASME JOURNAL OF ENGINEERING FOR GAS TURBINE AND POWER, Vol. 115, pp. 612–619.

Rosenberg, H. S., Oxley, J. H., and Barrett, R. E., 1992, "Selective Catalytic Reduction for NO_x Control at Cogeneration Plants," IGTI-Vol. 7, ASME Cogen-Turbo '92, pp. 409–417.

von Spakovsky, M. R., and Evans, R. B., 1993, "Engineering Functional Analysis—Part I and Part II," ASME *Journal of Energy Resources Technology,* Vol. 115, pp. 86–99.

von Spakovsky, M. R., and Frangopoulos, C. A., 1994, "The Environomic Analysis and Optimization of a Gas Turbine Cycle with Cogeneration," ASME-WAM, AES Vol. 33.

Weber, E., and Schmidt, D., 1991, "High and Low Dust SCR Processes," *Sulphur Dioxide and Nitrogen Oxides in Industrial Waste Gases: Emission, Legislation and Abatement,* D. Van Velzen, ed., ECSC, EEC, EAEC, Brussels and Luxembourg, pp. 223–234.

APPENDIX

The following equation has been used to evaluate the annualized capital cost of each component of the plant (Frangopoulos, 1991a):

$$Z_i^\$ = \mathrm{FCR} \cdot \Phi_i \cdot C_i^\$ / (3.6 \cdot 10^5 \cdot N),$$

where, in order not to complicate the analysis, the maintenance cost has been taken into consideration by a constant factor Φ_i. FCR is the annual fixed charge rate, obtained by the addition of several items: interest or return on investment, depreciation, interim replacements, property insurance, taxes, etc..

The values utilized for the analysis are

$$\mathrm{FCR} = 18.7\%$$

$$\Phi_i = 1.06$$

$$N = 8000 \text{ h/year}$$

The purchased cost $C^\$$ of each component can be estimated by means of equations written in terms of geometrical and manufacturing variables or in terms of performance and stream variables.

Further information about the component purchased cost equations are reported in Frangopoulos (1991a), Agazzani et al. (1995), Agazzani and Massardo (1996), Boehm (1987), and Lazzaretto et al. (1994). The cost equation for the SCR, in particular, has been provided in the text.

Dual Brayton Cycle Gas Turbine Pressurized Fluidized Bed Combustion Power Plant Concept

X. L. Yan

L. M. Lidsky

Longmark Power International Inc.,
One Kendall Square Suite 2200,
Cambridge, MA 02139

High generating efficiency has compelling economic and environmental benefits for electric power plants. There are particular incentives to develop more efficient and cleaner coal-fired power plants in order to permit use of the world's most abundant and secure energy source. This paper presents a newly conceived power plant design, the Dual Brayton Cycle Gas Turbine PFBC, that yields 45 percent net generating efficiency and fires on a wide range of fuels with minimum pollution, of which coal is a particularly intriguing target for its first application. The DBC-GT design allows power plants based on the state-of-the-art PFBC technology to achieve substantially higher generating efficiencies, while simultaneously providing modern gas turbine and related heat exchanger technologies access to the large coal power generation market.

Introduction

Fluidized bed combustion (FBC) is the basis of most modern coal-fired power systems. FBC is well suited to firing various quality coals or co-firing coals with other fuels, such as biomass and waste, with low emissions of pollutants. This has been demonstrated in conventional atmospheric FBC power plants. However, the conventional plants based on the Rankine steam turbine cycle are relatively inefficient. The efficiency can be slightly improved in the state-of-the-art (first generation) pressurized fluidized bed combustion (PFBC) combined cycle power plants that incorporate the more efficient Brayton gas turbine cycle to provide a small share (20–25 percent) of overall plant power generation.

Proposed advanced (second generation) PFBC combined cycle power plant designs increase the share of power generation from the gas turbine cycle to about 50 percent, by significantly raising the gas turbine inlet temperature and by using very high excess combustion air (in the range of 100–150 percent). These advanced designs require a partial coal gasification stage to produce the gaseous fuel needed to heat flue gas in a second combustor, in order to reach the required turbine inlet temperature. These designs also considerably increase the load and design requirements of the hot gas cleanup system. The quest for higher efficiency in the advanced PFBC designs has resulted in increased system complexity that adversely affects plant economics, operation, and development time. Other advanced designs, such as the integrated gasification combined cycle (IGCC) system, are similarly complex and offer no advantage of efficiency or cost over the advanced PFBC designs.

Dual Brayton Cycle Gas Turbine (DBC-GT) PFBC is a newly conceived power plant design that employs an innovative cycle arrangement to achieve clean and efficient power generation at competitive cost (Yan and Lidsky, 1996). The design is based on PFBC for coal combustion in conjunction with both a closed and an open Brayton cycle gas turbine that are connected in such fashion as to maximize the system performance, while reducing the technological demands on each of the components. The DBC-GT design surpasses the efficiency and environmental goals of other advanced designs, yet is substantially smaller, simpler, and thus less expensive. Furthermore, the DBC-GT provides a practical means to incorporate modern closed-cycle helium turbine into a commercially attractive fossil plant design.

DBC-GT Power Plant Concept

A schematic of the baseline DBC-GT power plant design is shown in Fig. 1. The plant consists of three major subsystems, the circulating PFBC system, the open-cycle gas turbine system, and the closed-cycle gas turbine system. At design conditions, approximately 75 percent of the total plant power output is provided by the closed-cycle gas turbine, while the remaining 25 percent is provided by the open-cycle gas turbine. In addition to power generation, the open-cycle gas turbine supplies compressed combustion air to the CPFBC, which produces hot flue gas for expansion in the open cycle turbine, and provides indirect heating to the closed cycle in an external fluidized bed heat exchanger (FBHX). A portion of the combustion air supplied by the open cycle is fed into the FBHX heater as fluidizing air before being injected into the combustor as tertiary air.

The CPFBC allows combustion of various quality coals with good atmospheric emission characteristics and extremely high firing capacities. Coal and limestone are mixed with water to form a paste that is then fed by a paste pump into the lower bed of the combustor. Coal is combusted to heat the solid particles contained in the combustor bed and to produce hot flue gas. Most of the thermal energy released from combustion is contained in the bed solids. Combustion takes place in the CPFBC with staged combustion air and at relatively low combustion temperatures to limit NO_x emissions, while limestone reacts with the coal bound sulfur.

The hot flue gas with entrained solids leaves the top of the combustor and enters cyclones, where the coarse solid particles are separated from the flue gas. The hot flue gas exiting the cyclones flows into ceramic filters for final filtration of the remaining particulate dust. The cleaned flue gas is then directed into the open-cycle turbine, which extracts work from the sensible heat of the flue gas to drive an electric generator and to drive air compressors to compress combustion air. The compressed combustion air is preheated by the turbine exhaust gas in a

---

Contributed by the International Gas Turbine Institute and presented at the International Gas Turbine & Aeroengine Congress & Exhibition, Orlando, FL, June 2–5, 1997. Manuscript received by the ASME Headquarters March 1, 1997. Paper No. 97-GT-123. Associate Technical Editor: H. A. Kidd.

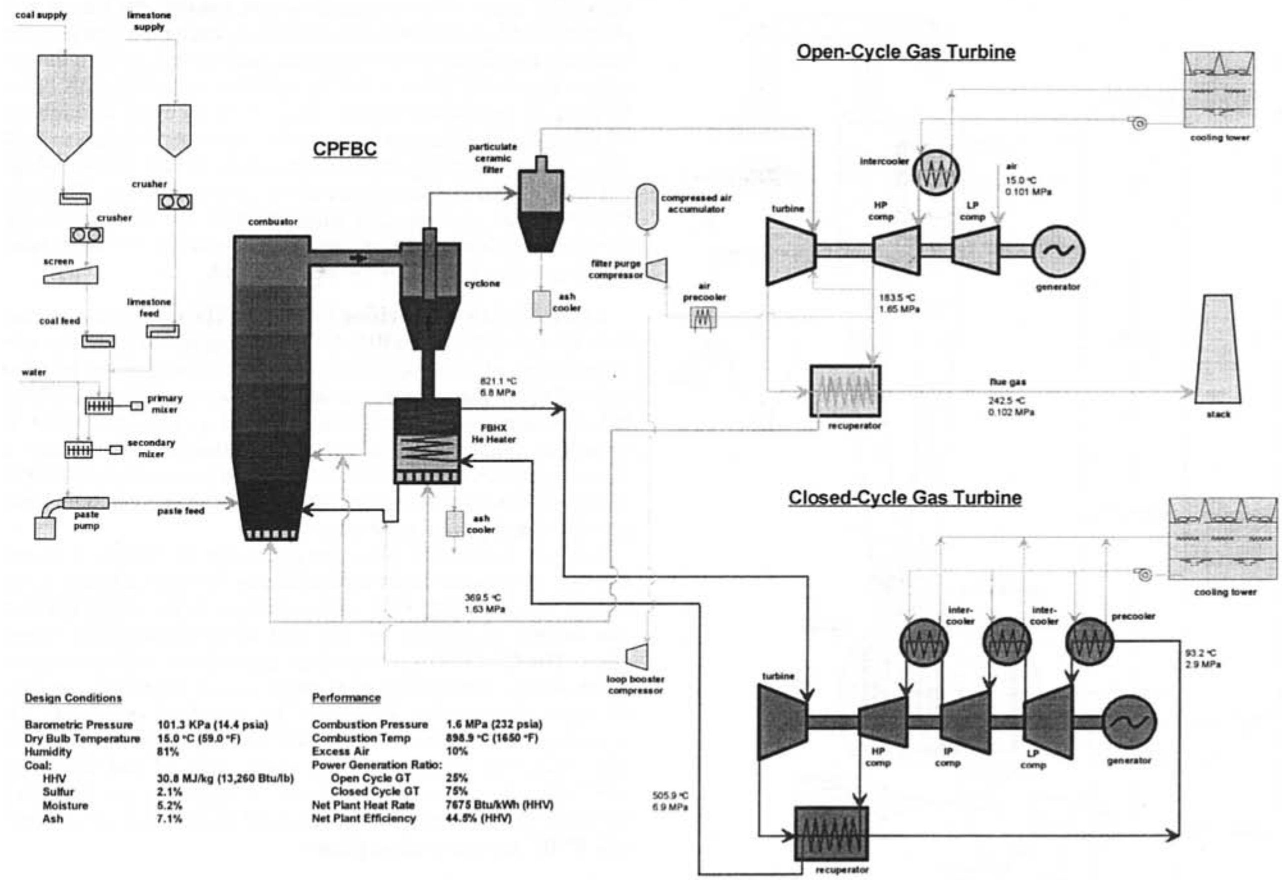

Design Conditions

Barometric Pressure	101.3 KPa (14.4 psia)
Dry Bulb Temperature	15.0 °C (59.0 °F)
Humidity	81%
Coal:	
HHV	30.8 MJ/kg (13,260 Btu/lb)
Sulfur	2.1%
Moisture	5.2%
Ash	7.1%

Performance

Combustion Pressure	1.6 MPa (232 psia)
Combustion Temp	898.9 °C (1650 °F)
Excess Air	10%
Power Generation Ratio:	
Open Cycle GT	25%
Closed Cycle GT	75%
Net Plant Heat Rate	7675 Btu/kWh (HHV)
Net Plant Efficiency	44.5% (HHV)

Fig. 1 Schematic of DBC-GT power plant

recuperator before it is delivered to the combustor. This is an important energy recovery step to attain high thermal efficiency for the high-pressure combustor system. The cooled flue gas from the recuperator is sent directly to stack for emission without further treatment.

The main energy transfer takes place in the FBHX external to the combustion zone of the circulating fluidized bed combustor. The hot solid particles captured in the cyclones contain the bulk of the combustion energy. These solid particles are circulated from the cyclones into the FBHX, wherein the sensible heat of the hot solid particles is transferred at high heat transfer rates to the working fluid (helium) of the closed-cycle gas turbine, which then converts the heat at high efficiency into shaft power to drive a second electric generator.

There are several design features that merit comment here. First, the DBC-GT design is in part aimed at finding a way to incorporate modern closed-cycle helium turbomachinery into a commercially attractive fossil plant design. A major impediment to the use of this very compact, very efficient technology was the inability to design a robust, economic gas heater. Fortunately, the external FBHX has precisely the attributes required for successful heater design:

- high and nearly uniform temperatures
- high and nearly uniform heat transfer coefficients
- pressurized environment
- fluidization of fine solids at low velocity
- essentially combustion-free atmosphere

This combination of properties minimizes tube thermal and mechanical stresses, assures low rates of chemical and mechanical attack on the tubing, and results in very compact (i.e., high volumetric heat transfer) heater design.

Furthermore, the DBC-GT design relies on the highly efficient, reliable, closed-cycle gas turbine for the majority of the plant power generation. The open-cycle gas turbine is used primarily as a heat recovery means rather than as a major contributor to total power output. Thus, it is not necessary to deviate from optimal combustor operating conditions to maximize open-cycle output by using high excess air or by raising turbine inlet temperature with resulting deleterious impact on component sizes, filter capacity, and environmental performance.

Finally, and most obviously, the DBC-GT replaces the Rankine cycle in conventional PFBC plants with a higher-performance Brayton cycle. This allows power plants employing PFBC technology to achieve substantially higher efficiencies, while simultaneously providing modern gas turbine and related heat exchanger technologies access to the large coal power generation market, which has been traditionally dominated by Rankine cycle steam turbine generators.

CPFBC System. Figures 2 and 3 depict elevation and plan views of a CPFBC system design for a 400 MWe DBC-GT plant. The CPFBC system employs separate pressure vessels to contain individual components—a modular design approach that is favored by industry to reduce pressure vessel costs and system installation requirements (Robertson and Bonk 1993; Rehwinkel et al., 1993). The major components of the CPFBC include a single combustor with a firing rate of 905 MWt (3089 $\times 10^6$ Btu/hr), four parallel cyclone/filter trains for flue gas cleanup, and a FBHX heater unit for heating the closed cycle. The pressure vessels are fabricated of carbon steels and protected with internal refractory linings (exclusive of the heater vessel) from the abrasive solids and hot gases. Because of its capacity for firing at extremely high power density, the combustor is very compact; the largest outer diameter of the combustor

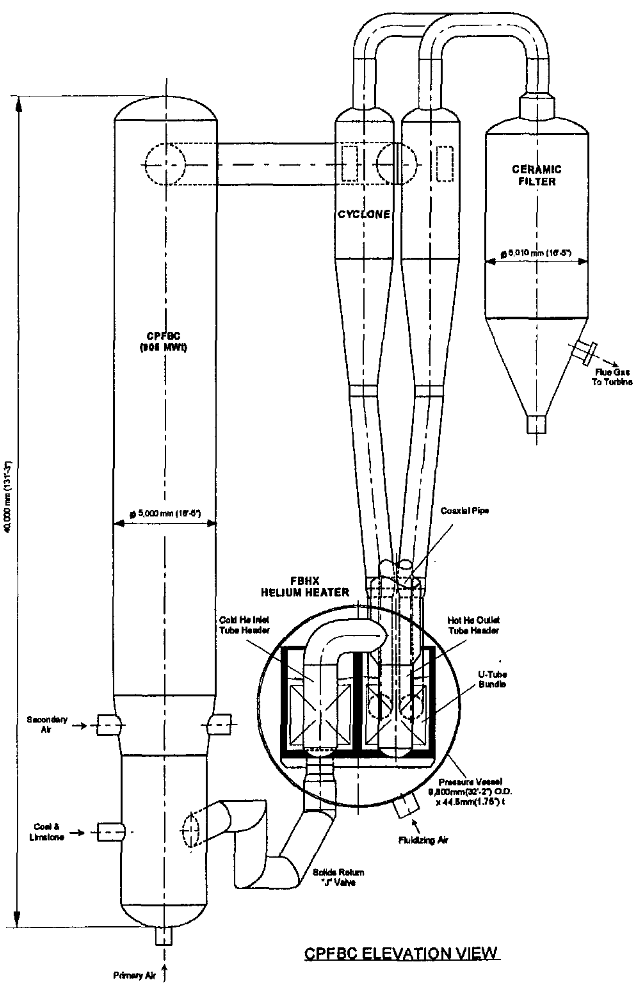

Fig. 2 CPFBC for 400 MWe DBC-GT power plant

pressure vessel is only 5.0 m (16 ft. 5 in.). The cyclones and filters are also compact modular units.

The horizontal pressure vessel of the FBHX helium heater encloses a pair of refractory-walled fluidized beds, each containing an identical U-tube bundle. The pressure vessel is cooled on the inside by cold stagnant air. The two tube bundles share common tubular headers for directing helium flows into and out of the tubes. The tube bundles have a heat duty of 2 × 300 MWt (2 × 1025 10^6 Btu/hr) and include a total heat transfer surface area of 2 × 6, 141 m^2 (2 × 66,098 $ft.^2$). Each tube bundle is immersed in a series of seven fluidized cells to facilitate heating the helium gas to the required exit temperature of 821.1°C (1510.0°F). To augment heat transfer, the bed solids are forced to flow, alternately, under and over the partition weirs from one cell to another to provide an overall cross-counter flow effect between the solids and helium and to avoid solids flow bypass. The distributed temperatures and heating duties among the multiple cells are detailed in Fig. 4.

Combustion-related corrosion on the heater tubes is minimized, since the external heater is essentially free of combustion. Tube erosion is similarly minimized because the particle beds in which the tubes are immersed are fluidized at very low velocity (0.3 m/s or 1 ft./s) with fine solids. These salubrious working conditions allow heater tubes fabricated of suitable high-temperature alloys with reasonable design margins to achieve a design lifetime of 30 years.

The overall dimensions of the heater steel pressure vessel are 9.8 m (32 ft. 2 in.) O.D., 45.3 m (148 ft. 7 in.) length, and 44.5 mm ($1\frac{3}{4}$ in.) wall thickness. The vessel weighs under 600 metric tons (660 tons). One approach to constructing the heater is to shop assemble it into two subassemblies, each of which contains one tube bundle in a half-length pressure vessel, to ship the two halves to site by barge (and by crawlers from barge to inland location if necessary) and to erect and join them through circumferential welding on the vessel and the tube headers in field. The size and shipping requirements of the heater subassemblies are well within the experience of the power industry. The combustor vessel, cyclone, and filter modules are all smaller than the heater modules. Therefore, they can easily be shop fabricated and shipped to site by barge or rail.

Open Cycle Gas Turbine System. The open-cycle gas turbine for the 400 MWe DBC-GT plant operates at a turbine inlet temperature of 889.0°C (1632.2°F) with a compressor pressure ratio of 16.8. The compressor air flow rate is 339.5 kg/s (748.5 lb/s). Compressor intercooling is used to deliver a cold air stream to enable effective recovery of turbine exhaust heat in the recuperator. It should be noted that intercooled and recuperated gas turbines are a well-established technology in both transportation and power generation.

The gas turbine for the open cycle can be chosen from any number of commercially available gas turbines without major design modification. One such machine is the ABB GT140P gas turbine developed for the 350 MWe P800 PFBC power plant. The GT140P is a twin-shaft gas turbine with compressor intercooling. Adjustable inlet guide vanes are used to control air flow rates to the combustor for part load operation. The operating conditions of the GT140P closely resemble the working conditions required by the open cycle of the 400 MWe DBC-GT plant. For smaller plants, a candidate gas turbine is the ABB GT35P, which has been used in a number of commercial PFBC demonstration plants.

Closed Cycle Gas Turbine System. The closed cycle gas turbine system is a compact, reliable, and efficient power conversion unit responsible for 75 percent of the total plant output. The cycle begins with the working gas being compressed sequentially in three compressor sections. Gas intercooling is provided between the compressor sections to reduce compressor power consumption. The gas discharged from the last compressor stage flows into one side of the recuperator to be heated by the turbine exhaust gas that passes through the other side of the recuperator. The preheated gas leaving the recuperator is then delivered into the FBHX heater, wherein it is heated to a final temperature of 821.1°C (1510.0°F) at a pressure of 6.8 MPa (981.9 psia). The hot gas is then directed into the turbine to drive the compressor and an electric generator. The gas exhausted from the turbine is passed into the recuperator to transfer its residual heat back to the cycle, after which it is cooled by the precooler before being fed into the compressor to start next cycle process.

Figure 5 illustrates the performance characteristics of the recuperated and intercooled Brayton helium turbine cycle. The design point is set at the optimal cycle pressure ratio of 2.50, where cycle efficiency peaks for the turbine inlet temperature of 821.1°C (1510.0°F). Although the selected turbine inlet temperature, which is limited by the heater, is considerably lower than those encountered in combustion gas turbines, the closed cycle yields 50 percent generating efficiency. The key to the high efficiency is performance augmentation by cycle intercooling and recuperation, using high-effectiveness and low-pressure-loss heat exchangers. Another factor that contributes significantly to the high performance is the high aerodynamic efficiencies of the turbomachine made possible by the high Reynolds numbers and extremely low Mach numbers characteristic of helium flows. These desired conditions enhance blading efficiency and eliminate the shock losses that commonly exist in air-breathing gas turbines.

The closed cycle system of the 400 MWe DBC-GT plant is rated at 300 MWe and is based on a conventional layout of

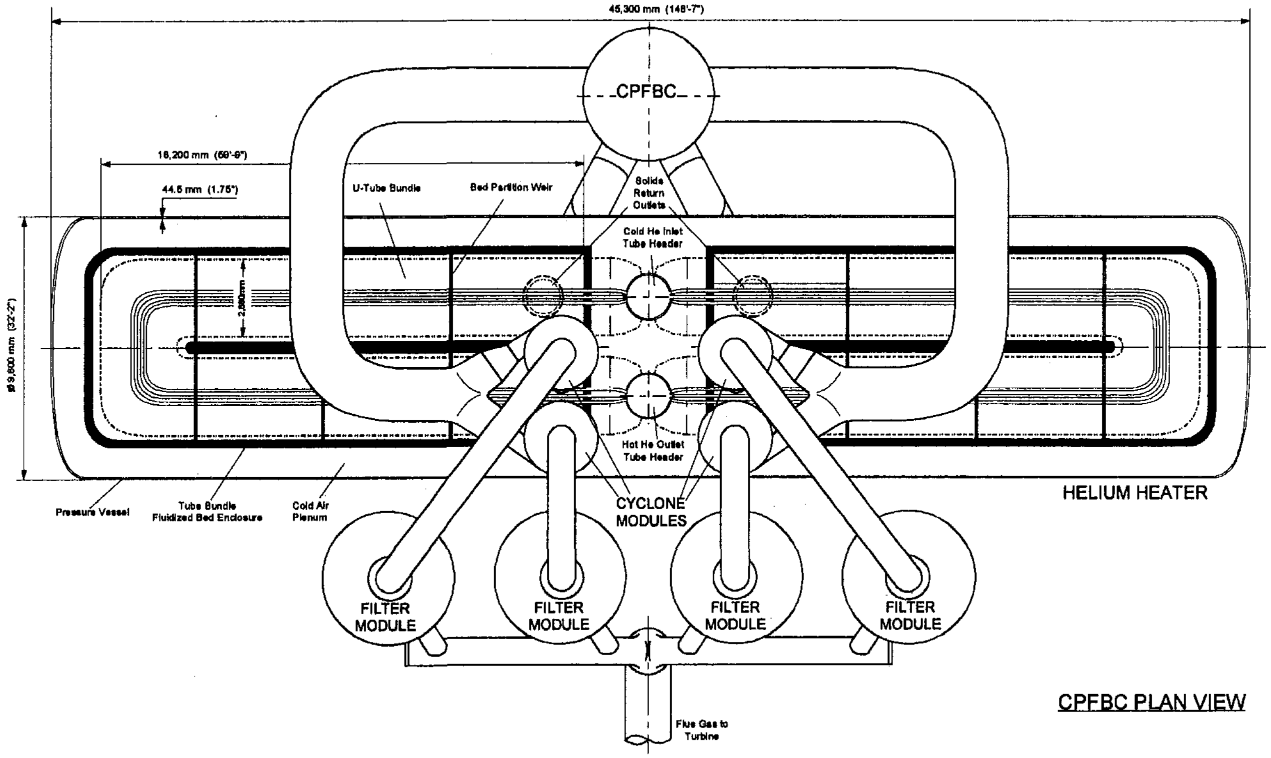

Fig. 3 Plan view of CPFBC for 400 MWe DBC-GT power plant

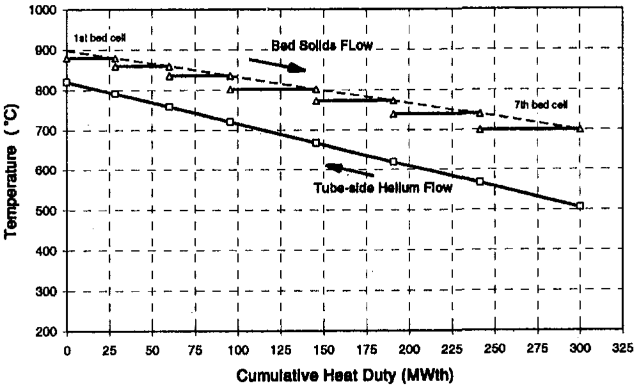

Fig. 4 FBHX temperature and heat duty distribution per tube bundle

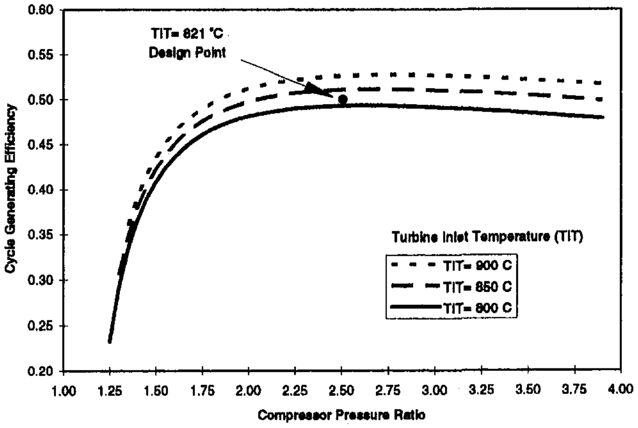

Fig. 5 Helium turbine cycle characteristics

turbomachinery, recuperator, precooler, and intercooler. The system layout is shown in Fig. 6 with key dimensions to indicate the compactness of the system. The small size is mainly attributable to the closed cycle's unique abilities to pressurize the system and to use helium rather than air as working fluid. Both the transport capacity and the thermal conductivity of helium are five times larger than those of air. This leads to high power density and small equipment size. It should be noted that helium is readily available at a cost negligible compared to the total operating cost of a plant.

The turbomachine is a single-shaft, axial-flow machine made up of three compressor sections and a single turbine section. The compressor has 10, 12, and 14 stages in the low, intermediate, and high-pressure sections, and the turbine has 11 stages. The maximum tip diameter of the compressor is 1.5 m (4 ft. 11 in.) and that of the turbine is 1.8 m (5 ft. 11 in.). Because of the low gas temperatures in the turbine, the vanes and buckets throughout the turbine stages are uncooled and made of conventional alloys. The turbomachine directly drives a synchronous electric generator. Conventional radial and thrust oil bearings are used on the turbomachine and generator rotors.

The recuperator is made up of two identical modular units. Each unit contains a plate-fin heat exchanger based on a design widely used in gas turbine power plants. The plate-fin design offers high surface compactness, and, thus, small unit size. The high-pressure helium greatly enhances heat transfer and minimizes pressure drop while providing an inert, nonfouling working environment compatible with the compact surface topology. The design effectiveness of the recuperator is 95 percent with a total pressure drop of 2.0 percent. The recuperator is easily designed to tolerate the anticipated number of thermal cycles and rapid transients over the plant's lifetime without scheduled maintenance.

The closed-cycle system uses four modular coolers of identical design to provide heat rejection. The coolers are helium-to-water heat exchangers of tube-and-shell construction. The helium flows in the tube side in a counter-cross flow arrange-

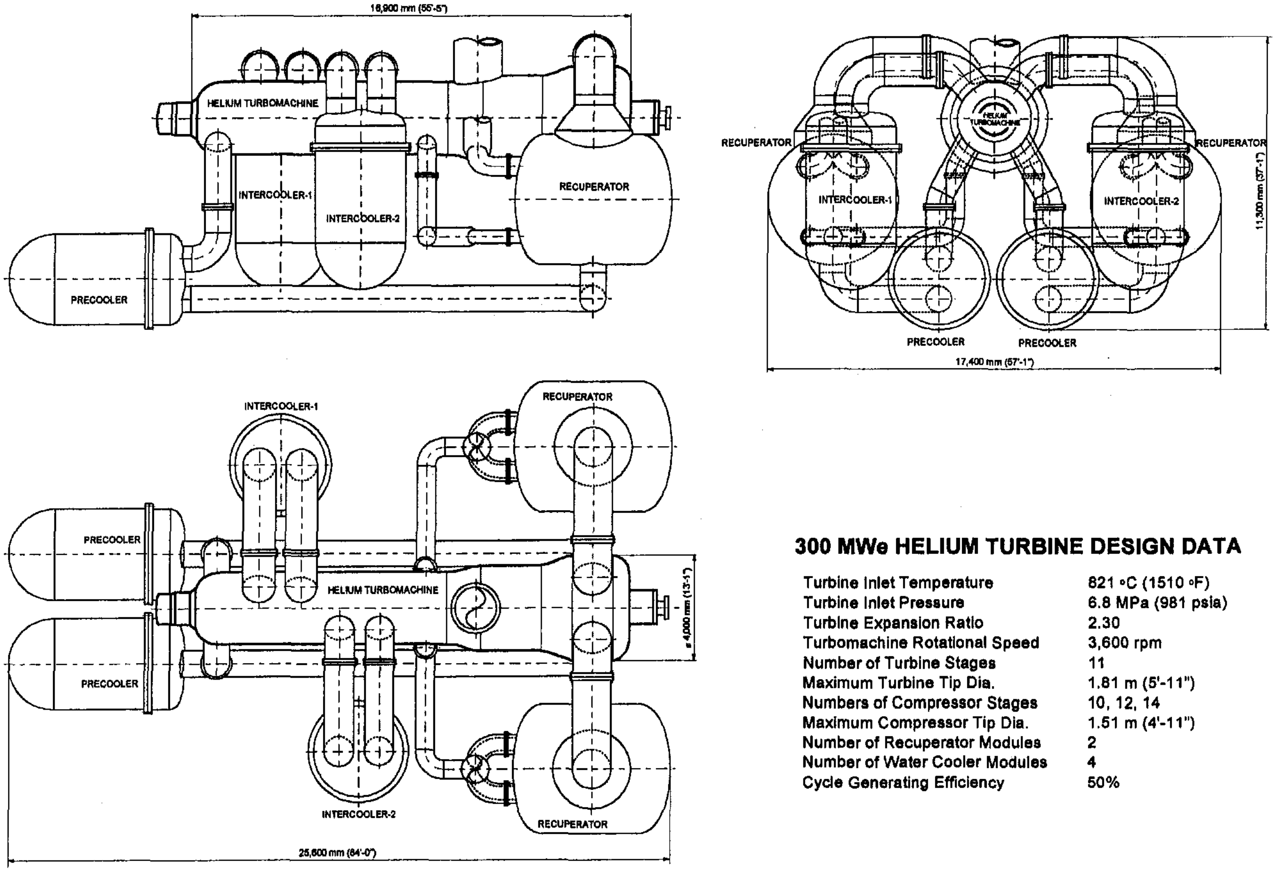

300 MWe HELIUM TURBINE DESIGN DATA

Turbine Inlet Temperature	821 °C (1510 °F)
Turbine Inlet Pressure	6.8 MPa (981 psia)
Turbine Expansion Ratio	2.30
Turbomachine Rotational Speed	3,600 rpm
Number of Turbine Stages	11
Maximum Turbine Tip Dia.	1.81 m (5'-11")
Numbers of Compressor Stages	10, 12, 14
Maximum Compressor Tip Dia.	1.51 m (4'-11")
Number of Recuperator Modules	2
Number of Water Cooler Modules	4
Cycle Generating Efficiency	50%

Fig. 6 Helium turbine system for 400 MWe DBC-GT power plant

ment with the shell-side cooling water. Two cooler modules operating in parallel are used as a precooler to cool the inlet gas flow to the low-pressure compressor section, while the remaining two modules are each used as an intercooler to cool the inlet gas flow to the low-pressure compressor section, while the remaining two modules are each used as an intercooler to cool the inlet gas flow to the intermediate and high-pressure compressor sections. The helium leaves the coolers at an exit temperature of 25.0°C (77.0°F) under the design basis ambient conditions (17.0°C (62.6°F) cooling water inlet temperature, 11.1°C (52.0°F) wet bulb ambient temperature, and 5.8°C (10.6°F) cooling tower approach temperature).

DBC-GT Power Plant Performance

Table 1 summarizes the performance data of a 400 MWe DBC-GT power plant burning Pittsburgh No. 8 Bituminous coal with a higher heating value of 30,843 kJ/kg (13,260 Btu/lb) and a sulfur content of 2.1 percent (a detailed analysis of the coal is provided in Table 3). The coal and limestone are mixed into a paste and fed by paste pumps into the combustor. The coal is burned in the combustor at 898.9°C (1650.0°F) and 1.6 MPa (232 psia) with 10 percent excess air. Limestone is added at a Ca/S molar ratio of 1.3 to achieve a minimum of 90 percent sulfur removal. The power generated by the open cycle gas turbine is 108.3 MWe, and the power generated by the closed cycle gas turbine is 300.8 MWe. The in-plant power consumption is only 6.4 MWe; the low in-plant power consumption is characteristic of Brayton gas turbine cycle. The net plant heat rate is 7675 Btu/kWh (HHV), equivalent to a net plant efficiency of 44.5 percent (HHV).

Table 2 compares the performance of the DBC-GT with those of alternative coal power generation technologies of both current and advanced designs. The potential ranges of efficiencies and economically practical plant sizes are listed for each technology. In contrast to the alternative systems, the DBC-GT allows high efficiency without system complexity and the resulting high costs of construction and operation. Because of simplicity in design and operation and because gas turbine cycles are not sensitive to scale size, the DBC-GT is able to function economically over a wide range of plant sizes. It is possible to further augment the efficiency in the advanced DBC-

Table 1 DBC-GT power plant performance

Combustor Firing Rate (HHV)	MWt (10^6Btu/hr)	905.6 (3090.1)
Combustion Temperature	°C (°F)	898.9 (1650.0)
Combustion Pressure	MPa (psia)	1.6 (232.0)
Combustion Air	kg/s (lb/s)	327.7 (722.5)
Excess Air	%	10.0
Coal Feed (Pittsburgh No. 8 Bitum.)	kg/hr (lb/hr)	105,706 (233,037)
Limestone Feed	kg/hr (lb/hr)	9,026 (19,898)
Ca/S Molar Ratio		1.3
Minimum Sulfur Retention	%	90.0
Total Ash Discharge	kg/hr (lb/hr)	18,548 (40,891)
Stack Gas Flow	kg/s (lb/s)	373.2 (822.7)
Stack Temperature	°C (°F)	242.5 (468.5)
Open-Cycle Gas Turbine Output	MWe	108.3
Closed-Cycle Gas Turbine Output	MWe	300.8
Gross Plant Output	MWe	409.1
In-Plant Power Consumption	MWe	6.4
Net Plant Output	MWe	402.7
Net Plant Heat Rate (HHV)	Btu/kWh	7675
Net Plant Efficiency (HHV)	%	44.5

Table 2 Performance comparison of coal power generation technologies

Coal Technologies	Efficiency (%, HHV)	Economic Sizes (MWe)
PC&AFBC Steam Cycle		
1800 psia/1000/1000 °F	35-36	100-200
2400 psia/1000/1000 °F	36-38	200-300
3500 psia/1000/1000 °F	38-39	300-500
1st Generation PFBC-CC	38-40	100-400
2nd Generation PFBC-CC	42-45	300-500
IGCC w/ HGCU	41-44	200-400
DBC-GT	**43-45**	**100-400**
Advanced DBC-GT	**46-48**	**400-600**

GT designs by employing a ''topping combustor'' to raise turbine inlet temperature and by using other design enhancement to permit efficiencies up to 48 percent (HHV). These advanced designs provide long-term growth potential for the DBC-GT.

Performance Sensitivity to Alternate Coals

The base coal for the foregoing DBC-GT performance data is a medium-sulfur, low-moisture Pittsburgh No. 8 bituminous coal. The effects of using alternate coals and feeding methods were studied for a 400 MWe DBC-GT plant. The two alternate coals studied were a high-sulfur, medium-moisture Illinois No. 6 bituminous coal and a low-sulfur, high-moisture Western subbituminous coal. These coals represent a wide spectrum of coals used in commercial power generation. Detailed analyses of these coals are provided in Table 3.

Each coal was studied under the following four alternate feeding methods:

- paste feed of coal as-received
- paste feed of coal, after 50 percent moisture depletion of coal feedstock
- pneumatic feed of coal as-received
- pneumatic feed of coal, after 50 percent moisture depletion of coal feedstock

Table 3 Analyses of alternate coals

		Pittsburgh No. 8 Bitum.	Illinois No.6 Bitum.	Western Subbitum.
Proximate Analysis				
Moisture	%	5.2	12.0	30.4
Ash	%	7.1	16.0	6.4
Volatile	%	36.7	33.0	31.1
Fixed Carbon	%	51.0	39.0	32.1
Higher Heating Value (HHV)	kJ/kg	30,843	23,493	18,655
	Btu/lb	13,260	10,100	8,020
Ultimate Analysis				
C	%	73.8	57.5	47.9
H	%	4.9	3.7	3.4
N	%	1.4	0.9	0.6
S	%	2.1	4.0	0.5
O	%	5.5	5.8	10.8
H2O	%	5.2	12.0	30.4
Ash	%	7.1	16.1	6.4
Coal Ash Analysis (dry)				
Phosphate Pentoxide, P2O5	%	0.4	0.2	0.8
Silica, SiO2	%	55.2	45.0	31.6
Ferric Oxide, Fe2O3	%	9.3	20.0	4.6
Alumina, Al2O3	%	24.8	18.0	15.3
Titanium Oxide, TiO2	%	1.2	1.0	1.1
Calcium Oxide, CaO	%	3.0	7.0	22.8
Magnesia, MgO	%	0.9	1.0	4.7
Sulfur Trioxide, SO3	%	2.3	3.5	16.6
Potassium Oxide, K2O	%	2.1	1.9	0.4
Sodium Oxide, Na2O	%	0.8	0.6	1.3
Undetermined		0.0	1.8	0.8

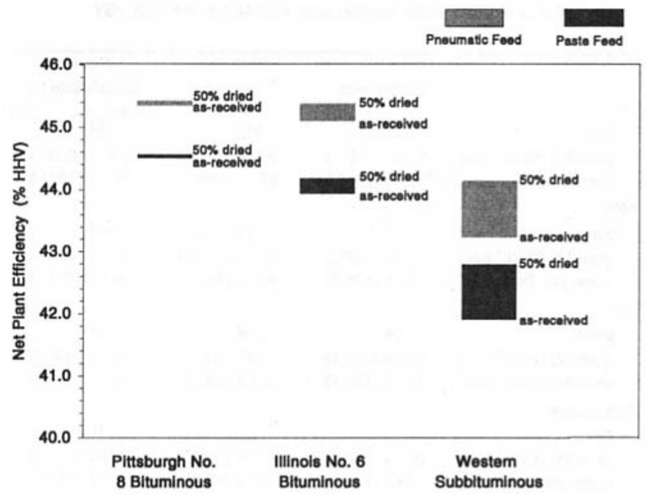

Fig. 7 Performance sensitivity to alternate coals and feeds

In paste feed, water is mixed with coal and limestone to form a paste which is then injected into the combustor by paste pumps. According to the typical requirements of paste pumping systems, the amount of water added for making the paste is assumed to be 18 percent by weight of the final paste for all three coals. This results in a total water content in the paste of about 22 percent for the Pittsburgh bituminous coal, 27 percent for the Illinois bituminous coal, and 43 percent for the Western subbituminous coal. In pneumatic feed, a transport air compressor and lock hopper system is utilized to feed coal and limestone. For depletion of coal moisture when appropriate, the waste heat of stack flue gas is used to dry the coal feedstock, without need for consuming additional fuel. The stack gas from the DBC-GT still contains sensible heat at a temperature of around 243°C (469°F) that could be utilized in many ways, including drying the feedstock, without adverse effect on power generation.

Figure 7 displays the performance sensitivity of the nominal 400 MWe plant to alternate coals and feeding methods. As seen, the performance is closely affected by the higher heating values of the coals, which are largely related to the moisture contents, and by their sulfur and ash contents. These properties affect solids handling duties for feedstock (coal and limestone) and in ash disposal. For example, the plant using the Illinois coal involves 38 percent more feedstock flow and 150 percent greater ash disposal than the one using the Pittsburgh coal. A higher moisture content incurs a larger latent heat loss from water evaporation during combustion, and, thus, lowers the thermal efficiency.

Using pneumatic feed, instead of paste feed, for all three coals leads to a significant improvement of plant efficiency, as it avoids the large heat loss from evaporation of the water added in making paste, and it also reduces the mass flow with attendant loss of stack heat.

The incentive for drying coal is greatest for the high-moisture, Western subbituminous coal, as seen in Fig. 7. When this coal is depleted of 50 percent of the coal-bound moisture, the net plant efficiency is increased by approximately 1 percent for both paste and pneumatic feed cases. The ability of the DBC-GT to achieve efficient power generation with low quality coals is an attractive design feature.

Environmental Impact

The DBC-GT offers outstanding environmental performance. The plant exceeds present emission requirements by large mar-

Table 4 Emission performance of 400 MWe DBC-GT*

Emissions	Pittsburgh No. 8 Bituminous	Illinois No. 6 Bituminous	Western Subbituminous
SO_2			
ppmv	159	361	54
gram/MJ (lb/10^6 Btu)	0.143 (0.331)	0.340 (0.791)	0.054 (0.125)
tonne/year (ton/year)	2645.6 (2916.2)	6315.2 (6961.2)	994.1 (1095.8)
NOx			
ppmv	48	48	48
gram/MJ (lb/10^6 Btu)	0.031 (0.072)	0.033 (0.076)	0.035 (0.081)
tonne/year (ton/year)	577.5 (636.6)	607.5 (669.6)	643.0 (708.7)
CO			
ppmv	24	24	24
gram/MJ (lb/10^6 Btu)	0.009 (0.022)	0.010 (0.023)	0.011 (0.025)
tonne/year (ton/year)	175.8 (193.8)	184.9 (203.8)	195.7 (215.8)
Particulates			
ppmw	10	10	10
gram/MJ (lb/10^6 Btu)	0.004 (0.009)	0.004 (0.010)	0.004 (0.010)
tonne/year (ton/year)	74.1 (81.7)	77.3 (85.2)	80.3 (88.5)

* based on coal HHV and at 65% capacity factor where applicable

gins. In fact, it is capable of achieving emission levels low enough to permit installation in or near urban areas.

The first direct benefit of the plant's high efficiency is low specific CO_2 discharge. Second, the clean burning capabilities of the CPFBC ensure low stack emissions of pollutants. Combustion in the CPFBC takes place at low temperature with staged combustion air, which typically limits the total NO_x emissions to less than 50 ppm. To control SO_2 emission, limestone is added during combustion to react with coal-bound sulfur to allow 90–95 percent sulfur capture at efficient limestone utilization. Finally, the filtration of flue gas by ceramic filters ensures dust concentration in the stack below 10 ppm.

Table 4 details the estimated atmospheric emissions from a 400 MWe DBC-GT plant for the three representative coals.

The Dual Brayton Cycle eases the requirements of plant waste heat rejection. The high cycle thermal efficiency minimizes waste heat rejection from the plant. Furthermore, the cycle rejects the waste heat over a broad high temperature range. As a result, the DBC-GT requires about half the circulating cooling water flow needed in a comparable combined-cycle plant, and employs correspondingly smaller circulating circuits and cooling towers. The high temperature heat rejection also makes dry (air) cooling feasible at those sites where cooling water resources are limited.

Commercialization

All of the technologies required by the DBC-GT are accessible for near-term commercialization. The CPFBC is a current, state-of-the-art technology that is being commercially developed and demonstrated by industries and government-sponsored projects throughout the world (Moore, 1993). A number of vendors are championing this technology, which is expected to enter the coal power generation market in the near future.

The open-cycle gas turbine required by the DBC-GT can be selected from several existing machines, some of which are already in operation in commercial PFBC power plants. The closed-cycle gas turbine is a proven, although relatively underutilized, technology. More than 20 closed-cycle gas turbine plants have been built and operated worldwide (Bammert, 1975; Zenker, 1988). Recent technological advances in industrial and aircraft gas turbines and modern numerical modeling techniques have provided the opportunity to substantially improve existing closed-cycle gas turbine technology. The development of closed-cycle helium turbine technology in recent years has had the benefit of extensive studies by the U.S. Department of Energy, electric utilities, and power equipment suppliers (U.S. DOE, 1994).

Development of a prototype plant, in an optimal size range of 100–200 MWe, would be the first step in commercial deployment. The prototype plant will provide the design basis and operational experience necessary for scale-up to larger sizes. In addition, the prototype plant is itself in a size range of commercial interest in many parts of the world.

Nearly 600 GWe of new electrical generating capacity addition is planned worldwide for the 1990s, and the same or greater power addition is anticipated for the first decade of the next century. Coal, the most abundant and reliable fossil fuel in the world, is predicted to be the choice of fuel for about 50 percent of worldwide power plant additions, at an average rate of 70 GWe per year over the next 10 to 20 years. Timely and successful development of the DBC-GT would make the technology well positioned to respond to the growing electric power demands worldwide. The simplicity, low cost, high efficiency and sound environmental performance of the DBC-GT should make the technology an attractive option in power generating markets.

References

Bammert, K., 1975, "A General Review of Closed-Cycle Gas Turbines Using Fossil, Nuclear and Solar Energy," Thiemig-Taschenbücher, Band 57 Verlag Karl Thiemig, Munich.

Moore, T., 1993, "A Brighter Future for PFBC," *EPRI Journal,* Dec. pp. 16–23.

Rehwinkel, H., Meier, H.-J., and Wedel, G. V., 1993, "Bubbling and Circulating Pressurized Fluidized Bed Combustion," *VGB Kraftwerkstechnik,* Vol. 73, No. 6, pp. 1–8.

Robertson, A., and Bonk, D., 1993, "Electric Utility Second-Generation Pressurized Fluidized Bed Combustion Plants," *Application of Fluidized-Bed Combustion for Power Generation,* proceedings, EPRI TR-101816, pp. 29-1–29-14.

U.S. Department of Energy, 1994, "MHTGR Development in the United States," *Progress in Nuclear Energy,* Vol. 28, No. 3, pp. 265–333.

Yan, X. L., and Lidsky, L. M., 1996, "Dual Brayton Cycle Gas Turbine Utilizing a Circulating Fluidized Bed Combustor," U.S. Patent No. 5,544,479.

Zenker, P., 1988, "Ten Years of Operating Experience with the Oberhausen Helium Turbogenerator Plant," *VGB Kraftwerkstechnik,* Vol. 68, No. 7, pp. 616–621.

M. T. Turner
Propulsion Systems Integration,
Rolls-Royce,
P.O. Box 3, Filton,
Bristol, BS12 7QE, United Kingdom

J. W. Chew
Mechanical Science Group,
Rolls-Royce,
Moor Lane,
Derby, DE24 8BJ,
United Kingdom

C. A. Long
Thermo-Fluid Mechanics Research Centre,
University of Sussex, Brighton,
Sussex, BN1 9QT,
United Kingdom

Experimental Investigation and Mathematical Modeling of Clearance Brush Seals

In this paper, an experimental program and a CFD based mathematical model using a brush seal at two bristle to rotor clearances (0.27 mm and 0.75 mm) are presented. The experimental program examined the radial pressure distributions along the backing ring, the axial pressure distribution along the rotor, and the mass flow through the seal through a range of pressure ratios while exhausting to atmosphere. The results from this experimental program have been used to further calibrate a CFD-based model. This model treats the bristle pack as an axisymmetric, anisotropic porous region, and is calibrated by the definition of nonlinear resistance coefficients in three orthogonal directions. The CFD analysis calculates the aerodynamic forces on the bristles, which are subsequently used in a separate program to estimate the bristle movements, stresses, and bristle and rotor loads. The analysis shows that a brush seal with a build clearance produces a very different flow field within the bristle pack to one with an interference, and the need to understand the bulk movements of the bristles. These are shown to be affected by the level of friction between the bristles and the backing ring, which has an important effect on the bristles wear and seal leakage characteristics.

1.0 Introduction

Since Ferguson [1] published his paper on brush seals in 1988, there has been an ever increasing interest in their usage and in the mechanisms that control their performance. The driving force behind this was the opportunity of using them as a direct replacement for labyrinth seals, giving a substantial improvement in leakage characteristics. It was recognised that if this was possible, particularly in the more arduous sealing positions of a gas turbine, significant improvements in cycle efficiencies could be achieved [2]. Although a brush seal looks very simple in its design, research and aero engine experience has shown the complex nature of the flow fields and mechanics. Braun et al. [3] showed that many different flow features of through flow exist in a seal. For example, rivering and jetting. Other authors have shown that there can be significant hystersis in their flow characteristics or bristle stiffening effects when a differential pressure is applied [4].

A schematic of the brush seal used is shown in Fig. 1, which is comprised of three main components: the brush pack, the side plate, and the backing ring. The brush pack is clamped between a side plate, on the high pressure side, and a backing ring, on the low pressure side giving support to the bristles. The construction is held together by a weld around the outer diameter. The bristles which are made from typically 0.076 mm diameter super-alloy wire are inclined in the orthogonal ($r-\theta$) plane at a "lay angle" of 45 deg to the radial direction, with a typical packing density of 200 bristle per mm circumference. To obtain good sealing characteristics, it is important that the geometry is suited to the environment in which the seal will be working. This may require the designer to decide what are the most important characteristics. These could be seal leakage, wear rates and service life, pressure bearing capacity, or tolerance of rotor to stator relative movements. This is particularly true when the seal is subject to the harsh environment of the gas turbine core where differential pressures of 1500 kPa, temperatures of 900 K, and surface speeds of 300 m/s are possible, with designers wanting to extend their operational range still further. Design variables for a brush seal include bristle length, diameter and material, backing ring to rotor clearance, bristle to rotor interference (or seal clearance), pack thickness, and bristle lay angle.

To understand brush seals better a number of mathematical models have been developed and published. These have ranged from full computational fluid dynamic (CFD) calculations, to one-dimensional porosity-type approaches. For example, Braun and Kudriatsev [5], calculated the flow through a two-dimensional array of circular pins within a laminar incompressible flow field. Dowler et al. [6], in comparison, used resistance coefficients that are estimated from work on cylindrical bodies in a cross-flow field. Many of the workers have also endeavoured to predict the bending of the bristles, carried out with the use of simple cantilever bending theory.

In a previous paper by Bayley and Long [7], the bristle pack was treated as an axisymetric, two-dimensional, anisotropic Darcian porous medium, incorporating a "porosity value" that is the ratio of the resistance coefficients in orthogonal directions. An experimental program was also presented that examined the pressure field axially along a static rotor, and radially down the backing ring (from which the porosity values were determined). This used a brush seal with an interference fit between the bristles and the static rotor. To enable the combination of both viscous and inertial effects, a non-Darcian approach was adopted in the paper by Chew et al. [8]. This again assumed that the bristle pack is a axisymetric, anisotropic porous region, but incorporates nonlinear resistance coefficients with the coefficients determined from the measurements by Bayley and Long [7, 9].

One of the main obstacles that brush seals need to overcome, before they are fully accepted as alternative to labyrinth seals in gas turbines, is the control of bristle wear, and, consequential, the increase of leakage flow. An increased brush seal flow can have a number of effects. Firstly, there will be a loss in performance by the leakage of high pressure air by-passing the combustion chamber and turbine rotor blades. There can also be a spoiling effect as the leakage flow returns to the main turbine

---

Contributed by the International Gas Turbine Institute and presented at the International Gas Turbine & Aeroengine Congress & Exhibition, Orlando, FL, June 2–5, 1997. Manuscript received by the ASME Headquarters March 15, 1997. Paper No. 97-GT-282. Associate Technical Editor: H. A. Kidd.

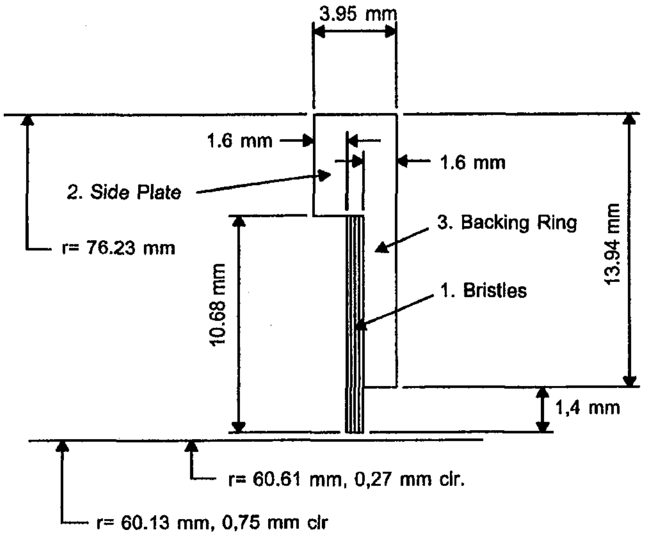

Fig. 1 Schematic of the experimental brush seal

gas stream, reducing turbine efficiency. In some cases, depending on the design of the secondary air system, the additional leakage flow can increase the downstream pressure of the seal, which affects the fine balance of the bearing loads.

What is sometimes more important to the designer is not the smallest flow possible, (as some flow may be required to stop hot gas ingestion), but a predictable and stable leakage, keeping the bearing loads within their design specifications, and maintaining optimum turbine efficiency. One way of achieving this is to design a brush seal with an initial "running" clearance, or, in other words, using a seal that has already been "worn-in". By having an initial running clearance, Ferguson [1] showed that the leakage flow would still be a quarter to one-fifth of what would be expected through an annular gap with similar dimensions, although current experience shows this to be slightly optimistic. The difference was put down to an effect, where the bristles close down the clearance under the influence of the differential pressure across the brush seal. This effect is called "blow down", which is now known to be due to the radial inward flow within the brush pack.

In this paper, the experimental work carried out by Bayley and Long [7] at the University of Sussex is extended to include clearance seals. These results have subsequently been used to further calibrate the Chew et al. [8] CFD model.

2.0 CFD Modeling

2.1 Mathematical Model. The brush seal model used is that described in detail in Chew et al. [8]. However, for completeness, a brief description is given here. The fluid dynamics model is based on the algorithm described by Moore [10], which incorporates the nonlinear, anisotropic porosity treatment of the brush. Aerodynamic bending forces on the bristle obtained from this calculation are used in a bending calculation routine based on first-order bending theory that estimates bristle deflections and associated forces.

Outside the bristle pack the CFD code solves the usual Reynolds-average, Navier-Stokes equations with a mixing length model of turbulence. In the present study, uniform total temperature of the air is assumed. Within the pack the following extra source (or body force) term is included in the momentum equations to account for the drag of the bristles on the air.

$$F_r = -\tilde{A}u\mu - \tilde{B}\rho|u|u, \qquad (1)$$

where F_r is the resistance force per unit volume, $\tilde{A}$ and $\tilde{B}$ are viscous and inertial resistance tensors, u is the mean velocity vector, μ denotes the dynamic viscosity, and ρ denotes the fluid density.

The resistance tensors are assumed constant throughout the brush with the principal directions aligned with the bristle in the axial direction and normal to the bristle in the axial plane. Thus, there are a total of six resistance coefficients, (a_s, a_n, a_z, b_s, b_n, and b_z) that can be defined and adjusted to calibrate the model. The boundary conditions for the CFD calculation requires the specification of the total pressure and flow angle at inlet, static pressure at exit, and no-slip on walls.

Once the CFD solution has been obtained, Eq. (1) may be used to calculate the aerodynamic forces on the bristle. Bending calculations then give the bristle deflections in both the axial direction and orthogonal plane. The most general model separates the pack into a number of bristle rows, but for the orthogonal plane bending calculation a bulk model can also be employed. This bulk model averages the aerodynamic forces across the bristle rows, but retains the variation along the bristle length. Beam flexure theory is then applied to obtain the deflection and shaft contact force associated with an average bristle. Friction between the bristle pack and the backing ring edge was neglected in the results presented by Chew et al. [8] but is included here. A simple model is used in which static and kinetic friction factors are assumed equal and constant. This involves the inclusion of the following forces in the bending calculation:

$$S = \min(\alpha R, F_{eq}), \qquad (2)$$

where S is the frictional force, α is the friction factor, R is the reaction between the bristle pack and the backing ring edge, and F_{eq} is the force required to maintain zero deflection for the bristle at some initial position. For the present results, the initial position was taken to be that assumed by the bristles prior to the application of the aerodynamic forces.

Nomenclature

$\tilde{\mathbf{A}}$ = viscous resistance tensor
a = principal viscous resistance coefficient
$\tilde{\mathbf{B}}$ = inertial resistance tensor
b = principal inertial resistance coefficient
$\mathbf{F}_r$ = resistance force per unit volume
F_{eq} = force required to maintain zero deflection
L = distance from shaft to side plate inner radius
p = absolute pressure
P^* = nondimensional pressure ($P^* = (p - p_u)/(p_u - p_d)$)
R = reaction between bristle pack and backing ring
R_p = pressure ratio ($R_p = p_u/p_d$)
r = radial coordinate
r_s = radius of shaft
S = frictional force
$\mathbf{u}$ = mean velocity vector
Y = nondimensional radial position ($(r - r_s)/L$)
z = nondimensional axial position relating to the pressure tapping no.
α = friction factor
ρ = density of fluid
μ = dynamic viscosity of fluid
θ = tangential coordinate

Subscripts

d = downstream
n = normal direction, to bristles (in $r - \theta$ plane)
u = upstream
s = parallel direction, to bristles
z = axial direction, to bristles

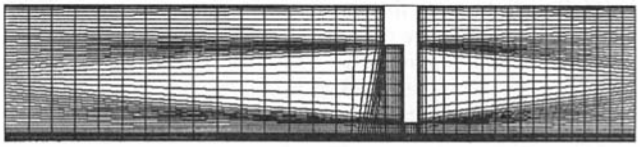

Fig. 2 Typical brush seal CFD mesh (76 × 52 Grid)

A typical grid used for the CFD calculations is given in Fig. 2 (this contains a 76 by 52 mesh). While full grid independence is not claimed, numerical tests as reported in Chew et al. and additional tests on clearance seals have shown that the level of accuracy is reasonable.

2.2 Choice of Resistance Coefficients. The method by which the resistance coefficients were chosen was described for an interference seal by Chew et al. [8]. This showed that the axial resistance's (a_z and b_z) principally controlled the mass flow, while the backing ring pressure distribution was affected mainly by the degree of anisotropy. It was found that an anisotropic ratio of $a_z = 60a_s = a_n$, with $a_z = 5.317 \times 10^{11}$, and $b_z = b_n = 1.998 \times 10^6$, with $b_s = 0$ gave a reasonable fit. (This implies that the resistance coefficients are equal in the axial and normal—to the bristles—directions, and there is no inertial resistance in the direction of the bristles, which might be expected.)

In the experimental work detailed in this paper, the build clearances were achieved by running with reduced shaft diameters. For these conditions, two methods of modeling were utilized. This assumes either that the bristle pack was "not blown down" (remaining in its built condition), or that the pack was fully "blown down", so that the bristle tips touched the shaft. For the undisturbed pack, the resistance coefficients were kept the same as the interference case given above. For the "blown down" pack, it was again assumed that $a_z = 60a_s = a_n$ and $b_s = 0$, but the values were "adjusted" to give a reasonable fit to the backing ring pressure distribution and mass flow measurements; these values are given in Table 1.

Using these coefficients, the CFD model was run for a number of pressure ratios in both the "not blown down" and "blown down" positions. The results from each of these runs were fed into the bending program to give indications of the movements of each of the bristle rows. The discussion below details the results from these calculations, with a comparison of the experimental to theoretical results.

3.0 Experimental Apparatus

A section through the test rig is shown in Fig. 3. The seal is clamped between the front cover plate and spacer rings. The nonrotating test piece forms a dummy "rotor", and the outer diameter of this is machined to give the appropriate static radial seal clearance between the bristle tips and rotor. Flow is supplied to the rig from a 400 kW Howden screw compressor, and the flow rate measured using an "Annubar". Air enters the rig through a hole in the rear cover plate. Thirty 10 mm holes and a 0.1 mm mesh-size, stainless steel gauge distribute the incoming air evenly into an annular plenum chamber upstream of the seal.

Table 1 Resistance coefficients for a "blown down" clearance seal

Interfer./ clearance	a_n	a_s	a_z	b_n	b_s	b_z
-0,27mm	5.317 x10^{11}	8.8617 x10^9	5.3170 x10^{11}	1.998 x10^6	0	1.998 x10^6
0,27 mm.	1.8284 x10^{10}	3.0473 x10^8	1.8284 x10^{10}	1.710 x10^5	0	1.710 x10^5
0,75 mm.	1.4 x10^9	2.3333x 10^7	1.4 x10^9	7.0 x10^4	0	7.0 x10^4

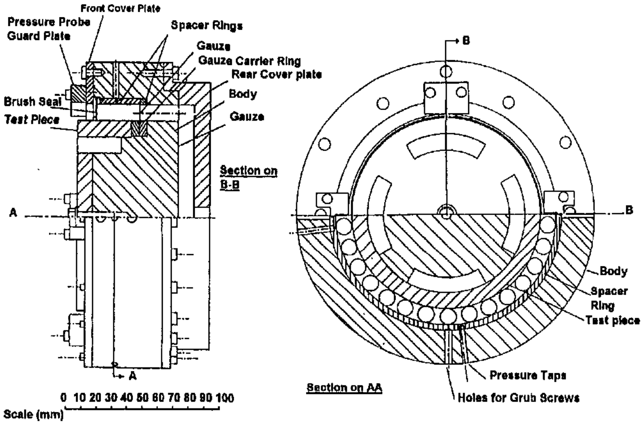

Fig. 3 Section through the brush seal experimental test rig

The pressure distribution in the radial and axial directions are measured by pressure tappings located in the backing ring and in the rotor surface. The radial pressure tappings are located at four different circumferential locations. Each set comprises five separate 0.25 mm diameter pressure tappings that are laser drilled in the backing ring at equally spaced intervals between the front plate and backing ring inside diameters. The test piece, or rotor, contains twenty-four 0.25 mm diameter axial pressure tappings. These are located at angular intervals of 15 deg, and separated by 0.06 mm in the axial directions. With this arrangement, 11 of the pressure tappings are expected to be under the bristle tips. The remaining tappings are to accommodate the expected axial deflections of the bristles and the uncertainty in the exact location of the brush seal in the housing. Tests were carried out for the range of upstream absolute pressures, between 108 kPa and 400 kPa. The pressures were measured by a 50-port Scanivalue. During the test, each of the measurement ports were opened for 0.5 s. Four complete sets of measurements would usually be made at a particular value of upstream pressure. There were only small variations in the four sets of scans, which have been assumed to be negligible, and, therefore, only averaged results have been presented.

Some tests were conducted with superimposed vibration. To allow transmission of this to the seal itself, the mass of the rig was supported on a separate frame using four springs and allowed to slide up and down on PTFE bushes. This allowed vibration levels of 10 mm/s at 300 Hz to be superimposed. The tests discussed were conducted with and without superposed vibration. However, this was found to make no significant difference to either the mass flow through the seals, the pressure distributions, or the observations of the bristle deflection. It was noted, however, that a shock loading applied to the body rig did make significant differences.

4.0 Results and Discussion

4.1 Fluid Dynamics. Examples of the predicted velocity fields in the vicinity of the seal for the 0.75 mm clearance seal are given in Fig. 4 for a pressure ratio of 2. Considering Fig. 4(*a*) first, the bristles in this brush are of an undisturbed bristle pack. The vector plot shows that the seal leakage occurs predominately underneath the bristle tips, while the flow in the brush pack is relatively weak, and, mainly, radially inwards, particularly in the front and rear bristle rows.

In Fig. 4(*b*), the seal and conditions are identical to Fig. 4(*a*); however, the bristles are assumed to have "blown down" under the aerodynamic force of the radial inward flow, which were observed experimentally by Ferguson [1], and the adjusted

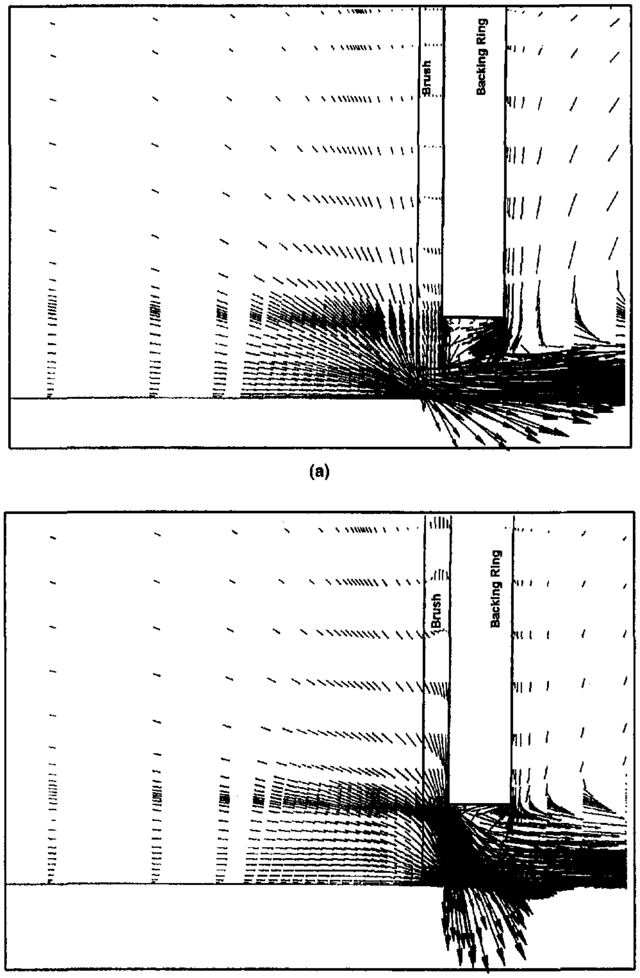

(a)

(b)

Fig. 4 (*a*) "Not blown down seal" 0.75 mm clearance, *Rp* = 2; (*b*) "Blown down seal" 0.75 mm clearance, *Rp* = 2

resistance coefficients are used. In this case, the flow field is similar to that of an interference seal, with the axial flow evenly distributed across the overhung bristle and a strong radially inward flow in front of the bristles and within the brush pack itself.

Having these two types of flow it can be seen that the mass flow through the seal can vary significantly depending on whether the seal is "blown down" or not. Initially, assuming that there are no three-dimensional effects and that the seal had a clearance under the bristle, the mass flow would be controlled by the bristle clearance gap, with the backing ring clearance a second-order effect. Whereas when the bristles are blown down, the flow would be controlled by the backing ring clearance. In reality, if this were the case, the mass flow rate would be close to an interference seal. By examination of the results presented in section 4.3, they are obviously not, a discrepancy that may be explained by the presence of nonaxisysmetric effects, such as rivering (Braun et al. [3]). A further explanation could come from the possibility of the bristle not blowing in fully and becoming "locked up" against the backing ring. This would be dependent on a number of factors, with the predominant factor being (1) the friction between the rear bristles and the backing ring, and (2) the ability of the bristles to slide over one another.

4.2 Pressure Distributions. Tests were conducted over the range of upstream gauge pressures $8 < p_0 < 270$ kPa, and approximately 40 tests were conducted for each radial clearance build. For all the tests, the air inlet temperature was about 20°C. The downstream gauge pressure (p_1) was equal to zero, and p_{at} was equal to, approximately, 100 kPa. In order to show the physical behavior of the seal, it is convenient to present these results in bands of pressure ratio, R_p.

4.2.1 Radial Pressure Distribution. The pressures, referred to as P^*, are nondimensionalized with respect to the upstream pressure p_u. These are plotted against Y, which is the nondimensional distance from the shaft. The variation of radial pressure distribution with pressure ratio for the two radial clearance builds is summarized in Fig. 5. At the lowest pressure ratio, there is a significant overall drop in pressure from $Y = 1$, at the outer radius of the front plate, to $Y = 0.2$, at the innermost pressure tapping. As the pressure ratio is increased, this overall pressure gradient is reduced. Similarly, increasing the radial build clearance also reduces the pressure gradient. This would be consistent with a reduction in the degree of anisotropy of the pack. This occurs in both clearances, and it implies that the radial component of the total mass flow reduces as the pressure ratio is increased. It is interesting to note that the experimental measurements for the 0.75 mm clearance seal show different forms of the radial pressure distribution; as the pressure ratio is increased from $R_p = 2$ to 3, the radial pressure gradient is significantly reduced.

The CFD modeling results for the radial pressure distribution with the assumption of a "not blown down" and "blown down" seals are also shown in Fig. 5 for the 0.75 mm clearance seal at a pressure ratio of 2. The fit between the experimental and theoretical results is considered reasonable. It also must be noted that the values are applied to the whole porous region and are constant for the whole range of pressure ratio modeled. In practice, this is unlikely to be the case since, as already detailed above, the degree of anisotropy appears to reduce as the pressure ratio increases. In simple geometrical terms, the bristles will be more packed together the further radially in you come. However, this may be counteracted by the splaying of the bristles tips, particularly at low pressures.

4.2.2 Axial Pressure Distribution. It is recognized that there was some discrepancy in the relative position of the pressure tappings for these tests and a variation in the pressure levels recorded so that the interpretation of these results should be treated with caution. For this reason, the results were not used in the model calibration, but some of the results are presented here for information.

The variation of measured axial pressure distribution for the 0.27 mm seal for various pressure ratios is shown in Fig. 6. Again, the pressure P^* is nondimensionalized, with the axis of abscissa, z, corresponding to the pressure tapping number. Some

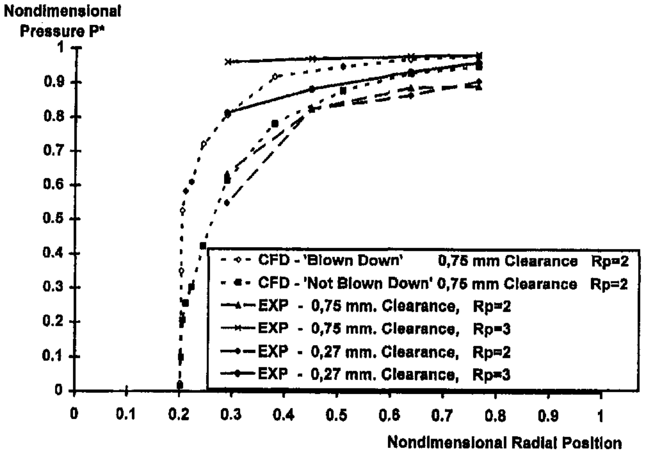

Fig. 5 Radial pressure distribution

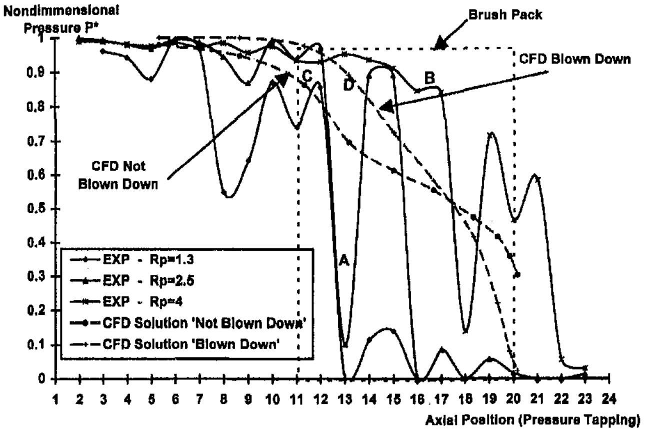

Fig. 6 Axial pressure distributions for the 0.27 mm clearance seal

scatter in the measurements is noted, and is believed to be due to circumferential variation for the bristles blowing inwards, with clumps of bristles moving down, and shielding individual pressure tappings. Another reason for the discrepancies may be due to the relative sizes of the pressure tapping holes (0.25 mm) and the 0.27 mm seal clearance.

Despite this scatter, the measurements indicate a sudden pressure drop as the flow enters the gap below the first line of bristles (A), which would be consistent with a vena-contracta effect. As the pressure ratio is increased and the bristles are observed to "blow down" and touch the rotor, the majority of the pressure drop occurs towards the rear of the brush pack, with the rate of pressure drop slightly reduced (B). (In Bayley and Long [7], the axial pressure distribution for a 0.25 mm interference seal show no vena-contracta effect). The CFD axial pressure distribution for the not "blown down" and "blown down" seal for a pressure ratio of 2 is also shown. This shows that the model predicts an initial pressure drop as the flow enters the pack, but is not as significant as the experimental results (C). For the "blown down" case the pressure drop is more even, and occurs further back in the pack (D).

4.3 Measured Mass Flows. The variation of measured mass flow through the brush seal with pressure ratio for each of the radial build clearances is shown in Fig. 7(*a*) and (*b*). As is to be expected, the mass flow is strongly dependent on the radial build clearance. For any clearance, the mass flow through the seal increases with pressure ratio. Although, when there is an initial clearance between the shaft and bristle tips, there is a rapid increase of mass flow. For the 0.27 mm radial build clearance tests, this occurs for $1 < R_p < 2$. For the tests with a 0.75 mm radial build clearance, the corresponding range is $1 < R_p < 2.5$. Above these pressure ratios, the mass flow increases less rapidly with increasing pressure ratio, which may suggest that this change occurs when the bristles make good contact with the surface of the shaft. In comparison, the measured flow given in Bayley and Long [7] for the case when there is an initial radial interference would appear to confirm this, with the flow increasing linearly with R_p. The results for the measured mass flow obtained from the 0.75 mm clearance seal when the test rig had been subjected to a shock load (high "*g*" case) are also given. These values are significantly lower than the nonshocked (low "*g*") cases, with the decrease in the flow indicating that the seal becomes more fully "blown down".

The results from the CFD modelling for the two cases are also shown, giving good agreement for both clearances. At the lower pressure ratios, the measured mass flows are in reasonable agreement with the CFD results for the not "blown down" case, at higher pressures there is better accord with the "blow down" CFD results.

4.4 Bending Model Results. Examples of results from the bending calculations are shown in Figs. 8 and 9. Note that constant aerodynamic forces are assumed in these calculations with values obtained from CFD solutions for the specific bristle pack locations.

Results from the frictionless bending model in which the pack is divided into 10 bristle rows are given in Fig. 8. These results here are for a pressure ratio of 2. Axial deflections are shown in Fig. 8(*a*) for a fully "blown down" 0.75 mm clearance seal. These show a maximum deflection of the order of 0.1 mm at the rear most bristles, and indicate bulging of the pack in front of the seal. Figure 8(*b*) gives the results from the orthogonal plane bending calculation. Here, the bristle to rotor load gives a measure of the aerodynamic "blow down" of the bristles. It is clear that the strongest forces occur on the downstream bristles and that the strength and distribution of the "blow down" force is dependent upon the clearance between the bristle pack and the rotor. Reducing the clearance reduces the strength of the blow down.

Figure 9 gives the results for orthogonal plane bending using the bulk model in which the aerodynamic forces are averaged over the bristle rows. Friction between the backing ring and the bristle pack is included in these calculations. The radial clearance predictions show that for sufficiently high friction factors the "blow down" of the pack is suppressed. The point at which this occurs is dependent upon both the pack-to-rotor clearance and the pressure ratio. This result is consistent with the experi-

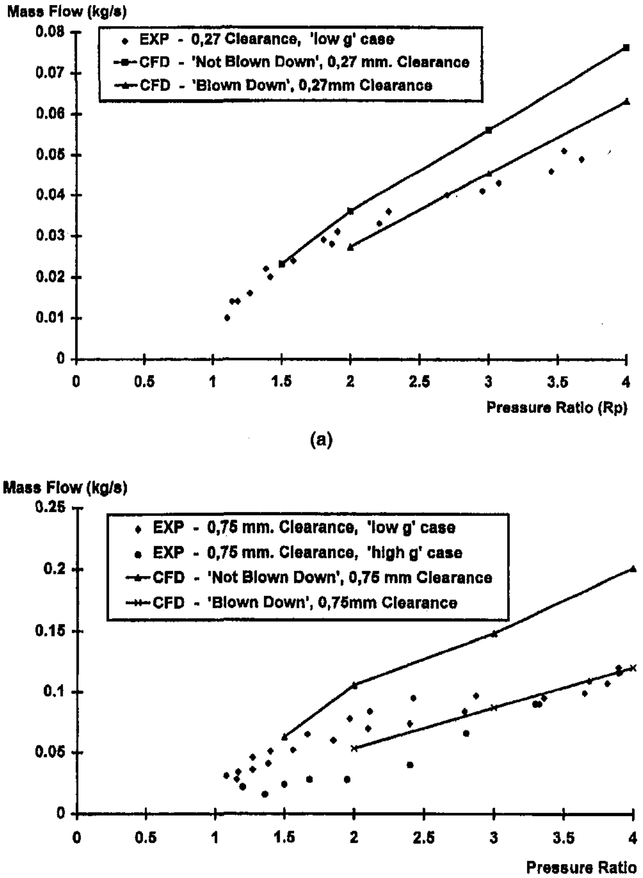

(a)

(b)

Fig. 7 (*a*) Mass flow versus *Rp* for the 0.27 mm clearance seal; (*b*) mass flow versus *Rp* for the 0.75 mm clearance seal

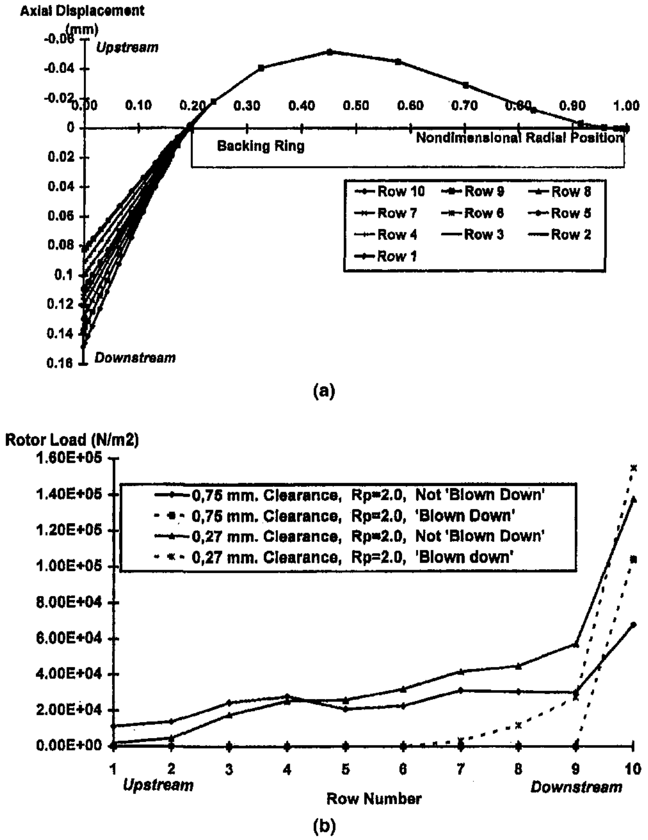

(a)

(b)

Fig. 8 (*a*) Axial displacement, 0.75 mm clearance seal, *Rp* = 2; (*b*) rotor loading due to aerodynamic forces

mentally observed effect of the high "*g*" force on flow rates for the 0.75 mm clearance seal (see Fig. 7).

This result shows theoretically the effects of hystersis and bristle stiffening described by Basu et al. [2] where the bristles can be "locked" against the backing ring and either cause an increase in leakage, or an increase in rotor to tip load. These effects have significant implications to the gas turbine designer, where rotor to stator relative movements are common. During accelerations (or deceleration) of a gas turbine, there are significant changes in the differential pressure as well as centrifugal rotor growth and thermal movements of the rotor and stator. If the brush seal becomes "locked" and the rotor moves away from the seal there will be a significant increase in leakage. Conversely, if the rotor moves towards the seal there will be large increase in the bristle to rotor loads causing a higher rate of wear.

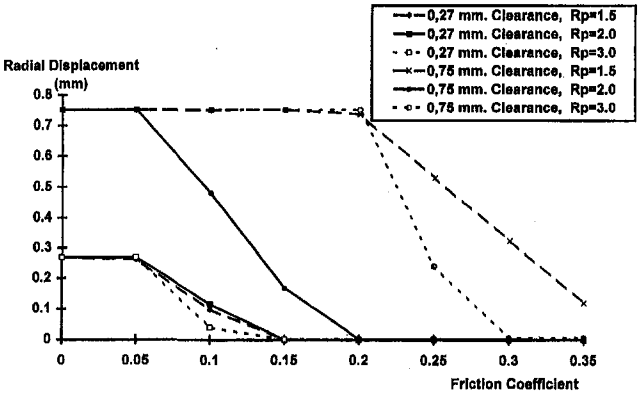

Fig. 9 Radial displacement of bristles

5.0 Conclusion and Possible Future Developments

Experiments have been conducted on clearance brush seals to measure the distribution of axial and radial pressures and their leakage characteristics, complementing previously published work using an interference seal. The clearances used were 0.27 mm and 0.75 mm, with pressure ratios of up to 4, with the seal flow exhausting to atmosphere. The results from these experiments have been used to further calibrate a CFD brush seal model. The code calculates the aerodynamic forces applied to the bristle, which can used in a bending calculation routine that yields information on the mechanics of clearance brush seals.

Consistent experimental results were obtained from the radial pressure distribution and leakage characteristic; however, the axial pressure distribution results needed careful interpretation. The results clearly showed that the flow through a brush seal is very dependant on the position of the bristles. If a brush seal is built with a clearance, the aerodynamic forces will tend to move the bristles towards the rotor. The movement is very dependent on the balance between the normal aerodynamic forces and the friction levels in the brush pack. Due to the "blow down" effect of the seal and the locking effect of the friction, building a seal with a clearance may not give the desired effect of reduced wear when associated with an environment where there is relative radial movement between rotor and brush pack.

The study further confirms that the use of a non-Darican approach can give good agreement to experimental results, even with the simplistic use of uniform resistance. However, it is noted that the experimental data is still somewhat limited and that there is clearly scope for further calibration of the model, as and when further data becomes available. There is a particular need for the pressure distribution within the pack rotor pressures and the mass flow. If improved pressure distribution data was available, it may show the need for the CFD model to contain variable resistance coefficients throughout the grid that were dependant upon the movement of the brush pack. To do this, it would also require a link between the bending routine and the CFD code to allow an iterative calculation to be carried out. Further areas of uncertainty are the pressure distribution within a seal, with a rotating rotor, and the effect on the bristle tips when placed within a boundary layer with a circumferential flow of 300 m/s.

The development of the CFD code and bending routine has generated a valuable research tool that can be used to aid the development of new brush seal designs and arrangements, in a quick and inexpensive manner, as a screening method to reduce the number of seal designs that are required to be manufactured and rig tested for proof of concept. It is also helping us to understand the complex mechanisms that affect the operation of brush seals.

6.0 Acknowledgments

The authors would like to thank Rolls Royce for their permission to publish this work, the MOD for their support, and their colleagues past and present at the University of Sussex, and Rolls Royce for their assistance in the many technical discussions that have taken place examining the experimental and theoretical results, particularly L. Lapworth, P. Millener, and P. Withers.

7.0 References

1 Ferguson, J. G., 1988, "Brushes as High Performance Gas Turbine Seals," ASME Paper No. 88-GT-182, presented at the Gas Turbine and Aeroengine Congress, The Netherlands.

2 Chupp, M. J., and Dowler, R. C., 1991, "Evaluation of Brush Seals for Limited-Life Engines," AIAA Paper No. 90-2140, presented at the 26th Joint Propulsion Conference, July 16–18, 1990, Orlando, FL.

3 Braun, M. J., Canacci, V., and Hendricks, R., 1990, "Flow Visualization in a Simulated Brush Seal," ASME Paper No. 90-GT-217, presented at the Gas Turbine and Aeroengine Congress, Brussels.

4 Basu, P., Datta, A., Johnson, R., Loewenthal, R., and Short, J., 1993, "Hystersis and Bristle Stiffening Effects of a Conventional Brush Seal," AIAA Paper No. 93-1996, presented at the 29th Joint Propulsion Conference, July 28–30, Monterery, CA.

5 Braun, M. J., and Kudriatsev, V. V., "A Numerical Simulation of the Brush Seal Section and Some Experimental Results," ASME *Journal of Turbomachinery*, Vol. 115, pp. 404–410.

6 Dowler, C. A., Chupp, R. E., and Holle, G. F., 1992, "Simple Effective Thickness Model for Circular Brush Seals," AIAA Paper No. 92-3192, presented at the 28th Joint Propulsion Conference, July 6–8, Nashville, TN.

7 Bayley, F. J., and Long, C. A., 1993, "A Combined Experimental and Theoretical Study of Flow and Pressure Distribution in a Brush Seal," ASME JOURNAL OF ENGINEERING FOR GAS TURBINES AND POWER, Vol. 115, No. 2, pp. 404–410.

8 Chew, J. W., Lapworth, B. L., and Millener, P. J., 1995, "Mathematical Modelling of Brush Seals," accepted in *Int. J. Heat & Fluid Flow.*

9 Long, C. A., private communications.

10 Moore, J. G., 1985, "Calculation of 3D flow without Numerical Mixing," AGARD Lecture Series No. 140 on 3D Computational Techniques Applied to Internal Flows in Propulsion Systems.

Fundamental Heat Transfer Experiments of Heat Pipes for Turbine Cooling

S. Yamawaki
Ishikawajima-Harima Heavy
Industries Co., Ltd.,
Advanced Technology Department,
Aero-Engine & Space Operations,
229, Tonogaya, Mizuho-Machi,
Nishitama-Gun, Tokyo 190-1297,
Japan

T. Yoshida

M. Taki

F. Mimura

National Aerospace Laboratory,
Chofu, Tokyo 182-8522,
Japan

Fundamental heat transfer experiments were carried out for three kinds of heat pipes that may be applied to turbine cooling in future aero-engines. In the turbine cooling system with a heat pipe, heat transfer rate and start-up time of the heat pipe are the most important performance criteria to evaluate and compare with conventional cooling methods. Three heat pipes are considered, called heat pipe A, B, and C, respectively. All heat pipes have a stainless steel shell and nickel sintered powder metal wick. Sodium (Na) was the working fluid for heat pipes A and B; heat pipe C used eutectic sodium-potassium (NaK). Heat pipes B and C included noncondensible gas for rapid start-up. There were fins on the cooling section of heat pipes. In the experiments, an infrared image furnace supplied heat to the heat pipe simulating turbine blade surface conditions. In the results, heat pipe B demonstrated the highest heat flux of 17 to 20 W/cm^2. The start-up time was about 6 minutes for heat pipe B and about 16 minutes for heat pipe A. Thus, adding noncondensible gas effectively reduced start-up time. Although NaK is a liquid phase at room temperature, the start-up time of heat pipe C (about 7 to 8 minutes) was not shorter than the heat pipe B. The effect of a gravitational force on heat pipe performance was also estimated by inclining the heat pipe at an angle of 90 deg. There was no significant gravitational dependence on heat transport for heat pipes including noncondensible gas.

Introduction

To improve the performance of gas turbines, the specifications for turbine inlet temperature continue to increase while cooling air flow is kept to a minimum. Generally, compressor discharge air has been used as the primary coolant of turbine components in cooling schemes that may involve convective, film, and impingement cooling methods. The temperature of the compressor discharge air increases with increasing pressure ratio of the gas turbine, reducing convective heat transfer inside the turbine blades. Alternative cooling schemes have been considered by many researchers. Although there are effective alternative coolants such as steam and water for an industrial gas turbine, an aero-engine can't use such alternative coolants. Currently, a heat pipe cooling is one of the most realistic alternative cooling schemes for a future aero-engine.

The super/hypersonic transport propulsion system research project has been conducted in Japan since 1989. The combined cycle engine, which is operated as a turbo-fan engine from takeoff to flight Mach number 3, is considered. A turbine inlet temperature is planned in the 1700°C class. A heat pipe turbine cooling system is being considered to protect turbine blades from such high temperatures while reducing cooling air flow and still maintaining high thrust at a high Mach number flight condition. The advantage of using heat pipes for a turbine cooling depends on heat transfer rate through heat pipes instead of cooling air.

Recently, Anderson et al. (1993a) studied the heat pipe cooling of future turbo-shaft engines. Silverstein et al. (1994), Gottschlich and Meininger (1992) carried out a feasibility study of heat pipe turbine vane cooling in an advanced military fighter engine. The calculated benefits from heat pipe cooling of vanes was a reduction in specific fuel consumption of 1.6 percent and an increase in specific shaft horsepower of 1.8 percent for a turboshaft engine and a reduction in SFC of 0.2 percent and an increase in thrust of 7.2 percent for a military fighter engine.

Our concept of heat pipe cooling shown in Fig. 1 resembles one of Silverstein et al. A difference is that we use cooling air for the leading edge and trailing edge region because we understand that heat pipes cannot transfer all the heat required to maintain an acceptable turbine blade temperature over the whole surface. Local maximum heat flux on a turbine blade may exceed the heat pipe specifications. Furthermore, the heat pipe can't cool the thin trailing edge region since a vapor space of the heat pipe is required.

Acceleration may effect heat pipe performance. Heat pipes are set at several angles in this concept to check that heat transfer rate of each heat pipe is not affected by gravitational force in steady conditions. Furthermore, the heat pipe must overcome the acceleration force in a flight maneuver. Although 10 g acceleration force are assumed in military engines, normal flight conditions mean low acceleration for a civil engine.

Also important is how fast heat pipes start, especially for aero-engines. Generally, a high temperature heat pipe uses alkali metal, which is solid phase at room temperature. It should thaw quickly in start-up. Previously, Yoshida et al. (1993) demonstrated the start-up time of a sodium heat pipe with screen mesh wick was about 90 minutes. That should be reduced to less than the typical start-up to take-off time.

We can demonstrate a short start-up time as well as high heat transfer rate of heat pipes. To reduce start-up time of liquid metal heat pipe, the inclusion of noncondensible gas is effective, as demonstrated by Ponnappan and Chang (1994). Anderson (1993a) stated that sintered powder metal wick produced a rapid start-up for an alkali metal heat pipe. It has a high capillary force that overcomes the high pressure drop during start-up.

In this paper, in order to estimate the feasibility of a heat pipe cooling system, we tried to confirm heat transfer rate, start-up time, and effect of gravitational force for three heat pipes. All heat pipes have a nickel sintered powder metal wick for high capillary pumping power. The effect of including a noncondensible gas and the phase of the working fluid at start temperature on cold start-up time are considered.

Contributed by the International Gas Turbine Institute and presented at the International Gas Turbine & Aeroengine Congress & Exhibition, Orlando, FL, June 2–5, 1997. Manuscript received by the ASME Headquarters March 15, 1997. Paper No. 97-GT-438. Associate Technical Editor: H. A. Kidd.

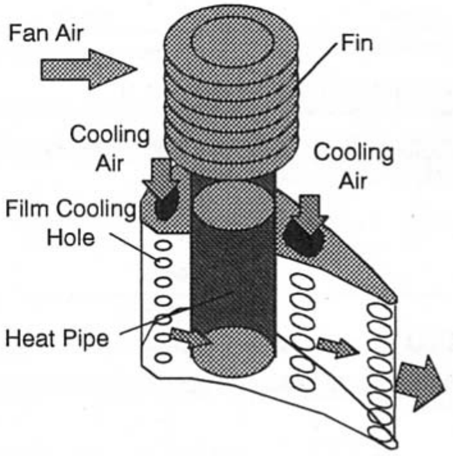

Fig. 1 **A concept of heat pipe turbine vane cooling**

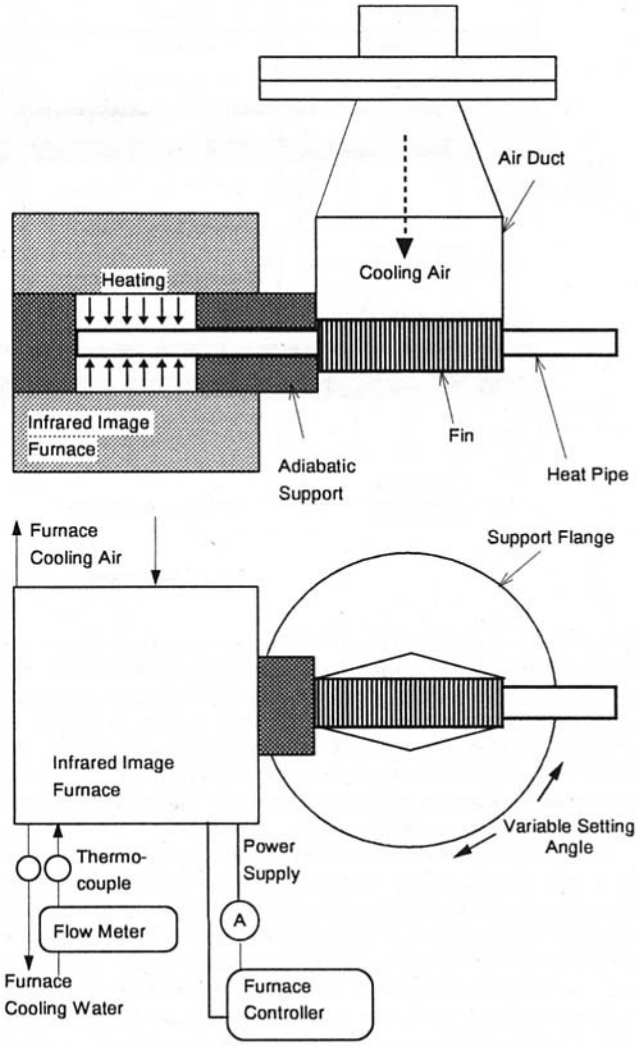

Fig. 2 **Experimental setup for heat pipe test**

Experiment

Figure 2 shows the experimental setup of heat pipe performance tests. In order to simulate a turbine vane, we selected an infrared image furnace, which can heat very rapidly at high heat flux, and heated a 100 mm length from the end of heat pipe. The heat pipe is supported by ceramic as an adiabatic section. An air duct is set to the fin of heat pipe condenser section. We didn't use cooling air for the results presented here. To confirm an effect of gravitational force on heat transfer rate and start-up time, the heat pipe setting angle can be changed from horizontal to vertical dispositions.

The configuration used to test the three heat pipes called heat pipes A, B, and C, respectively, are shown in Fig. 3. All the heat pipes have approximately the same dimensions. The outer diameter is 21.3 mm and the length is 460 mm. A nickel sintered powder metal wick and an artery were installed. For its low cost, the material of the heat pipe shell was stainless steel. There were fins in the condenser section. Heat pipe A has 40 square fins of 43.2 mm width, 0.74 mm thickness, 4 mm pitch, and 160 mm total length. Heat pipes B and C have 20 square fins of 31.55 mm width, 0.74 mm thickness, 4 mm pitch, and 80 mm total length. The reason why heat pipes B and C have smaller fins is that heat pipe A could not start because of too much heat loss from the condenser fins during start-up. Since the total length of the heat pipes were the same in active condenser length of heat pipes B and C were longer than the heat pipe A. The difference of inactive condenser length has negligible effect for heat pipes. The length of the evaporator is 100 mm, which is selected from furnace size. The adiabatic section has a length of 100 mm, which is selected as the same length as the evaporator length. Although the heat pipe dimensions are not based on the particular engines, our purpose of this experiment is to estimate fundamental heat transfer performance of heat pipes. The data will be useful for confirming predicted heat transfer performance in a feasibility study. Figure 4 shows a typical cross section of a heat pipe. There is an artery in the bottom of the heat pipe, and a thick nickel sintered powder metal wick installed inside the heat pipe shell. Detailed dimensions of the wick and artery were not supplied by Thermacore, which manufactured these heat pipes. These configurations are shown in the literature (Anderson, 1993b).

To confirm the effect of including a noncondensible gas, heat pipes B and C contained argon gas. The optimal pressure of argon gas should be determined for the best operation of each type of heat pipe considered. After several tests by Theremacore, 1 torr of argon gas was chosen; a similar pressure gave good results for Ponnapan and Chang. Sodium (Na) was the working fluid for heat pipes A and B; heat pipe C used an eutectic mixture of sodium and potassium known as NaK. A NaK heat pipe was demonstrated by Anderson (1993c). Eutectic NaK has a melting

Nomenclature

Ai = surface area of heating section
C = coefficient
di = pipe inner diameter
do = pipe outer diameter
hi = internal heat transfer coefficient for the air flow pipe
Nu = Nusselt number
q = heat flux
Q = heat transport rate
R = thermal resistance
le = length of heating section
T_{ow} = pipe outer surface temperature
T_{cb} = bulk mean temperature of air inside the air flow pipe
T_{we} = averaged surface temperature on the evaporator
T_{wc} = averaged surface temperature on the condenser
Re = Reynolds number
Pr = Prandtl number
X = length from heating start point
λ_m = heat conductivity of pipe material
λ_{cb} = heat conductivity of air based on film temperature

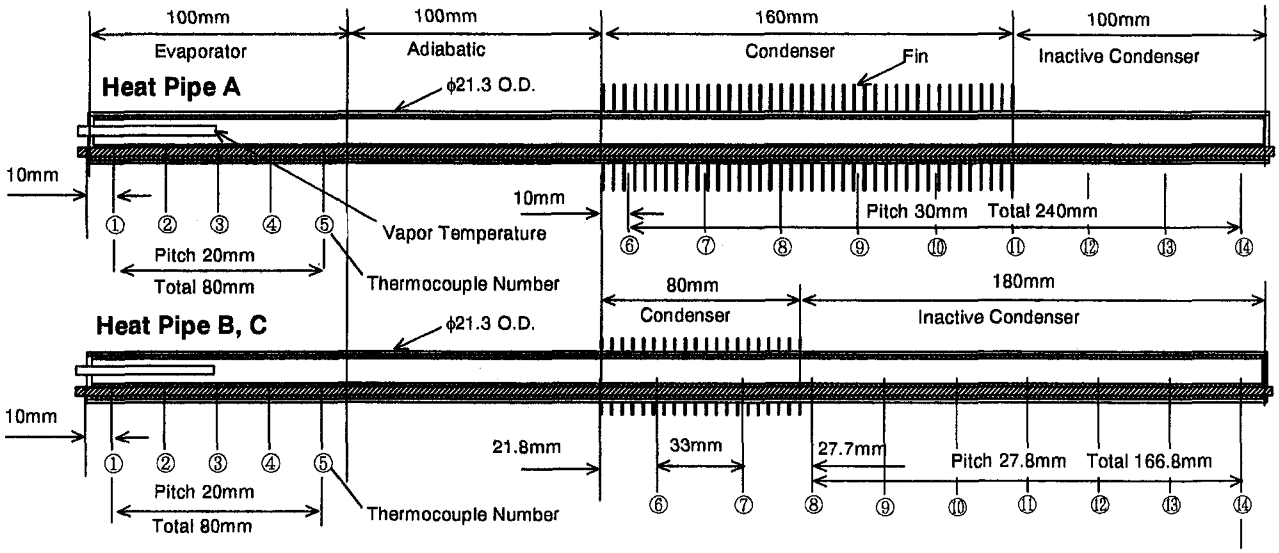

Fig. 3 Heat pipes dimensions and thermocouple locations

temperature of −12°C. When a sodium heat pipe is started up, the sodium is frozen. The sodium gradually melts as the thermal front propagates down the heat pipe. Working fluid can not be returned from the condenser to the evaporator until sodium is melted. In contrast, the start-up of a NaK heat pipe is simplified since the NaK is liquid at room temperature, eliminating the thawing associated with a sodium or potassium heat pipe. Table 1 summarizes the three heat pipe configurations.

In experiments, the surface temperature distribution along the heat pipe and the vapor temperature inside the heat pipe were measured by thermocouples. Electric power input to the furnace was estimated by measuring current and voltage. Thermocouple locations are shown in Fig. 3. Thermocouples on the evaporator and inactive condenser were set in wells in the heat pipe shell. For the condenser fin section, the junction of the thermocouple was attached on the heat pipe surface. For heat pipe A, the first experiment, temperature measurements were slightly poor. All measurements were controlled by a personal computer. The minimum time interval of measurements was every 3 seconds.

Since the furnace was cooled by water and air protecting the heater and mirror, large amounts of heat losses were unavoidable. A calibration was carried out to estimate actual heat input to the heat pipe. An air flow pipe was set instead of the heat pipe, as shown in Fig. 5. Actual heat transfer rate was estimated by measurements of the pipe surface temperature and air flow rate. If we know heat transfer coefficient inside the pipe at an air flow Reynolds number, we can calculate heat flux by Eq. (1) and Eq. (2).

$$q = (T_{ow} - T_{cb}) \Bigg/ \left(\frac{1}{h_i} + \frac{A_i \ln (d_o/d_i)}{2\pi \lambda_m l_e} \right) \qquad (1)$$

$$\mathrm{Nu} = \frac{h_i d_i}{\lambda_{cb}} = \left(1 + \frac{C}{(X/d_i)} \right) \times 0.022\ \mathrm{Re}^{0.8}\ \mathrm{Pr}^{0.5} \qquad (2)$$

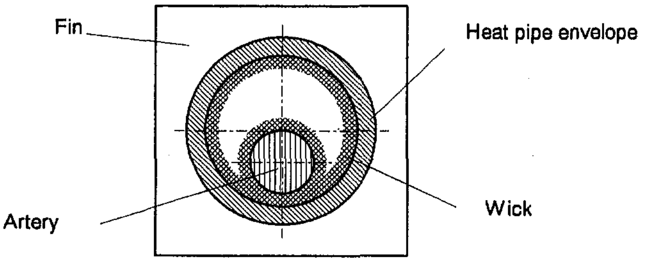

Fig. 4 Heat pipe typical section

Since the upstream length of the furnace was more than 10 times the inner diameter, the air flow inside the pipe must be fully developed turbulent flow. However, heating for the air flow pipe was begun in the furnace suddenly. The thermal boundary layer was developing in the heating section. According to Kays and Crawford (1980), C in Eq. (2) is about 1.4 for this experiment. To estimate internal heat transfer coefficient, we carried out a heat transfer experiment for the same pipe as shown in Fig. 6. A sheath heater was fit around the pipe, and a 50 mm thick glass wool was wrapped around the pipe and the heater. We can estimate heat flux from electrical power input to the heater by estimating heat loss from insulated glass wool surface as well as heat conduction along the pipe.

Results and Discussion

Calibration of Heat Input to the Heat Pipe. Figure 7 shows some results of the air pipe heat transfer experiments. The heat loss through the insulation is estimated from a correlation of natural convection from the horizontal pipe surface with the measured insulation temperature; it is to be about 10 to 15 percent of the power input. Actual heat input is estimated by subtracting the calculated heat loss from the measured input power. Figure 8 shows the relations of Nusselt number and Reynolds number for the air flow pipe internal heat transfer. The Nusselt number was 1.2 times greater than the case of fully developed pipe flow. It agrees with the case of $C = 1.4$ and $X/di = 6.21$ in Eq. (2).

Based on this result, we carried out the air flow pipe test with the furnace, and estimated the furnace efficiency defined by a ratio of actual heat transfer rate and supplied electric power shown in Fig. 9. The efficiency increased from 15 percent to 20 percent with increasing pipe temperature (400°C to 600°C). Data scatter was caused by variation of power input and the cooling water flow rate of the furnace. With the assumption that the efficiency continues to increase above 20 percent at even higher temperatures, we assumed a minimum of 20 percent efficiency over the high temperature test range.

Table 1 Heat pipes configurations

	A	*B*	*C*
Working Fluid	Sodium (Na)	Sodium (Na)	NaK
Non-Condensible gas	No	Yes	Yes

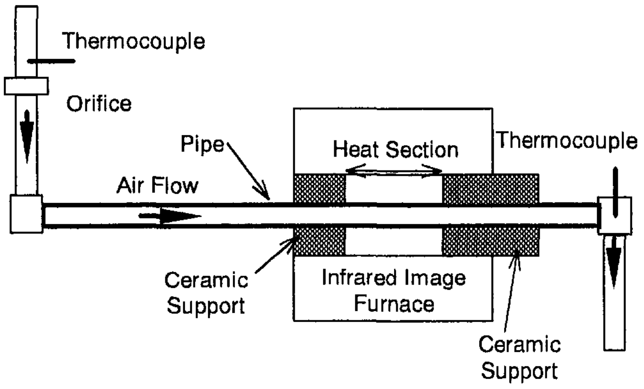

Fig. 5 Experimental setup for the air flow pipe test

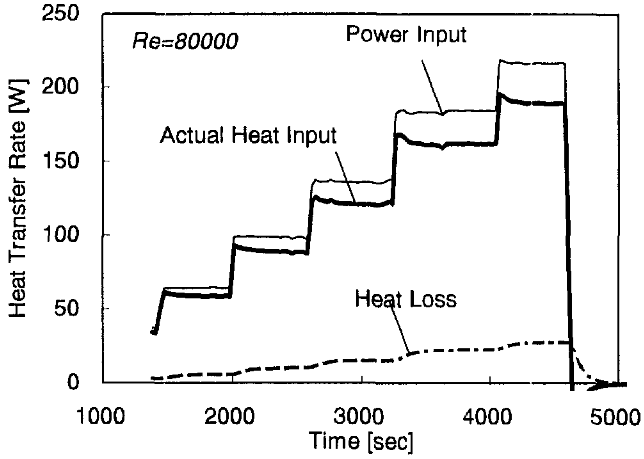

Fig. 7 Example results of the internal heat transfer measurement

Heat Pipe A. Figure 10(*a*) shows the transient temperature profile at specified axial locations for heat input into the horizontal heat pipe A. During the cold start-up, a ceramic sheet was wrapped around the fins to reduce heat loss in the condenser because the heat pipe could not start with the original fin configuration. After start-up, the ceramic sheet was taken away. After power input, temperatures on the evaporator (#2, #5) and of the vapor increased rapidly, and remained around 600°C, as limited by the sonic limit. A small hot spot was observed in the evaporator (#2) around 800 seconds after power input, indicating insufficient liquid return. After the power was reduced slightly, the hot spot disappeared, and no hot spots were seen during the remainder of the start-up. After about 14 minutes (840 seconds), the temperature near the edge of the condenser fins (#10) exceeded 500°C. The heat pipe started, since temperatures on the evaporator and condenser increased simultaneously with increase of heat input. After 1800 seconds, the ceramic sheet around the fins was taken away. Then, temperatures on the condenser decreased rapidly and heat input was increased to keep temperatures on the condenser above 500°C. After that, the highest heat transport rate, 1400 W, was recorded. The axial temperature profile at specified times after power input are shown Fig. 10(*b*). The propagation of a thermal front down the heat pipe is clearly visible.

Heat Pipe B. Figure 11(*a*) shows transient temperature profiles at specified axial locations for heat input into the horizontal heat pipe B. Although the temperature profile resembles that of heat pipe A, the scale of time is changed. After 6 minutes (360 seconds), temperatures on the condenser (#6 to #8) increased rapidly above 500°C. The start-up time decreased drastically with the assistance of included noncondensible gas. Axial temperature profiles at specified times after power input are shown Fig. 11(*b*). Since noncondensible gas collected in the edge of the heat pipe, lower temperatures were shown in the inactive condenser.

Figure 12(*a*) shows transient temperature profiles at specified axial locations for heat input into the vertical heat pipe B. Since the evaporator sat above the condenser, liquid working fluid must return from the condenser to the evaporator by overcoming the gravitational force—the most severe configuration for start-up and heat transport. Although the heat transport rate slightly decreased, the start-up time was almost the same as the time as for horizontal orientation. Axial temperature profiles at specified time after power input are shown in Figure 12(*b*). The temperature on the edge of the evaporator increased at the highest heat transport. That might signify a dry out condition caused by insufficient liquid return.

Heat Pipe C. Figure 13(*a*) shows transient temperature profiles at specified axial locations for heat input into the horizontal heat pipe C. In spite of using liquid working fluid, NaK, the time to the temperature rise at the edge of the condenser fin was not as short as the time of heat pipe B. Furthermore, dry out appeared at the edge of the evaporator at a lower heat input. The axial temperature profiles at specified times after power input are shown in Fig. 13(*b*). Lower temperatures were observed in the inactive condenser, which may have been caused by overcharging of noncondensible gas. This is also a possible reason for low heat transport rate.

Discussion. Figure 14 shows comparison of heat transport rate as well as heat flux on the evaporator at specified set angles, horizontal is 0 deg and vertical is 90 deg. The highest heat transport rate, 1520 W, was recorded for the heat pipe A at −12 deg, which means the condenser was above the evaporator.

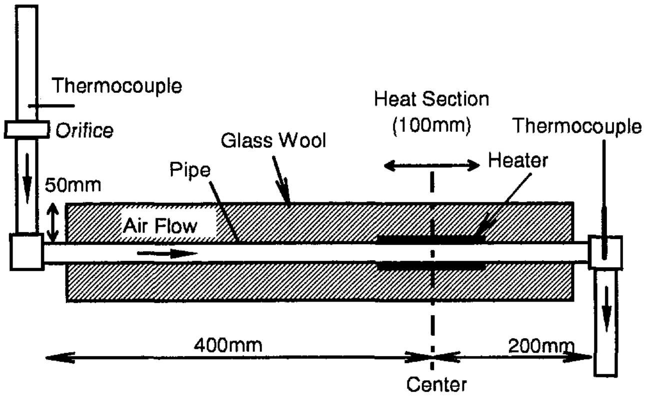

Fig. 6 Test apparatus for internal heat transfer measurement

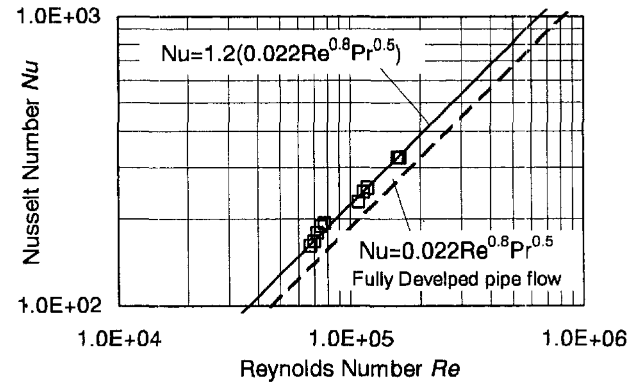

Fig. 8 Correlation of internal heat transfer

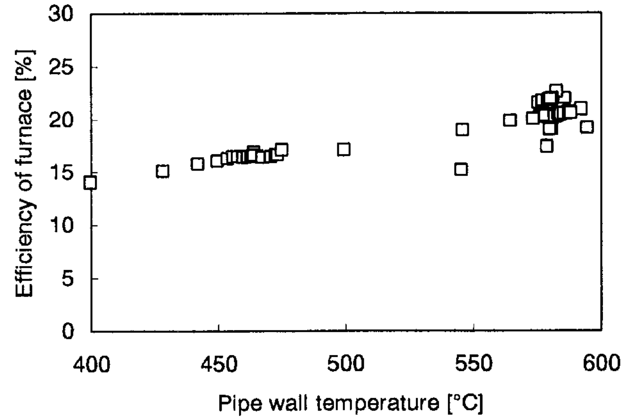

Fig. 9 Efficiency of infrared image furnace

Horizontally, heat pipes A and B demonstrated 1300–1400 W performance, which was equivalent to 20 W/cm^2 of heat flux on the evaporator surface. But when vertical, heat pipe B showed 1125 W (16.8 W/cm^2), and heat pipe A showed a lower heat transport rate, 800 W (11.9 W/cm^2). Heat pipe A shows a high dependency on a set angle because of no noncondensible gas. Although heat pipe C had the lowest heat transport rate, dependence on a set angle was the same as for heat pipe B. In this experiment, we tried to apply forced convection across the condenser fins to increase the heat transport rate, but it was unacceptable because temperatures on the condenser decreased rapidly below 500°C, and the hot spot appeared on the evaporator. The temperature of 500°C may correspond to the interfacial vapor temperature, called transition temperature by Cao and Faghri (1992), between the continuum and rarefied vapor flows in the heat pipe. Temperatures on the condenser should be kept above the interfacial temperature even in the case of high heat transport. Since the limitation of heat transfer rate depends on the operational heat pipe shell temperature, it will be able to increase by using a high temperature material instead of stainless steel.

Figure 15 shows a comparison of start-up time, defined as the time when temperatures reached 500°C in the condenser, for three heat pipes. Heat pipe B shows the shortest start-up time and no dependence on a set angle. On the other hand, heat pipe A needed longer start-up time, about 16 minutes, and showed a slight dependence on a set angle. Data scatter was produced by poor temperature measurements because thermocouples were mounted on the surface for heat pipe A but in-

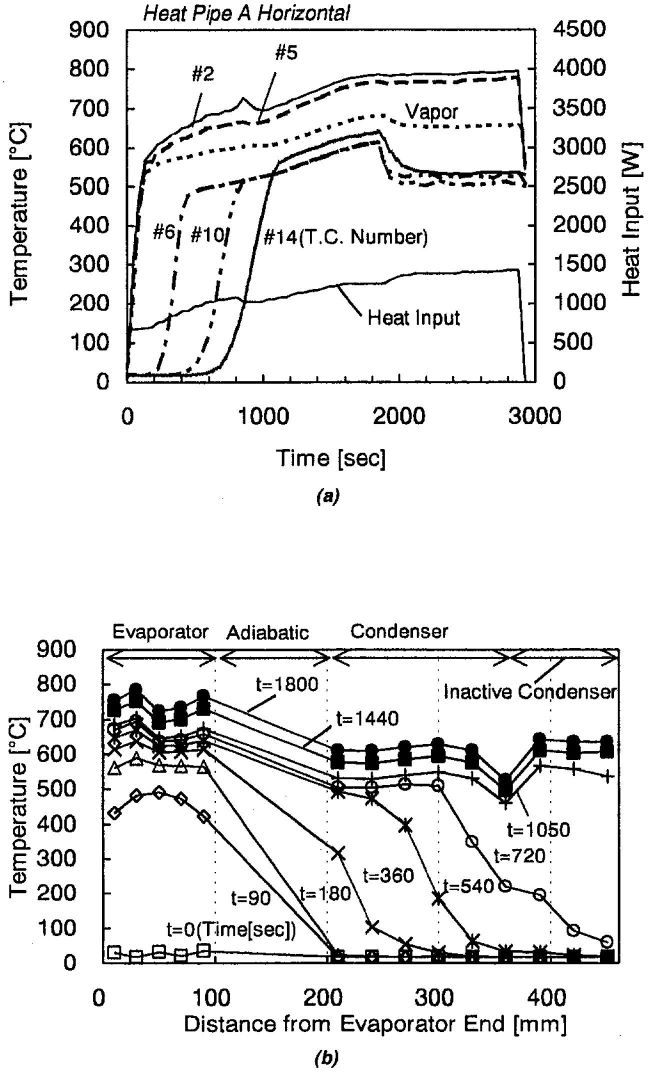

(a)

(b)

Fig. 10 Temperature profiles for the horizontal heat pipe A: (*a*) transient temperature profiles at specified axial locations; (*b*) axial temperature profiles at specified times.

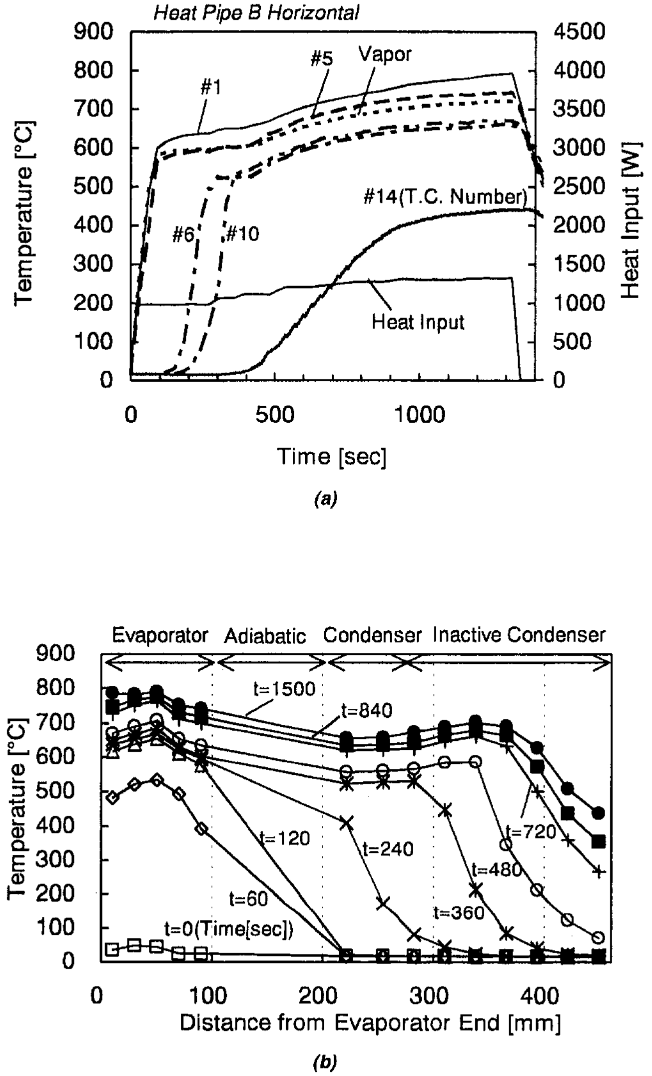

(a)

(b)

Fig. 11 Temperature profile for the horizontal heat pipe B: (*a*) transient temperature profiles at specified axial locations; (*b*) axial temperature profiles at specified times.

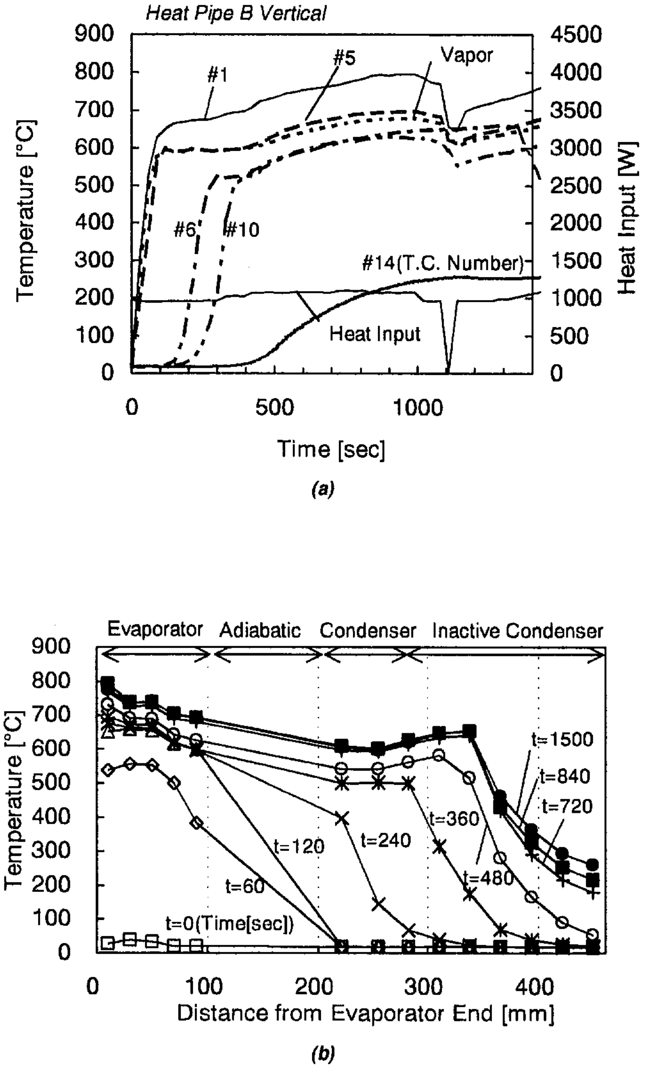

Fig. 12 Temperature profiles for the vertical heat pipe B: (*a*) transient temperature profiles at specified axial locations; (*b*) axial temperature profiles at specified times.

serted in wells for heat pipes B and C. Although heat pipe C, with the NaK working fluid, did not need to thaw during start-up, the start-up time was longer than sodium heat pipe B (7 to 8 minutes). A slight dependence on a set angle appeared. Nevertheless, it is clear that by including a noncondensible gas effectively, start-up time as well as the gravitational force effect is decreased.

To design a heat pipe cooling system, the heat pipe performance, such as thermal resistance and heat transport limitations, must be predicted. Figure 16 shows thermal resistance, R, of the horizontal heat pipe B. Definition of thermal resistance is as follows:

$$R = (T_{we} - T_{wc})/Q. \qquad (3)$$

Measured thermal resistance increased and then decreased rapidly during the start-up. Six minutes (360 seconds) of start-up time were also apparent in the profile of thermal resistance. Predicted thermal resistance after the start-up are also shown in Fig. 16. There is a big difference due to the estimation of equivalent heat conductivity of the wick and artery.

Figure 17 shows operating points in a plot of operating vapor temperature and heat transport for the horizontal heat pipe B. During the start-up, operating points were plotted near the sonic limit of the heat pipe. So, during start-up the heat transport was

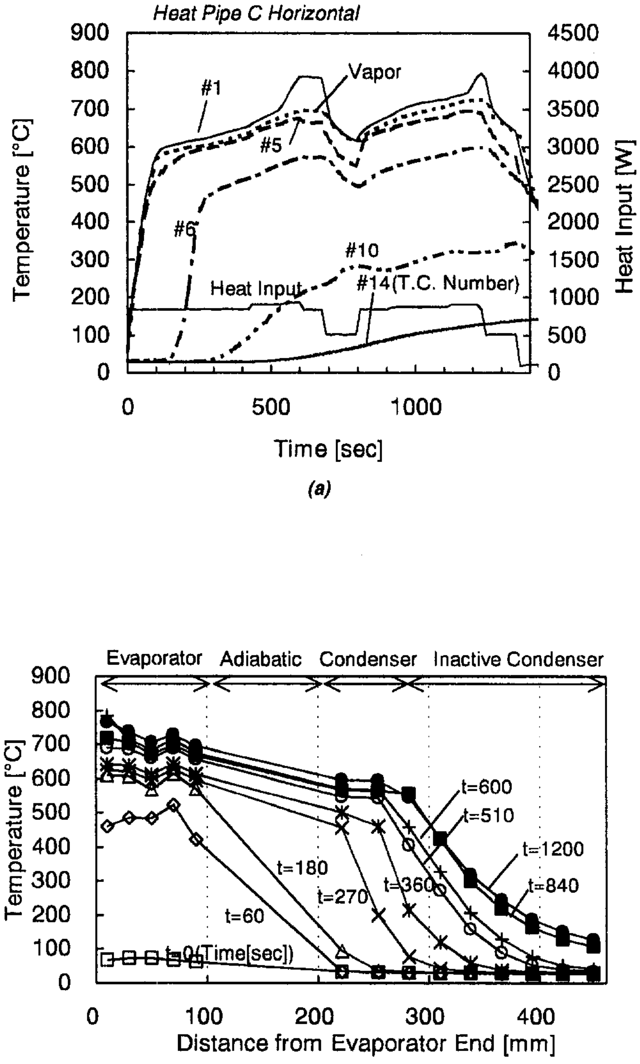

Fig. 13 Temperature profiles for the horizontal heat pipe C: (*a*) transient temperature profiles at specified axial locations; (*b*) axial temperature profiles at specified times.

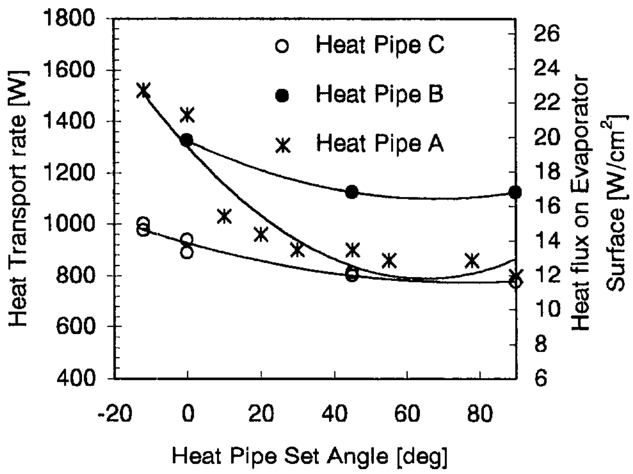

Fig. 14 Comparison of heat transfer rate at specified set angle for three heat pipes

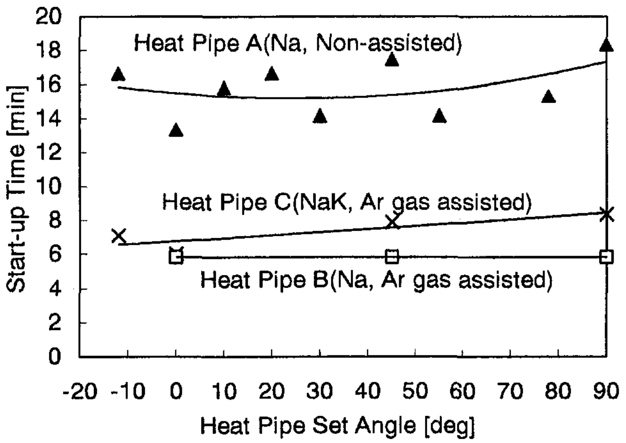

Fig. 15 Comparison of start-up time at specified set angle for three heat pipes

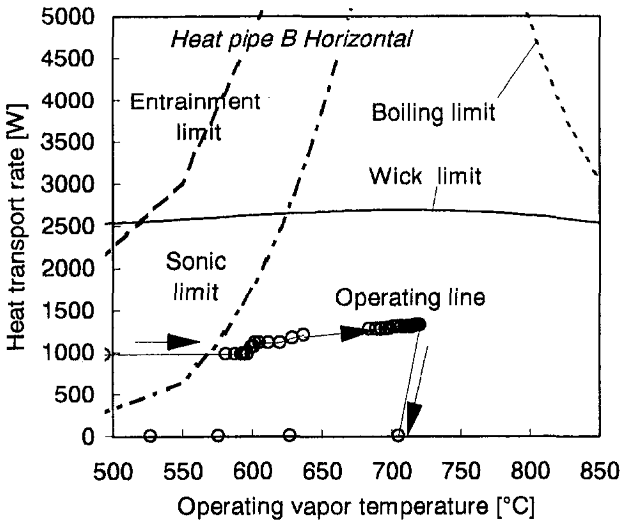

Fig. 17 Comparison of predicted operating limits and measured operating points

limited by the sonic limit. But, in the highest heat transport conditions, the wick limit predicted twice the actual limitation of heat transport. All heat transport limits were calculated according to a heat pipe text book (Chi, 1976). Although prediction of heat transport limitations must be improved, there are many unknowns in characterizing the powder metal wick and artery configuration.

Figure 18 shows a trial evaluation of a heat pipe applied to an aero-engine at flight Mach number 3 and turbine inlet temperature of 1700°C. In this evaluation, we compared the decrease of fuel consumption for an hour of supersonic flight, and assumed additional weight for heat pipe cooling system. Cooling air flow reduction, roughly calculated from a comparison between the heat pipe evaporator, available heat flux, and averaged heat flux on the vane, was required to overcome the disadvantage of additional weight. Current status yields about a 13 percent reduction of cooling air flow, which is calculated from 16.8 W/cm^2 of available heat flux for the vertical heat pipe B and about 125 W/cm^2 of averaged vane surface heat flux reduced by film cooling and thermal barrier coating. More than 20 percent of cooling air flow reduction is required to show an advantage by applying the heat pipe cooling system. Further improvements are required in order to use heat pipes for turbine cooling, i.e., increasing heat transport rate as well as decreasing start-up time.

For real application of heat pipes in the aero-engines, the reliability as well as the performance of the heat pipe should be confirmed. The effect of strong accelerations in a flight maneuver and an accident will be confirmation. A safety when heat pipes are broken in an operation should be demonstrated, because alkali metal reaction with moist air must be contained. A detailed configuration of a heat pipe cooling system with one body of vane and heat pipe for reducing heat resistance, a support of the heat pipe against a vibration and thermal expansions with sealing, a casing configuration introducing fan air to the condenser for minimize of heat pipe total length will be considered.

Conclusions

Fundamental heat transfer experiments were carried out for three kinds of heat pipes that may be applied to turbine cooling in a future aero-engine. Several important findings were obtained through experiments. A summary of this paper is as follows:

1 Heat pipe B, which has nickel sintered powder metal wick and sodium working fluid including noncondensible argon gas,

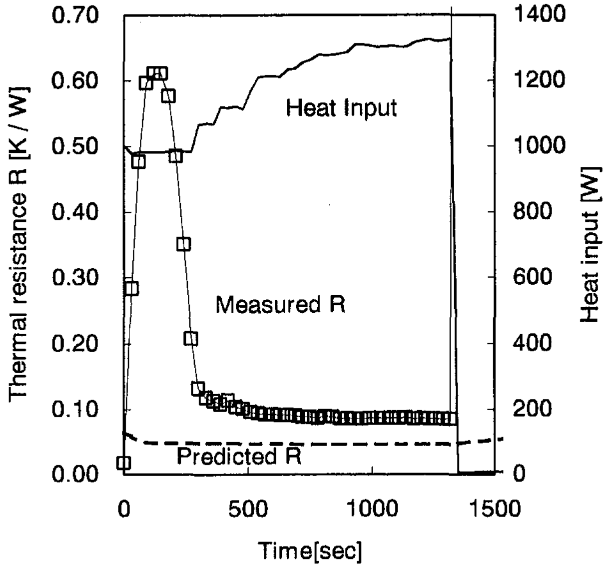

Fig. 16 Thermal resistance of the horizontal heat pipe B

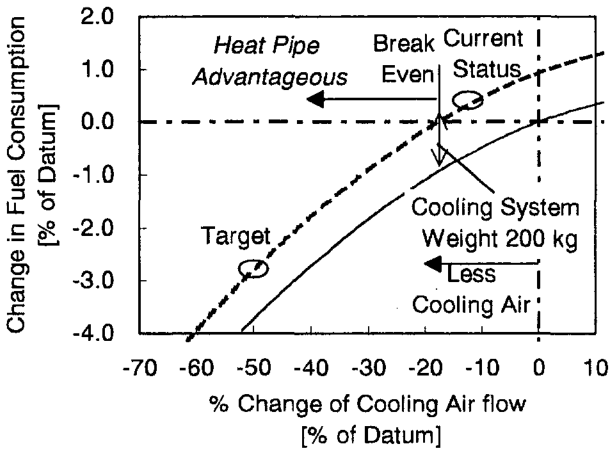

Fig. 18 Trial evaluation of a heat pipe applied to an aeroengine

demonstrated a higher heat transport rate for several heat pipe set angles and the shortest start-up time, about 6 minutes.

2 Heat pipe A, like heat pipe B but without noncondensible gas, recorded a higher heat transport rate than heat pipe B, about 1425 W, in the horizontal disposition. But, heat pipe A's heat transport rate was gravity sensitive, and reduced at high set angle conditions when the evaporator is set above the condenser. Start-up time is longer, 16 minutes, than heat pipe B.

3 The sodium-potassium (NaK) working fluid (in heat pipe C) did not show any advantages to being in a liquid phase at room temperature during start-up. The heat transport rate did not increase when compared to sodium working fluid. Skipping the thawing period during start-up is apparently not important to reduce start-up time.

4 Inclusion of noncondensible gas is effective for reducing start-up time and reducing the effect of gravitational forces on heat transport.

Although the heat transport was not enough to show a clear advantage using heat pipes, there are still several areas for improvement that can be pursued—such as using a high temperature shell material and reducing heat pipe length. Thus, a new turbine cooling system using heat pipes is a prime candidate for future aero-engines.

Acknowledgments

This work has been conducted under a contract with NEDO (the New Energy and Industrial Technology Development Organization) as a part of the National Research and Development Program "Industrial Science and Technology Frontier Program" on Super/Hypersonic Transport Craft Propulsion Systems of AIST (the Agency of Industrial Science and Technology), MITI (Ministry of International Trade and Industry).

References

Anderson, W. G., Hoff, S., and Winstanley, D., 1993a, "Heat Pipe Cooling of Turboshaft Engines," ASME Paper 93-GT-220.

Anderson, W. G., 1993b, "Negative Pressure in Alkali Metal Heat Pipes," AIAA Paper 93-3904, ASME/AIChE 29th National Heat Transfer Conference.

Anderson, W. G., 1993c, "Sodium-Potassium (NaK) Heat Pipe," *Heat Pipes and Capillary Pumped Loops*, A. Faghri et al., eds., ASME HTD-Vol. 236, pp. 47–53.

Cao, Y., and Faghri, A., 1992, "Analysis of High Temperature Heat Pipe Startup from the Frozen State: Part 1—Numerical Simulation," *Topic in Heat Transfer—Volume 3*, ASME HTD-Vol. 206-3.

Chi, S. W., 1976, *Heat Pipe Theory and Practice: A Source Book*, Practical Technology Series, Hemisphere, Bristol, PA.

Kays, W. M., and Crawford, M. E., 1980, *Convective Heat and Mass Transfer*, 2nd ed., McGraw-Hill, NY, p. 270.

Ponnappan, R., and Chang, W. S., 1994, "Startup Performance of a Liquid Metal Heat Pipe in Near Vacuum and Gas-Loaded Modes," *Journal of Thermophysics and Heat Transfer*, pp. 164–171.

Silverstein, C. C., Gottschlich, M. J., and Meininger, M., 1994, "The Feasibility of Heat Pipe Turbine Vane Cooling," ASME Paper 94-GT-306.

Yoshida, T., Taki, M., Mimura, F., Kumagai, T., Maya, T., and Yamawaki, S., 1993, "A New Cooling System for Ultra High Temperature Turbines," *11th International Symposium on Air Breathing Engines*, proceedings, pp. 749–756.

Experience in Applying the New UK Procedure for Creep Rupture Data Assessment to Gas Turbine Materials

C. K. Bullough
European Gas Turbines Ltd.,
Cambridge Rd.,
Whetstone, Leicester,
LE8 6LH, United Kingdom

A new procedure being developed in British Standards for the assessment of creep-rupture data is described and evaluated with trial data sets of gas turbine blading materials. The procedure is applied in phases. An important development by statistical experts is a framework for the main assessment phase that uses maximum-likelihood fitting methods for the treatment of unfailed test points and error variance. The framework selects models from a standard suite (together with any other linear models supplied by the assessor) using statistical criteria, but also incorporates metallurgical judgement. The improved representation of the experimental data compared with previous fitting methods and the associated statistical tests indicate that the new procedure can be used to derive rupture strength values for gas turbine materials with confidence.

Introduction

Reliable creep rupture data are a fundamental requirement for the design of hot-section gas turbine components, and creep rupture testing represents a significant proportion of the development and characterization costs of a new material. For the design to be safe without being over-conservative, it is essential to derive accurate rupture design values using the most appropriate methods. It is perhaps surprising, therefore, that many data sets continue to be analyzed using relatively simplistic methods, such as the Larson Miller parameter with the constant $C = 20$, when considerable work over the last 30–40 years has led to improved descriptions of material behavior (see, for example, the reviews of the state of the art in Conway 1969; EPRI 1979; Dulieu, 1982). Even when alternative time-temperature parameters or other predictive models are investigated, there is no agreed criterion for choosing the parameter with the best "fit". Ironically, the only general agreement is that predictive models with the best "statistical" fit are not necessarily the most suitable for extrapolation to the design conditions of interest.

Recent round-robin assessments of large, multi-cast data sets of boiler and pressure materials, demonstrated significant differences in the predicted rupture strength values (Holdsworth, 1996a). This round-robin was associated with the development of Post-Assessment Tests for predictive models to ensure their physical realism, adequate representation within the range of data, and reproducibility in extrapolation. Within Europe, Post Assessment Tests are increasingly applied in order for the assessment results to be accepted, and have been shown to improve consistency of predicted strength values (Holdsworth, 1996b). During the same development period, British Standards Institution commissioned a program of work within Panel ISE 73/-/4, "Creep Rupture Assessment Methodology," leading to a new, unambiguous procedure, to be published as PD6605, representing the state of the art. Fundamental improvements to the statistical methods are included; notably, the treatment of variance heterogeneity and the explicit inclusion of unfailed test data using maximum likelihood estimation methods, in addition to the formal inclusion of several of the Post-Assessment Tests.

In the present investigation, the benefits of new techniques developed for PD6605 (Draft) have been evaluated by applying them to typical trial data sets of conventionally cast and single-crystal gas turbine blade materials. One consideration is that, unlike boiler and pressure vessel steels, gas turbine materials are produced to closer tolerances, so that the scatter in test data is likely to be smaller, and, therefore, less difficult to deal with. On the other hand, gas turbine material test data set sizes are often much smaller, are of shorter duration, and cover a wider temperature range. They therefore present a challenge for any assessment method.

Elements of the Procedure

Four separate, largely sequential phases in the assessment are identified in the procedure and are illustrated in the flow diagram (Fig. 1).

- In the initiation phase, the scope of the assessment (principally the material specification) is agreed, and the data collated.
- In the pre-assessment phase, data are summarized, anomalous test points are reviewed, and (if necessary) the specification may be revised. Isothermal plots of the data are also examined to check for inflections, and the best-tested casts are selected.
- In the main assessment phase, a suite of standard models, together with any user defined models, are fitted to the data, and a shortlist of models are compiled by statistical and visual examination. Tests for physical realism and accuracy within the range of the data are performed. A preferred model is chosen from the shortlist by considering robustness in extrapolation and the effect of influential casts.
- During a post-assessment phase, the chosen model is examined for its extrapolative capability. The need for a change in material specification (restriction of compositional range for example) may also be investigated. The main assessment may need to be repeated for the revised specification.

The overall objective in developing this procedure has been to incorporate state-of-the-art, but easy-to-use, statistical methods

---

Contributed by the International Gas Turbine Institute and presented at the International Gas Turbine & Aeroengine Congress & Exhibition, Orlando, FL, June 2–5, 1997. Manuscript received by the ASME Headquarters March 1, 1997. Paper No. 97-GT-118. Associate Technical Editor: H. A. Kidd.

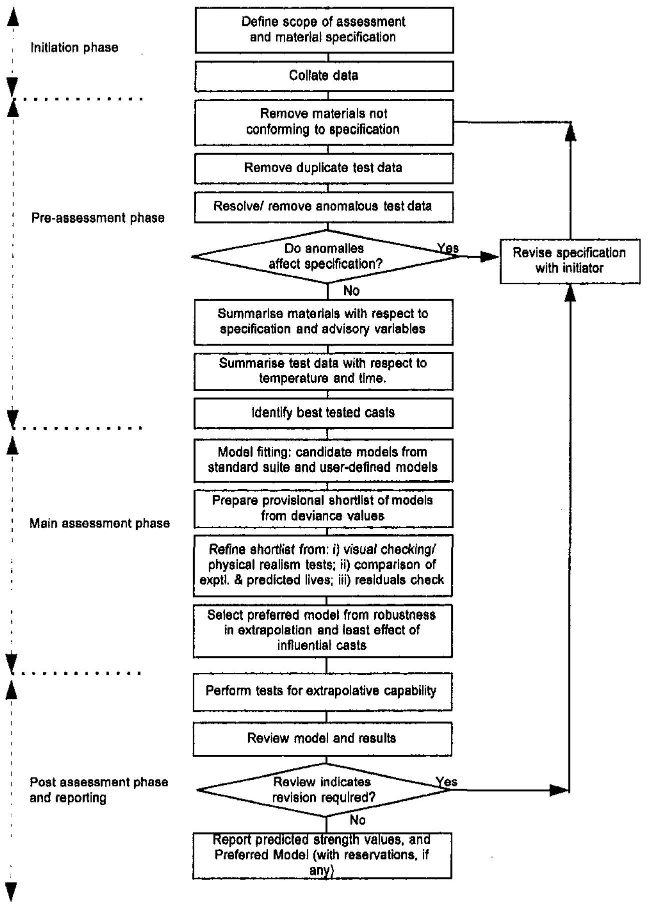

Fig. 1 Simplified flow diagram of the draft PD 6605 assessment procedure

while retaining the best aspects of metallurgical expertise and judgement.

Pre-Assessment

The principal objective of the pre-assessment phase is to provide a sufficiently large, error-free and characterized data set for input into the main assessment. In effect, this is merely what is required by good practice on the part of the assessor. Nevertheless, the formal procedure ensures that minimum standards are met and the results are recorded for future reference.

Simple aspects, such as the removal of duplicate points (which may inadvertently arise when large data sets from several sources are periodically updated) and the examination of anomalous rupture data (either genuine or due to mistaken entry) will not be considered further here.

During the pre-assessment phase of PD6605 (draft), however, there is the provision to revise the specification on inspection of the rupture data for anomalies. This is because data for piping and pressure vessel steels are generally collected according to fairly broad heat treatment ranges, and preliminary examination of rupture behavior sometimes points to the need to narrow or subdivide that range. (For example, there are two property sets for Type 321 steel with different heat treatment ranges in PD6525, 1990; namely, grades 321S51-490 and 321S51-510.)

An important aspect of the pre-assessment phase is to characterize the data set to provide information for the subsequent main assessment phase and to provide a record for future consideration. One table (not shown) is produced in which the information on the collated materials is compared against the specification variables and any other variable judged important by the assessor (typically, product size and residual elements). Other tables summarize the distribution of the test data (e.g., Table 1) and the distribution of the unique materials with respect to temperature and duration. At the same time, a number of best-tested casts (i.e., unique materials with the most extensive test data) are identified. The rupture data of three of these casts are examined to check for points of inflection and other aspects that would affect the choice of predictive model in the main assessment phase.

Main Assessment—The Statistical Framework

The main-assessment phase is based on a rigorous statistical framework developed at the University of Lancaster, UK. In essence, a number of linear regression models, including those already currently in use together with any others, is examined to produce a shortlist, which is refined until a preferred model is chosen. Both statistical techniques and metallurgical judgement are used to make the final choice; they are described later in the paper. Two novel features that are used throughout the framework, however, are error models other than the conventional log-normal distribution and the treatment of unfailed test points by survival analysis.

Error Model. Work on steels for pressure purposes has demonstrated that errors in fitting creep rupture test failure times are not truly random with respect to the independent variables, temperature, and stress. This is in contradiction to one of the basic assumptions of least squares linear regression. Plots of error (the difference between the log of rupture life and the log of the predicted median rupture life) versus each of the independent variables appears to be "funnel shaped". The width of the scatter band increases with increasing absolute temperature and logarithm of stress. Heteroscedastic error models are therefore introduced through fitting the shape factor in the failure distribution with temperature and stress terms (Table 2).

Further trials on example data sets caused the team at Lancaster University to conclude that creep rupture test failure times were not log-normal, as is generally assumed. Other essentially bell-shaped error distributions were investigated, and a heteroscedastic Weibull model gave a significantly better fit. Exceptionally, when the lower confidence interval poorly reflects the number of failed points, a heteroscedastic log-logistic model is preferred instead.

Unfailed Test Points. The majority of creep rupture data sets contain tests that have not proceeded to rupture, either because the tests are continuing or because they have been discontinued. However, such "censored" data are often of high value, being at test conditions where failure, if it had occurred, would help define the shape of the curve at long times. Moreover, the discontinuation of long-term tests after a fixed duration automatically results in a conservative estimate of life. Unfailed test points may be addressed by (1) manual adjustment of curves, (2) "estimating" the failure life, for example, from strain-time data, and (3) using the unfailed lifetime directly during statistical fitting process.

The procedure developed for PD6605 (draft) favours the last option, primarily because the other options are either arbitrary or require strain-time data that are often unavailable. In essence, a survival analysis approach is adopted that from the failed data population, estimates the probability of failing within the time on test. An iterative technique uses this information and maximum likelihood methods to estimate the coefficients of both the predictive and error models. Long duration unfailed tests that have reached or exceeded the predicted median life of the failed data population have a large effect on the coefficients. Consequently, the inclusion of unfailed test points almost always results in a counter-clockwise rotation of the median failure line on log (σ) versus log (t_r^*) plots relative to the same

Table 1 Distribution of creep rupture data of a conventionally cast material with respect to source, temperature, and duration (draft PD6605—Preassessment)

Test Materials	Temp	Number of tests with specified durations (italics indicate unfailed tests)																						$t_{r\ max}$	σ_{min}	Source				Total			%B of total
	°C	<100h		100-200h		200-500h		500-1000h		1-2kh		2-5kh		5-10kh		10-20kh		20-30kh		30-50kh		50-70kh				(B)							
		B	*UB*	B	*UB*	B	*UB*	B	*UB*	B	*UB*	B	*UB*	B	*UB*	B	*UB*	B	*UB*	B	*UB*	B	*UB*	B	B	1	2	3	4	B	*UB*	B+UB	
Insufficient information	550	1						1						1				1			*3*			24,621	560				4	4	*3*	7	1
	600	2				1				1		1		1				1		1	*1*			34,268	498				8	8	*1*	9	1
	650	5				3				3				1						1				36,804	520	6			7	13		13	2
	700	1		2		3		3		2		3		2		3				1	*1*			35,938	265				20	20	*1*	21	3
	732	2		1		1		2		1		1												2,069	450			2	6	8		8	1
	750	2		6		13	*1*	6		5		5		4		2	*1*	2		4		1		59,857	208	17	3		30	50	*2*	52	7
	760	2				3		1																599	441				6	6		6	1
	800	2		1		2		2		3		3		3		4				2	*2*			43,396	114				22	22	*2*	24	3
	816	12	*1*	40		34	*1*	50	*1*	38	*1*	19		3		1								10,211	124	2		34	161	197	*10*	207	28
	850	4		9		19		10		16		14		22		9		1						21,454	120	52	2		50	104	*1*	105	15
	870	41		25		20		9		23	*1*	12		4		6	*3*	4		1				41,131	78.8	1		9	135	145	*6*	151	21
	900	5		2		2		3		2		4		7		2	*1*	1	*1*	1	*2*			37,994	31	4			25	29	*5*	34	4
	927	2		10		6		24		2				1										7,072	80	1		9	35	45		45	6
	929	1		1								1												4,008	80				3	3		3	0
	930	2		2		4		2		4		1												3,996	70		1		14	15	*1*	16	2
	950					1				1		2					*2*							4,521	30	4				4	*2*	6	1
	980	2		3		4		1		3		3												3,768	40			4	12	16	*2*	18	2
	1000					1				1		1												4,962	32				3	3		3	0
	1050	2		1						1														1,091	30				4	4		4	1
	Total, or (max/min)	88	*1*	103		117	*2*	114	*1*	106	*2*	70		49		27	*7*	10	*1*	11	*9*	1		59,857	30	87	6	58	545	696	*36*	732	99

model fitted with only the failed data. Even a few long-term unfailed data beyond the median line of the failed data population can cause a rotation leading to a slight but significant increase in extrapolated strength values (Fig. 2).

Main Assessment—Model Selection

Potential candidates for the model selection process are listed in Table 2. Note that lower order polynomial models may also be selected, and the analyst may also supply his own model provided it is linear in parameters.[1] The first part of the main assessment is to provide a provisional shortlist of up to six candidate models on the basis of several standard model forms

---

[1] The Manson-Haferd and "MMR" models are strictly nonlinear; however, these models may be linearized by scanning through a range of T_o and selecting the value that yields the lowest deviance.

Table 2 Predictive models and error models (draft PD6605—main assessment)

Algebraic forms	
$\ln(t_r^*) = \beta_o + \beta_1 \log(T) + \beta_2 \log(\sigma) + \beta_3 T^{-1} + \beta_4 \sigma T^{-1}$	Soviet Model 1
$\ln(t_r^*) = \beta_o + \beta_1 \log(T) + \beta_2 \log(\sigma) T^{-1} + \beta_3 T^{-1} + \beta_4 \sigma T^{-1}$	Soviet Model 2
$\ln(t_r^*) = \beta_o + \beta_1 \log(T) + \beta_2 \sigma + \beta_3 \sigma^2 + \beta_4 T + \beta_5 T^{-1}$	Minimum Commitment Method (A=0) (Manson, 1968, and Goldhoff, 1973)
Mendelson-Manson-Roberts parametric equations	
$\ln(t_r^*) = F(\sigma)(T - T_o)^r / \sigma^{-q} + \beta_5$	
where: $F(\sigma) = \beta_o + \beta_1 \log(\sigma) + \beta_2 \log(\sigma)^2 + \beta_3 \log(\sigma)^3 + \beta_4 \log(\sigma)^4$	
$\ln(t_r^*) = F(\sigma)(T - T_o) + \beta_5$	Manson-Haferd, 1953.
$\ln(t_r^*) = F(\sigma) / (T - T_o) + \beta_5$	Termed: "MMR"
$\ln(t_r^*) = F(\sigma) / (T) + \beta_5$	Larson-Miller, 1952.
$\ln(t_r^*) = F(\sigma)(T) + \beta_5$	Manson-Haferd, $T_o=0$
Other parametric forms	
$\ln(t_r^*) = F(\sigma) + \beta_5 / T$	Orr-Sherby-Dorn, 1954.
$\ln(t_r^*) = F(\sigma)(T) + \beta_5 T$	Manson-Succop, 1956.
User defined models	
$\ln(t_r^*) = G(\sigma, T)$	Any model linear in parameters, eg.
$\ln(t_r^*) = \beta_o + \beta_1 \log(T) + \beta_2 \sigma + \beta_3 \sigma^2 + \beta_4 T + \beta_5 T^{-1} + \beta_6 \sigma T^{-1.5}$	Used for Conventionally-Cast material data set
Error Models	
$g(\eta, \alpha) = \alpha \ln 2 \exp(-\alpha\eta) t^{\alpha-1} \exp[-\ln 2 \exp(-\alpha\eta) t^{\alpha}]$	Weibull
$g(\eta, \alpha) = \dfrac{\alpha \exp(-\eta)[t \exp(-\eta)]^{\alpha-1}}{\{1 + [t \exp(-\eta)]^{\alpha}\}^2}$	Log-logistic
where $\alpha = \exp(\gamma_o + \gamma_1 T + \gamma_2 \log(\sigma))$	Shape factor containing error heterogeneity
and $\eta = Md[\ln(t_r^*) \mid T, \sigma]$	Median of the logarithm of failure time, t_r* hours.
stress, σ MPa, temperature, T K, model coefficients $\beta_o, \beta_1 \ldots \beta_6$	

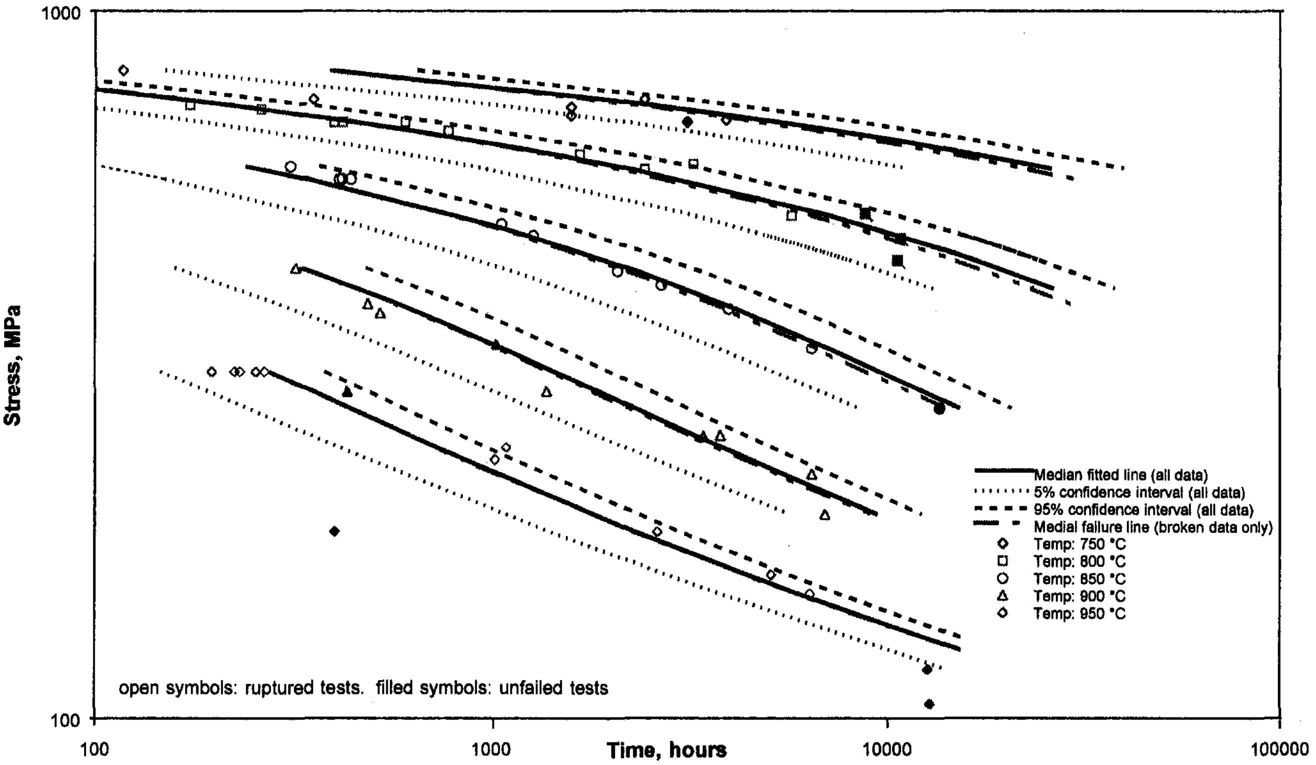

Fig. 2 The effect of unfailed test data on the median failure time of single crystal turbine blade material (data at temperatures above 950°C not shown)

and the lowest deviance for best statistical goodness of fit). The list will typically contain:

- two of the "Soviet Model 1", "Soviet Model 2", and the "Minimum Commitment Method $(A = 0)$" models;
- four models of the Mendelson-Manson-Roberts type;
- or the user's own predictive models may also be added.

Metallurgical judgement is introduced by visual examination of the plots of the shortlisted models against the data on log (stress) versus log (time) axes. Isothermal lines are also drawn from the predictive model at 25°C intervals, within and slightly outside of the range of data to ensure that there is no crossover, come-together, or turn-back between 10 and 10^6 hours and above 0.8 times the lowest experimental rupture stress.

Further model checks include an examination of the derivative of the model $-\delta \log (t_f^*)/\delta \log (\sigma)$ versus stress to ensure that the slope of the curve does not become unrealistically "steep" within the range of the application. Isothermal curves suggesting sigmoidal behavior when none was apparent in the behavior of the best-tested casts would similarly cause a model to be rejected. An isothermal plot of the predicted versus the observed behavior is also used to check how many points fall below the lower 95 percent confidence interval compared with the 2.5 percent predicted.

Results from these tests for a data set of conventionally cast blading materials are given in Table 3.

Robustness in Extrapolation. Ideally, an optimum predictive model for a data set would represent the rupture behavior over an entire range of temperature and stress. It should also be capable of extrapolation since most data sets are of a too-short duration compared with the required design lives (extrapolation of three or more times the longest rupture point is common). The techniques developed for PD6605 (draft) test for extrapolative capability by culling 30 percent of the lowest stress data at each temperature (15 percent for metallurgically active steels). A statistic "P" is then derived, which compares the predicted failure times of the full and culled data set at the lowest test stress.

Influential Casts. An optimum predictive model would also be relatively insensitive to influential casts, otherwise a small change in the number of rupture data of that cast could have large consequences for the predicted strength values. A technique was developed to test for the influence of casts by removing each one in turn, refitting the model, and examining the effect on extrapolation. Of course, a material may be influential yet still conform to the specification. The purpose of this technique is, therefore, not to identify materials that should be re-evaluated, but to select the model that is least affected by the removal of the influential cast from the data set. A test statistic is usually derived, but it could not be for the data sets illustrated, as the individual casts were insufficiently described.

Post-Assessment. The concept of "Post Assessment Tests" has been developed by the European Creep Collaborative Committee, Working Group 1, to provide objective test criteria of predictive models arising from a wide range of assessment procedures (Holdsworth, 1996b). The tests fall into three categories, one of which ("tests of physical realism") is already fully integrated into the procedure developed for PD6605 (draft). A second category "fit within the range of the data" is partly implemented in the form of isothermal plots of the predictive rupture lives versus experimental rupture lives (Fig. 3). The mean slope of the line (0.88) falls within the permitted limits of 0.78 to 1.22, and the line falls within the ±log 2 boundary lines at 100 and 100,000 hours; therefore, the predictive model passes this test. (Incidentally, such plots often demonstrate the fact that the width of the scatter band decreases with decreasing stress, thus confirming the need for heteroscedastic error models during the main assessment.) An additional test examines the behavior of the best-tested casts in similar fashion.

The post assessment tests on extrapolative capability also investigate the effect of culling data, both in terms of test dura-

Table 3 Preliminary model selection during the assessment of creep rupture data set of conventionally cast turbine blade material (draft PD6605—main assessment)

Model	Deviance value	Visual Check vs the data.	Checks of Physical Realism (isothermal plots, derivatives plots, no. of points below lower confidence interval).	Residuals check (PAT2.1),
Soviet Model 1	9666.66	Poor fit	Pass	Not evaluated
Minimum Commitment Method (A=0)	9643.5	Best of standard models	Pass	Not evaluated
Manson-Haferd (order = 4, T_0=0)	9628.5	Acceptable fit	Pass	Not evaluated
Manson-Haferd (order = 3, T_0=0)	9680.78	Sigmoidal behaviour implied	Pass	Not evaluated
Orr-Sherby-Dorn (order = 4)	9723.02	Poor fit at low T's	Pass	Not evaluated
Orr-Sherby-Dorn (order = 3)	9785.22	Poor fit at low T's	Pass	Not evaluated
"User Defined" (based on Minimum Commitment Method (A=0) + interaction term, see Table 2)	9546.14	Best fit at T's of interest	Pass - 1.91% of points below lower confidence interval.	Pass - see eg. Figure 3

tion and in terms of stress. These tests directly examine the effect of culling on predicted strength values at 300,000 hours. A full reassessment is required using the culled data set. Since 300,000 hours is an excessively long duration for a gas turbine blade, proposals for the modification of these tests for turbine materials are under consideration.

At the conclusion of the main and post assessment phases, there are additional tests that permit the assessor to evaluate if a poor fit was due to some hitherto unsuspected metallurgical influence on properties (Fig. 1). If this influence can be proven, there is an option of revising the material specification and repeating the assessment.

Discussion

The work reported here summarizes the new UK procedure for creep rupture assessment that is being prepared for British Standard Document PD6605. Previously, a large number of trials were performed by panel members of ISE73/-/4 on pressure vessel steel product data sets. It is believed that this is the first report of applying the procedure to data sets of gas turbine materials.

The principal benefit of the procedure prepared for PD6605 (draft) is that it offers a sound statistical framework, which may accommodate the benefits of metallurgical judgement. The procedure is reproducible and relatively nonsubjective. EGT's experience is that it is relatively easy to implement since modular GLIM 4 (Francis et al., 1993) programs have been prepared by Lancaster University for inclusion in the published standard. In addition, the model parameters may be readily output in ASCII format, permitting them to be used in other packages (e.g., spreadsheets) for further manipulation or presentation.

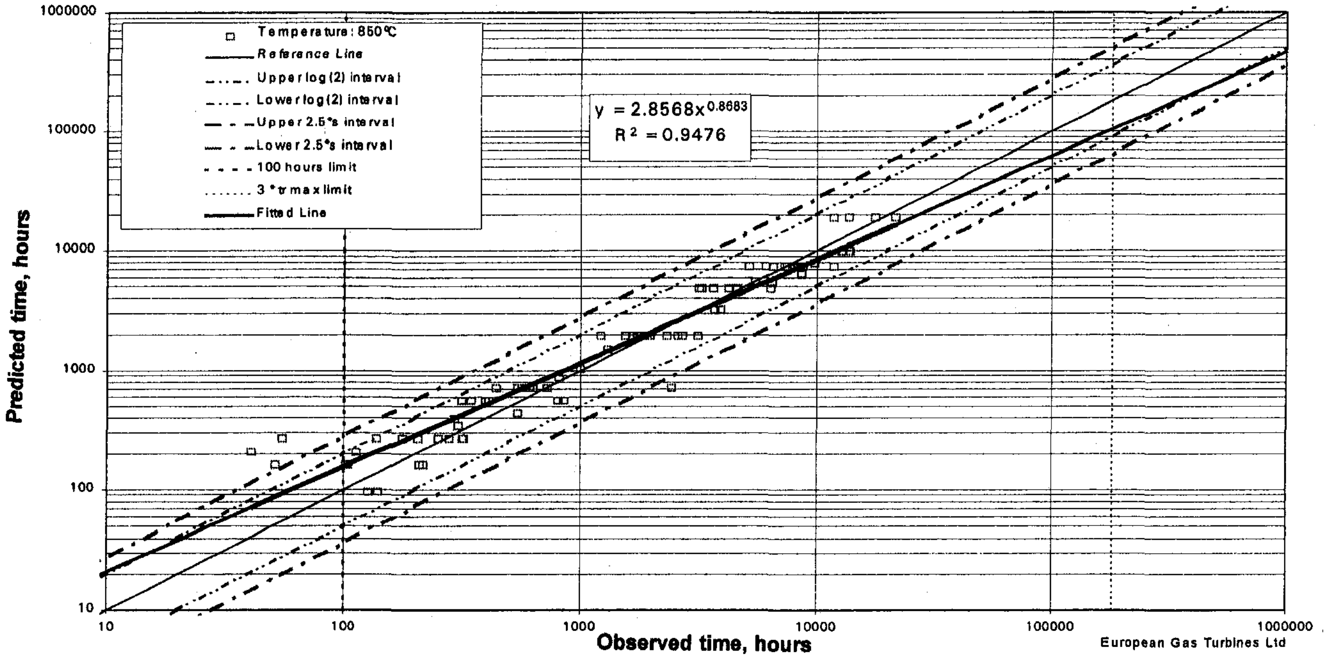

Fig. 3 A comparison of experimental and predicted lives of a conventionally-cast turbine blade material at 850°C

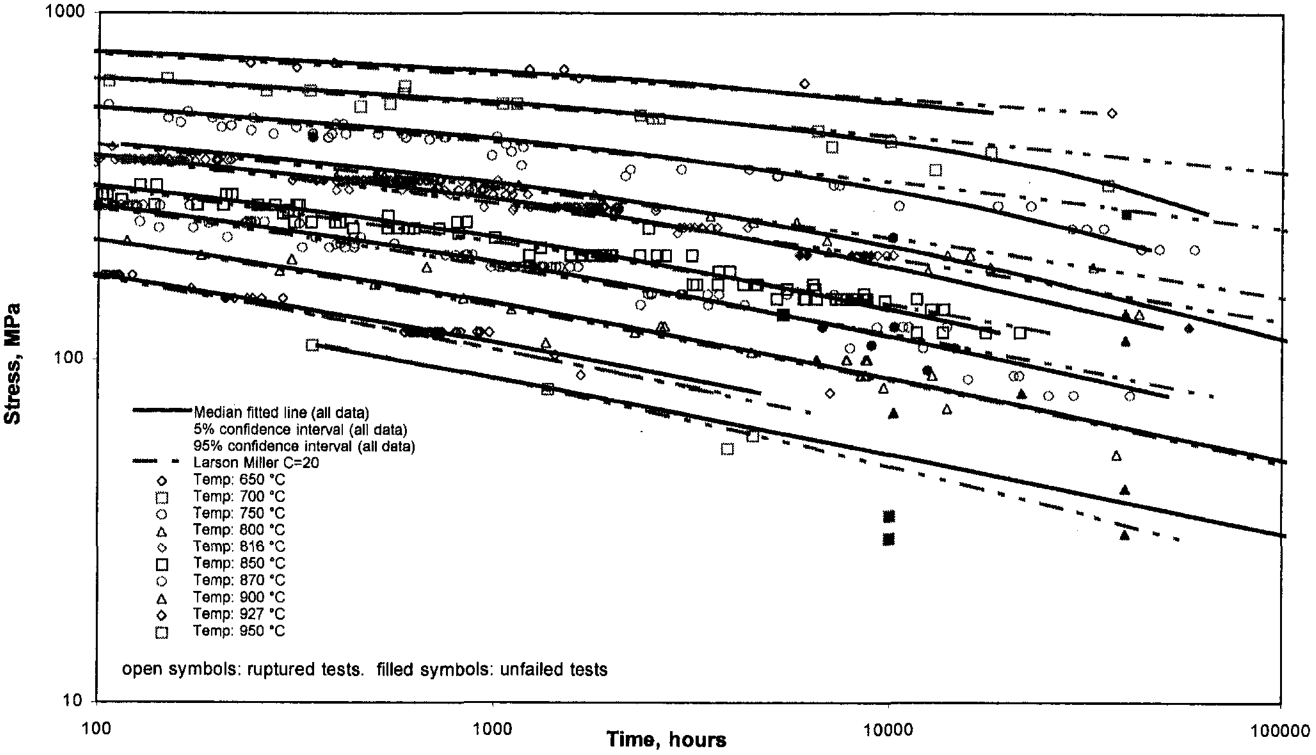

Fig. 4 A comparison of median fitted line from the new procedure with an existing Larson Miller (*C* = 20) fit for creep rupture data of a conventionally-cast turbine blade material

Pressure vessel steel creep rupture data sets are generally extensive, and the materials are well characterized. On the other hand, gas turbine materials data sets are less extensive and, as here, must be drawn from a variety of sources, including the assessor's own test laboratory, manufacturers' test data, collaborative programs, and the open literature. Due to a lack of information, it is often difficult, if not impossible, to demonstrate that the materials have been produced to the required specification. Furthermore, lack of detailed information on, say, heat treatment parameters prevents consideration of improvements to the specification. These observations strongly indicate the need for maintained sources of test data, such as those described in a companion paper (Piearcey and Bullough, 1997).

The relatively large number of fitted parameters (up to 10) and the use of heteroscedastic error models means that the procedure cannot be used for small data sets (a lower limit of 100 data points is, from experience, thought to apply). Most data sets exceed this limit (for example, there were 732 and 152 points in the of conventionally cast and single crystal trial data sets, respectively). A further consideration is the fact that data sets on gas turbine materials typically extend over a greater temperature range (350–400°C), whereas steels for pressure purposes are usually tested over a smaller range (150–200°C). The shorter range of test durations in gas turbine data sets is the result of a combination of the shorter anticipated lives of gas turbine blades and high costs. The present experience suggests that models with greater temperature flexibility are required for gas turbine data sets. For example, an adaptation of the Minimum Commitment Method ($A = 0$) model with an additional stress/temperature interaction term was necessary to fit one of the data sets investigated.

The present results for a conventionally cast turbine blading material are further illustrated in Fig. 4, together with the results of an earlier assessment on the same data set by the Larson Miller Method (assuming $C = 20$, 4th order polynomials, and least squares fitting). The new procedure's representation of the experimental data, particularly at temperatures and stresses of interest, is improved, compared with the earlier assessment, and it avoids the danger of optimistic extrapolation. This improved fit together with the associated statistical tests provide a good indication that the new procedure can be used to derive reliable rupture strength values for gas turbine materials.

Acknowledgments

The author wishes to thank colleagues in BSI Panel ISE73/-/4, in ECCC Working Group 1, and within the Materials Group and Methods Group at MEC Whetstone for helpful discussions. In particular, the statistical developments in the main assessment section of this paper are the result of work by Prof. R. Davies and colleagues at the University of Lancaster, UK. Post Assessment Tests are an original concept of the European Creep Collaborative Committee.

This paper is published with the permission of European Gas Turbines Ltd.

References

BS PD 6525, 1990, *Elevated Temperature Properties for Steels for Pressure Purposes: Part 1—Stress Rupture Properties,* British Standards Institution, London, UK.

BS PD 6605 (draft), *Guidance on the Methodology for the Analysis of Stress Rupture Data,* British Standards Institution, London, UK. (For further information contact either the author, or Dr. S. R. Holdsworth, GEC ALSTHOM Turbine Generators, Newbold Road, Rugby, CV21 2NH, UK.)

Conway, J. B., 1969, *Stress-Rupture Parameters: Origin, Calculation and Use,* Gordon and Breach, New York.

Dulieu, D., ed., 1982, "The Properties of Steels at High Temperatures," CEC Report: EUR 7615 EN.

EPRI Publication FP-1062, 1979, final report of research project 638-1, Electric Power Institute, Palo Alto, CA.

Francis, B., Green, M., Payne, C., eds., 1993, "GLIM System Release 4 Manual," Clarendon Press, Oxford, UK.

Goldhoff, R. M., 1973, "Towards the Standardization of Time-Temperature-Parameter in Elevated Temperature Data Analysis," Proceedings of Conference on Creep and Fatigue, ASTM, Philadelphia, PA.

Holdsworth, S. R., 1996a, ''Review of WG1 Evaluation of Creep Rupture Data Assessment Methods. Recommendation Validation,'' *European Creep Collaborative Committee Recommendations—Appendix C of Volume 5,* Doc Ref. 5524/MC/68 Issue II. (For further information contact Dr. S. R. Holdsworth, GEC ALSTHOM Turbine Generators, Newbold Road, Rugby, CV21 2NH, UK)

Holdsworth, S. R., 1996b, ''Guidance for the Assessment of Creep Rupture, Creep Strain and Stress Relaxation Data,'' European Creep Collaborative Committee Recommendations—Volume 5, Doc Ref. 5524/MC/68 Issue II. (For further information contact Dr. S. R. Holdsworth, GEC ALSTHOM Turbine Generators, Newbold Road, Rugby, CV21 2NH, UK)

Ivarrson, B., 1986, ''Evaluation of Different Methods for Extrapolation of Creep Rupture Data,'' Report IM-1794, Swedish Institute for Metals Research, Stockholm, Sweden.

Larson, F. R., Miller, J., 1952, ''A Time-Temperature Relationship for Rupture and Creep Stresses,'' Trans., ASME, Vol. 74, pp. 765–775.

Manson, S. S., 1968, ''Time-Temperature-Parameters—A Re-evaluation and Some New Approaches,'' *Proceedings of Materials Engineering Congress,* ASM Publication D8-100, ASM, Metals Park, OH, p. 1.

Manson, S. S., Haferd, A. M., 1953, ''A Linear Time-Temperature Relation for Extrapolation of Creep and Stress-Rupture Data,'' NACA TN 2890.

Manson, S. S., Succop, G., 1954, ''Stress Rupture Properties of Inconel 700 and Correlation on the Basis of Several Time-Temperature Parameters,'' ASTM STP No 174., ASTM, Philadelphia, PA, p. 40.

Orr, L. R., Sherby, O. D., Dorn, J. E., 1954, ''Correlations of Rupture Data for Metals at Elevated Temperatures,'' Transactions, ASM, Vol. 46, pp. 113–128.

Piearcey, B. J., and Bullough, C. K., 1997, ''An On-line Materials Database for the Design of Gas Turbine Components,'' ASME Paper 97-GT-167, presented at Turbo Expo '97—Land Sea and Air, June 2–5, 1997, Orlando, FL.

Development and Turbine Engine Performance of Three Advanced Rhenium Containing Superalloys for Single Crystal and Directionally Solidified Blades and Vanes

R. W. Broomfield

D. A. Ford

J. K. Bhangu

Rolls-Royce plc,
Elton Road Materials Center, P.O. Box 31,
Derby and Bristol, U.K.

M. C. Thomas

D. J. Frasier

P. S. Burkholder

Allison Engine Company (Rolls-Royce plc),
Indianapolis, IN

K. Harris

G. L. Erickson

J. B. Wahl

Cannon-Muskegon Corporation,
SPS Technologies, Inc.,
Muskegon, MI

Turbine inlet temperatures over the next few years will approach 1650°C (3000°F) at maximum power for the latest large commercial turbofan engines, resulting in high fuel efficiency and thrust levels approaching 445 kN (100,000 lbs.). High reliability and durability must be intrinsically designed into these turbine engines to meet operating economic targets and ETOPS certification requirements. This level of performance has been brought about by a combination of advances in air cooling for turbine blades and vanes, design technology for stresses and airflow, single crystal and directionally solidified casting process improvements, and the development and use of rhenium (Re) containing high γ' volume fraction nickel-base superalloys with advanced coatings, including full-airfoil ceramic thermal barrier coatings. Re additions to cast airfoil superalloys not only improves creep and thermo-mechanical fatigue strength, but also environmental properties including coating performance. Re dramatically slows down diffusion in these alloys at high operating temperatures. A team approach has been used to develop a family of two nickel-base single crystal alloys (CMSX-4® containing 3 percent Re and CMSX®-10 containing 6 percent Re) and a directionally solidified, columnar grain nickel-base alloy (CM 186 LC® containing 3 percent Re) for a variety of turbine engine applications. A range of critical properties of these alloys is reviewed in relation to turbine component engineering performance through engine certification testing and service experience. Industrial turbines are now commencing to use this aero developed turbine technology in both small and large frame units in addition to aero-derivative industrial engines. These applications are demanding, with high reliability required for turbine airfoils out to 25,000 hours, with perhaps greater than 50 percent of the time spent at maximum power. Combined cycle efficiencies of large frame industrial engines are scheduled to reach 60 percent in the U.S. ATS programme. Application experience to a total 1.3 million engine hours and 28,000 hours individual blade set service for CMSX-4 first stage turbine blades is reviewed for a small frame industrial engine.

Introduction

During the last 30 years, turbine inlet temperatures have increased by about 500°C (900°F). About 70 percent of this increase is due to more efficient design of air cooling for turbine blades and vanes, particularly the advent of serpentine convection and film cooling, and the use of full airfoil thermal barrier ceramic coatings, while the other 30 percent is due to improved superalloys and casting processes. The greatest advances in metal temperature and stress capability for turbine airfoils have been the result of the development of single crystal superalloy, casting process, and engine application technology pioneered by Pratt and Whitney (P&W) (Gell et al., 1980).

Maximum metal temperatures approaching 1130°C (2066°F) have been flight-qualified for CMSX-4 turbine blades at maximum engine power during accelerated, simulated mission endurance testing (ASMET) (Fullagar et al., 1994). Full airfoil and platform advanced thermal barrier coatings have been certified for commercial turbine engine use, with the capability to increase gas temperatures by 100°C (180°F), or reduce metal temperatures commensurately to dramatically improve turbine blade life (PW, 1994).

Allison's unique dual-wall Lamilloy® quasi-transpiration cooling technology applied to CMSX-4 single crystal airfoils facilitates a further 222°C (400°F) to 333°C (600°F) turbine inlet temperature capability increase over the next five years. The Castcool™ Lamilloy® technology combines film leading and trailing edge airfoil cooling, with the dual-wall Lamilloy cooling in the rest of the airfoil in a one piece single crystal casting, further improving the cost of manufacture. The fine detail and complexity of these components bring manufacturing considerations to the forefront (Harris et al., 1990; Burkholder et al., 1995) (Fig. 1).

The compositions of the first generation single-crystal superalloys that have attained turbine engine application status are shown in Table 1. These alloys are characterized by similar creep-rupture strength. However, they exhibit variations in single crystal castability, residual γ/γ' eutectic phase content fol-

---

Contributed by the International Gas Turbine Institute and presented at the International Gas Turbine & Aeroengine Congress & Exhibition, Orlando, FL, June 2–5, 1997. Manuscript received by the ASME Headquarters March 1, 1997. Paper No. 97-GT-117. Associate Technical Editor: H. A. Kidd.

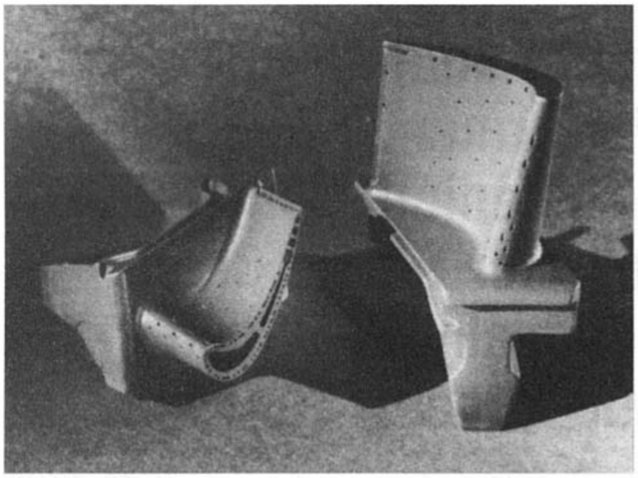

Fig. 1 AE 301X Castcool first stage blade—CMSX-4 Alloy

Table 1 First generation single crystal superalloys

Nominal Composition, wt. %

Alloy	Cr	Co	Mo	W	Ta	V	Cb (Nb)	Al	Ti	Hf	Ni	Density (kg/dm³)
PWA 1480	10	5	-	4	12	-	-	5.0	1.5	-	BAL	8.70
René N4	10	8	2	6	5	-	.5	4.2	3.5	.2	BAL	8.56
SRR 99	8	5	-	10	3	-	-	5.5	2.2	-	BAL	8.56
RR2000	10	15	3	-	-	1	-	5.5	4.0	-	BAL	7.87
AM1	8	6	2	6	9	-	-	5.2	1.2	-	BAL	8.59
AM3	8	6	2	5	4	-	-	6.0	2.0	-	BAL	8.25
CMSX-2	8	5	.6	8	6	-	-	5.6	1.0	-	BAL	8.56
CMSX-3	8	5	.6	8	6	-	-	5.6	1.0	.1	BAL	8.56
CMSX -6	10	5	3	-	2	-	-	4.8	4.7	.1	BAL	7.98
SX 792	12	8	2	4	5	-	-	3.4	4.2	-	BAL	8.25

lowing solution heat treatment, absence or presence of carbides, impact and mechanical fatigue properties (HCF & LCF), environmental oxidation and hot corrosion properties, coating performance, and density.

Turbine engine experience with the first generation single-crystal alloys has resulted in process developments being combined with Re additions to improve and maximize overall properties of the turbine airfoil components (Harris et al., 1990). Microstructures can be optimized to be fully solutioned and HIP'ed, to contain neither γ/γ' eutectic phase, nor regions of incipient melting, carbides, nor microporosity (Fullagar et al., 1994). The published compositions of the Re containing single crystal alloys are shown in Table 2.

Component cost considerations, particularly for commercial aero and industrial turbine engines, have resulted in the development of the three Re containing DS superalloys (Table 3). These alloys have similar creep-rupture strength to the first generation single-crystal superalloys. PWA 1426 (Cetel et al., 1992) is used 50 percent solutioned, René 142 (Ross and O'Hara, 1992) close to 100 percent solutioned, and CM 186 LC as-cast (Harris et al., 1992; Caruel et al., 1996). The absence of a solutioning requirement with CM 186 LC not only lowers cost and improves manufacturability (no recrystallization or incipient melting problems), but also provides excellent transverse intermediate temperature ductility and transverse low cycle fatigue (LCF) properties.

Alloy Development

Development in the CM family of single-crystal superalloys has been in the following two general directions since the inception of CMSX-2® and CMSX-3® alloys (Harris et al., 1983, 1986):

- Partial replacement of tungsten (W) with increasing Re. Lowering of chromium (Cr) to accommodate the increased alloying with acceptable phase stability.
- Partial replacement of titanium (Ti) by tantalum (Ta). Re is a key element, and the magnitude of the improvement that it provides in creep and LCF strength at 950°C (1742°F) is illustrated in Figs. 2 and 3. As an example, changing from a non-Re containing alloy SRR99 to a 6 percent Re alloy CMSX-10 (RR 3000) increases creep strength at 500 hours life by 46 percent and increases fatigue strength at 20,000 cycles life by 59 percent. These improvements are less when corrected for alloy density differences.

In order to understand these improvements, the distribution of Re through the microstructure has been studied in some detail on three scales: dendritic, microscopic, and atomic.

Distribution of Rhenium

On the dendritic scale, it is well known that Re segregates strongly to the dendrite centers and that even after a solution/homogenization heat treatment, a uniform distribution is not

Nomenclature

ASMET = accelerated simulated mission endurance test
ATS = advanced turbine system
B = boron
C = carbon
CGR = crack growth rate
DS = directionally solidified, columnar grain
DPT = durability proof testing
EDAX = energy dispersive x-ray micro-analysis
EFH = engine flight hours
ETOPS = extended over water, twin engine certification requirements
HCF = high cycle fatigue
HIP = hot isostatic pressing
HP = high pressure
IP = intermediate pressure
ISA = International Standard Atmosphere (15°C)
kN = kilo newton
LCF = low cycle fatigue
LMP = Larson-Miller parameter
LNG = liquid natural gas
MFB = machined-from-blade
MW(e) = mega-watt
NGV = nozzle guide vane
OPR = overall pressure ratio
ppm = part per million
S = sulfur
Si = silicon
SEM = scanning electron microscope
T = temperature
TBC = thermal barrier coating
TCP = topologically close-packed phase
TEM = transmission electron microscope
TET = turbine entry temperature
TF = thermal fatigue
TFCIL = thermal fatigue crack initiation life
TMF = thermomechanical fatigue
TTT = transformation-time-temperature
WDX = wavelength dispersive microanalysis
Zr = Zirconium
[N] = combined nitrogen
[O] = combined oxygen
γ = gamma phase
γ' = gamma prime phase
$\Delta\epsilon_{mec}$ = change in mechanical strain
K_T = stress concentration factor

Table 2 Re containing single crystal alloys

Nominal Composition, wt. %

Alloy	Cr	Co	Mo	W	Ta	Cb (Nb)	Re	Al	Ti	Hf	Ni	Density (kg/dm³)
CMSX-4	6.5	9	.6	6	6.5	-	3	5.6	1.0	.1	BAL	8.70
PWA 1484	5	10	2	6	9	-	3	5.6	-	.1	BAL	8.95
SC 180	5	10	2	5	8.5	-	3	5.2	1.0	.1	BAL	8.84
René N5	7	8	2	5	6	-	3	6.2	-	.2	BAL	8.63
René N6	4	12	1	6	7	-	5	5.8	-	.2	BAL	8.97
CMSX -10	2	3	.4	5	8	.1	6	5.7	.2	.03	BAL	9.05

achieved (Table 4). In the Rolls-Royce materials specifications for CMSX-4 and CMSX-10 (RR 3000), a different approach to measuring dendritic segregation following solution/homogenization heat treatment has been taken. A large number of measurements of Re, W, and Ta levels are made across a section perpendicular to crystal growth, and the standard deviations associated with the distributions for each element are calculated. An upper limit is set for the standard deviation for each element; the limits vary from one alloy to the other, but they do not vary by component in a given alloy. The solution/homogenization heat treatments developed for both alloys are designed to minimise residual dendritic microsegregation and hence to maximize phase stability.

On a microscopic scale, the composition of the γ' phase has been measured in both CMSX-4 and in an early variant of CMSX-10 (RR 3000) containing 5.3 percent Re (RR 2067) using EDAX micro-analysis on thin TEM foils. The alloy and γ' phase compositions were as shown in Table 5.

The γ' compositions were much more similar to each other than were the alloy compositions, basically $(Ni, Co)_3(Al, Ta)$ with some Cr, W, and Ti dissolved. The Re contents in the γ' were low, and, so, on the basis that both CMSX-4 and CMSX-10 (RR 3000) contain about 70 vol. percent γ', this implies average Re levels in the γ phase of about 6 wt. percent and 13 percent (by weight), respectively, in the two alloys. It is not surprising, therefore, that under conditions, where dislocation movement is confined to the γ phase, Re additions are very powerful strengtheners.

Atom-probe micro-analyses of Re containing modifications of PWA 1480 and CMSX-2 alloys reveal the occurrence of short-range order in the γ matrix (Blavette et al. 1986, 1988). Small Re clusters (approximately 1.0 μm in size) are detected in the alloys. The Re clusters act as efficient obstacles to dislocation movement in the γ matrix channels compared to isolated solute atoms in solid solution, and, thereby, they play a significant role in improving alloy strength. The benefits of Re to mechanical properties can be seen in situations where dislocation movement within the γ phase matrix channels is controlling. Where dislocations pass readily through both γ and γ' phases, the strength advantage is smaller. Dislocations travel mainly within the γ matrix channels at higher temperatures >850°C (1562°F). A consistent benefit for CMSX-4, for example, is seen in tensile strength, creep, and stress-rupture strength over the temperature range of 850–1050°C (1562–1922°F), where the temperature capability advantage is at least 30°C (54°F) over SRR 99.

Table 3 Re containing DS alloys

Nominal Composition, wt. %

Alloy	Cr	Co	Mo	W	Ta	Re	Al	Ti	Hf	C	B	Zr	Ni	Density (kg/dm³)
PWA 1426	6.5	12	2	6	4	3	6.0	-	1.5	.10	.015	.03	BAL	8.6
René 142	6.8	12	2	5	6	3	6.2	-	1.5	.12	.015	.02	BAL	8.6
CM 186 LC	6.0	9	.5	8	3	3	5.7	.7	1.4	.07	.015	.005	BAL	8.70

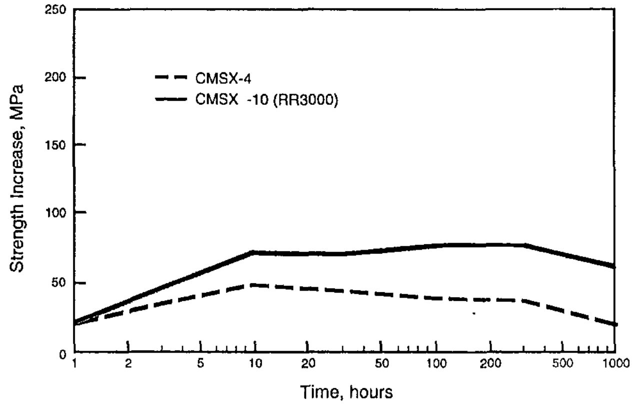

Fig. 2 The strength advantage of Re containing single crystals over SRR 99—1 percent creep strain, 950°C (1742°F) (Not density corrected)

Further work on the distribution of Re on the atomic scale is being undertaken at Oxford University using atom-probe micro-analysis. In fully heat-treated CMSX-10 (RR 3000), a pronounced buildup of Re has been observed adjacent to the γ' particles—as one might expect since Re is a slow-diffusing element which is rejected by the growing γ' (Fig. 4).

Influence of Re Upon Selected Properties

The influence of Re is all-pervasive in this class of superalloy, but five areas have been selected: stability of γ' at high temperatures, effect of Re distribution upon primary creep behavior, oxidation performance, thermal fatigue, and, finally, LCF properties.

Stability of γ'. γ' stability is important in terms of resistance to coarsening and re-solutioning of γ' during coating or brazing operations. CMSX-4 has good performance in this respect, as indicated by a recent paper (Miglietti and Pennefather, 1996). These workers measured γ' size following a wide range of brazing/diffusion heat treatments up to 1240°C (2264°F). These times and temperatures have been combined via the Larson-Miller parameter (LMP) (Fig. 5); there is steady γ' growth up to a LMP of 30,000, but much faster growth thereafter. The 30,000 value corresponds, for instance, to 3 hours at 1190°C (2174°F) (a typical brazing condition). It is interesting to note that the resistance to γ' coarsening appears to be improved by the 1140°C (2085°F) intermediate age used for CMSX-4. As-solution-treated CMSX-4 was soaked for various times and temperatures by Roan (1996), and in this condition (3 hours at 1190°C (2174°F), caused significant dissolution of the cubic γ'. Quite probably, the Re "wall" at the γ/γ' interface, observed in the atom-probe work, is effective in restricting growth and dissolution of the γ'.

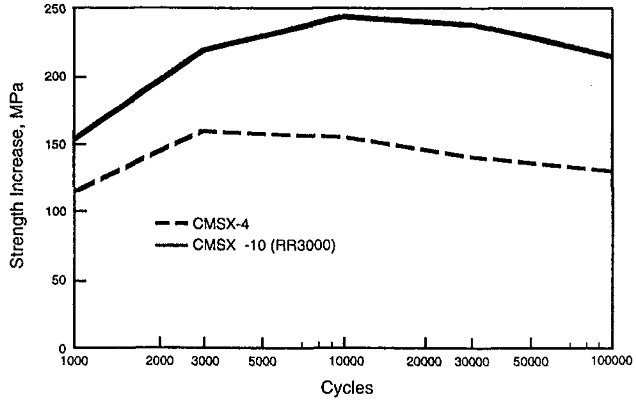

Fig. 3 The strength advantage of Re containing single crystals over SRR 99—low cycle fatigue, 950°C (1742°F)

Table 4 CMSX-4 alloy

0.25" (6.4 mm) ϕ Test Bar Allison Solution/Homogenisation Heat Treatment + Double Aged

SEM-WDX Analysis (wt. %)

	Center of Primary Dendrite	Interdendritic Region
Cr	5.8	5.7
Co	9.7	9.8
Ni	BAL	BAL
W	6.1	4.2
Mo	.6	.7
Ti	.9	1.0
Al	5.7	6.4
Re	3.7	1.9
Ta	5.0	6.5
Hf	.06	.05

γ' stability is further improved in the 6 percent Re alloy CMSX-10 (RR 3000). During creep tests at 1175°C (2147°F), a stable γ' rafted structure developed in a few hours, and was still stable after 60 hours testing (Fig. 6).

Primary Creep Behavior. During the development of CMSX-10 (RR 3000) it was noted that the magnitude of primary creep varied with the casting source. Times to rupture were fairly consistent, but the times to 1 percent creep strain on samples from the "good" source were between two and four times as long as those from the "worst" source. When the standard homogeneity check was carried out, a good correlation was observed between homogeneity and creep life; the standard deviation for Re was 1.23 percent in the worst samples, falling to 0.6 percent in the best ones. The casting source with the highest thermal gradient and solidification rate gave the lowest standard deviation for Re. A proposed explanation for this effect follows.

In cast and heat-treated single crystals, the dislocations are concentrated in interdendritic regions (Pollack and Argon, 1992). As deformation occurs, these dislocations multiply and spread throughout the structure. In more heavily segregated test pieces, the dislocation motion through the γ matrix channels at the start of the 1080°C (1975°F) test (ie., primary creep) will therefore occur in regions low in rhenium, and, hence, low in creep strength. A rapid rate of primary creep would therefore be expected. In the most segregated sample referred to above, it was estimated that the weakest 10 percent of the structure contained only 3.0–4.3 percent Re and 4.5 percent W; so, it might be comparable with homogeneous CMSX-4 with 2.9 percent Re + 6.4 percent W. Once dislocations have spread throughout the structure, the overall creep rate will be a function of the average composition of the alloy, hence segregation has less effect upon the stress-rupture life.

Table 5 Alloy and γ' phase compositions

	Co	Cr	Mo	W	Re	Al	Ti	Ta
Nominal wt. %								
RR2067	8.0	3.4	0.48	6.1	5.3	5.6	1.0	7.6
CMSX-4	9.7	6.5	0.6	6.4	2.9	5.6	1.0	6.5
Gamma Prime (γ'), wt. %								
RR2067	5.2	1.9	1.0	5.6	1.9	6.1	1.25	11.4
CMSX-4	6.1	2.7	0.55	5.75	1.4	6.2	1.4	10.7
Gamma Prime (γ'), at. %								
RR2067	5.5	2.3	0.6	1.9	0.65	14.1	1.6	3.9
CMSX-4	6.4	3.2	0.35	1.9	0.45	14.2	1.75	3.6

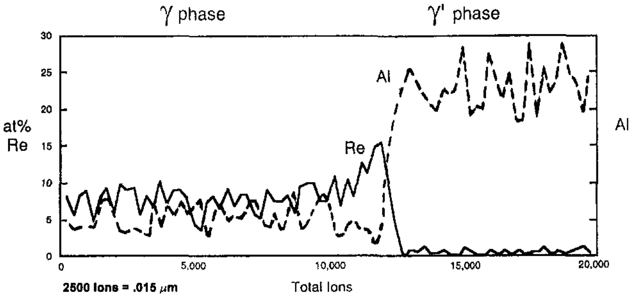

Fig. 4 Re distribution across γ and γ' phases CMSX-10 (RR 3000)

Oxidation Behavior. The oxidation performance of 3 percent and 6 percent Re containing single crystal alloys at 1100°C (2012°F) for instance, is remarkably good bearing in mind the low Cr content of these materials. Normally, in cast superalloys with 5.5–6.2 percent aluminum (Al) (Strangman, et al., 1980) one would not expect a stable, protective α alumina film to form with less than about 8 percent Cr present, yet CMSX-10 (RR 3000) has quite good performance in this respect, with only 2 percent Cr. Once again, Re could be the key element. Research (Chen and Little, 1995) showed that Re did not enter the oxide film, but it did concentrate in the γ' depleted zone beneath the oxide. Figure 7 is taken from the work of Chen and Little (1995), and demonstrates twice as much Re in this region than in the base alloy. It is proposed that this Re concentration slows down the diffusion of elements such as Ti into the aluminium oxide scales, so increasing the oxide scale stability. Residual ppms (10–20 ppm) of yttrium (Y) and lanthanum (La) have been shown to dramatically improve the bare oxidation resistance and coating performance on CMSX-4 alloy (Fig. 8, 9, and 10) (Thomas et al., 1994; Korinko et al., 1996) when the sulfur (S) content of the alloy is <2 ppm.

It has also been found that La gives improved control of its ppm chemistry in the single crystal casting process compared to Y. It is now also known that the La and Y tie-up the residual S as very stable sulfides. The latest burner rig data indicates ppm combinations of La + Y may give the best results at 1038°C (1900°F) and 1093°C (2000°F) test temperatures. S weakens the strong Van der Waal's bond between the alumina scale and the base alloy.

Phase Stability. One aspect of critical importance in these high Re superalloys is the metallurgical stability, ie., the rate of formation of topologically close packed phases (TCPs).

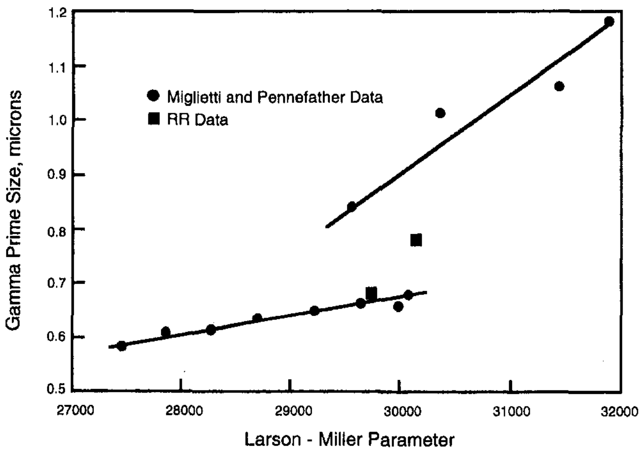

Fig. 5 Gamma prime size in CMSX-4 verses soaking condition, hrs/°C

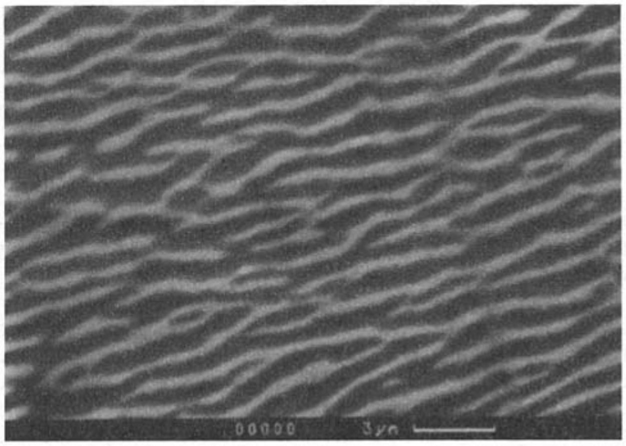

Fig. 6 Rafted γ/γ' structure in CMSX-10 (RR 3000) after 1 percent creep strain in 60 hours at 1175°C (2147°F)

These are not present significantly in the practical use of CMSX-4, but in CMSX-10 (RR 3000), the operating conditions of components have to be carefully considered against the TTT curve for formation of these phases. CMSX-4 shows continuing linear relationships for log stress to log stress-rupture life (Fig. 11), with no fall-off due to excessive TCP phase formation, out to the extent of current testing: 5600 h at 1121°C (2050°F), 12,400 h at 1093°C (2000°F), and 17,000 h at 982°C (1800°F). The composition of these TCP phases has been established by Chen and Little (1995), as shown in Table 6.

Unlike the γ' phase referred to earlier, the compositions of the TCP phases formed are clearly different in the two alloys. They are both basically Ni-Cr-W-Re, but the Re:W ratio in particular is much higher in CMSX-10 (RR 3000), reflecting the basic chemistry differences of the two alloys.

The important factor from a turbine engine performance viewpoint is, of course, the effect that these TCP phases have upon mechanical properties. Some TCP phases, particularly in multi-grain cast superalloys, have a marked embrittling effect, but these do not; their effect is to reduce creep strength when a certain volume fraction is formed by concentrating Re and W into an ineffective form, in effect, de-alloying the material. During the CMSX-10 (RR 3000) development program, the amount of TCP phase was estimated by a point-counting technique. The point was counted if it fell either on a TCP needle or on its γ' envelope, so, in effect, the proportion of the structure that was other than the normal $\gamma + \gamma'$ was measured. To give one example, unstressed exposure of CMSX-10 (RR 3000) for 250 hours at 1100°C (2012°F) gave an area fraction of TCP's of 5 percent, but this had no deleterious effect upon the impact strength, high or low cycle fatigue strength of the alloy. A substantial deviation in creep strength was only seen when the area fraction of TCP's approached 20 percent. In that condition,

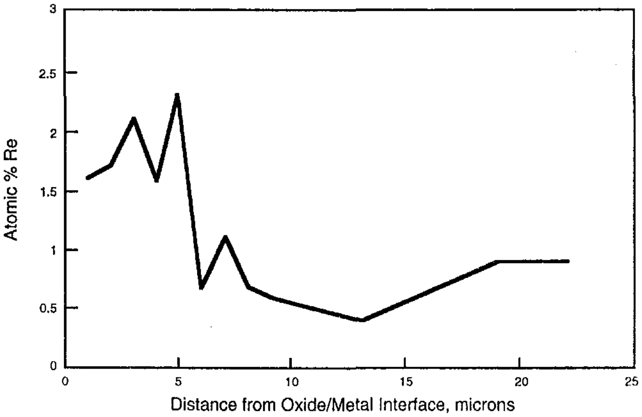

Fig. 7 Re distribution beneath the oxide/metal interface

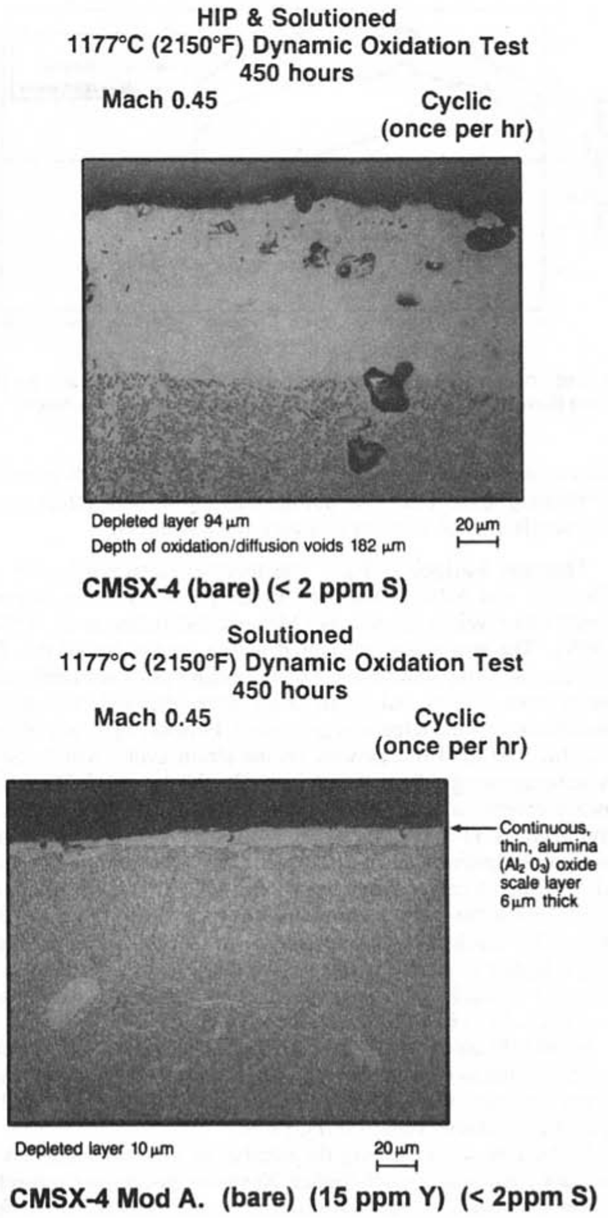

Fig. 8

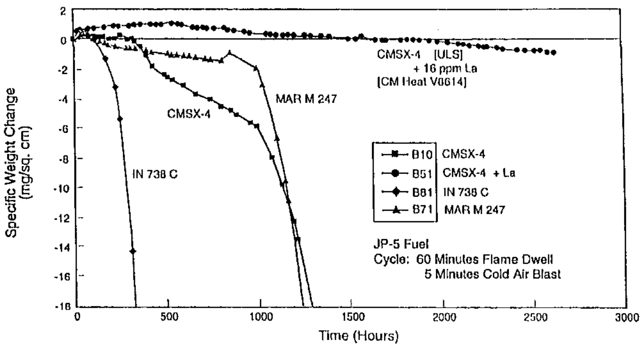

Fig. 9 Becon burner rig—dynamic cyclic oxidation bare alloys 1038°C (1900°F), 0.4 Mach

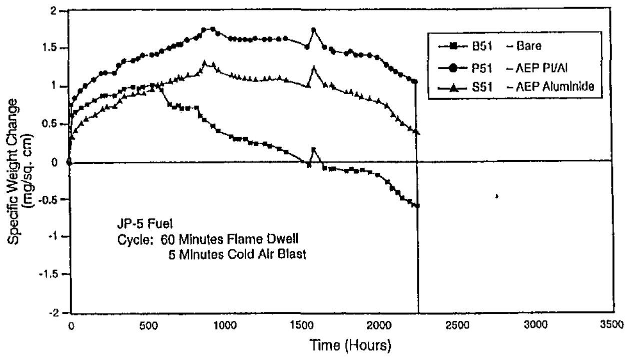

Fig. 10 Becon burner rig—dynamic cyclic oxidation CMSX-4 + La (16 ppm) Bare and Coated (CM Heat V8614) 1038°C (1900°F) 0.4 Mach

the creep elongation was still in the range of 13 to 18 percent, confirming these TCP's do not have an embrittling effect upon this single crystal alloy at this area fraction level.

Thermal Fatigue (TF). The thermal fatigue behavior of CMSX-4 and SRR99 has been investigated on blade-shaped, single-edge wedge specimens (Meyer-Olbersleben et al., 1992, 1996). The strain was measured at the wedge tip of the TF specimens. Temperature-mechanical strain cycles with different mean strain values and strain ratios were obtained. The strain distribution on the edge was presented. Further, TF crack initiation life and total life depend on the strain cycle, which itself is temperature-gradient dependent. On the basis of TF strain measurements, a new TMF cycle was introduced. An integrated approach for TF and TMF investigations was proposed. Preliminary investigations show that under the test conditions used, TF cycling is more damaging than TMF. TF crack initiation mechanisms for both superalloys were identified. Finally, the higher TF crack initiation resistance of CMSX-4 is explained by its higher oxidation resistance combined with a higher mechanical strength of its γ' depleted zone and γ/γ' microstructure (Fig. 12) (Meyer-Olbersleben, 1996).

In SRR99 and CMSX-4, residual cast microporosity on the wedge tip led to stress concentration. For both alloys under high strain loading, cracks always initiate on these porosities at the specimen surface (Figs. 12(*a*), (*b*)).

Under low strain loading the number of thermal cycles (N_i) to crack initiation is much higher. Nevertheless, the same mechanism of crack initiation on microporosities was observed for CMSX-4, Fig. 12(*d*). For SRR99, a complex mechanism of oxidation/spallation/reoxidation combined with the effect of the residual cast microporosity was identified as the crack initiation mechanism, Fig. 12.

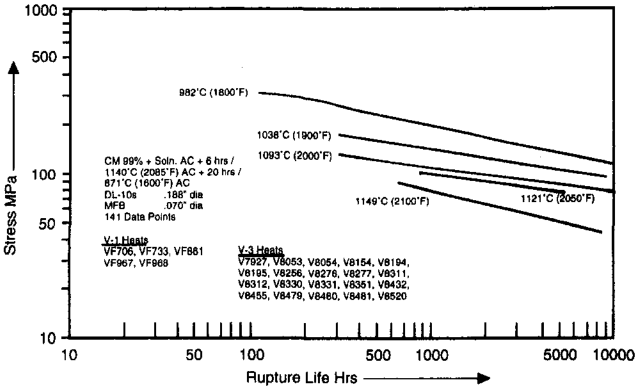

Fig. 11 Stress—rupture CMSX-4 alloy (average 001)

Table 6 TCP phases (wt %)

	Ni	Co	Cr	Mo	W	Re	Al	Ti
CMSX-4	20	8	9	2	28	28	1	4
CMSX -10 (RR3000)	30	2	6	1	10	44	2	5

Wedge tips of CMSX-4 specimens remained almost intact during low strain loading even after very high numbers of thermal cycles (Fig. 12(*d*)), showing its high resistance to oxidation. However, the wedge tips of SRR99 specimens were highly damaged by oxide-scale spalling.

For both alloys investigated, crack initiation was always observed only after an incubation period, which is dependent upon the strain range and the maximum temperature of the thermal cycle. All cracks were initiated at the wedge tip surface and propagated towards the bulk. For all tests, an initial increase in the crack growth rate (CGR) was followed by a pronounced decrease when the crack length was between 2–3 mm. The exact beginning of this crack growth retardation depends upon $\Delta\epsilon_{\mathrm{mec}}$ and T_{max}.

The reduction of thermal gradients in the specimen depth and subsequent decrease in thermal strains and stresses at the crack tip is the main reason for crack growth retardation on blade-shaped specimens. For longer cracks, the lower temperature and the lower interaction with oxygen should also be considered as an additional cause. No significant difference in the CGR was observed between SRR99 and CMSX-4 for the same TF test conditions.

HIP treatments were found to enhance TF resistance by closing the microporosity.

Low Cycle Fatigue (LCF). CMSX-4 shows a benefit over non-Re containing alloys when the time-dependent LCF mode is in operation, where dislocation activity and crack growth are

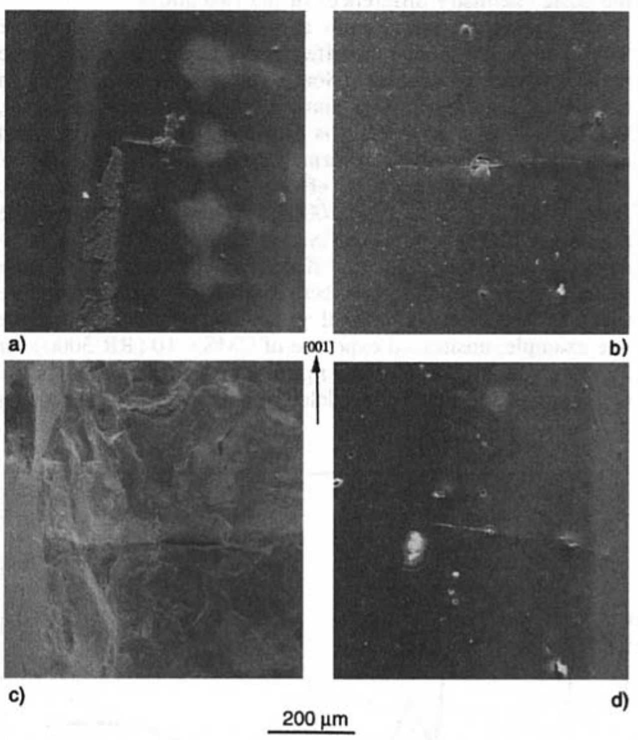

a) SRR 99, T_{max}=1150°C, $\Delta\varepsilon_{mec}$=0.75%, Ni= 680,
b) CMSX-4®, T_{max}=1150°C, $\Delta\varepsilon_{mec}$=0.75%, Ni=1080,
c) SRR 99, T_{max}=1150°C, $\Delta\varepsilon_{mec}$=0.53%, Ni= 5200,
d) CMSX-4®, T_{max}=1100°C, $\Delta\varepsilon_{mec}$=0.48%, Ni=28000.

Fig. 12 View of the wedge tip, SEM micrographs

Table 7 Strain controlled LCF 950°C (1742°F) R = O

Nf at 0.7% Strain	Cycles
DS Mar M 002 [Long]	10,000
DS CM 186 LC [Long]	19,000
CMSX-4 (001) [Unhipped]	50,000
CMSX-4 (001) [Hipped]	~100,000

mainly confined to the γ matrix phase. If the LCF data are plotted as stress for a given cyclic life versus temperature, the temperature advantage of CMSX-4 over SRR99 is about 45°C (81°F), which is similar to the creep strength advantage at high temperatures.

Under cycle-dependent conditions, where dislocations and cracks slice through γ and γ' phases alike, the improvement for CMSX-4 is less. However, if an improved fatigue performance is required in this regime, there is a solution: HIP'ing. In both plain specimens and notched specimens ($K_T = 2.2$), fatigue failures initiate at single crystal casting microporosity, and the fatigue life at a given cyclic stress and temperature can be related to the size and shape of the micropores (one 100 μm interdendritic micropore is more damaging than hundreds of 30 μm spherical pores at their normal uniform spacing in single crystal castings).

The LCF life improvement at 950°C (1742°F) of the Re containing alloys and HIP'ing is shown in Table 7.

Castability

RR investment foundries have cast well over 150 tons of Re containing superalloys over the last 10 years. Principle applications are turbine blading for both military and civil engines. During the period of introduction, RR has worked closely with CM and has evaluated, in-depth, the alloys CM 186 LC, CMSX-4, and CMSX-10 (RR 3000). Each alloy has presented the foundry with interesting challenges, and, as a result, considerable understanding of each alloy's behavior has been gained.

From a castability viewpoint, CMSX-4 performed well, with little difference observed in grain selection and quality to first generation alloys such as RR2000 and SRR99 when cast under conditions developed for these alloys. However, a revision of casting conditions showed CMSX-4 to be less prone to freckle chains and freckle generated defects than SRR99. Production experience has confirmed the general absence of these defects. CMSX-4 has shown no particular propensity to high angle boundary formation and recrystallization at 1.6 percent critical strain, as is typical of other single crystal alloys.

During the development of CMSX-10 (RR 3000), over 10 chemistry iterations were considered to meet the castability and mechanical property objectives, including microstructural stability. The development program showed certain chemistries to be sensitive to freckle formation, particularly at low casting temperatures. However, a satisfactory combination of mechanical properties were achieved, and production experience has shown no excessive tendency to any common single crystal defect. Foundry yields are in line with first and second generation single crystal alloys.

Table 8 lists the critical chemistries of the twenty-one 3629 kg (8000 lb.) blend heats of CMSX-4 manufactured to date. The ability to recycle CMSX-4 and foundry revert to these high quality standards that ensure the blend heats perform quite as well as 100 percent virgin heats has resulted in significant single crystal component cost reduction, which, along with significant advances in single crystal casting technology, result in turbine airfoil yields often >90 percent.

CM initiated a collaboration with RR in 1987 to establish the castability of a series of CM 186 LC alloy variants with chemical iterations controlling the level of the grain boundary strengthening elements C, Zr, and B and the residual element Si.

The castability assessment consisted of studies of the propensity to DS grain boundary cracking, porosity, and ceramic shell/core reaction. RB211 HP and IP turbine blades were cast with a variety of casting conditions and mould assembly designs to understand the behavior of the various chemical modifications. The results of these trials showed the benefit of reducing Si and

Table 8 Critical chemistry (wt % or ppm) CMSX-4 alloy blend V-3 3629 kg (8000 lb) heats

HEAT #	BLEND RATIO	C ppm	S ppm	B ppm	[N] ppm	[O] ppm	Al	Ti	Zr ppm	Si	Fe
V8331	50R/50V	18	2	<20	2	2	5.63	1.02	18	.01	.040
V8481	50R/50V	17	2	<20	2	1	5.67	1.02	25	.02	.026
V8562	50R/50V	20	2	<20	1	1	5.61	1.04	17	.02	.037
V8563	50R/50V	21	2	<20	1	1	5.66	1.02	22	.01	.036
V8634	50R/50V	21	2	<20	1	1	5.63	1.02	17	.01	.040
V8640	60R/40V	25	2	<20	1	1	5.63	1.03	17	.02	.038
V8653	50R/50V	19	2	<20	1	1	5.65	1.03	32	.01	.037
V8656	50R/50V	23	2	<20	2	1	5.64	1.02	30	<.01	.032
V8657	50R/50V	22	2	<20	1	1	5.66	1.03	30	.01	.030
V8676	50R/50V	18	2	<20	2	2	5.66	1.04	17	.01	.031
V8820	60R/40V	28	4	<20	1	2	5.66	1.01	22	.01	.045
V8821	60R/40V	27	3	<20	2	1	5.68	1.01	21	.01	.044
V8848	60R/40V	32	3	<20	1	1	5.70	1.01	18	.01	.059
V8857	50R/50V	30	2	<20	1	1	5.68	1.02	39	.01	.061
V8876	60R/40V	24	3	<20	2	2	5.65	1.01	32	.01	.051
V8877	60R/40V	27	3	<20	3	1	5.65	1.01	32	.01	.044
V9042	60R/40V	24	3	<20	1	1	5.65	1.03	24	.01	.053
V9081	50R/50V	30	3	<20	1	2	5.67	1.02	39	<.02	.054
V9119	40R/60V	30	1	<20	1	1	5.64	1.02	10	<.01	.067
V9179	50R/50V	25	2	<20	1	1	5.66	1.02	60	<.01	.089
V9180	60R/40V	26	3	<20	1	1	5.64	1.03	17	<.01	.067
MEAN		24	2	<20	2	1	5.65	1.02	25	.01	.041
STD. DEV.		4	.6	–	.6	.4	.02	.01	7	–	.010

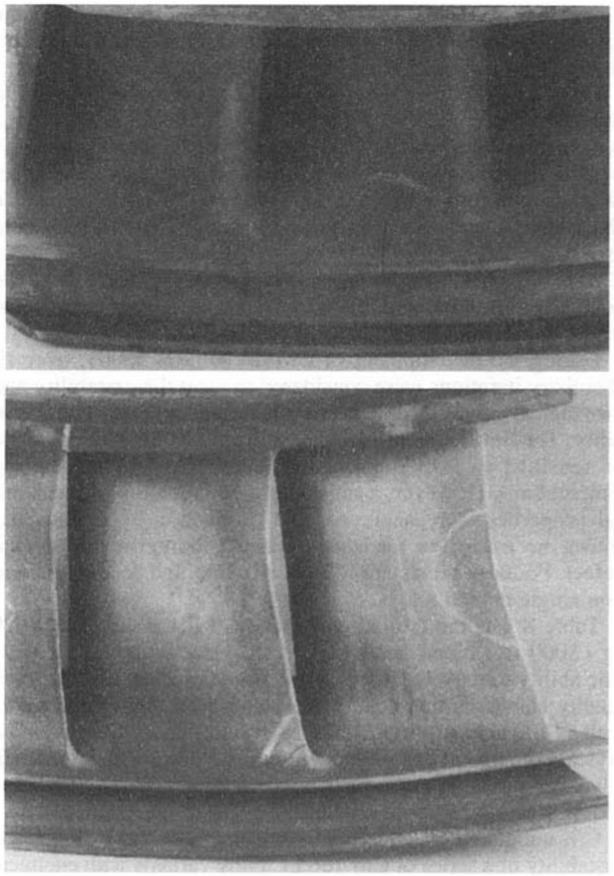

Fig. 13 IN 738°C cooled equiaxed second vane following 300 hr of DPT testing—leading edge outerband and trailing edge airfoil cracking

Zr levels to minimize any tendency for DS grain boundary cracking. The optimized chemistry showed no adverse foundry problems or other unusual problems. Casting yields, based on rejections associated with the alloy, were very high and equivalent to the best materials evaluated by RR. Grain structure defects such as freckle chains were not encountered.

Although no components are in production at RR with this alloy, castings have been produced for both military and civil demonstrator engines. These castings were produced from mixed virgin/revert ingot utilising scrap 3 percent Re containing CMSX-4 alloy and balancing virgin elements to create the CM 186 LC composition.

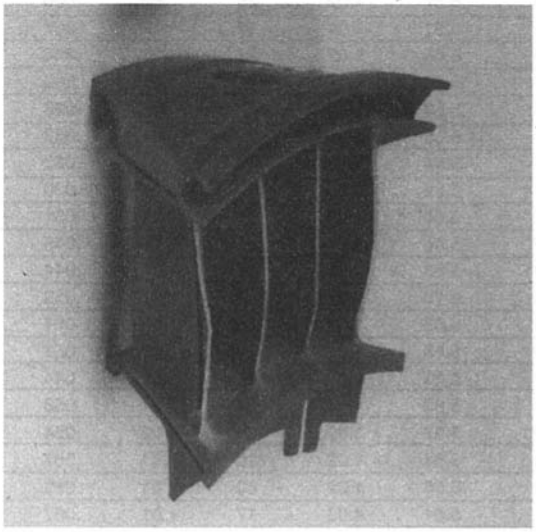

Fig. 14 IN 738 C cooled equiaxed 2nd vane following 300 hr of DPT testing—trailing edge airfoil bowing

Fig. 15 Dimensional inspection results of the CMSX-4 uncooled second vane airfoils as-new and following 150 hr of DPT AE Series Engine Testing

Allison Engine Test Results

Initial engine design for the T 406, AE 2100, and AE 3007 engines incorporated a variety of nickel-base superalloys in the high pressure turbines, including CMSX-3, IN 738 C, and MAR M 247. These alloys launched and certified this family of gas turbine aero engines; however, increased demand for higher power and lower specific fuel consumption has necessitated increased turbine entry temperatures. To accommodate the increase in temperature, improved airfoil alloys must be utilized. Significant development, as well as certification testing, has been done with CMSX-4.

The family of aero gas turbines mentioned above currently has amassed 7700 hours of high pressure turbine testing using CMSX-4; the distribution is 2360, 2790, and 2550 hours for the HPT 1 blade, HPT2 vane, and HPT2 blade, respectively. The HPT 1 blade (Fig. 18) is an air-cooled component, while the HPT 2 vane and blade have been tested and certified utilizing no cooling air. Turbine airfoils manufactured from CMSX-4 have performed successfully in a number of key test vehicles: engine #ps468 (150 hour development type test), engine #A300717 (official 150 hour FAA type test), engine #A300130 (500 hour development Accelerated Simulated Mission Endurance Test (ASMET)), engine #A300704 (official FAA over-temperature test), and engine #A300131 (official 1000 hour ASMET). Post-test inspections generally include a visual, dimensional, and nondestructive dye penetrant inspection; metallurgical evaluation has also been done, but this has been limited due to its destructive nature, and the desire to reuse the turbine hardware. In addition to full engine testing, component testing

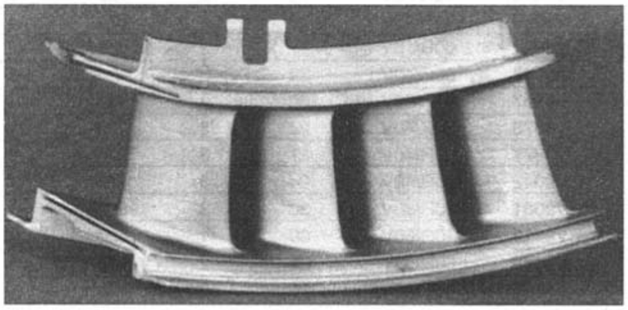

Fig. 16 CMSX-4 uncooled second vane segment following 150 hr of AE series engine DPT testing

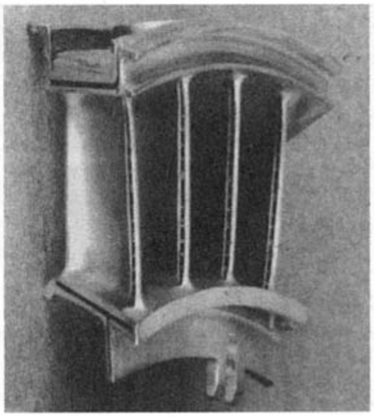

Fig. 17 CMSX-4 uncooled second vane segment following 150 hr of AE series engine DPT testing

on a hot fatigue rig has been used to quantify the endurance limit for a representative sample of CMSX-4 blades.

Only very limited distress has been noted in the CMSX-4 airfoils after testing, and the engine results indicate that the relative improvement for CMSX-4 is perhaps greater than originally anticipated. This has been particularly true for the multi-airfoil segmented second vane (Burkholder, et al., 1995); this vane (Figs. 13–17) has passed a 500 hour ASMET and currently is undergoing testing in a 1000 hour ASMET test. At the 900 hour mark, the engine was disassembled and visually inspected. The CMSX-4 vanes were found to be in excellent condition with only minor indications of any hot section damage.

Figures 19–22 show the γ, γ' microstructures of a CMSX-4 HPT 1 cooled turbine blade following 1093 h of ASMET testing in a AE series engine. It is apparent that at 50 percent span, the convex wall has only seen modest temperatures with higher and similar temperatures at the concave wall and leading edge and with the highest temperatures at the trailing edge, particularly the concave side.

With this successful development and certification database, flight test engines have already been shipped using CMSX-4 airfoils, and production AE 3007A engines incorporating CMSX-4 airfoils shipped in late 1996.

Rolls-Royce Military Engine Experience

Pegasus HP1 and HP2 Turbine Blades. The F402-RR-408 engine in service with the USMC is now being fitted with "sand tolerant" HP1 and HP2 turbine blades in single crystal CMSX-4. Fleet service experience to date includes 25 engines fitted with these blades, the lead engine being at 291 hours (Jan. 1997).

Development bench engine testing has now demonstrated a service life of 2000 hours (2 off ASMET tests, each of 530 h endurance running time), after which the blades were in good condition (Fig. 23). Turbine entry temperatures reached 1397°C (2547°F, 1670°K) simulating ISA + 34°C conditions.

Pegasus LP1 Turbine Blade. A development program has just been carried out with the LP1 blade cast in CMSX-4. The production part is in SRR99. This has been pursued in order to both increase creep life in service and to enable engine uprate capability. An ASMET cyclic endurance test has just been successfully carried out on a set of CMSX-4 LP1 turbine blades (530 h test). It is planned to offer this modification to the customers for the engine.

Pegasus LP1 Vane. In order to extend the life of the current equiaxed C1023 alloy LP1 NGV, it is proposed to cast the vane in CMSX-4. Castings are due in January 1997, with endurance testing starting late 1997.

Pegasus HP2 Vane. The current HP2 NGV is cast in equiaxed PD21 alloy, and suffers from leading edge oxidation/"burning" in earlier versions of the Pegasus engine, resulting in a high reject rate at overhaul. To increase the life of the component, a customer-funded program has been initiated to validate a vane cast in CMSX-4. It is anticipated that this will offer a 100°C (180°F) increase in material property capability. Castings are due in January 1997 and, following endurance testing, will be offered as a modification.

Adour LP Vane. Two engine sets of castings (Fig. 24) have been produced in CMSX-4 alloy for development testing. The current material is equiaxed C1023. One of these sets has

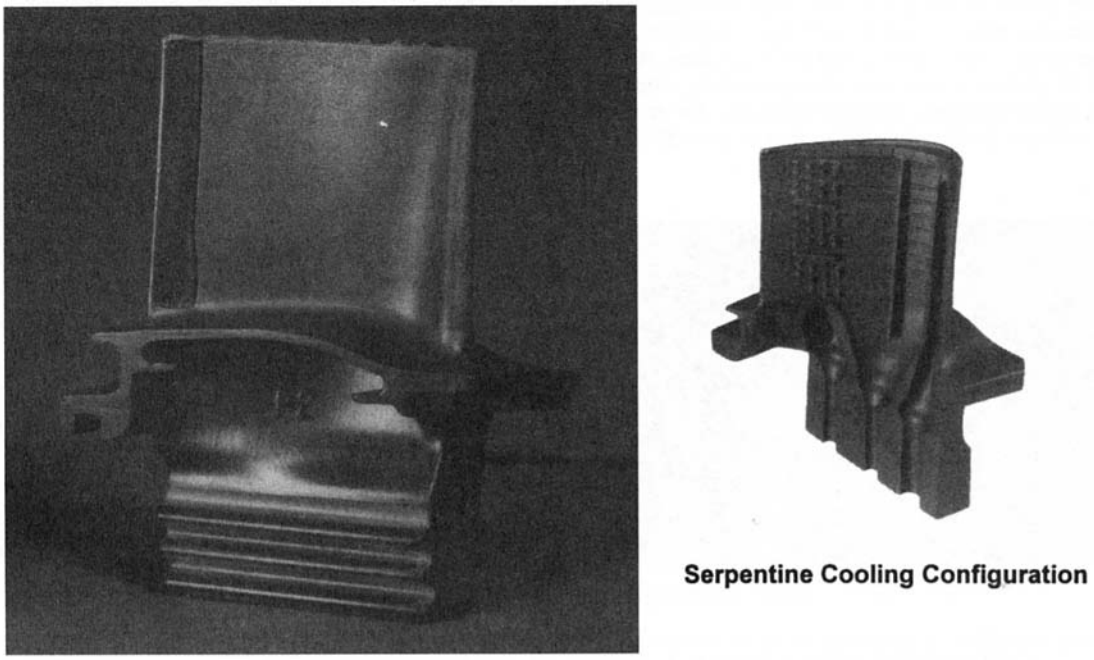

Serpentine Cooling Configuration

Fig. 18 AE series HP1 turbine blade following ASMET engine testing—CMSX-4 alloy

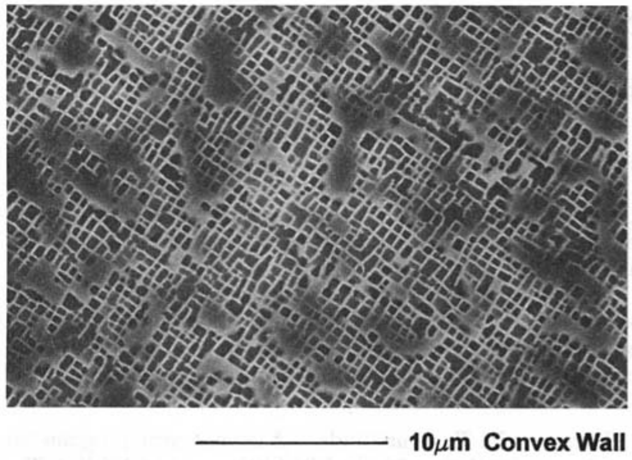

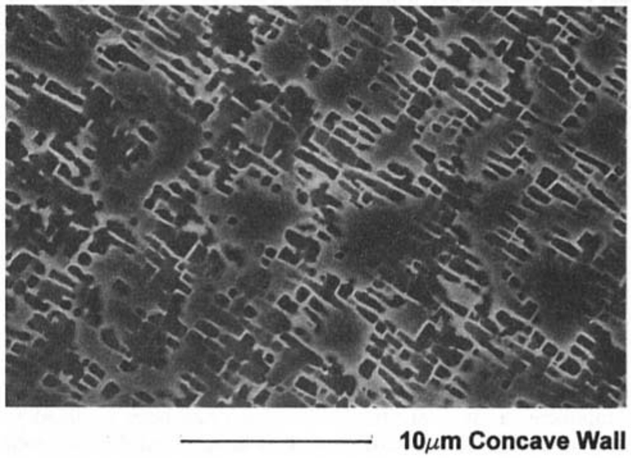

Fig. 19 SEM micrographs γ, γ' microstructure AE series HPT 1 cooled turbine blade CMSX-4 alloy following 1093 hr of ASMET testing. 50 percent airfoil span N^R second RIB.

been machined, and is currently carrying out engine testing with total running time now at 10 h (Jan. 1997).

Adour HP Vane. CMSX-4 casting trials have been carried out as singles and now are being carried out as triples. These vanes are currently conventionally cast in C1023 alloy. An order for 10 sets of parts of triples has been placed to support the 2000 h life engine program. Finished parts are due mid 1997 for engine testing—leading to certification in late 1998.

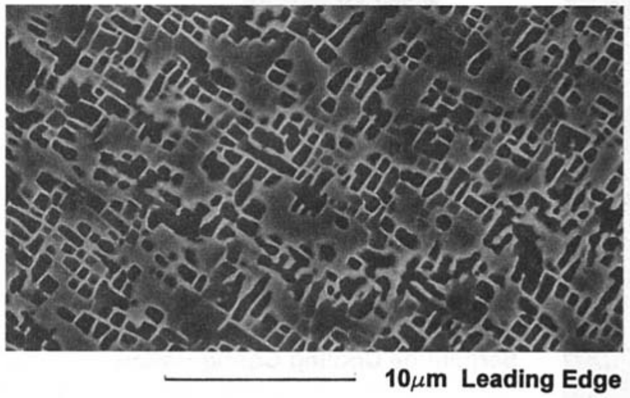

Fig. 20 SEM micrographs γ, γ' microstructure AE series HPT 1 cooled turbine blade CMSX-4 alloy following 1093 hr of ASMET testing. 50 percent airfoil span.

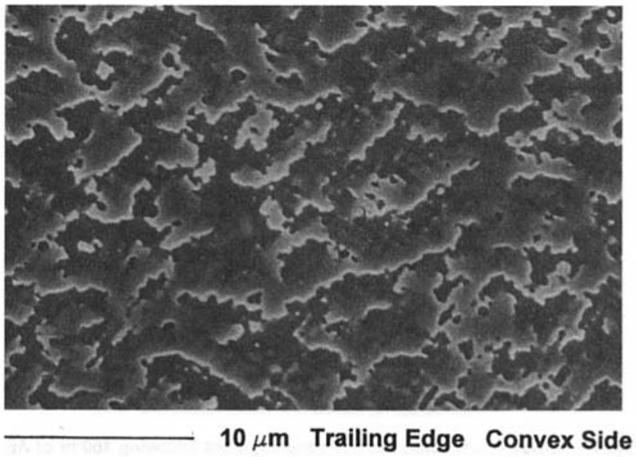

Fig. 21 SEM micrographs γ, γ' microstructure AE series HPT 1 cooled turbine blade CMSX-4 alloy following 1093 hr of ASMET testing. 50 percent airfoil span trailing edge.

Adour HP and LP Turbine Blades. For the 2000 h engine life initiative, it is planned to introduce CMSX-4 HP and LP turbine blades to replace the existing DS MAR M 002 and SRR 99 alloys, respectively. Design work is completed.

Rolls-Royce Civil Engine Experience

The RB211 and Trent family of engines power many of the large civil aircraft being used for passenger carrying service, including L1011, B747, B757, B767, A330, and B777.

All currently manufactured engines in the RB211 family feature a high bypass ratio, a wide chord fan, and a 3-shaft system. The 3-shaft concept, apart from providing a more optimized matched thermodynamic cycle, incorporates an intermediate pressure (IP) shaft which rotates significantly slower than the high pressure shaft, enabling the IP turbine blade to remain uncooled. Figure 25 shows the general arrangement of Trent turbofan engine, showing the components where Re containing superalloys are used.

Earlier versions of the RB211 family were certificated with directionally solidified MAR M 002 nickel-based alloy HP and IP turbine blades. However, the continual drive for improved specific fuel consumption has resulted in increased overall pressure ratios (OPRs) and turbine entry temperatures

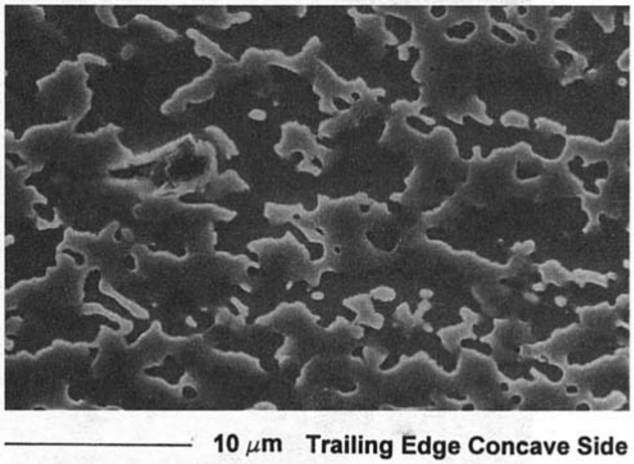

Fig. 22 SEM micrographs γ, γ' microstructure AE series HPT 1 cooled turbine blade CMSX-4 alloy following 1093 hr of ASMET testing. 50 percent airfoil span trailing edge.

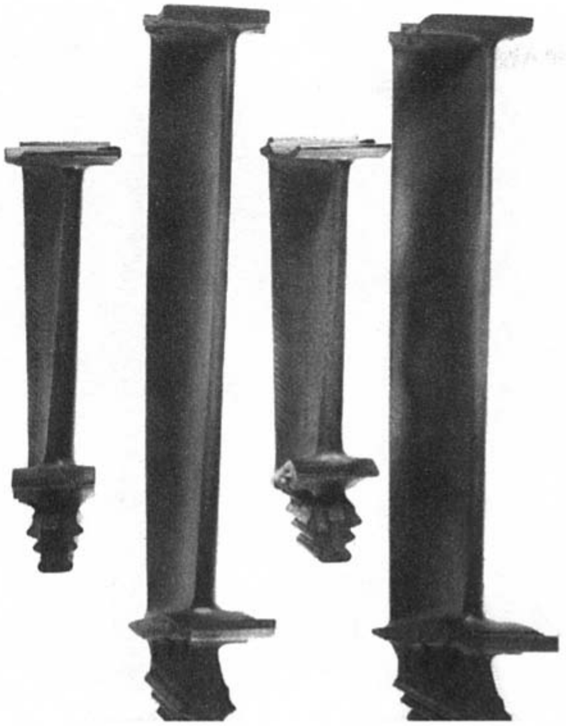

Fig. 23 **Pegasus CMSX-4 HP1 and HP2 turbine blades (leading edge). On the right: aluminised L106 (×2 ASMETS) On the left: pack aluminised (×1 ASMET)**

(TETS). The latter are now routinely above 1527°C (2781°F, 1800°K) during a 150 h type test, approximately 200°C (360°F) higher than the melting point of the materials used in the high pressure turbine. The cycle efficiency is also improved by minimum use of cooling air in the high pressure turbine, which in turn requires improved material properties and cooling techniques. Additionally, the airfoil material must be capable of accepting protective coatings, and, in particular, thermal barrier coatings (TBCs).

It was these considerations that led Rolls-Royce to select CMSX-4 and CMSX-10 (RR3000) for the following engine applications after an intensive materials characterization program in laboratories in addition to casting trials to establish viable production processes (Table 9).

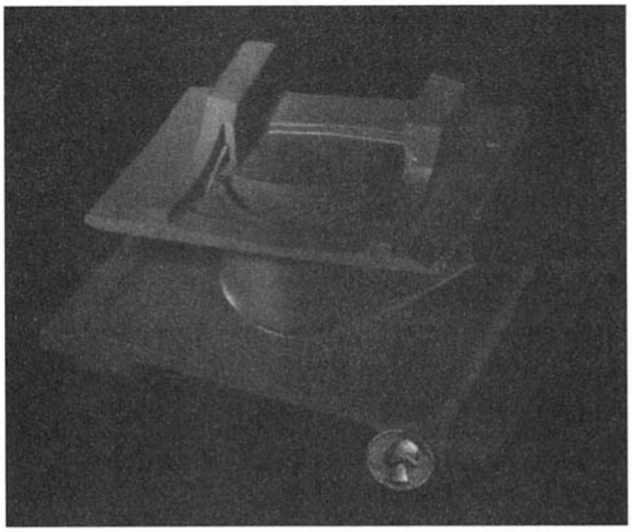

Fig. 24 **Adour LP vane CMSX-4 alloy—as-cast**

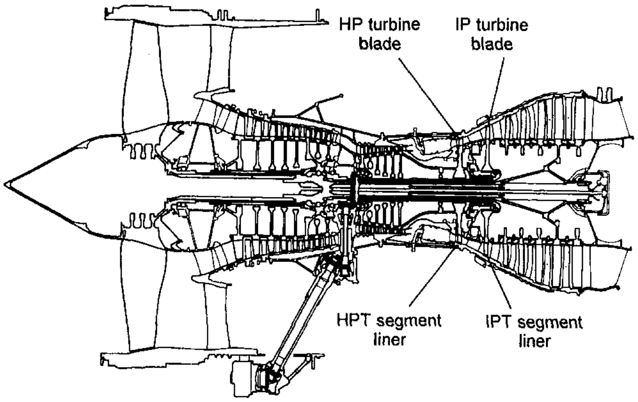

Fig. 25 **Trent turbofan**

The HP turbine blade applications were driven by the need to minimize the amount of cooling air used, without incurring creep penalties either in the airfoil or the shroud. All blades were subjected to rigorous bench engine test programs that included temperature surveys, dynamic measurements, feed air pressure and 150 h type tests, and realistic simulated service cycle tests. The condition of the RB211-524G/H CMSX-4 blade after 5000 cycles is compared to the DS blade after 3750 cycles in Fig. 26.

The Trent 800 HP blade, shown in Fig. 27, represents the most advanced application of CMSX-4 operating at the highest OPR and TET—essentially as a cantilevered blade, but with a shroud for aerodynamic performance and performance retention advantage. This blade is currently being evaluated with a full airfoil advanced TBC system for higher thrust versions of the Trent 800.

The IP turbine blade in a 3-shaft engine enables the blade to operate uncooled, and, hence, results in improved cycle efficiency relative to a 2-shaft engine where the second stage HP turbine blade must be cooled. Because the blade is uncooled, operating at about 1000°C (1832°F), the successive increases in TET have demanded materials with better creep and oxidation properties. Figure 28 shows IP turbine blades in CMSX-10 (RR 3000) alloy that met the Trent demands for improved creep resistance. The condition of the IP turbine blades after all of the bench tests has been excellent.

Finally, the use of CMSX-4 is being extended to HP and IP shroud segments, which form the rotor path, to overcome the component plastic deformation seen in certain applications. Analytical work has shown that the improved creep properties of CMSX-4 will result in components which will not incur the plastic strain. The hardware is currently undergoing bench engine evaluation.

Table 9 **CMSX-4 and CMSX 10 (RR 3000) applications**

Component	Project	Material	Bench Hours	Lead Service Cycles	Date of Entry into Service
High-Pressure Turbine Blade - Cooled	RB211-524G/H	CMSX-4	3300	3050	Dec 94
	Trent 700	CMSX-4	5200	2000	Mar 95
	Trent 800	CMSX-4	4750	800	Apr 96
IP Turbine Blade - Uncooled	Trent 700	CMSX-4	5200	2000	Mar 95
	Trent 800	CMSX -10 (RR3000)	4750	800	Apr 96
HP and IP Shroud Segment Liners	RB211-524G/H Trent 700 Trent 800	CMSX-4	–	–	–

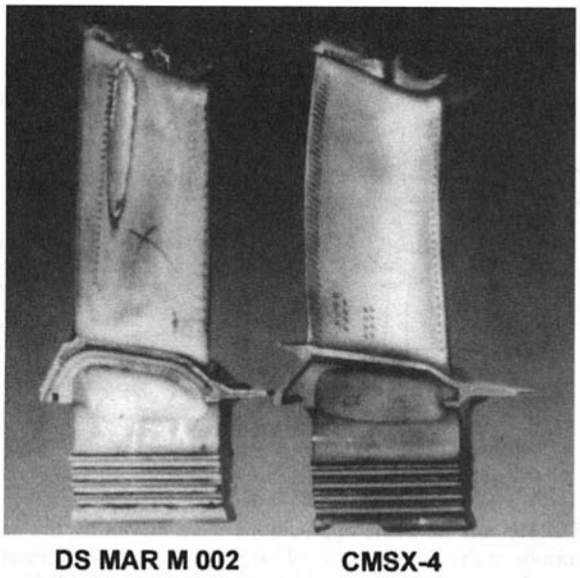

Fig. 26 Comparison between DS MAR M 002 blade (left) and CMSX-4 blade (right) following endurance engine testing

Other Engine Experience

Solar® Turbines, Inc. has reported that six years of field experience for CMSX-4 first stage blades in the MARS 100 industrial turbine has been excellent. Total running time for the 132 engines in the field is 1.25 million h, with the blades and Pt/Al coatings in good condition when examined at engine overall after 26,000–28,000 h service. The MARS 100 engines tend to spend at least 50 percent of their running time at maximum power with natural gas or liquid natural gas (LNG) as the predominant fuel (Harris, et al., 1992; Kubarych and Aurrecoechea, 1993; Brentnall, et al., 1997). Figure 29 shows a photomicrograph from a MARS 100 first stage CMSX-4 turbine blade after over 25,000 service hours. The CMSX-4 substrate alloy is coated with a platinum aluminide coating applied by a pack cementation process (RT-22). The photomicrograph was obtained from an axial airfoil section near the blade tip, at the convex wall near the leading edge. Coating condition appears to be excellent.

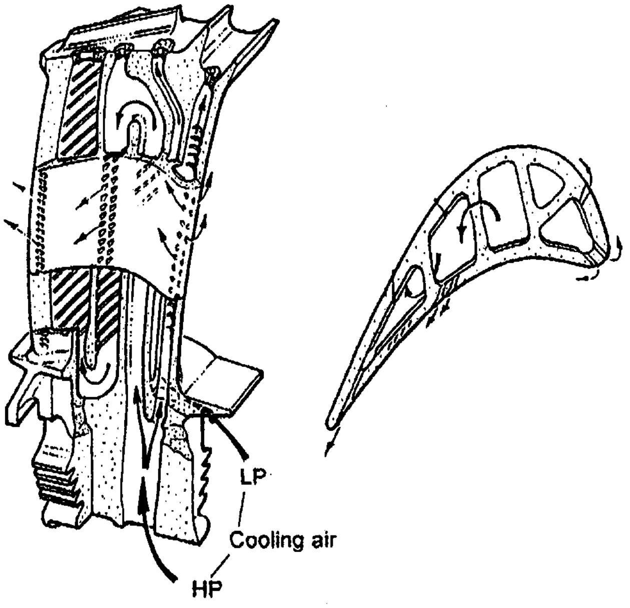

Fig. 27 Trent 800 HP blade cast in CMSX-4

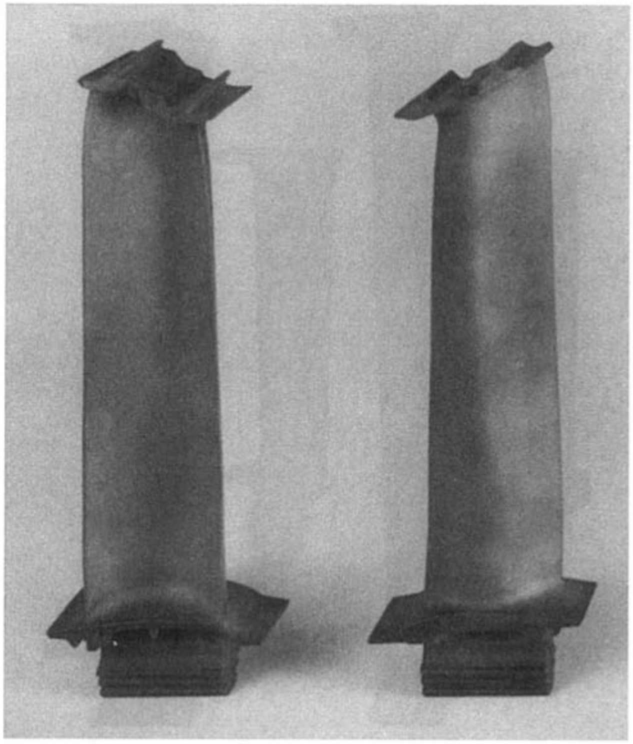

Fig. 28 Trent 890 IP turbine blades CMSX-10 (RR 3000) alloy following ETOPS engine testing

SNECMA has successfully completed initial 400 equivalent cycle ASMET-type military engine testing with DS HP vanes in CM 186 LC alloy with good results; this confirms the excellent transverse LCF properties and coating performance of the alloy (Bourguignon et al., 1996).

European Gas Turbines Ltd. has now validated blading in both CM 186 LC and CMSX-4 alloys for application to their range of industrial gas turbines. CM 186 LC has been chosen as a cost effective DS HP rotor blade alloy for the Typhoon gas turbine to provide enhanced life margins at its latest 4.9 MW(e) rating (Figs. 30 and 31). This cooled blade (Fig. 32) is now in full production, and first engine deliveries with this standard of blade commenced in September 1996. The performance of the alloy in the foundry has been very encouraging with no problems encountered

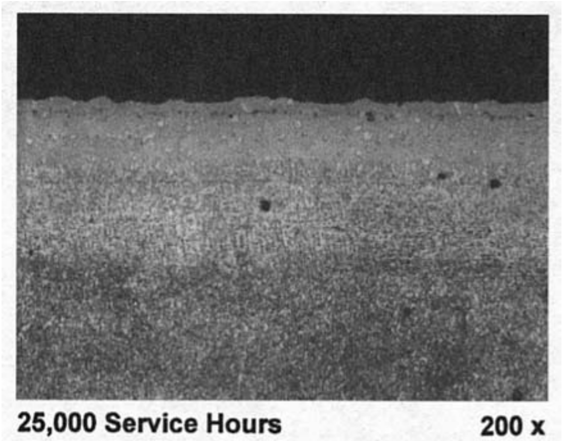

Fig. 29 MARS 100 first stage CMSX-4 turbine blade—airfoil axial section near blade tip—convex wall near leading edge

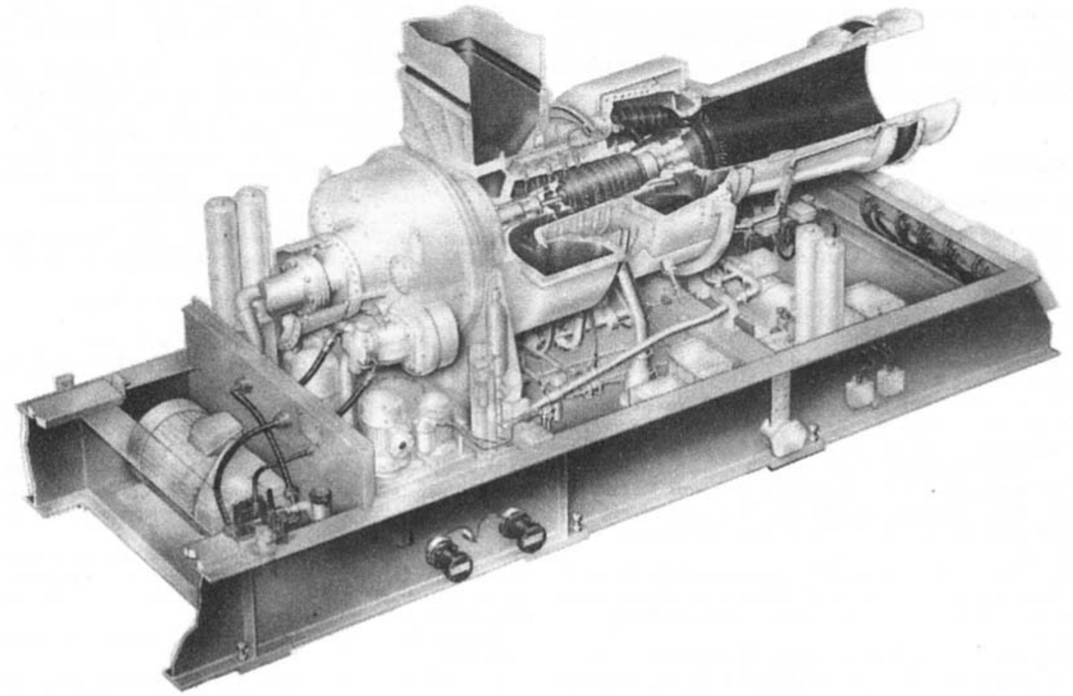

Fig. 30 Typhoon industrial engine

during casting development and with yields approaching 90 percent early in production. The first application of CMSX-4 is for an uncooled HP rotor blade in the Hurricane 1.6 MW(e) gas turbine to replace the γ'/ODS alloy blade previously specified for this application.

For both applications, the blades have been fully validated in development engine testing. This has included strain gauge testing to determine in-engine vibration modes and to establish HCF margins, infra-red pyrometry to measure blading metal temperatures, and a cyclic endurance test to simulate up to three years of cyclic operation in service.

An extensive in-house materials testing program on both materials has been in place to provide the mechanical and physical property data necessary for design, to provide long term creep data, and to carry out corrosion and oxidation testing and coating trials. The latter have confirmed the acceptability of these alloys for long-term industrial gas turbine applications with the selected layered silicon aluminide coating system (Sermalloy 1515).

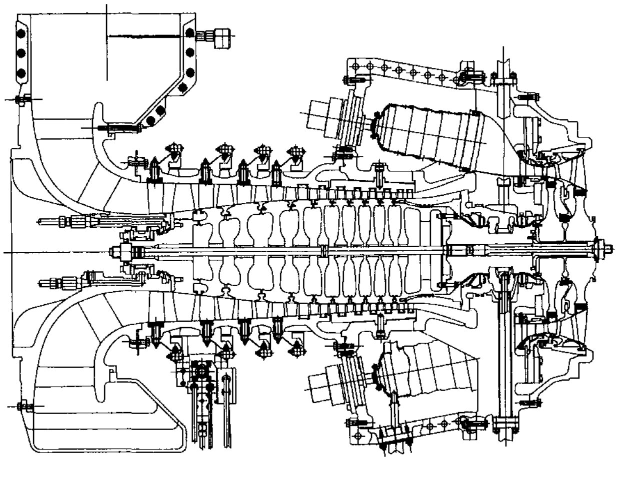

Fig. 31 Typhoon general arrangement

Further applications of these alloys in the EGT product range are currently being pursued.

Summary

The year 1997 is seventy-two years since the discovery of the metallic element Re. Over the last ten years, Re has been successfully and used as a critical strengthening element in cast nickel-base superalloys for single crystal and directionally solidified turbine airfoils.

Fig. 32 Typhoon cooled HP turbine blade DS CM 186 LC alloy

Turbine engine tests and service experience has generally exceeded expectations for the Re containing superalloys. This paper explains these results relating alloy properties to turbine engine component performance for three of the alloys.

Acknowledgments

The authors wish to acknowledge the significant contributions to this work from many personel at RR, Allison, Solar, EGT, SNECMA, CM, Howmet, and PCC (Airfoils).

References

Bachelet, E., and Lamanthe, G., 1986, National Symposium—Single Crystal Superalloys, Viallard-de-Lans, France.

Blavette, D., Caron, P., and Khan, T., *Scripta Met*, Vol. 20, No. 10.

Blavette, D., Caron, P., and Khan, T., "An Atom-Probe Study of Some Fine Scale Microstructural Features in Ni-Base Single Crystal Superalloy," 6th International Symposium, TMS, Warrendale, PA, pp. 305–314.

Brentnall, W. D., Aurrecoechea, J. M., Rimlinger, C. M., Harris, K., Erickson, G. L., Wahl, J. B., 1997, "Extensive Industrial Gas Turbine Experience With Second Generation Single Crystal Alloy Turbine Blades," *ASME (IGTI) Turbo Expo '97*, ASME, NY.

Burkholder, P. S., Thomas, M. C., Frasier, D. J., Whetstone, J. R., Harris, K., Erickson, G. L., Sikkenga, S. L., and Eridon, J. M., 1995, "Allison Engine Testing CMSX-4 Single Crystal Turbine Blades and Vanes," *IOM 3rd International Charles Parsons Turb. Conf. Proc.*,

Caruel, F., Bourguignon, S., Lallement, B., Fargeas, S., DeBussac, A., Harris, K., Erickson, G. L., and Wahl, J. B., 1996, "SNECMA Experience With Cost Effective DS Airfoil Technology Applied Using CM 186 LC™ Alloy," *Turbine Development and Application*, ASME, NY.

Cetel, A. D., and Duhl, D. N., 1992, "Second Generation Columnar Grain Nickel-Base Superalloy," 7th International Symposium, TMS, Warrendale, PA, pp. 287–296.

Cetel, A. D., and Duhl, D. N., 1988, "Second-Generation Nickel-Base Single Crystal Superalloy," 6th International Symposium, TMS, Warrendale, PA, pp. 235–244.

Chen, J. H., and Little, J. A., 1995, unpublished work, Cambridge University, UK.

Doner, M., and Heckler, J. A., 1985, "Effects of Section Thickness and Orientation on the Creep-Rupture Properties of Two Advanced Single Crystal Alloys," *Aerospace Technical Conference*,

Erickson, G. L., 1996, "The Development and Application of CMSX-10," 8th International Symposium, TMS, Warrendale, PA, pp. 35–44.

Ford, D. A., and Arthey, R. P., 1984, "Development of Single Crystal Alloys for Specific Engine Application," 5th International Symposium, TMS, Warrendale, PA, pp. 115–124.

Fullagar, K. P. L., Broomfield, R. W., Hulands, M., Harris, K., Erickson, G. L., and Sikkenga, S. L., 1994, "Aero Engine Test Experience with CMSX-4® Alloy Single Crystal Turbine Blades," 1996, ASME JOURNAL OF ENGINEERING GAS TURBINES AND POWER, Vol. 118, No. 2, pp. 380–388.

Garrett, U.S. Patent #4,935,072.

Gell, M., Duhl, D. N., and Giamei, A. F., 1980, "The Development of Single Crystal Superalloy Turbine Blades," 4th International Symposium, TMS, Warrendale, PA, pp. 205–214.

Gell, M., Duhl, D. N., Gupta, D. K., and Sheffler, K. D., 1987, *JOM*, pp. 11–15.

Giamei, A. F., and Anton, D. L., 1985, "Rhenium Additions to a Ni-Base Superalloy: Effects on Microstructure," *Met Trans A. 16A*, pp. 1997–2005.

Goulette, M. J., Spilling, P. D., and Arthey, R. P., 1984, "Cost Effective Single Crystals," 5th International Symposium, TMS, Warrendale, PA, pp. 167–176.

Harris, K., Erickson, G. L., and Schwer, R. E., 1983, "Development of the Single Crystal Alloys CMSX-2 and CMSX-3 For Advanced Technology Turbines," ASME Paper no. 83-GT-244.

Harris, K., Erickson, G. L., and Schwer, R. E., 1984, "MAR M 247 Derivations—CM 247 LC® DS Alloy, CMSX® Single Crystal Alloys, Properties and Performance," 5th International Symposium, TMS, Warrendale, PA, pp. 221–230.

Harris, K., Erickson, G. L., and Schwer, R. E., 1986, "CMSX Single Crystal, CM DS and Integral Wheel Alloys Properties and Performance," *Cost 50/501 Conf. Liége Proc.*, pp. 709–728.

Harris, K., Erickson, G. L., and Schwer, R. E., Frasier, D. J., and Whetstone, J. R., 1990, "Process and Alloy Optimization for CMSX-4 Superalloy Single Crystal Airfoil," *Cost Conference Liége, Proc. Part II*, pp. 1281–1300.

Harris, K., Erickson, G. L., Sikkenga, S. L., Brentnall, W. D., Aurrecoechea, J. M., and Kubarych, K. G., 1992, "Development of the Rhenium Containing Superalloys CMSX-4 and CM 186 LC For Single Crystal Blade and Directionally Solidified Vane Applications in Advanced Turbine Engines," 7th International Symposium, TMS, Warrendale, PA, pp. 297–306.

Holmes, J. W., et al., and O'Hara, K. S., 1988, "Thermal Fatigue Testing of Coated Monocrystalline Superalloys," *ASTM STP 942*, ASTM, West Conshohocken, PA, pp. 672–691.

Khan, T., and Brun, M., 1989, *Symposium on Single Crystal Alloys*, MTU/SMCT, Munich.

Korinko, P. S., Barber, M. J., and Thomas, M. C., 1996, "Coating Characterization and Evaluation of DS CM 186 LC and SX CMSX-4," *Coatings/Materials Interactions*, ASME, NY.

Kubarych, K. G., and Aurrecoechea, J. M., 1993, "Post Field Test Evaluation of an Advanced Industrial Gas Turbine First Stage Turbine Blade," *TMS/ASM Mat Wk '93 Proc.*, TMS, Warrendale, PA.

Meyer-Olbersleben, F., Rézai-Aria, F., and Goldschmidt, D., 1992, "Investigation of the Thermal Fatigue Behavior of Single Crystal Nickel-Based Superalloys SRR 99 and CMSX-4," 7th International Symposium, TMS, Warrendale, PA, pp. 785–794.

Meyer-Olbersleben, F., Engler-Pinto, Jr., C. C., and Rézai-Aria, F., 1996, "On Thermal Fatigue of Nickel-Based Superalloys," *Thermomechanical Fatigue Behavior of Materials*, 2nd Vol., ASTM STP 1263 M. J. Verrilli and M. G. Castelli, eds., ASTM, West Conshohocken, PA.

Miglietti, W. M., and Pennefather, R. C., 1996, *Coatings/Materials Interactions*, ASME, NY.

Pessah, M., Caron, P. and Khan, T., 1992, "Effect of μ Phase on The Mechanical Properties of a Nickel-Base Single Crystal Superalloy," 7th International Symposium, TMS, Warrendale, PA, pp. 567–576.

Petrov, D. A., and Tumanov, A. T., 1973, "The Use of Single Crystal Blades," *Aircraft Engineering No. 9.*

Pollack, T. M., and Argon, A. S., 1992, *Aeta Metallurgica at Materialia*, Vol. 40, pp. 1.

PW 2037 Engine Display, 1994, Farnborough Air Show (PWA), Pratt & Whitney.

Roan, F., 1996, private communication.

Ross, E. W., and O'Hara, K. S., 1996, "René N4: A First Generation Single Crystal Turbine Airfoil Alloy With Improved Oxidation Resistance, Low Angle Boundary Strength and Superior Long Time Rupture Strength," 8th International Symposium, TMS, Warrendale, PA, pp. 19–25.

Ross, E. W., and O'Hara, K. S., 1992, "René 142: A High Strength, Oxidation Resistant DS Turbine Airfoil Alloy," 7th International Symposium, TMS, Warrendale, PA, pp. 257–265.

Strangman, T. E., et al., 1980, "Development of Exothermically Cast Single Crystal MAR M 247 and Derivative Alloys," 4th International Symposium, TMS, Warrendale, PA, pp. 215–224.

Thomas, M. C., Helmink, R. C., Frasier, D. J., Whetstone, J. R., Harris, K., Erickson, G. L., Sikkenga, S. L., and Eridon J. M., 1994, "Allison Manufacturing, Property and Turbine Engine Performance of CMSX-4 Single Crystal Airfoils," *Cost 501 Conf Proc*, Liége.

Walston, W. S., O'Hara, K. S., Ross, E. W., Pollock, T. M., and Murphy, W. H., 1996, "René N6: Third Generation Single Crystal Superalloy," 8th International Symposium, TMS, Warrendale, PA, pp. 27–34.

Wortmann, J., Wege, R., Harris, K., Erickson, G. L., and Schwer, R. E., 1988, "Low Density Single Crystal Superalloy CMSX-6®," *7th World Conference on Investment Casting Proc.*, Munich.

Wukusick, C. S., and Buchakjian, L., Jr., 1991, "Improved Property—Balanced Nickel-Base Superalloys for Producing Single Crystal Articles," UK Patent Application no. GB 2 235 697 A.

Wukusick, C. S., 1980, Directional Solidification Alloy Development, final report, NAVAIR Contr. N62269-78-C-0315.

Yamazaki, M., et al., 1984, "Alloy Design for High Strength Nickel-Base Single Crystal Alloys," 5th International Symposium, TMS, Warrendale, PA, pp. 157–166.

Yukawa, N., et al., 1988, "High Performance Single Crystal Superalloys Developed By The d-Electrons Concept," 6th International Symposium, TMS, Warrendale, PA, pp. 225–234.

Coating Life Prediction Under Cyclic Oxidation Conditions

K. S. Chan
kchan@swri.org

N. S. Cheruvu

G. R. Leverant

EPRI Materials Center
for Combustion Turbines,
Southwest Research Institute,
6220 Culebra Road,
P. O. Drawer 28510,
San Antonio, TX 78228-0510

The hot gas path section components of land based turbines require materials with superior mechanical properties and good hot corrosion and oxidation resistance. These components are generally coated with either a diffusion coating (aluminide or platinum aluminide) or with an overlay coating (MCrAlY) to provide additional hot corrosion and/or oxidation protection. These coatings degrade due to inward and outward diffusion of elements during service. Outward diffusion of aluminum results in formation of a protective oxide layer on the surface. When the protective oxide spalls, aluminum in the coating diffuses out to reform the oxide layer. Accelerated oxidation and failure of coating occur when the Al content in the coating is insufficient to reform a continuous alumina film. This paper describes development of a coating life prediction model that accounts for both oxidation and oxide spallation under thermal mechanical loading as well as diffusion of elements that dictate the end of useful life. Cyclic oxidation data for aluminide and platinum aluminide coatings were generated to determine model constants. Applications of this model for predicting cyclic oxidation life of coated materials are demonstrated. Work is underway to develop additional material data and to qualify the model for determining actual blade and vane coating refurbishment intervals.

Introduction

Protective coatings in land-based turbines generally fail by oxidation, spallation, and localized corrosion (Nesbitt, 1989). The latter occurs when a continuous protective oxide layer, e.g., alumina, cannot be formed on the coating surface due to the depletion of the oxide-forming element (e.g., Al). The loss of the oxide-forming element from the coating can take place by the following three means: (1) oxidation; (2) spallation; and (3) inward diffusion of the oxide-forming element into the substrate. These degradation mechanisms must be taken into account when considering the failure and the useful life of a coating.

Several attempts have been made (Nesbitt and Heckel, 1984; Lee et al., 1987; Nesbitt, 1989a, 1989b; Nesbitt and Barrett, 1993), with successful results, to predict coating life based on consideration of cyclic oxidation, spallation, and diffusion of oxide-forming elements. Two criteria have been proposed for defining the onset of coating failure: (1) a critical Al content (Nesbitt and Barrett, 1993), and (2) a nonzero volume fraction of the β phase in the aluminide coatings (Lee et al., 1987). These earlier life prediction approaches, however, were based on an empirical spallation model that contains temperature-dependent material constants (Probst and Lowell, 1988; Lowell et al., 1991). Evaluation of these material constants for the temperature of interest for land-based turbine applications could sometimes be difficult. Extrapolation of material constants determined from short time tests performed at higher temperatures to the lower temperatures in field conditions usually lead to uncertain, if not unreliable, lifetime estimates. As a result, there is a need for a more accurate and reliable life prediction model for coatings and coated components.

The objective of this article is to present a new coating life model that is suitable for predicting the useful life of MCrAlY and aluminide coatings. The model includes treatment of oxidation, spallation, and outward and inward diffusion of oxide forming elements. The new mechanism-based model differs from previous models in the treatment of oxide spallation by adapting a fracture mechanics approach that results in explicit relationships between weight of oxide spalled and relevant physical and mechanical properties of the oxide. As a consequence, possible temperature dependence of material parameters is easily defined, and any extrapolation of model constants with temperature, if necessary, can be justified and done with confidence. In addition to the coating life model, experimental data have also been generated to provide input to the model, as well as independent data for verifying the model prediction. For the present investigation, the oxidation, spallation, and lifetime predictions of aluminide and platinum aluminide coatings are considered. Inward diffusion of the oxide-forming element, Al, into the substrate is not considered here because of the lack of diffusivity data for the constituent phases in the coatings.

Experimental Procedure

Material and Coatings. Flat rectangular test specimens (30 × 16 × 1.5 mm) were machined from the root section of a fully heat-treated GTD-111 turbine blade using electro-discharge machining process. The specimens were ground to produce a surface finish of 8–16 RMS. The nominal compositions of GTD-111, aluminide coating, and the PtAl coating are given in Table 1. In the fully heat-treated condition, GTD-111 exhibits a bimodal distribution of primary (cuboidal) and secondary (spherical) gamma prime particles. Both coatings show a microstructure of equiaxed β (NiAl) grains in the as-processed condition.

The specimens were coated with either aluminide or platinum aluminide using a modified low activity cementation process that produces an outward diffusing coating. The outward diffusion coating process is described elsewhere (Shankar, 1988; Smith and Boone, 1990). For application of platinum aluminide coating, the specimens were electroplated with an approximately 10 μm thick layer of platinum prior to a CVD aluminizing treatment. These processes produced nominal coating thicknesses of 33.8 μm and 65 μm, for aluminide and platinum aluminide coatings, respectively.

Cyclic Oxidation Testing. The cyclic oxidation tests were performed in the cyclic oxidation testing facility at SwRI, which consists of a furnace, a forced air cooling system, and a com-

---

Contributed by the International Gas Turbine Institute and presented at the International Gas Turbine & Aeroengine Congress & Exhibition, Orlando, FL, June 2–5, 1997. Manuscript received by the ASME Headquarters March 15, 1997. Paper No. 97-GT-389. Associate Technical Editor: H. A. Kidd.

Table 1 Nominal composition of GTD-111 in weight percent

Material	C	Cr	Co	Mo	W	Pt	Ta	Ti	Al	Zr	Ni
GTD-111	0.10	14	9.5	1.5	3.8	—	2.8	4.9	3.0	0.01	Bal.
Aluminide Coating	—	2.8	7.0	0.4	—	—	2.4	0.7	29.5	—	Bal.
PtAl Coating	—	4.1	5.7	0.3	—	15	2.9	2.0	19.9	—	Bal.

puter controlled moving arm that transfers the coated specimens in and out of the furnace and to the cooling system, and vice versa. During cyclic oxidation tests, the specimens were inserted in the furnace that was maintained at 1065.5°C (1950°F). They were held in the furnace for 55 minutes and then moved to the cooling system and cooled by forced air for five minutes. The specimens took approximately four minutes to reach the test temperature and one minute to cool from the test temperature to room temperature. They were then returned to the furnace, and the thermal cycle was repeated. The cyclic oxidation test was interrupted at specified intervals to weigh the specimens. After 1000 cycles, micro-sections were prepared from aluminide and platinum aluminide coated specimens for metallographic evaluation. The microstructure and coating composition were determined using optical and scanning electron microscopy and energy dispersive spectroscopy (EDS).

Coating Life Model

A recently developed cyclic oxidation model (Chan, 1997) is extended for predicting the cyclic oxidation behavior and the usable life of a coating. The proposed coating life model is basically a computer program, dubbed COATLIFE, that contains a number of subroutines that perform specific functions and describe various degradation mechanisms on a cycle-by-cycle basis. The development of the cyclic oxidation model is described elsewhere (Chan, 1997), while an extension of the model for predicting the usable life of coatings is presented here.

Figure 1 shows a schematic of the cyclic oxidation model and the proposed methodology for predicting the usable life of a coating. The important ingredients in the coating life model are (1) oxidation kinetics, (2) oxide fracture and spallation, (3) overall kinetics of cyclic oxidation and depletion of the oxide-forming element, and (4) a life predicting scheme based on a critical concentration of Al for the formation of a protective oxide layer. A brief description of these essential features of the model is presented in the next four sections.

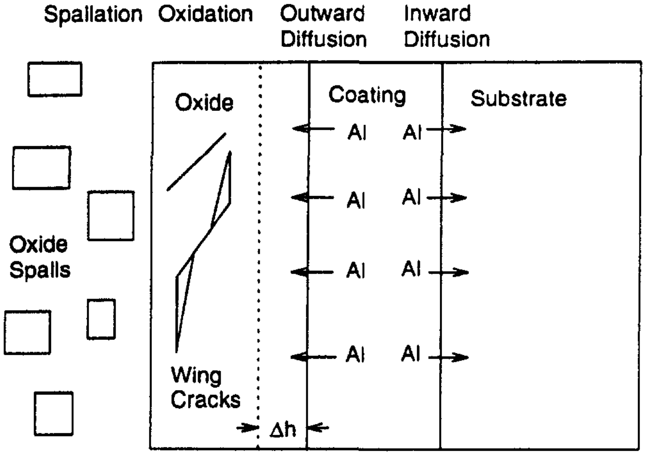

Fig. 1 Schematics of degradation mechanisms treated in the COATLIFE model

1 Oxidation Kinetics. The weight of oxide, W_{ox}, formed during a thermal cycle is modeled using the parabolic growth equation given by

$$W_{ox} = Z\sqrt{k_p t}, \qquad (1)$$

where k_p is the oxidation kinetic constant, t is time of oxidation, and Z is the ratio of the molecular weight of the oxide to the atomic weight of oxygen in the oxide. Equation (1) relates the weight of oxide formed to the weight of oxygen gained by the coating. After spallation occurs at the end of a thermal cycle, the thickness of the oxide is reduced, leading to an increase in the oxidation rate. This increase in the oxidation rate after spallation is modeled by using the concept of an equivalent time introduced by Probst and Lowell (1988). The equivalent time, t_e, for cyclic oxidation corresponds to the time required to form an oxide layer of identical thickness under isothermal conditions. The equivalent time, t_e, is calculated at each cycle based on the cycle time and the current thickness of oxide layer on the coating surface.

2 Spallation. A recent analysis of oxide spallation shows that the weight of oxide spalled, W_s, during a thermal cycle is given by (Chan, 1997)

$$W_s = q\Delta T^2 \left[\frac{W_{ox}}{W_o}\right]^{1+m}, \qquad (2)$$

where

$$q = \frac{\zeta_o W_o \sin^2 2\psi \sin^3 \psi}{\pi}\left[\frac{E_{ox}\Delta\alpha\sqrt{l_o}}{K_{ox}}\right]^2, \qquad (3)$$

is the spallation constant, m is the spallation exponent, and ΔT is the temperature drop. The parameter q in Eq. (2) incorporates material parameters concerning the length (l_o), angle (ψ), and density (ζ_o) of microcracks, the Young's modulus (E_{ox}), fracture toughness (K_{ox}), and the difference in the CTE, $\Delta\alpha$, between the oxide and the coating. The referenced weight, W_o, is arbitrary and can be taken as 1 mg/cm^2 or any other convenient value. Consequently, only the constants q and m need to be evaluated from experimental data if one adopts a phenomenological approach. On the other hand, an explicit relationship between q and other materials properties in Eq. (3) provides valuable insight about the spallation process and the possible dependence of the parameter q on the test temperature. It also allows one to calculate the q parameter if the values for ζ_o, ψ, E_{ox}, $\Delta\alpha$, l_o, and K_{ox} are known. In the present paper, the values for q and m were evaluated from the experimental weight change data.

3 Overall Kinetics of Cyclic Oxidation. The overall kinetics of cyclic oxidation has been modeled as a process that involves the formation and spallation of oxides during thermal cycling. The weight of oxide remained, W_r, on the coating surface after a thermal cycle can be expressed as (Probst and Lowell, 1988; Lowell et al., 1991)

$$W_r = W_{ox} - W_s, \qquad (4)$$

where W_{ox} and W_s are given by Eqs. (1) and (2), respectively. Expressions for the cumulative weight change, total weight of oxide spalled, and the weight of aluminum loss have been formulated as a function of number of thermal cycles. The expression for the cumulative weight change per unit area, W_c, after n thermal cycles is (Probst and Lowell, 1988; Lowell et al., 1991)

$$W_c(n) = (1/Z)W_r(n) - (1 - 1/Z)\,\left(\sum_{1}^{n} W_s(n)\right), \qquad (5)$$

while the cumulative metal loss, W_m, of the oxide-forming element from the coating due to oxidation and spallation is given by (Probst and Lowell, 1988; Lowell et al., 1991)

$$W_m(n) = (1 - 1/Z)\,\left[W_r(n) + \sum_{1}^{n} W_s(n)\right] \qquad (6)$$

for the nth cycle. The parameters of W_{ox}, W_r, W_s, W_c, W_m, t_e, and weight gain, W_g, are calculated for each of the thermal cycles.

4 Life Prediction Methodology. The loss of the oxide-forming element from the coating, which is aluminum for the systems considered here, can occur by two routes. One is by outward diffusion of Al to form an oxide scale that spalls either partly or wholly during thermal cycling, while the other is by inward diffusion into the substrate. When inward diffusion of Al into the substrate is absent or sluggish compared to outward diffusion, the surface recession and the aluminum content in the coating at the nth cycle are calculated on the basis of a flux and mass balance of Al loss caused by oxidation and spallation. The volume fraction of the β phase (NiAl), $V_\beta(n)$, in the coating at the nth cycle is calculated using the lever rule and is given by

$$V_\beta = 1 \quad \text{for} \quad X_{\text{Al}} \geq X_{\text{Al}}^{\beta} \qquad (7)$$

and

$$V_\beta(n) = \frac{X_{\text{Al}}(n) - X_{\text{Al}}^{*}}{X_{\text{Al}}^{\beta} - X_{\text{Al}}^{*}} \quad \text{for} \quad X_{\text{Al}}^{\beta} \geq X_{\text{Al}}(n) \geq X_{\text{Al}}^{*} \qquad (8)$$

where X_{Al}^{β} is the aluminum content in the β phase at the $\beta/(\gamma' + \beta)$ phase boundary, and X_{Al}^{*} is the aluminum content in the γ' phase at the $(\gamma' + \beta)/\gamma'$ phase boundary.

The remaining life, RL, is defined based on the assumption that the useful life of the coating is zero when the volume fraction of the β phase is zero, leading to

$$RL = \frac{X_{\text{Al}}(n) - X_{\text{Al}}^{*}}{X_{\text{Al}}(0) - X_{\text{Al}}^{*}} \quad \text{for} \quad X_{\text{Al}}(0) \geq X_{\text{Al}}(n) \geq X_{\text{Al}}^{*}, \qquad (9)$$

which gives a remaining life of unity when $X_{\text{Al}}(n) = X_{\text{Al}}(0)$ but a zero remaining life when $X_{\text{Al}}(n) \leq X_{\text{Al}}^{*}$.

Comparison of Model Prediction and Experimental Data

There are three material constants in the coating life model that are evaluated from the experimental data. They are the oxidation kinetic constants, k_p, the spallation constant, q, and the spallation exponent, m. Other material input includes the coating thickness, h, the aluminum content of β, X_{Al}^{β}, at the $\beta/(\gamma' + \beta)$ phase boundary, and the aluminum content of γ', X_{Al}^{*}, at the $(\gamma' + \beta)/\gamma'$ phase boundary. The value of k_p was determined from the weight change data for short time prior to the maximum in the weight change versus time curve using Eq. (1) by assuming that spallation was negligible within this time frame. The initial values for q and m were determined using the procedures described elsewhere (Chan, 1997). These values were then further refined by comparison of model calculation and experimental data until good agreement was obtained. The values for X_{Al}^{β} and X_{Al}^{*} were determined by performing EDS on individual phases. A summary of the material constants for the aluminide and Pt-modified aluminide coatings is presented in Table 2. For all calculations presented in this paper, inward diffusion of Al into the substrate was ignored because of the lack of diffusivity data for the β and γ' phases.

Figure 2 presents the experimental and calculated weight change curves for the GTD-111 alloy coated with aluminide and PtAl coatings. These experimental data were used to obtain the material constants in the oxidation kinetics and spallation equations. In both cases, the model reproduced the experimental weight change curves fairly accurately.

In addition to weight change, the model also computed the values for the weight gain, W_g, weight of oxide remaining, W_r, on the surface, weight of oxide spalled, W_s, and weight of metal (Al) loss, W_m, from the coating. Figure 3 presents the results for the PtAl coated specimen as a function of number of thermal cycles. The calculated results indicated that a steady-state condition occurred at about 500 cycles, where W_g and W_r remained constant, while W_s and W_m increased and W_c decreased at essentially constant rates. The steady-state condition occurs when the rate of oxidation equals the rate of spallation during a thermal cycle. Under this circumstance, the rate of Al loss from the coating also equals the spallation rate.

The Al contents in the aluminide and PtAl coatings are presented as a function of thermal cycles in Fig. 4. For the aluminide coating, the model predicted an Al content of 23 percent after 1000 cycles, compared to 21 percent observed experimentally. The calculated Al content for the PtAl coating, after 1000 cycles, is 35.6 percent, compared to a measured value of 30.3 percent. The aluminide coating exhibited a higher Al loss than the PtAl coating because of faster oxidation and spallation kinetics, due to a higher k_p value. Despite a slightly higher value for the spallation constant, q, the PtAl coating manifested less spallation because the amount of oxide spalled per cycle increases linearly with q, but increases nonlinearly according to a power-law on the weight of oxide formed.

The calculated coating thickness is compared against experimental measurement in Fig. 5. The initial thickness of the aluminide coating was 33.8 μm and it decreased to about 24 μm after 1000 cycles. In contrast, the PtAl coating decreased from 65 μm to 61 μm after the same number of cycles. The smaller surface recession in the PtAl coating was the result of a larger initial coating thickness and a lower Al loss. These are substantial variations in the experimental value of the coating thickness. The average values of the measured thickness are in good agreement with the model predictions.

Figure 6 presents the calculated and measured volume percents of the β phase for the aluminide and PtAl coating, respectively. Because of Al loss, the aluminide coating started to lose

Table 2 Material parameters for aluminide and Pt-modified aluminide coatings

Coating	Thickness, μm	k_p(mg^2/cm^4/h)	q, mg/cm^2/°C^2	m	X_{Al}^{β} (at. %)	X_{Al}^{*} (at. %)
Aluminide	33.8	1.6x10^{-3}	1.2x10^{-9}	2.63	34	19
Pt-Modified Aluminide	65	1.0x10^{-3}	2.0x10^{-9}	2.0	34	19

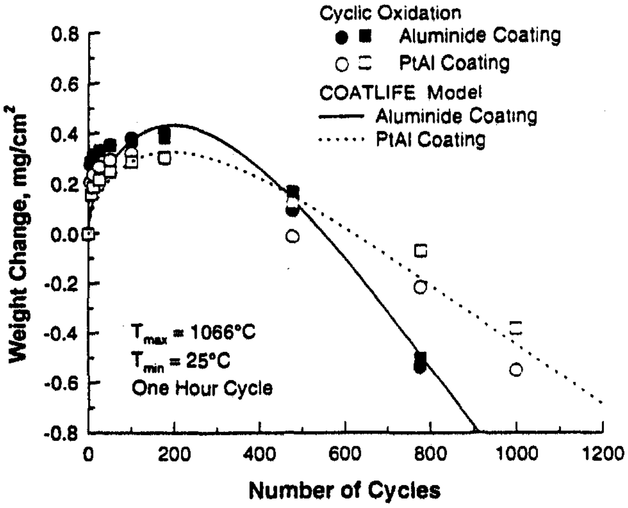

Fig. 2 Experimental weight change data compared against model calculation for coated GTD-111

β phase and to show the presence of γ' after 400 thermal cycles. The depletion of β phase was complete at about 1150 cycles where the Al content fell below 19 percent, Fig. 6. The calculated volume fraction of β phase was 27.7 percent after 1000 cycles, compared to 12 percent observed experimentally. In comparison, the PtAl coating was able to maintain a β microstructure up to 2000 cycles. A complete depletion of β phase did not occur until after 4220 cycles, at an Al content of 19 percent, Fig. 6. The amount of β phase measured was 76 percent after 1000 cycles, compared to 100 percent in the prediction.

The predicted remaining life is presented as a function of thermal cycles in Fig. 7. The predicted coating lives are 1150 and 4220 cycles for the aluminide and PtAl coatings, respectively. The relationship between remaining life and number of cycles is a nonlinear one. As a result, any linear extrapolation of experimental data or model calculation at short times (small number of cycles) to long times (large number of cycles) is likely to yield unreliable lifetime estimates. The PtAl coating is predicted to have a longer life than the aluminide coating because of the lower oxidation and spallation kinetics and a larger thickness in the PtAl coating.

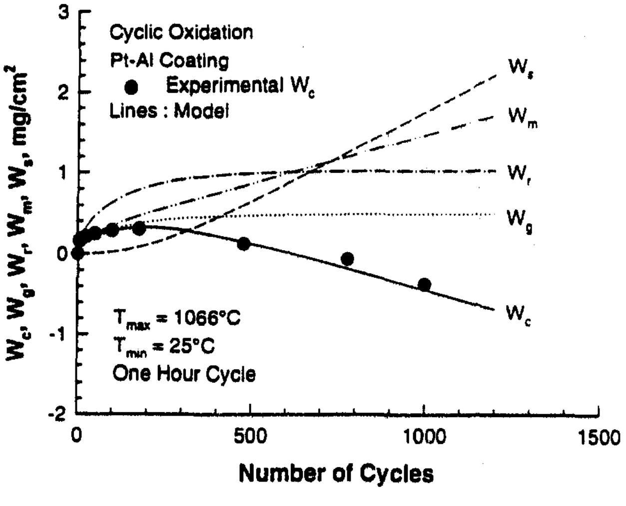

Fig. 3 Calculated results for weight gain (W_g), weight of oxide remained (W_r) on the coating surface, weight of oxide spalled (W_s), and weight of Al loss (W_m) from the coating compared against the calculated and experimental weight change data for the Pt-modified aluminide coating

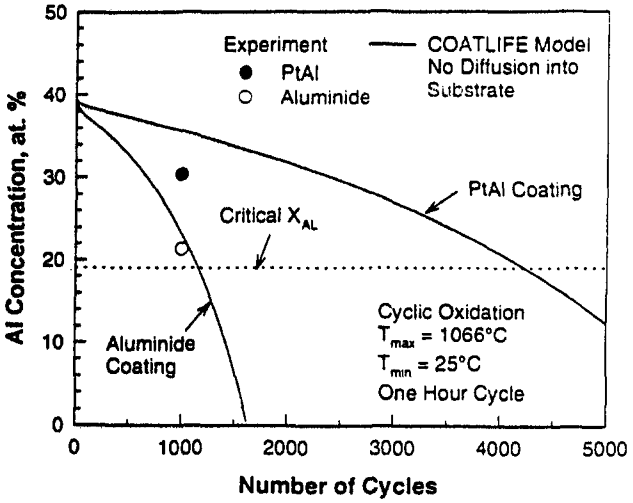

Fig. 4 Comparison of predicted and observed Al content as a function of thermal cycles

Discussion

The useable life of an aluminide coating relies on the presence of a sufficient amount of aluminum in the coating to form a protective alumina film that reduces the rate of oxidation. The life of a coating can be considered to be exhausted when the aluminum content in the coating is insufficient to form a continuous oxide film so that accelerated oxidation occurs at the uncovered substrate. There are three possible sources of aluminum loss from an aluminide coating, which are (1) outward diffusion of Al to the oxide film, (2) oxide spallation, and (3) inward diffusion of Al to the substrate.

Comparison of model prediction against experimental data indicates that the model overpredicted the Al content by 2 percent for the aluminide coating and about 5 percent for the PtAl coating. The accuracy of Al content determined by the EDS technique was ±2 percent. Thus, the agreement was well within the experimental scatter for the aluminide coating, but not for the PtAl coating. The discrepancy might be attributed to Al loss due to inward diffusion to the substrate, which was not included in the current model calculation. The discrepancy observed in the amount of β phase in the PtAl coating might be caused by the use of the lever rule for a binary system, instead of that for a ternary system. The approximation was necessary because of the lack of a ternary phase diagram for the Pt-Ni-Al system.

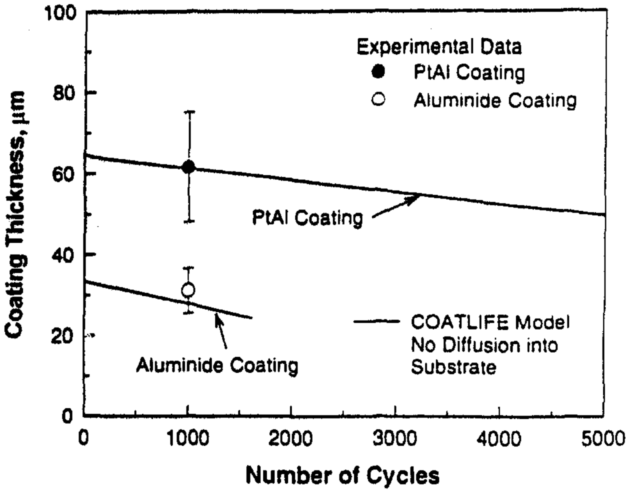

Fig. 5 Calculated and measured values of the coating thickness as a function of thermal cycles

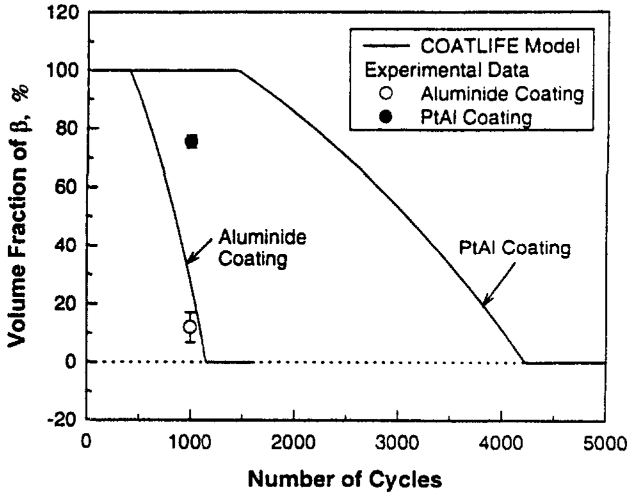

Fig. 6 Predicted volume percent of β compared against experimental data

Indirect evidence of inward diffusion of Al into the substrate is provided in Fig. 8(*a*) and (*b*) for aluminide and PtAl coatings, respectively. In both cases, the coating has a $\beta + \gamma'$ microstructure while the neighboring area containing distributed finger-like particles is the interdiffusion zone. Compared with the as-coated material, the interdiffusion zone had grown and the particles within it had coarsened. The Al content within the interdiffusion zone was also higher than the substrate. EDS analyses of the substrate showed a slight increase in Al content from 4 percent to 6.5 percent after cyclic oxidation.

This result suggested that the slight overprediction of Al content in the coating by the model is the consequence of not treating the inward diffusion of Al into the substrate. Conversely, the fairly good agreement obtained between the model and experimental data indicates that the main degradation mechanisms in the coating are oxidation and spallation. The error introduced by ignoring inward diffusion is small for the aluminide coating, but is somewhat larger for the PtAl coating. An improvement in the lifetime prediction requires taking into account the Al loss due to inward diffusion.

The proposed model is still in the developmental stage. Many aspects of coating degradation mechanisms have not been incorporated (e.g., effects of microstructure, substrate, reactive elements, etc.) nor discussed because of the lack of space. Although further improvements are required, the model nevertheless provides a framework from which quantitative predictions of coating lives of laboratory specimens can be made. Work is currently underway to generate additional material data, to develop new techniques for determining local temperatures at blades and vanes, and to qualify the model for determining actual blade and vane coating refurbishment intervals.

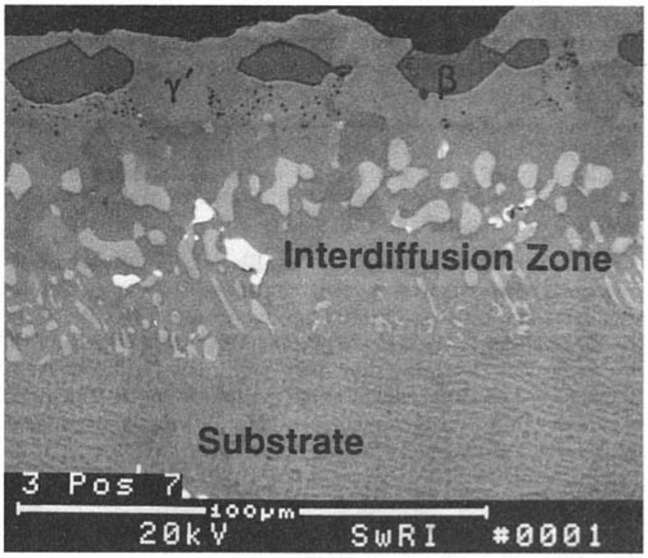

(a) Aluminide Coating

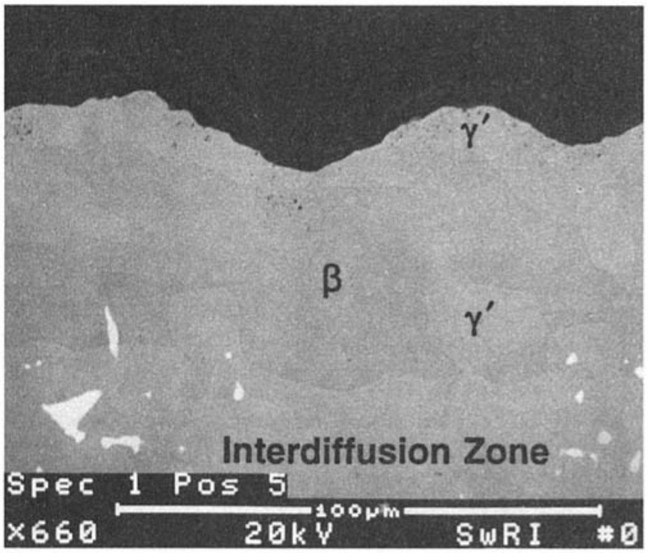

(b) PtAl Coating

Fig. 8 Microstructures of the coating and the interdiffusion zone after 1000 cycles

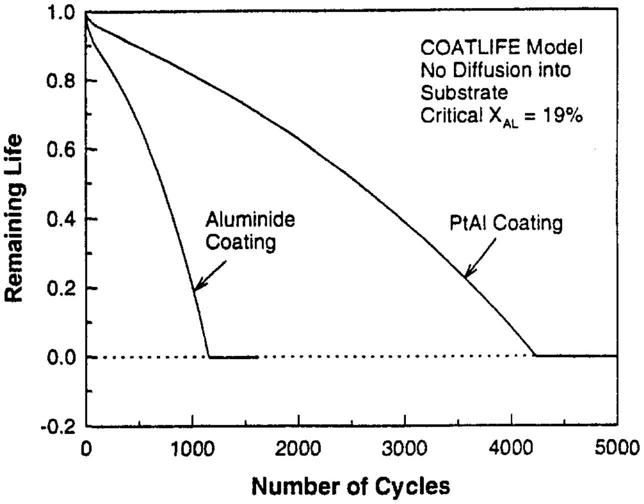

Fig. 7 Remaining lives predicted for aluminide and PtAl coatings

Conclusions

1 A life prediction model has been developed for certain coatings used for land based gas turbines. The coating life model is capable of representing the oxidation, spallation, and failure of aluminide and PtAl coatings.

2 The lifetimes of aluminide coatings can be predicted based on a critical Al content that corresponds to the minimum Al content below which the volume fraction of the β phase becomes zero.

3 Both oxidation and spallation are modeled accurately by the coating life model. The main degradation mechanisms in the aluminide coatings are oxidation and spallation.

4 The predicted Al content, volume fraction of the β phase, and the coating recession are in reasonable agreement with the experimental data. The model predictions of Al content tend to be on the high side because inward diffusion of Al into the substrate was not included in these calculations. Further improvement in the accuracy of the coating life prediction requires consideration of inward diffusion of Al into the substrate.

Acknowledgments

This work was supported by the Electric Power Research Institute's Materials Center for Combustion Turbines at Southwest Research Institute (SwRI) through Contract No. RP3643-01, Dr. George H. Quentin, Program Manager. Discussion of this work with Dr. Henry Bernstein, SwRI, and Dr. James Nesbitt, NASA-Lewis Research Center, is acknowledged. The technical assistance by Ms. Fawn Cobia and the clerical assistance by Ms. Patty Soriano, SwRI, are appreciated.

References

Chan, K. S., 1997, "A Mechanics-Based Approach to Cyclic Oxidation," *Met. Mat. Transactions A,* Vol. 28A, pp. 411–422.

Lee, E. Y., Charter, D. M., Biederman, R. R., and Sisson, Jr., R. D., 1987, "Modeling the Microstructural Evolution and Degradation of M-Cr-Al-Y Coatings During High Temperature Oxidation," *Surface and Coatings Technology,* Vol. 32, pp. 19–39.

Lowell, C. E., Barrett, C. A., Palmer, R. W., Auping, J. V., and Probst, H. B., 1991, "COSP: A Computer Model of Cyclic Oxidation," *Oxidation of Metals,* Vol. 36, No. 1/2, pp. 81–112.

Nesbitt, J. A., 1989, "Diffusional Aspects of the High-Temperature Oxidation of Protective Coatings," *Diffusion Analysis & Applications,* A. D. Romig, Jr., and M. A. Dayananda, eds., TMS, Warrendale, PA, pp. 307–324.

Nesbitt, J. A., 1989, "Predicting Minimum Aluminum Concentrations for Protective Scale Formation on Ni-base Alloys," *Journal of Electrochemical Society,* Vol. 136, pp. 1518–1527.

Nesbitt, J. A., and Barrett, C. A., 1993, "Predicting the Oxidation-Limited Lifetime of β NiAl," *Structural Intermetallics,* R. Darolia, J. J. Lewandowski, C. T. Liu, P. L. Martin, D. B. Miracle, and M. V. Nathal, eds., TMS, Warrendale, PA, pp. 601–609.

Nesbitt, J. A., and Heckel, R. W., 1984, "Modeling Degradation and Failure of Ni-Cr-Al Overlay Coatings," *Thin Solid Films,* Vol. 119, pp. 281–290.

Probst, H. B., and Lowell, C. E., 1988, "Computer Simulation of Cyclic Oxidation," *Journal of Metals,* Vol. 40, No. 10, pp. 18–21.

Shankar, S., 1985, Methods of Forming Protective Diffusion Layer on Nickel Cobalt and Iron Base Alloys, U.S. Patent No. 4,525,814.

Smith, J. S., and Boone, D. H., 1990, "Platinum Modified Aluminides-Present Status," presented at ASME International Gas Turbine and Aero Engine Congress and Exposition, Paper No. 90-GT-319, June 11–14, Brussels, Belgium.

K. T. Millsaps

G. L. Reed

Marine Propulsion Laboratory,
Department of Mechanical Engineering,
Naval Postgraduate School,
Monterey, CA 93943

Reducing Lateral Vibrations of a Rotor Passing Through Critical Speeds by Acceleration Scheduling

A method is presented for reducing the lateral response of an imbalanced rotor accelerating or decelerating through its first lateral bending critical speed by using a variable acceleration rate. A lumped parameter model along with a numerical integration scheme is used to simulate the response of a simply supported, single disk rotor during fast acceleration and deceleration through critical speed. The results indicate that the maximum response and/or the total vibrational energy of a rotor passing through the critical speed can be reduced significantly by using a variable acceleration schedule. That is, reducing the acceleration rate after the nominal critical speed is passed. These predictions were verified experimentally for a single disk rotor.

1 Introduction

Rotating machines are designed to avoid resonance by operating either below or above the first lateral bending critical speed. These are referred to as subcritical and supercritical operation, respectively. There are several advantages to supercritical designs including reduced system weight and cost. However, there is a problem in that the rotor must pass through one or more critical speeds (resonances) when being started and again when coming to rest.

Large amplitude lateral vibrations occurring during these transitions can cause tip rubs of airfoils and seals in turbomachines as well as increased bearing reactions. In order to avoid damage due to rubbing, nominal tip clearances are specified well in excess of those necessary for steady-state supercritical operation. This degrades a turbomachines aerodynamic performance. In particular, larger clearances create lower efficiencies for both turbines and compressors and lower the stall margin in compressors. Therefore, methods to reduce vibrations during transition through critical speeds can offer substantial benefits.

The first published analysis of an oscillator accelerating through resonance was due to Lewis [1] in 1932. While this single degree of freedom, constant amplitude forcing model approximates the behavior of a rotor; the real force due to an imbalance scales quadratically with rotor speed. Analytical solutions were obtained in terms of Fresnel integrals, and solutions were given for various constant acceleration rates and damping levels. These classical results qualitatively predict the observed behavior of an accelerating or decelerating rotor. The maximum amplitude for a quickly accelerating or decelerating rotor is significantly smaller than the corresponding steady-state response near resonance. Furthermore, there is a shift in the instantaneous speed at which the maximum vibration amplitude occurs. This apparent shift in the critical speed occurs at a higher speed for accelerating rotors and lower one for decelerating rotors.

Pöschl [2] and Baker [3] obtained similar results to those of Lewis. Meuser and Weibul [4] extended the analysis to include a cubic nonlinear spring in the system, and McCann and Bennett [5] analyzed a multi-degree-of-freedom system subject to a constant acceleration. Fearn and Millsaps [7] obtained asymptotic approximations for the maximum amplitude and the time at which it occurs for a rotor with constant acceleration or deceleration. Gluse [8] provided an analysis which predicted when a system will fail to accelerate through critical speed due to the back torque of the whirling rotor. Finally, Ishida et al. [9] investigated the stability of a rotor with a nonlinear spring characteristic accelerating through critical speed at a constant rate.

Filippov [13] provided analytical solutions for single degree of freedom oscillator systems, in terms of indefinite integrals, for several acceleration schedules. The cases treated include constant acceleration and deceleration, as well as linearly and quadratically increasing and decreasing angular accelerations.

To the best knowledge of the authors, no analysis nor experimental results for the case of a rotor accelerating at a nonconstant rate appears in the open literature.

Current industry practice is to accelerate a rotor at a constant rate as quickly as possible through critical speed, therefore reducing the time during which the rotor is near its natural frequency, hence reducing the energy input into the lateral mode. High levels of damping are used to dissipate the energy of the vibration. This elevated damping level can be in excess of what is optimum for the design supercritical operation.

This paper presents an analysis of the lateral response of a simple rotor to variable acceleration. It was discovered that scheduling the acceleration through critical can reduce the maximum amplitude and total energy of the lateral vibrations. Preliminary experimental results on a simple, single disk rotor verified the model predictions.

2 Analytical Model

An analytical model for a rotor accelerating at an arbitrary rate was developed. It is a linear, two-degree-of-freedom, lumped mass-spring-damper model with both direct and cross stiffnesses and damping, as shown in Fig. 1.

The equivalent modal properties obtained for the disk, shaft and bearings are used for mass (M), stiffness (K_{ij}), and damping (C_{ij}). The system properties are assumed to be independent of rotor speed. The variable amplitude and frequency forcing due to the small eccentric mass imbalance, m, is lo-

---

Contributed by the International Gas Turbine Institute and presented at the International Gas Turbine & Aeroengine Congress & Exhibition, Orlando, FL, June 2–5, 1997. Manuscript received by the ASME Headquarters March 7, 1997. Paper No. 97-GT-234. Associate Technical Editor: H. A. Kidd.

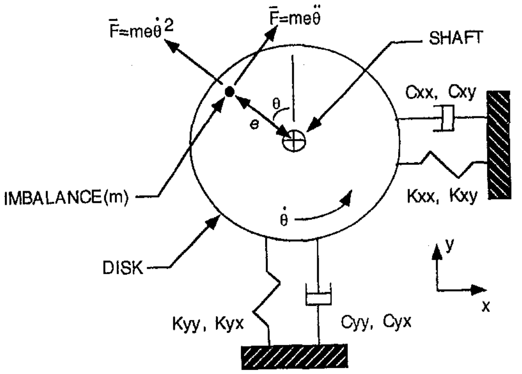

Fig. 1 Two-degree-of-freedom lumped mass and stiffness model of rotating shaft and disk assembly with direct and cross-coupled linear stiffness and damping

cated a distance e away from the rotational center. The rotor starts from rest at $\theta = 0$ at $t = 0$, and has an instantaneous speed and acceleration of $\dot{\theta}$ and $\ddot{\theta}$, respectively. Summing the forces in the x and y-directions yields the following equations of motion:

$$\begin{bmatrix} M & 0 \\ 0 & M \end{bmatrix}\begin{Bmatrix} \ddot{x} \\ \ddot{y} \end{Bmatrix} + \begin{bmatrix} C_{xx} & C_{xy} \\ C_{yx} & C_{yy} \end{bmatrix}\begin{Bmatrix} \dot{x} \\ \dot{y} \end{Bmatrix} + \begin{bmatrix} K_{xx} & K_{xy} \\ K_{yx} & K_{yy} \end{bmatrix}\begin{Bmatrix} x \\ y \end{Bmatrix}$$
$$= me\begin{Bmatrix} \ddot{\theta}\cos\theta - \dot{\theta}^2\sin\theta \\ \ddot{\theta}\sin\theta + \dot{\theta}^2\cos\theta \end{Bmatrix}. \quad (1)$$

This system can be rewritten in terms of a set of four first order equations as

$$\dot{x}_2 = \left(\frac{me}{M}\right)(\ddot{\theta}\cos\theta - \dot{\theta}^2\sin\theta) - \left(\frac{C_{xx}}{M}\right)x_2 - \left(\frac{C_{xy}}{M}\right)y_2 - \left(\frac{K_{xx}}{M}\right)x_1 - \left(\frac{K_{xy}}{M}\right)y_1, \quad (2)$$

$$\dot{x}_1 = x_2, \quad (3)$$

$$\dot{y}_2 = \left(\frac{me}{M}\right)(\ddot{\theta}\sin\theta + \dot{\theta}^2\cos\theta) - \left(\frac{C_{yy}}{M}\right)y_2 - \left(\frac{C_{yx}}{M}\right)x_2 - \left(\frac{K_{yy}}{M}\right)y_1 - \left(\frac{K_{yx}}{M}\right)x_1, \quad (4)$$

and

$$\dot{y}_1 = y_2. \quad (5)$$

A fourth order Runge-Kutta scheme was used to numerically integrate these equations to find the rotor displacements, $x(t)$ and $y(t)$. The initial conditions for the time marching can be taken either with the rotor at rest or from some arbitrary rotational speed, $\omega = \dot{\theta}$. Since these are linear, constant coefficient equations, the solution for the rotor displacements, $\vec{x}$, can be written in integral form as

$$\vec{x} = \int_0^t h^*(t-\tau)\vec{f}(\tau)d\tau, \quad (6)$$

where $\vec{x}$ is the solution vector, h^* is the system transfer function, and $\vec{f}$ is the unbalance forcing. This type of solution is useful when optimizing the acceleration schedule for minimum response.

For steady-state response, the model can be reduced to a single-degree-of-freedom (radial) system. However, for an accelerating rotor, both radial and tangential components are necessary.

This model uses a prescribed angular position as a function of time for the disk. If instead, a prescribed torque schedule is imposed, a third equation is necessary. This type of model would be necessary if the driving torque were not sufficient to "enforce" a prescribed position (velocity, acceleration) schedule. In fact, as shown by Gluse [8], it may not be possible to accelerate through critical speed with a small torque and a large mass eccentricity due to the "back-torque" resulting from the shaft's lateral motion.

3 Model Validation

The model and solution procedure were verified against the analytical results of Lewis [1] and by comparing the results obtained for a very low acceleration rate to steady-state results. To compare with Lewis, the forcing, $f(t)$, is given by

$$f(t) = P\cos(\pi h t^2 + \phi), \quad (7)$$

where P is the magnitude (constant) of the forcing function, h is the acceleration of the system in cycles per second per second, and ϕ is the initial phase angle of the exciting force. The number of free vibrations the system would make from time zero to t is denoted by r. The nondimensional acceleration rate, q, is given by

$$q = \frac{\omega_n^2}{h}, \quad (8)$$

where ω_n is the natural frequency of the system, and h is the acceleration. The term q can also be stated as the value of r at which the instantaneous frequency of the exciting force is equal

Nomenclature

C_{xx}, C_{yy} = modal direct damping (Ns/m)
C_{xy}, C_{yx} = modal cross damping (Ns/m)
E_t = kintic energy of lateral motion (J)
e = radial location of eccentric mass (m)
h = shaft acceleration rate (rads/s2)
h^* = impulse response function
I_{zz} = polar moment of inertia (m^4)
$i = \sqrt{-1}$
K = stiffness (N/m)
K_{xx}, K_{yy} = modal direct stiffness (N/m)
K_{xy}, K_{yx} = modal cross stiffness (N/m)
M = modal mass of the disk (kg)
m = eccentric mass (kg)
P = amplitude of Force (N)
P_{in} = power input to rotor disk (w)
$q = \omega_n^2/h$ = nondimensional acceleration [1]
$R = Kx/P$ = nondimensional amplitude [1]
$\bar{R} = \sqrt{x^2 + y^2}$ = amplitude of rotor vibration (m)
T = applied torque (Nm)
t = time (s)
x, y = orthogonal shaft displacements (m)
$\theta(t)$ = angle of eccentric mass (rads)
$\dot{\theta} = \omega$ = angular velocity (rads/s)
$\ddot{\theta}$ = instantaneous shaft acceleration (rads/s2)
ϕ = initial phase angle (rads.)
ω_n = natural bending frequency (rads/s)
ζ = damping ratio [1]

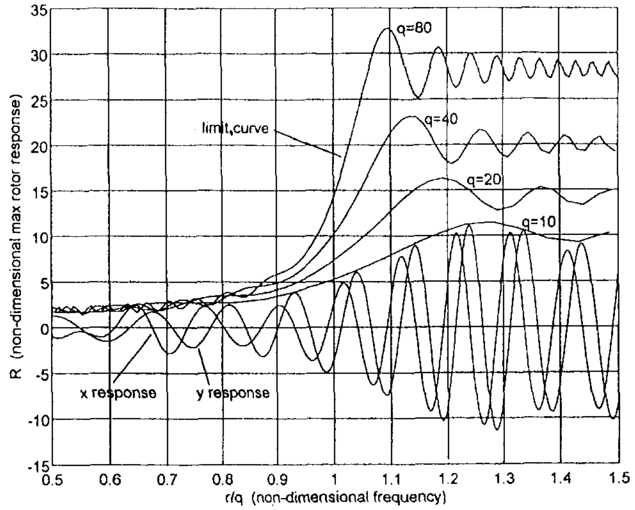

Fig. 2 Nondimensional amplitudes, $x(t)$ and $y(t)$, are shown for $q = 10$ along with the maximum radial response, R, for zero damping. Also shown are limit curves for several lower values of q, which correspond to higher acceleration rates.

to the natural frequency of the system. A lower value of q implies a faster acceleration—fewer cycles to get to critical. The nondimensional frequency is r/q and is equal to unity at the natural frequency. The nondimensional amplitude, R, is given by

$$R = \frac{Kx}{P}, \tag{9}$$

where x is the displacement, K is the system stiffness, and P is the magnitude of the forcing function. The results obtained by the model match very closely (to within 0.2 percent) with the solution of Lewis.

Figure 2 shows results from the model for zero damping. A plot of the $x(t)$ and $y(t)$ displacements of a rotor accelerating quickly through critical ($q = 10$) are shown along with the limit curve (radial displacement) for this case. The limit curves for slower acceleration (higher q) are also shown.

4 Model Predictions: Acceleration Scheduling

4.1 Constant Acceleration and Deceleration. For simplicity, symmetric stiffness and damping coefficients and no cross terms will be used in the predictions in this section. The parameters used in the calculations to be presented, which are given in Table 1, are nominally equal to the experimental facility's modal properties.

Table 1 Rotor kit specifications and modal properties used in calculations

Total length of shaft	45.7 cm (18 in)
Size of disk	7.62 dia × 2.45 cm
Distance between bearings	35.6 cm
Mass of disk	0.8090 kg
Diameter of shaft	0.9525 cm (0.375 in)
Disk Position (Centered)	17.8 cm
Shaft material	4140 LAHS Steel.
Length of bearing	0.6350 cm
Nominal bearing clearance	0.00254 cm
Bearing type	Plain oilyte bronze
$C_{xx} = C_{yy}$	7.087 N-s/m (0.04 lbf-s/in) ($\zeta = 0.0115$)
$K_{xx} = K_{yy}$ (used in section 4)	87,700 N/m (495 lb$_f$/in)
K_{xx} (used in section 5)	87,700 N/m (495 lb$_f$/in)
K_{yy} (used in section 5)	89,500 N/m (505 lb$_f$/in)
Modal Mass, M	1.0807 kg (2.383 lb$_m$)
m	0.00100 kg (0.0353 oz)
e	0.0305 m (1.200 in)

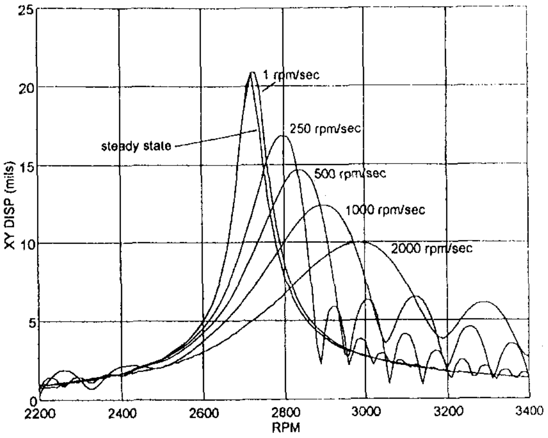

Fig. 3 Radial amplitude of vibration for a rotor with several acceleration rates. The characteristics of the rotor are given in Table 1.

The model was used to predict the vibration amplitude of the rotor as a function of time, $\bar{R}(t)$, which is given by

$$\bar{R}(t) = \sqrt{x^2(t) + y^2(t)}, \tag{10}$$

where $x(t)$ and $y(t)$ are the instantaneous orthogonal displacements. Figure 3 gives predictions from the model for acceleration rates of 0 (steady state), 1, 250, 500, 1000, and 2000 rpm/s, respectively. The amplitude is reduced by approximately 50 percent for the highest acceleration case from the steady-state solution, and there is a shift from about 2700 rpm to about 3000 rpm of the apparent critical speed. The same generic behavior occurs for the case of a decelerating rotor, as shown in Fig. 4. However, the apparent critical moves to a lower speed.

Figure 5 shows predictions for a constant acceleration rate with various levels of damping. With no damping, the vibrational energy that is put into the rotor during the time when the rotor was near the natural frequency is "locked in" since there is no way to dissipate it. These are, essentially, free vibrations in the way that even if the forcing were stopped, they would persist. The oscillation period is close to the undamped natural period of the rotor. When damping is present, the vibrational energy is quickly dissipated once the speed is sufficiently far from the critical speed.

4.2 Nonconstant Acceleration and Acceleration Scheduling. One striking feature of the curves shown in Figs. 3 and 4, is that the amplitude for the cases with fast acceleration is lower than the slower ones near the rotor's natural frequency.

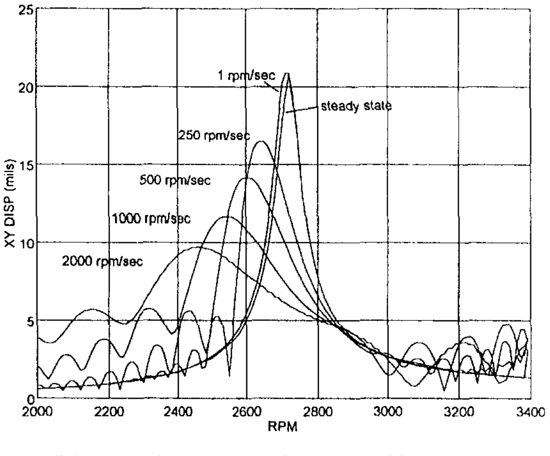

Fig. 4 Radial amplitude of vibration for a rotor with several deceleration rates. The characteristics of the rotor are given in Table 1.

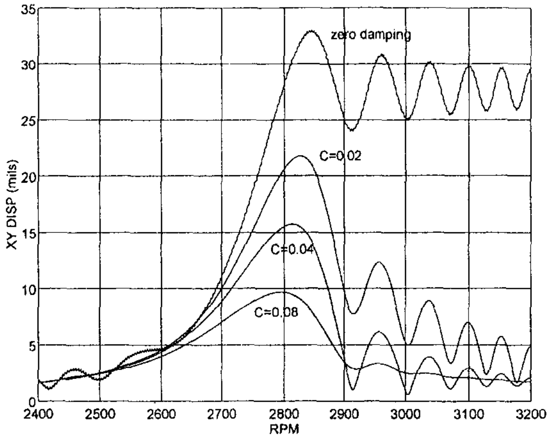

Fig. 5 Effect of damping on the ring down of energy stored in the rotor while passing through critical. The acceleration rate is 360 rpm/s (q = 338).

However, at higher speeds, the steady-state response is actually lower than the fast acceleration curves.

This leads to the possibility that a variable acceleration, with an initial high acceleration followed by a reduced acceleration, may yield a lower peak response as well as a reduced total vibrational energy. This concept of acceleration scheduling is illustrated in Fig. 6. A high acceleration rate is applied to the rotor until some instantaneous angular velocity past the natural frequency. Then, the acceleration rate is reduced to a much lower rate, and the response follows the lower response curve out to the steady-state response.

This is the simplest form of acceleration scheduling, with a simple step change in angular acceleration. Presumably, even better schedules can be obtained by prescribing an optimum schedule as a function of time, or more precisely the rotor phase.

The model was used to investigate the effectiveness of acceleration scheduling. It was found that this method can reduce the maximum amplitude and the total lateral vibrational energy. Trial and error was used with a simple step change in $\ddot{\theta}$. The maximum acceleration was fixed at h = 2000 rpm/s (q = 62), and the equations were integrated past the normal resonance. Then, the acceleration was reduced in a step fashion to 250 rpm/s (q = 493). The behavior immediately after the switch occurred is very sensitive to the exact phase of the eccentric mass at the time of the switch. This should be expected since the rotor must tend to the steady-state solution for a supercritical rotor which is "heavy side in" (phase = −180 deg). Figure 7 shows predictions for a case for such an acceleration schedule. The maximum amplitude of the response is about 10 percent less than that of the continuous 2000 rpm/s acceleration response. The "ring down" after the critical speed is much more rapid for the case of the scheduled rotor than for the constant high acceleration case.

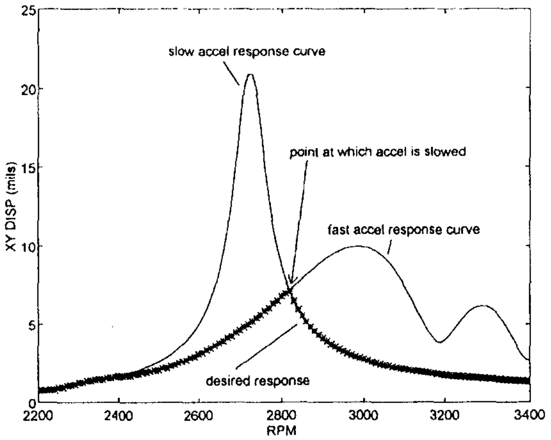

Fig. 6 *Cartoon of how changing acceleration rate (scheduling) from a high rate to a low rate after critical speed is reached can lead to a lower response*

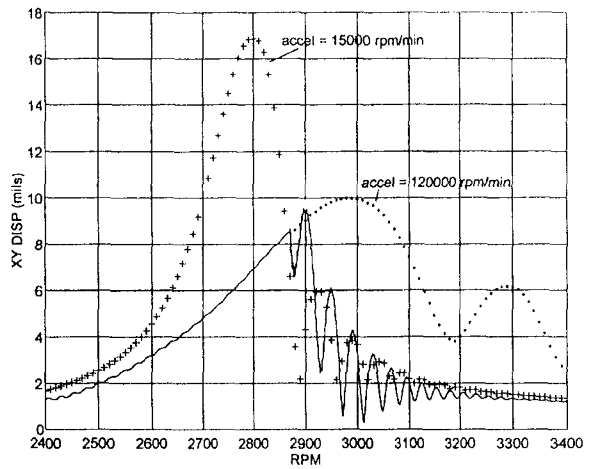

Fig. 7 *Model predictions for 3 cases. Envelope of radial response at a constant high acceleration (120,000 rpm/min), envelope of radial response at a constant low acceleration (15,000 rpm/min), and time resolved radial response for the fast acceleration (120,000 rpm/min) followed by a reduced acceleration (15,000 rpm/min).*

4.3 Energy Considerations. If the maximum amplitude of vibration during the acceleration transient is to be reduced, the energy fed into the rotor's lateral vibration should be minimized, and this energy must be removed quickly by the action of damping.

The energy for the lateral vibration is drawn from the rotational energy of the shaft by means of the eccentric whirling mass, m. The external power input to the shaft, P_{in}, due to the external torque, T, is

$$P_{in} = T\omega, \tag{11}$$

where ω is the instantaneous angular velocity. The total energy in the shaft at any given time is divided between the rotational kinetic energy (if there is no torsional vibration), E_r, given by

$$E_r = \tfrac{1}{2} I_{zz}\omega^2, \tag{12}$$

where I_{zz} is the polar moment of inertia, and the total (potential and kinetic) energy of the lateral vibration E_t, given by

$$E_t = \tfrac{1}{2} M(\dot{x}^2 + \dot{y}^2) + \tfrac{1}{2} K(x^2 + y^2). \tag{13}$$

To reduce the energy transfer from the rotational motion to the lateral mode, the relative phase between the back torque pulsation from the lateral motion of the eccentric imbalance mass and the shaft angular motion should be driven as far away from 0 deg (in phase) as possible. If the average of the absolute value of the relative phase during acceleration can be kept larger than $\pi/2$, the energy in the lateral mode will be extracted by the rotational mode. This leads to the possibility that a high bandwidth active torque control can be used to virtually eliminate lateral vibrations.

Finally, direct damping is beneficial in reducing the response during acceleration and deceleration through critical speeds.

5 Experimental Confirmation

5.1 Overview. Experiments were conducted to verify that acceleration scheduling is capable of reducing lateral vibrations

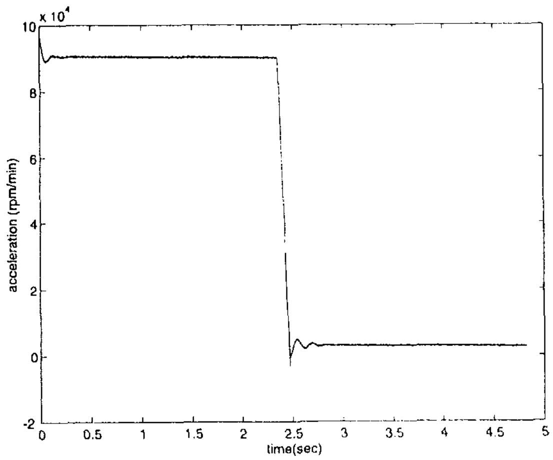

Fig. 8 Measured acceleration schedule which produced the lowest maximum response

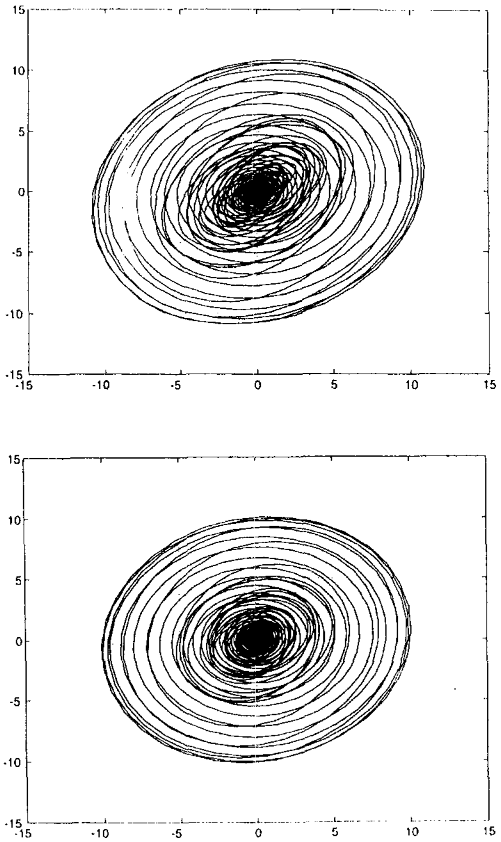

Fig. 9 Comparison of orbits from the model calculated with the measured acceleration schedule (*a*) to orbits that were directly measured (*b*). Distances are in mils.

in real hardware. The results to be presented are preliminary in that precise control of the acceleration rate was not possible with the experimental facility used. However, it was possible to reduce the acceleration rate in a noncontrolled manner and measure it. The measured acceleration rates were used as input to the model. The predicted responses with the measured acceleration rates were compared to the experimental orbits—for model validation. Reduced lateral responses were found for some schedules, as predicted by the model.

5.2 Facility Description. The experimental facility is based on a Bently Nevada Rotor Kit [11] mounted on an isolation table as shown in Fig. 10. The configuration of the rotor for all experiments and the modal parameters used in the numerical model, which reflect this configuration, are given in Table 1. The direct stiffness in the vertical (y) direction is slightly larger than the horizontal (x) direction due to gravitation [12]. Hence, slightly different $K_{ii}s$ were used than those of section 4 of the paper. The stiffness coefficients along with the direct damping were obtained by a parameter identification procedure extracted from steady-state experimental orbit data, which correspond closely to static modal response tests [12]. While there is split resonance due to the nonisotropic stiffness properties, the nominal critical speed is approximately 2720 rpm.

As designed, the motor controller is capable of fixed speeds in the range of 0–12,000 rpm or constant acceleration/deceleration rates up to 15,000 rpm/min. The highest acceleration rate corresponds to $q = 493$ for the configuration used, which is a relatively slow acceleration. Therefore, the feedback resistor in the controller was replaced to allow for a greater acceleration. With this modification the highest acceleration rate was nearly 90,000 rpm/min ($q = 82$). This reduced the stability of the controller somewhat, and, thus, created less damped oscillations when sudden changes in acceleration were input.

The motor controller was not capable of following a prescribed acceleration schedule. Instead, the acceleration was manually reduced at a fraction of a second after the nominal critical speed was reached. Several runs were made to capture the change at the correct point by trial and error. The motor controller did not yield a simple step change from a constant high acceleration rate to a constant low one. The instantaneous shaft speed was measured by recording successive signals from the 96 count/revolution optical encoder attached to the end of the shaft. This was done with an HP-53318 Modulation Domain Analyzer. The whirl orbits (x and y) and the shaft speed history were recorded.

5.3 Results and Comparison to Model. The measured acceleration schedule from the experiment that produced the largest reduction in the maximum amplitude of vibration is shown in Fig. 9. After the start up transient, there is a fairly constant acceleration rate until the time when the controller is altered. At this point, an undershoot is created followed by a damped oscillation until the lower acceleration rate is stabilized.

This measured acceleration schedule, $\ddot{\theta}(t)$, was used as an input to the model to predict the orbit response. These results are is shown in Fig. 10(a). For direct comparison, the actual response measured with the same acceleration schedule is shown in Fig. 10(b).

Table 2 gives a summary of the maximum response amplitude from the model and experiments for steady-state operation, the maximum acceleration rate, and the best scheduled acceleration.

5.4 Discussion of Results. The measured orbits compare favorably to those predicted by the model, as can be seen in Fig. 10. In addition, the differences between the predictions

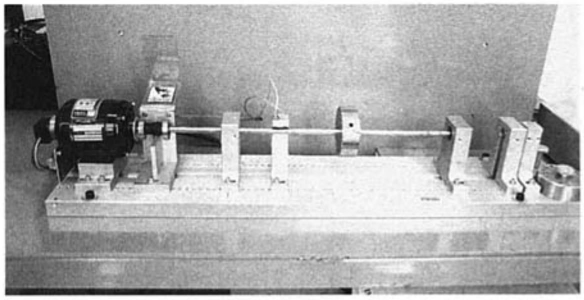

Fig. 10 Experimental rotor facility. From left to right is (1) optical encoder, (2) controllable electric motor, (3) shaft coupling, (4) main shaft, (5) inboard bearing, (6) *x* and *y*-proximeters, (7) disk, and (8) out board bearing, motor controller.

Table 2 Maximum response, $\bar{R} = \sqrt{x^2 + y^2}$ (mils), predicted by the model and measured in the experimental rotor facility for steady state, a fast constant acceleration and with the acceleration schedule given in Fig. 9. Typical experimental uncertainty is about 0.2 mils

	Model	Experiment
Steady-state	20.5	20.5
Constant acceleration (90,000 rpm/min)	12.0	12.2
Scheduled acceleration (Best Case)	10.9	10.7

of maximum rotor deflection from the simple model and the experimental results are typically within 3 percent, which is close agreement. This indicates that the model contains all the dominant physical characteristics necessary for accurate predictions in both steady state as well as transient operation. This is true at least for the range of parameters used in this investigation and with a motor which can deliver sufficient torque so as to prescribe the acceleration.

The model predicted a maximum amplitude of 12 mils for a constant acceleration of 90,000 rpm/min and a 10.9 mil amplitude for the "optimum" schedule. This is a 9 percent reduction. The measured reduction was even larger (12 percent reduction). However, due to the nature of the experimental procedure (the measurements are not directly repeatable) and the magnitude of the experimental uncertainty, a great deal of confidence cannot be placed on this particular number. The model and the experimental results both indicate that a reduced acceleration rate, once the nominal critical speed is reached, can lead to a reduced lateral response.

6 Conclusions

The validated linear, planar two-dimensional rotor model was used to show that it is possible to reduce lateral vibrations in a rotor by using a reduced acceleration rate after reaching the rotor's natural frequency. Preliminary experimental results support this conclusion.

While all the efforts described focused on simple rotors, the general technique should be applicable to a standard rotor with more complex characteristics including several vibration modes, gyroscopic coupling, etc. This method should also be applicable to decelerating rotors.

It should be possible to further reduce the vibration amplitude and/or the total vibrational energy by developing optimum acceleration schedules for a given application. However, such a schedule may require very high bandwidth sensing and actuation to implement. Also, rapid changes in the torque will excite torsional vibrations.

If this technique can be implemented effectively in real turbomachinery, tighter tip clearances can be specified in lighter machines, yielding higher performance.

7 Acknowledgments

This work was sponsored by NAVSEA03-Z. The authors would like to express their gratitude to Mr. John Hartranft, Mr. Dan Grohgan, and Mr. Phil Matis of NAVSEA for their interest and support.

8 References

1 Lewis, F. M., 1932, "Vibration During Acceleration Through a Critical Speed," *Transactions of the ASME,* Vol. 54, pp. 253–261.

2 Pöschl, 1933, "Das Anlaufen eines einfaches Schwingers", Ingenieur-Archiv, IV bd, p. 98.

3 Baker, J. G., 1939, "Mathematical-Machine Determination of the Vibration of Accelerated Unbalanced Rotor," *Journal of Applied Mechanics,* Vol. 6, p. A1.

4 Meuser, R. B., and Weibel, E. E., 1948, "Vibration of a Nonlinear System During Acceleration Through Resonance," *Journal of Applied Mechanics,* Vol. 15.

5 McCann, Jr., G. D., and Bennett, R. R., 1949, "Vibrations of Multifrequency Systems During Acceleration Through Critical Speeds," *Journal of Applied Mechanics,* Vol. 16, p. 375.

6 Dornig, A., 1957, "Transients in Simple Undamped Oscillators Under Inertial Disturbances," *Journal of Applied Mechanics,* June, pp. 217–223.

7 Fearn, R. L., and Millsaps, K., 1967, "Constant Acceleration of an Undamped Simple Vibrator Through Resonance," *Journal of the Royal Aeronautical Society,* Aug., p. 567.

8 Gluse, M. R., 1967, "Acceleration of an Unbalanced Rotor Through its Critical Speeds," *Naval Engineers Journal,* Feb., pp. 135–144.

9 Ishida, Y., Yamamoto, T., and Murakami, S., 1992, "Nonstationary Vibration of a Rotating Shaft with Nonlinear Spring Characteristics During Acceleration Through a Critical Speed," *JSME International Journal,* Series III, Vol. 35, No. 3.

10 Reed, G. L., 1995, "Theoretical and Experimental Investigation of the Response of a Rotor Accelerating Through Critical Speed," M.S. thesis, Department of Mechanical Engineering, Naval Postgraduate School, Monterey, CA.

11 Bently Rotor Kit, 1988, *Operating Manual,* Bently Nevada Corporation.

12 Millsaps, K. T., and Vejvoda, C. E., 1996, "Origin of Split Resonance and Backward Whirl in a Simple Rotor," International Gas Turbine Conference, Birmingham, UK, June 10–13, ASME Paper No. 96-GT-80.

13 Filippov, A. P., 1956, *Vibrations of Elastic Systems,* Academy of Sciences, Ukrainian SSR, Kiev, pp. 145–151.

B. M. Antkowiak
C. S. Draper Laboratory, Inc.,
555 Technology Square,
Cambridge, MA 02139

F. C. Nelson
College of Engineering,
Tufts University,
Medford, MA 02155

Rotodynamic Modeling of an Actively Controlled Magnetic Bearing Gas Turbine Engine

This paper summarizes the development of a finite element rotordynamic solution used in a closed loop simulation for a magnetic bearing rotor system in a gas turbine engine. A magnetic bearing controlled rotor is analyzed, and the state dynamics matrix [A], the shaft control influence matrix [B], and the sensor matrix [C] are constructed. Bode plots of the state-space transfer function are also constructed and compared to the results of the rotor dynamic model.

Introduction

Two of the most serious concerns of high-speed rotating machines are the large amplitudes at critical speeds and the instabilities associated with internal damping. Either of these conditions can be catastrophic, and it is important that both of these mechanisms be understood. The inclusion of magnetic bearings presents an additional problem in the response characteristics of the rotor as it directly interacts with the control design. By developing a state-space plant model of a high-speed rotor model and integrating the rotordynamics directly with the control system, the closed-loop response of the shaft can be simulated.

This paper presents a method and practical application of this technique for a high-speed jet engine. This engine is intended to operate supercritically and is suspended by two radial and one axial magnetic bearing. No coupling is considered between the axial and radial bearings. Disturbances from rotor imbalance, starter-generator loads, and inertia loads due to aircraft maneuvers can be included in the model.

Finite Element Model

The rotordynamic model is constructed using finite elements based on the work of Nelson (1977). The element includes rotary inertia, gyroscopic moments, and shear effects. The complete derivations of the element shape functions, done by Nelson (1976), will not be repeated here. However, a review of the coordinate transformation will be repeated, because of their key role in the development of the rotor equations of motion and the rotor state-space model.

The element has 8 degrees of freedom (DOF), or 4 DOF per node. The element is oriented along the $+X$-axis with positive rotation determined by the right-hand rule. Two reference systems are used to describe its motion. A rotating reference (x, y, z) is defined relative to a fixed reference (X, Y, Z) by a single rotation φ about the X-axis. The physical displacements of the rotor can then be given in rotating or fixed frame coordinates as

$$\{q\}^T = [V \quad W \quad B \quad \Gamma] \tag{1a}$$

$$\{p\}^T = [v \quad w \quad \beta \quad \gamma]. \tag{1b}$$

The relative motion of a point on the element can now be shown in the rotating coordinate systems in Fig. 2. The transformation from the rotational coordinates to the fixed frame coordinates can then be written as

$$\{q\} = [T]\{p\} \tag{2a}$$

$$\{\dot{q}\} = \dot{\phi}[T']\{p\} + [T]\{\dot{p}\} \tag{2b}$$

$$\{\ddot{q}\} = [T](\{\ddot{p}\} - \dot{\phi}^2\{p\}) + [T'](\ddot{\phi}\{p\} + 2\dot{\varphi}\{\dot{p}\}), \tag{2c}$$

where $[T]$ and $[T']$ are orthogonal matrices

$$[T] = \begin{bmatrix} \cos\phi & -\sin\phi & 0 & 0 \\ \sin\phi & \cos\phi & 0 & 0 \\ 0 & 0 & \cos\phi & -\sin\phi \\ 0 & 0 & \sin\phi & \cos\phi \end{bmatrix} \tag{3a}$$

$$[T'] = \begin{bmatrix} 0 & -1 & 0 & 0 \\ +1 & 0 & 0 & 0 \\ 0 & 0 & 0 & -1 \\ 0 & 0 & +1 & 0 \end{bmatrix} [T]. \tag{3b}$$

The individual rotor element matrices are assembled into global matrices for mass, $[M]$, stiffness, $[K]$, and gyroscopics, $[G]$. External damping is represented as viscous damping in matrix $[Cd]$. The resulting equation of motion as developed in Nelson (1977) can be represented in fixed frame coordinates as

$$[M]\{\ddot{q}\} + ([G] + [Cd])\{\dot{q}\} + [K]\{q\} = \{Q_c\}\cos\Omega t + \{Q_s\}\sin\Omega t + \{F\}, \tag{4}$$

or in rotational coordinates as

$$[M]\{\ddot{p}\} + \omega(2[\hat{M}] + (1 - \psi)([G] + [Cd]))\{\dot{p}\} + ([K] - \omega^2([M] - (1 - 2\psi)[\tilde{M}]))\{p\} = \{Q\} + \{F_c\}\cos\Omega t + \{F_s\}\sin\Omega t. \tag{5}$$

The symmetric matrix $[\tilde{M}]$, which appears in the rotating reference equation, is the assembled rotary mass matrix part of $[M]$, and $[\hat{M}]$ is a skew symmetric matrix that results from the coordinate transformation.

Rotordynamic Model

The equation of motion for a rotor can, therefore, be written in terms of fixed or rotational coordinate frames. Since this paper deals with the development of a plant model for a control simulation, the fixed frame equation of motion (4) is more

---

Contributed by the International Gas Turbine Institute and presented at the International Gas Turbine & Aeroengine Congress & Exhibition, Orlando, FL, June 2–5, 1997. Manuscript received by the ASME Headquarters February 3, 1997. Paper No. 97-GT-13. Associate Technical Editor: H. A. Kidd.

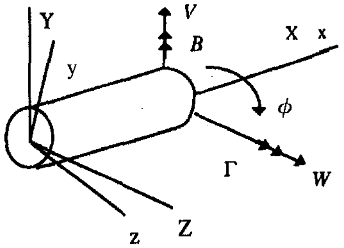

Fig. 1 Element coordinate systems

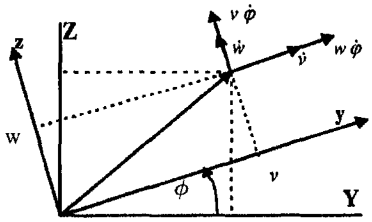

Fig. 2 Relative motion of a point on the shaft

advantageous and will be used. The undamped homogeneous part of this equation is

$$[M]\{\ddot{q}\} + ([G])\{\dot{q}\} + [K]\{q\} = \{0\}. \tag{6}$$

A solution method to calculate the rotor dynamic equation of motion uses the state-space variable defined as

$$\{\delta\}^T = [q, \dot{q}] \tag{7}$$

and the identity as

$$[[M], [0]]\{\dot{\delta}\} + [[0], -[M]]\{\delta\} = \{0\}. \tag{8}$$

Combining Eqs. (7) and (8) results in:

$$[R]\{\dot{\delta}\} + [S]\{\delta\} = \{0\}, \tag{9}$$

where

$$[R] = \begin{bmatrix} [G] & [M] \\ [M] & [0] \end{bmatrix} \quad [S] = \begin{bmatrix} [K] & [0] \\ [0] & -[M] \end{bmatrix}. \tag{10a, b}$$

If a trial solution is assumed in the form

$$\{\delta\} = \{\Phi\}e^{\lambda t}, \tag{11}$$

Eq. (9) becomes

$$\lambda[R]\{\Phi\} = -[S]\{\Phi\}. \tag{12}$$

This equation can be solved with a standard eigenvalue solver for the eigenvalues and eigenvectors. The eigenvalues will occur in complex conjugate pairs. The real part corresponds to an exponential decay, while the imaginary part provides the oscillation. These eigenvalue pairs represent forward and backward whirl conditions. When the shaft speed matches that of the whirl frequencies, synchronous whirl develops. Synchronous whirl is a necessary condition for the occurrence of a critical speed.

State Space Control Model

Eigenvectors can also be calculated for the undamped and nonrotating equation of motion. These eigenvalues, $[\omega^2]$, and eigenvectors, $[\underline{\Phi}]$, can be solved with the equation of motion

$$[M]\{\ddot{q}\} + [K]\{q\} = \{0\} \tag{13}$$

or by rewriting it as an eigenvalue equation as follows:

Nomenclature

$[A]$ = state dynamics matrix of dimension $2n \times 2n$
$[B]$ = control influence matrix of dimension $2n \times m$
$[C]$ = sensor distribution matrix of dimension $m \times 2n$
$[Cd]$ = external assembled element damping matrix
$[D]$ = feedback controller matrix $m \times m$
$[G]$ = assembled element gyroscopic matrix
$[\underline{G}]$ = modal reduced gyroscopic matrix $[G]$
$[I]$ = identity matrix
$[K]$ = assembled element stiffness matrix
$[L]$ = reduced modal DOF force transformation matrix
$[M]$ = assembled element mass matrix
$[\tilde{M}]$ = assembled element rotor inertia part of $[M]$
$[\hat{M}]$ = transformed mass matrix
$\{Q\}$ = element internal (unbalance) force
$\{F\}$ = element external force
$[R]$ = state-space mass and gyroscopic matrix
$[S]$ = state-space stiffness matrix
$[T]$, $[T']$ = transformation matrices
V, W = translation shaft displacement in (Y, Z)
X, Y, Z = fixed frame coordinates
m = number of selected DOF, $m < n$
n = number of modes
$\{p\}$ = physical displacement vector relative to (y, z)
$\{q\}$ = physical displacement vector relative to (Y, Z)
$\{u\}$ = physical force vector relative to (Y, Z)
v, w = translation shaft displacements in (y, z)
x, y, z = rotating frame coordinates
φ, B, Γ = shaft rotations about (X, Y, Z)
β, γ = shaft rotations about (y, z)
$\{\alpha\}$ = state-space variable in modal coordinates
$[\Phi]$ = eigenvectors
$[\underline{\Phi}]$ = undamped Eigenvectors
Ω = spin speed = $\dot{\varphi}$
$\{\delta\}$ = state-space variable in fixed physical coordinates
$[\omega^2]$ = eigenvalues of the nonrotating undamped equation of motion
ω = whirl speed
ψ = spin/whirl ratio
λ = eigenvalues of the rotor equation of motion
$\{\eta\}$ = vector of modal displacements and velocities
$\{\zeta\}$ = linear viscous damping ratio

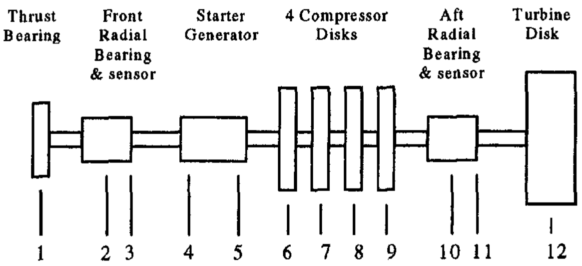

Fig. 3 Rotor components and sensor/actuator locations

$$\omega^2[K]^{-1}[M]\{\underline{\Phi}\} = \{\underline{\Phi}\}. \tag{14}$$

Using the eigenvalues, $[\omega^2]$, and eigenvectors, $[\underline{\Phi}]$, Eq. (4) can be represented in modal coordinates, η, as

$$\{\ddot{\eta}\} + (2[\zeta\omega] + [\underline{G}])\{\dot{\eta}\} + [\omega^2]\{\eta\} = [\underline{\Phi}]^T[L]\{u\}, \tag{15}$$

where

$$\{q\} = [\underline{\Phi}]\{\eta\} \tag{16a}$$

$$[\omega^2] = \begin{bmatrix} \ddots & & \\ & \omega^2 & \\ & & \ddots \end{bmatrix} \tag{16b}$$

$$[\underline{\Phi}]^T[M][\underline{\Phi}] = [I] \tag{16c}$$

$$[\underline{\Phi}]^T[G][\underline{\Phi}] = [\underline{G}] \tag{16d}$$

$$[\underline{\Phi}]^T[K][\underline{\Phi}] = [\omega^2] \tag{16e}$$

$\{\zeta\}$ = modal damping ratios for external damping
$\{u\} = m \times 1$ matrix of forces at m locations, where $m < n$
$[L]$ = an $n \times m$ matrix that inflates the $m \times 1$ $\{u\}$ force matrix to an $n \times 1$ force matrix

The state-space model can then be constructed so that it represents the dynamics of the rotor in a finite number of states, where each state represent a vibrational mode of the rotor. If a state vector is chosen as

$$\{\alpha\}^T = [\eta, \dot{\eta}], \tag{17}$$

then the state-space model takes the following form:

$$\{\dot{\alpha}\} = [A]\{\alpha\} + [B]\{u\}. \tag{18}$$

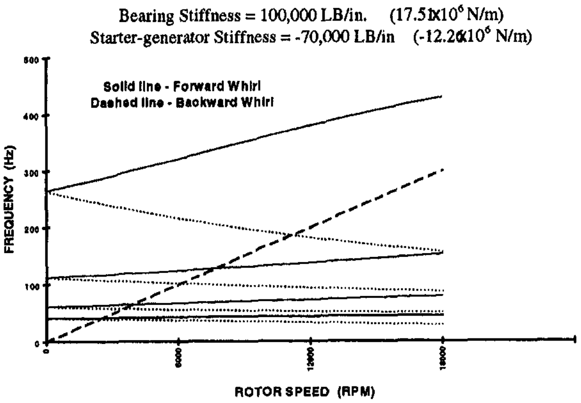

Fig. 4 Campbell diagram

Table 1 Forward whirl critical speeds

Mode 1 (RPM)	2,551
Mode 2 (RPM)	3,914
Mode 3 (RPM)	7,661
Mode 4 (RPM)	29,850

The output in physical coordinates is

$$\{q\} = [C]\{\alpha\}. \tag{19}$$

The vector $\{\alpha\}$ is the modal displacements and velocities of the rotor in state space. The input force, $\{u\}$, is applied through the matrix, $[B]$, and the output, $\{q\}$, is the shaft physical displacement and velocity in Y and Z-coordinates. To satisfy the equation of motion, the steady-state dynamics matrix $[A]$ has the specific form of

$$[A] = \begin{bmatrix} [0] & [I] \\ -[\omega^2] & -(2[\zeta\omega] + [\underline{G}]) \end{bmatrix}. \tag{20}$$

For convenience, $[\underline{G}]$ will be calculated for a shaft velocity of unity ($\Omega = 1$ radian/s) and, therefore, must be multiplied by the desired speed of the shaft in radians/s for different rotor speeds. The state-space actuator matrix $[B]$ and sensor matrix $[C]$, are then

$$[B] = \begin{bmatrix} [0] \\ [\underline{\Phi}]^T[L] \end{bmatrix} \tag{21}$$

$$[C] = [[\underline{\Phi}] \quad [0]]. \tag{22}$$

To reduce the number of states, a modal reduction can be applied to the mass, stiffness, and gyroscopic matrices by eliminating higher frequency modes. By reducing n to the desired number of modes, i, the $[M]$, $[K]$, and $[\underline{G}]$ matrix size is reduced accordingly. The normalization scheme consists of setting

$$[\underline{\Phi}_i]^T[M][\underline{\Phi}_i] = [I] \tag{23a}$$

$$[\underline{\Phi}_i]^T[G][\underline{\Phi}_i] = [\underline{G}] \tag{23b}$$

$$[\underline{\Phi}_i]^T[K][\underline{\Phi}_i] = [\omega_i^2], \tag{23c}$$

where $[\underline{\Phi}_i]$ is the modal matrix truncated at the ith mode.

Note that $[\underline{G}]$ remains a nondiagonal matrix. The modal reduction method employed here, based on modal superposition, is routinely used when damping is involved. In the case, where there is only nominal amounts of damping and/or the gyroscopic forces are small, the natural frequencies and mode shapes do not appreciably change, and this procedure is reasonable. However, care must be taken to assure that this procedure does not lose valuable information by eliminating an excessive number of modes.

Application to a Magnetic Bearing Gas Turbine Engine

A finite element model of a magnetic bearing rotor was constructed with 91 nodes and 90 elements. The major components

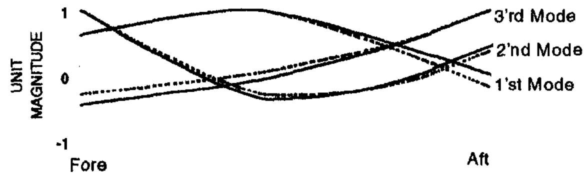

Fig. 5 Natural frequency mode shapes at 2,551 RPM

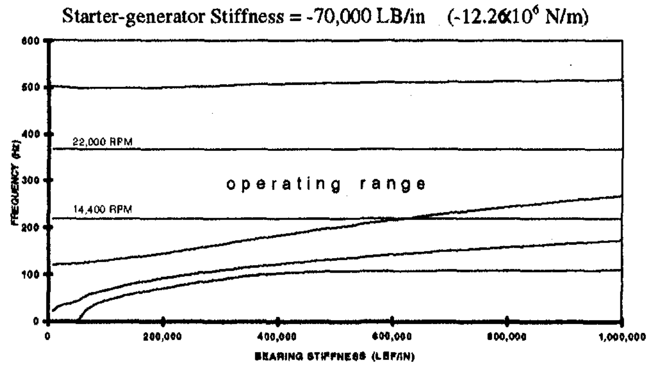

Fig. 6 Rotor critical speed map

of this rotor system are shown schematically in Fig. 3, with the 12 actuator-sensor matrix locations.

A rotordynamic analysis was performed using Eq. (12) and an isotropic radial bearing stiffness of 100,000 lb/in, (17.51×10^6 N/m), at each radial bearing. A starter-generator negative stiffness was applied to each end of the starter-generator, locations 4 and 5 in Fig. 3, for a total equivalent stiffness of −70,000 lb/in, (-12.26×10^6 N/m). The first four whirl frequency pairs have been plotted on a Campbell Diagram in Fig. 4. The upper line in each whirl speed pair indicates forward whirl, while the lower is backward whirl. The diagonal line represents equal frequency and rotor speed. The intersection of this line with the whirl speed indicates a synchronous whirl condition. The occurrence of critical speeds at the various synchronous whirl conditions is determined by a forced response analysis.

The forward and backward mode shapes have also been computed for the shaft critical speeds. The mode shapes of the first 3 whirl frequencies at the shaft first critical speed of 2,551 RPM have been normalized to 1 and are shown in Fig. 5. The first three mode shapes at the 2nd and 3rd critical speed are similar and are not shown.

The actual magnetic bearing stiffness will vary with frequency. Therefore, critical speeds for various mechanical spring rates of the bearings were calculated. The resultant critical speed versus bearing stiffness is shown in Fig. 6. No critical speeds exist in the operating range of the rotor for bearing stiffness up to 600,000 lb/in (105.1×10^6 N/m).

The purpose of the development of the state-space matrices is to use them in simulations of the closed-loop response dynamics of the rotor. For this application, the mechanical bearing stiffness and damping are zero in the state-space matrices or plant system. These stiffness will be provided by applying external forces as a function of the shaft displacement $\{q\}$. The results, without constraints to ground, should then have four zero-frequency, rigid-body modes. In addition, the number of modes was chosen to be 24 for a total of 48 states. Table 2 lists these natural frequencies associated with the unconstrained rotor at zero rotor speed.

Modal damping was input through the ζ damping term in the $[A]$ matrix from Eq. (20). A value of 1 percent of critical damping will be used in this rotor model for all 24 modes. Note that this method of applying modal damping represents external damping to ground and will always be stabilizing. This approach is only good for small amounts of damping since large values of internal damping can reduce the maximum rotor speed obtainable at the onset of instability.

Table 2 Rotor free-free natural frequencies

Mode #	Frequency (Hz)	Mode #	Frequency (Hz)
1 - 2	0.0	13 - 14	1119.
3 - 4	0.0	15 - 16	1418.
5 - 6	101.5	17 -18	2120.
7 - 8	260.6	19 - 20	2284.
9 - 10	497.0	21 - 22	2974.
11 - 12	719.8	23 - 24	3298.

From the resulting eigenvectors, the $[B]$ and $[C]$ matrices were constructed for 12 actuator and sensor locations on the shaft, see Fig. 3. These 12 locations and 24 modes of Table 2 comprise a matrix of displacement and velocity eigenvector pairs in the $[B]$ and $[C]$ matrices.

A feedback control system was then run in MATLAB to verify that the dynamics of the control matrices matched those of the mechanical bearing rotor system. To accomplish this, the mechanical bearing stiffness and negative starter generator stiffness were added to a feedback controller in matrix $[D]$. The feedback control system is shown in Fig. 7.

Bode plots for the rotor transfer function have been made for the zero, minimum (13,400 rpm), and maximum (22,000 rpm) rotor operational speeds for the free-free rotor, $[D] = [0]$, and for the constrained and loaded rotor. These are shown in Fig. 8 with the amplitude expressed in decibels. The units of amplitude, x, are displacement in feet divided by the applied force in pounds (.00571 m/N). The input forcing function is applied in the Y-direction at the turbine disk and the output is in the Y and Z-directions at the bearings. The traces in Fig. 8 represent a transfer function from a force applied at the turbine to the displacement at the bearing in the Y and Z-directions. For the first two plots (Fig. 8(a) and 8(d)) there is no Z output since there is no coupling at zero rotor speed. The two additional traces in Figs. 8(b), 8(c), 8(e), and 8(f) represent the transfer function coupling from the Y to Z-coordinates at rotor speed due to the speed dependent Coriolis forces.

The Bode plot for the free-free rotor, Fig. 8(a), at zero rotor speed shows the expected resonance frequency of 101.5 Hz (6090 rpm). An interesting phenomenon of these resonant frequencies (poles) can be noticed as the rotor spins up in speed in Figs. 8(b) and 8(c). First, the poles bifurcate. This can be best observed by noticing that the 101.5 Hz peak in Fig. 8(a) becomes two peaks in Fig. 8(b), one slightly lower and the other somewhat higher than 101.5 Hz. This frequency pair are the backward and forward critical speeds, respectfully. Second, the coupling between the Y and Z-axis increases because of the Coriolis terms. Third, the lowest resonant frequency, which does not exist in the zero spin speed case, increases with speed to approximately 30 Hz at 22,000 rpm. This subsynchronous frequency is the precessional frequency of the rotor and is essentially a rigid body motion.

The supported rotor, Fig. 8(d), at zero spin speed shows resonant frequencies at 41.6, 61.2, and 109.0 Hz. These correspond to the natural frequencies of the nonrotating shaft. Furthermore, at increasing rotor speeds, Fig. 8(e) and 8(f), they bifurcate into the forward and backward whirl frequencies as predicted in Fig. 4. This comparison shows that the control matrices contain the dynamics of the rotating shaft and that a sufficient number of modes were retained. Simulations of the

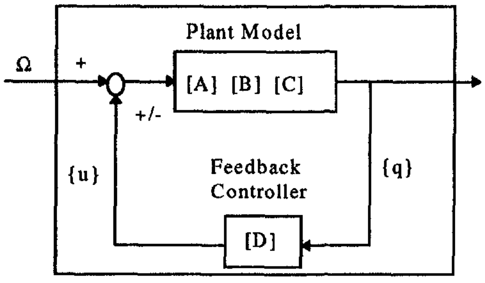

Fig. 7 Feedback control loop

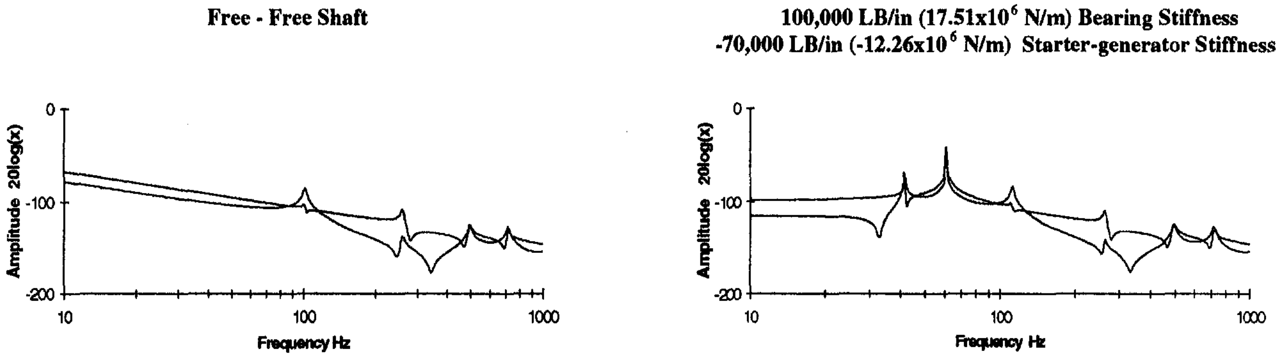

(a) 0 RPM Rotor Speed (d)

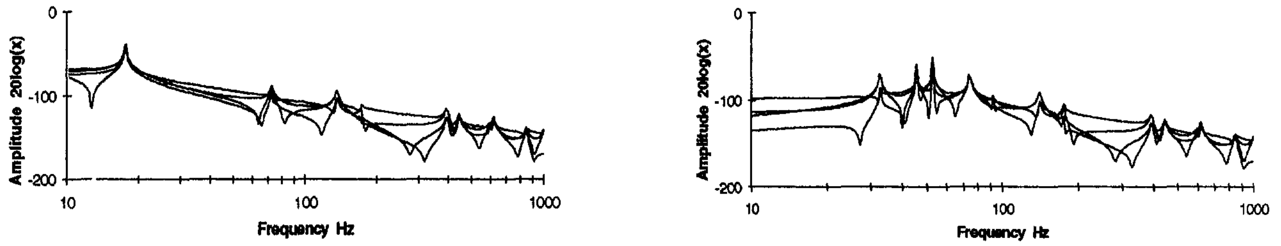

(b) 13,400 RPM Rotor Speed (e)

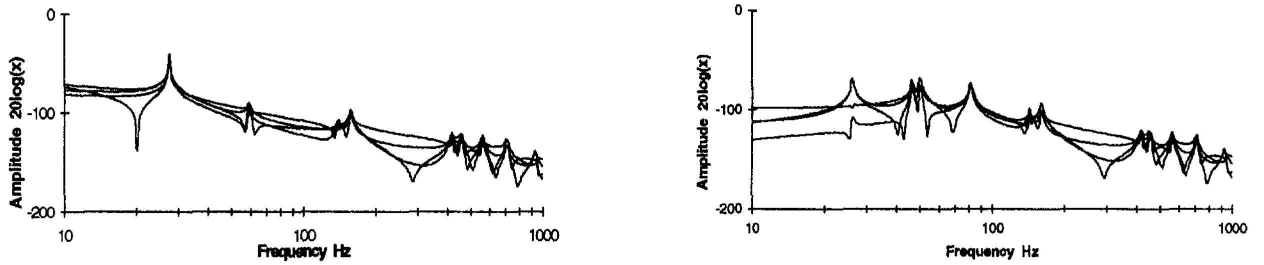

(c) 22,000 RPM Rotor Speed (f)

Fig. 8 Bode plots of the rotor transfer function

above rotordynamic model on magnetic bearings with frequency-dependent properties is presented in Scholten (1997).

Summary

A reduced order rotordynamic state-space, transfer-function model of a rotor has been presented. It appears to be adequate to capture the essential closed loop dynamics of the rotating components of a high speed jet engine. In a separate study, Part II, Scholten (1996) uses the results of these state space control matrices in a simulation model to develop a control system for this shaft.

References

Nelson, H. D., 1977, "A Finite Rotating Shaft Element Using Report ERC Timoshenko Beam Theory," Engineering Research Center report no. ERC-R-77023, Arizona State University, Tempe, AZ, p. 61.

Nelson, H. D., and McVaughn, J. M., 1976, "The Dynamics of Rotor-Bearing Systems Using Finite Elements," *ASME Journal of Engineering for Industry*, May, pp. 593–603.

Scholten, J. R., 1997, "A Magnetic Bearing System for High Temperature Gas Turbine Applications," *Rotor Dynamics*, Turbo Expo '97, ASME, New York.

Direct Prediction of the Effects of Mistuning on the Forced Response of Bladed Disks

M. P. Mignolet
mignolet@enuxsa.eas.asu.edu

W. Hu
Department of Mechanical and
Aerospace Engineering,
Arizona State University,
Tempe, AZ 85287-6106

In this paper, a novel approach to determine reliable estimates of the moments of the steady-state resonant response of a randomly mistuned bladed disk is presented, and the use of these moments to accurately predict the corresponding distribution of the amplitude of blade vibration is described. The estimation of the moments of the response is accomplished first by relying on a "joint cumulant closure" strategy that expresses higher order moments in terms of lower order ones. A simple modeling of the error terms of these approximations is also suggested that allows the determination of an improved, or accelerated, estimate of the required moments. The evaluation of the distribution of the amplitude of blade response is then accomplished by matching the moments computed by the cumulant closure with those derived from a three-parameter model recently derived. A first order approximation of the moments obtained for a simple structural model of a bladed disk yields a new parameter that can be used as a measure of the localization of the forced response. Then, numerical results demonstrate that the method provides extremely accurate estimates of the moments for all levels of structural coupling which in turn lead to a description of the amplitude of blade response that closely matches simulation results. Finally, a comparison with existing perturbation techniques clearly shows the increased accuracy obtained with the proposed joint cumulant closure formulation.

Introduction

Blade-to-blade variations in their geometry and structural properties (mistuning) occur during the manufacturing process and/or as a consequence of in-service wear. Although small, these variations have been shown in a long series of investigations (see, in particular, the early works of Whitehead (1966) and Ewins (1969) and the more recent studies of Ottarsson and Pierre (1995)) to be the potential source of very large changes, in particular, increases of the forced response of bladed disks, and have been linked to high cycle fatigue problems. The numerous studies that have been published on this topic have provided a lot of insight into and some limited prediction capabilities of the damaging effects of mistuning but have not solved all issues. In this context, note that this problem is especially difficult because of the highly nonlinear dependence of the resonant response of a bladed disk on its structural properties.

In addition to useful but expensive Monte Carlo simulation studies (see, for example, Basu and Griffin (1986) and Kielb and Kaza, (1984)), perturbation techniques have been used to predict the properties and sensitivity of the forced response of the blades. In some of these studies (see, for example, Sinha (1986) and Sinha and Chen (1989)), the mistuning is assumed small enough so that the tuned response can be used as a zeroth order solution of the problem. Then, a series expansion solution of the forced response is obtained in terms of powers of the mistuning terms. Accordingly, it is found that the ratio of the magnitude of the mistuned impedances to the damping level plays an important role in the sensitivity of the system to small changes in the blade properties. In other investigations (see, for example, Wei and Pierre (1988)), it has been argued that the blade-to-blade coupling should be considered as the small term on which the perturbation solution is based. These analyses emphasize, in particular, the role of the ratio of the magnitude of the mistuning to the blade-to-blade coupling strength. In fact, both of these types of perturbations provide valuable insight into the behavior of the forced response in the two limits of strongly and weakly coupled bladed disks, respectively. Unfortunately, recent investigations (Ottarsson and Pierre, 1995) have suggested that the most damaging effects of mistuning might occur in the middle zone, where none of these two perturbation schemes provides a good approximation of the characteristics of the forced response.

Recently, Mignolet and Lin (1996) derived, under some mild conditions, a three-parameter model that has provided an almost perfect match of the probability density function of the amplitude of response of the blades at resonance. Further, this model has been found to be applicable in both ranges of weakly and strongly coupled bladed disks. This result represents a major step toward the accurate prediction of the effects of random mistuning on the structural dynamics of bladed disks over the entire range of coupling strengths. To complete this task, however, it is necessary to dispose of an equally reliable technique for the evaluation of the first moments of the blade response, i.e., mean and variance, from which the three parameters of the corresponding distribution can be uniquely determined. The accurate computation of these moments and their use in connection with the three-parameter model to reliably estimate the probability density function of the amplitude of blade response represent the objectives of the present investigation.

Bladed Disk Structural Dynamics

Modeling the bladed disk as a linear N-degree-of-freedom system leads to the set of N equations of motion

$$M\ddot{\underline{X}} + C\dot{\underline{X}} + K\underline{X} = \underline{F}(t), \tag{1}$$

where M, C, and K denote, respectively, the $N \times N$ mass, damping and stiffness matrices of the system, while $\underline{F}(t)$ and $\underline{X}(t)$ represent the time dependent excitation and response vectors the jth components of which will be written as $F_j(t)$ and $X_j(t)$, $j = 1, 2, \ldots, N$.

Contributed by the International Gas Turbine Institute and presented at the International Gas Turbine and Aeroengine Congress and Exhibition, Orlando, FL, June 2–5, 1997. Manuscript received by the ASME Headquarters March 15, 1997. Paper No. 97-GT-404. Associate Technical Editor: H. A. Kidd.

In the presence of a harmonic excitation of the form

$$F_j(t) = F_j^{(c)} \cos(\omega t + \psi_j) + F_j^{(s)} \sin(\omega t + \psi_j)$$
$$= \mathrm{Re}[\tilde{F}_j e^{i(\omega t + \psi_j)}] \quad j = 1, 2, \ldots, N, \quad (2)$$

where $\tilde{F}_j = F_j^{(c)} - iF_j^{(s)}$, $F_j^{(c)}$, $F_j^{(s)}$, ω, and ψ_j are constants, it is readily shown that the system reaches a steady-state response of the form

$$X_j(t) = U_j \cos(\omega t + \psi_j) + V_j \sin(\omega t + \psi_j)$$
$$= \mathrm{Re}[\tilde{X}_j e^{i(\omega t + \psi_j)}] \quad j = 1, 2, \ldots, N, \quad (3)$$

where $\tilde{X}_j = U_j - iV_j$. Introducing Eq. (2) and (3) into Eq. (1) leads to the linear system of algebraic equations

$$H\underline{\tilde{X}} = \underline{\tilde{F}}, \quad (4)$$

where

$$\underline{\tilde{X}}^T = [\tilde{X}_1 \;\; \tilde{X}_2 \;\; \ldots \;\; \tilde{X}_N] \quad \text{and}$$
$$\underline{\tilde{F}}^T = [\tilde{F}_1 \;\; \tilde{F}_2 \;\; \ldots \;\; \tilde{F}_N] \quad (5,6)$$

and where the superscript symbol T denotes the operation of matrix transposition. Finally, the elements of the $N \times N$ impedance matrix H can be expressed as linear combinations of the components of the mass, damping, and stiffness matrices. This linearity implies that the matrix H corresponding to a mistuned system can be written in terms of its tuned counterpart $\bar{H}$ as

$$H = \bar{H} + \Delta H, \quad (7)$$

where the elements of ΔH are proportional to the random fluctuations in the structural properties of the blades. Then, the steady-state response of the disk can be written as

$$\underline{\tilde{X}} = (\bar{H} + \Delta H)^{-1}\underline{\tilde{F}}. \quad (8)$$

Determination of the Moments

Definitions. The expression for the steady-state response of the bladed disk given by Eq. (8) readily leads to a representation of the mean response vector $\underline{\mu_{\tilde{X}}}$ in the form

$$\underline{\mu_{\tilde{X}}} = E[\underline{\tilde{X}}] = E[(\bar{H} + \Delta H)^{-1}\underline{\tilde{F}}] = E[(\bar{H} + \Delta H)^{-1}]\underline{\tilde{F}}, \quad (9)$$

where the symbol $E[\quad]$ denotes the operation of mathematical expectation. Note that the last equality in Eq. (9) holds only if the forces are purely deterministic. Similarly, two second moment matrices of the response vector $\underline{\tilde{X}}$ can be expressed as

$$K_{\underline{\tilde{X}\tilde{X}}} = E[\underline{\tilde{X}\tilde{X}^T}] = E[(\bar{H} + \Delta H)^{-1}\underline{\tilde{F}\tilde{F}^T}(\bar{H} + \Delta H)^{-T}] \quad (10)$$

and

$$\hat{K}_{\underline{\tilde{X}\tilde{X}}} = E[\underline{\tilde{X}\tilde{X}}^{*T}]$$
$$= E[(\bar{H} + \Delta H)^{-1}\underline{\tilde{F}\tilde{F}}^{*T}(\bar{H} + \Delta H)^{-*T}], \quad (11)$$

where * denotes the operation of complex conjugation. From the vector $\underline{\mu_{\tilde{X}}}$ and the matrices $K_{\underline{\tilde{X}\tilde{X}}}$ and $\hat{K}_{\underline{\tilde{X}\tilde{X}}}$ the first and second order moments of the response of all the blades can be extracted. Specifically,

$$E[U_j] = \mathrm{Re}\{E[\tilde{X}_j]\}; \quad E[V_j] = -\mathrm{Img}\{E[\tilde{X}_j]\}; \quad (12, 13)$$

$$E[U_jU_k] = \tfrac{1}{2}\,\mathrm{Re}\{E[\tilde{X}_j\tilde{X}_k] + E[\tilde{X}_j\tilde{X}_k^*]\} \quad (14)$$

$$E[U_jV_k] = -\tfrac{1}{2}\,\mathrm{Img}\{E[\tilde{X}_j\tilde{X}_k] - E[\tilde{X}_j\tilde{X}_k^*]\} \quad (15)$$

$$E[V_jV_k] = -\tfrac{1}{2}\,\mathrm{Re}\{E[\tilde{X}_j\tilde{X}_k] - E[\tilde{X}_j\tilde{X}_k^*]\}. \quad (16)$$

A Series Expansion Solution. Although Eqs. (9)–(16) provide exact representations of the first moments of the response, the extreme complexity of the mathematical expressions of the elements of the matrix $(\bar{H} + \Delta H)^{-1}$, in terms of the corresponding components of $\bar{H}$ and ΔH, prevents the direct use of these relations in practical applications.

To resolve this difficulty, it has been suggested (see for example Sinha (1986) and Sinha and Chen (1989)) to proceeded with a Neumann expansion of the matrix $(\bar{H} + \Delta H)^{-1}$ in the form

$$(\bar{H} + \Delta H)^{-1} = (I_N + \bar{H}^{-1}\Delta H)^{-1}\bar{H}^{-1}$$
$$\approx \bar{H}^{-1} - (\bar{H}^{-1}\Delta H)\bar{H}^{-1} + (\bar{H}^{-1}\Delta H)^2\bar{H}^{-1}$$
$$+ \ldots + (-1)^n(\bar{H}^{-1}\Delta H)^n\bar{H}^{-1}, \quad (17)$$

where I_N denotes the $N \times N$ identity matrix. The convergence of the above series requires that the eigenvalues of the matrix $\bar{H}^{-1}\Delta H$ all be less than one in magnitude for all possible sets of random structural properties of the blades. Since this condition is difficult to test practically, one can turn to an approximate analysis based on the respective eigenvalues of the matrices $\bar{H}^{-1}$ and ΔH. To this end, note first that the eigenvalues of $\bar{H}^{-1}$ correspond to the steady-state modal amplitudes of response of the tuned system at the excitation frequency ω. Thus, at resonance, one of these eigenvalues will be approximately of the order of $1/2\zeta_j^{(m)}k_j^{(m)}$, where $\zeta_j^{(m)}$ and $k_j^{(m)}$ are the modal damping ratio and stiffness of the mode excited. Further, the magnitude of the remaining eigenvalues will be strongly dependent on the spacing between natural frequencies of the tuned bladed disk. In this context, it has often been noted (see Wei and Pierre (1988) for a discussion) that the blade-to-blade coupling is small so that the natural frequencies of the bladed disk form a series of densely populated groups of frequencies. Then, at resonance, there is not just one but a few eigenvalues of $\bar{H}^{-1}$ that are of the order of $1/2\zeta_j^{(m)}k_j^{(m)}$.

The eigenvalues of ΔH are, as the elements of this matrix, random variables, and, thus, cannot be predicted with absolute certainty. However, it can be expected that they typically will be of the order of σ_k, $\sigma_c\omega$, or $\sigma_m\omega^2$, where σ_k, σ_c, and σ_m denote the standard deviations of the stiffnesses, damping coefficients, and masses of the blades.

Combining these two separate analysis, it is found that the eigenvalues of the matrix $\bar{H}^{-1}\Delta H$ are, for certain sets of structural properties of the blades, of the order of $\sigma_k/2\zeta_j^{(m)}k_j^{(m)}$, $\sigma_m/2\zeta_j^{(m)}m_j^{(m)}$, or $\sigma_c/2\zeta_j^{(m)}\sqrt{k_j^{(m)}m_j^{(m)}}$, where $m_j^{(m)}$ is the modal mass of the mode excited. Further, the probability that these approximate bounds for the eigenvalues of the matrix $\bar{H}^{-1}\Delta H$ are reached or exceeded increases as the structural coupling between the blades decreases because of the corresponding increase in the number of eigenvalues of $\bar{H}^{-1}$ that are close to $1/2\zeta_j^{(m)}k_j^{(m)}$.

The availability of the above eigenvalue estimates allows for a simple, approximate assessment of the reliability of the series expansion given in Eq. (17). Consider, as a typical example, a bladed disk in which only the blade stiffnesses are random with a common standard deviation equal to 2 percent of the tuned modal stiffness. Further, as a representative value, select the corresponding modal damping ratio to be $\zeta_j^{(m)} = 0.01$. Then, $\sigma_k/2\zeta_j^{(m)}k_j^{(m)} = 1$, which represents the maximum allowable value for the eigenvalues of $\bar{H}^{-1}\Delta H$ for the series expansion of Eq. (17) to converge!

It can be concluded from the above discussion that the Neumann expansion given in Eq. (17) does not provide a general purpose technique for the reliable estimation of either the response vector $\underline{\tilde{X}}$ or its moments.

A different perspective on the limitations of Eq. (17) can be obtained by first rewriting Eq. (8) in the form

$$\underline{\tilde{X}} = \bar{H}^{-1}\underline{\tilde{F}} - \bar{H}^{-1}\Delta H\underline{\tilde{X}}. \tag{18}$$

Then, inserting this expression for the complex response vector $\underline{\tilde{X}}$ on the right-hand side of Eq. (18) leads to the relation

$$\underline{\tilde{X}} = \bar{H}^{-1}\underline{\tilde{F}} - \bar{H}^{-1}\Delta H(\bar{H}^{-1}\underline{\tilde{F}} - \bar{H}^{-1}\Delta H\underline{\tilde{X}}). \tag{19}$$

Repeating this process n times finally yields the exact formula

$$\underline{\tilde{X}} = \bar{H}^{-1}\underline{\tilde{F}} - (\bar{H}^{-1}\Delta H)\bar{H}^{-1}\underline{\tilde{F}} + (\bar{H}^{-1}\Delta H)^2\bar{H}^{-1}\underline{\tilde{F}} + \ldots$$
$$+ (-1)^n(\bar{H}^{-1}\Delta H)^n\bar{H}^{-1}\underline{\tilde{F}} + (-1)^{n+1}(\bar{H}^{-1}\Delta H)^{n+1}\underline{\tilde{X}}. \tag{20}$$

The presence of the response vector $\underline{\tilde{X}}$ on both sides of the above equation indicates that this representation is in fact implicit. To obtain an explicit relationship, it is necessary to provide a closure to the recursive evaluation of the vector $\underline{\tilde{X}}$ as given by Eq. (20). Comparing Eq. (17) and (20), it is seen that the series expansion, Eq. (17), is obtained from the exact representation, Eq. (20), by neglecting its last term, i.e., $(-1)^{n+1}(\bar{H}^{-1}\Delta H)^{n+1}\underline{\tilde{X}}$. This assumption is justifiable, as discussed above, when the largest eigenvalue of $\bar{H}^{-1}\Delta H$ is smaller than 1 and n is large enough. These conditions can be assessed by standard numerical techniques when the mistuning term ΔH is specified. However, in the present context of the determination of the first moments of the response of randomly mistuned bladed disks, Eq. (9)–(16), it would be necessary to evaluate the magnitude of the largest eigenvalue of the matrix $\bar{H}^{-1}\Delta H$ for all possible combinations of values of the elements of the mistuning matrix ΔH. Since it is clearly impossible to accomplish this task, one must focus on the estimation of the expectations of the form $E[(\bar{H}^{-1}\Delta H)^{n+1}\underline{\tilde{X}}]$. To this end, note that the nth moment of a random variable Z, $E[Z^n]$, does not, in general, tend to zero as $n \to \infty$. As an example, let Z be normally distributed with zero mean and standard deviation σ. Then,

$$E[Z^n] = \begin{cases} \dfrac{n!}{(n/2)!}\left(\dfrac{\sigma}{\sqrt{2}}\right)^n & \text{for even } n, \\ 0 & \text{for odd } n. \end{cases} \tag{21}$$

Considering the behavior of $E[Z^n]$ as a function of n, it is found that $E[Z^n] \to \infty$ as $n \to \infty$, independently of the magnitude of the standard deviation σ. However, for small values of this parameter, the moments $E[Z^n]$ first decrease until n approximately equals $1/\sigma^2$, then they increase monotonically.

These observations clearly indicate that the term $E[(\bar{H}^{-1}\Delta H)^{n+1}\underline{\tilde{X}}]$ cannot be neglected no matter how large n is selected; this term must either be approximated, or an additional constraint must be expressed. This task will be accomplished in the sequel by relying on the concept of cumulants.

Cumulants. Given the moments $E[Z^n]$ of a random variable, its characteristic function $M_Z(\theta)$ can be computed as

$$M_Z(\theta) = E[e^{i\theta Z}] = \sum_{n=0}^{\infty} \frac{(i\theta)^n}{n!} E[Z^n]. \tag{22}$$

Although this complex-valued function has many important properties in probability theory, its natural logarithm, the log-characteristic function, is of interest here. Specifically, this function admits a Taylor expansion of the form

$$\ln M_Z(\theta) = \kappa_1(i\theta) - \tfrac{1}{2}\kappa_2\theta^2 + \ldots = \sum_{n=1}^{\infty} \kappa_n \frac{(i\theta)^n}{n!}, \tag{23}$$

where κ_n is termed the nth order cumulant of the random variable Z. The cumulants provide a description of the random variable Z that is equivalent to the one provided by the moments. In fact, these two sets of characteristics are related to each other through a general relationship that expresses the nth order cumulant κ_n in terms of the moments $E[Z^m]$ for $m \le n$ (Lin and Cai, 1995). For $n = 1$, 2, and 3, this relationship yields

$$\kappa_1 = E[Z] \quad \kappa_2 = E[Z^2] - \{E[Z]\}^2 \tag{24, 25}$$

and

$$\kappa_3 = E[Z^3] - 3E[Z^2]E[Z] + 2\{E[Z]\}^3. \tag{26}$$

Cumulant Closure. Besides these similarities, important differences exist between cumulants and moments. Of great importance in the present context is the fact that $\kappa_n = 0$ for $n > 2$, if the random variable Z is Gaussian distributed. Further, it has been observed that the cumulants $\kappa_3, \kappa_4, \ldots$ of many non-Gaussian random variables encountered in engineering applications are small and that the neglect of one of them often provides a good approach to the estimation of the dominant features of this random variable (Ibrahim, 1985; Lin and Cai, 1995). This property is the basis for the present estimation technique of the moments of the forced response of mistuned bladed disks. Specifically, the joint moments of the form $E[(\bar{H}^{-1}\Delta H)^{n+1}\underline{\tilde{X}}]$ will be selected so that the corresponding $(n + 1)$st joint cumulant, κ_{n+1}, vanishes (nth order cumulant closure).

Example: Second Order Cumulant Closure. To illustrate the application of the above strategy, consider the determination of the mean values and the second moments of the response of a general mistuned bladed disk through a second order joint cumulant closure. For simplicity, assume first that the mistuning in the structural properties of the bladed disk has zero mean, i.e., $E[\Delta H] = 0$. Then, taking the expected value of both sides of Eq. (19) yields

$$E[\underline{\tilde{X}}] = \bar{H}^{-1}\underline{\tilde{F}} + \bar{H}^{-1}E[\Delta H\bar{H}^{-1}\Delta H\underline{\tilde{X}}]. \tag{27}$$

In terms of components, this matrix-vector equation can be rewritten as

$$E[\tilde{X}_j] = \sum_{k=1}^{N} \bar{H}_{jk}^{-1}\tilde{F}_k + \sum_{k,l,q,s=1}^{N} \bar{H}_{jk}^{-1}\bar{H}_{lq}^{-1}E[\Delta H_{kl}\Delta H_{qs}\tilde{X}_s], \tag{28}$$

where $\bar{H}_{jk}^{-1}$ and ΔH_{jk} denote the jk elements of the matrices $\bar{H}^{-1}$ and ΔH, respectively.

Next, the joint third cumulant of the random variables ΔH_{kl}, ΔH_{qs}, and $\tilde{X}_s$, which is defined as (Lin and Cai, 1995)

$$\kappa_3 = E[\Delta H_{kl}\Delta H_{qs}\tilde{X}_s] - E[\Delta H_{kl}\Delta H_{qs}]E[\tilde{X}_s]$$
$$- E[\Delta H_{kl}\tilde{X}_s]E[\Delta H_{qs}] - E[\Delta H_{qs}\tilde{X}_s]E[\Delta H_{kl}]$$
$$+ 2E[\tilde{X}_s]E[\Delta H_{qs}]E[\Delta H_{kl}], \tag{29}$$

is set to zero. Relying on the zero mean property of the elements of ΔH, this condition reduces simply to

$$E[\Delta H_{kl}\Delta H_{qs}\tilde{X}_s] = E[\Delta H_{kl}\Delta H_{qs}]E[\tilde{X}_s]. \tag{30}$$

Combining Eq. (28) and (30) finally yields the linear system of algebraic equations

$$E[\tilde{X}_j] - \sum_{s=1}^{N} \{ \sum_{k,l,q=1}^{N} \bar{H}_{jk}^{-1}\bar{H}_{lq}^{-1}E[\Delta H_{kl}\Delta H_{qs}] \} E[\tilde{X}_s]$$
$$= \sum_{k=1}^{N} \bar{H}_{jk}^{-1}\tilde{F}_k, \tag{31}$$

which is easily solved for the mean values $E[\tilde{X}_j] = E[U_j] - iE[V_j]$.

Note the complete generality of the present formulation that does not assume that the elements of the mistuning matrix ΔH are independent of each other, nor that the mistuning statistics are the same for each blade, nor any other specific property of the tuned or mistuned system. However, if the tuned and mistuned properties of all the blades are identical, the above set of N equations in N unknowns, N being the total number of degrees of freedom on the entire disk, can be reduced to a $p \times p$ system of equations, where p is the number of degrees of freedom per blade. In any case, denoting by σ^2 a typical variance of the elements ΔH_{kl}, it is seen that Eq. (31) can be written succinctly as

$$A(\sigma^2)E[\underline{\tilde{X}}] = \bar{H}^{-1}\underline{\tilde{F}}. \qquad (32)$$

It should be noted that the role of the mistuning variance σ^2 is quite different in the cumulant closure strategy and in the series expansion, Eq. (17). Namely, it affects both the left and right-hand sides (for higher order cumulants) of the equations in the former approach, while it is present only as a perturbation, i.e., on the right-hand side in the latter technique.

Once the mean values $E[\tilde{X}_j]$ have been computed, higher order moments of the response and the mistuning elements, such as $E[\Delta H_{lq}\tilde{X}_j]$, can also be determined from Eq. (18)–(20). Specifically, multiplying Eq. (18) by ΔH_{lq} and taking expectations of both sides yields the relation

$$\begin{aligned} E[\Delta H_{lq}\tilde{X}_j] &= -\sum_{k,s=1}^{N} \bar{H}_{jk}^{-1} E[\Delta H_{lq}\Delta H_{ks}\tilde{X}_s] \\ &= -\sum_{k,s=1}^{N} \bar{H}_{jk}^{-1} E[\Delta H_{lq}\Delta H_{ks}]E[\tilde{X}_s], \qquad (33) \end{aligned}$$

where the last equality again results from the application of the second order cumulant closure condition, Eq. (30).

The knowledge of all the moments involving the first power of the response vector $\underline{\tilde{X}}$ allows, in turn, the determination, by an appropriate cumulant closure scheme, of the second moment matrices $K_{\underline{\tilde{X}}\underline{\tilde{X}}}$ and $\hat{K}_{\underline{\tilde{X}}\underline{\tilde{X}}}$ of the mistuned response. Specifically, relying again on the second order cumulant closure, postmultiply Eq. (18) by $\underline{\tilde{X}}^T$ and take expectations of both sides of the resulting equation. This process yields the relation

$$K_{\underline{\tilde{X}}\underline{\tilde{X}}} = E[\underline{\tilde{X}}\underline{\tilde{X}}^T] = \bar{H}^{-1}\underline{\tilde{F}}E[\underline{\tilde{X}}^T] - \bar{H}^{-1}E[\Delta H\underline{\tilde{X}}\underline{\tilde{X}}^T] \qquad (34)$$

or, in terms of components,

$$E[\tilde{X}_k\tilde{X}_j] = \sum_{l=1}^{N} \bar{H}_{kl}^{-1}\tilde{F}_l E[\tilde{X}_j] - \sum_{l,q=1}^{N} \bar{H}_{kl}^{-1} E[\Delta H_{lq}\tilde{X}_q\tilde{X}_j]. \qquad (35)$$

Setting to zero the third joint cumulant of ΔH_{lq}, $\tilde{X}_q$, and $\tilde{X}_j$ yields the condition (see Eq. (29))

$$\begin{aligned} &E[\Delta H_{lq}\tilde{X}_q\tilde{X}_j] \\ &\quad = E[\tilde{X}_q]E[\Delta H_{lq}\tilde{X}_j] + E[\tilde{X}_j]E[\Delta H_{lq}\tilde{X}_q]. \qquad (36) \end{aligned}$$

Since the four terms appearing in the right-hand side of the above equation have been determined during the first moments computation, see Eq. (32) and (33), the second moments of the response, $E[\tilde{X}_k\tilde{X}_j]$, can directly be obtained from Eq. (35) and (36). Finally, a similar analysis yields estimates of $E[\tilde{X}_k\tilde{X}_j^*]$, and all second order moments can be determined from Eq. (14)–(16). If necessary, higher order moments of the response could be obtained by proceeding similarly. Computational issues are always very important in all mistuning analyses. In this light, it should be noted that the determination of the moments according to a second order cumulant strategy requires only the solution of a set of linear equations of the same order as the number of degrees of freedom per blade, i.e., as a tuned analysis. Similarly, the third order cumulant approximation requires a computational effort equivalent to the solution of a full disk. In both cases, this is substantially less than a Monte Carlo analysis that requires many (several hundred to several thousand) solutions of the full disk!

Acceleration of Convergence. The determination of the moments of the response of mistuned bladed disks by relying on an nth order cumulant closure scheme can be shown to involve the solution of systems of linear algebraic equations of sizes that increase with the order n. Thus, it is desirable to make the best use possible of low order (2nd, 3rd, . . .) results. This smart use of resources can be accomplished by considering the tuned values (which can be shown to correspond to a first order cumulant closure approximation), 2nd, 3rd, . . . order cumulant closure results not as separate approximate values of the moments, but rather as a convergent sequence of estimates of these values. Then, an acceleration of convergence procedure can be used to forecast the limit of this sequence that corresponds to an order $n \to \infty$ cumulant closure.

To illustrate this procedure, let w_n represent any of the moments sought. Then, this approximation can be expressed as

$$w_n = w_\infty + \Delta w_n, \qquad (37)$$

where w_∞ is the exact value of the moment and Δw_n is the nth order error, or fluctuation. An improved, or accelerated, estimate of w_∞ can be extracted from a set of closure approximations w_n, $n = 1, 2, 3, \ldots$ by modeling the fluctuation terms Δw_n, for example, as a sum of real and complex exponentials, as is done in connection with the Aitken-Shanks transformation (see Greenberg, 1978). That is, let

$$\Delta w_n = \sum_j \alpha_j e^{\lambda_j n}. \qquad (38)$$

This representation of the error terms is quite flexible since it can account for a purely exponential decay or growth, when the parameters λ_j are real, for harmonic fluctuations, when the coefficients λ_j occur in complex conjugate pairs, and are purely imaginary, but also for a harmonically fluctuating, exponentially modulated behavior, when the complex parameters λ_j are present in conjugate pairs. Under this assumed model, it can be shown that the closure estimates w_n, $n = 1, 2, 3, \ldots$, satisfy a linear recurrence relation of the form (see, for example, Oppenheim and Schafer (1975))

$$w_n + a_1 w_{n-1} + a_2 w_{n-2} + \ldots + a_m w_{n-m} = b_0 \qquad (39)$$

for some coefficients a_j, $j = 1, 2, \ldots, m$ and b_0.

The determination of these $m + 1$ parameters requires the knowledge of at least the $2m + 1$ closure results w_n, $n = 1, 2, \ldots, 2m + 1$. Indeed, given these estimates, a linear system of equations for the coefficients a_j and b_0 can be obtained by expressing Eq. (39) for $n = m + 1, m + 2, \ldots, 2m + 1$.

Finally, an accelerated estimate of the moment of the response can be obtained as

$$(w_\infty)_{acc} = \frac{b_0}{1 + \sum_{j=1}^{m} a_j}. \qquad (40)$$

Setting $m = 1$ and using the results of the 1st (=tuned), 2nd, 3rd, . . . order cumulant closure yields an accelerated estimate $(w_\infty)_{acc}$ of any moment w_n in the form

$$(w_\infty)_{acc} = \frac{w_3 w_1 - w_2^2}{w_3 - 2w_2 + w_1}. \qquad (41)$$

Distribution of the Amplitude of Response

Once the moments of the mistuned response of the blades have been determined, it is necessary to estimate the probability density function of the amplitude of response, from which the important issue of fatigue life can reliably be addressed. An accurate model of this function has recently been derived by Mignolet and Lin (1996) by relying on an "adaptive" perturbation scheme (Lin and Mignolet, 1997). According to this technique, the forced response of the blade is computed as a sum of its modal contributions, each of which is either computed exactly or approximated depending on whether the corresponding natural frequency is close or far from the excitation frequency. Relying on this strategy and the central limit theorem, it was found that the amplitude of forced response can be modeled as

$$A_j^2 = \frac{\overline{y}_1^2}{\overline{y}_2^2 + 1}, \tag{42}$$

where $\overline{y}_1$ is a normal random variable with mean $\overline{\mu}_1$ and standard deviation $\overline{\sigma}_1$, and $\overline{y}_2$ is a normal random variable with zero mean and standard deviation $\overline{\sigma}_2$. Further, it has been argued on the basis of a simple bladed disk model that the random variables $\overline{y}_1$ and $\overline{y}_2$ are independent. Then, the probability density function of the amplitude A_j can be expressed as

$$p_A(a) = \frac{1}{\pi \overline{\sigma}_1 \overline{\sigma}_2} \int_1^\infty \frac{s^2}{\sqrt{s^2 - 1}} \exp\left[-\frac{s^2 - 1}{2\overline{\sigma}_2^2} \right]$$

$$\times \left\{ \exp\left[-\frac{(as - \overline{\mu}_1)^2}{2\overline{\sigma}_1^2} \right] + \exp\left[-\frac{(as + \overline{\mu}_1)^2}{2\overline{\sigma}_1^2} \right] \right\} ds. \tag{43}$$

The three parameters $\overline{\mu}_1$, $\overline{\sigma}_1$, and $\overline{\sigma_2}$ can be determined from the knowledge of the three moments $E[V_j]$, $E[V_j^2]$, and $E[U_j^2]$, see Eq. (13), (14), and (16), through the relations

$$E[V_j] = \sqrt{\frac{\pi}{2}} \frac{\overline{\mu}_1}{\overline{\sigma}_2} \exp\left[\frac{1}{2\overline{\sigma}_2} \right] erfc\left[\frac{1}{\sqrt{2}\,\overline{\sigma}_2} \right] \tag{44}$$

$$E[A_j] = E[\sqrt{U_j^2 + V_j^2}] \approx E[V_j] + \frac{1}{2} \frac{E[U_j^2]}{E[V_j]}$$

$$= \frac{1}{\sqrt{2\pi}} \frac{\overline{\mu}_1}{\overline{\sigma}_2} \exp\left[\frac{1}{4\overline{\sigma}_2^2} \right] K_0\left[\frac{1}{4\overline{\sigma}_2^2} \right] \tag{45}$$

and

$$E[A_j^2] = E[U_j^2] + E[V_j^2]$$

$$= \sqrt{\frac{\pi}{2}} \frac{\overline{\sigma}_1^2 + \overline{\mu}_1^2}{\overline{\sigma}_2} \exp\left[\frac{1}{2\overline{\sigma}_2} \right] erfc\left[\frac{1}{\sqrt{2}\,\overline{\sigma}_2} \right], \tag{46}$$

where K_0 and *erfc* are the modified Bessel's function of order 0 and the complimentary error function, respectively. Thus, given estimates of $E[V_j]$, $E[V_j^2]$, and $E[U_j^2]$, the above three nonlinear equations can be solved for the parameters $\overline{\mu}_1$, $\overline{\sigma}_1$, and $\overline{\sigma}_2$. Then, the probability density function of the amplitude of blade response, $p_A(a)$, can be evaluated for all values a by numerically performing the integral given in Eq. (43). This function can, in turn, be used to evaluate all quantities of interest. For example, the probability that the amplitude lies in the interval $[a_1, a_2]$ can be determined by integrating $p_A(a)$ over the domain $a \in [a_1, a_2]$. Although performing these tasks analytically is extremely challenging, they represent only routine numerical computations.

Example of Application

In order to demonstrate the value, both phenomenological and computational, of the cumulant closure technique described in the previous sections, a simple model of a bladed disk was selected in which each blade is represented by a single-degree-of-freedom system (see Fig. 1). Following previous investigations (Sinha, 1986; Sinha and Chen, 1989), the blades will be assumed to have the same mass ($m = 0.0114$ kg), damping coefficient ($c_j = 1.443$ Ns/m, approximately 1 percent of the critical value), but have different stiffnesses. Specifically, the parameters k_j are selected to be independent Gaussian random variables with mean $k_t = 430{,}000$ N/m and standard deviation $\sigma_k = 8{,}000$ N/m. Further, the aerodynamic and structural coupling between blades is modeled by springs and dashpots of common values k_C and c_C. In the present study, different values of k_C will be used, but the parameter c_C is set to zero in all cases. With these assumptions, the matrices $\overline{H}$ and ΔH can be written as

$$\overline{H} = \begin{bmatrix} h_1 & -h_2 & 0 & \cdot & 0 & -h_2 \\ -h_2 & h_1 & -h_2 & \cdot & 0 & 0 \\ 0 & -h_2 & h_1 & \cdot & 0 & 0 \\ \cdot & \cdot & \cdot & \cdot & \cdot & \cdot \\ 0 & 0 & 0 & \cdot & h_1 & -h_2 \\ -h_2 & 0 & 0 & \cdot & -h_2 & h_1 \end{bmatrix} \tag{47}$$

and

$$\Delta H = \begin{bmatrix} k_1 & 0 & 0 & \cdot & 0 & 0 \\ 0 & k_2 & 0 & \cdot & 0 & 0 \\ 0 & 0 & k_3 & \cdot & 0 & 0 \\ \cdot & \cdot & \cdot & \cdot & \cdot & \cdot \\ 0 & 0 & 0 & \cdot & k_{N-1} & 0 \\ 0 & 0 & 0 & \cdot & 0 & k_N \end{bmatrix}, \tag{48}$$

where

$$h_1 = (k_t - m\omega^2 + 2k_C) + ic\omega \tag{49}$$

and

$$h_2 = k_C \tag{50}$$

when $N > 2$.

It is further assumed that the blades are subjected to a resonant rth engine order excitation of the form of Eq. (2) with

$$F_j^{(c)} = F_0 \quad F_j^{(s)} = 0 \quad j = 1, 2, \ldots, N \tag{51}$$

$$\omega = \omega_r = \sqrt{\frac{k_t + 4k_C \sin^2\left(\dfrac{\pi r}{N}\right)}{m}} \quad \text{and} \tag{52}$$

$$\psi_j = \frac{2\pi}{N} r(j - 1) = (j - 1)\Delta\psi. \tag{53}$$

In all numerical examples presented below, the value $F_0 = 1$N has been used.

Second Order Cumulant Closure. Since the first order cumulant closure is, in fact, equivalent to the analysis of the tuned system, the results of the second order scheme should be regarded as only first approximations of the true moments. Nevertheless, the simplicity of the equations it involves allows to obtain an important, qualitative picture of the effects of mistuning on the forced response of bladed disks.

It has been assumed, in the beginning of this section, that both the tuned and mistuned characteristics of the blade properties were the same for each blade. Then, it is expected that each blade will be characterized by the same moments so that $E[U_j] = E[U_s]$, $E[V_j] = E[V_s]$, $E[U_j^2] = E[U_s^2]$, etc. for $j \neq s$. Further, the assumptions of independence and identical distribution of the stiffnesses k_j imply, together with the form of the matrix ΔH, that

$$E[\Delta H_{kl} \Delta H_{qs}] = \sigma_k^2 \delta_{kl} \delta_{kq} \delta_{qs}, \tag{54}$$

where δ_{kl} denotes the Kronecker symbol which equals 1 when $k = l$ and 0 otherwise. Using the above results, it is found that Eq. (31) reduces to the single algebraic equation

$$\{1 - \sigma_k^2 \overline{H}_{jj}^{-1} [\sum_{k=1}^{N} \overline{H}_{jk}^{-1}]\} E[\tilde{X}_j] = [\sum_{k=1}^{N} \overline{H}_{jk}^{-1}] F_0. \tag{55}$$

The term on the right-hand side of the above equation can be recognized as the tuned response of the system. Since this term can be directly computed as $F_0/(ic\omega)$, it is concluded that

$$\sum_{k=1}^{N} \bar{H}_{jk}^{-1} = \frac{1}{ic\omega} \qquad (56)$$

so that Eq. (55) can be written as

$$\left\{1 - \frac{\sigma_k^2 \bar{H}_{jj}^{-1}}{ic\omega}\right\} E[\tilde{X}_j] = \frac{F_0}{ic\omega}. \qquad (57)$$

The determination of the term $\bar{H}_{jj}^{-1}$ requires a more thorough analysis of the properties of the tuned system. More specifically, the circulant character of the matrix $\bar{H}$ implies that its inverse, $\bar{H}^{-1}$, is also circulant and that the discrete Fourier transforms of their respective elements are inverse of each other. Using this property it can be shown that

$$\bar{H}_{jj}^{-1} = \frac{z_0}{k_C(1 - z_0^2)} \left[\frac{2}{1 - z_0^N} - 1\right], \qquad (58)$$

where N denotes the number of blades, and z_0 is the complex number of modulus $|z_0| < 1$, which satisfies the quadratic equation

$$z_0^2 - \frac{(ic\omega + 2k_C \cos \Delta\psi)}{k_C} z_0 + 1 = 0. \qquad (59)$$

Aside from this mathematical definition, the complex number z_0 is a very physical quantity; it characterizes the propagation of a disturbance from blade-to-blade along the disk. In fact, its modulus, $|z_0| < 1$, represents the fraction of the disturbance that is transmitted from one blade to the next. In the absence of damping ($c = 0$), Eq. (59) yields the two solutions $z_0 = e^{i\Delta\psi}$ and $z_0 = e^{-i\Delta\psi}$, which both possess a unit modulus, as expected, since there is no dissipation in the system and the frequency of the excitation (disturbance) ω matches exactly the undamped natural frequency of the tuned system (see Eq. (52)). The corresponding, infinite, value of $\bar{H}_{jj}^{-1}$ is simply indicative of the lack of a steady-state solution. As the damping level increases, the modulus of z_0 becomes less than one, and $\bar{H}_{jj}^{-1}$ remains finite. Interestingly, it is seen from Eq. (58) that the part of $\bar{H}_{jj}^{-1}$ that is first affected by the presence of a small damping is the term z_0^N that represents the fraction of the magnitude of a disturbance that is observed at its point of origin after it has completed one revolution across the disk. This term will be very close to zero, even when $c\omega/k_C \ll 1$ (or $|z_0| \approx 1$), provided that the number of blades, N, is large enough. With this small approximation, it is found that by combining Eqs. (57) and (58), the mean response of the bladed disk is independent of the number of blades it supports. In fact, this finding is not surprising; if a disturbance is dissipated before it propagates at least once around the disk, the circular geometry of the system will not be reflected, and the system will behave as if it had an infinite number of blades. With this small assumption and some algebraic manipulations, it is found that Eq. (58) becomes

$$\bar{H}_{jj}^{-1} = \frac{z_0}{k_C(1 - z_0^2)} = \pm \frac{1}{\sqrt{(-c^2\omega^2 - 4k_C^2 \sin^2 \Delta\psi) + i(4c\omega k_C \cos \Delta\psi)}}, \qquad (60)$$

where the + (−) sign must be selected when $\cos \Delta\psi > 0$ ($\cos \Delta\psi < 0$).

Localization Factor of the Forced Response. In assessing the worth of the cumulant closure approach to the determination of the moments of the forced response, it should first be emphasized that this technique is not a perturbation scheme; no assumption on the magnitude of either the mistuning variance σ_k^2 or the coupling stiffness k_C was made. This statement should also be clear from Eq. (57) and (60) since the corresponding mean response $E[\tilde{X}_j]$ is not represented as a series expansion of any variable σ_k^2 or k_C. In fact, these quantities, together with the damping term $c\omega$ are present in Eq. (57) through a single, dimensionless, quantity $\sigma_k^2 \bar{H}_{jj}^{-1}/ic\omega$. Further, if it is assumed that k_C is "large", $\sigma_k^2 \bar{H}_{jj}^{-1}/ic\omega$, is "small", and the mean response of the blades can be expressed as a power series of σ_k^2, i.e.,

$$E[\tilde{X}_j] = \left[1 + \frac{\sigma_k^2 \bar{H}_{jj}^{-1}}{ic\omega} + \left(\frac{\sigma_k^2 \bar{H}_{jj}^{-1}}{ic\omega}\right)^2 + \ldots\right] \frac{F_0}{ic\omega}. \qquad (61)$$

When it is the coupling stiffness k_C that is the smaller term, one can proceed similarly with a power series expansion in k_C of the term $[1 - \sigma_k^2 \bar{H}_{jj}^{-1}/ic\omega)]$, with respect to its value at $k_C = 0$, i.e., $[1 + (\sigma_k^2/c^2\omega^2)]$.

The above finding that Eq. (57) admits separate series expansion in the limit of "large" and "small" k_C clearly indicates that the cumulant closure method is not a perturbation technique with respect to a specific configuration (the tuned system, the uncoupled disk, or any other configuration) but rather an approximation strategy over the entire range of values of the system parameters. On this basis and in view of the preeminent role of $\sigma_k^2 \bar{H}_{jj}^{-1}/ic\omega$ in Eq. (57), it is suggested to introduce the modulus of this dimensionless quantity as the localization factor for forced response, γ_F, i.e.,

$$\gamma_F = \left|\frac{\sigma_k^2 \bar{H}_{jj}^{-1}}{ic\omega}\right| = \frac{\sigma_k^2}{c\omega[(c^2\omega^2 + 4k_C^2 \sin^2 \Delta\psi)^2 + (4c\omega k_C \cos \Delta\psi)^2]^{1/4}}. \qquad (62)$$

Then, it is seen from Eq. (61) and (62) that $\gamma_F = 1$ represents the limit of convergence of the large coupling series approximation.

The plots of the real and imaginary parts and modulus (γ_F) of $\sigma_k^2 \bar{H}_{jj}^{-1}/ic\omega$, see Fig. 2 and 3, for the parametric values given above and both the zeroth and third engine order ($r = 0, 3$) demonstrate that these quantities display a very rapid behavior in the domain $k_C \in [0, c\omega]$. Further, both the real part of $\sigma_k^2 \bar{H}_{jj}^{-1}/ic\omega$ and γ_F exhibit a monotonic behavior with maxima at $k_C = 0$ equal to $\pm\sigma_k^2/c^2\omega^2$ ("+" for γ_F and "−" for $\mathrm{Re}[\sigma_k^2 \bar{H}_{jj}^{-1}/ic\omega]$). On the contrary, the imaginary part of $\sigma_k^2 \bar{H}_{jj}^{-1}/ic\omega$, which is associated with the mean value $E[U_j]$, displays a sharp maximum at an intermediate value of k_C, $k_C \approx 0.4c\omega$.

Acceleration of Convergence. The method of acceleration of convergence described by Eq. (41) was used in connection with the tuned response of the system (=first order), and the results of the second and third order cumulant closure technique to provide estimates of the moments $E[U_j]$, $E[V_j]$, $E[U_j^2]$, and $E[V_j^2]$ for the single-degree-of-freedom per blade model shown in Fig. 1 with the numerical values given above. Displayed in

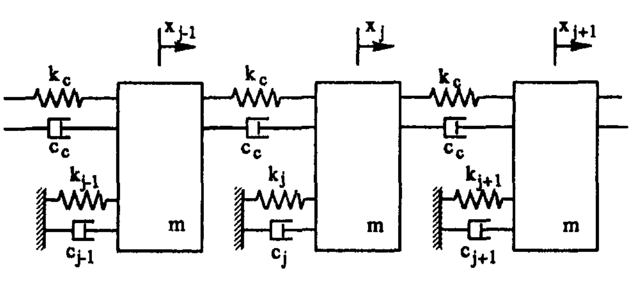

Fig. 1 One d.o.f. per blade bladed disk model

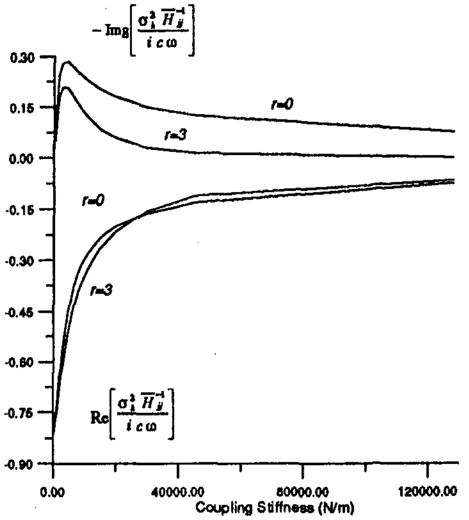

Fig. 2 Real and imaginary parts of $\sigma_k^2 \overline{H}_{jj}^{-1}/ic\omega$, Eq. (60), as a function of coupling stiffness for zeroth and third engine order

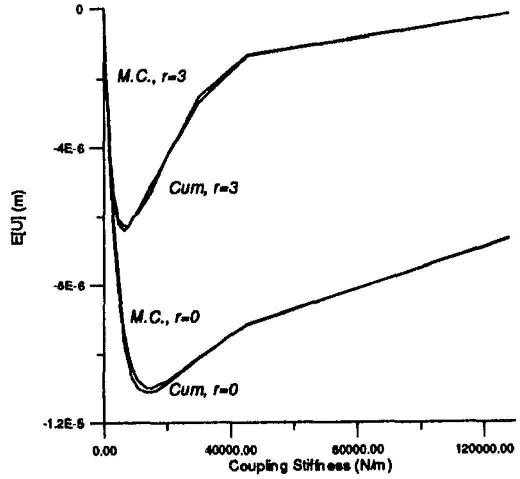

Fig. 4 Comparison of values of $E[U_j]$ computed by Monte Carlo simulation (M.C.) and cumulant closure (Cum) for zeroth and third engine orders

Fig. 4 is a comparison of the cumulant closure estimates of $E[U_j]$ and the corresponding exact means computed by Monte Carlo simulation for values of the coupling stiffness $k_C \in [0, 128000]$ N/m (for both zeroth and third engine orders). It is clearly seen that the acceleration of convergence has provided extremely accurate estimates of $E[U_j]$ for all values of k_C and for both engine orders. The corresponding comparison for $E[V_j]$, presented in Fig. 5, confirms the reliability of the cumulant closure technique with acceleration of convergence. The accuracy of the estimates of the second moments $E[U_j^2]$ and $E[V_j^2]$ was found to be excellent as well, except in the domain $k_C \in [0, 6000]$ where the acceleration of convergence underestimated the exact values of these moments. Since, in that small domain, the system is almost uncoupled, the "weak" coupling series expansion (Wei and Pierre, 1988) was used to provide an improved estimate of the moments. Then, an interpolation strategy was employed to obtain a uniformly valid expression for $E[U_j^2]$ and $E[V_j^2]$. This approximation and the exact values, computed by Monte Carlo simulation, are presented in Fig. 6 and 7. Clearly, the accuracy of these estimates is excellent. Additional results, not presented here, have been obtained with double and half the damping used in Figs. 4–7. In all cases, reliable estimates of the moments have been obtained, although a decrease in accuracy with decreasing damping (below 1 percent of critical) has been observed. In these cases, it is recommended to rely also on the results of the fourth order cumulant.

Distribution of the Amplitude of Response. The accurate estimates of the moments $E[V_j]$, $E[U_j^2]$, and $E[V_j^2]$, which have been obtained by relying on the cumulant closure technique with acceleration of convergence, have been used to first predict the values of the three parameters $\bar{\mu}_1$, $\bar{\sigma}_1$, and $\bar{\sigma}_2$, by solving Eq. (44)–(46). Then, estimates of the probability density function of the amplitude of response can be determined from Eq. (43) by numerical integration. Shown in Figs. 8 and 9 are the probability density functions corresponding to the reference coupling stiffness, $k_C = 45{,}430$ N/m, and to both the zeroth and third engine order excitation, respectively—computed by Monte Carlo simulation (M.C.) and by the cumulant closure technique coupled with Eq. (43)–(46). The excellent agreement between these two sets of curves, especially in the important high amplitude tail of the distribution, demonstrates the accuracy of not only the cumulant closure technique, but also the three-parameter model derived by Mignolet and Lin (1996).

Comparison With Perturbation Solutions. It has been shown in the previous sections that the proposed joint cumulant closure strategy provides a reliable basis for the estimation of both the moments and the probability density function of the amplitude

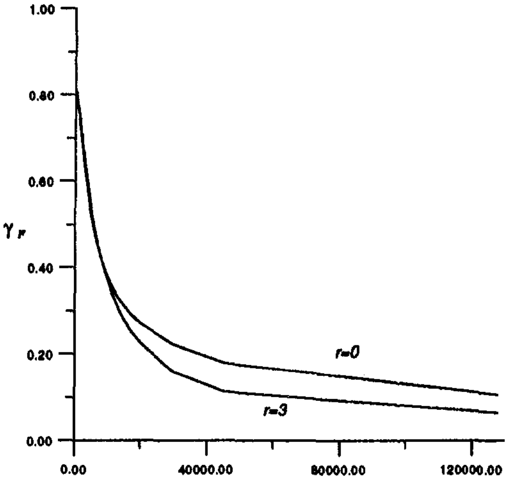

Fig. 3 $\gamma_F = |\sigma_k^2 \overline{H}_{jj}^{-1}/ic\omega|$, Eq. (62), as a function of coupling stiffness for zeroth and third engine order

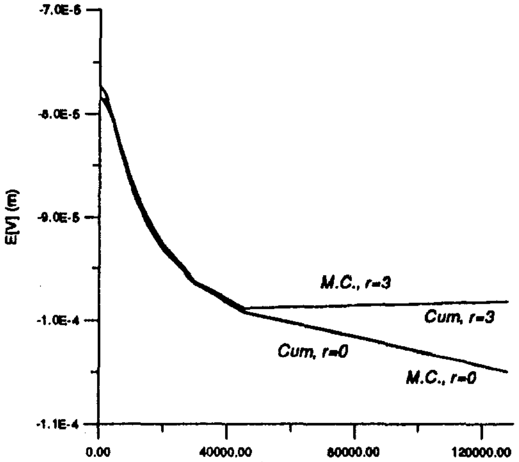

Fig. 5 Comparison of values of $E[V_j]$ computed by Monte Carlo simulation (M.C.) and cumulant closure (Cum) for zeroth and third engine orders

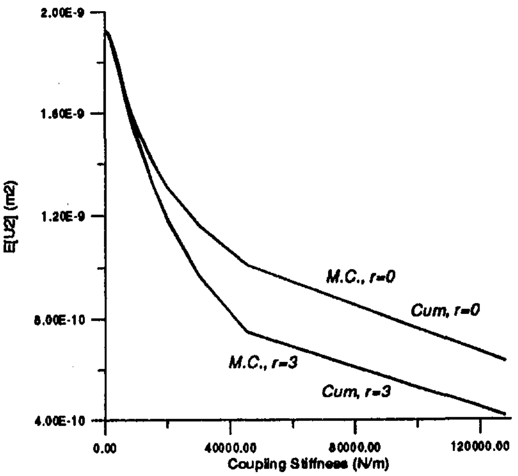

Fig. 6 Comparison of values of $E[U_j^2]$ computed by Monte Carlo simulation (M.C.) and cumulant closure (Cum) for zeroth and third engine orders

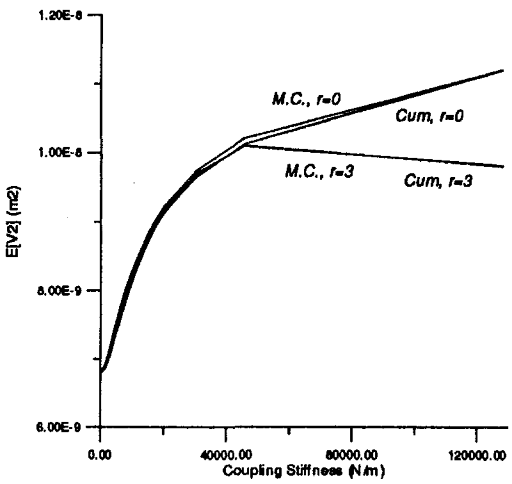

Fig. 7 Comparison of values of $E[V_j^2]$ computed by Monte Carlo simulation (M.C.) and cumulant closure (Cum) for zeroth and third engine orders

of blade response. It is now in order to assess the advantages of this formulation with respect to published perturbation approaches, i.e., the "regular" perturbation method (Sinha and Chen, 1989) and the "modified" one (Wei and Pierre, 1988). Shown in Table 1 are the percentages of error of the estimates of $E[V_j]$ obtained by these two techniques and by the present strategy for a third engine order excitation and for various values of k_C. These results clearly show that the applicability of both the regular and the modified perturbation techniques to the prediction of the mean value $E[V_j]$ is limited to very large and very low values of k_C, respectively. Further, additional data, not presented here for brevity, has demonstrated that the errors on the other moments of the response are, in fact, consistently larger for both methods and for all values of the coupling stiffness. Finally, in analyzing this table, note in particular that the study of the maximum of the blade response (see Ottarsson and Pierre (1995)) has emphasized the neighborhood of $k_C = 8000$ N/m as a worst case scenario. Then, an error in the critical area of at least 10 percent on all moments should be expected by using any of the two perturbation techniques.

This error, which might at first be considered admissible, leads to dramatic errors in the probability density function of the amplitude of blade response. To demonstrate the sensitivity of this function to small changes/errors in the moments, the coupling stiffness was selected as $k_C = 20{,}000$ N/m and the probability density function of the blade response was computed by Monte Carlo and by relying on Eq. (43)–(46) with the estimates of the moments computed by (i) the proposed cumulant closure and (ii) by the regular perturbation for $E[V_j]$ and by the cumulant closure for the other moments. In view of the numerical results presented in Table 1, it is seen that the cases (i) and (ii) differ only by a variation, in the first moment, of approximately 2 percent. Yet, as can be observed on Fig. 10, this small change in $E[V_j]$ leads to a dramatic error in the estimate of the probability density function of the amplitude of blade response! Thus, the prediction of the probabilistic features of the forced response cannot be accurately accomplished on the basis of the published perturbation techniques. On the contrary, the cumulant closure strategy does provide the required reliable estimates of the moments.

Summary

In this investigation, the determination of reliable estimates of the values of the first few moments of the resonant response of a mistuned bladed disk and their use in estimating the distribution of the amplitude of blade vibration have been addressed. The contributions of this study can be summarized as follows.

1 A novel technique for the estimation of the moments of the forced response has been described that relies on the neglect of one of the "joint cumulants" of the response and the mistuned structural properties. Although these characteristics of the response are intimately related to the moments, they generally display a more stable behavior than the moments do, and, thus, are more suited to be approximated. It was demonstrated that this approach, which involves only the solution of linear algebraic equations, is not a perturbation scheme but is an estimate of all required moments over the entire range of blade-to-blade coupling strengths. Further, the technique is adaptive in the sense that the accuracy of the estimates of the moments can be improved by imposing the neglect of a higher order joint cumulant. The computational issues of this approach were briefly addressed, and it was noted that the determination of the moments according to a second order cumulant strategy requires only the solution of a set of linear equations of the same order as the number of degrees of freedom per blade, i.e. as a tuned analysis. Similarly, the third order cumulant approximation requires a computational effort equivalent to the solution of a full disk. In both cases, this is substantially less than a Monte Carlo analysis that requires many (several hundred to several thousand) solutions of the full disk!

2 The investigation of the first order approximation (second order cumulant closure) of the moments of the forced response has shown that these characteristics depend on the blade-to-blade coupling, the damping in the system, and the mistuning

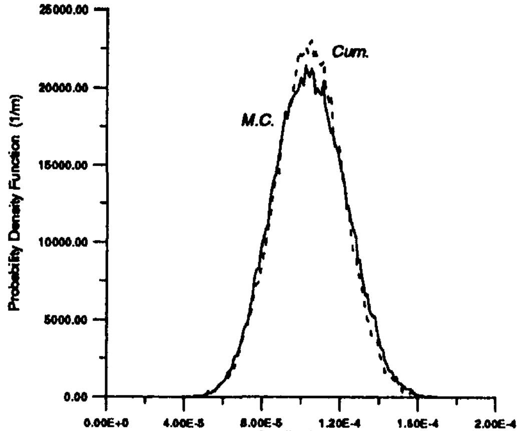

Fig. 8 Probability density function of the amplitude of blade response computed by Monte Carlo simulation (M.C.) and through cumulant closure and Eq. (43)–(46) (Cum.), zeroth engine order

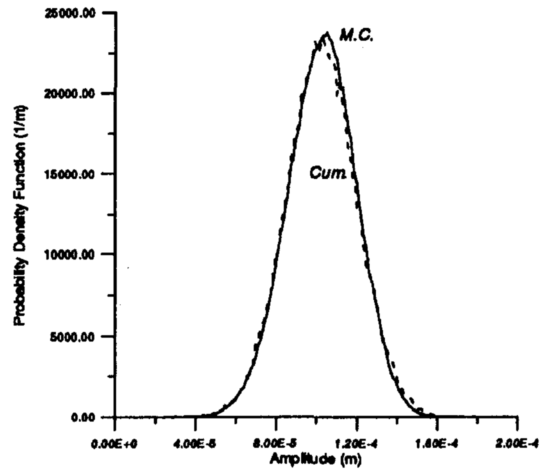

Fig. 9 Probability density function of the amplitude of blade response computed by Monte Carlo simulation (M.C.) and through cumulant closure and Eq. (43)-(46) (Cum.), third engine order

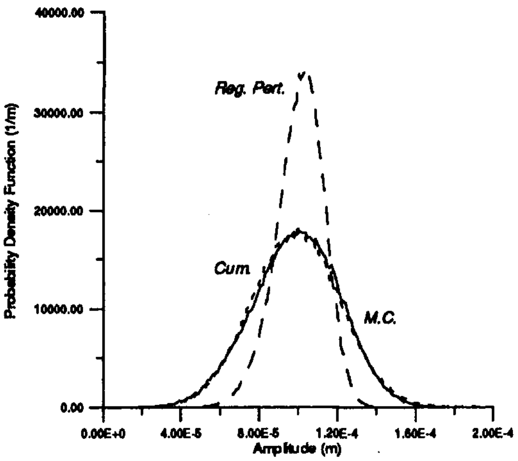

Fig. 10 Probability density function of the amplitude of blade response computed by Monte Carlo simulation (M.C.) and Eq. (43)-(46) through cumulant closure (Cum.) and regular perturbation (Reg. Pert.), k_c = 20,000 N/m, third engine order

level through a single complex parameter $(\sigma_k^2 \bar{H}_{jj}^{-1}/ic\omega$, see Eq. (58) and (60)), the modulus of which $(\gamma_F$, see Eq. (62)) is a bonafide measure of the localization effect of the forced response of the bladed disk. This parameter was found to sharply and monotonically increase, see Fig. 3, as the blade-to-blade coupling is reduced below the damping level in the system.

3 An acceleration of convergence scheme was introduced that relies on the estimates of the moments computed by a first (=tuned analysis), second, and third order cumulant closure approach to yield an improved approximation of the exact values of these moments. This acceleration of convergence was accomplished by modeling the fluctuations of the sequence of estimates of the moments with respect to their true values as linear combinations of exponentials terms (real or complex). This representation of the fluctuations is quite flexible but is also very convenient since the corresponding sequence of estimates satisfies a linear difference equation, the coefficients of which are readily determined from a linear system of equations. Once these parameters have been computed, revised, or accelerated, estimates of the moments are easily obtained, see Eq. (40) or (41).

4 The connection between the computed moments and the distribution of the amplitude of blade response has been accomplished by relying on a recently introduced three-parameter model of its probability density function. Given the moments of the response, the three parameters of the model can be determined by solving Eqs. (44)-(46). Then, the probability density function of the amplitude of blade response is determined by performing the numerical integration of Eq. (43).

5 A numerical assessment of the reliability of the estimates of the moments obtained by the proposed method was accomplished by considering a one-degree-of-freedom per blade bladed disk model in which the level of the structural coupling between the blades was varied. The results of this parametric study clearly demonstrate that the accelerated estimates of the moments of the response are extremely close to their exact values in all cases investigated. In fact, a maximum relative error of 1 percent was generally observed. These estimates of the moments were then used to predict the distribution of the amplitude of blade response. Again, an excellent agreement with Monte Carlo simulation results was obtained, see Fig. 8 and 9. Finally, a comparison with existing perturbation approaches has clearly demonstrated the increased accuracy obtained with the proposed joint cumulant closure formulation, see Fig. 10 and Table 1.

Table 1 Errors in the prediction of the first order moment $E[V_j]$ obtained by using the "regular perturbation" technique (fourth order), the "modified perturbation" technique (second order in k_C), and the accelerated cumulant closure

k_C (N/m)	2,000	4,543	8,000	11,000	15,000	20,000	45,430
Error (%) Reg. Pert.	99.96	25.90	11.05	7.00	3.95	2.03	0.38
Error (%) Mod. Pert.	0.82	4.14	11.20	22.90	42.40	79.90	430.97
Error (%) Acc. Cum.	1.22	0.46	0.18	0.14	0.18	0.11	0.08

Acknowledgment

The financial support of this work by the Naval Surface Warfare Center, Caderock Division, Department of the Navy, Bethesda, MD 20084 is gratefully acknowledged.

References

Basu, P., and Griffin, J. H., 1986, "The Effects of Limiting Aerodynamic and Structural Coupling in Models of Mistuned Bladed Disk Vibration," *Journal of Vibration, Acoustics, Stress, and Reliability in Design,* Vol. 108, pp. 132-139.

Ewins, D. J., 1969, "The Effects of Detuning Upon the Forced Vibrations of Bladed Disks," *Journal of Sound and Vibration,* Vol. 9, pp. 65-79.

Greenberg, M. D., 1978, *Foundations of Applied Mechanics,* Prentice-Hall, Englewood Cliffs, New Jersey.

Ibrahim, R. A., 1985, *Parametric Random Vibrations,* Research Studies Press, John Wiley and Sons, New York.

Kielb, R. E., and Kaza, K. R. V., 1984, "Effects of Structural Coupling on Mistuned Cascade Flutter and Response," ASME JOURNAL OF ENGINEERING FOR GAS TURBINES AND POWER, Vol. 106, pp. 17-24.

Lin, C. C., and Mignolet, M. P., 1997, "An Adaptive Perturbation Scheme for the Analysis of Mistuned Bladed Disks," ASME JOURNAL OF ENGINEERING FOR GAS TURBINES AND POWER, Vol. 119, pp. 153-160.

Lin, Y. K., and Cai, G. Q., 1995, *Probabilistic Structural Dynamics: Advanced Theory and Applications,* McGraw-Hill, New York.

Mignolet, M. P., and Lin, C. C., 1996, "A Novel Limit Distribution for the Analysis of Randomly Mistuned Bladed Disks," ASME Paper 96-GT-414, presented at Turbo Expo '96, Birmingham, United Kingdom.

Oppenheim, A. V., and Schafer, R. W., 1975, *Digital Signal Processing,* Prentice-Hall, Englewood Cliffs, New Jersey.

Ottarsson, G., and Pierre, C., 1995, "On the Effects of Interblade Coupling on the Statistics of Maximum Forced Response Amplitudes in Mistuned Bladed Disks," *Proceedings of the Structures, Structural Dynamics and Materials Conference,* AIAA-95-1494-CP, pp. 3070-3078.

Sinha, A., 1986, "Calculating the Statistics of Forced Response of a Mistuned Bladed Disk Assembly," *AIAA Journal,* Vol. 24, pp. 1797-1801.

Sinha, A., and Chen, S., 1989, "A Higher Order Technique to Compute the Statistics of Forced Response of a Mistuned Bladed Disk," *Journal of Sound and Vibration,* Vol. 130, pp. 207-221.

Wei, S.-T., and Pierre, C., 1988, "Localization Phenomena in Mistuned Assemblies with Cyclic Symmetry: Part II—Forced Vibrations," *Journal of Vibration, Acoustics, Stress, and Reliability in Design,* Vol. 110, No. 4, pp. 439-449.

Whitehead, D. S., 1966, "Effect of Mistuning on the Vibration of Turbomachines Blades Induced by Wakes," *Journal of Mechanical Engineering Science,* Vol. 8, pp. 15-21.

The Effect of Misalignment on Rotor Vibrations

J. L. Nikolajsen
Staffordshire University,
School of Engineering,
Stafford, ST18 0AD,
England

Rotors with three or more fluid-film bearings (or fluid seals) have "redundant" supports, and, therefore, interdependent bearing loads that are generally unknown both in magnitude and direction. The steady-state bearing eccentricities and the dynamic stiffness and damping coefficients of the bearings are, therefore, also unknown since both are functions of the bearing loads. Thus, the dynamic behavior of multibearing rotors generally cannot be predicted with good accuracy without access to a procedure for calculating the steady-state bearing loads and eccentricities. This paper outlines such a procedure in terms of both the influence coefficient method, the transfer matrix method, and the finite element method. Radial bearing misalignment and flexibility of the bearing back-up structures are accounted for. Once the eccentricities are available, the bearing stiffness and damping coefficients can be calculated in the usual way and used to predict critical speeds, instability threshold speed, and rotor response to imbalance. A numerical example is presented that illustrates some of the nonlinear effects of bearing support redundancy, notably the large variations in instability threshold speed with radial bearing misalignment. The example shows how the method can be used to determine the level of bearing misalignment that leads to optimum rotor stability. It is concluded that no simple guide lines exist by which optimum stability can be achieved. Neither perfect bearing alignment nor equal load sharing between bearings necessarily lead to optimum stability.

Introduction

Some types of turbomachinery, such as pumps and turbogenerators, have rotors with several journal bearings and/or fluid seals. The resulting support redundancy makes the steady-state bearing loads interdependent and difficult to calculate. The bearing eccentricities and the dynamic bearing coefficients are equally difficult to obtain since both are nonlinear functions of the bearing loads. Bearing misalignment and flexibility of the back-up structure further complicates the calculations. Thus, poor accuracy can be expected in the predicted rotordynamic characteristics for machines with multibearing rotors unless specially designed software is used to calculate the bearing loads or eccentricities. As an example, it is well-known that if a plain journal bearing is misaligned so that it does not carry its full load, it becomes a potential source of rotor instability. However, since bearing alignment is usually adjustable, it could potentially be used as a means of improving rotor stability. The problem is that the adjustments leading to optimum stability are generally unknown and difficult to determine because of the interdependence between the bearing loads.

This paper provides a method for calculating the coupled bearing loads and eccentricities for multibearing rotor systems, thus allowing the dynamic characteristics of such rotors to be determined with the same accuracy as for simple rotors without support redundancy. Any rotor system can be analyzed as long as the usual bearing and seal data are available relating the steady-state load (Sommerfeld number) to eccentricity and attitude angle. For unsymmetric bearings, this data is required for all load directions. The analysis procedure, briefly stated, is to calculate the steady-state bearing eccentricities and attitude angles from a nonlinear simultaneous equation system derived from force and moment equilibrium equations for the rotor. The implementation of the method will be outlined in terms of both the IC (influence coefficient) method, the FE (finite element) method, and the TM (transfer matrix) method because of the fundamental differences between the three. Once the eccentricities have been determined, the hydrodynamic stiffness and damping coefficients for all the bearings can be calculated in the usual manner, and the natural frequencies, mode shapes, unbalance response, and instability threshold speed can be predicted with standard rotor programs (e.g., Lund (1974); Nelson (1976)) with the same accuracy as for rotors without support redundancy.

This work builds in part on theory developed in Nikolajsen (1978), Nikolajsen and Gajan (1988), and Kelly (1989). The only other published works in this area, known to the author, are those of Rieger (1970) and Takagi (1980). Rieger (1970) appears to be the first to analyze misalignment effects, but his method is too rudimentary for practical use. Takagi (1980) mentions a practical method in existence, but gives no details. Other publications on multibearing rotors, including Tondl (1965) and Morton (1972), ignore the effect entirely.

Bearing Eccentricity Calculation

The steady-state bearing eccentricities are calculated here with the assumption that no moment reactions occur either at the bearings or at the seals. This is still the conventional assumption, although theoretical moment coefficients are available for seals, see, for example, Childs (1981). The following derivations can be extended to include such moment reactions. Implementation in terms of both the IC, FE, or TM method is described for use in rotor programs based on these methods. The IC method is considered to be conceptually the simplest and will be presented first.

The Influence Coefficient Method. Figure 1 shows the steady-state equilibrium position J of the journal within the flexibly supported bearing. Three forces, acting on the journal, are in static equilibrium: P (the bearing's share of the

---

Contributed by the International Gas Turbine Institute and presented at the 41st International Gas Turbine and Aeroengine Congress and Exhibition, Birmingham, United Kingdom, June 10–13, 1996. Manuscript received by the ASME Headquarters January 31, 1996. Paper No. 96-GT-373. Associate Technical Editor: J. N. Shinn.

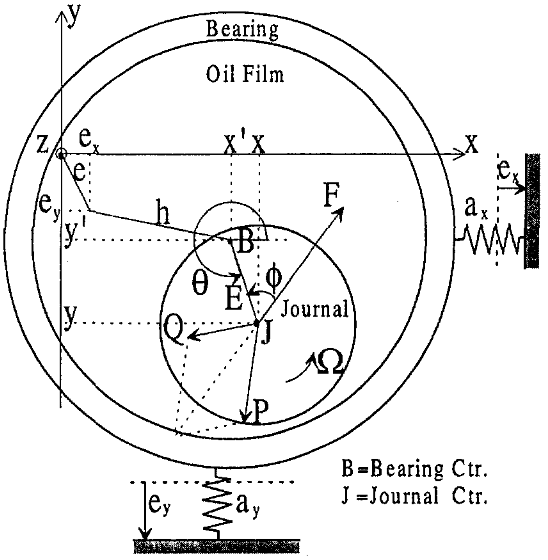

Fig. 1 Steady-state equilibrium in journal bearing

rotor weight), F (the hydrodynamic fluid-film force), and Q (the elastic restoring force from the shaft). Thus, for bearing no. j

$$Q_{xj} = F_j \cos(\theta_j - \phi_j) - P_{xj}$$

$$Q_{yj} = F_j \sin(\theta_j - \phi_j) - P_{yj}. \qquad (1)$$

P is, by definition, set equal and opposite to the support reactions that would exist if all the bearings and seals were replaced by perfectly aligned pinned supports. P can, therefore, be found by the standard flexibility influence coefficient method for statically indeterminate beams, see, for example, Argyris (1958). The influence coefficients for a shaft with variable cross section can be derived as outlined in Vernon (1967). They are listed in Nikolajsen (1978).

Figure 2 shows the total static shaft displacements at the bearing locations, z_1 through z_4, for a four-bearing rotor. The shaft displacements consist of (1) the elastic shaft deflections d, relative to the end bearings, (2) the bearing eccentricities E, (3) the elastic displacements h of the flexible bearing housings, and (4) the bearing misalignments e relative to the end bearings, as measured before the rotor is installed. By means of Fig. 2, the following generalized expressions can be deduced for the elastic shaft deflections d:

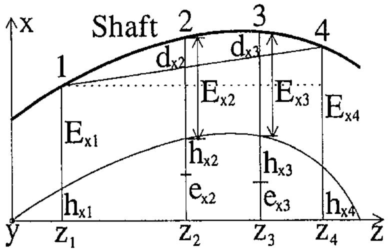

Fig. 2 Shaft displacement components

$$d_{xi} = -(E_{xl} + h_{xl})(z_n - z_i)/(z_n - z_l) + E_{xi} + h_{xi} + e_{xi} - (E_{xn} + h_{xn})(z_i - z_l)/(z_n - z_l)$$

$$2 \le i \le n - 1 \qquad (2)$$

$$d_{yi} = -(E_{yl} + h_{yl})(z_n - z_i)/(z_n - z_l) + E_{yi} + h_{yi} + e_{yi} - (E_{yn} + h_{yn})(z_i - z_l)/(z_n - z_l).$$

The bearing housing displacements h can be expressed in terms of the hydrodynamic bearing forces F and the housing flexibilities a by

$$\begin{aligned} h_{xi} &= a_{xi} F_i \cos(\theta_i - \phi_i) \\ h_{yi} &= a_{yi} F_i \sin(\theta_i - \phi_i). \end{aligned} \quad 1 \le i \le n \qquad (3)$$

Alternative expressions for d can be written in terms of the shaft elastic restoring forces Q and the shaft flexibility influence coefficients a_{ij} as follows:

$$d_{xi} = -\sum_{j=2}^{n-1} a_{ij} Q_{xj} = -\sum_{j=2}^{n-1} a_{ij}[F_j \cos(\theta_j - \phi_j) - P_{xj}]$$

$$2 \le i \le n - 1 \qquad (4)$$

$$d_{yi} = -\sum_{j=2}^{n-1} a_{ij} Q_{yj} = -\sum_{j=2}^{n-1} a_{ij}[F_j \sin(\theta_j - \phi_j) - P_{yj}],$$

where Q has been substituted from Eqs. (1).

Equations (2), (3), and (4) combine to give

$$-[c_1\epsilon_1 \cos\theta_1 + a_{x1}F_1 \cos(\theta_1 - \phi_1)](z_n - z_i)/(z_n - z_l)$$
$$+ c_i\epsilon_i \cos\theta_i + a_{xi}F_i \cos(\theta_i - \phi_i)$$
$$+ \sum_{j=2}^{n-1} a_{ij}[F_j \cos(\theta_j - \phi_j) - P_{xj}]$$

Nomenclature

a_{ij} = flexibility influence coefficient for simply supported shaft = radial deflection of station i due to unit force at station j
a_{xi}, a_{yi} = back-up structure flexibilities at bearing (or seal) no. i
c = radial bearing (or seal) clearance
d = elastic shaft deflection
e = radial bearing (or seal) misalignment
E = bearing (or seal) eccentricity or elastic modulus of shaft material
F = hydrodynamic fluid-film force
h = bearing (or seal) housing radial displacement
I = second moment of area of shaft cross section
K, k = seal stiffness (direct and cross-coupled)
l = length of shaft element
n = number of bearings and seals
N = total number of shaft stations
P = external force on journal
Q = internal shaft elastic restoring force
x, y = radial displacements
z = axial bearing (or seal) location
$\epsilon = E/c$ = bearing (or seal) eccentricity ratio
θ, ϕ = angular displacements
θ = direction angle of E
ϕ = bearing attitude angle
μ = oil viscosity
Ω = shaft rotational speed

$$
\begin{aligned}
&-[c_n\epsilon_n \cos\theta_n + a_{xn}F_n \cos(\theta_n - \phi_n)] \\
&\qquad\qquad \times (z_i - z_l)/(z_n - z_l) + e_{xi} = 0 \qquad (5)
\end{aligned}
$$

and

$$
\begin{aligned}
&-[c_1\epsilon_1 \sin\theta_1 + a_{y1}F_1 \sin(\theta_1 - \phi_1)](z_n - z_i)/(z_n - z_l) \\
&\quad + c_i\epsilon_i \sin\theta_i + a_{yi}F_i \sin(\theta_i - \phi_i) \\
&\quad + \sum_{j=2}^{n-1} a_{ij}[F_j \sin(\theta_j - \phi_j) - P_{yj}] \\
&\quad -[c_n\epsilon_n \sin\theta_n + a_{yn}F_n \sin(\theta_n - \phi_n)] \\
&\qquad\qquad \times (z_i - z_l)/(z_n - z_l) + e_{yi} = 0. \qquad (6)
\end{aligned}
$$

Moment equilibrium of the external forces for the entire shaft about the end bearing positions results in

$$\sum_{j=1}^{n-1} [F_j \cos(\theta_j - \phi_j) - P_{xj}](z_n - z_j) = 0 \qquad (7)$$

$$\sum_{j=1}^{n-1} [F_j \sin(\theta_j - \phi_j) - P_{yj}](z_n - z_j) = 0 \qquad (8)$$

$$\sum_{j=2}^{n} [F_j \cos(\theta_j - \phi_j) - P_{xj}](z_j - z_l) = 0 \qquad (9)$$

$$\sum_{j=2}^{n} [F_j \sin(\theta_j - \phi_j) - P_{yj}](z_j - z_l) = 0. \qquad (10)$$

Equations (5) through (10) constitute a set of $2n$ nonlinear simultaneous equations from which the magnitudes ϵ and directions θ of the n eccentricity ratios can be found. The equations are nonlinear because the bearing forces F_j are nonlinear functions of ϵ_j and θ_j, as given in the literature, e.g., Lund (1965). For seals, however, F is usually assumed to be a linear function of ϵ, see Childs (1981).

Equations (5) through (10) were solved by a combined steepest-descend/Newton-Raphson iteration algorithm due to Powell (1970). The method was found to be efficient and stable with almost global convergence.

The Finite Element Method. Using a standard finite element rotor model, e.g., Nelson (1976), the steady-state equilibrium equations for a flexible rotor can be written as follows:

$$[K_0]\{X\} = \{F\} - \{P\}, \qquad (11)$$

where $[K_0]$ is the unsupported shaft FE stiffness matrix (a known matrix of order four times the number of shaft stations). Vector $\{X\}$ contains the x and y-components of the radial and angular shaft displacements at all the FE nodes, including the bearing and seal-eccentricity components E_x and E_y, which are being sought. $\{F\}$ is an unknown vector containing the x and y-components of the hydrodynamic bearing and seal forces, which are known functions of the bearing and seal eccentricity components E_x and E_y. $\{P\}$ is a known vector containing x and y-components of all the external forces acting on the journal, including the rotor weight.

By reference to Fig. 1, the x and y-components of the bearing eccentricity E, can be expressed as the difference between the location of the journal center and the location of the bearing center, i.e.,

$$
\begin{aligned}
E_x &= x - x' \\
E_y &= y - y'. \qquad (12)
\end{aligned}
$$

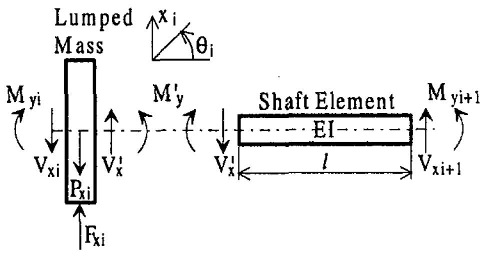

Fig. 3 Discrete shaft model for transfer matrix analysis

Also, the hydrodynamic bearing forces $F_x(E)$ and $F_y(E)$ can be expressed in terms of the housing flexibilities a_x and a_y, and the bearing misalignments e_x and e_y as

$$
\begin{aligned}
F_x &= (e_x - x')/a_x \\
F_y &= (e_y - y')/a_y
\end{aligned}
$$

from which

$$
\begin{aligned}
x' &= e_x - a_xF_x \\
y' &= e_y - a_yF_y. \qquad (13)
\end{aligned}
$$

Substitution of Eqs. (12) and (13) into Eqs. (11) leads to

$$
\begin{aligned}
[K_0]\{\{X'\} + \{E\}\} &= [K_0]\{\{e\} - \{aF\} + \{E\}\} \\
&= \{F\} - \{P\}
\end{aligned}
$$

or

$$[K_0]\{E\} = [[I] + [K_1]]\{F\} - \{P_1\}, \qquad (14)$$

where $\{P_1\} = \{P\} + [K_0]\{e\}$ is a known vector of constant forces. $[K_1]$ is equal to $[K_0]$, except for the columns associated with bearing and seal locations that have been multiplied by the support flexibilities a_x and a_y. $[I]$ is the identity matrix. $\{E\}$ contains the desired x and y-components of the bearing eccentricities at the bearing locations and it contains the absolute shaft displacements at all other stations.

Seal forces are usually assumed to be known linear functions of the seal eccentricities, but nonlinear functions of rotational speed. Thus, if seals are present, the seal forces can be expressed as

$$\begin{Bmatrix} F_x \\ F_y \end{Bmatrix} = -\begin{bmatrix} K & k \\ -k & K \end{bmatrix}\begin{Bmatrix} E_x \\ E_y \end{Bmatrix}, \qquad (15)$$

which can be substituted into Eq. (14) at the seal locations to simplify the calculations.

Equation (14) is a nonlinear equation system from which the bearing eccentricities $E = (E_x, E_y)$ can be found. If a Newton-Raphson iteration procedure is used, and if derivatives rather than finite differences are used in the Jacobian matrix, then it is advantageous to note that some of the derivatives turn out to be the bearing stiffness coefficients that are known functions of the bearing eccentricity, see, for example, Lund (1965).

The Transfer Matrix Method. Figure 3 shows the usual lumped mass and massless flexible shaft elements used in rotordynamic analysis based on the *TM* method, see, for example, Lund (1974). The rotor is assumed here to be in steady-state equilibrium. Using the standard TM procedure, it can be verified that transfer across a mass and beam-element combined is given by

$$\begin{Bmatrix} x \\ y \\ \theta \\ \phi \\ V_x \\ V_y \\ M_y \\ M_x \\ 1 \end{Bmatrix}_{i+1} = \left[\begin{array}{cccc|cccc|c} 1 & 0 & l & 0 & l^3/(6EI) & 0 & l^2/(2EI) & 0 & (P_x - F_x)_i l^3/(6EI) \\ 0 & 1 & 0 & l & 0 & l^3/(6EI) & 0 & l^2/(2EI) & (P_y - F_y)_i l^3/(6EI) \\ 0 & 0 & 1 & 0 & l^2/(2EI) & 0 & l/(EI) & 0 & (P_x - F_x)_i l^2/(2EI) \\ 0 & 0 & 0 & 1 & 0 & l^2/(2EI) & 0 & l/(EI) & (P_y - F_y)_i l^2/(2EI) \\ \hline 0 & 0 & 0 & 0 & 1 & 0 & 0 & 0 & (P_x - F_x)_i \\ 0 & 0 & 0 & 0 & 0 & 1 & 0 & 0 & (P_y - F_y)_i \\ 0 & 0 & 0 & 0 & l & 0 & 1 & 0 & l(P_x - F_x)_i \\ 0 & 0 & 0 & 0 & 0 & l & 0 & 1 & l(P_y - F_y)_i \\ \hline 0 & 0 & 0 & 0 & 0 & 0 & 0 & 0 & 1 \end{array}\right] \begin{Bmatrix} x \\ y \\ \theta \\ \phi \\ V_x \\ V_y \\ M_y \\ M_x \\ 1 \end{Bmatrix}_i , \quad (16)$$

where the eight top elements of the last column of the matrix are nonzero at the bearing and seal locations only. Shear flexibility has been omitted in Eq. (16) for clarity, but can easily be included in the usual manner. If seals are present and the seal forces are considered linear, then further simplification can be achieved by substitution of Eq. (15).

The effect of bearing and seal support flexibility and radial misalignment is included, as before, by substitution of Eqs. (12) and (13), giving

$$\begin{Bmatrix} E_x \\ E_y \\ \theta \\ \phi \\ V_x \\ V_y \\ M_y \\ M_x \\ 1 \end{Bmatrix}_{i+1} = \left[\begin{array}{c|c|c} & & (P_x - F_x)_i l^3/(6EI) - (a_x F_x - e_x)_i + (a_x F_x - e_x)_{i+1} \\ A_{11} & A_{12} & (P_y - F_y)_i l^3/(6EI) - (a_y F_y - e_y)_i + (a_y F_y - e_y)_{i+1} \\ & & (P_x - F_x)_i l^2/(2EI) \\ & & (P_y - F_y)_i l^2/(2EI) \\ \hline & & (P_x - F_x)_i \\ A_{21} & A_{22} & (P_y - F_y)_i \\ & & l(P_x - F_x)_i \\ & & l(P_y - F_y)_i \\ 0\ 0\ 0\ 0 & 0\ 0\ 0\ 0 & 1 \end{array}\right] \begin{Bmatrix} E_x \\ E_y \\ \theta \\ \phi \\ V_x \\ V_y \\ M_y \\ M_x \\ 1 \end{Bmatrix}_i , \quad (17)$$

where A_{11} through A_{22} are the four 4×4 submatrices outlined in Eq. (16).

The basic solution procedure goes as follows:

(i) choose initial values of eccentricity components E_x and E_y at all the bearing locations;

(ii) make a transfer across the entire shaft, using Eq. (17), to get

$$\begin{Bmatrix} E_x \\ E_y \\ \theta \\ \phi \\ V_x \\ V_y \\ M_y \\ M_x \\ 1 \end{Bmatrix}_N = \left[\begin{array}{c|c|c} & & \\ B_{11} & B_{12} & b_1 \\ & & \\ \hline & & \\ B_{21} & B_{22} & b_2 \\ & & \\ 0\ 0\ 0\ 0 & 0\ 0\ 0\ 0 & 1 \end{array}\right] \begin{Bmatrix} E_x \\ E_y \\ \theta \\ \phi \\ V_x \\ V_y \\ M_y \\ M_x \\ 1 \end{Bmatrix}_1 . \quad (18)$$

(iii) Substitute the boundary conditions (usually zero forces and moments at the ends) to get

$$\begin{bmatrix} B_{21} \end{bmatrix} \begin{Bmatrix} E_x \\ E_y \\ \theta \\ \phi \end{Bmatrix}_1 = -\begin{Bmatrix} b_2 \end{Bmatrix}; \quad (19)$$

(iv) calculate $\{E_x, E_y, \theta, \phi\}_1$ from the linear equation system (19);

(v) use the corresponding full state vector $\{E_x, E_y, \theta, \phi, 0, 0, 0, 0\}_1$ in a transfer from station no. 1 to bearing no. 1. The resulting transfer matrix will look similar to Eq. (18), with nonzero elements in the last column resulting only from the last transfer as the bearing is reached. Thus, the two first lines of the matrix equation represent two nonlinear equations from which improved values of the eccentricity components at bearing no. 1 can be derived, for example by Newton-Raphson iteration. This procedure in repeated between bearings no. 1 and 2, etc. to calculate improved values of all the bearing eccentricities;

(vi) go back to (ii) until convergence.

Numerical Example

The three methods described above have been programmed and included in rotordynamic programs based on the IC, FE, and TM methods, respectively. They have been thoroughly tested and found to produce consistent results. One of the test cases is presented here, for the rotor-system shown in Fig. 4, to illustrate the analysis procedure and to provide some insight into the static and dynamic behavior of multibearing rotors.

The rotor system shown in Fig. 4 consists of two lumped masses carried by a massless shaft supported by four identical plain journal bearings. The shaft and the bearing stiffnesses are of the same order of magnitude. The bearings were realistically dimensioned with regard to mean bearing pressure, minimum oil-film thickness, oil flow, friction loss, and temperature rise.

A damped free vibration analysis was carried out using the IC method, extended for eccentricity calculation, as described

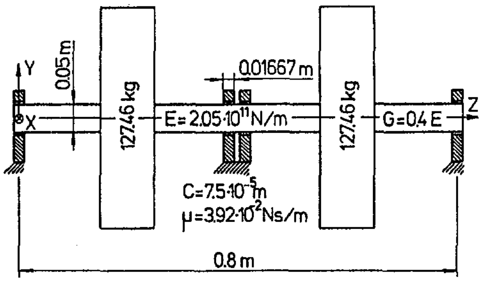

Fig. 4 Sample multibearing rotor

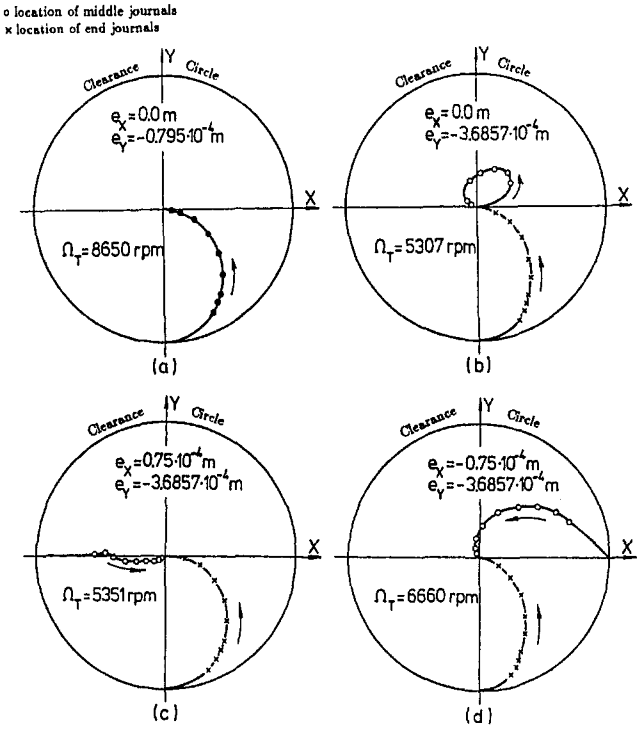

Fig. 5 Steady-state bearing loci

above. The Sommerfeld Number, the attitude angle, and the usual eight bearing stiffness and damping coefficients for the bearings were determined from graphs given in Woodcock (1971). The bearing loads are generally not vertical for a multibearing rotor so it becomes necessary to perform a coordinate transformation of the bearing coefficients as outlined for example in Nikolajsen (1973).

The calculated steady-state journal positions as functions of speed are shown in Fig. 5 for selected misalignments e of the middle double-bearing relative to the two end bearings. The instability threshold speed Ω_T is also indicated. The arrows indicate the direction of motion of the journal centers for increasing speed. The points on the loci correspond to speeds that are continually doubled from a low of 500 rpm through 1000 rpm, 2000 rpm, etc. up to 128,000 rpm to get traces of the entire loci, although in practice Ω_T sets an upper limit for the speed.

In Fig. 5(*a*), the vertical misalignment has been chosen such that the total static bearing loads on all four bearings are equal at all speeds. In Fig. 5(*b*), the misalignment is such that the middle journals are concentric in the bearings at zero speed. This leads to the unusual situation of increasing eccentricity for increasing speed (below 1000 rpm). The loci of Figs. 5(*c*) and (*d*) result when horizontal misalignment equal to the bearing clearance is also added.

Figure 5 shows that both the bearing loci and the instability threshold speed depend in a complex manner on the magnitude and direction of misalignment. For example, Figs. 5(*c*) and 5(*d*) suggest that, for this rotor, misalignment in the negative x-direction results in better stability than the same misalignment in the positive x-direction. However, if the x-misalignments are increased to $\pm 4.28 \times 10^{-4}$ m, then the threshold speeds become 10,795 rpm and 10,141 rpm respectively, thus reversing the trend.

In Fig. 6, the instability threshold speed has been plotted as a function of vertical misalignment of the middle bearing pair. Optimum stability occurs at a misalignment of about -0.25×10^{-4} m (vertically down). This corresponds to neither equal load sharing nor perfect alignment, although it is close to both for this rotor. The minimum threshold speed occurs as expected at a misalignment that unloads either the middle bearings or the end bearings. The steep drop from maximum to minimum threshold speed indicates that the bearings must be aligned within relatively close tolerances to avoid a serious drop in stability.

Figure 6 also shows that with a vertical misalignment of $(-0.5 \pm 0.5) \times 10^{-4}$ m, the threshold speed would be in the range 8800 rpm to 8500 rpm, which is close to optimum. By inspection of Fig. 4 and without access to Fig. 6, it would seem reasonable to position the bearings for zero misalignment to make them all carry approximately the same load. If this were done to within the same tolerance of $\pm 0.5 \times 10^{-4}$ m ($\frac{2}{3}$ of the bearing clearance), then the threshold speed could be anywhere between 8800 rpm and 7500 rpm, i.e., it may be 1000 rpm lower than could be achieved with access to Fig. 6.

Bearing support flexibilities of 1.2×10^{-7} m/N were introduced in the x and y-directions for the misalignment configuration shown in Fig. 5(*b*). This reduced the operating misalignment from -3.69×10^{-4} m to -2.45×10^{-4} at 6000 rpm so the middle bearings were no longer completely unloaded. As a result, the threshold speed increased from 5307 rpm to 6342 rpm. Thus, bearing support flexibility may stabilize a multibearing rotor, whereas in general it is considered destabilizing because it lowers the first critical speeds and the instability threshold speed is often close to twice the first critical speed. Finally, according to Fig. 6, superior stability can be achieved by severe bearing misalignment but this is generally unacceptable due to the adverse effect on other parameters, such as the minimum film thickness.

Conclusions

A complex relationship has been shown to exist between radial bearing misalignment and stability of a multibearing rotor. Neither perfect alignment nor equal load sharing between bearings can be relied upon to give optimum stability. Numerical analysis is necessary to predict the "misalignments" and the tolerances on alignment that will ensure an adequate stability margin. Bearing support flexibility can improve the stability of badly aligned rotors. However, it could reduce the stability of a well-aligned rotor by lowering the natural frequency in which the rotor goes unstable. The complex relationship between misalignment and threshold speed, illustrated here, suggests that improper alignment could be responsible for some of the unexplained cases of turbomachinery instability which occur from time to time. It is recommended that misalignment effects be investigated in such cases using one of the methods outlined above. These methods are useful for all types of fluid-film bearings and seals whose dynamic characteristics vary with eccentricity ratio.

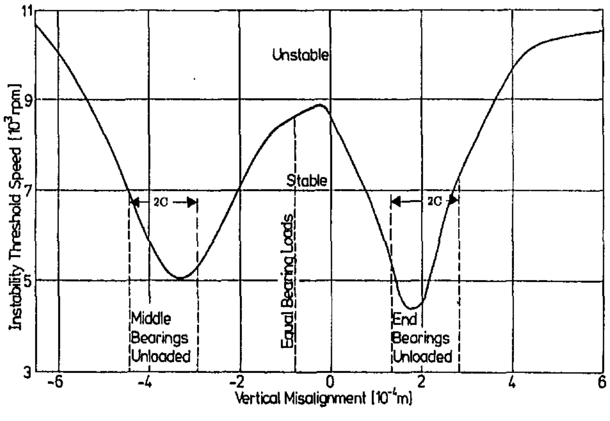

Fig. 6 Rotor stability chart

For rotors with many bearings and seals, the required parametric studies become very time consuming unless they are automated. This can be done for example by linking the rotor program with a standard nonlinear optimization program that considers the threshold speed to be a nonlinear function of the misalignments and seeks to maximize this function.

Acknowledgments

This work was supported by the Engineering and Physical Sciences Research Council, UK and by the Turbomachinery Research Consortium at Texas A&M University. The paper was prepared at Staffordshire University.

References

Argyris, J. H., 1958, "On the Analysis of Complex Elastic Structures," *Applied Mechanics Reviews,* ASME, New York, Vol. 11, No. 7, pp. 331–338.

Childs, D., 1981, "Rotordynamic Moment Coefficients for Finite-Length Turbulent Seals," Paper presented at the IFTOMM Conf on Rotordynamic Problems in Power Plants.

Kelly, J. H., 1989, "Analysis of Multi-Stage Centrifugal Pumps Using Transfer Matrices," MSc thesis, Texas A&M University, College Station, TX.

Lund, J. W., 1965, "Rotor-Bearing Dynamics Design Technology, Part III: Design Handbook for Fluid-Film Type Bearings," Technical Report AFAPL-TR-64-45, U.S. Air Force.

Lund, J. W., 1974, "Stability and Damped Critical Speeds of a Flexible Rotor in Fluid-Film Bearings," ASME *Journal of Engineering for Industry,* Vol. 96, Ser. B, No. 2, pp. 525–533.

Morton, P. G., 1972, "Analysis of Rotors Supported Upon Many Bearings," *Journal of Mechanical Engineering Science,* Vol. 14, No. 1, pp. 25–33.

Nelson, H. D., and McVaugh, J. M., 1976, "The Dynamics of Rotor-Bearing Systems Using Finite Elements," ASME *Journal of Engineering for Industry,* Vol. 98, No. 2, pp. 593–601.

Nikolajsen, J. L., 1973, "The Effect of Variable Viscosity on the Stability of Plain Journal Bearings and Floating-Ring Journal Bearings," ASME *Journal of Lubrication Technology,* Vol. 95, No. 4, pp. 447–456.

Nikolajsen, J. L., 1978, "Modelling and Control of Rotor-Bearing Systems," Ph.D. dissertation, University of Sussex, UK.

Nikolajsen, J. L., and Gajan, R. J., 1988, "A New Computer Program for Pump Rotordynamic Analysis," *Proceedings of the Fifth International Pump Users Symposium,* pp. 11–16.

Powell, M. J. D., 1970, "A Fortran Subroutine for Solving Systems of Non-Linear Algebraic Equations," (from Rabinowitz, P., "Numerical Methods for Non-Linear Algebraic Equations," Gordon & Breach), pp. 115–161.

Rieger, N. F., 1970, "Study of Misalignment Effects on Performance of Multi-Bearing Rotor," ASME paper no. 70-DE-71.

Takagi, M., et al., 1980, "Analysis and Design of Centrifugal Pumps Considering Rotor Dynamics," paper presented at the Second International Conference on Vibration in Rotating Machinery, Cambridge, UK, pp. 43–51.

Tondl, A., 1965, "Notes on the Problem of Self-Excited Vibrations and Non-Linear Resonances of Rotors Supported in Several Journal Bearings," *Wear Magazine,* Vol. 8, pp. 349–357.

Vernon, J. B., 1967, *Linear Vibration Theory—Generalized Properties and Numerical Methods,* John Wiley & Sons, New York.

Woodcock, J. S., 1971, "Dynamic Characteristics of a Journal Bearing Oil-Film," PhD dissertation, University of Sussex, UK.

The Diesel Engine for Cars—Is There a Future?

F. F. Pischinger
FEV Motorentechnik,
GmbH & Co. KG,
Neuenhofstrabe 181,
D-52078 Aachen

The diesel engine is known as the most fuel efficient combustion engine. Its acceptance for use in passenger cars, however, varies geographically. Today, the diesel car plays an important role in Europe; in France, for instance, it is achieving a remarkable market share of about 42 percent, while in the US its market penetration can be neglected. Many questions are expressed concerning the future of diesel powered cars. The question affecting market acceptance is as follows: can the significantly better fuel efficiency of a diesel car outweigh perceived detrimental characteristics? Such unfavorable properties are thought to be low specific power, objectionable noise, higher exhaust emissions (including smoke), and higher vehicle price. These features are closely influenced by the state of passenger car diesel engine technology. This technology state and its potential must be evaluated with respect to current and future demands, for instance, tighter exhaust emission regulations. In addition, the commercial value and consumer acceptance of high fuel economy must be evaluated. It is clear that the ultimate result of weighing the pros and cons will depend not only on technological factors, but also on political factors such as fuel taxation. Regarding the state of technology, the diesel car is very promising. First, by employing a direct injection combustion system, the fuel efficiency can be improved by about 15 percent over current swirl chamber engines. Furthermore, the specific power (hp/ltr) can be increased by efficient supercharging to achieve values of today's gasoline engines. By tuning the combustion system, low noise engine design features and incorporation of careful noise reduction measures on the vehicle, the noise behavior of a spark ignited vehicle can be reached. Exhaust emissions can currently be reduced to a level to satisfy today's European and US Tier 1 emission limits. However, significant development effort remains. More stringent emission levels (California US, Tier 2 ULEV, and Stage 3 in Europe) require further advancements in diesel combustion. The strong development potential of 4-valve engines and new unique injection systems is evident. In addition, there are promising developments with lean NO_x catalysts and regenerative particulate filters. These technologies offer the potential to meet the very stringent future emission standards. It is anticipated that the sophisticated technology needed to meet these standards will make the future diesel car more expensive compared to a gasoline fueled vehicle. This raises the issue of what price will the consumer pay for the higher fuel economy of a diesel car. In light of the worldwide rapid increase in passenger car population and of the dwindling oil reserves and their global distribution, the fuel efficient diesel engine will play an important role in the future of passenger cars.

1 Introduction

The diesel engine is the most fuel efficient combustion engine known. Its use in applications such as trucks, buses, agricultural equipment, ships, and power stations is firmly established. For passenger cars, however, its position differs very much geographically. As Fig. 1 shows, the diesel car has a market share of about 20 percent in Europe (in France, for instance, a record share of about 42% (in 1996), while in the USA its penetration into the market can be neglected.

A simple reason for this uneven distribution in market shares is different fuel prices and car tax rates. As an example, Fig. 2 shows that in France and in Germany, due to lower taxes, diesel fuel is about 25 percent cheaper than the mostly used European premium gasoline, whereas in the USA fuel prices are much less loaded by taxes and there is no significant difference between prices of diesel and gasoline. As an example for differences in annual car tax rates, Fig. 3 shows relative figures for comparable medium sized cars, with the gasoline car being rated 100 percent. In Germany, the diesel car is taxed nearly four times as high as the gasoline vehicle, which might explain, at least partially, the difference in diesel market share compared to France where there is no difference between diesel and gasoline car tax.

Beyond these differences in taxation, there are historical circumstances and technology related pros and cons for diesel versus gasoline cars. For decades in most European countries the diesel car has the image of an exceptionally fuel efficient and durable vehicle. Over time, an increasing fraction of European consumers have valued these properties higher than historic drawbacks of the diesel car such as lower power, higher noise, and higher price.

During the last decade in Europe, the introduction of the low emission gasoline engine with three-way catalyst challenged the exhaust emission capability of the passenger car diesel—especially the particulate emission of the diesel, which has become the target of environmental concern. Even though no proof of serious health hazards caused by the particulate concentrations in urban areas could so far be found, such discussions contributed to a certain degree of uneasiness among some diesel car buyers, especially in Germany, and gave rise to questions about the future of the diesel car.

This leads to the following general questions: what will be the future of the diesel car? Will the trend in Europe toward increased diesel share continue, be stopped, or be reversed?

Contributed by the Internal Combustion Engine Division and presented at the Fall Technical Conference of the ASME Internal Combustion Engine Division, October 20–23, Springfield, OH. Manuscript received by the ASME Headquarters January 20, 1998. Associate Technical Editor: D. Assanis.

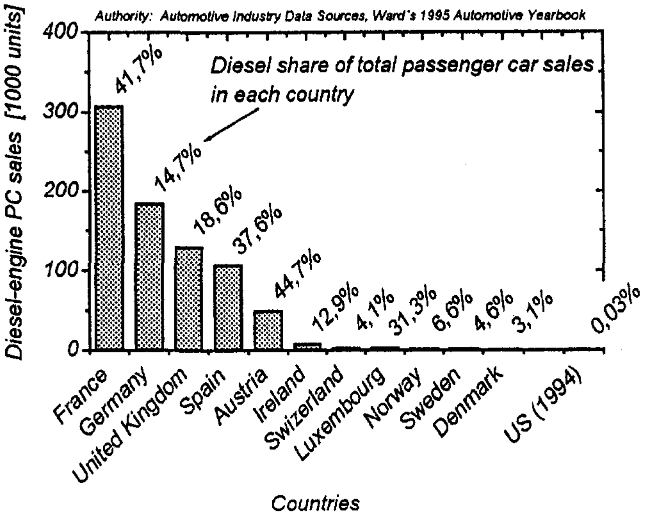

Fig. 1 Diesel-engine passenger car sales in Western Europe (January–April 1996) and US (1994)

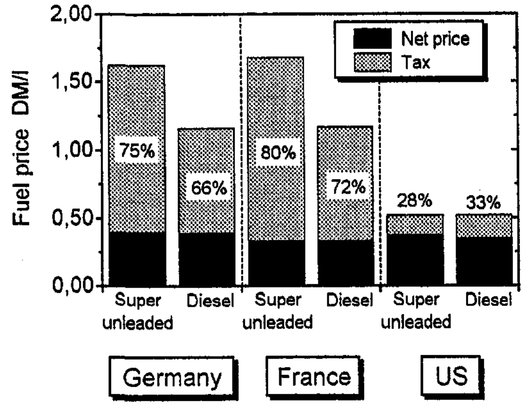

Fig. 2 Comparison of fuel prices for diesel engine and gasoline engine passenger cars (tax in percentage of fuel price)

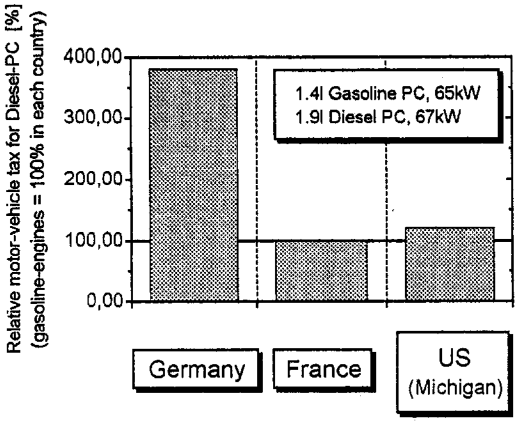

Fig. 3 Comparison of motor-vehicle taxes for diesel engine and gasoline engine passenger cars

Will the US car market begin to accept diesel technology? Can diesel technology cope with future noise and exhaust emission regulation?

To predict the future role of the diesel car, a thorough evaluation of today's state of passenger car diesel technology and its future potential must be compared to the existing and future requirements. Such a projection follows.

2 State of Technology

Power Density. Among the historical drawbacks of the passenger car diesel is the lower power density, even if this was accepted by diesel car supporters. However, over the last few years a significant change took place in power density, as Fig. 4 shows. The power output per liter increased up to 45 kW (60 hp) due to improved combustion process, higher turbocharging, and use of improved materials. With direct injected 4-valve prototype diesel engines even 50 kW/ltr (67 hp/ltr) can be reached, thus able to compete with many of today's gasoline engines, especially in the US.

Fuel Efficiency. The relative improvement goes even further with improved fuel efficiency, as shown in Fig. 5, thereby improving still more the diesel engine's biggest asset. The step from prechamber and swirl chamber (IDI) engines to direct injected (DI) diesels improved the minimum effective specific fuel consumption by about 15 percent. Today's DI diesel engines reach values below 200 g/kWh (0.329 lb/hph). Still more impressive is the advantage of the DI diesel engine at part load operation. Figure 6 shows a comparison of specific fuel

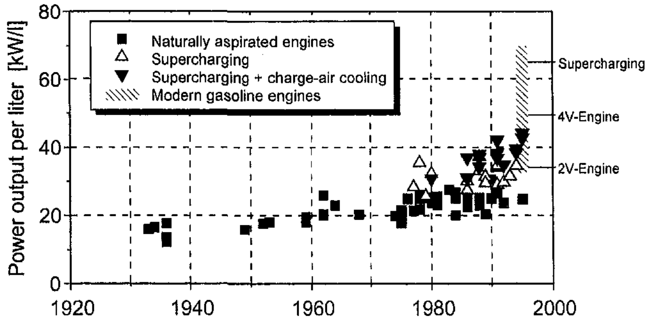

Fig. 4 Power output per liter history of passenger car diesel engines

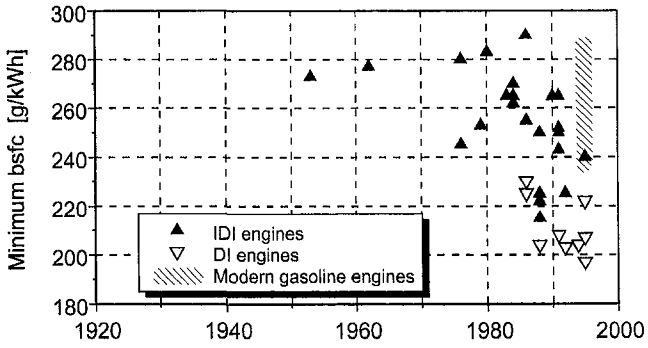

Fig. 5 Minimum brake specific fuel consumption history of passenger car diesel engines

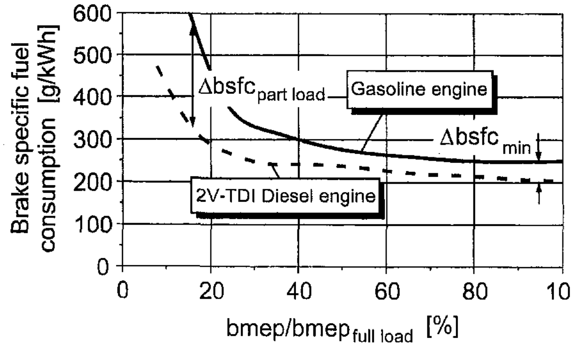

Fig. 6 Brake specific fuel consumption of diesel engines compared to gasoline engines (part load, 2000 rpm)

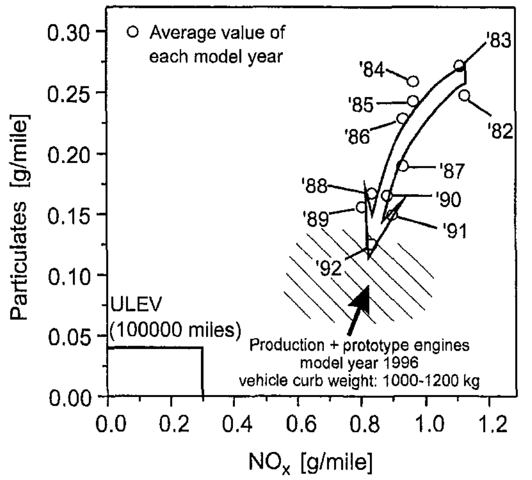

Fig. 7 Pollutant emissions history of diesel engine passenger cars (FTP 75 - test)

consumption for a turbocharged direct injected (TDI) car diesel against that of a very good naturally aspirated gasoline engine versus load at 2000 rpm. For the full load range the diesel advantage is about 20 percent, whereas at lower part load, which is typical for city driving, it is in the range of 40 percent. It should be remarked here that due to the higher density of diesel fuel, which corresponds to a higher energy density, the volumetric fuel consumption of a diesel is already about 12 percent lower compared to a gasoline fueled engine. A further bonus for the diesel comes from better fuel efficiency under cold starts compared to the SI engine. Altogether under average driving conditions the TDI diesel car has an advantage in volumetric fuel efficiency of between 30 and 40 percent, compared to a similarly powered modern gasoline vehicle.

Exhaust Emissions. As is well known, there exists a trade-off between fuel efficiency and exhaust emissions. It is, therefore, remarkable that such fuel efficiency improvements have been reached while meeting today's exhaust emission requirements. Compared to a decade ago, remarkable improvements in exhaust emissions have been reached as Fig. 7 shows for particulate and NO_x emissions in the FTP 75 test. NO_x emissions could be reduced by about 30 percent, while at the same time particulate emissions have reduced by more than 60 percent. However, it is evident that there is still significant improvement necessary especially for NO_x emissions to reach future more stringent emission standards, such as California's ULEV standard. Concerning CO and HC emissions, diesel engines have an inherent advantage, however, these standards have been reduced over the last decade.

Noise Emission. During the last decade, noise emissions of passenger car engines have improved considerably. This holds true for SI engines as well as for diesels as can be seen in Fig. 8. Mainly, due to the lower combustion noise, SI engines show on average a lower level. However the best diesel engines can compete with SI engines in their upper noise band. This could be achieved by tuning the combustion system and low noise engine design features for DI passenger car diesels. Together with careful noise reduction measures on the vehicle, the noise behavior of a good gasoline car can be reached with a DI diesel under most operation conditions.

Technology. Today's technology, to reach state-of-the-art figures in all disciplines above, employs, among other things, 2-valves per cylinder, direct injection, distributor-type fuel-injection pump, turbocharging with charge air cooling, exhaust gas recirculation (EGR), oxidation catalyst, electronic control for fuel injection, EGR and charge air pressure, low noise engine structure, and noise silencing measures on the vehicle. It is clear that with these technologies it is difficult to keep the price of the diesel car close to the price of the gasoline version. However, it has been found in Europe that the customers are willing to pay a higher price for the very fuel efficient diesel car.

3 Technology for the Future

The goals that must be reached to assure a bright future for the car diesel engine are numerous. The most important objectives are to reach future stringent emission standards such as California ULEV and European Step 3 and beyond, while achieving a further decrease in noise levels. While accomplishing these goals, the fuel economy should be further improved or maintained at today's low level. Further improvements in power density would, of course, be advantageous in combination with high torque at low engine speed. However, this should be achieved without adding to much additional cost to the diesel car.

Chemical Thermodynamics. The crucial task for lowering diesel emissions is to improve particulate and NO_x emissions simultaneously—a difficult task since there is usually a trade-off between these two emissions. To determine if this task is at all possible, basic fundamentals of chemical thermodynamics must be explored.

Figure 9 shows a typical mixture distribution in a diesel injection spray just prior to ignition, ranging from rich in the spray core to lean in the spray edge. The diagram above shows the temperature history of the zones with different relative air-fuel ratios (λ) that proceed from the curve of mixture temperature before combustion up to the curve of burned gases after combustion. The diagram also shows the zones of soot and NO_x formation, the darker shadowed zones indicating higher formation rates. It can be seen that in an indicated target λ-range, combustion is possible without soot formation and only very low NO_x formation. Thus, in principle, smokeless, low NO_x diesel combustion should be possible if the mixture formation could be narrowed to the required mixture ratio. This may not be possible with the combustion of typical sprays. However, even if soot formation cannot be completely avoided, there is a possibility to burn the soot during the high temperature combustion process, as is shown in the diagram on the right side of the figure. This of course requires intensive mixing at the beginning of the expansion process while the temperatures are still on a high level, however not too high because of NO_x formation. Thereby, the soot generated can be burned nearly completely during the process.

It can be concluded that a careful mixing strategy is the key to low emission diesel combustion. Since mixing is controlled by fuel injection as well as by air motion in the combustion chamber, both processes must be developed concurrently. Fu-

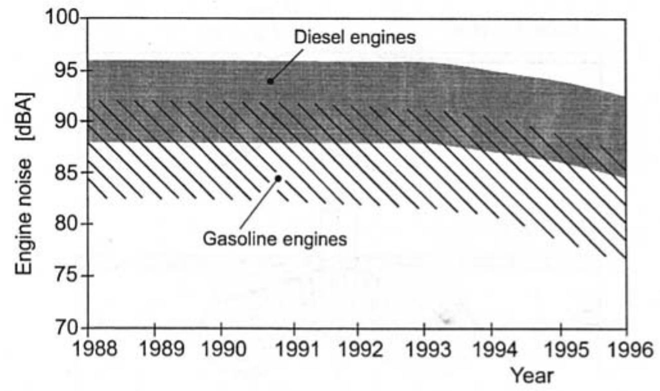

Fig. 8 Engine noise emissions history of passenger car diesel and gasoline engines 1988–1996 (full load, 3000 rpm, 1 m distance)

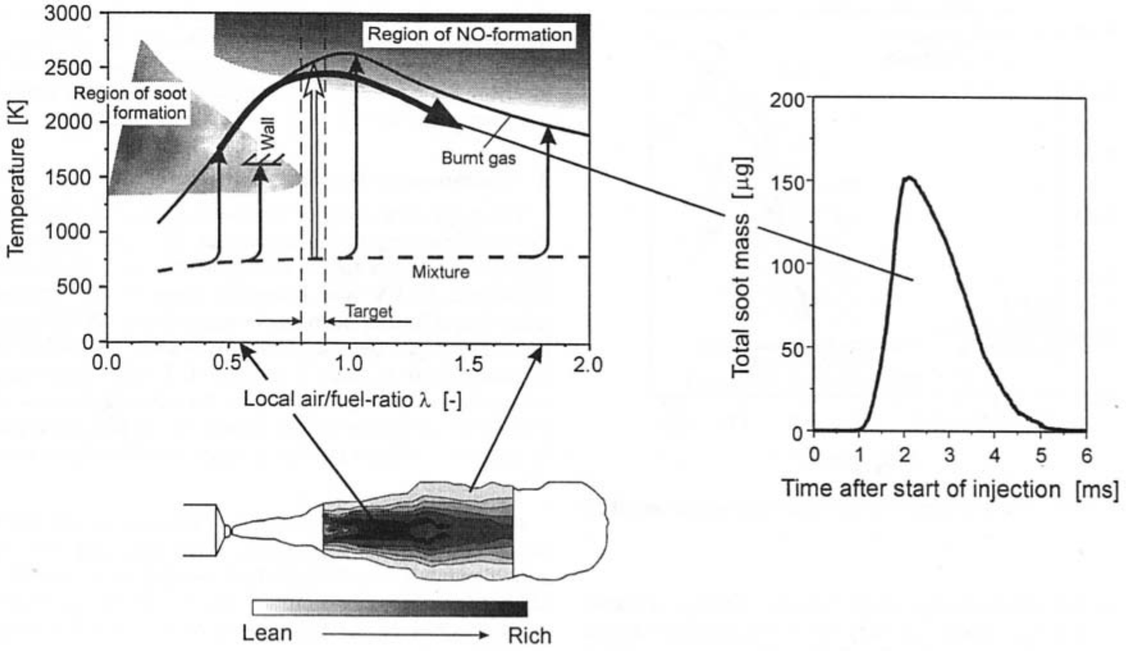

Fig. 9 Soot formation and nitrogen oxide formation in a diesel fuel spray and its dependence on stoichiometric air/fuel ratio

ture diesel combustion development approaches follow these guidelines. Typical design features which address this fact are discussed below.

4-Valve Technology. It is obvious that the mixing process during fuel injection into the combustion chamber is influenced by the position of the injector as well as by the symmetry of the air flow during injection. Achieving the best mixing conditions for a typical multispray injection of a DI diesel engine requires equally good conditions for all sprays of the injector. Figure 10 shows the typical arrangement for today's 2-valve passenger car diesel engines. The inclined injector is positioned off-center and sprays into the asymmetrical flow in an eccentric combustion chamber. By contrast, the 4-valve design incorporates a centrally mounted vertical injector with completely symmetric sprays and a symmetric flow field in a concentric combustion chamber. In addition, the four instead of two valves improve the gas exchange process.

Figure 11 shows the influence of different 4-valve arrangements on swirl number c_u/c_a and flow coefficient α_k as measured on a special steady-state flow rig. Swirl number c_u/c_a indicates the degree of air rotation around the cylinder axis produced by the intake process which for efficient fuel-air mixture formation should be in the range of 1.5 and 1.9 for 4-valve high speed passenger car diesel engines. The flow coefficient is influenced by the arrangement of the intake valves and the required swirl number. It can be seen in Fig. 11 that the twisted valve arrangement produces the highest flow coefficient, and, thereby, the best breathing capability of the engine at the required swirl intensity. The twin arrangement, which is known from larger diesel engines, and the tandem arrangement are found to be inferior. The advantage of four valves over two valves also can be seen in Fig. 11.

Thorough investigations on a future diesel prototype engine conducted by FEV have proven that a twisted 4-valve arrangement could be realized in a cost effective and durable design. Views of the ''Diesel Future'' cylinder head are shown in Fig. 12. It can be seen that even with a central vertical injector a single overhead camshaft design was possible.

Another advantage of the 4-valve technology is the capability to produce variable swirl by port deactivation as shown in Fig. 13. By increasingly closing the short intake port of the twisted arrangement, for example, by employing a throttle flap, the swirl number can be increased effectively. This is important in

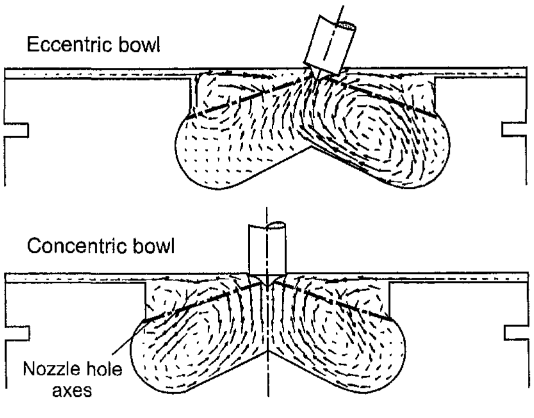

Fig. 10 Comparison of two-valve and four-valve concept with regard to flow in the combustion chamber (piston at TDC)

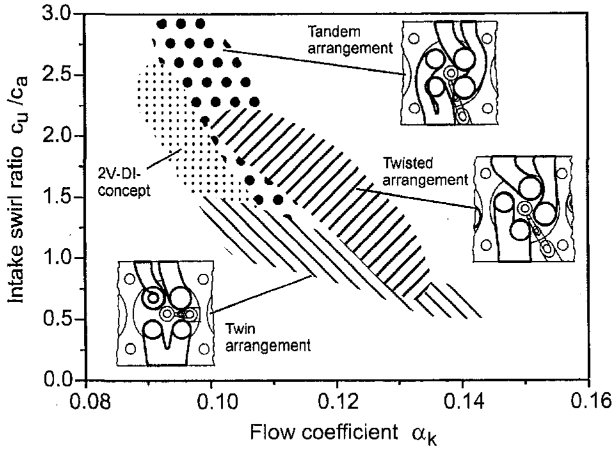

Fig. 11 Flow quality of different port concepts for four-valve DI diesel engines

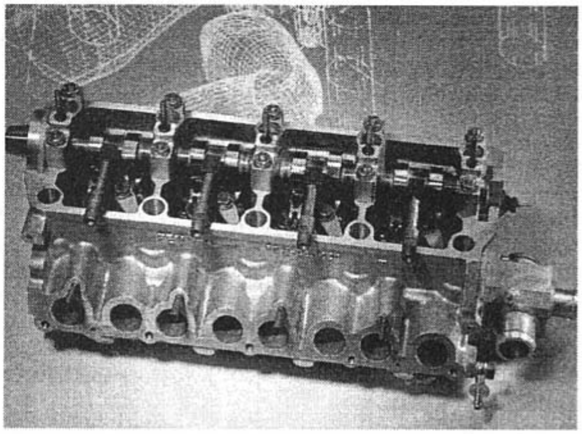

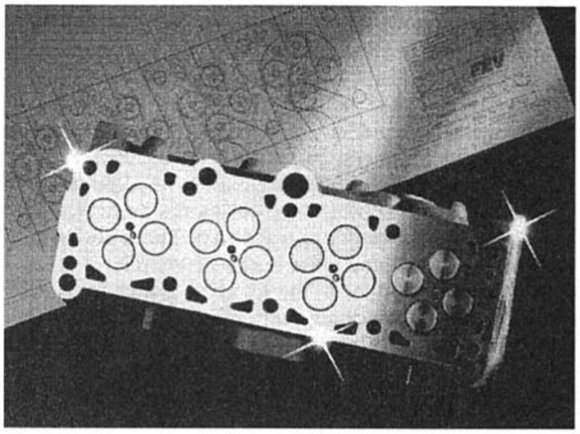

Fig. 12 Flow characteristics of four-valve DI diesel engines for deactivation of short intake port

order to enhance fuel/air mixing, and, thereby, to reach high torque at low engine speed. The associated decrease in flow coefficient is not detrimental for low speed operating conditions.

By careful optimization of this 4-valve arrangement, even in combination with current production distributor-type fuel injection pumps, an increase in engine power could be achieved. As full load bmep versus engine speed curves show for such a turbocharged 4-cylinder engine (Fig. 14), torque over a wide speed range and maximum power could be increased by about 15 percent over the 2-valve engine. Of course, maximum cylinder pressure was limited to the same level for both versions.

Still more impressive are the associated improvements in exhaust emissions, as shown in Fig. 14, which range between 20 and 30 percent. In addition, the fuel consumption (specific fuel consumption b_e) could be improved by about 4 percent.

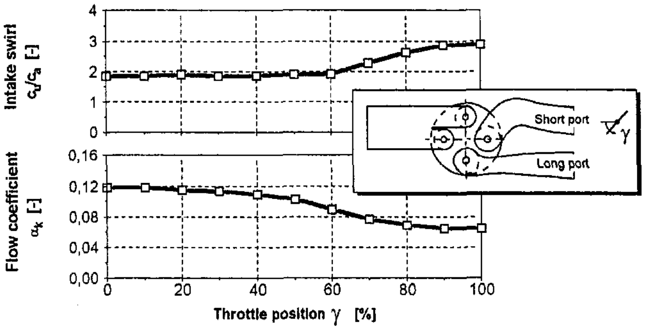

Fig. 13 Flow characteristics of four-valve DI diesel engines for deactivation of short *intake port

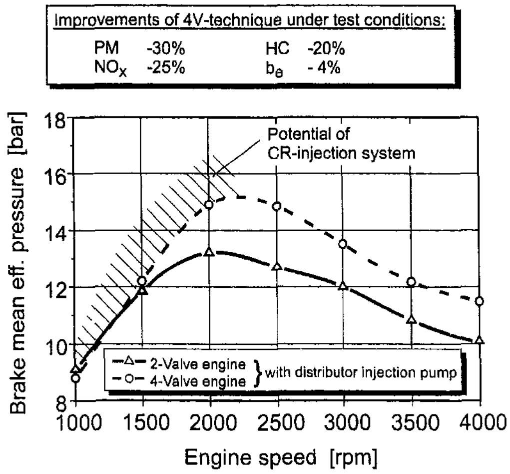

Fig. 14 Improvements of four-valve DI diesel engines under test conditions

However, with a conventional cam-actuated injection pump, a drawback in combustion still remains at very low engine speeds, if the system is tuned for high power. This has a negative effect on low end torque, as Fig. 14 shows. In this case, advanced fuel injection concepts such as common rail (CR) systems can provide further improvement.

Fuel Injection Technology. For cam-actuated fuel injection systems, there is always a strong dependence of injection pressure level on engine speed. Furthermore, the potential to shape the pattern of injection rate versus time is restricted by cam design. These limitations can be overcome by application of a common rail fuel injection system. Such systems can produce injection pressure levels largely independent from speed and load by feeding a fuel rail with electronically controlled permanent fuel flow from a high pressure fuel pump. The fuel rail subsequently feeds the injector on each cylinder. Injection timing and injection quantity per cylinder and cycle is typically controlled by electromagnetic valves on each injector. Such systems for passenger car diesel engines currently under development will soon be introduced in the market.

The application of common rail technology requires a special tuning of the combustion system to optimize mixture formation. Thereby, using the high pressure capability of the injection system at low engine speed, low end torque can be improved considerably, as previously seen in Fig. 14.

In addition, the capability of CR systems for pilot injection can be used to reduce combustion noise. Here, best results can be obtained by carefully tuning of pilot fuel quantity and separation time. As an example, the trade-off between exhaust smoke (Bosch smoke number) and maximum pressure rise as a function of pilot injection quantity is shown in Fig. 15 for a typical city driving part load operation point. To avoid an increase in soot formation, while considerably reducing the noise-generating pressure rise, an injection quantity between 0.5 and 1.0 mm^3/cycle is desirable. This is a difficult task for an electromagnetic valve, which also tends to restrict rate shaping. Therefore, piezoelectric valve actuators for CR systems are under development and offer additional advantages in the future.

Noise reduction achieved by application of an experimental piezoelectric CR system is shown in Fig. 16. A reduction of about 10 to 15 dBA can be reached in the critical high frequency range. Although a distinct disadvantage in combustion noise exists compared to low noise spark ignited engines, the noise of the improved passenger car diesel can be further compensated by low noise design of the engine structure and cost effective measures on the vehicle.

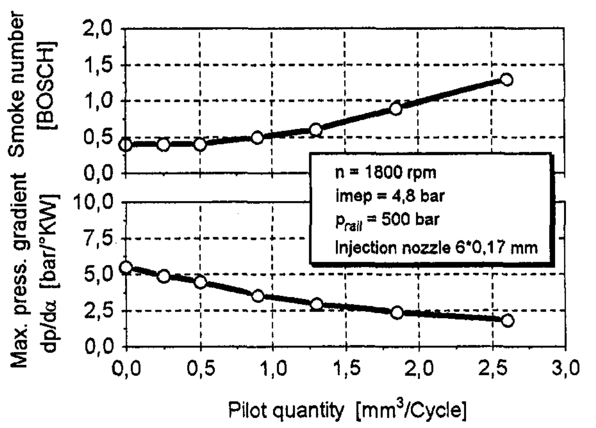

Fig. 15 Common rail system: influence of pilot quantity on black smoke emission and pressure gradient

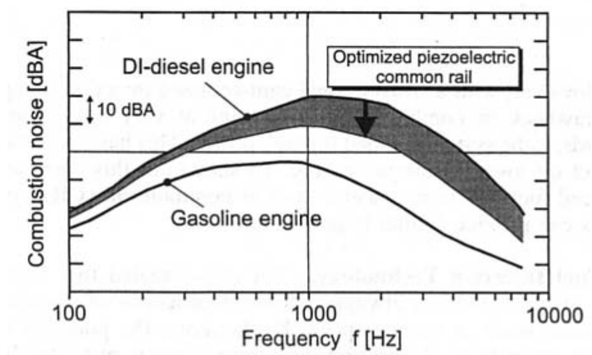

Fig. 16 Combustion noise of modern passenger car engines: potential of optimized *piezoelectric common rail (part load, medium speed)

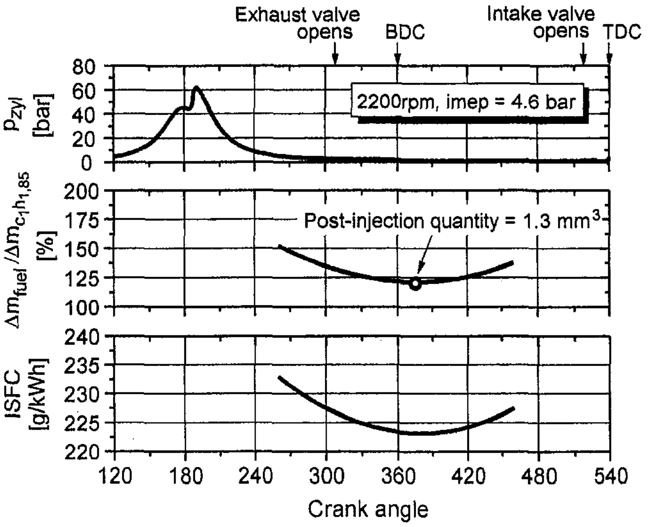

Fig. 17 Common rail injection system: influence of post-injection timing (constant HC-emission = 1500 ppm C_2H_8)

In addition to all these advantages, a common rail system offers the possibility of post-injection. Post-injection is an effective method to discretely supply the exhaust gas with a certain level of hydrocarbons as reducing agent for a lean-NO_x catalyst. It is possible to synchronize the post-injected fuel for lowest oxidation rate. Figure 17 shows the following quantities versus post-injection timing for a required HC-level of 1500 ppm C_3H_8 at a part load operating point: cylinder pressure, ratio of total supplied fuel mass to produced mass of HC, and the corresponding indicated specific fuel consumption. The highest HC formation efficiency and correspondingly lowest fuel consumption is reached with post-injection period near BDC.

Exhaust Aftertreatment. By application of the features mentioned above in combination with state-of-the-art technology, not only are high specific output and improved fuel efficiency possible, but also engine-out exhaust emissions will be improved considerably. However, these levels may not be sufficient to reach future emission goals even with application of current production oxidation catalysts. This is especially true for larger passenger cars and light trucks. Therefore, additional measures for exhaust gas after treatment must be investigated. Two such techniques are particle storage reactors and lean-NO_x catalysts.

Particle storage reactors, also called particulate traps, collect particulates on a special surface, such as a porous ceramic, and burn them such that the unit is not overloaded. Overloading the particulate trap not only can cause plugging and severe loss in engine load and efficiency, but also can destroy the unit by overheating in the case of quick oxidation. Today, a rather promising method is under development that combines two methods for easy regeneration of the storage reactor with the principle shown in Fig. 18. A small amount of additive is added to the fuel that, after combustion, makes the particles reactive for low temperature oxidation in the trap. The additive can be carried as a lifetime supply on board of vehicle or it can be added to future diesel fuel in the refinery. Under most driving conditions, exhaust temperature are sufficiently high to burn all the particulates in due time. This has already been proven in ongoing vehicle tests. Under certain extreme driving patterns, such as repeated severe winter cold starting followed exclusively by short distance driving, this method may not function properly. Therefore, the patented self-supported filter regeneration (SFR) system for burning the trapped particulate by electric flame initiation, especially at low temperatures, is combined with the additive method. The energy necessary for ignition is moderate.

With such a regenerative trap, particulate emission can be reduced by more than 80 percent. As indicated in Fig. 19, for a large car this can be used to allow an increase in the degree of exhaust recirculation, thereby lowering NO_x emissions. As this may not be completely sufficient to reach very low emission limits (ULEV), catalytic NO_x converters for O_2-containing exhaust gases—so-called lean-NO_x catalysts—are an important technology to be combined with future passenger car diesels.

All lean-NO_x catalysts require a reducing agent to function. From a practical point of view, diesel fuel would be a desirable candidate, especially when it is supplied by a common rail system without the need for additional hardware. Under laboratory conditions, conversion rates of up to 60 percent can be

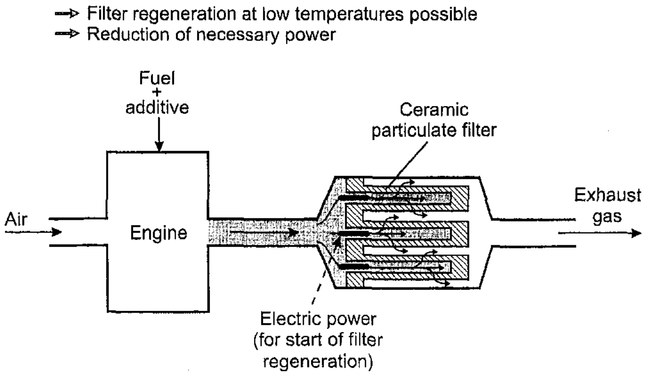

Fig. 18 FEV particulate filter system (self-supported filter regeneration, SFR-system) in combination with fuel additive

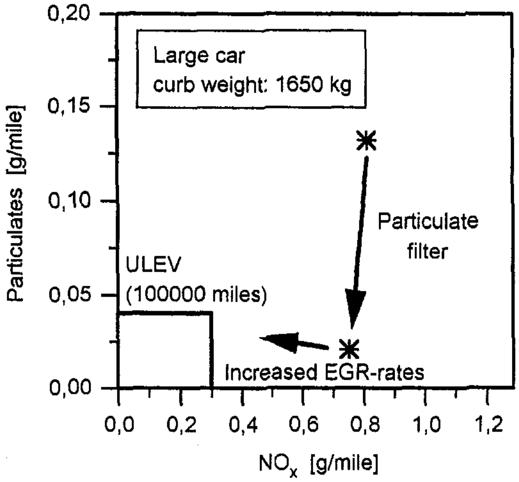

Fig. 19 **Influence of particulate filter and increased ERG-rates on particulate and nitrogen oxide emissions (FTP 75 test)**

reached. Figure 20 shows that for a diesel engine under steady-state operation, a maximum of 40 percent conversion rate is reached. Depending on hydrocarbon/NO_x ratio and actual temperature levels, lower values are expected in practical application. Presently, conversion rates of 20 to 25 percent seem realistic for vehicle operation. Thus, a technological achievement is still necessary for future applications.

If urea is used as a reducing agent such an achievement is already reached. Urea is a non-toxic agent which can be dissolved in water. Unfortunately, an additional liquid on board a vehicle that requires refilling in intervals (e.g., about 28 l/10,000 km) to function properly cannot easily be accepted. Nevertheless, the results with this technology for NO_x reduction are very encouraging. As shown in Fig. 21 for a large car, a 80 percent NO_x reduction could be reached in the FTP 75 test. This can also be regarded as an encouraging result for further work on lean-NO_x catalytic systems in general.

4 Summary and Conclusions

The role of the diesel engine for passenger cars in the world market is characterized by historical and technology features as well as by other critical boundary conditions. In spite of the higher price of a diesel vehicle, its high fuel efficiency and durability combined with fuel price factors has led to an increasing market share in Europe.

Meanwhile, car diesel engine technology has further improved and mitigated many passenger car historical problems with diesel engines. By introduction of a tailored direct injection electronically controlled combustion system, the fuel efficiency is improved by about 15 percent over today's swirl chamber engines. Furthermore, the specific power (hp/ltr) could be increased by efficient supercharging to values of current gasoline engines. By tuning the combustion system and including low noise engine design features with careful noise reduction measures on the vehicle, the noise behavior of a good gasoline car can be reached under most operating conditions. Exhaust emissions have been reduced to levels that satisfy current European and US Federal Tier 1 emission limits.

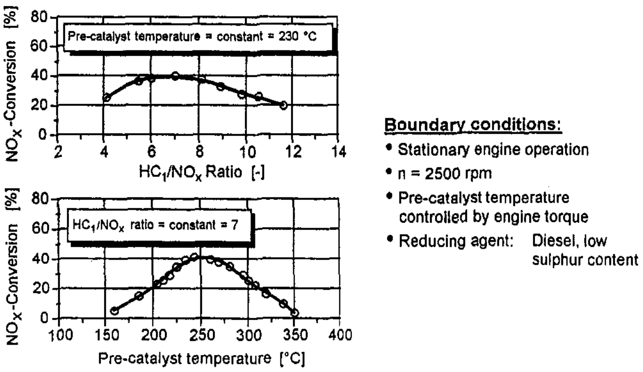

Fig. 20 **Characteristic of NO_x conversion with lean NO_x/HC technology**

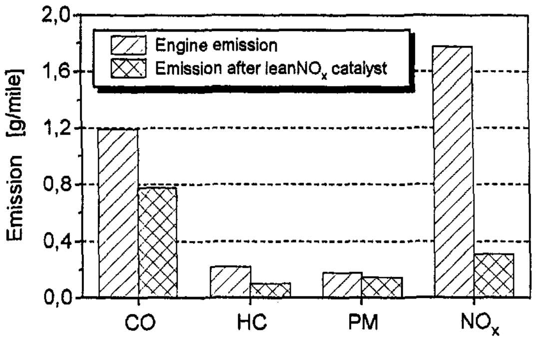

Fig. 21 **Selective catalytic NO_x reduction with urea**

Meanwhile, advancements to improve the properties of passenger car diesel and comply with future, more stringent emission levels are ongoing. Great potential, especially with 4-valve engines and new unique injection systems, is already evident. Other features not discussed within this paper, such as improved turbocharger technology, new EGR-concepts, downsizing, etc., will also contribute to increased attraction of the diesel car. In addition, there is promising work with lean-NO_x catalysts and regenerative particulate traps ongoing. These technologies offer good chances to meet the very stringent emission levels of the future.

Although there are some promising technologies, such as common rail injection to reduce the cost of a diesel engine, it can be expected that some highly sophisticated technology may be needed in the future to meet increasing consumer and exhaust emission standards. These technologies may continue to keep the future diesel car more expensive compared to a gasoline fueled vehicle. Whether this factor will be accepted by the consumer will strongly depend on other boundary conditions such as fuel price and taxes. In view of the worldwide rapid increase in passenger car population and the limited world fuel resources, the boundary conditions of the future should favor the car diesel. Considering all these arguments, the future of the car diesel is expected to be very promising and challenging.

T. Murayama
Hokkaido Automotive Engineering College,
2-6 Nakanoshima, Toyohina-Ku,
Sapporo 062, Japan

T. Chikahisa
Hokkaido University,
Sapporo, Japan

Y. Fujiwara
Hokkaido Institute of Technology,
Sapporo, Japan

Diesel Engine Smoke Reduction by Controlling Early Thermal Cracking Process and Activation Later Stage Combustion

In this investigation, extensive soot reduction was attempted with two parallel approaches: blending of oxygenated fuel and generation of strong turbulence during the combustion process. In the early stage of usual diesel combustion, the droplets in the spray are thermally cracked to low boiling point components as C2 to C5 due to the shortage of oxygen, and these components result in the formation of soot. To control the thermal cracking process, the addition of oxygenated additives to the fuel was attempted. As a result, remarkable soot reduction was obtained by adding small amounts of oxygen to the fuel. To generate strong turbulence, a small chamber connected to the main combustion chamber was added and small amount of fuel were injected into the chamber, resulting in significant soot reduction. Additionally, a clearly apparent NO_x reduction was obtained by the mixing control.

Introduction

In early 1960, J. S. Meurer of MAN proposed a unique combustion system by pointing to the rapid combustion due to ignition of accumulated mixture during the ignition lag period as a defect in conventional diesel combustion. After ignition, the gas temperature in the cylinder locally rises to over 2000°C [1, 2]. During this period, the ignition lag of the injected fuel becomes very short and the combustion proceeds without sufficient time for mixture formation. Under this condition, thermal cracking of the fuel proceeds at very high speed, while the diffusion of oxygen from the surrounding air proceeds by physical mixing speed. As a result, not enough oxygen is supplied to the spray, and the thermal cracking of the fuel rises to a dehydrogenation, condensation polymerization reaction, which produces polynuclear aromatic hydrocarbon (PAH), a pre-soot material. The result is a great deal of soot formed in the early stages of combustion [3].

In the Meurer's M-engine, most of the fuel is sprayed along the wall of the spherical combustion chamber encasing in the piston to cover the wall with a film. The wall temperature is maintained at about 340°C by oil cooling of the inner face of the piston and fuel evaporates progressively from the wall to form a uniform mixture, which does not give rise to thermal cracking [1, 2].

With this evaporative combustion, the fuel quantity needed to initiate combustion becomes relatively small, and the pressure rise due to combustion is not so rapid. This results in smooth, smokeless operation.

Unfortunately, this combustion system has demerits; so, the M-engine disappeared from the market despite the excellent idea of evaporative combustion from the walls to suppress the intensive thermal cracking in early combustion.

In Meurer's concept, high pressure injection is not only necessary but can be harmful for the suppression of intensive thermal cracking and soot formation in the early stage of combustion because a fine spray will increase the flammable mixture formed during the ignition lag period. Under the microscope, the mixture is not uniform and the shortage of oxygen around the spray worsens.

Thirty years have passed since the days of M-combustion, and today high pressure injection is the most powerful tool to suppress smoke. For example, Advanced Combustion Engineering of Japan (ACE) reported smokeless combustion at $\lambda = 1.5$, without sacrificing thermal efficiency, by a 150 ~ 160 MPa injection pressure and timing retardation. In this case, a small nozzle is necessary to suppress increased NO_x and noise and to maintain thermal efficiency. In spite of the longer injection duration, better thermal efficiency is assured by improved mixing with the fine spray and enhanced micro turbulence resulting in a shortening of combustion. The large amount of soot produced in the early stage of combustion is not emitted from the exhaust as it re-combusts in the diffusive combustion period. With high pressure injection, the flash boiling of a part of the injected fuel and enhanced inclusion of air into the spray will suppress soot formation, while micro turbulence will promote the re-combustion of soot in the diffusive combustion period [4].

There are works in progress to reduce smoke without increasing injection pressure. For example, combustion in prechamber engines [5], application of alcohol fuels [6], water in oil emulsions [7], and bio-fuels [8]. With emulsified fuel, micro-explosions of water in the spray droplet enhances the mixing process of fuel and air. Biofuels and alcohol fuels reduce smoke apparently due to the oxygen in the fuel molecules. In alcohol fuels, there is a flash boiling effect because of the relatively low boiling points of the fuels.

As described here, there are two very different approaches to decrease smoke from diesel engines: low and high pressure injection.

The authors have studied promotion of oxidation of thermally cracked components in early combustion, especially low carbon and low boiling point components, with water in oil emulsions, alcohols, and methyl ester of biofuels as oxygenate fuels, and also several oxygenate additives like oxides, ethers, carbonates, etc.

To activate the later stage of combustion and to promote the recombustion of soot, the authors have injected a small amount of fuel in the later stage of combustion through an auxiliary combustion chamber to introduce strong turbulence in the main

---

Contributed by the Internal Combustion Engine Division and presented at the 18TH Annual Fall Technical Conference of the ASME Internal Combustion Engine Division, Fairborn, OH, October 20–23, 1996. Manuscript received by the ASME Headquarters September 22, 1997. Associate Technical Editor: D. Assanis.

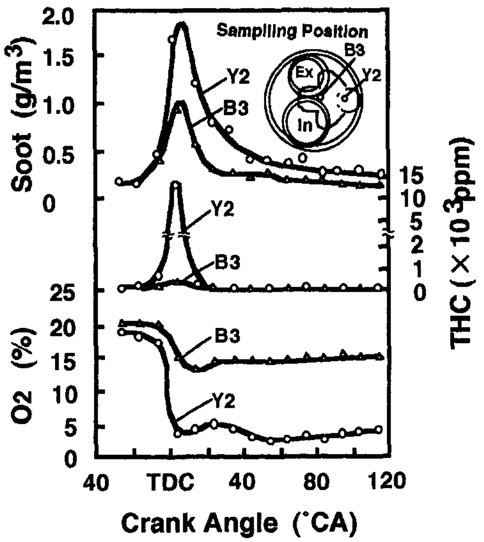

Fig. 1 Soot, THC, and oxygen in both combustion chambers under any crank angle

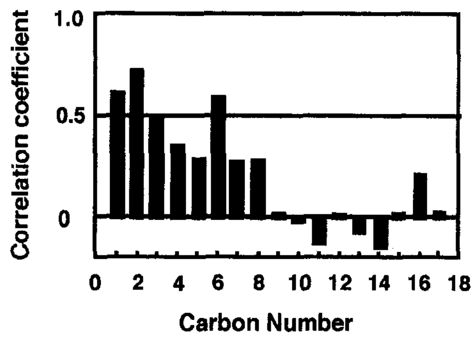

Fig. 3 Correlation between the density of soot and carbon number of hydrocarbons

chamber. By this system, the intensity of turbulence and its production time could be controlled independently from the main injection. Using this idea, a low pressure injection could be utilized, and when an over-rich mixture was introduced, simultaneous reductions of NO_x and smoke may be realized without sacrificing thermal efficiency.

Smoke Produced in the Early Stage of Combustion and its Suppression by the Oxygenate Fuel or Oxygenate Additives

Figure 1 shows the amount of soot and oxygen at any crank angle measured by high speed gas sampling with a pre-chamber engine. In the early stage of combustion, there is a great deal of oxygen in the combustion chamber but a large amount of soot is produced. A large part of the soot may re-combust in the proceeding diffusive combustion period and the remainder is emitted from exhaust [3].

Despite the large amount of oxygen in the early stage of combustion, a great deal of soot is produced because the speed of the diffusive supply of oxygen to the spray cannot keep up with the rapid thermal cracking of the fuel by heat transfer from the surroundings just after ignition. As a result, a great deal of low-boiling-point hydrocarbons is produced, and, by condensation polymerization, these hydrocarbons produce polynuclear aromatic hydrocarbon (PAH) soot precursors, which are emitted from exhaust [9, 10]. Figure 2 shows the cracked components in the exhaust, and Fig. 3 shows the correlation between the soot and hydrocarbons. With increases in soot, low-boiling-point hydrocarbon in the exhaust (i.e., methane or ethylene, etc.) and polymerization of PAH proceeds, as shown in Fig. 4. That is, polymerization of PAH is also proceeds under intensive formation of soot [11].

As explained above, the production of large amounts of soot early in the combustion may occur due to differences in the speed of cracking of fuel and in the diffusion of oxygen from the surroundings. Then, oxygen exists in the fuel molecule as a biofuel, and the cracked components would directly oxidize and smoke formation would be suppressed. Figure 5 shows photographs of a diesel oil, rapeseed oil, and its methyl ester spray. In the case of biofuels, engine performance including smoke is similar to diesel oil in spite of extremely large droplet size, and rather smooth operation is possible. However, when naturally aspirated engines are operated for long durations with biofuels, there may be carbon deposition on the nozzle tip or piston rings may stick. With methyl ester, a spray similar to diesel oil was obtained with engine performance similar to the original biofuel and diesel oil [12, 13].

By using alcohol fuels, such as methanol or ethanol, smokeless operation of diesel engines is possible, but because of the extremely low cetane number, an ignition aid is necessary. In the case of a biofuel and its methyl ester, no modification of the engine is necessary because of the high cetane number of the fuels.

Although not economically practiced as a main fuel, a small amount of mixing of oxygenate additives to diesel oil may form a premium diesel oil. So, we would like to report on the smoke suppressing effect of dimethyl carbonate (DMC) as an oxygenate additive [14, 15].

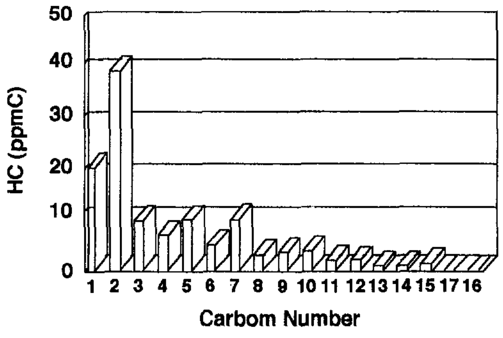

Fig. 2 Thermally cracked components in the exhaust (hydrocarbons)

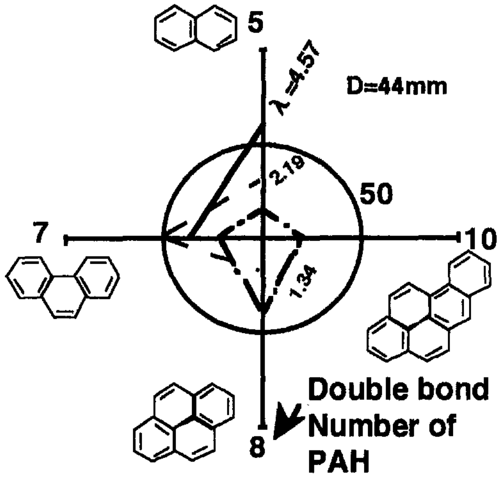

Fig. 4 Polymerization of PAH in the SOF

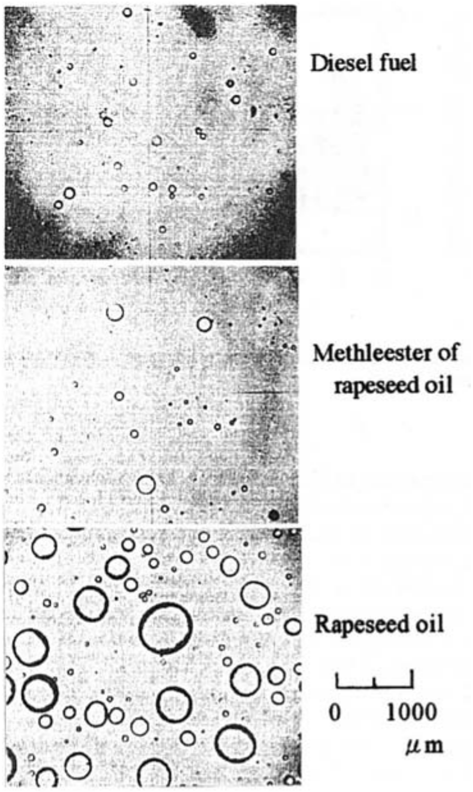

Fig. 5 Droplet size of various fuels

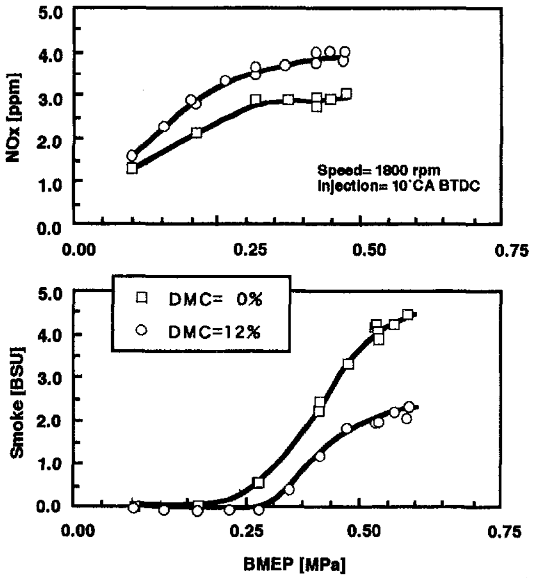

Fig. 6 Load characteristics on NO_x and smoke emissions for DMC = 0 percent and 12 percent by volume at 1800 rpm

The test engine was a single cylinder DI engine with 100 mm bore and 105 mm stroke, a BIP-type combustion chamber combined with the 0.28 mm diameter injector nozzle hole.

Oxygenated fuel additive DMC was used in the test. The selection criteria for oxygenates include additive solubility, the flash point of the blend, the viscosity of the blend, the solubility of water in the resultant blend, and the water partitioning potential of the additive. As a fuel oxygenated additive, DMC met such requirements and also had no objectionable odor. Yearlong use of DMC blended fuel did not cause fuel line damage, and it showed good solubility with diesel fuel. The DMC can be made from the reaction of CO and methanol, with an expected cost of $1 per liter in large scale production. The properties of DMC are shown below.

Dimethyl Carbonate	C3H6O3
Molecular Structure	H3C—O—C—O—CH3 ‖ O
C:H:O by Mass	6:1:8
Stoichiometric Air DMC Ratio	3.51:11
Density at 20°C	1.07 kg/l
Heating Value	15780 kJ/kg
Solubility	13.9g/100g with water

Since the solubility of DMC in water is high, it may be extracted from fuel with separated water. However, this did not happen during tests. Commercial diesel fuel was used as the baseline fuel.

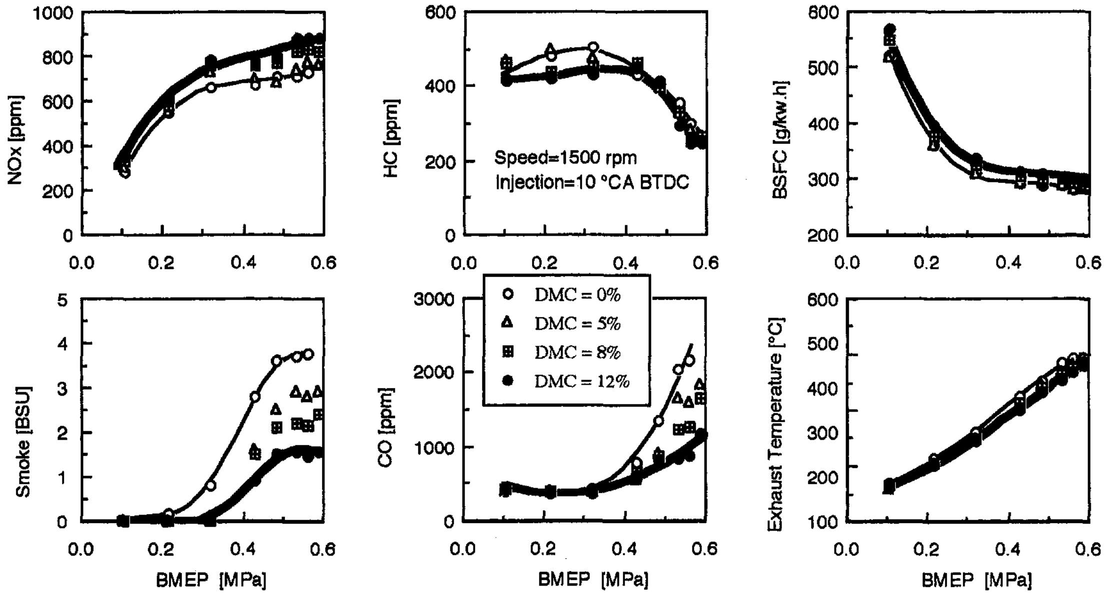

Fig. 7 The effect of DMC addition on load characteristics with engine speed 1500 rpm and injection at 10 deg CA BTDC

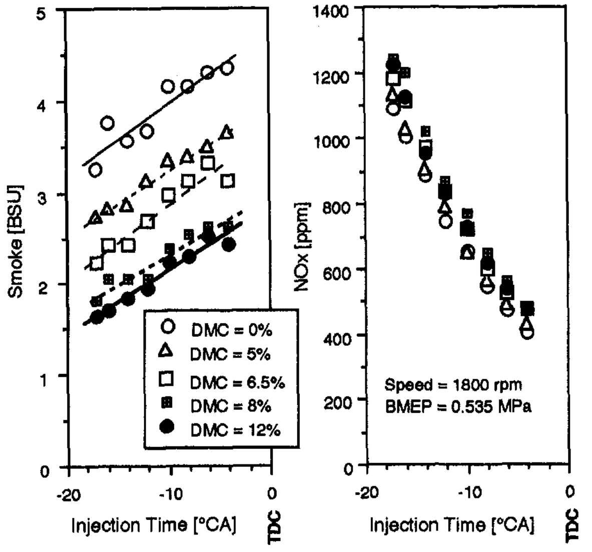

Fig. 8 The effect of fuel injection timing on NO_x and smoke emissions for different DMC concentrations

A constant-volume combustion bomb was used to observe the effects of DMC addition. The cylinder was 100 mm in diameter, and 30 mm wide fitted with quartz windows at each end, permitting optical access to the entire chamber. A high-speed video camera was used to record the flames generated by the combustion process.

After evacuation of air, the combustion chamber was loaded with a mixture of ethylene, oxygen, and nitrogen at an initial room temperature. The mixture was then ignited with a spark, providing a diesel-like condition for the following spray combustion. The oxygen concentration of the premixed combustion gas before the spray injection was set to 21 percent by volume.

Thermal cracking analysis was conducted to study the mechanism of particulate formation with DMC. The analysis was conducted in a nonpressurized furnace. Fuel was pushed through the capillary at different furnace temperatures and with different surrounding gases. Gas-chromatograph analyses were performed to determine the thermally cracked species under different conditions.

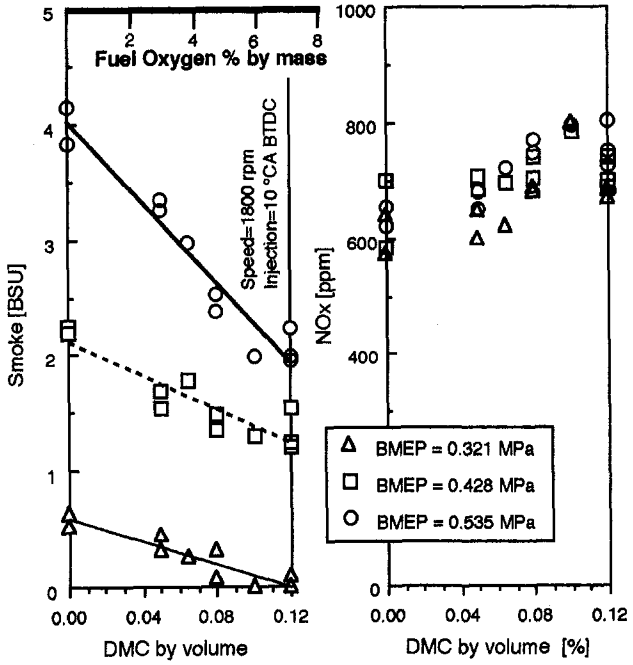

Fig. 9 The effect of fuel DMC Concentration on smoke and NO_x emissions

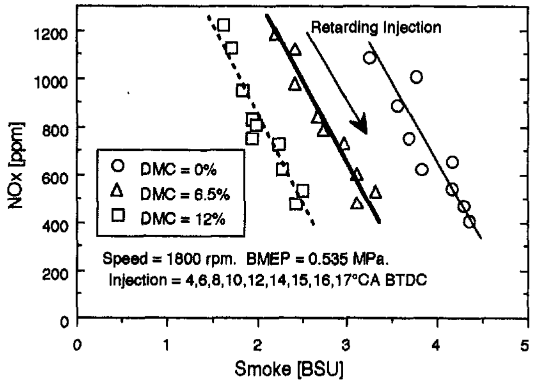

Fig. 10 The trade-off relation for NO_x and smoke when fuel injection is retarded for DMC = 0 percent, 6.5 percent, and 12 percent

The present investigation used two arrangements, one for lower boiling point hydrocarbons and one for higher boiling point hydrocarbons. The thermal cracking analyses were conducted on pure DMC, diesel fuel, and DMC blended diesel fuel, in nitrogen and oxygen environments.

DMC Addition Test. Figure 6 shows the basic effect of DMC on NO_x and smoke formation for a single cylinder engine. The DMC reduces smoke strongly at heavy loads, while NO_x increases some what. Comprehensive results are provided in Fig. 7, with the engine operating at 1500 rpm. Specific fuel consumption increases slightly as the DMC content increases because of decreased heating value. Using the heating value of DMC, it was confirmed that the thermal efficiency was identical both with and without DMC addition. The noticeable reductions in HC, CO, and exhaust temperature also indicate that the DMC addition improves combustion efficiency because the concentration (ppm values) closely corresponds to the amount of emissions in the naturally aspirated engine. This is also reflected in the increase in NO_x formation. Although specific fuel consumption increased, the engine thermal efficiency was maintained with the DMC addition here.

Figure 8 used injection timing as the variable at 1800 rpm and high load operation. Smoke increases and NO_x decreases when the injection timing is retarded. When DMC was added, a significant amount of smoke reduction was observed, and

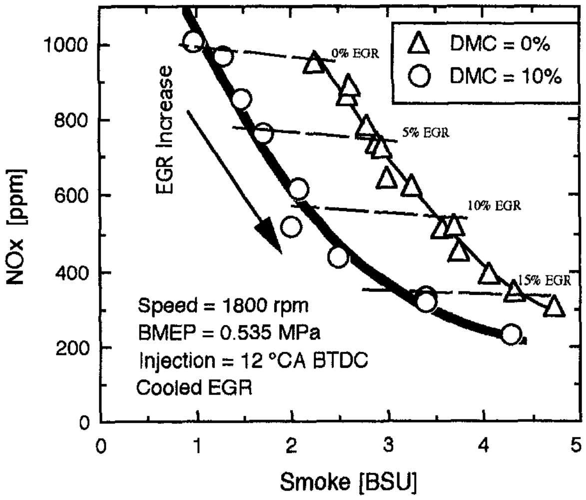

Fig. 11 The combined effect of EGR and DMC on NO_x and smoke

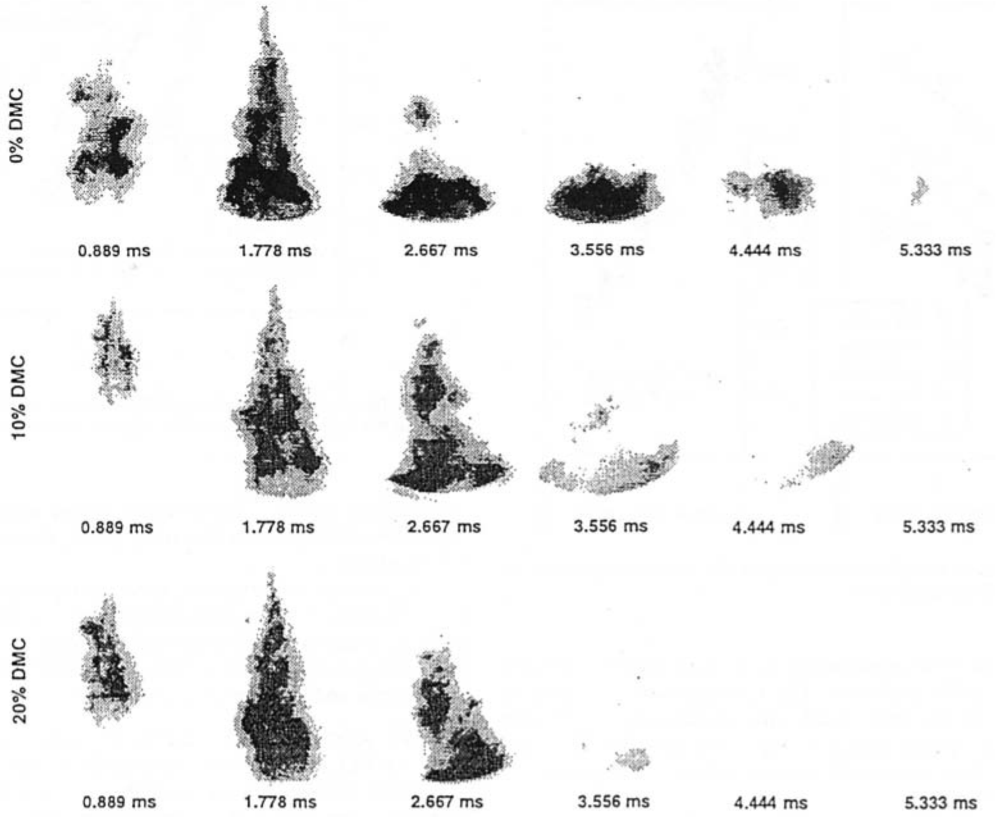

Fig. 12 The effect of DMC addition on the development of flame illumination. The time parameter refers to the time of the zero flame frame, the last with no illumination frame before ignition.

there were only slight increases in NO_x. As shown in Figs. 6 to 8, a smoke reduction of 35–50 percent was attained for a wide range of operation with 8 ~ 12 percent of DMC in the fuel.

Figure 9 shows the relationship between smoke levels and DMC concentration. The DMC is also represented as fuel oxygen concentration in the figure. For different load levels, smoke reduces directly with DMC content, while NO_x increases to a lesser extent. The figure also indicates that DMC addition has a stronger effect on smoke at higher load operation, indicated by the increased slope of the smoke data. However, such load effects are not reflected in the NO_x plot.

As DMC content increases, the rate of smoke decrease is much larger than the NO_x increase, which results in a better trade off between NO_x and particulate than with other methods, like injection timing retardations, as shown in Fig. 10.

With combined use of EGR and DMC, substantial reductions in NO_x and smoke were obtained simultaneously for the 10 percent DMC operation, Fig. 11.

Constant-Volume Combustion Bomb Observations. The effect of DMC was observed with the constant volume combustion bomb, and the results are shown in Fig. 12. The flame images were captured with a high-speed video camera at 13,500 frames/sec, with a resolution of 128 × 128 pixels. The oxygenated fuel significantly reduced the particulate luminosity and the luminosity disappears faster, indicating decreased smoke formation.

In these tests, fuel was injected through a single hole nozzle into a combustion chamber containing quiescent working fluids with engine like temperature and pressure.

Thermal Cracking Analysis. When thermal cracking is performed with nitrogen as the sole surrounding gas, the cracking of pure DMC generated some CO and CO2, which apparently suppressed the formation of ethylene, as shown in Figs. 13 and 14. Reductions in ethylene, in turn, is thought to have hindered the formation of benzene, as shown in Fig. 15. The effect of DMC on ethylene and benzene reduction was also shown with the DMC blended fuel, as compared with the reference fuel, Figs. 14 and 15. The suppression of ethylene and then benzene formation was observed in oxygen-nitrogen environments, see Figs. 13 to 15. Such suppression also took place for aromatics with two or more rings, Fig. 16.

The experimental observation suggested that during the initial stage of thermal cracking—before the oxygen component is separated from the fuel—a part of the oxygen in the DMC

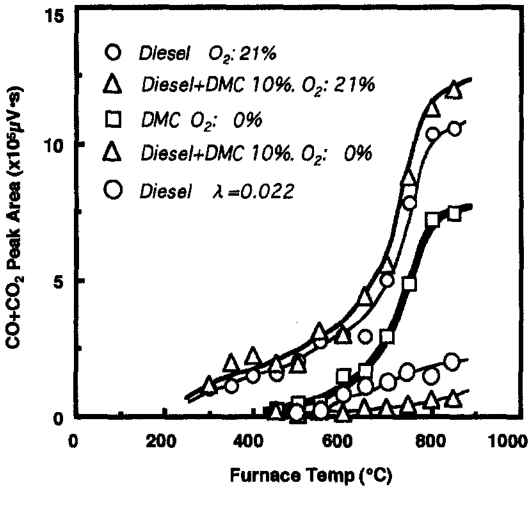

Fig. 13 The effect of DMC on the formation of CO and CO_2 in nitrogen and oxygen environments for the lower boiling point condition

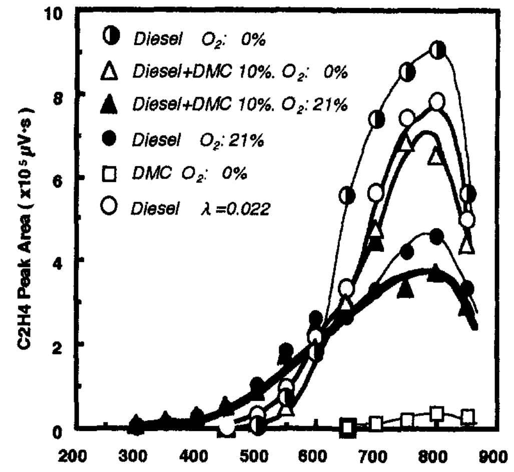

Fig. 14 The effect of DMC on the formation of ethylene in nitrogen environments for the lower boiling point condition

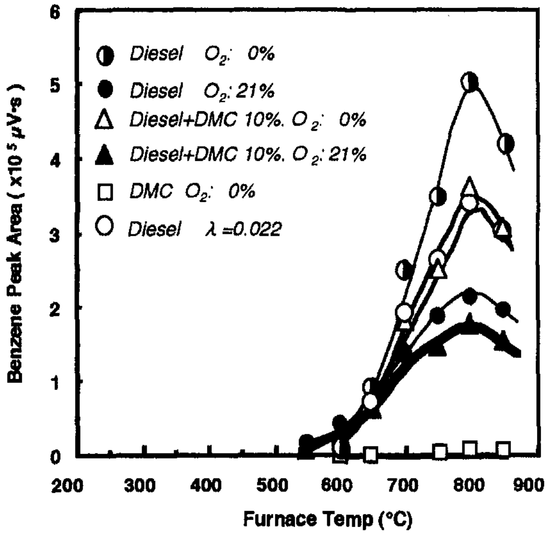

Fig. 15 The effect of DMC on the formation of benzene in nitrogen and oxygen environments for the lower boiling point condition

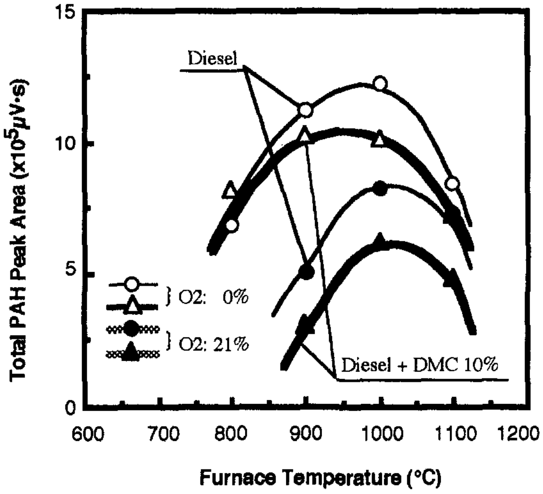

Fig. 16 The effect of DMC addition on the formation of total PAH in nitrogen and oxygen environments for the higher point condition

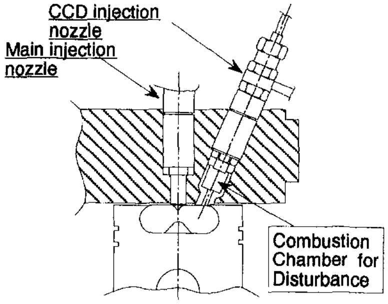

Fig. 17 Structure of the CCD system

was consumed during the cracking and polymerization of the blended fuel, and this reduced the formation of unsaturated cracked constituents, such as ethylene, etc. Thus, reductions in the formation of particulate can be expected through the suppressed benzene and polynuclear aromatic hydrocarbons (PAH).

When a small amount of O_2 was added in nitrogen-dominated environments to substitute the amount of oxygen contained by the 10 percent DMC addition ("diesel $\lambda = 0.022$" in the figures), there was little change in the suppression of ethylene and benzene, see Figs. 14 and 15. This suggests that the quantity of oxygen was much more important than the structure of the oxygen contained in the fuel.

Introduction of Strong Turbulence in Later Stage of Combustion

To reduce smoke effectively without increasing NO_x emission, it is important to maintain a moderate initial combustion and have an active secondary combustion. This is also the optimum combustion pattern for thermal efficiency because of the short and retarded combustion. When the initial combustion is made fuel rich followed by the activated combustion (two-stage combustion in the followings), the NO_x emission may be lowered with high thermal efficiency and low smoke because of the controlled mixture change process. In this section, the results of introducing strong turbulence in the later stage of combustion is presented together with an analysis of the smoke reduction mechanism in the process. The results of the two-stage combustion are also presented.

In the present research, the activation of the secondary combustion was attempted by introducing strong turbulence with the equipment described below.

The CCD System. The basic engines used in this research are four stroke, single cylinder, naturally aspirated direct injection diesel engines, with displacements of 694 and 1425 cc. The 694 cc engine (rated speed: 3600 rpm) was used in most of the experiments, except in Fig. 18, where the 1425 cc engine (rated speed: 1200 rpm) was used. A turbulence generating cell and auxiliary injection system are equipped to the base engine as shown in Fig. 17. This cell is referred to as the combustion chamber for disturbance (CCD), and the system and the auxiliary injection to the CCD are referred to as the "CCD system" and "CCD injection" in the following. Small amounts of fuel are injected into the CCD, and the jet of this burned gas is injected into the main combustion chamber, where it generates strong turbulence. The volume of the CCD corresponds to 5.5 percent of the total clearance volume. The injection timing and fuel ratio of the CCD injection were 10 deg after top dead center (ATDC) and comprised 10 percent of the total injected fuel, as established previously [16].

Results Of CCD Combustion. Figure 18 shows smoke, NO_x, and brake specific fuel consumption (BSFC) for different brake mean effective pressures (BMEP) with and without CCD

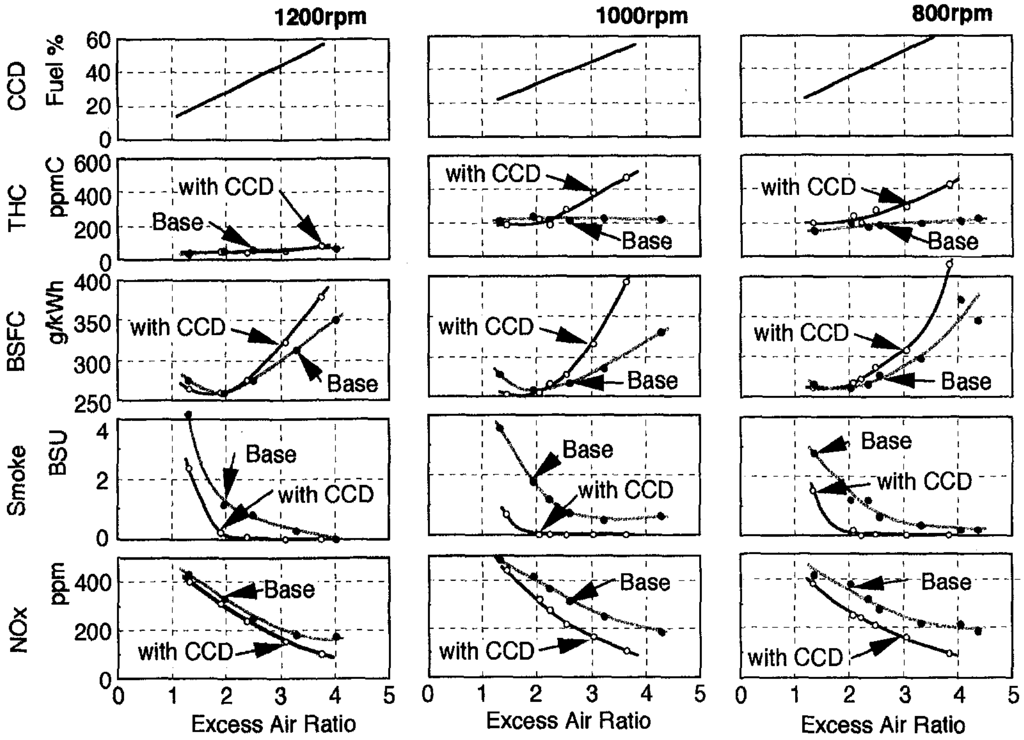

Fig. 18 Performance of the CCD system at various engine speeds and loads

injection. The abscissa is the engine load expressed as the excess air ratio. The engine speeds are 1200, 1000, and 800 rpm, and the injection timing of the main fuel is 10 deg crank angle before top dead center (BTDC) with the 1425 cc engine. The amount of fuel injected into the CCD is constant, and equal to 20 percent of the total fuel amount at a load of 0.37 MPa. The engine load is controlled by the fuel injected into the main chamber.

The figure shows that the CCD system reduces smoke very effectively. The smoke density is 0 above an excess air ratio of 2 and is below 2 Bosch Smoke Units even at an excess air ratio of 1.2. With the CCD injection the brake specific fuel consumption becomes poorer, and total hydrocarbon (THC) increases at partial loads because the ratio of the CCD fuel amount relative to the total fuel increases at partial loads. At full loads the BSFC is slightly better with CCD injection, and THC is as low as that without CCD injection. The decreased fuel consumption at high loads was attributed to the shorter combustion due to the enhanced mixing. The NO_x emissions with CCD injection are slightly lower than with the standard engine, and it was approximately equal to the standard engine in most of the experiments.

This confirms that the introduction of strong turbulence in the later stage of combustion is very effective in reducing smoke, while NO_x is maintained at the level of the standard engine. Generally, NO_x tends to increase when smoke decreases, but the result here indicates that the system improves the trade-off relationship between NO_x and smoke. This may be attributed to the fact that the turbulence is generated late in the combustion process, and is like the initial combustion where a large part of the NO_x forms. Deterioration in BSFC and hydrocarbons at partial loads were effectively prevented by decreasing the CCD fuel amount and injecting it at the main injection timing.

Smoke Reduction Process With Turbulence. To investigate the formation and oxidation process of particulate in the cylinder, particulate from the combustion chamber was sampled during the combustion process. The apparatus consists of a needle type high speed gas sampling valve, a particulate trap filter, a gas sampling chamber, and a vacuum pump. The sampling valve opening corresponds to 10 deg crank angle at an engine speed of 1440 rpm. The sampling time is indicated by the central crank angle at the sampling. Particulate concentrations were determined by measuring the filter weight before and after sampling and the volume of sampled gas. Details of the apparatus and procedures are given in reference [17].

Figure 19 shows the particulate concentrations in the main chamber for three cases. The case with CCD injection, without CCD injection, and the case when the amount of fuel corresponding to the amount of the main fuel with the CCD injection was injected into the main chamber only ("Main inj. only" in the figure). The excess air ratio is 1.5, except for the third case. In the third case, the excess air ratio is 1.8 because the total amount of injected fuel is reduced by the amount of the subinjection fuel.

As can be seen from Fig. 19, the particulate concentrations show a similar changes as they peak early in the combustion period and decrease as the oxidation proceeds. Comparing the

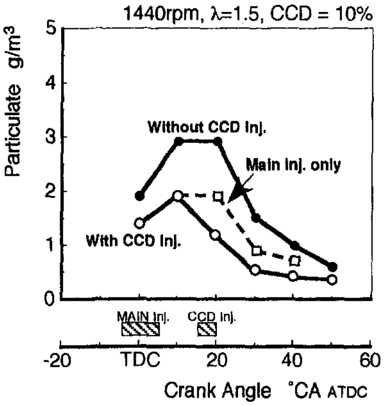

Fig. 19 Changes in particulate density sampled in the main combustion chamber

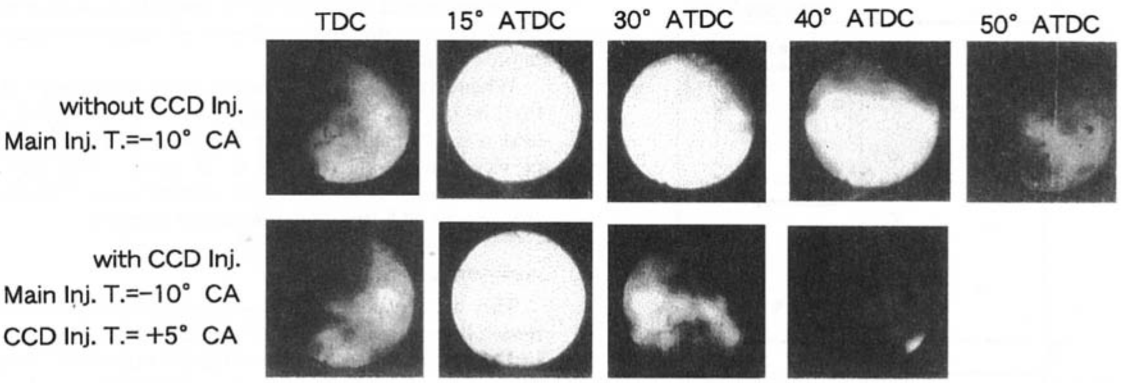

Fig. 20 Images (or comparison) of combustion processes with and without CCD injection (high speed photograph)

three cases in detail clearly shows the effect of the turbulence. The particulate concentration with the CCD injection is equal to that of the main injection, only early in the combustion period. This would be expected, as the amounts of fuel injected into the main chamber are equal in both cases. When the CCD injection starts, the particulate concentration begins to reduce rapidly, even though the amount of total fuel has increased. This increase is due to the addition of the secondary fuel. The reduction in smoke density shows that the turbulence promotes oxidation of the particulate formed at the early stage.

From a comparison of the particulate concentrations with and without the CCD injection given the same excess air ratio, we found that the peak value without the CCD injection is higher. This shows that greater quantities of particulate were formed at the early stage. It is thought that the difference in peak values is caused by the difference in amounts of fuel injected into the main chamber, judging from the fact that the peak value with CCD injection is the same as that with the main injection only.

The results of the gas sampling experiment show that the smoke reduction effect of the CCD system consists of the following two mechanisms: (1) promotion of particulate oxidation by strong turbulence generated from the CCD; and (2) reduction in particulate formation due to the decreased fuel quantity injected in the main chamber.

Next, a closer examination of the effect of the turbulence on particulate oxidation by in-cylinder observation. Figure 20 shows photos of the main chamber with and without the CCD injection during the combustion period using an optical glass fiber and a high speed camera. The engine speed is 1440 rpm, and the excess air ratio is 2.0. There were no differences between the pictures with and without the CCD injection for the period from ignition to the time when the flame has spread over the whole chamber (15 deg ATDC). In the later period, however, it is observed that the flame disappears rapidly at 30–40 deg. ATDC with the CCD injection, in contrast to the case without the CCD injection, where the flame remains after 50 deg ATDC.

Two-Stage Combustion. Next, it was attempted to reduce NO_x while keeping the smoke level low with the two-stage combustion concept. To form the initial rich mixture, pistons are equipped with a small cavity of 72 percent of the basic piston cavity as shown in Fig. 21. The rest is air cavity, with the extra air available for the secondary combustion. The total volume of the air and the main cavities are equal to the basic cavity volume. The type 1 piston has a circular air cavity around the top clearance area, separated from the main cavity. The type 2 piston has the air volume at the top of the cavity, while in type 3 it is in the bottom of the cavity. The last two pistons do not have a clear separation between the air and the main cavities.

Figure 21 compares the results for these pistons with that of the basic piston. A 10-hole nozzle was used for the small cavity pistons and this gave better emission performance than the original 4-hole nozzle. With the basic piston, the original 4-hole nozzle was used as the best matched injector. All of the three pistons for the two stage combustion, where CCD injection is applied, show significantly lower NO_x emissions than the basic engine. However, without CCD injection significantly more smoke was emitted. With CCD injection, smoke levels apparently decreased and became lower than the basic piston level when injection timing was optimized, as shown in the figure. The type 1 piston decreased smoke at relatively early injection timings, while the type 2 piston decreased smoke at late injection timings. Type 3 had the highest smoke emissions of the three. Thus, by optimizing two-stage combustion, it was shown that simultaneous reduction of NO_x and smoke may be possible.

Figure 22 shows the trade-off curves for NO_x versus specific fuel consumption and smoke. The small cavity combustion chambers with the CCD system are shown for the basic engine and with the CCD system. At each condition, the injection timings were varied. The figure shows that the fuel consumption with the small cavity is similar to that of the base engine, although it does not reach the level of the base engine with the

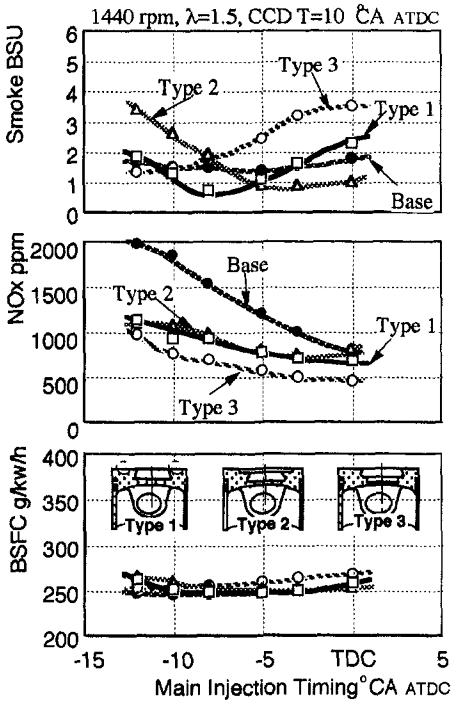

Fig. 21 Engine performance with various piston configuration in the two-stage combustion

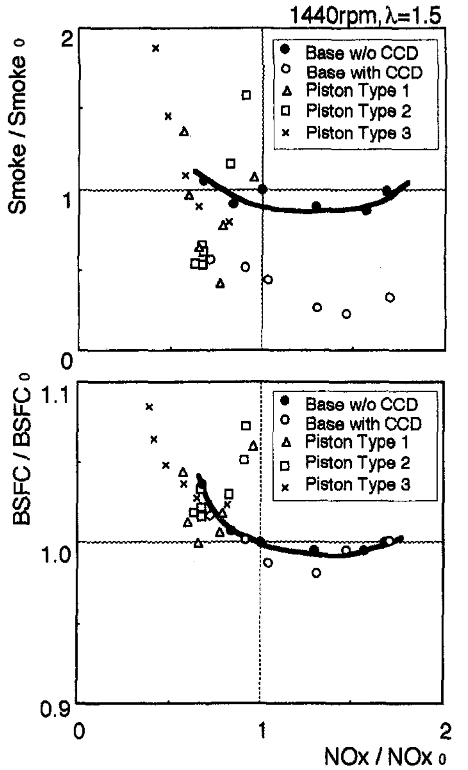

Fig. 22 Trade-off curves for the various two-stage combustion pistons and the base engine with and without CCD

CCD system. It also shows that the NO_x and smoke decrease simultaneously with the use of type 1 and type 2 pistons, something that cannot be achieved by simple retardation of injection timing with the basic engine.

The above findings show that "rich, high turbulence combustion," i.e. two-stage combustion, offers great potential for simultaneous improvements in smoke and NO_x emitted from diesel engines.

Conclusion

This work focused on determining ways to minimize smoke emissions while keeping good thermal efficiency and NO_x emission levels.

To suppress soot formation due to thermal cracking with the shortage of oxygen in the early intensive combustion, dimethyl carbonate as an oxygenate additive was utilized. As a result, smoke was reduced almost linearly with DMC concentration directly in proportion to fuel oxygen content. With 10 percent of DMC contained in the fuel, a smoke reduction of 35 ~ 50 percent was attained.

To completely burn the remaining soot at the late stage of combustion, the CCD system (combustion chamber for disturbance system) was very effective in the following two ways: (1) promotion of particulate oxidation by strong turbulence generated from the CCD; and (2) reduction in particulate formation due to decreased fuel quantities injected in the main chamber.

When a rich mixture is formed at the initial stage of combustion, NO_x decreases significantly to 30 percent even with high heat release during the early combustion. So, the combination of oxygenate additives and CCD system with rich mixtures could offer great potential for simultaneous improvements in smoke and NO_x emitted from diesel engines.

Acknowledgment

This work was financially supported by Ube Industries Ltd., research program RC-107 of the JSME, and Isuzu Motor Co. Ltd. provided support in procuring the experimental equipment. The authors were fortunate to have the assistance of many graduate students of Hokkaido University and Hokkaido Institute of Technology, whose contributions were invaluable in the accomplishments of the research reported here.

References

1 Meurer, J. S., 1956, "Evaluation of Reaction Kinetics Eliminates Diesel Knock—The M-Combustion System of MAN," SAE-Trans. Vol. 64.

2 Meurer, J. S., 1962, "Multifuel Engine Practice," SAE-Trans. Vol. 70.

3 Murayama, T., Fujiwara, Y., and Tosaka, T., 1992, "The Properties, Formation, and Oxidation of Soot Particulate in Diesel Engines," ASME ICE-Vol. 17.

4 Tabata, T., et al., 1995, "Effects of Multi-Hole Nozzle with Throttle Construction on Diesel Combustion and Emission with High-Pressure Fuel Injection," SAE-950607.

5 Murayama, T., 1969, "An Experimental Study on the Performance of a Multifuel Engine: Part 1—Applied to a Precombustion Chamber Engine," *Bulletin of the JSME,* Vol. 12-50, p. 311.

6 Murayama, T., et al., 1988, "Potential and Problems in Alcohol Fuel Combustion Techniques in Diesel Engines," *Proc. of the International Symposium on Alcohol Fuels,* Vol. 6.

7 Murayama, T., et al., 1978, "Experimental Reduction of NO_x, Smoke, and BSFC in a Diesel Engine Using Uniquely Produced Water Fuel (Zero to 80%) Emulsion," SAE Trans. 780224.

8 Murayama, T., 1994, "Evaluating Vegetable Oil as a Diesel Fuel," *INFORM,* Vol. 5, No. 10, p. 1138.

9 Tosaka, T., Fujiwara, Y., and Murayama, T., 1989, "The Effect of Fuel Properties on Diesel Engine Exhaust Particulate Formation," SAE Paper 890421.

10 Fujiwara, Y., Fukazawa, S., Tosaka, S., and Murayama, T., 1984, "Formation of Soot Particulates in the Combustion Chamber of a Precombustion Chamber Type Diesel Engine," SAE Paper 840417.

11 Murayama, T., Yamane, K., Chikahisa, T., and Miyamoto, N., 1988, "Measurement of Particulate and Unburnt Hydrocarbon Emissions for Diesel Engines," SAE Paper 880343.

12 Murayama, T., Takagi, N., Oh, Y., Miyamoto, N., Itow, K., and Chikahisa, T., 1984, "Low Carbon Flower Buildup, Low Smoke, and Efficient Diesel Operation with Vegetable Oils by Conversion to Mono-Esters and Blending with Diesel Oil or Alcohols," SAE Trans. 841161.

13 Murayama, T., Miyamoto, N., Chikahisa, T., and Yamane, K., 1986, "Effect of Super Heating of Heavy Fuels on Combustion and Performance in DI Diesel Engines," SAE-Trans. 860306.

14 Murayama, T., Zheng, M., Chikahisa, T., Oh, Y., Fujiwara, Y., Tosaka, S., Yamashita, M., and Yoshitake H., 1995, "Simultaneous Reductions of Smoke and NO_x from a DI Diesel Engine with EGR and Dimethyl Carbonate," SAE Trans. 952518.

15 Liotta, F. J., and Montalvo, D. M., 1993, "The Effect of Oxygenated Fuels on Emissions from a Modern Heavy-Duty Diesel Engine," SAE Paper 932730.

16 Murayama, T., and Chikahisa, T., 1990, "Reduction of Smoke and NO_x Emissions by Active Turbulence Generated in the Late Combustion Stage in D.I. Diesel Engines," ICE-Vol. 11, ASME, New York.

17 Konno, M., Chikahisa, T., and Murayama, T., 1993, "An Investigation on the Simultaneous Reduction of Particulate and NO_x by Controlling Both the Turbulence and the Mixture Formation in DI Diesel Engines," SAE Paper 932797.

F. Trenc

S. Rodman

Department of Mechanical Engineering,
University of Ljubljana,
Asuerceva 6,
Ljubljana, Slovenia, SLO-1000
ferdinand.trenc@fs.uni-lj.si

L. Skerget

M. Delic

Department of Mechanical Engineering,
University of Maribor,
Maribor, Slovenia

Optimum Cylinder Cooling for Advanced Diesel Engines

Continuous demand for higher specific engine output simultaneously introduces problems of higher mechanical and thermal stresses of the engine components. Uneven temperature distribution in the cylinder wall of a diesel engine, especially when air-cooled, is well known. Peak local temperatures, large circumferential and longitudinal temperature gradients provoke deformations that, in turn, affect the reliability of the engine. As the result of intensive numerical and experimental investigations, a horizontal, curved channel fed with engine lubrication oil was introduced in the upper part of the air-cooled cylinder. Optimization of the channel design, its position, and determination of suitable asymmetrical split oil flow have led to more favorable cylinder temperature distribution, similar to that obtained by advanced water-cooled engines. Analyses of the local laminar oil-flow phenomena and local heat transfer distribution in curved channels are discussed in the paper and can be successfully applied to advanced liquid-cooled engines.

Description of the Problem

A portion of heat released in the combustion process in an internal combustion engine is dissipated from the engine surfaces to different coolers. Heat transfer through the engine cylinder is the object of this paper. Liquid, water-based cooling is generally used to cool cylinder liners of the advanced diesel engines. Air-cooling is, on the other hand, suitable for small petrol engines, diverse industrial engines, and the engines for special purpose, off-road vehicles. Three cooling media are therefore applied to cool the engine: water, air, and engine lubrication oil. If water is replaced by the lubrication oil, only two cooling media remain, and the reliability of the engine can be substantially improved. Full oil-cooling has been applied to smaller industrial engines only. Air-cooling of the engine cylinders requires sophisticated design and increased cooling surfaces. Trenc et al. (Trenc, 1992, 1993; Trenc and Pavletic, 1993; Trenc et al., 1994; Trenc and Primozic, 1994; Trenc et al., 1995) report the following: "If physical properties of the cooling air are also taken into account, maximum limiting specific engine output of about 21 kW/liter swept volume can be expected for the turbocharged, aftercooled, and air-cooled diesel engines." This limit is defined as follows: (*a*) by the peak temperatures of the inner wall (working surface) of the cylinder that amounts, in the case of an air-cooled engine, to approximately 200°C. These peak temperatures are located in the upper working part of the cylinder, i.e., in the cylinder transverse section that is defined by the extreme upward position of the top piston ring (ring reversal); (*b*) by the maximum cylinder circumferential temperature gradients, or simply by its temperature asymmetry (defined by the difference between the peak and the minimum circumferential temperature at the same cylinder transverse section) that amounts to over 40°C; and (*c*) by the average longitudinal temperature gradients in the upper working part of the cylinder liner that exceed 1°C/mm cylinder length (Transverse sections 0-I-II in Fig. 3). These temperature gradients are mostly consequence of the axial heat fluxes from the intake and exhaust channel flow through the cylinder head to the cylinder contact surface and of the radial heat fluxes from the combustion process that diminishes during the working stroke of the piston. The heat sources mentioned above generate an uneven temperature distribution circumferentially and longitudinally through the cylinder wall. This temperature pattern is typical also for water cooled cylinders and will be described later.

Ideally, a perfect cooling system would result in isotherms of moderate temperatures around and along the cylinder wall. "Increased temperature asymmetry, due to high local temperatures and temperature gradients in a real engine (the art of cylinder cooling is less important) are located in the upper quarter of the cylinder height," reported Trenc (1992) and Trenc and Primozic (1994). In the lower part of the cylinder, almost isothermal circumferential temperature distribution can be met. Absolute temperature level there depends mostly on the cooling art and its design (longer cooling water jacket); it is also affected by the heat transfer to the engine crankcase. If lower wall temperatures of approximately 140–150°C are typical for an air-cooled engine, corresponding temperatures in a conventional water-cooled cylinder do not exceed 120°C. The first conclusion could be that the top of the cylinder shall be cooled intensively (to avoid longitudinal temperature gradients and too high peak cylinder wall temperatures), selectively around its periphery (to avoid excessive temperature asymmetry), and less intensively in the lower half of the cylinder (cylinder temperatures that are lower than the saturation temperature of the combustion products can provoke corrosion effects on the cylinder working surface and have to be avoided (Dobovisek et al., 1989).

Solution of the Problem

A rectangular curved channel fed with engine lubrication oil was inserted in the upper part of a baseline, air-cooled cylinder. Configuration of the channel was designed according to available technological possibilities and the results of the local heat transfer analyses. After trials with single oil flow channel design and symmetrical split oil flow, proposed by Trenc (1992), and Trenc et al., (1994), an asymmetrical split oil-flow channel was introduced to more effectively cool the baseline air-cooled cylinder. Results of the experimental and numerical analyses proposed by Šelih et al. (1993) were used for the optimization process of the prototype four-cylinder, TC and IC combined air-oil cooled TAM BF 513LC family engine. Layout of three channel designs for additional oil-cooling of the baseline air-cooled engine and their principal geometry is shown in Fig. 1. Results concerning research work with the channel DOH3 are described by Trenc (1992), Trenc and Pavletič (1993), and

---

Contributed by the Internal Combustion Engine Division for publication in the ASME JOURNAL OF ENGINEERING FOR GAS TURBINES AND POWER. Manuscript received by the ASME Headquarters December 20, 1997. Associate Technical Editor: D. Assanis.

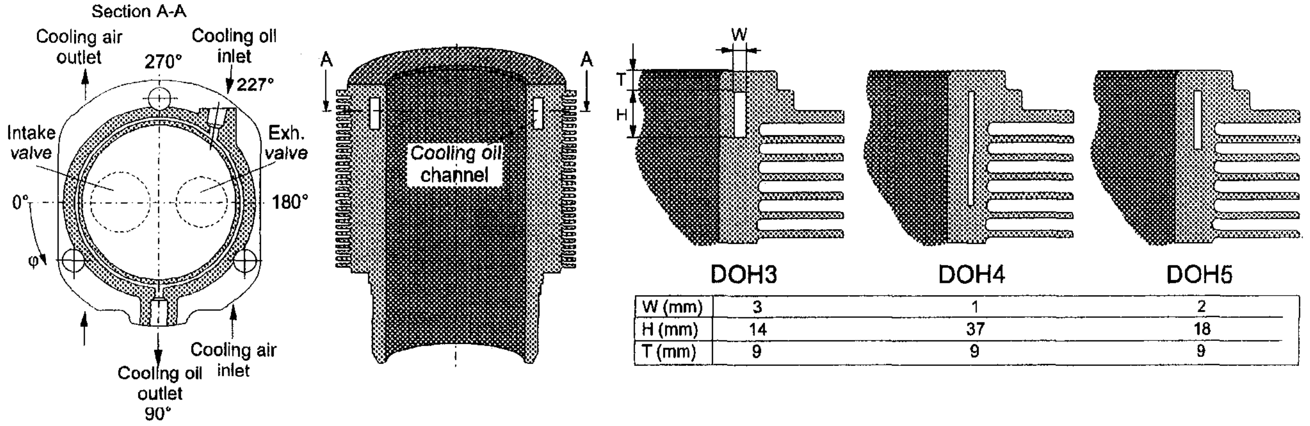

	DOH3	DOH4	DOH5
W (mm)	3	1	2
H (mm)	14	37	18
T (mm)	9	9	9

Fig. 1 Layout of the cylinder combined air-oil cooling with 3 versions of channel design

Šelih et al. (1993), whereas DOH4 and DOH5 channel design versions, together with some measured and computed heat transfer data and oil mass flow data were presented by Trenc et al. (1995). The position and relative size of the intake and exhaust valve in the cylinder head is schematically presented on the left side of Fig. 1. Relative size of the channel geometry, other geometrical details, and oil mass flow data were presented in the Trenc's patent (1993). Transverse section of the cylinder (left) shows asymmetrical cooling channel branches: the shorter with bigger portion of the cooling oil spreads along the hottest area of the cylinder (vicinity of the exhaust valve and outlet of the hot cooling-air), whereas the longer branch with less oil covers the region of the intake valve and therefore lower cylinder temperatures. The oil jet enters the channel in the zone where peak cylinder temperatures are located. It strikes the inner channel wall, prevents the formation of the boundary layer, and, therefore, dramatically (locally) increases the heat transfer coefficient. Ma et al. (1990) reported that local heat fluxes of the range 10^6 W/m^2 can be met when jets of impinging viscous fluids are concerned. The effect of the intensive heat transfer at the cooling oil inlet provokes a sink of local temperatures and levels the circumferential temperature asymmetry. Design and control of partial oil flows in two channel branches is very simple and was described and patented by Trenc (1993).

Figure 2 shows circumferential temperature distribution of the inner cylinder wall and in the transverse cylinder section where the top piston ring reaches its extreme position (ring reversal). The results of the experimental work with three-channel cooling design solutions (baseline air-cooled DOH3 on Fig. 2 as well as on Fig. 3) are very similar to those reported by Trenc et al. (1993) and for the DOH4 Trenc et al. (1995); engine running conditions were the same for all three cooling designs presented, and they refer to the engine rated (peak) torque. Optimum quantity (mass flow $\dot{m}$ = 0.08 kg/s) of the cooling oil was determined during the optimization procedure on the prototype engine for the described operating point and 0.11 kg/s for the engine rated power. Temperatures of the inner cylinder and both channel walls (measured 1.3 mm from the working surface) were taken by 58 0.2 mm diameter NiCr-Ni thermocouples; their position is schematically shown by the control sections 1 to 9 in Fig. 2 and 0–IX in Fig. 3.

Circumferential temperature asymmetry of the baseline cylinder was additionally leveled by the impinging jet of the cooling oil and the DOH3 and DOH4 versions. Influence of more intensive cooling and lower cylinder temperatures in the longer channel branch of the channel DOH4 (Fig. 2) is the direct consequence of larger oil flow there. This was proved by the results of the subsequent laser-assisted oil velocity measurements and numerical simulations of the channel flow dynamics. Heat transfer in shorter channel branch is, according to Fig. 2, approximately the same for DOH3 and DOH4. Higher heat fluxes of the DOH4 channel (Fig. 9) were compensated by lower oil rate through the shorter branch of the DOH4 channel branch reported (Delič et al., 1996; Rodman et al., 1996).

Optimum DOH design is defined by the reasonably high ratio between the heat dissipated by the cooling oil, and the moderate pressure losses in the channel. Measured pressure drop of the oil in the DOH4 channel is (by approximately 50 percent) higher in comparison with channel DOH3 at lower oil flows (00.07 kg/s) and roughly the same at larger flow rates ($\dot{m}$ > 0.12 kg/s), where channel inlet and outlet pressure drops become predominant (Rodman, 1996). The absolute value of the pressure drop in the channel DOH4 that includes inlet, outlet, and line pressure losses never exceeded 6.10^4 Pa per engine cylinder at the engine rated conditions. Extra power consumption of the oil pump for the model engine BF 4L 513LC was therefore calculated to be 240 W; it represents less than 0.16 percent of the measured rated engine brake effective power, and is within the range of the engine test and accuracy.

Longitudinal measured temperature distribution in the cylinder wall and average temperature gradients of a water, air, and

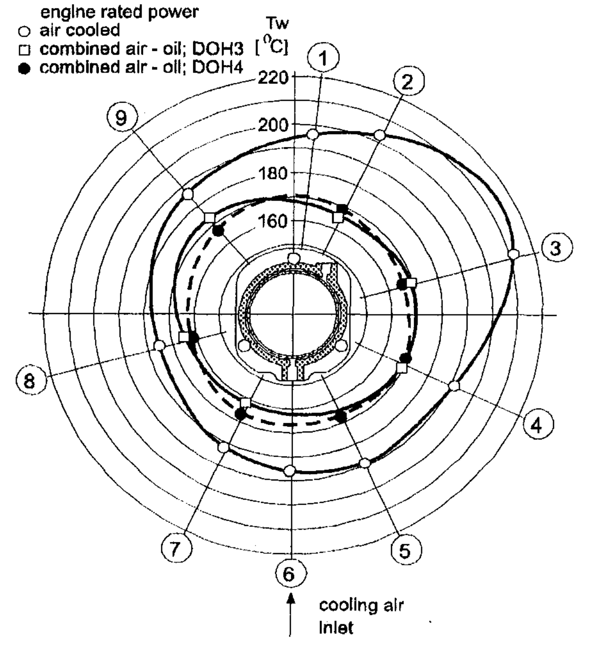

Fig. 2 Circumferential temperature distribution in the cylinder wall (1.3 mm from the inside surface) for 3 DOH configurations

cooling	engine rated power [%]	ΔT/Δl hotest section '3'	[°C/mm] coolest section '8'
○ —— air cooled	100	0,82	0,42
□ —— combined cooled DOH3	100	0,27	0,24
△ - - - water cooled	100	0,59	0,19
● —— combined cooled DOH4	100	0,65	0,35

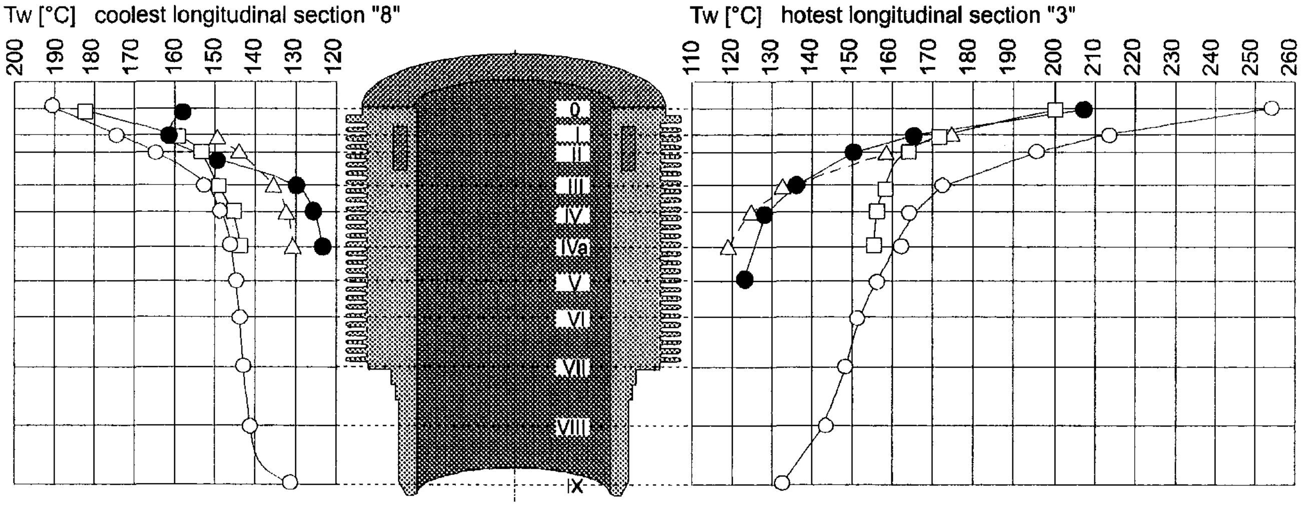

Fig. 3 Measured longitudinal cylinder wall temperature distribution for different cooling systems

combined air-oil cooled engine for the same (rated) engine running conditions are presented in Fig. 3. Some data (water and DOH3) were again taken from the previously reported data (Trenc, 1993) for better comparison. The left part of the diagram shows temperatures in the relatively "coolest" (section No. 8, Fig. 2), and the right part shows the temperatures in the "hottest" (section 3, Fig. 2) longitudinal cylinder section. Owing to its reduced height ($H = 14$ mm), influence of the additional cooling with the DOH3 channel design on the lower (air-cooled only) part (temperatures) of the cylinder is insignificant. On the other hand, DOH4 with its longer channel (Fig. 1) also intensively cools the lower part of the cylinder. Its temperature distribution and its average longitudinal temperature gradient is very similar to that of a water-cooled engine. The long jacket of a conventional water-cooled Diesel engine cools the bottom half of the cylinder to less than 120°C. For an optimum cooling system, a higher temperature would be more favorable. In the case of highly rated diesel engines, problems of piston cooling could be overcome by an extra oil channel at the bottom of the cylinder wall.

Numerical Model for Local Thermo-Hydraulic Conditions in the Channel

Hydraulic Conditions of the Oil in a Curved Channel. Previous experimental and two-dimensional numerical investigations of the temperature distribution within the cylinder wall were reported by Trenc et al. (1992) and Selih et al. (1993). Constant (measured) local oil temperature and heat transfer coefficient (from Trenc (1992)) in the channel wall were prescribed in the two-dimensional model for the two selected cylinder longitudinal sections (3 and 8, Fig. 2). Besides temperatures along the internal and top (contact to cylinder head) cylinder wall, together with the prescribed convective boundary conditions for the air-cooled fins, do not give sufficient explanation of the local oil flow and heat transfer phenomena in the oil channel. The problem of the channel flow was therefore later solved numerically by itself and presented by Delič et al. (1995, 1996). Adiabatic boundary conditions were prescribed for the inlet and outlet section of the channel as well as for the top and the bottom channel walls. Mean measured temperatures of the inner and outer channel wall were determined during the previous experiments on the engine and were kept constant along the channel length. Mass flow and the temperature of the incoming oil and reference pressure in the outlet channel section were also prescribed according to the experiments. The TASCflow 2.4 computer program based on the finite volume method was applied to solve problems of transport phenomena in the undeveloped laminar flow of incompressible viscous fluid. Expressions that include variation of physical properties of the cooling oil by temperature were defined (especially the change of the kinematic viscosity of the engine lubrication oil with the temperature) and used for the calculations. Local temperatures of the oil were progressively computed along the channel length and took into account the change of the oil viscosity. To obtain good convergence of the computed results, a fine mesh consisting of 261.460 nodes was applied by Delic et al. (1995). Layout of the finest mesh for the channel DOH4 flow (left) and the calculated streamlines (right) of the oil flow for the same channel geometry are presented in Fig. 4. Results of numerical computation gave velocity profiles of the oil flow at different locations of the channel. Integration of the calculated velocities (over the channel transverse cross section) for the oil mass flow mentioned before indicated that 77.8 percent of the flow feeds the shorter branch, and only 22.2 percent feeds the longer branch (Delic et al., 1996). Influence of the selected boundary conditions on the results of computations and comparison with laser-measured velocities in the channel DOH4 led to a discrepancy in the branch flows that didn't exceed 8 percent.

A very sophisticated flow pattern develops in the channel inlet region that crucially affects flow and heat transfer in both channel branches. It generally depends on the channel geometry (aspect ratio) and the oil mass flow. Curves of constant oil velocities in the four indicated locations of the channel DOH4 (transverse channel sections A1 to A4; flow symmetry allows presentation of one half of the channel only) are presented in Fig. 5. The oil jet first strikes the inner wall of the channel (section A4), and then spreads toward the channel branches.

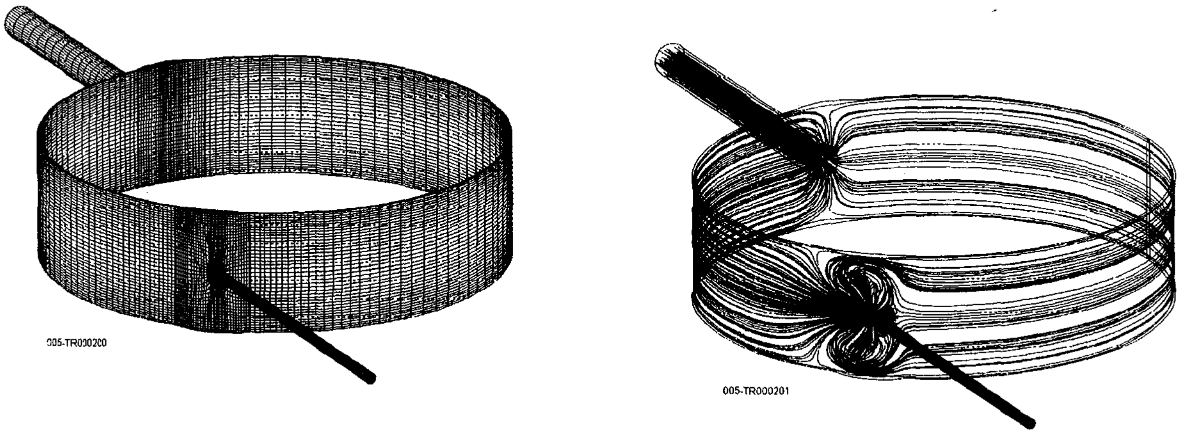

Fig. 4 Finest mesh for flow calculations (left) and streamlines of the DOH4 flow (right)

In a short time after entering the branch (section A1), the peak flow velocity decreases to one third of its initial value.

Influence of the centrifugal forces on liquids in curved channels and especially in wider channels (smaller aspect ratio channels) and higher Reynolds numbers have been reported by different authors. Fluid transverse motion towards the outer, top, and bottom channel wall consequently occurs, and the fluid is forced into a spiral motion. The location of top fluid velocities moves from the inner to the outer channel wall. Transverse secondary flow appears in the inlet channel section as the consequence of the impinging oil-jet. It spreads along both channel branches and generates reverse flows. Reverse flows obstruct general motion of the coolant, and decrease the effective mass flow through the channel. This is also the reason why greater aspect ratio channels are more efficient for heat transfer. If the channel aspect ratio is increased, viscosity forces prevail, and together with higher channel friction, prevent reverse flows in the channel. The flow pattern is more regular and two velocity peaks close to the top and bottom channel wall appear. Figure 6 shows computed axial velocity distribution in the coolant inlet section for the bigger aspect ratio DOH4 channel (*a*, *b*, and *c*) at $\frac{1}{4}$, $\frac{1}{2}$, and $\frac{3}{4}$ of the channel height, and smaller aspect ratio channel DOH3 (*d*) at $H = \frac{1}{2}$. The bottom part (*d*) of Fig. 6 clearly shows that reverse flow enters the left (higher-flow) channel branch, and that peak velocities are located close to the inner channel wall. No reverse flow exists in the narrower DOH4 channel. The above described flow configuration dramatically affects heat transfer capability of the channels and will be discussed later again. Computed results were tested and compared to the measured data. A laser anemometer (LDA) together with a model transparent cylinder was used for this purpose. Results of measured axial velocities in the channel transverse section that corresponds to the position angle $\varphi = 205$ deg (on Fig. 1) are presented in Fig. 7. Comparisons between computed and measured data show good agreement. Two typical velocity peaks can be seen close to the top and bottom channel wall. Integration of particular measured velocity components gives (together with the appropriate density values) mass flows that differ from the integral measured oil flow by less than 2 percent. Combination of any integrated mass flows through any transverse control section in the high flow and low flow branch shows better than 1.7 percent accuracy.

Heat Transfer Results in a Curved Channel. As it was mentioned in the last paragraph, spiral flow of the cooling oil is formed along the channel branches. The "pitch" of this spiral defines zones where peak velocities come closest to the inner or outer channel walls, making the laminar boundary layer of the cooling oil thinner, and making local cooling more efficient. The boundary layer is first destroyed in the zone where oil

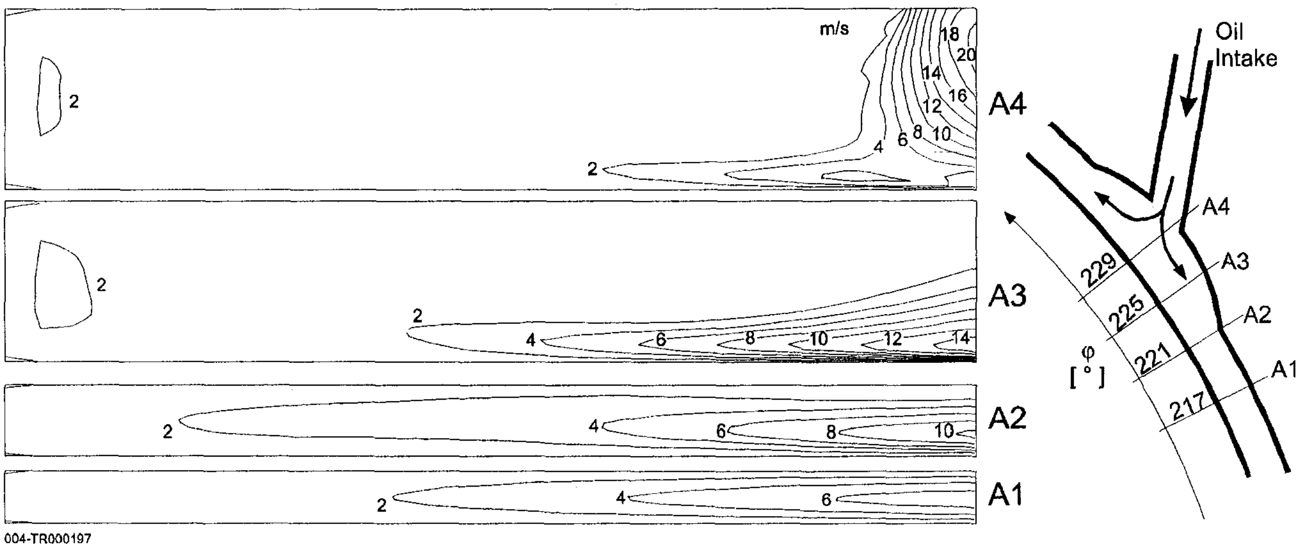

Fig. 5 Isolines of velocity in the channel inlet zone and transverse sections A1, A2, A3, and A4

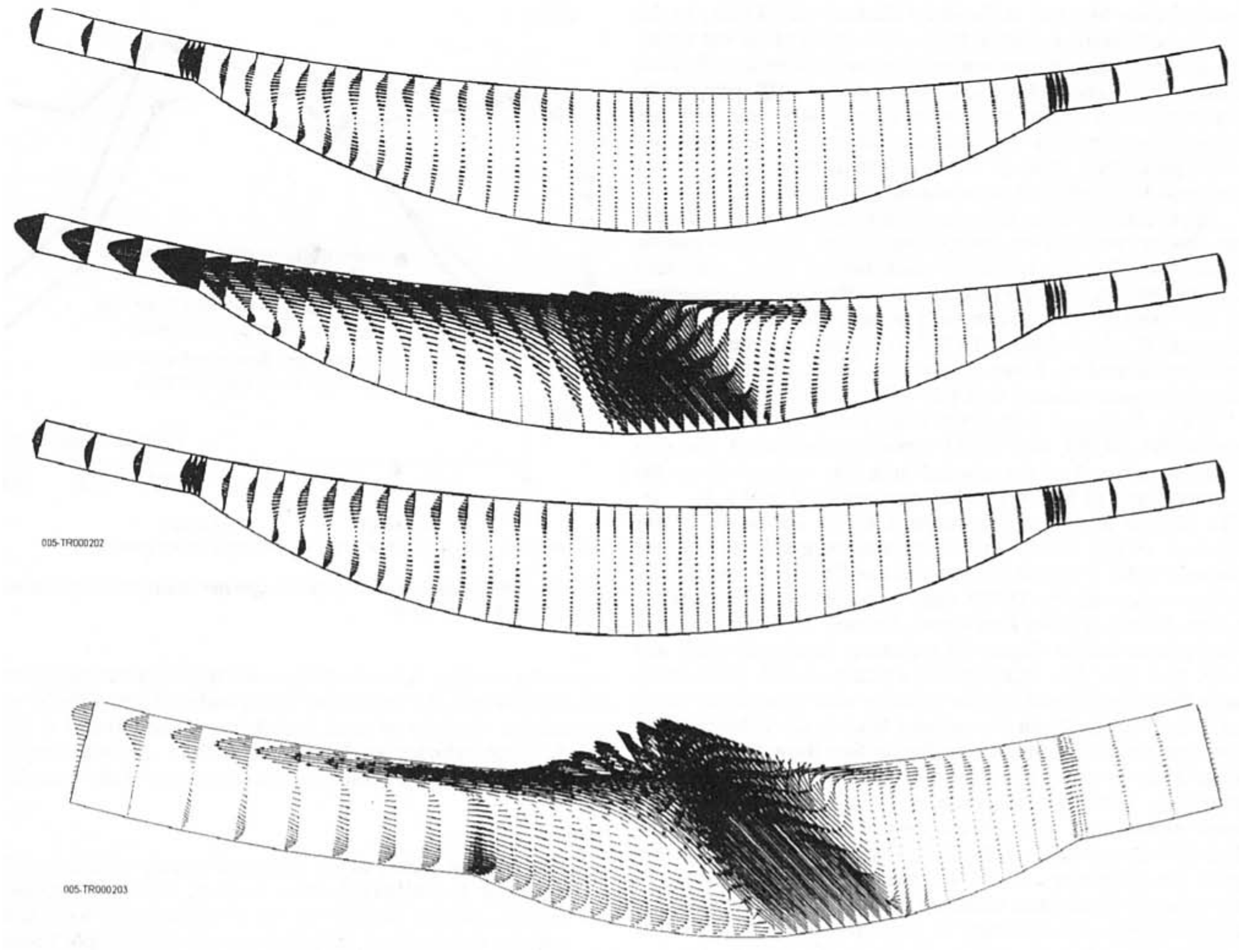

Fig. 6 Axial velocity distribution in the inlet zone for the channel DOH4: (*a*) 1/4H; (*b*) 1/2 H; (*c*) 3/4 H; and for the channel DOH3, (*d*) 1/2 H.

leaves the inlet zone and enters particular channel branches. Local maxima of the heat flux therefore occur at the contractions and expansions of the channel. Average calculated heat flux data along the inner and outer wall of the DOH4 channel are presented in Fig. 8; internal or external channel wall surface ($H \times$ channel length) was taken into account for particular heat flux calculations. Peak values correspond to the contractions at the channel inlet and outlet sections. Heat flux distribution follows the velocity distribution in the channel: the largest velocity

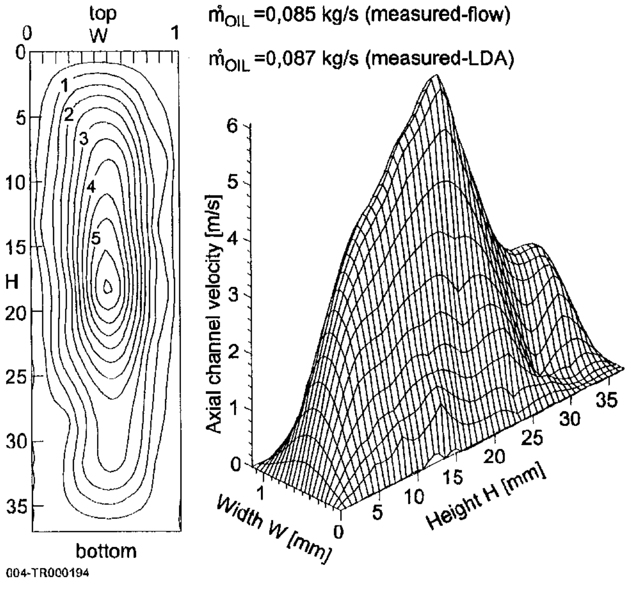

Fig. 7 Axial flow velocity distribution at φ = 205°; LDA measurements.

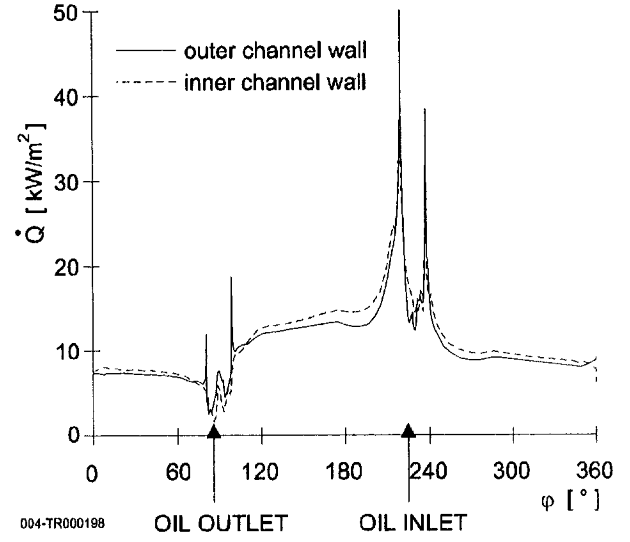

Fig. 8 Average heat flux through inner and outer wall of the DOH4 channel

gradients are first met at the inner channel wall. Owing to the channel curvature and spiral flow, the location of the top velocity gradients then moves toward the outer channel wall. Heat fluxes of both channel walls are equal at $\varphi = 110°$. Moving on towards the oil outlet, heat fluxes through the outer wall are larger. From Fig. 8 one can conclude that heat transfer capability of the presented ''channel'' cooling system covers exactly local demands for cooling of an advanced IC Engine.

Approximately three times more heat can be transferred from the channel walls in the zone of the highest cylinder temperatures (oil inlet zone). At the same time a ''hot'' (shorter) channel branch is by 50 percent more effective in comparison to the ''cooler'' (longer) channel branch. The situation can be changed if wider channel DOH3 is applied. As the result of stronger secondary flows, larger heat fluxes can be obtained along the outer channel wall ($\varphi = 90$–$200°$).

In Fig. 9 average heat fluxes along the channel branches of the DOH3, DOH4, and DOH5 version are presented. Calculations were based on the channel area that corresponds to the surface (sum) of both vertical channel walls ($2 \times H \times L_{\text{channel}}$). The highest heat fluxes correspond to the narrowest DOH4 channel, owing to the very steep velocity gradients near the channel walls. It should be observed that DOH4 channel is only 1 mm wide, whereas DOH3 channel is more than three times wider. Radial cylinder heat fluxes decrease exponentially with the cylinder height. Figure 10 represents measured radial and axial heat flux data from the top contact section (connection with the cylinder head) of the cylinder with the cylinder head: axial heat fluxes (from the cylinder head to the cylinder) near the cylinder running surface are bigger than those 5.8 mm away from it (in the radial direction from the combustion chamber), especially where the influence of the exhaust channel is the most pronounced. Heat fluxes were determined by applying Fourier's law of heat conduction and by the use of the thermopiles (to determine ΔT in the material more accurately) at the exactely determined locations. Details concerning heat flux measurements can be found in the reference of Trenc et al. (1995). Heat flows from the cylinder to the cylinder head in the zone of the engine intake channel; it flows in the opposite direction when exhaust channel is concerned. This is the main reason why temperature asymmetry in the upper part of the cylinder is so pronounced and why very careful and locally selected cooling of the upper part of the cylinder must be applied. We can learn from the previous analyses that correct cooling of modern engine cylinders must follow local requirements for cooling. Axial heat fluxes decrease dramatically from the top towards the bottom of the cylinder; Trenc (1995) reported that the ratio of axial heat fluxes at the top and at two thirds of the cylinder height amounts to 20:1, and that there is no need for intensive cooling of the lower part of the cylinder.

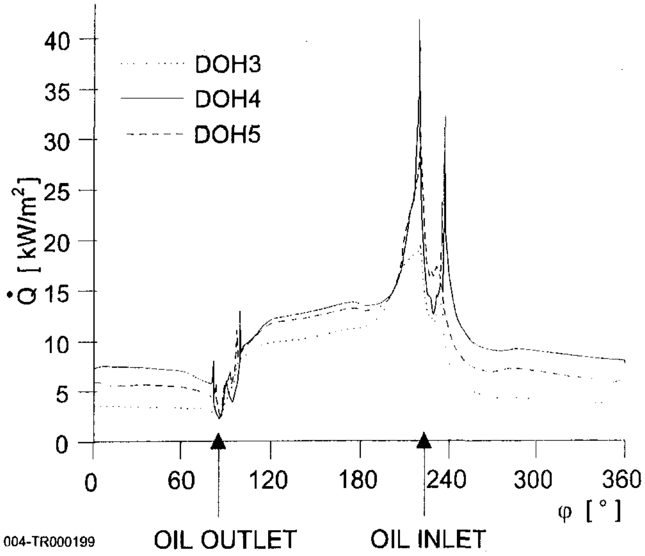

Fig. 9 Average heat flux along the channels DOH3, DOH4, and DOH5

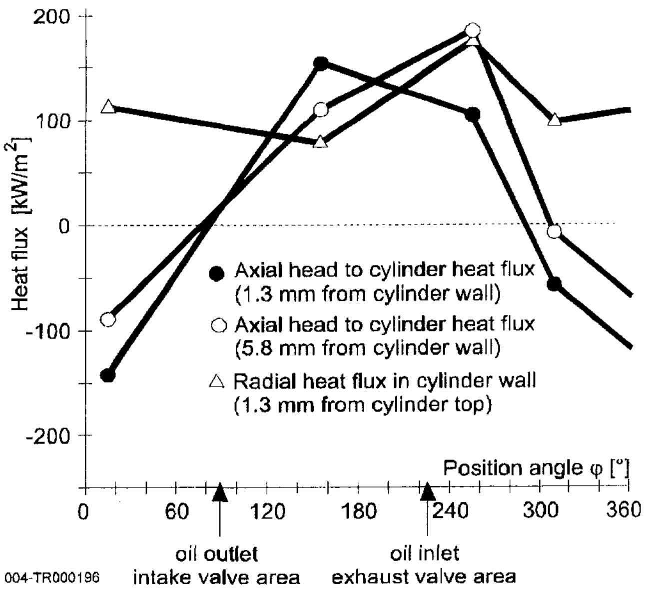

Fig. 10 Cylinder radial and cylinder-to-cylinder head axial heat flux distribution; measured data.

Conclusion

1 The cooling jacket of an advanced engine cylinder shall therefore be relatively short (1/3 of the total cylinder length), narrow (to control and to obtain better local heat transfer distribution), and with asymmetrically positioned inlet and outlet of the coolant flow.

2 Less energy for transport of the coolant is needed when laminar flow with reduced flow friction and ''short cooling jacket'' is applied.

3 If there is special demand for more intensive cooling of the piston skirt when it is close to the BDC, another small horizontal channel with lubrication oil can be used for supplemental cooling.

4 Variable circumferential cooling channel geometry (converging and diverging) or asymmetric split flow with adjusted inlet coolant nozzle can be applied to obtain better circumferential temperature distribution, especially in the upper part of the cylinder liner.

5 DOH4 was selected as the compromise design solution; optimum oil cooling of the upper third of the cylinder was achieved by very good heat transfer and relatively low pressure drop of the mostly undeveloped laminar flow; the geometrical aspect ratio of the channel corresponds to the technological and load capacity requirements of the baseline air-cooled cylinder.

6 Oil has good cooling properties for an ICEngine: during engine warming-up period and at lower engine loads it acts more as a heat insulator (shorter warming-up period).

7 There is no fear of overheating the cooling oil: 5 kg/min per cylinder suffice for safe engine specific output 23 kW/dm^3. Corresponding inlet-outlet oil temperature difference never exceeds 7°C, as reported Trenc et al. (1995).

Acknowledgment

The authors wish to record their appreciation of the Ministry of Science and Technology of the Republic of Slovenia for their financial support.

References

Delic, M., Skerget, L., Zagar, L., and Trenc, F., 1995, "Thermo-Hydraulic Conditions of Laminar Fluid Flow in Narrow Channels," *Journal of Mechanical Engineering,* Vol. 41, No. 7–8, Ljubljana, Slovenia, pp. 219–228.

Delic, M., Skerget, P., and Trenc, F., 1996, "Flow Phenomena of Laminar Split-Oil Flow in a Curved Horizontal Channel," *4th Int. Conference, Heat Transfer '96,* Computational Mechanics Publications, Southampton, UK, pp. 115–124.

Dobovisek, Z., and Humski, F., 1989, "Survey of the Literature on the Cooling Problems Concerning Air-Cooled Cylinders of Diesel Engines," *Seminar Work, Dep. of Mech. Engineering,* Technical Faculty of Maribor, Maribor, Slovenia, pp. 21–22.

Ma, C. F., Sun, H., Auracher, H., and Gomi, T., 1990, "Local Convective Heat Transfer from Vertical Heated Surfaces to Impinging Circular Jets of Large Prandtl Number Liquids," *Proceedings of the 4th Int. Conference on Heat Transfer,* No. 4-MC-16, Hemisphere Publishing Corporation, NY, pp. 441–446.

Rodman, S., Delic, M., Oberdank, K., Trenc, F., and Skerget, P., 1996, "Comparison of Experimental and Numerical Results and Analyses of the Oil-Flow in a Curved Channel," *Proceedings of the Conference Kuhljevi dnevi,* Sl.društvo za mehaniko, Gozd Martuljek, Slovenija, pp. 169–176.

Selih, J., Trenc, F., Damjanic, F. B., and Pavletic, R., 1993, "Thermal Analysis of an Air Cooled Internal Combustion Engine Cylinder Liner," *Int. Conference 8th on Numerical Methods for Thermal Problems,* Vol. VIII, Part 2, Pineridge Press, Swansea, UK, pp. 1334–1345.

Šelih, J., Damjanic, F., B., Trenc, F., and Pavletic, R., 1993, "A Novel Cylinder Cooling System of Air-Cooled Engines," *Int. Journal for Engineering Modelling,* Vol. 6, No. 1–4, pp. 45–50.

Trenc, F., 1992, "Analysis of Temperature Distribution in an Air-Cooled Diesel Engine," Dr. Thesys No. 137/D, University of Ljubljana, Faculty of Mechanical Engineering, Ljubljana, Slovenia.

Trenc, F., and Pavleti, R., 1993, "Combined Air-Oil Cooling on a Supercharged TC&IC TAM Diesel Engine," ASME *Journal of Engineering for Gas Turbines and Power,* Vol. 115, No. 4, pp. 742–746.

Trenc, F., 1993, Kuehlung eines an einen Verbrennungs-kolbenmotorkopf angrenzender Motorzylinderabschnits; Deutsche Patentamt, Anmeldung No. 4344 696.5, Muenchen, 1993.

Trenc, F., Volf, V., and Skerget, L., 1994, "Further Development of the Combined Air-Oil Cooling on a Diesel Engine," *Int. FISITA Congress,* Vol. 1, Paper No. 945024, pp. 215–222.

Trenc, F., and Primozic, J., 1994, "Combined Air-Oil Cooling of the TAM Prototype Diesel Engine," *Journal of Mechanical Engineering,* Vol. 40, No. 1-2, 1994, Ljubljana, Slovenia, pp. 55–65.

Trenc, F., Primozic, J., and Vuksanovic, B., 1995, "Analysis of Combined Air-Oil Cooling Effectiveness of Diesel Engine Cylinders," *Journal of Mechanical Engineering,* Vol. 41, No. 5-6, Ljubljana, Slovenia, pp. 187–196.

J. Yang
Senior Technical Specialist.

R. W. Anderson
Senior Staff Technical Specialist.

Ford Motor Company,
Scientific Research Laboratory, MD 2629,
20000 Rotunda Drive, P.O. Box 2053,
Dearborn, MI 48121-2053

A New Criterion for Judging SI Engine In-Cylinder Pressure Development for Its Effect on Combustion Noise

The effect of engine in-cylinder pressure development on combustion noise is studied based on measured pressure traces and the attenuation-curve theory by Austen and Priede (1958). A new criterion is proposed that correlates better to the noise levels predicted by the attenuation theory than the commonly used maximum pressure rise rate. The effect of engine bore size on combustion noise is studied next with the same engine speed, the same piston mean speed, or the same power output, respectively. For the first two cases, a smaller bore size results in a lower noise level.

Introduction

Noise is an IC engine problem that needs to be controlled. While exhaust noise is suppressed by a muffler, engine noise is induced primarily by cyclic variations of the in-cylinder pressure caused by compression and combustion. For SI engines, slow combustion usually results in a quiet engine. But, slow combustion can result in lower engine thermal efficiency. Because the form of the cylinder pressure development is critical for both noise and thermal efficiency, a suitable criterion is required for the engine designer to judge various forms of in-cylinder pressure curves for their effect on combustion noise. Such criteria proposed so far include the maximum cylinder pressure, the maximum pressure rise rate (MPRR), and the maximum rate of change of the pressure rise rate. It has been found that MPRR is the best criterion among the three, especially for engines at high speed (Priede, 1980; Mesurier and Stansfield, 1931). This criterion will be evaluated in this study with particular interest on engines of varying bore size.

The effect of cylinder pressure on engine noise can be studied by analyzing the cylinder pressure spectrum. Priede (1956) showed a satisfactory correlation between the cylinder pressure spectra and the emitted noise. Later, Austen and Priede (1958) proposed an ''attenuation curve'' theory, which established the relationship between cylinder pressure level (CPL) and sound pressure level (SPL):

$$\text{CPL (dB)} - \text{Attenuation (dB)} = \text{SPL (dB)}.$$

A particular merit of this theory is that it separates the effect of the engine structural attenuation and the effect of the cylinder pressure variation on combustion noise. The theory will be used in this study.

A Study on Noise Criteria

Criterion Evaluation. The commonly used criterion, MPRR, was evaluated using 31 full-load pressure traces from a single cylinder SI engine with a bore of 90.2 mm. Control parameters, such as spark timing, number of intake valves, and engine speed were varied so that the pressure traces had different forms and MPRR. Ten such pressure traces are shown in Fig. 1.

Due to the difficulty in precisely measuring engine combustion noise, the SPL was determined by applying the attenuation curve theory of Austen and Priede (1958). Because the attenuation curve of the tested engine was not available, six attenuation curves provided by Austen and Priede (1958) and Priede (1980) were used. One of the attenuation curves was for a gasoline engine, and five for diesel engines. The maximum difference in attenuation of these curves in the audible frequency range was 13 dB, corresponding to a difference of 20 fold in sound energy intensity. Shapes of the curves are also different. Thus, these curves can be used to study the effect of various engine structures on SPL.

There might be an issue in applying these smoothed attenuation curves. These curves were determined by measuring the SPL in octave or narrower bands (Austen and Priede, 1958). Thus, valleys in the attenuation curves, which correspond to the natural frequencies of vibration modes, were smoothed. The smoothed attenuation curve, however, may not be a problem for this study. The major goal here is to determine the SPL in a wide frequency range or in octave bands in the same way as the attenuation curves were determined.

Figure 2 shows typical results of calculations applying the attenuation curve theory. The cylinder pressure spectrum of a pressure trace within an engine cycle was first calculated through a finite Fourier transform. Then, applying the attenuation curve of an SI engine (Austen and Priede, 1958), the sound pressure spectrum could be determined. For both spectra, the energy in octave bands was summed, respectively, to obtain pressure levels in each band. Energy in five octave bands in the audible range, from 150 to 4800 Hz, was summed to obtain the total SPL. In this study, the unit of pressure level and spectra was dB above 2×10^{-5} N/m^2. Unless otherwise specified, the attenuation curve for an SI engine was from Austen and Priede (1958), and the engine speed was 1500 rpm.

Total SPL versus MPRR for all the 31 measured pressure traces are plotted in Fig. 3. There is a general correlation between the total SPL and the MPRR with a slope of about 4.35 dB/(bar/cad). But, this correlation is not completely satisfactory. For the two cases circled in Fig. 3, the total SPL of a pressure trace having a higher MPRR of 2.67 bar/cad was even lower than that having a lower MPRR of 1.83 bar/cad. Further study on these two cases shows that the amplitudes of the pressure spectra with a higher MPRR are higher only in the frequency range below 300 Hz. In the more critical frequency range, above 300 Hz, its amplitudes are comparable to, or even lower than, that with a lower MPRR, resulting in slightly lower total SPL.

The effect of engine speed on noise can be studied by using the same crank-angle resolved pressure data from a single speed.

Contributed by the Internal Combustion Engine Division. Manuscript received by the ASME Headquarters November 21, 1997. Associate Technical Editor: D. Assanis.

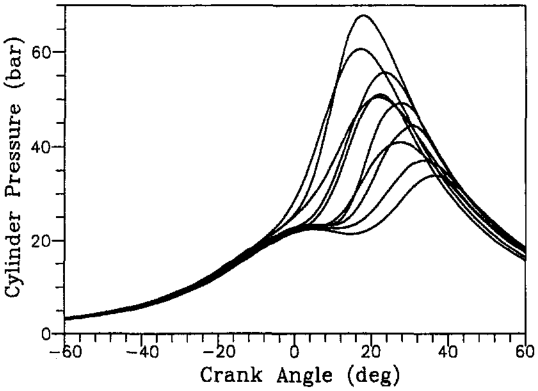

Fig. 1 Ten measured cylinder pressure traces at full load

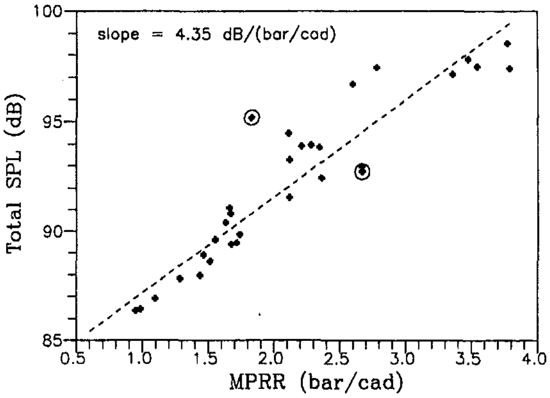

Fig. 3 Correlation between the predicted total SPL and the MPRR using 31 pressure traces at an engine speed of 1500 rpm

Assuming that the pressure traces are measured at a higher engine speed, the cylinder pressure spectra generated by finite Fourier transform will shift to higher frequencies. The total SPL of the measured pressure traces from a single speed calculated at three engine speeds are shown in Fig. 4. The predicted total SPL strongly depends on engine speed but less strongly on the MPRR in bar/cad. Such strong dependence on engine speed can also be seen if the predicted total SPL is plotted versus MPRR in bar/ms. The criterion of MPRR alone cannot correlate well with the total SPL at different engine speeds for a given engine structure. It should be pointed out that for a particular engine, the pressure traces at different engine speeds are different. This is because the burning rates and heat transfer rates are not proportional to the engine speed, although they increase with the engine speed. Thus, for a real engine, the combustion noise level at a high engine speed may be close to but lower than that predicted in this study.

A New Criterion. Because the criterion of MPRR is unsatisfactory, a new criterion is established based on the following analysis. First, the peaks of the SI engine noise spectra are usually in the frequency range of 400–1000 Hz (Austen and Priede, 1958). Next, the slopes of the six attenuation curves determined by Austen and Priede (1958) in the frequency range from 200 to 800 Hz were similar and nearly constant. Beyond 800 Hz, the slopes of the attenuation curves diverged, and the curves became more flat. This higher frequency range, however, was of less importance. Hence, the similarity between the attenuation curves within the most critical frequency range can be used to establish a new method to judge the pressure curves for their effect on engine combustion noise.

For any SI engine pressure trace, the sound pressure spectra in a frequency band from 300 to 2000 Hz can be calculated by subtracting a "standard attenuation line" (SAL) from the cylinder pressure spectra. This SAL can be considered as a most critical portion of an attenuation line for a "standard engine." The proposed SAL is

Attenuation

$$= \begin{cases} 80 - 60 \log_{10} (f/800) & \text{for } f = 300 \sim 800 \\ 80 - 45 \log_{10} (f/800) & \text{for } f = 800 \sim 1200\,. \\ 72.08 - 25 \log_{10} (f/1200) & \text{for } f = 1200 \sim 2000 \end{cases}$$

Then, the sound energy of the resulting sound pressure spectra in the specified band is summed to obtain a nominal SPL, which is an Attenuated CPL (ACPL) by the SAL. It can be used as a criterion in judging any SI engine pressure trace. The proposed SAL and the six attenuation curves of Austen and Priede (1958) and Priede (1980) are compared in Fig. 5. The proposed SAL imitates the most critical portion of the attenuation curves of Austen and Priede (1958). The ACPL is approximately a subset of the total SPL. Therefore, correlation between the SPL and the ACPL should be very good and independent of engine speed.

The calculated total SPL versus the ACPL of the 31 measured pressure traces are plotted in Fig. 6. The correlation is much better than that of Fig. 3. The new correlation is also independent of engine speed, as shown in Fig. 7, in which the same set of the 31 pressure traces was used for predictions at different engine speeds. Further study has shown that the linearity and the scattering of the correlations are insensitive to the selection of the SAL. This means that the method itself, rather than the selection of the SAL, results in a good correlation.

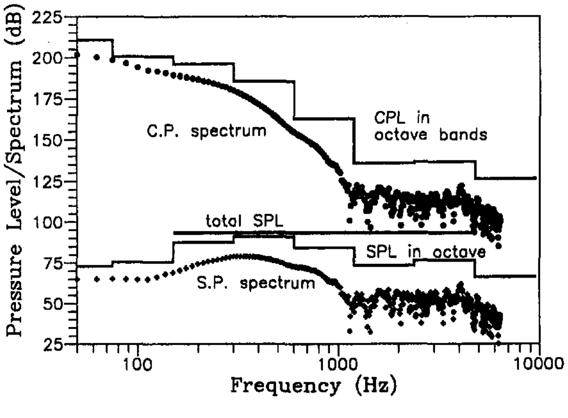

Fig. 2 An example of applying the attenuation curve theory

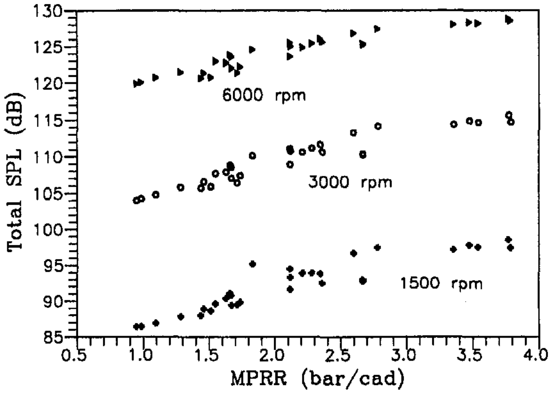

Fig. 4 Correlation between the predicted total SPL and the MPRR using 31 pressure traces at three engine speeds

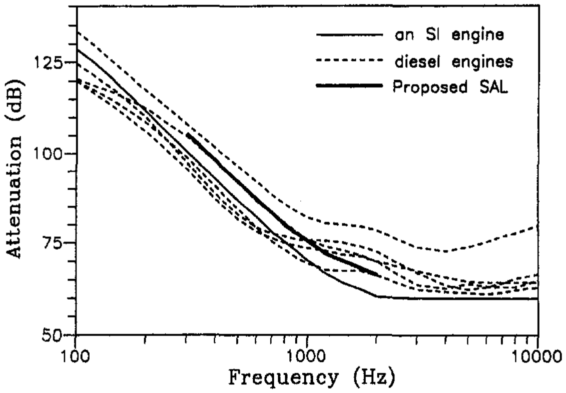

Fig. 5 Comparison of six attenuation curves of Austen and Priede (1959) and Priede (1980), and a proposed SAL

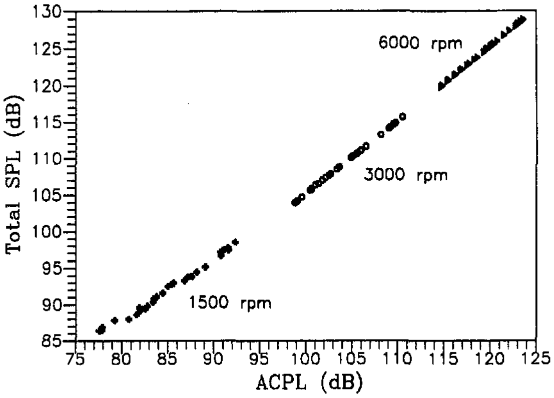

Fig. 7 Correlation between the predicted total SPL and the ACPL using 31 pressure traces at three engine speeds

To further evaluate this conclusion, the effect of various engine structures on the new criterion was studied. The SAL was applied to the six engine structures of Austen and Priede (1958) and Priede (1980). As shown in Fig. 8, the new criterion works well for all the six engine structures.

A relationship between the two criteria is shown in Fig. 9. It was established by finding the corresponding ACPL for a given MPRR through SPL at different engine speeds. Because the correlation of SPL versus MPRR is not very good, a regression of the data points has to be made, and the established relationship between MPRR and ACPL is only an approximation. If a different engine structure is used, the same pressure trace will generate different SPL. But, ACPL and MPRR of the pressure trace remain the same. Therefore, the established relationship based on one engine structure is applicable to other engines. Using this figure, one can estimate the ACPL from known MPRR and engine speed.

A Study on the Effect of Bore Size

In regulating the development of in-cylinder pressure for noise control, the effect of engine size on noise should be considered. An empirical correlation between the noise level and the size of an SI engine has been established (Challen, 1975; Priede, 1979):

$$I \sim B^5,$$

where I is sound intensity, and B is bore size. There were arguments as to whether noise level was proportional to B^5 or B^6, but the difference was small.

The reason for the low noise level with smaller bore size is analyzed below. Periodic variation of the in-cylinder gas pressure excites vibration of the engine structure. This vibration then produces pressure waves in the surrounding air. Because the in-cylinder gas excites vibration of the engine structure through the combustion chamber surface and the engine structure broadcasts noise through its surface, combustion noise should be proportional to the surface area, $I \sim B^2$. The effect of reducing bore size on noise level can be expressed by an upward shift of the attenuation curve. But, this effect alone cannot explain the empirical correlation of $I \sim B^5$.

Another effect of bore size on combustion noise is through its effect on the natural frequencies of the engine structure. For geometrically similar engines, natural frequencies of the structure are inversely proportional to the size, i.e., $f \sim B^{-1}$, according to vibration theory (Timoschenko, 1928). The geometrical similarity, however, may not exist for small engines due to the limitations of casting and machining. Walls of a small engine can be as thick as a larger engine. In this case, natural frequencies of the structure will be inversely proportional to square of the bore, i.e., $f \sim B^{-2}$, (Timoschenko, 1928). A small bore size thus results in high natural frequencies.

Because an engine structure broadcasts combustion noise through structural vibration, response of the engine structure to the exciting waves depends on natural frequencies of the structure. When the frequency of an exciting wave is much different than any of the natural frequencies of the structure, the amplitude of the structural vibration will be small because of more attenuation by the structure. The shape of the attenuation curves determined by Austen and Priede (1958) depends on the natural frequencies of the engine structure. When the natural frequencies of the engine structure increase by a ratio of two, for example, each corresponding point in the attenuation curve will

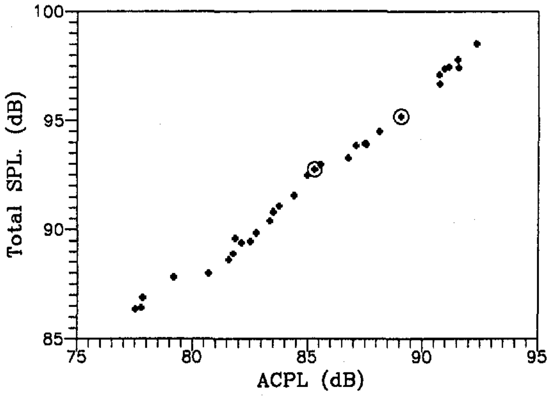

Fig. 6 Correlation between the predicted total SPL and the ACPL using 31 pressure traces at an engine speed of 1500 rpm

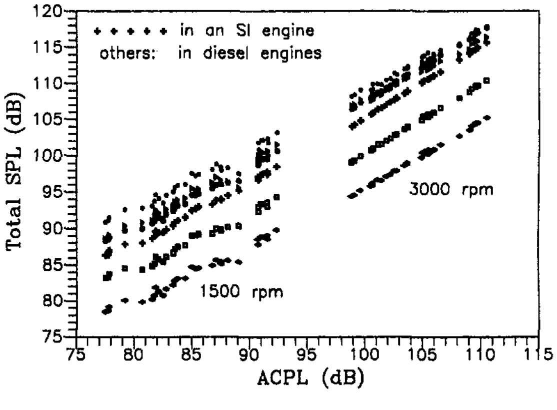

Fig. 8 Correlation between the predicted total SPL and the ACPL using six engine structures (Austen and Priede, 1959; Priede, 1980) at two engine speeds

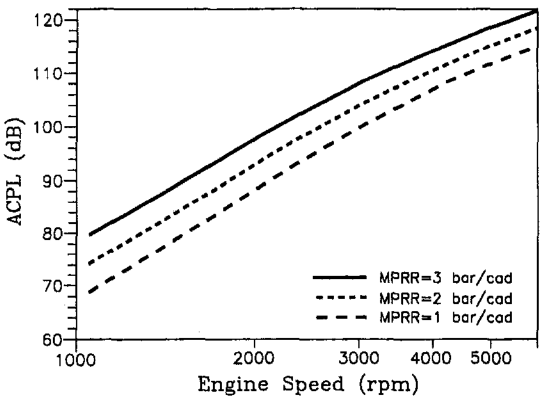

Fig. 9 Relationship between ACPL and MPRR at different engine speed using the attenuation curve of an SI engine (Austen and Priede, 1958)

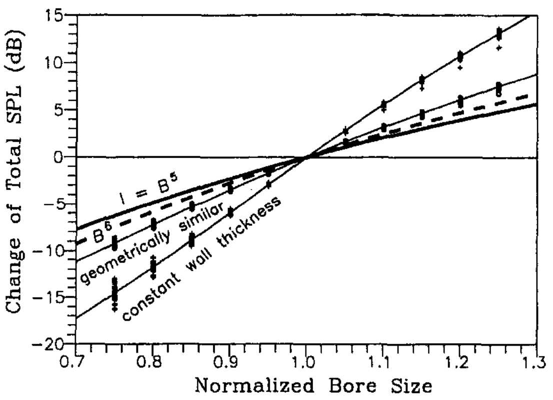

Fig. 11 Comparison of the predicted total SPL versus the bore size at an engine speed of 1500 rpm using 31 pressure traces, and two empirical correlations

shift to the high frequency direction by the same ratio. In a logarithm coordinate, this corresponds to a horizontal shift of the attenuation curve without changing its shape.

Figure 10 shows the effect of bore size on the change of attenuation. If the bore size decreases with a ratio of 1/1.414, the attenuation curve shifts up by 3 dB due to the decrease of surface area. Attenuation also increases due to the shift of the attenuation curve to higher frequencies because of the increased structural rigidity. This increase has been calculated assuming geometrically similar or constant wall thickness, corresponding to a natural frequency ratio of 1.414 or 2.0, respectively. As shown, the increase in attenuation by reducing the bore size mainly results from the increase in natural frequencies of the structure.

Because of the change of attenuation, reducing bore size results in a lower noise level, as shown in Fig. 11. The empirical correlations of $I \sim B^5$ and $I \sim B^6$ are also plotted in the figure for comparison. They are close to but do not fall between the predicted SPL assuming geometrically similar and constant wall thickness. This difference may result from a number of reasons. First, the change of damping due to the change of bore size is not considered. Second, the mixture burning rates of the engines may have been different when the empirical correlations were established. Third, the structures of these engines might be neither geometrically similar nor have the same wall thickness. These can have an effect on the measured outcome.

Engines with different bore size may be operated at different speed. If they are operated at the same piston mean speed, the sliding speed of the piston rings and the mechanical stresses caused by inertial forces will be the same, assuming the engines are geometrically similar. Engine speed will be inversely proportional to the bore size. Figure 12 shows the predicted total SPL as a function of bore size when the baseline engine is operated at 1500 rpm. The predicted total SPL increases with the bore size for both cases.

In another case, assuming the power output and the brake mean effective pressure (BMEP) of the engines remain the same, engine speed will be inversely proportional to the third power of the bore size. Because of the high speed, the predicted noise levels of small engines are higher than that of large engines. But, the assumption of the same power output is not practical. For example, small engines are used for smaller cars, which usually require less power.

Because the predicted noise levels of small-bore engines are lower using the same pressure trace, restrictions on the pressure development of smaller engines can be looser. This trend can be seen in Fig. 13, which shows the predicted "allowed MPRR" as a function of bore size with the same noise level at an engine speed of 1500 rpm. Since the relationship between ACPL and MPRR has been established (Fig. 9), the corresponding "allowed ACPL" can also be determined and shown in Fig. 13. Figure 13 also shows the MPRR of some production engines. Despite the fact that their structures are different and their noise levels may be different, the trend of the production engine's MPRR is consistent with the predictions.

Conclusions

Studies based on measured pressure traces of an SI engine and the attenuation curve theory show the following:

- The correlation between the total SPL and the MPRR is unsatisfactory due to the scatter of the data points and the dependence on engine speed.

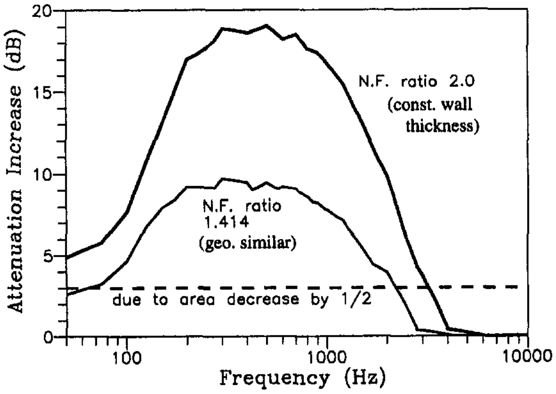

Fig. 10 Increase in attenuation due to the decrease in bore size assuming geometrically similar and constant wall thickness, respectively

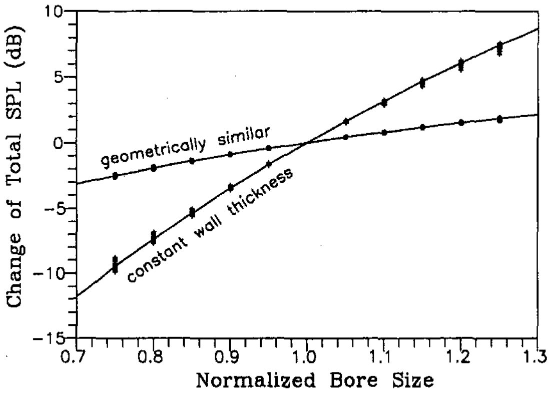

Fig. 12 Comparison of the predicted total SPL versus the bore size at the same piston mean speed using 31 pressure traces

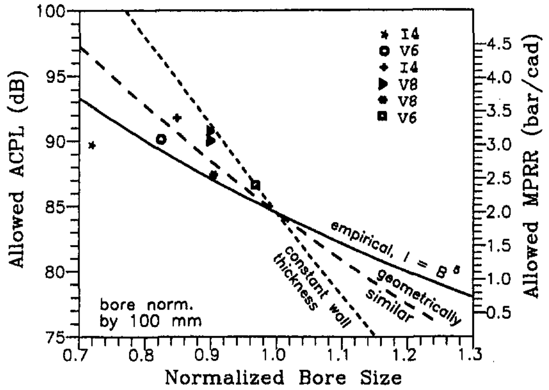

Fig. 13 Predictions of the allowed MPRR and ACPL with the same noise level at an engine speed of 1500 rpm, and the measured MPRR of some production engines

- A new criterion of ACPL is proposed to judge the pressure curve for its effect on SI engine combustion noise. Correlation between the total SPL and the ACPL is much better than that of the MPRR, and is independent of engine speed.
- A relationship between the MPRR and the ACPL is established based on an SI engine structure. Because the relationship is applicable to six different engine structures, it should be applicable to other engines.
- Decreasing the bore size increases the natural frequencies of the engine structure, resulting in an increase in noise attenuation.
- At the same engine speed or at the same piston mean speed, engines with smaller bore result in lower noise levels. Therefore, the allowable MPRR or ACPL should increase as the bore size decreases.

Acknowledgments

The author thanks Drs. D. Brehob, J. Yi, and Y. Shen for helpful discussions, Mr. R. Whiteaker and Mr. P. Sleeman for measuring pressure data, and Mr. R. Stein, Mr. W. Stockhausen, and Mr. K. Cope for the production engine data.

References

Austen, A. E. W., and Priede, T., 1958, "Origins of Diesel Engine Noise," presented at the Symposium on Engine Noise and Noise Suppression, The Inst. Mech. Engrs., London.

Challen, B. J., 1975, "The Effect of Combustion System on Engine Noise," SAE 750798.

Le Mesurier, L. J., and Stansfield, R., 1931, "Fuel Testing in Slow and High Speed Diesel Engines," *J. of Petroleum Technology,* Vol. 17, p. 387.

Priede, T., 1956, *The Origins of Diesel Engine Noise,* Report No. C.29147, CAV Ltd.

Priede, T., 1979, "Problems and Developments in Automotive Engine Noise Research," SAE 790205.

Priede, T., 1980, "In Search of Origins of Engine Noise—An Historical Review," SAE 800534.

Timoschenko, 1928, *Vibration Problem in Engineering,* Constable, p. 309.

Oil Layer as Source of Hydrocarbon Emissions in SI Engines

K. Min

W. K. Cheng
wkcheng@mit.edu

Massachusetts Institute of Technology
Sloan Automotive Lab, Bldg. 31-165,
Cambridge, MA 02139-4307

The role of lubrication oil film on the cylinder liner as a source of hydrocarbon emissions in spark-ignition engines is assessed. First, the ''source strength'' is examined via an analytical model of the gasoline vapor absorption/desorption process. The solution shows that depending on engine operating conditions, there are three regimes. The process could be (1) limited by the gas side diffusion process, (2) limited by the liquid phase diffusion process, with the absorbed fuel fully penetrating the oil layer thickness (thin oil film regime), and (3) again limited by the liquid phase diffusion process, but with the absorbed fuel penetration depth small compared to the oil layer thickness (thick oil film regime). In regime (1), the source strength (the integrated absorption or desorption flux over one cycle) is proportional to the inverse of the square root of the rpm, but independent of oil layer parameters. In regimes (2), the strength is proportional to the oil film thickness divided by the Henry's constant. In regime (3), the strength is independent of the oil film thickness, but is proportional to the fuel penetration depth divided by the Henry's constant. Then, the oxidation of the desorbed fuel (using iso-octane as fuel) is examined with a one-dimensional reaction/diffusion model. The novel feature of the model is that the desorbed fuel is being exposed to the piston crevice hydrocarbon, which is laid along the liner as the piston descends. At stoichiometric conditions, the oxidation of the crevice HC is reduced by the presence of the desorbed HC from the oil layer.

Introduction

The absorption and desorption of fuel by the lubrication oil layer has been identified as an important mechanism for hydrocarbon (HC) emissions in spark-ignition engines [1]. The mechanism works as follows. In the intake, compression and the early part of the expansion process, the fuel vapor in the charge, being soluble in the lubrication oil, gets absorbed in the oil film on the cylinder liner. When the oil layer is covered by burned gas (which has very little HC) in the expansion and exhaust process, the absorbed fuel is desorbed. When this desorbed fuel is not oxidized in the remaining part of the engine process, it contributes to the exhaust HC emissions.

While the above process had been well established in static experiments using a combustion bomb [2, 3], results from engine experiments are not as definitive. For example, by using special engines, higher HC emissions were observed when the engine was operating with lubrication oil than without [4, 5]; also, higher HC emissions correlated with higher solubility of the fuel species in the oil. In another engine experiment relating the speciated HC emissions to the fuel component solubility in the oil layer, no correlation was found [6]. Therefore, there is a need to understand the basic nature of the oil layer HC mechanism to assess its effect on engine HC emissions.

There are three important pieces to the oil layer mechanism: the amount of HC that is stored and released in the layer (this amount could be interpreted as a HC ''source strength''); the degree that the release HC is oxidized; and the relative magnitude of oil layer HC emissions relative to the other HC mechanisms. To address these pieces, an analytical solution for the ''source strength'' (as characterized by the amplitude of the absorption/desorption HC flux) is first derived for an idealized situation. The purpose is to utilize this solution to identify the different regimes of the process. Then, a detailed numerical simulation is presented of the transport of HC into and out of the oil layer and the oxidation of the desorbed HC. An important feature of this simulation is that the desorbed HC is released in the presence of the HC ejected from the piston top land crevice; hence, there is significant interaction between the two sources of HC.

Analytical Model for the Oil Layer Absorption/Desorption Process

The purpose of the analytical model is to provide a closed form solution of an idealized oil layer absorption/desorption process so that the overall behavior of the process could be extracted from the solution. In particular, several regimes of behavior could be identified. It will be seen that the scaling dependence of the absorption/desorption flux on the physical parameters, such as the diffusivity of the fuel species in the oil layer and the engine rpm, are very different in each regime. Moreover, depending on the engine running condition, the oil layer mechanism may operate in more than one regime.

There has been substantial work on modeling the oil layer absorption/desorption mechanism [7–10]. The basic model for diffusion of HC in the oil layer is described in reference [7]. Detailed application to engine via one-dimensional oil layer model is described in references [8] and [9]. The one-dimensional flux results were incorporated in a three-dimensional simulation in reference [10]. In these models, however, assumptions were made regarding the physical processes involved: for example, there is negligible gas side diffusion resistance in references [7] and [9]; the penetration depth in the oil layer is small compared to the oil film thickness in reference [8] and [10]. To model the process comprehensively, such assumptions are relaxed here.

The Model. The model assumes a one-dimensional oil layer of thickness δ occupying the space x from $-\delta$ to 0. (See the nomenclature section for the definition of symbols.) The oil

---

Contributed by the International Combustion Engine Division and presented at The Fall Technical Conference of the ASME Internal Combustion Engine Division, Springfield, OH, October 20–23, 1996. Manuscript received by the ASME Headquarters November 21, 1997. Associate Technical Editor: D. Assanis.

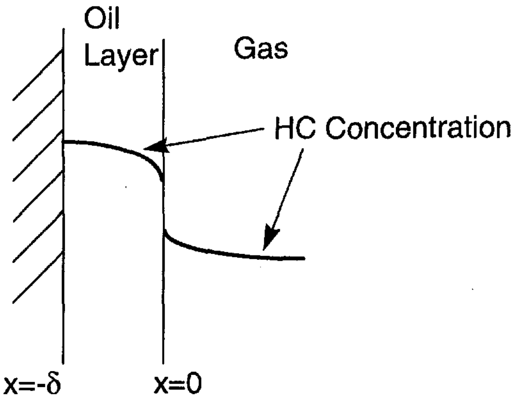

Fig. 1 Schematic showing the desorption process of the oil layer HC mechanism

layer is exposed to the charge at $x = 0$ (see Fig. 1). The HC concentration in the bulk charge would fluctuate sinusoidally as $n_\infty \operatorname{Re}(e^{i\omega t})$. In one engine cycle, the charge HC to which the oil layer is exposed to takes the value of the fresh mixture during intake, increases during the compression process, and decreases to zero when the oil layer is in contact with the burned gas. The sinusoidal fluctuation in our model may be interpreted as a Fourier component of the actual periodic varying concentration. Of special interest is the fundamental Fourier component.

The partial differential equations and the boundary conditions that describe the oil layer mechanisms are as follows. (In the following, primed quantities denote properties in the oil layer; unprimed quantities denote properties in the gas phase.) In the oil layer

$$\frac{\partial n'}{\partial t} = D' \frac{\partial^2 n'}{\partial x^2} \quad -\delta < x < 0. \tag{1}$$

On the gas side

$$\frac{\partial n}{\partial t} = D \frac{\partial^2 n}{\partial x^2} + \frac{\partial}{\partial t} [n_\infty \operatorname{Re}(e^{i\omega t})] \quad 0 < x < \infty. \tag{2}$$

At the boundary conditions at the liner surface, the diffusion flux is zero:

$$\partial n'/\delta x(-\delta) = 0. \tag{3}$$

At the oil/gas interface, the HC concentration on the oil side and on the gas side are related by Henry's Law:

$$n'(0) = n(0) n^* RT'/H \tag{4}$$

and the diffusion flux is continuous, as follows:

$$D' \partial n'/\partial x(0-) = D \partial n/\partial x(0+). \tag{5}$$

The boundary condition at the bulk gas is

$$n(t, x = \infty) = n_\infty \operatorname{Re}(e^{i\omega t}). \tag{6}$$

For constant diffusivities, the analytical solution to Eqs. (1)–(6) for the HC flux (molar concentration per unit area per unit time) at the oil/gas interface is

$$\text{Flux} = n_\infty \sqrt{(\omega D)} \operatorname{Re}\left\{ \frac{-\Lambda g(\delta/\delta_p)}{1 + \Lambda g(\delta/\delta_p)} e^{i(\omega t + \pi/4)} \right\}. \tag{7}$$

In this expression, δ_p is the HC penetration depth in the oil layer, where

$$\delta_p = \sqrt{(D'/\omega)}. \tag{8}$$

The factor Λ is a measure of the ratio of the liquid side to the gas side boundary layer resistance to mass diffusion:

$$\Lambda = \frac{n^* RT'}{H} \sqrt{\frac{D'}{D}} \tag{9}$$

The factor $n^* RT'/H$ in Eq. (9) accounts for the difference in the HC concentrations at the two sides of the oil/gas interface.

The function $g(\delta/\delta_p)$ is defined by

$$g(\delta/\delta_p) \equiv \tanh\left(\frac{\delta}{\delta_p} \frac{(1 + i)}{\sqrt{2}}\right) \tag{10}$$

Note that for small δ/δ_p, $g \simeq (\delta/\delta_p)(1 + i)/\sqrt{2}$; for large δ/δ_p, $g \simeq 1$.

Oil Layer Absorption/Desorption Regimes. The structure of Eq. (7) may be interpreted as follows:

(1) The factor $\sqrt{(\omega D)}$ is the diffusion velocity on the gas side. Thus, $n_\infty \sqrt{(\omega D)}$ is the HC flux if the HC transport is limited by the gas side diffusion resistance.

(2) The factor $\Lambda g/(1 + \Lambda g)$ describes the effect of HC diffusion in the oil layer. For large value of Λ, the diffusion in the oil layer is fast compared to the gas side so that the gas side diffusion resistance is limiting. Then this factor $\simeq 1$, and the flux amplitude is:

Nomenclature*

c_p = specific heat at constant pressure
D = diffusivity of HC in gas phase
D' = diffusivity of HC in oil layer
g = defined in Eq. (10)
H = Henry's constant (Pa)
h = heat transfer coefficient
Le = Lewis number
Nu = Nusselt number
n = molar HC concentration in gas (mole/cc)
n' = molar HC concentration in oil (mole/cc)
n_∞ = amplitude of the fuel molar concentration fluctuation in the bulk gas (mole/cc)
n^* = molar concentration of the oil (mole/cc)
P_i = intake manifold pressure
R = universal gas constant (8.314 J/mol-k)
Re( ) = real part of a complex expression
Re = Reynolds number
rpm = engine speed, revolution per minute
T = gas temperature
T_{BL} = average gas side boundary layer temperature
T' = oil layer temperature
t = time
x = coordinate perpendicular to cylinder wall
W = molecular weight of fuel HC
W^* = molecular weight of the lubricant
δ = oil layer thickness
δ_p = HC penetration depth in oil layer; $\delta_p = \sqrt{(D'/\omega)}$
Λ = defined by Eq. (9)
ρ = gas density
ρ^* = oil density
μ = viscosity of oil
ω = angular frequency
ξ = position along liner normalized by stroke

Subscripts

r = at reference condition

---

* All primed quantities refer to properties in the oil layer; unprimed quantities refer to properties in the gas phase.

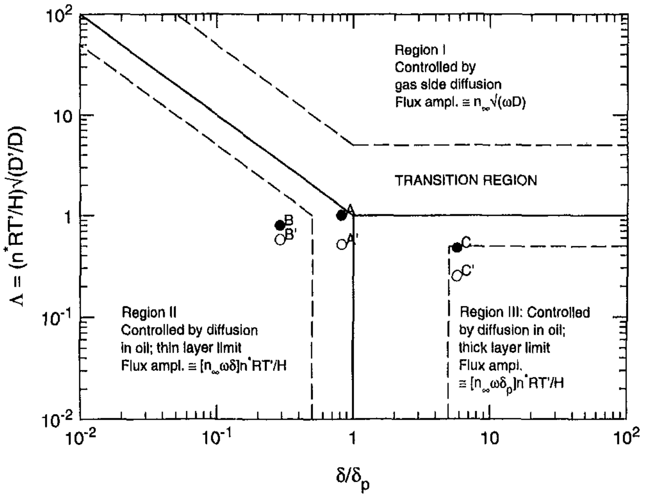

Fig. 2 Regimes of the oil layer absorption/desorption mechanism. The points A and A′ are for toluene and iso-octane at 1500 rpm, 0.4 bar P_i, 90°C liner temperature. The points B and B′ are for 1000 rpm, WOT, 120°C. The points C and C′ are for 3000 rpm, 0.4 bar, 25°C.

$$\text{Flux ampl} \simeq n_\infty \sqrt{(\omega D)}. \tag{11}$$

Note that the expression for Λ is the square root of the ratio of diffusivities, multiplied by the factor $n^*\mathbf{R}T'/H$ to account for the difference in concentration in the oil layer and in the gas phase. Normally the diffusivity in oil is much less than than that in the gas phase; $\sqrt{(D'/D)} \sim 10^{-2}$. The factor $n^*\mathbf{R}T'/H$, however, could bring the value of Λ to ~ 1 for HC species of high solubility (low H).

(3) For small value of Λ, the transport process is limited by the HC diffusion in the oil layer. There are two sub-regimes in this regime, depending on the HC penetration depth in the oil layer. When the oil layer is thick ($\delta \gg \delta_p$), the result is independent of the oil layer thickness δ ($g \simeq 1$ in Eq. (10)), and is proportional to the penetration depth δ_p; then, the amplitude in Eq. (7) simplifies to

$$\text{Flux ampl} \simeq [n_\infty \omega \delta_p] n^* RT'/H. \tag{12}$$

The above expression reflects the fact that the portion of the oil layer beneath the penetration depth does not play a role in the process.

(4) In the other sub-regime, the oil layer is thin and the absorbed HC fully penetrates the layer. Then, $g \simeq (\delta/\delta_p)(1 + i)/\sqrt{2}$ in Eq. (10), and the flux amplitude in Eq. (7) simplifies to

$$\text{Flux ampl} \simeq [n_\infty \omega \delta] n^* RT'/H. \tag{13}$$

Note that the flux is no longer dependent on δ_p. Equation (13) is identical to Eq. (12) except with δ replacing δ_p.

The above discussion indicates that the regimes of oil layer absorption/desorption behavior depends on the following two nondimensional parameters: the ratio of the oil layer thickness to penetration depth δ/δ_p, and the ratio of the liquid-side to gas-side diffusive resistance Λ. These regimes are mapped on Fig. 2. For small δ/δ_p, the amplitude term in Eq. (7) reduces to

$$\text{Flux} \simeq n_\infty \sqrt{(\omega D)}\ \mathrm{Re}\left\{ \frac{\Lambda \delta/\delta_p \dfrac{(1+i)}{\sqrt{2}} e^{i(\omega t + \pi/4)}}{1 + \Lambda \delta/\delta_p \dfrac{(1+i)}{\sqrt{2}}} \right\}, \tag{14}$$

which further reduces to the expression in Eq. (13) when $\Lambda\delta/\delta_p$ is small. Thus, the boundary between Regions I and II in Fig. 2 is drawn along $\Lambda\delta/\delta_p = 1$.

The boundaries between the regions on Fig. 2 are drawn at where the relevant parameters are equal to 1. The region where these parameters are in the range of 0.5 to 5 are designated as transition regions. The three regions are:

Region I. The absorption/desorption mechanism is limited by the gas phase diffusion resistance. The amplitude of the HC flux at the oil/gas interface is given by Eq. (11).

Region II. The absorption/desorption mechanism is not limited by the gas phase diffusion resistance. The HC fully penetrates the thin oil layer. The amplitude of the HC flux at the oil/gas interface is given by Eq. (13).

Region III. The absorption/desorption mechanism is not limited by the gas phase diffusion resistance. The HC does not fully penetrate the thick oil layer. The amplitude of the HC flux at the oil/gas interface is given by Eq. (12).

Application to Engine. In engine application, the particular regime for oil layer mechanism and the scaling law (as a function of engine speed, load, etc.) for the absorption/desorption flux depends on the operating condition. In general, values of parameters such as δ and D in the above model would change as a function of the time within a cycle and as a function of the location of the oil layer. Only estimates of these values, which are representative for a cycle, are given here for the purpose of identifying the operating regime. The detailed, spatially and crank-angle resolved calculation of the absorption and desorption process will be given in a later section.

In the following, the relationship of the various parameters to the engine variables (rpm, intake pressure, etc.) is discussed first. Then numerical values for the parameters are evaluated at a reference engine operating point. Finally, scaling laws are given for the departure from this reference condition.

Scaling of δ/δ_p. In classical lubrication theory for an oil ring of width b, the oil film thickness δ to support a normal stress σ is

$$\frac{\delta}{b} \propto \sqrt{\frac{\mu V}{\sigma b}}, \tag{15}$$

where V is the sliding velocity that is proportional to the engine rpm. (In this discussion, the thickness of the oil layer on the liner is assumed to be proportional to the thickness of that under the top ring.) The normal stress, σ, is proportional to the gas loading, which scales with the intake pressure. (The ring tension is neglected in this estimate.) Thus, the scaling for δ is

$$\delta = \delta_r \sqrt{\frac{\mu}{\mu_r} \frac{\text{rpm}}{\text{rpm}_r} \frac{P_{i_r}}{P_i}}. \tag{16}$$

In this and subsequent expressions, the subscript r denotes the reference condition.

Using the information quoted in reference [2], the HC diffusivity in oil, D', is proportional to the oil temperature T' (in K). Then, from Eq. (8), the penetration depth is

$$\delta_p = \delta_{p_r} \sqrt{\frac{\text{rpm}_r}{\text{rpm}} \frac{T'}{T'_r}}. \tag{17}$$

Combining Eqs. (16) and (17), the scaling law for δ/δ_p is

$$\frac{\delta}{\delta_p} = \left(\frac{\delta}{\delta_p}\right)_r \frac{\text{rpm}}{\text{rpm}_r} \sqrt{\frac{\mu(T')}{\mu_r} \frac{P_{i_r}}{P_i} \frac{T'_r}{T'}}. \tag{18}$$

Thus, δ/δ_p is proportional to the engine rpm and is inversely proportional to the square root of intake pressure. The absolute value of the oil layer temperature, T', does not change appreciably, so the factor $\sqrt{(1/T')}$ does not change much over the op-

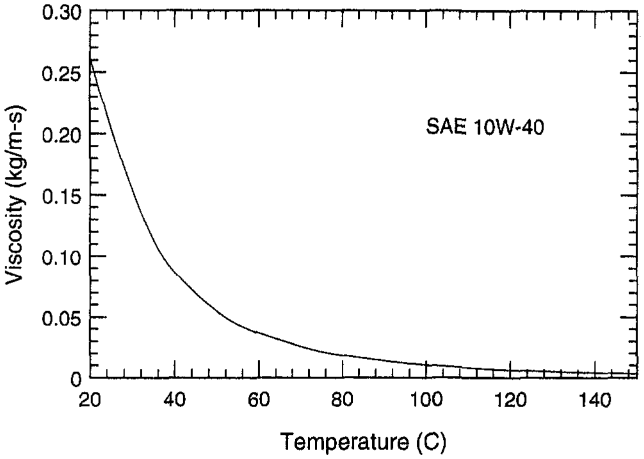

Fig. 3 Viscosity of a typical SAE 10W40 oil

erating range. The viscosity μ, however, is very sensitive to T', and the dependence is modeled by the Vogel Eq., as follows:

$$\mu(T') = \rho^* A \exp(B/(C + T')), \tag{19}$$

where A, B, and C are empirical constants. The viscosity for a typical SAE 10W40 oil is shown in Fig. 3. The value for μ changes over a factor of 10 from a cold engine condition (~25°C) to a warmed-up condition (~90°C). Thus, the regime for oil layer absorption/desorption could change substantially during engine warm-up.

Scaling of Λ. The value of Λ (defined in Eq. (9)) is a measure of the relative liquid side to gas side diffusion resistance. The factor $n^*\mathbf{R}T'/H$ accounts for the concentration difference of the two sides. Typical Henry's constants for iso-octane (a paraffin) and toluene (an aromatic) in a lubricant [11] are shown in Fig. 4. The temperature dependence of H is similar for both compounds; they increase by approximately a factor of 3 to 3.5 over the 90 to 150°C range. Since the density of the lubricant does not change significantly over the liner temperature range, the value of n^* ($=\rho^*/W^*$, where ρ^* and W^* are the density and molecular weight of the lubricant) is roughly independent of operating condition. Thus,

$$n^*\mathbf{R}T'/H \sim \frac{T'}{H(T')}.$$

From reference [2], the oil side diffusivity, D', is proportional to T'. The gas side diffusivity, D, may be obtained by the analogy between mass and heat transfer (assuming that the effective Lewis number is unity). Then,

$$D \sim D_{\text{laminar}}\,\text{Nu}$$

In general, the heat transfer process, and, thus, the Nusselt number, Nu, changes over the cycle. To obtain representative values, the cycle-averaged heat transfer correlation of reference [12] is used: $\text{Nu}_\propto \text{Re}^{0.75}$. Then, relating the Reynolds Number to the operating condition of the engine,

$$D \propto \frac{T_{BL}^{.38}\,\text{rpm}^{.75}}{P_i^{0.25}},$$

where T_{BL} is the average temperature of the gas side boundary layer for calculating the viscosity. Using the above relationships, the scaling law for Λ is, therefore,

$$\Lambda = \Lambda_r \frac{\left(\frac{T'}{T'_r}\right)^{1.5}\left(\frac{P_i}{P_{i_r}}\right)^{.13}\left(\frac{T_{BL_r}}{T_{BL}}\right)^{.19}\left(\frac{\text{rpm}_r}{\text{rpm}}\right)^{.38}}{\frac{H(T')}{H_r}}. \tag{20}$$

In the above expression, the subscript r denotes the reference value. The boundary layer temperature, T_{BL} may be taken as the average of that of the bulk charge and of the wall. In a cycle, T_{BL} may change substantially. In Eq. (20), however, $\Lambda \sim T_{BL}^{-.19}$, and is, therefore, not very sensitive to the value of T_{BL}. Thus, a cycle-averaged value for T_{BL} suffices. Note that the major dependence in Eq. (20) comes from the sensitivity of $H(T')$ to temperature. This sensitivity, however, is offset somewhat by the $T'^{1.5}$ factor.

Operating Points. To study the regimes of the oil layer HC mechanism in an engine, a reference operating point is chosen. Then, departure from this point could be calculated using the scaling laws in Eq. (18) and (20).

The reference operating point is chosen to be at 1500 rpm and 0.4 bar intake pressure for a SI engine of 86 mm bore and 86 mm stroke (500 cc displacement). The engine is assumed to be fully warmed-up, with the liner temperature at 90°C. This condition is typical of the engine testing reference point used by engine companies, and is representative of the medium speed, light load operation in the FTP cycle.

The engine oil is a 10W40 crude oil-based lubricant with the Henry's constants for various hydrocarbons measured in reference [11] (oil D in the reference). The molecular weight is 500; the density is 881 kg/m^3.

The oil film thickness, δ, is obtained from the two-dimensional laser fluorescence measurement of reference [14], in which δ is measured to be ~0.8 μm at 1500 rpm, 0.69 bar intake pressure, and 80°C liner temperature. This value of δ is scaled to the reference condition by Eq. (16); thus, δ_r is 0.74 μm.

In reference [2], a value of 0.7×10^{-10} m^2/s is used for D', the diffusivity of HC in oil. In reference [9], values of 1.3 and 1.5×10^{-10} m^2/s are used. An average value of 1.2×10^{-10} m^2/s is used here. Using this value, the penetration depth at 1500 rpm is 0.9 μm. Thus, the reference value at 1500 rpm, 0.4 bar P_i for δ/δ_p is

$$\left(\frac{\delta}{\delta_p}\right)_r = 0.82. \tag{21}$$

At the reference operating condition, the Nusselt number Nu

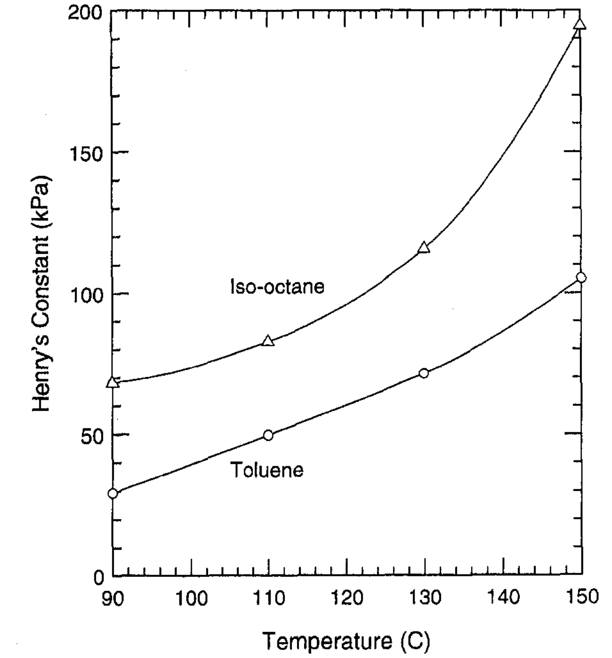

Fig. 4 Henry's constant for toluene and iso-octane in a crude oil-based 10W40 lubricant; data converted from reference [11]. (Original data were for the modified Henry's constant.)

~ 2 [12]. The laminar mass diffusivity of a dilute binary mixture for toluene and iso-octane in air are obtained from the Schmidt number given in reference [15]. (The value of iso-octane is not listed in in reference [15]. The *n*-octane value is used.) Using the values of H in Fig. 4, the reference values for Λ are

$$\Lambda_r \text{ (Toluene)} = 1.01,$$
$$\Lambda_r \text{ (Iso-octane)} = 0.52. \tag{22}$$

The reference operating points for toluene and iso-octane from Eq. (21) and (22) are marked as A and A' in Fig. 2. Thus, they are in the middle of the transition region: neither the thin/thick oil layer approximation nor the gas/oil layer diffusion limiting case could be used.

At high load, high liner temperature and low rpm, the oil layer thickness decreases and the absorption/desorption mechanism would operate in the thin oil layer regime. At 1000 rpm, WOT and at liner temperature of 120°C, the operating points for toluene and iso-octane are marked as B and B' in Fig. 2.

At low liner temperature, low intake pressure and high rpm, the oil layer thickens. At 3000 rpm, 0.4 bar intake pressure and at liner temperature of 25°C, the operating points for toluene and iso-octane are marked as C and C' in Fig. 2.

The above discussion leads to that depending on operating condition, the oil layer absorption/desorption mechanism could be in different regimes. At medium speed, light load condition (the reference point) the process is in the transition region so that there is no single rate limiting process. Therefore, it is necessary to employ a numerical simulation that encompasses both the oil side and gas side diffusion processes to study the mechanism.

Numerical Simulation of the Oil Layer Hydrocarbon Mechanism

The detailed process of the oil layer mechanism is simulated numerically in the following. The numerical model includes the effect of nonuniform oil film thickness and temperature along the liner, variation of the charge condition in the cycle, the covering and uncovering of the oil layer by the piston, and the desorption of the oil layer to the crankcase. The in-cylinder oxidation of the desorbed HC is also calculated. An important feature of the latter process is that the HC from the oil layer is desorbed into the crevice gas from the piston top land crevice.

The model combines the oil layer diffusion model of reference [9], the gas side diffusion and oxidation model of reference [16], and the piston ring-crevice flow model of reference [17]. It is briefly described in the following.

The oil layer on the cylinder liner is divided into 91 segments along the piston stroke. The length of each segment corresponds to a 2 deg displacement of the piston. A one-dimensional analysis (in the direction perpendicular to the liner surface) is carried out for each segment throughout an engine cycle. The HC molar concentration in the oil layer satisfies Eq. (1) and the boundary conditions of Eqs. (3), (4), and (5). When the segment is exposed to a nonreactive gas medium such as the unburned gas or the crank case gas, the mass flux boundary condition on the gas side (the RHS of Eq. (5)) is specified by the analogy between mass and heat transfer.

$$D \left.\frac{\partial n}{\partial x}\right|_{0+} = \frac{h[n(\infty) - n(0)]}{W\rho c_p \,\mathrm{Le}^{2/3}}, \tag{23}$$

where Le is the Lewis number, and h is the heat transfer coefficient given by the Woschni correlation (see reference [13]). The term $n(0)$ signifies the presence of the gas-side diffusion resistance.

When the oil layer is covered by unburned gas during the intake, compression, and the early part of the expansion process before the flame reaches the wall, $n(\infty)$ is the HC in the bulk charge calculated by a zero-dimensional cycle simulation program.

The oil layer segments above the fist ring are exposed to the charge gas. Those below are assumed to be exposed to the crankcase gas. Then, the value for $n(\infty)$ is the crankcase HC concentration, which is taken to correspond to a HC mole fraction of 7000 ppm C_1.

The outflow of crevice gas from the top land commences after peak cylinder pressure. The formulation for the reaction/diffusion species equation and the energy equation is identical to the crevice gas oxidation model described in reference [16]: it is an initial value problem (starting from the moment the liner is uncovered by the piston) with the initial concentration at the oil layer surface now supplied both by the crevice gas and the desorption flux. Furthermore, the boundary condition at $x = 0$ (the oil layer/gas interface) is now made compatible with the absorption/desorption from the oil layer. Thus, both the Henry's constant relationship, Eq. (4), and the flux matching conditions, Eq. (5), hold. The solution is obtained from solving the oil-layer diffusion and the gas-side reaction/diffusion equations simultaneously. A Crank-Nicholson scheme was used to solve the discretized finite difference equation. The specification of the initial temperature profile and the details of the numerical procedure are described in reference [16]. The calculation was carried out over several engine cycles until the concentration values within each cycle converged.

The simulation was carried out for the following engine specification:

Engine: Ricardo Hydra Mark III

Equivalence Ratio	1.0
Residual Gas	20 percent
Oxygen in Burned Gas	1 percent (by mole)
Bore/Stroke	86 mm/86 mm
Compression Ratio	8.29
IVO	4°BTC
IVC	49°BBC
EVO	54°BBC
EVC	16°ATC
Piston Top Land Height	7.87 mm

This engine has a hemispherical head and the piston top flushes with the top of the liner at TDC position.

Two sets of liner temperatures were considered. At the warm-up condition, the liner temperature was assumed to be 100°C (373°K) at the top and it dropped to 80°C (353°K) linearly over the stroke length. At cold condition, the liner temperature was assumed to be uniform at 30°C (303°K).

A lubricant film model [18] was used to evaluate the oil-film thickness. For each oil segment, the average value over a cycle was used because of the uncertainty in modeling the inter-segment transport of the oil. Typical results are shown in Fig. 5 (solid line). The drop in the oil film thickness at the top 30 mm of the liner is due to the exposure of the layer to the high cylinder pressure of compression and combustion. The thinning out of the film near the top of the liner is due to transition to mix and boundary lubrication. A simple analytical fit (dotted line in Fig. 5) to this thickness was used in the absorption/desorption calculation.

Absorption and Desorption in the Absence of the Crevice Hydrocarbon. To understand the absorption and desorption mechanism, the process was first examined without the presence of the crevice hydrocarbon, and the chemical reactions were switched off. Then, the process was purely diffusive.

The engine condition was at 2000 rpm, 0.4 bar intake pressure, stoichiometric condition. The fuel concentration of the unburned gas in the cylinder calculated by a cycle simulation is shown in Fig. 6. The concentration increases rapidly at the later part of the compression process. The oil layer is assumed to be exposed to the burned gas after 400°CA (40° ATC).

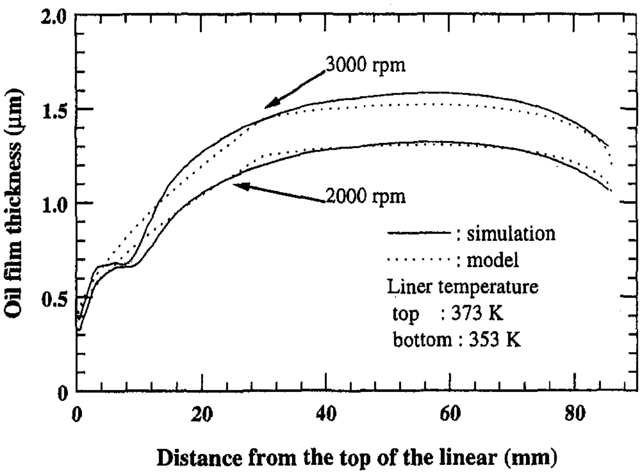

Fig. 5 Oil film thickness profile. Liner temperature varies linearly from 373K at the top to 353K at the bottom.

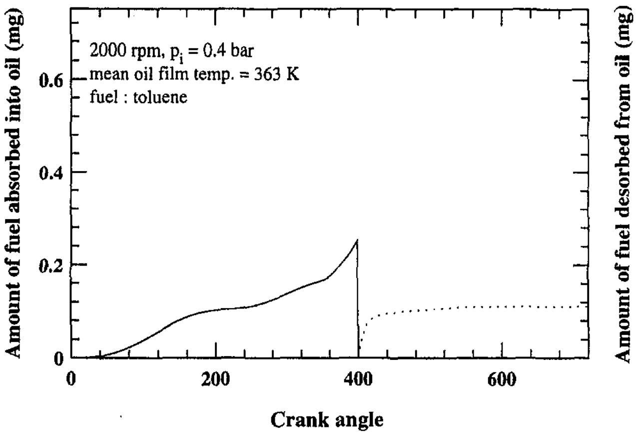

Fig. 8 Cumulative fuel absorbed into the oil layer (solid line) and desorbed to the combustion chamber (dotted line) in one engine cycle; warm-up engine condition (363°K mean liner temperature). The difference between the two end values is the amount desorbed to the crankcase.

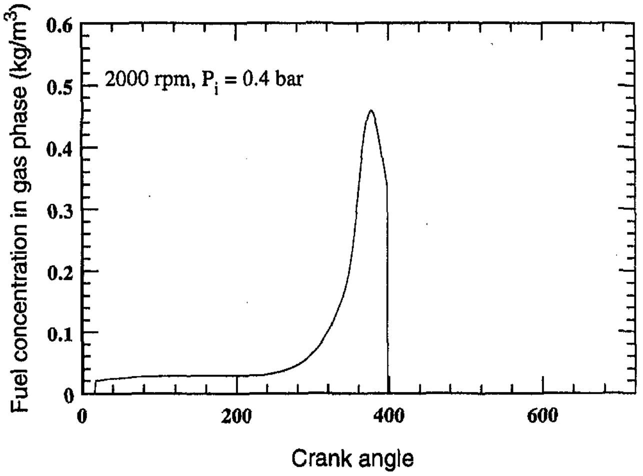

Fig. 6 Fuel concentration of the unburned gas used for the oil layer absorption/desorption simulation

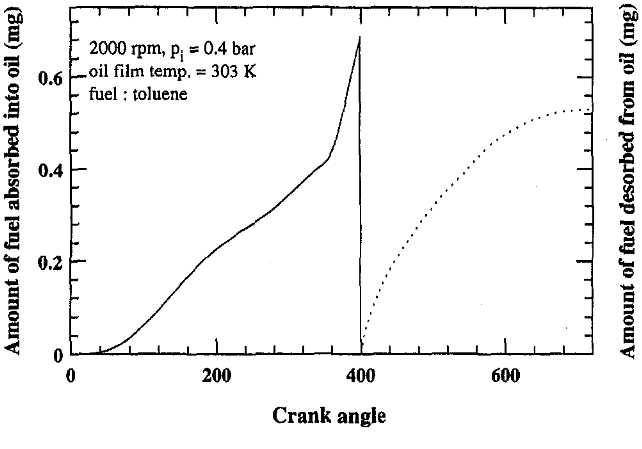

Fig. 7 Cumulative fuel absorbed into the oil layer (solid line) and desorbed to the combustion chamber (dotted line) in one engine cycle; cold engine condition (303°K liner temperature). The difference between the two and values is the amount desorbed to the crankcase.

The cumulative amount of fuel absorbed into the oil layer at a cold engine condition (303°K liner temperature) is shown in Fig. 7 (solid line). The rate of increase is fastest at the end because of the higher HC concentration on the gas side at that time, which more than compensates for the less exposed area as the piston comes up to the top. When the oil layer is covered by the burned gas, $\sim$5 percent of the fuel in the charge is absorbed.

The cumulative amount of fuel desorbed into the combustion chamber under the same condition is shown in Fig. 7 as the dotted line. The desorption process persists throughout much of the expansion and exhaust process. Approximately 80 percent of the absorbed fuel desorbs into the combustion chamber. The remaining 20 percent desorbs into the crankcase.

The corresponding results for a warmed-up engine (liner temperature 373°K at the top; 353°K at the bottom; mean temperature 363°K) are shown in Fig. 8. Compared to the cold engine, the amount of fuel absorbed is much lower and the desorption process is much faster—all of the desorption occurs within the expansion stroke. These differences could be explained by the higher value of the Henry's constant at the higher temperature. Approximately 2 percent of the fuel in the charge is absorbed. Of the absorbed fuel, $\sim$50 percent desorbs into the combustion chamber, and the rest desorbs into the crankcase.

Referring to Fig. 2, the operating condition in this example lies in Region II (warmed-up case) and Region III (cold engine case). Note that for both regions, the absorption/desorption flux is proportional to $1/H$. Thus, as H increases with temperature, the amount absorbed decreases. This is illustrated in Fig. 9. (For this figure, the oil temperature has a linear profile: the top is 10°K hotter than the mean; the bottom is 10°K cooler.) The plot in Fig. 9(*b*) is nonlinear with respect to $1/H$ because of the T' dependence of other factors in the process. Also, note that absorption is higher for toluene, which has a lower H (more soluble) than iso-octane.

The amount of fuel absorbed (as percentage of fuel in the charge) versus engine speed is shown in Fig. 10. In the cold engine, the absorbed amount decreases with rpm (the solid symbol in Fig. 10). This could be explained as follows. Because of the high lubricant viscosity, the oil film is thicker than the penetration depth; the oil layer mechanism operates in Region III. Then, according to Eq. (12), the flux is proportional to $\omega\delta_p$. Since $\delta_p \sim 1/\sqrt{\omega}$, the flux is proportional to $\sqrt{\omega}$. The amount absorbed in one cycle is proportional to the product of the flux and the cycle time, which $\sim 1/\omega$. Thus, the overall dependence of the absorbed amount is $\sim 1/\sqrt{\omega}$. This explains the decreasing trend in Fig. 10 for the low temperature case.

For the 363°K oil temperature case in Fig. 10 (open symbol), the oil film is thin because of the lower viscosity. When the penetration depth is larger than the oil film thickness, the absorption/desorption mechanism operates in Region II of Fig. 2.

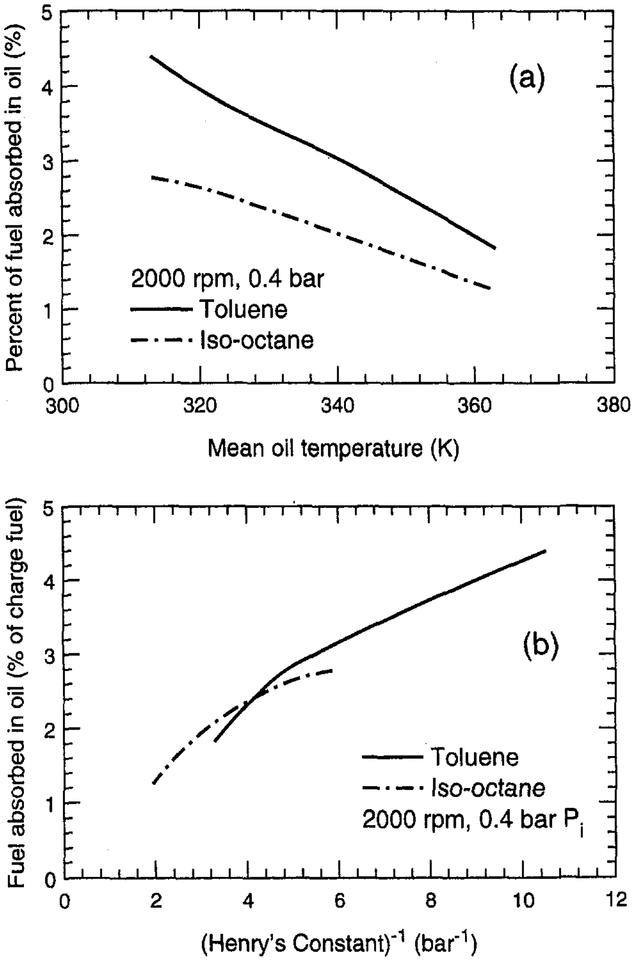

Fig. 9 The total amount of fuel absorbed in the oil layer, as percentage of fuel in the charge, (*a*) versus oil temperature and (*b*) versus reciprocal of Henry's constant

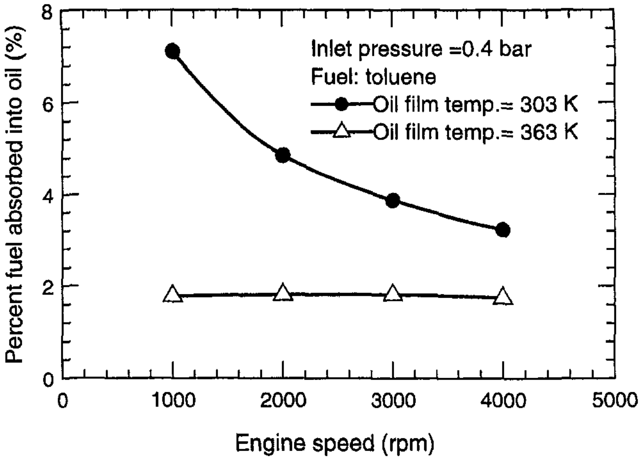

Fig. 10 Amount of fuel absorbed in the oil layer (as percentage of the fuel in the charge) versus engine speed

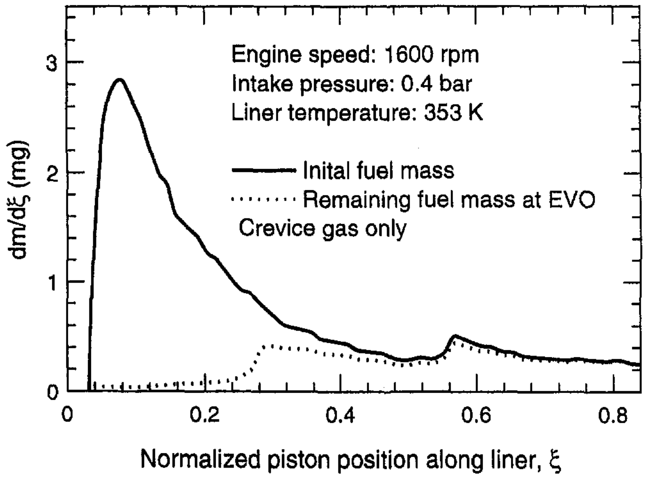

Fig. 11 Crevice-only HC mechanism. ξ is liner position normalized by the stroke; *y*-axis is HC mass per unit (normalized) length. Solid line is mass laid down by piston crevice out flow; dotted line is that remains at EVO after in-cylinder oxidation.

In this regime, the flux ∝ ω; the amount absorbed (∝ product of flux and time per cycle) is thus independent of ω. This explains the independence of the amount to rpm in Fig. 10.

Oxidation of the Desorbed Fuel in the Presence of Crevice Hydrocarbon. The fuel used to study numerically the complete absorption/desorption/oxidation process was iso-octane. A pseudo-one-step kinetic rate [19] for HC oxidation was obtained by fitting the detailed reacting mechanisms of reference [20]:

$$\frac{d[C_8H_{18}]}{dt} = -2.5 \times 10^{17}[C_8H_{18}][O_2]e^{-25000/T}. \qquad (24)$$

Here, [ ] denotes concentration in mole/cc, and T is in °K. The energy released was calculated by assuming that the products are in equilibrium.

The engine condition was stoichiometric at 1600 rpm, 0.4 bar intake pressure. The warmed-up engine temperature was used: the top of the liner was at 100°C (373°K), and drops linearly to 80°C (353°K) at the bottom.

As a reference, the HC source due to the crevice mechanism alone (without the oil layer) is shown in Fig. 11. The horizontal axis coordinate ξ is the position along the liner normalized by the stroke; $\xi = 0$ corresponds to the top of the liner. Exhaust valve opens at $\xi = 0.8$. The vertical axis is the mass of HC per unit length (normalized) laid down on the liner by the crevice outflow from the piston land (solid line of the plot), and that survives the in-cylinder oxidation to the EVO point (dotted line). Note that most of the HC released at the top of the liner is oxidized [16]. Approximately 25 percent of the total crevice HC survives to EVO.

The HC source due to the oil layer alone is shown in Fig. 12. The distribution of the total HC mass desorbed from the oil layer to the combustion chamber is shown as the solid line. Note that the top 15 percent of the liner is responsible for almost all the desorbed HC. This is because (*a*) the majority of the fuel is absorbed in the top part, and (*b*) the lower part has a longer exposure to the crankcase and desorbs substantially there.

Almost all (91 percent) of the desorbed HC survives oxidation to the EVO point (dotted line in Fig. 12). In this example, 1 percent O_2 was introduced in the burned gas. That was not sufficient to provide substantial oxidation of the desorbed fuel. (This lack of oxidation is in contrast to the crevice gas. This is because the crevice gas is primarily stoichiometric unburned mixture with oxygen premixed in it already.)

The combined case of desorption from oil layer and crevice out flow is shown in Fig. 13. Note that the HC "source" mass from both mechanisms is not equal to the sum of the individual mechanism. This is because the desorption process is changed in the presence of the crevice gas. The source comprises 17 percent from the desorbed fuel from the oil layer and 83 percent from the crevice mechanism.

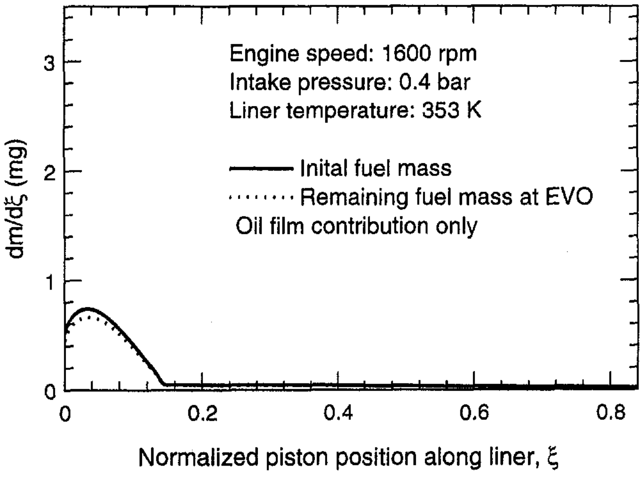

Fig. 12 Oil layer-only HC mechanism. See caption of Fig. 11 for axis definition. Solid line is the total mass (per unit normalized length) desorbed from the oil layer to the combustion chamber. Dotted line is the amount that survives in-cylinder oxidation to the EVO point.

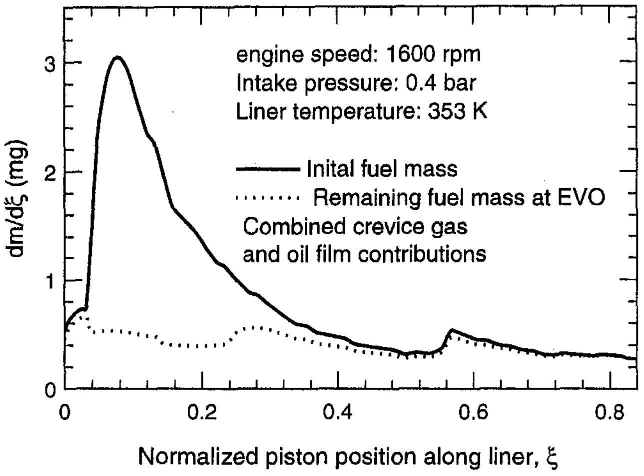

Fig. 13 Combined oil layer and crevice mechanism. See caption of Fig. 11 for axis definition. Solid line is the HC mass (per unit normalized length) released along the liner from both mechanisms. (This is not equal to the sum of Fig. 11 and 12; see text). Dotted line is mass that survives to EVO.

Because the desorption process is not important for the lower part ($\sim\frac{2}{3}$) of the liner, the results there in Fig. 13 is the same as those in Fig. 11. In the upper part, however, because of the insufficient oxygen available due to the presence of neat fuel from the oil layer, a significant amount of HC survives oxidation. As a result, the HC distribution is roughly uniform along the liner at EVO. The total HC survived is ~46 percent of the total source.

Discussion

The result that there is only significant HC from the oil layer mechanism in the upper 15 percent or so of the liner (Fig. 12) could offer an explanation for the results from reference [6]—that there is no significant contribution from the oil layer mechanism to the engine-out HC emissions. So far we have considered the oil layer as a HC "source", and its oxidation during the expansion process. To contribute to the engine-out HC emissions, however, we need to consider the subsequent oxidation in the blow-down process when the exhaust valve is open, and in the exhaust port. It is likely that there is vigorous mixing between the boundary layer on the top part of the liner and the hot burned gas in the blowdown process. If the the oil layer mechanism mainly contributes to the HC located at the top of the liner, this HC is likely to be oxidized when mixed into the the hot burned gas during the blowdown process. (Even at an excess of fuel, the HC will be oxidized to CO and H_2.) Hence, the oil layer mechanism would not contribute to the engine-out HC emissions. This may be what was observed in reference [6].

Conclusions

The oil layer as a source of HC mechanism is examined. Analytical solution to a simplified oil layer absorption/desorption process is first constructed. From the solution, three operating regimes are identified. The process could be (1) limited by the gas side diffusion process, (2) limited by the liquid phase diffusion process, with the absorbed fuel fully penetrating the oil layer thickness (thin oil film regime), and (3) again limited by the liquid phase diffusion process, but with the absorbed fuel penetration depth small compared to the oil layer thickness (thick oil film regime). Reduced solutions of the HC flux at the gas/oil layer interface in each of these regimes are given. Then, a detailed numerical model was used to study the oil layer HC mechanism. An important feature of the model is the inclusion of the crevice mechanism so that fuel is desorbed from the oil layer to the crevice out flow. Most of the oil layer HC comes out of the top 15 percent of the liner because (*a*) there is a larger amount absorbed there, and (*b*) the lower part of the liner desorbs significantly into the crankcase. The desorption process is affected by the crevice mechanism because of the covering of the oil layer by the crevice HC. Furthermore, because the desorbed HC is neat fuel as compared to a premixed mixture in the crevice gas, there is a significant deficiency in oxygen supply in the presence of the desorbed fuel when the engine is operating at stoichiometric condition. As a result, there is less overall in-cylinder oxidation of the combined oil layer/crevice source.

Acknowledgment

This research was supported by an Industrial Consortium for Engine Research. The member companies were Chrysler Motor Co., Ford Motor Co., General Motors Corp., Peugeot S. A., Renault, and Volvo Car Co.

References

1 Cheng, W. K., Hamrin, D., Heywood, J. B., Hochgreb, S., Min, K. D., and Norris, M., 1993, "An Overview of Hydrocarbon Emissions Mechanisms in Spark-Ignition Engines," SAE Transaction, Vol. 102, Paper 932708.

2 Kaiser, E. W., Adamczyk, A. A., and Lavoie, G. A., 1981, "The Effect of Oil Layers on the Hydrocarbon Emissions Generated During Closed Vessel Combustion," *Proceeding of the 18th Symp. (International) on Combustion,* Pittsburgh, PA, pp. 1881–1889. The Combustion Inst.

3 Adamczyk, A. A., and Kach, R. A., 1984, "A Combustion Bomb Study of Fuel-Oil Solubility and HC Emissions From Oil Layers," *Proceeding of the 20th Symp. (International) on Combustion,* The Combustion Inst., Pittsburgh, PA, pp. 37–43.

4 Ishizawa, S., and Takagi, Y., 1987, "A Study of HC Emission From a Spark Ignition Engine: The Influence of Fuel Absorbed into Cylinder Lubricating Oil Film," *JSME International Journal,* Vol. 30, No. 260, pp. 310–317.

5 Gatellier, B., Trapy, J., Herrier, D., Quelin, J. M., and Galliot, F., 1992, "Hydrocarbon Emissions of SI Engines as Influenced by Fuel Absorption-Desorption in Oil Films," SAE Paper 920095.

6 Kaiser, E. W., Siegl, W. O., and Russ, S. G., 1995, "Fuel Composition Effects on Hydrocarbon Emissions from a Spark Ignition Engine—Is Fuel Absorption in Oil Significant?" SAE Paper 952542.

7 Carrier, G., Fendell, F., and Feldman, P., 1981, "Cyclic Absorption/Desorption of Gas in a Liquid Wall Film," *Comb. Sc. and Tech.,* 25, pp. 9–19.

8 Dent, J. C., and Laksminarayanan, P. A., 1983, "A Model for Absorption and Desorption of Fuel Vapor by Cylinder Lubricating Oil Films and Its Contribution to Hydrocarbon Emissions," SAE Paper 830652.

9 Schramm, J., and Sorenson, S. C., 1989, "A Model for Hydrocarbon Emissions in an SI Engine," SAE Paper 890622.

10 Shih, L. K., and Assanis, D. N., 1992, ''Modeling Unburned Hydrocarbon Formation due to Absorption/Desorption Processes into the Wall Oil Film,'' *Symp. on Mechanism and Chemistry of Pollutant Formation and Control from ICE,* Div. of Petroleum Chemistry, American Chemical Society, pp. 1479–1497.

11 Schramm, J., and Sorenson, S. C., 1991, ''Solubility of Gasoline Components in Different Lubricants for Combustion Engines Determined by Gas-Liquid Partition Chromatography,'' *J. of Chromatography,* Vol. 538, pp. 241–248.

12 Taylor, C. F., and Toong, T. Y., 1957, ''Heat Transfer in Internal Combustion Engines,'' ASME Paper 57-HT-17; model summarized in reference [13].

13 Heywood, J. B., 1988, *Internal Combustion Engine Fundamentals,* McGraw-Hill, Inc., New York, NY.

14 Inagaki, H., Saito, A., Murakami, M., and Konomi, T., 1995, ''Development of Two-Dimensional Oil Film Thickness Distribution Measuring System,'' SAE Paper 952436.

15 Rohsenow, W., and Choi, H., 1961, *Heat, Mass, and Momentum Transfer,* Prentice-Hall, Inc., Englewood Cliffs, NJ.

16 Min, K., and Cheng, W. K., 1995, ''Oxidation of the Piston Crevice Hydrocarbon During the Expansion Process in a Spark Ignition Engine,'' *Combust. Sc. and Tech.,* Vol. 106, pp. 307–326.

17 Namazian, M., and Heywood, J. B., 1988, ''Flow in the Piston-Cylinder-Ring Crevices of a Spark-Ignition Engine: Effect on Hydrocarbon Emissions, Efficiency, and Power,'' SAE Paper 820088.

18 Tian, T., Wong, V. W., and Heywood, J. B., 1996, ''A Piston Ring-Pack Film Thickness and Friction Model for Multigrade Oils and Rough Surfaces,'' SAE Paper 962032.

19 Wu, K. C., 1994, ''Chemical Kinetic Modeling of Oxidation of Hydrocarbon Emissions in Spark Ignition Engines,'' MS thesis, Dept. of Mech. Eng., MIT, Cambridge, MA.

20 Axelsson, E. I., Brezinsky, K., Dryer, F. L., Pitz, W. J., and Westbrook, C. K., 1986, ''Chemical Kinetic Modeling of the Oxidation of Large Alkane Fuels: n-Octane and Iso-Octane,'' *Proceed. of the 21st Symp. (Int.) on Combustion,* The Comb. Inst., Pittsburgh, PA, pp. 783–793.

H. Nehme
Graduate Research Assistant.

N. G. Chalhoub
Associate Professor.

N. Henein
Professor.

Department of Mechanical Engineering,
Wayne State University,
5050 Anthony Wayne Drive,
Detroit, MI 48202

Development of a Dynamic Model for Predicting the Rigid and Flexible Motions of the Crank Slider Mechanism

A continuous model is developed to predict the rigid and flexible motions of the piston assembly/connecting rod/crankshaft mechanism for a single cylinder engine. The model accounts for the torsional vibration and the out-of-plane transverse deformation of the crankshaft along with the out-of-plane transverse deformation of the connecting rod. The eigenvalue problem of the crankshaft, including the counterweights, the flywheel, and the crank gear, is solved to obtain the analytical expressions for the elastic modes of the crankshaft. The resulting mode shapes are then used in the assumed modes method to approximate the structural flexibility terms. The differential-algebraic equations of motion are obtained by implementing the Lagrange principle. The digital simulation results illustrate the role played by the topological nonlinearities inherent in the system and reveal the relationships with which the rigid and flexible motions of the crank-slider mechanism would interact.

1 Introduction

The dynamics of the crankshaft and the reciprocating engine components are playing an increasing role in the assessment of engine performance and structural design. They are included in algorithms for detecting engine misfire (Lee and Rizzoni, 1995), for determining the instantaneous frictional losses in engines (Rezeka and Henein, 1984; Uras and Patterson, 1983), and for estimating the mean indicated pressure (Taraza, 1993a; Taraza 1993b). Moreover, detailed models of the crank-slider mechanism serve to assess the performance of a new engine design under wide range of operating conditions. These models can determine the noise and vibration levels that are being used as an important criteria for evaluating the engine quality (Kawazoe and Zhang, 1991). Furthermore, they provide a tool for performing three-dimensional dynamic stress analyses that are instrumental in predicting crankshaft fatigue failures (Kawazoe and Zhang, 1991; Priebsch et al., 1993; Carrato and Fu, 1986).

By and large, the work done in this area can be classified as lumped mass modeling (Taraza, 1993a; Bremer, 1979) or distributed mass modeling of the crank-slider mechanism (Kawazoe and Zhang, 1991; Priebsch et al., 1993; Carrato and Fu, 1986; Okamura et al., 1995). The leading techniques used in the development of distributed mass models are the finite element method (FEM) and the transfer matrix method (TMM). The finite element method tends to be more computationally intensive than the transfer matrix method, even for a relatively simple crankshaft structure.

Most of the distributed mass models have focused on predicting the rigid body motion of the crank-slider mechanism along with the three-dimensional deformation of the crankshaft. The connecting rod is usually represented by a lumped mass system since it is stiffer than the crankshaft. The lower end of the connecting rod is divided into two equal masses that are attached at the two ends of the crankpin. Whereas the inertial forces, associated with the reciprocating upper end of the connecting rod along with the piston mass, are lumped with the equivalent gas force and directly applied at the two ends of the crankpin (Morita and Okamura, 1995; Okamura et al., 1995; Kawazoe and Zhang, 1991; Priebsch et al., 1993).

In the present study, a distributed mass model is derived to predict the rigid and flexible motions of the piston assembly/connecting rod/crankshaft mechanism of a single cylinder engine. The distributed mass of the crankshaft and the connecting rod are accounted for in the formulation. Only the piston is treated as a rigid body. The model takes into consideration the torsional and out-of-plane transverse deformations of the crankshaft along with the out-of-plane transverse deformation of the connecting rod. The assumed modes method is used in this work to approximate the structural flexibility terms. The admissible functions, required for the implementation of this method, are chosen to represent the elastic modes of both the crankshaft and the connecting rod. The analytical expressions for the mode shapes of the crankshaft structure are not available in the literature. As a consequence, a detailed eigenvalue problem of the crankshaft, including the counterweights, the flywheel and the crank gear, is formulated to determine the natural frequencies and the mode shapes of the crankshaft. The current work treats the crankjournals, crankpins, and crankarms as simple beam elements and the flywheel, crank gear, and counterweights as rigid bodies, as opposed to treating the crankjournals and crankpins as simple rods with the crankarms and counterweights idealized by jointed simple beams (Okamura et al., 1995).

The focus of this work is to investigate the role played by the topological nonlinearities that are inherent in the crank-slider mechanism and to explore the relationships with which the rigid and flexible motions would interact. Moreover, the combination resonances, that may appear in the system response, are investigated.

The piston assembly/connecting rod/crankshaft mechanism, considered in this study, is schematically illustrated in Fig. 1. The formulation of the eigenvalue problem is presented in the next section. The dynamic model is derived in section 3. The digital simulation results are included in section 4. They predict the rigid and flexible motions of the crank-slider mechanism in the case of a free rotation of the crankshaft as well as under

---

Contributed by the Internal Combustion Engine Division and presented at The Spring Technical Conference of the ASME Internal Combustion Engine Division, April 27–30, 1997, Fort Collins, CO. Manuscript received by the ASME Headquarters December 2, 1997. Associate Technical Editor: D. Assanis.

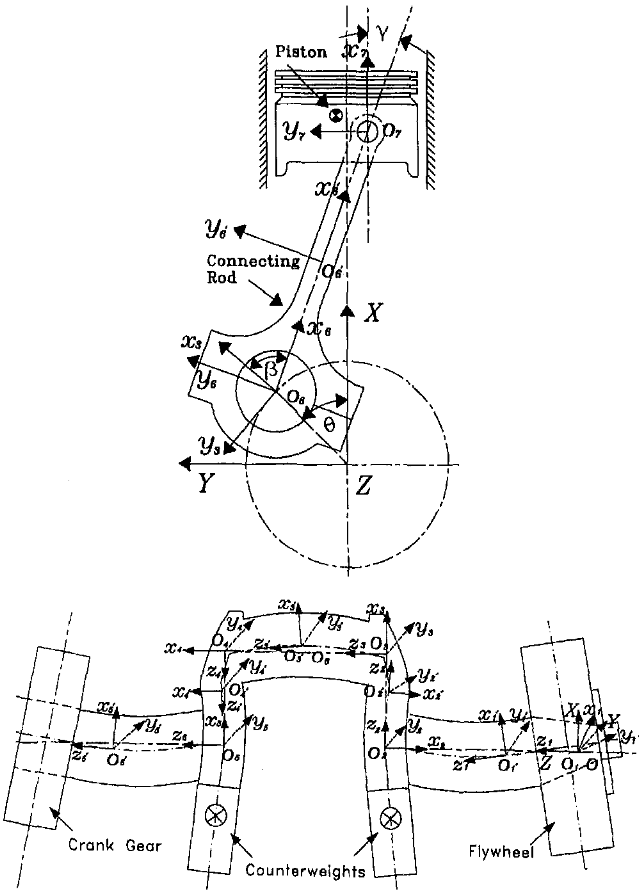

Fig. 1 Schematic of the piston assembly/connecting-rod/crankshaft mechanism

firing conditions. They also illustrate the various combination resonances that are induced by the system nonlinearities. Subsequently, the work is summarized and the main conclusions are highlighted.

2 Eigenvalue Problem of the Crankshaft

The assumed modes method is implemented to discretize the terms representing the torsional and out-of-plane transverse deformations of the crank-slider mechanism. These terms are written as linear combinations of the products of time-dependent generalized coordinates and admissible functions of spatial coordinates as follows (Meirovitch, 1986):

$$\phi(z_i, t) = \sum_{j=1}^{3} \phi^{(j)}(z_i)q_j(t)$$

$$W_{cs}(z_i, t) = \sum_{j=1}^{3} W_{cs}^{(j)}(z_i)q_j(t)$$

$$W_{cr}(x_6, t) = W_{cr}^{(1)}(x_6)q_4(t). \qquad (1)$$

The admissible functions, $\phi^{(j)}$ and $W_{cs}^{(j)}$, are selected herein to be the eigenfunctions representing the first three elastic modes of the torsional and out-of-plane transverse deformations of a free-free crankshaft, respectively. Similarly, $W_{cr}^{(1)}$ is considered to be the first elastic mode of the out-of-plane transverse deformation of a pinned-pinned beam. Note that the connecting rod is much stiffer than the crankshaft. Therefore, its structural deformation can be adequately represented by only considering the first elastic mode.

The eigenfunctions of a single beam are readily available in the literature (Young and Felgar, 1949). However, one has to solve the eigenvalue problem of the crankshaft, including the counterweights, the flywheel and the crank gear, in order to obtain the analytical expressions for the crankshaft mode shapes. This is done by partitioning the crankshaft into five beam elements, as shown in Fig. 1. The flywheel, the counterweights, and the crank gear are treated as rigid bodies that are connected to nodes 1, 2, 5, and 6, respectively (see Fig. 1). The transfer function matrix, relating the deformations and forces at one end of the ith beam element to those of the other end, can be written based on the Euler-Bernoulli beam theory as

$$\underset{\sim}{V}_i(0) = G_i \underset{\sim}{V}_i(L_i) = G_i\{\underset{\sim}{D}_i(L_i) | \underset{\sim}{F}_i(L_i)\}^T$$
$$= G_i\{W_{cs,z_i}\; W_{cs}\; \phi | \bar{M}\; \bar{V}\; \bar{T}\}^T_{z_i=L_i}$$

Nomenclature

A_i, m_i = cross-sectional area and mass of the ith beam element, respectively
EI_i = flexural rigidity of the ith beam element
$\underset{\sim}{F}(q, \dot{q})$ = vector including all inertial, stiffness and gravitational acceleration terms
GJ_i = torsional stiffness of the ith beam element
g, ρ = gravitational acceleration and density, respectively
L_i, L_6 = length of the ith beam element of the crankshaft and the connecting rod, respectively
$\bar{M}$, $\bar{V}$, $\bar{T}$ = bending moment, shear force and torque applied at the extremity of the beam element, respectively
$M(\underset{\sim}{q})$ = inertia tensor of the crank-slider mechanism
P_{gas} = cylinder gas pressure

$\underset{\sim}{Q}^{NC}$ = nonconservative generalized force vector
r = distance from the counterweight mass center to the Z-axis
T_{load} = engine load torque
W = out-of-plane transverse deformation
(x_i, y_i, z_i) = coordinates of an arbitrary point in the undeformed configuration of the ith beam element
μ = mass per unit length
ϕ = torsional vibration of the crankshaft
$\underset{\sim}{\omega}_j$ = rotation vector of the jth rigid body
ω_{n_j} = natural frequency of the jth elastic mode of the crankshaft
θ = crank angle
$(\ )_{cr}$ = a "cr" subscript refers to a variable associated with the connecting rod

$(\ )_{cs}$ = a "cs" subscript refers to a variable associated with the crankshaft
$(\ )_{cw1,cw2}$ = a "$cw1$" or a "$cw2$" subscript denotes a variable associated with the first or the second counterweight, respectively
$(\ )_{fl}$ = a "fl" subscript denotes a variable associated with the flywheel
$(\ )_{gr}$ = a "gr" subscript denotes a variable associated with the crank gear
$(\ )_p$ = a "p" subscript denotes a variable associated with the piston
$(\ )_{,z_i}$ = a "z_i" subscript indicates a differentiation with respect to z_i
$(\dot{\ })$, $(\ddot{\ })$ = a dot or a double dot over any symbol denotes first or second derivative with respect to time

$$G_i = \begin{bmatrix} a_{11} & a_{12} & 0 & a_{14} & a_{15} & 0 \\ a_{21} & a_{22} & 0 & a_{24} & a_{25} & 0 \\ 0 & 0 & a_{33} & 0 & 0 & a_{36} \\ a_{41} & a_{42} & 0 & a_{44} & a_{45} & 0 \\ a_{51} & a_{52} & 0 & a_{54} & a_{55} & 0 \\ 0 & 0 & a_{63} & 0 & 0 & a_{66} \end{bmatrix} \qquad (2)$$

where the a_{ij} terms denote nonzero entries of the above transfer function matrix. Their expressions are given in appendix A.

The boundary conditions of the beams that are attached at the ith node have to be selected such that the curves corresponding to the transverse deformation and its slope along with the torsional vibration of the crankshaft remain continuous at that node. Moreover, the linear and angular momentum balance equations at the ith node are defined by a H_i matrix. They reflect the dynamics of the rigid body that may be attached at that node. It should be pointed out that H_i becomes a null matrix in the absence of such a rigid body. Appendix A provides the expressions for the H_i matrices that correspond to the nodes which have a rigid body attached to them. All the boundary conditions at the $(i + 1)$th node can be combined and expressed as follows

$$\begin{aligned} \underset{\sim}{Y}_i(L_i) &= T_{(i,i+1)} \underset{\sim}{Y}_{i+1}(0) \\ &= \begin{bmatrix} R_{(i+1)_{3\times 3}} & | & 0_{3\times 3} \\ ---- & | & ---- \\ H_{(i+1)_{3\times 3}} & | & R_{(i+1)_{3\times 3}} \end{bmatrix} \underset{\sim}{Y}_{i+1}(0) \\ & \qquad i = 1, \ldots, 4 \end{aligned} \qquad (3)$$

where $R_{(i+1)}$ represents an $\alpha_{(i+1)}$ rotation around the y_i-axis. It can be expressed as

$$R_{(i+1)} = \begin{bmatrix} \cos \alpha_{(i+1)} & 0 & -\sin \alpha_{(i+1)} \\ 0 & 1 & 0 \\ \sin \alpha_{(i+1)} & 0 & \cos \alpha_{(i+1)} \end{bmatrix}. \qquad (4)$$

From the crankshaft geometry, one can set $\alpha_2 = \alpha_5 = 90$ deg and $\alpha_3 = \alpha_4 = -90$ deg (see Fig. 1). It should be emphasized that both $R_{(i+1)}$ and $H_{(i+1)}$ components of $T_{(i,i+1)}$ are responsible for coupling the out-of-plane transverse deformation and the torsional vibration of the crankshaft.

For mathematical convenience, the formulation of $T_{(fl,1)}$, corresponding to the first node where the flywheel is attached, is defined as

$$\begin{aligned} \begin{Bmatrix} \underset{\sim}{D}_1(0) \\ --- \\ \underset{\sim}{F}_1(0) \end{Bmatrix} &= T^{-1}_{(fl,1)} \begin{Bmatrix} \underset{\sim}{D}_1(0) \\ --- \\ \underset{\sim}{D}_1(0) \end{Bmatrix} \\ &= \begin{bmatrix} I_{3\times 3} & | & 0_{3\times 3} \\ -- & | & -- \\ 0_{3\times 3} & | & H_{1_{3\times 3}} \end{bmatrix} \begin{Bmatrix} \underset{\sim}{D}_1(0) \\ --- \\ \underset{\sim}{D}_1(0) \end{Bmatrix}. \end{aligned} \qquad (5)$$

Whereas, the formulation of $T_{(5,gr)}$, corresponding to the last node where the crank gear is connected, is given by

$$\begin{aligned} \begin{Bmatrix} \underset{\sim}{D}_5(L_5) \\ --- \\ \underset{\sim}{F}_5(L_5) \end{Bmatrix} &= T_{(5,gr)} \underset{\sim}{D}_5(L_5) \\ &= \begin{bmatrix} I_{3\times 3} \\ -- \\ H_6 \end{bmatrix} \underset{\sim}{D}_5(L_5) \end{aligned} \qquad (6)$$

The eigenvalue problem can now be formulated as

$$\begin{aligned} \begin{Bmatrix} \underset{\sim}{D}_1(0) \\ --- \\ \underset{\sim}{D}_1(0) \end{Bmatrix} &= T_{(fl,1)} \begin{Bmatrix} \underset{\sim}{D}_1(0) \\ --- \\ \underset{\sim}{F}_1(0) \end{Bmatrix} \\ &= T_{(fl,1)} \left(\prod_{i=1}^{4} G_i T_{(i,i+1)} \right) G_5 T_{(5,gr)} \underset{\sim}{D}_5(L_5) \\ &= \begin{Bmatrix} Y_{1_{3\times 3}} \\ --- \\ Y_{2_{3\times 3}} \end{Bmatrix} \underset{\sim}{D}_5(L_5) \end{aligned} \qquad (7)$$

The above equation can be rewritten in the following form:

$$[Y_1 - Y_2] \underset{\sim}{D}_5(L_5) = \underset{\sim}{0} \qquad (8)$$

Note that $[Y_1 - Y_2]$ is a singular matrix. Its entries are solely dependent on $\lambda_{w_i}^{(j)}$ and $\lambda_{t_i}^{(j)}$, which, in their turn, can be expressed with respect to the crankshaft natural frequency, ω_{n_j}, as follows

$$\lambda_{w_i}^{(j)} = \left(\frac{\mu \omega_{n_j}^2}{EI_i} \right)^{1/4} \quad \lambda_{t_i}^{(j)} = \left(\frac{\mu \omega_{n_j}^2}{GA_i} \right)^{1/2} \qquad (9)$$

The characteristic polynomial of $[Y_1 - Y_2]$ is set to zero and solved numerically to determine the natural frequencies of the crankshaft. The mode shapes of the crankshaft are defined with respect to the elastic modes of the five beam elements. The expressions of the jth elastic modes of the transverse and torsional deformations at an arbitrary point on the ith beam element can be written as

$$\begin{aligned} W_{cs}^{(j)}(z_i) &= A_i^{(j)} a_i(\lambda_{w_i}^{(j)}, z_i) + B_i^{(j)} b_i(\lambda_{w_i}^{(j)}, z_i) \\ &\quad + C_i^{(j)} c_i(\lambda_{w_i}^{(j)}, z_i) + D_i^{(j)} d_i(\lambda_{w_i}^{(j)}, z_i) \\ \phi^{(j)}(z_i) &= E_i^{(j)} e_i(\lambda_{t_i}^{(j)}, z_i) + F_i^{(j)} f_i(\lambda_{t_i}^{(j)}, z_i) \end{aligned} \qquad (10)$$

The reader is referred to appendix A for the expressions of the spatial functions $a_i(\lambda_{w_i}^{(j)}, z_i)$ to $f_i(\lambda_{t_i}^{(j)}, z_i)$. Furthermore, the above formulation demonstrates that six constants, $A_i^{(j)}$ to $F_i^{(j)}$, need to be evaluated in order to fully define the above jth elastic modes for the ith beam element. However, the crankshaft structure entails five such beam elements (see Fig. 1). This results in 30 constants that have to be numerically determined before the jth modes of the torsional and transverse deformations of the crankshaft can be obtained. These constants can be evaluated by writing three equations, representing the linear and angular momentum balance, for each node in the crankshaft structure. The remaining equations can be obtained by imposing the continuity conditions corresponding to the displacement and slopes at each node starting with node 2 and ending with node 5. This brings up the total number of equations to 30, out of which only 29 are independent. It should be mentioned that the connectivity conditions along with the linear and angular momentum balance equations have been used earlier in the formulation during the derivation of the $T_{(i,i+1)}$'s transformation matrices. The 29 independent equations serve to express 29 constants with respect to the 30th one. The latter, which can be arbitrarily selected, is assigned herein to normalize the eigenfunction of the crankshaft.

3 Dynamic Modeling

A dynamic model is developed to predict the rigid and flexible motions of the piston assembly/connecting rod/crankshaft mechanism of a single cylinder internal combustion engine. The current model treats the piston as a rigid body that can only move along the centerline of the cylinder. Thus, the derivations do not account for piston lateral displacements or tilting. Furthermore, the flywheel, the crank gear and the counterweights are modeled as rigid bodies.

An inertial coordinate system, (X, Y, Z), is fixed at point O. In addition, seven noninertial rotating coordinate systems, $\{(x_i, y_i, z_i), i = 1 \text{ to } 7\}$, are assigned to the piston, the connecting rod and the five beam elements of the crankshaft. This is illustrated in Fig. 1. Furthermore, the clearance between the piston assembly and the cylinder liner along with the clearances in the journal bearings, the crankpin, and the piston pin have been ignored in the current study.

To systematically represent the structural flexibility of the crank-slider mechanism, six floating coordinate systems, $\{(x_{i'}, y_{i'}, z_{i'}), i' = 1 \text{ to } 6\}$, are assigned to the compliant five beam elements of the crankshaft and the connecting rod (see Fig. 1). It should be emphasized that $z_{1'}$ to $z_{5'}$ and $x_{6'}$ axes are chosen to remain tangent to the neutral axes of their respective beam elements. As a result, the overall displacement of $O_{i'}$ and the orientation of $(x_{i'}, y_{i'}, z_{i'})$ with respect to (x_i, y_i, z_i) will reflect the total deformation of the ith beam at $O_{i'}$. Therefore, one can define the 4 × 4 structural flexibility transformation matrix as

$$T_i^{i'} = \left[\begin{array}{ccc|c} 1 & -\phi(z_i, t) & 0 & 0 \\ \phi(z_i, t) & 1 & W_{cs,z_i}(z_i, t) & W_{cs}(z_i, t) \\ 0 & -W_{cs,z_i}(z_i, t) & 1 & z_i \\ \hline 0 & 0 & 0 & 1 \end{array}\right] \quad i = 1, \ldots, 5$$

$$T_6^{6'} = \left[\begin{array}{ccc|c} 1 & -W_{cr,x_6}(x_6, t) & 0 & x_6 \\ W_{cr,x_6}(x_6, t) & 1 & 0 & W_{cr}(x_6, t) \\ 0 & 0 & 1 & 0 \\ \hline 0 & 0 & 0 & 1 \end{array}\right] \quad (11)$$

The extended absolute position vector of any point on the ith beam element of the crankshaft can be systematically determined from

$$\{\underset{\sim}{r}_{cs}^{(i)^T} | 1\}^T = [\prod_{j=1}^{i} T_{j-1}^{j}] T_i^{i'} \{x_{i'} \quad y_{i'} \quad 0 \quad | \quad 1\}^T \quad (12)$$

Ignoring Poisson's ratios, $x_{i'}$ and $y_{i'}$ will become equal to x_i and y_i. In addition, T_{j-1}^{j} defines the origin and orientation of the jth coordinate system with respect to the $(j-1)$th frame in the nominal rigid body configuration of the crankshaft. It can be written in the following general form:

$$T_{(j-1)}^{j} = \left[\begin{array}{ccc|c} \cos\alpha_j & 0 & \sin\alpha_j & 0 \\ 0 & 1 & 0 & 0 \\ -\sin\alpha_j & 0 & \cos\alpha_j & L_j \\ \hline 0 & 0 & 0 & 1 \end{array}\right]$$

$$j = 2, 3, 4, 5 \quad (13)$$

It should be mentioned that T_0^1 accounts for the rigid body motion of the crankshaft. It is given by

$$T_0^1 = \left[\begin{array}{ccc|c} \cos\theta & -\sin\theta & 0 & 0 \\ \sin\theta & \cos\theta & 0 & 0 \\ 0 & 0 & 1 & 0 \\ \hline 0 & 0 & 0 & 1 \end{array}\right] \quad (14)$$

Now, the extended absolute position vector of any point on the connecting rod can be expressed as

$$\{\underset{\sim}{r}_{cr}^{T} | 1\}^T = T_0^1 T_1^2 T_2^3 T_3^{3'} T_{3'}^{6} T_6^{6'} \{0 \quad y_{6'} \quad z_{6'} \quad | \quad 1\}^T \quad (15)$$

where $(x_{3'}, y_{3'}, z_{3'})$ represents a floating coordinate system whose origin is fixed at $z_3 = L_3/2$. $T_{3'}^{6}$ is given by

$$T_{3'}^{6} = \left[\begin{array}{ccc|c} \cos\beta & \sin\beta & 0 & 0 \\ -\sin\beta & \cos\beta & 0 & 0 \\ 0 & 0 & 1 & 0 \\ \hline 0 & 0 & 0 & 1 \end{array}\right] \quad (16)$$

where β is a superfluous coordinate which is introduced to describe the rigid body motion of the connecting rod with respect to the crankshaft. The mass center of the piston can be located from

$$\{\underset{\sim}{r}_{p}^{T} | 1\}^T = T_0^1 T_1^2 T_2^3 T_3^{3'} T_{3'}^{6} T_{6^e}^{6'} T_{6_e'}^{7} \{x_7^* \quad y_7^* \quad z_7^* \quad | \quad 1\}^T \quad (17)$$

where $(x_{6_e'}, y_{6_e'}, z_{6_e'})$ represents a floating coordinate system whose origin is fixed at $x_6 = L_6$. $T_{6_e'}^{7}$ is given by

$$T_{6_e'}^{7} = \left[\begin{array}{ccc|c} \cos\gamma & -\sin\gamma & 0 & 0 \\ \sin\gamma & \cos\gamma & 0 & 0 \\ 0 & 0 & 1 & 0 \\ \hline 0 & 0 & 0 & 1 \end{array}\right] \quad (18)$$

where γ is a superfluous coordinate representing the rigid body motion of the piston with respect to the connecting rod.

Now, the kinetic energy of the crank-slider mechanism can be obtained from

$$K.E. = \tfrac{1}{2} \sum_{i=1}^{5} \int_{m_i} \dot{\underset{\sim}{r}}_{cs}^{(i)} \cdot \dot{\underset{\sim}{r}}_{cs}^{(i)} dm_i + \tfrac{1}{2} \sum_{j} (m_j \dot{\underset{\sim}{r}}_j \cdot \dot{\underset{\sim}{r}}_j + \underset{\sim}{\overline{\omega}}_j^T I_j \underset{\sim}{\overline{\omega}}_j)$$

$$+ \tfrac{1}{2} \int_{m_{cr}} \dot{\underset{\sim}{r}}_{cr} \cdot \dot{\underset{\sim}{r}}_{cr} dm_{cr} \quad j = fl, cw1, cw2, gr, p$$

$$\underset{\sim}{\overline{\omega}}_{fl} = (-\dot{W}_{cs,z_1} \quad \dot{\theta} W_{cs,z_1} \quad \dot{\theta} + \dot{\phi})_{z_1=0}^{T}$$

$$\underset{\sim}{\overline{\omega}}_{cw1} = (-\dot{W}_{cs,z_1} \quad \dot{\theta} W_{cs,z_1} \quad \dot{\theta} + \dot{\phi})_{z_1=L_1}^{T}$$

$$\underset{\sim}{\overline{\omega}}_{cw2} = (-\dot{W}_{cs,z_5} \quad \dot{\theta} W_{cs,z_5} \quad \dot{\theta} + \dot{\phi})_{z_5=0}^{T}$$

$$\underset{\sim}{\overline{\omega}}_{gr} = (-\dot{W}_{cs,z_5} \quad \dot{\theta} W_{cs,z_5} \quad \dot{\theta} + \dot{\phi})_{z_5=L_5}^{T}$$

$$\{\underset{\sim}{\overline{\omega}}_p^T | 0\}^T = T_7^{3'} (-\dot{W}_{cs,z_3} \quad \dot{\theta} W_{cs,z_3} \quad \dot{\theta} + \dot{\phi} \quad | \quad 0)_{z_3=L_3/2}^{T}$$

$$+ T_7^{6'} (0 \quad 0 \quad \dot{\beta} + \dot{W}_{cr,x_6} \quad | \quad 0)_{x_6=L_6}^{T}$$

$$+ (0 \quad 0 \quad \dot{\gamma} \quad | \quad 0)^T \quad (19)$$

Next, the strain energy stored in the crank-slider mechanism along with the potential energy due to the force of gravity can be computed from

$$P.E. = \tfrac{1}{2}\sum_{i=1}^{5}\left(\int_0^{L_i} EI_i(W_{cs,z_iz_i})^2 dz_i + \int_0^{L_i} GJ_i(\phi_{,z_i})^2 dz_i\right)$$

$$+ \tfrac{1}{2}\int_0^{L_6} EI_6(W_{cr,x_6x_6})^2 dx_6 + \sum_{i=1}^{5}\int_0^{L_i} \rho A_i g\underset{\sim}{I}.\underset{\sim}{r}{}_{cs}^{(i)} dz_i$$

$$+ \int_0^{L_6} \rho A_6 g\underset{\sim}{I}.\underset{\sim}{r}_{cr} dx_6 + \sum_j (m_j g\underset{\sim}{I}.\underset{\sim}{r}_j)$$

$$j = fl,\ cw1,\ cw2,\ gr,\ p \tag{20}$$

where the datum line is considered to coincide with the inertial Z-axis.

The virtual work done by the nonconservative generalized forces is

$$\delta W_{NC} = -P_{\text{gas}}A_p\underset{\sim}{I}.\delta\underset{\sim}{r}_p - T_{\text{load}}\underset{\sim}{K}.\{-\delta W_{cs,z_5}\underset{\sim}{i}_5 + W_{cs,z_5}\delta\theta\underset{\sim}{j}_5$$

$$+ (\delta\theta + \delta\phi)\underset{\sim}{k}_5\}_{z_5=L_5} + \int_0^{L_2}\{\underset{\sim}{F}{}_{ax}^{(2)}.[-\tfrac{1}{2}\delta([W_{cs,z_2}]^2)\underset{\sim}{k}_2]\}dz_2$$

$$+ \int_0^{L_4}\{\underset{\sim}{F}{}_{ax}^{(4)}.[\tfrac{1}{2}\delta([W_{cs,z_4}]^2)\underset{\sim}{k}_4]\}dz_4$$

$$+ \int_0^{L_6}\{\underset{\sim}{F}{}_{ax}^{(6)}.[-\tfrac{1}{2}\delta([W_{cr,x_6}]^2)\underset{\sim}{i}_6]\}dx_6 \tag{21}$$

where the first two terms represent the virtual work done by the cylinder gas pressure and the engine load torque, respectively. The remaining terms capture the stiffening effect induced by the centripetal acceleration of the system. Ignoring the dependence of the axial forces on the structural flexibility terms and on the gravitational acceleration, the centrifugal force along the direction of the axial geometric shortening of the connecting rod can be written as

$$\underset{\sim}{F}{}_{ax}^{(6)} = \left\{\rho A_6(\dot\theta - \dot\beta)^2\left[\left(L_2L_6\cos\beta + \frac{L_6^2}{2}\right)\right.\right.$$

$$\left.- \left(L_2x_6\cos\beta + \frac{x_6^2}{2}\right)\right] + m_p(\dot\theta - \dot\beta + \dot\gamma)^2(L_2\cos\beta$$

$$\left.+ L_6 + x_7^*\cos\gamma - y_7^*\sin\gamma)\right\}\underset{\sim}{i}_6 \tag{22}$$

Whereas, the centrifugal forces along the direction of the axial geometric shortening of the second and fourth beam elements of the crankshaft can be expressed as

$$\underset{\sim}{F}{}_{ax}^{(2)} = \left\{\frac{1}{2}m_2\dot\theta^2L_2\left[1 - \left(\frac{z_2}{L_2}\right)^2\right]\right.$$

$$+ \tfrac{1}{2}m_{cr}(\dot\theta - \dot\beta)^2\left[L_2 + \frac{L_6}{2}\cos\beta\right] + \tfrac{1}{2}m_3\dot\theta^2L_2$$

$$+ \tfrac{1}{2}m_p(\dot\theta - \dot\beta + \dot\gamma)^2(L_2 + L_6\cos\beta$$

$$\left.+ x_7^*\cos(\beta - \gamma) + y_7^*\sin(\beta - \gamma)\right\}\underset{\sim}{k}_2$$

$$\underset{\sim}{F}{}_{ax}^{(4)} = -\left\{\frac{1}{2}m_4\dot\theta^2L_4\left[2\left(\frac{z_4}{L_4}\right) - \left(\frac{z_4}{L_4}\right)^2\right]\right.$$

$$+ \tfrac{1}{2}m_{cr}(\dot\theta - \dot\beta)^2\left[L_4 + \frac{L_6}{2}\cos\beta\right]$$

$$+ \tfrac{1}{2}m_3\dot\theta^2L_4 + \tfrac{1}{2}m_p(\dot\theta - \dot\beta + \dot\gamma)^2(L_2 + L_6\cos\beta$$

$$\left.+ x_7^*\cos(\beta - \gamma) + y_7^*\sin(\beta - \gamma)\right\}\underset{\sim}{k}_4 \tag{23}$$

Note that the effect of the centrifugal force of the connecting

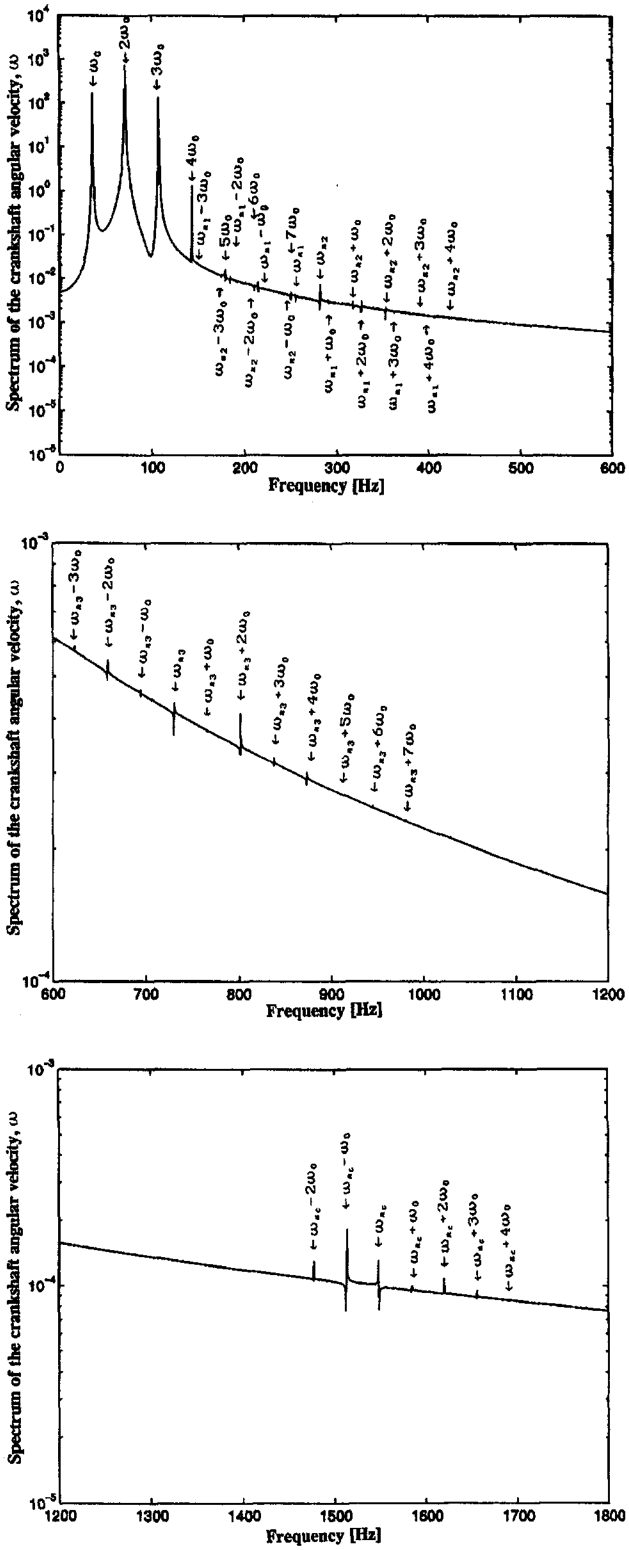

Fig. 2 Frequency spectrum of the crankshaft angular velocity in the case of a free motion with an initial rigid body rotation of the crankshaft

rod and the piston are equally distributed on the second and fourth beam elements of the crankshaft.

It should be mentioned that three coordinates θ, β, and γ have been used in the formulation to describe the rigid body motion of the slider-crank mechanism. To eliminate the superfluous coordinates, two constraint equations are imposed to prevent the piston from tilting or to move away from the centerline of the cylinder in the $\underset{\sim}{J}$-direction. The constraint equations are defined to be

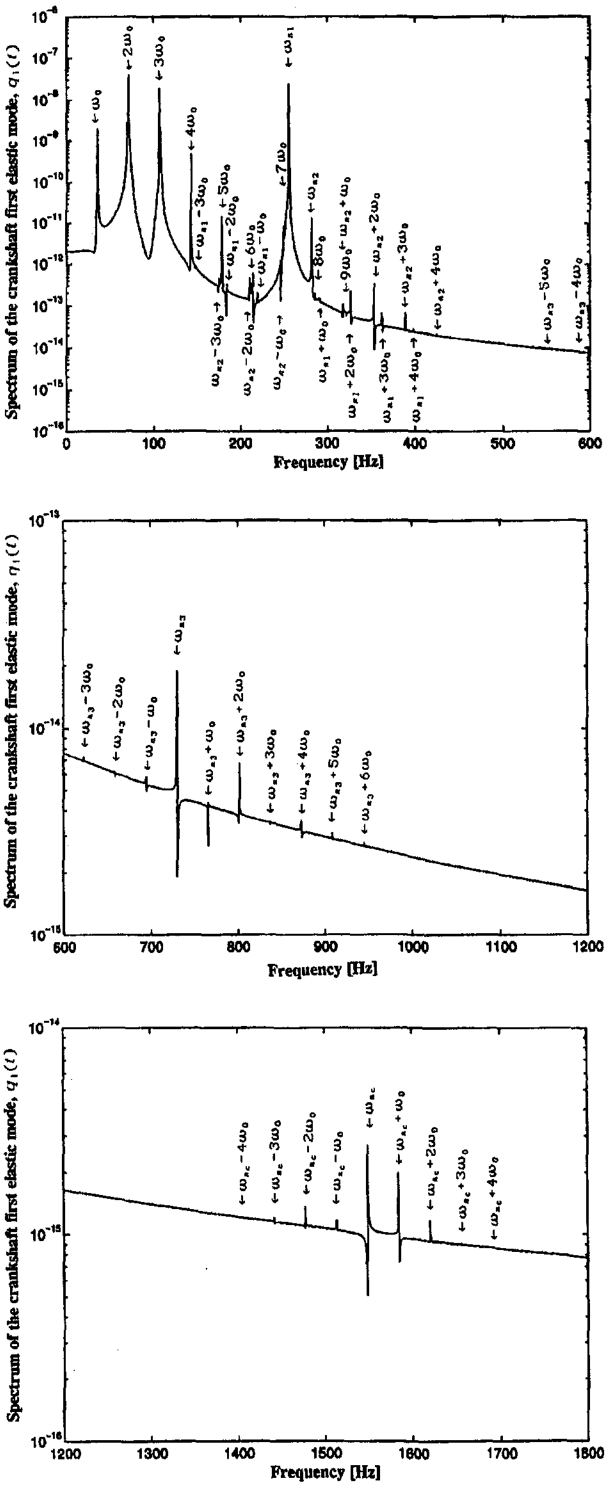

Fig. 3 Frequency spectrum of the first elastic mode of the out-of-plane transverse deformation of the crankshaft in the case of a free motion with an initial rigid body rotation of the crankshaft

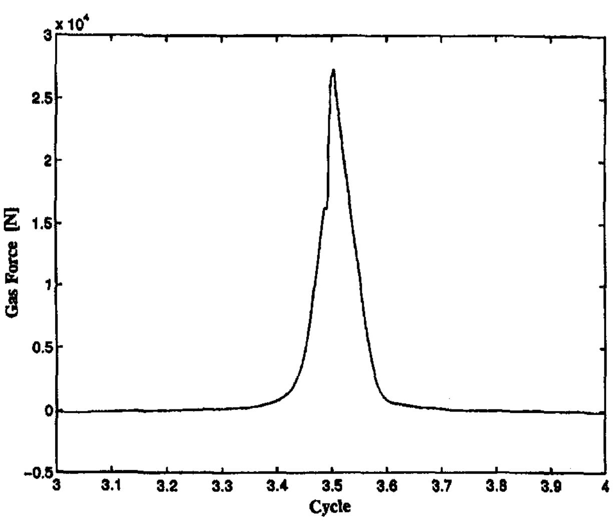

Fig. 4 Cylinder gas force

$$\underset{\sim}{\omega}_p\cdot\underset{\sim}{k}_7 = 0 \qquad (24a)$$

$$\underset{\sim}{r}_p^*(t)\cdot\underset{\sim}{J} = \text{const.} \qquad (24b)$$

The Lagrange principle is implemented to obtain the equations of motion for the crank-slider mechanism. The resulting equations are highly nonlinear, stiff, coupled, second order, ordinary differential equations that can be written in the following compact form:

$$M(\underset{\sim}{q})\ddot{\underset{\sim}{q}} + \underset{\sim}{F}(\underset{\sim}{q}, \dot{\underset{\sim}{q}}) = \underset{\sim}{Q}^{NC} + \underset{\sim}{\lambda}^T s_1(\underset{\sim}{q})$$

$$\underset{\sim}{q} = [\theta \quad \beta \quad \gamma \quad q_1 \quad q_2 \quad q_3 \quad q_4]^T \qquad (25)$$

where the generalized coordinates have to satisfy the above constraint equations. Differentiating Eq. (24a) once and Eq. (24b) twice with respect to time and writing the results in a compact form, one gets

$$s_1\ddot{\underset{\sim}{q}} + \underset{\sim}{s}_2 = \underset{\sim}{0} \qquad (26)$$

To numerically integrate the set of differential-algebraic (D-A) equations, the scheme used by Glocker and Pfeiffer (1992) is implemented whereby the Lagrange multiplier vector, $\underset{\sim}{\lambda}$, is given by

$$\underset{\sim}{\lambda} = -(s_1M^{-1}s_1^T)^{-1}(\underset{\sim}{s}_2 + s_1M^{-1}\underset{\sim}{h}) \qquad (27)$$

where $\underset{\sim}{h}$ is $\underset{\sim}{Q}^{NC} - \underset{\sim}{F}(q, \dot{q})$. Note that the constraint equations are independent, then s_1 has a full rank. Moreover, $M(q)$ is a positive definite matrix. Therefore, the inverse of $s_1M^{-1}s_1^T$ will always exist.

It should be pointed out that neither the structural damping nor the viscous damping are considered in the current model of the slider crank mechanism. This is because the current formulation will be used in a broader study that will focus on predicting the instantaneous frictional losses in internal combustion engines.

The equations of motion of the slider-crank mechanism are numerically integrated by the Gear's method which is best suited to handle stiff equations (Gear, 1971).

4 Digital Simulation Results

The equations of motion of the crank-slider mechanism are integrated in the time domain and in the event-based domain. The time-based results are used herein to perform a Fast-Fourier Transform (FFT) analysis in order to assess the effect of topological nonlinearities on the system response and to examine the relationships with which the rigid and flexible motions of the crank-slider mechanism would interact. The time-based integration requires a very small time increment to ensure that rapidly changing events are well represented in the digital simulations. Therefore, to avoid the large computation time required by the time-based integration, the results that did not require FFT analysis were generated by the event-based (crank-angle based) integration.

The time-based results are generated for the case of a free motion of the crank-slider mechanism with the initial angular velocity of the crankshaft, $\dot{\theta}(0)$, being equal to 225 rad/sec. Consequently, the frequency, ω_o, of the periodic rigid body motion of the crankshaft becomes 35.81 Hz. The topological nonlinearities, brought about by the motion of the connecting rod, have resulted in superharmonic resonances, $n\omega_o$ with $n = 1, 2, \ldots,$ appearing in the frequency spectrum of the angular velocity of the crankshaft (see Fig. 2). The effect of the rigid body motion on the structural flexibility is manifested by having ω_o and its superharmonic resonances appearing in the frequency spectrums of the first three elastic modes of the crankshaft and the first elastic mode of the connecting rod. Due to the lack of space, only the frequency spectrum of the first elastic mode of the crankshaft is shown in Fig. 3.

Moreover, the effect of topological nonlinearities on the structural flexibility of the system is manifested by the presence of combination resonances, $\omega_{n_i} \pm n\omega_o$, in the frequency spectrums of the elastic modes of the crankshaft and the connecting rod (see Fig. 3). Similarly, the combination resonances are appearing in the frequency spectrum of the crankshaft angular velocity; thus, exhibiting the effect of the flexible motion on the rigid body motion (see Fig. 2).

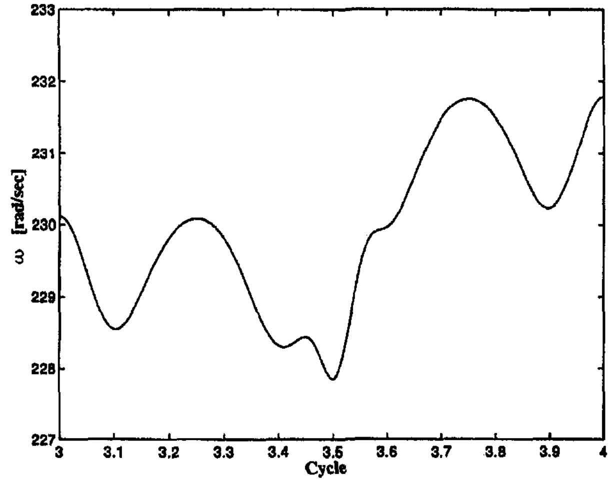

(a) Cycle No. 4

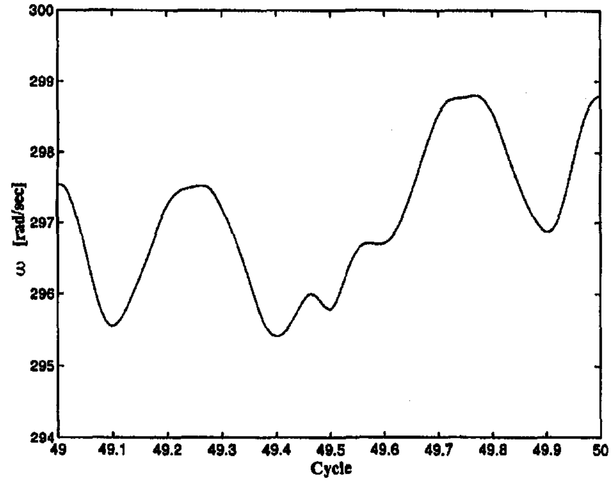

(b) Cycle No. 50

Fig. 5 Predicted crankshaft angular velocity in the case of an actual cylinder gas force with an initial rigid body rotation of the crankshaft

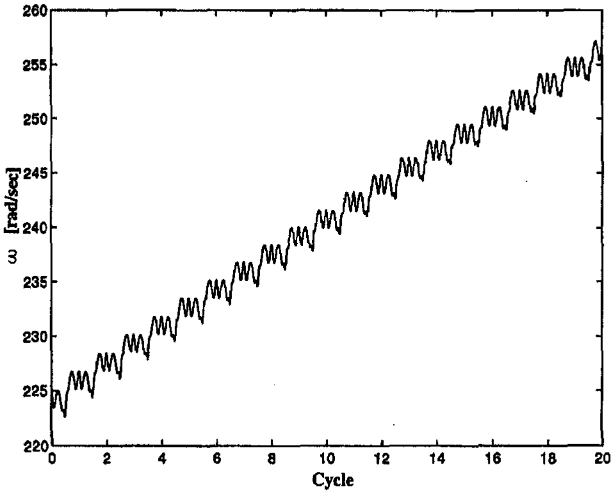

Fig. 6 Predicted crankshaft angular velocity in the case of an actual cylinder gas force with an initial rigid body rotation of the crankshaft

Next, the rigid and flexible motions of the crank-slider mechanism are predicted under engine firing conditions. The results were generated based on a gas pressure curve, depicted in Fig. 4, which was measured in a single-cylinder, four-stroke cycle, direct-injection diesel engine. The crankshaft angular velocity during the fourth and the fiftieth cycles are shown in Figs. 5(*a*) and 5(*b*), respectively. The results demonstrate that the crankshaft angular velocity decreases as the piston is accelerated from a zero speed at TDC to its maximum speed that can be reached at around 70 deg crank angle from TDC. Beyond that point, the piston starts decelerating and the crankshaft speed increases to reach a maximum value at BDC. Once again, at the beginning of the compression stroke, the crankshaft speed starts decreasing in order to set the piston in motion. This transfer of kinetic energy from the crankshaft to the piston reaches its maximum value at around 70 deg crank angle from TDC. Beyond that point, the crankshaft speed begins to increase. However, the resistive effect, stemming from the build-up of the gas pressure, will overcome the gain in the crankshaft kinetic energy for the remaining portion of the compression stroke. As a result, the crankshaft speed will significantly decrease until the pis-

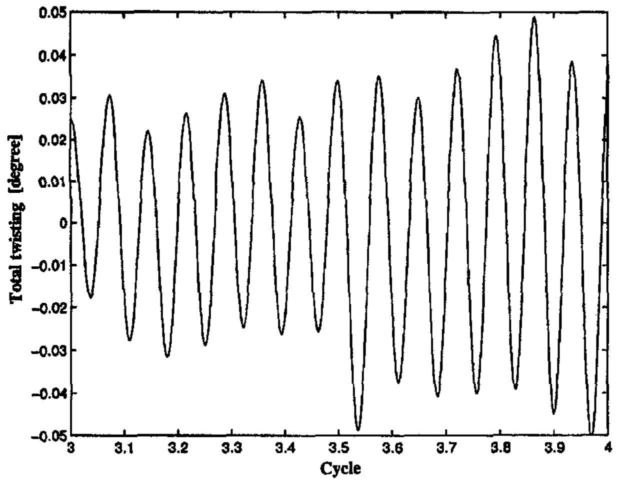

Fig. 7 Predicted total twisting of the crankshaft in the case of an actual cylinder gas force with an initial rigid body rotation of the crankshaft

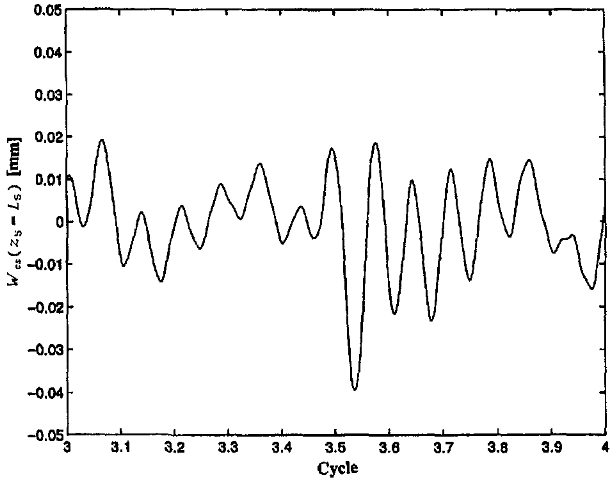

Fig. 8 Predicted out-of-plane transverse deformation of the crankshaft at the crank gear in the case of an actual cylinder gas force with an initial rigid body rotation of the crankshaft

ton reaches TDC. At that moment, the work of the gas force becomes positive, which leads to a significant increase in $\dot{\theta}$. Similarly, the last dip in $\dot{\theta}$ during the exhaust stroke can be related to the exchange of the kinetic energy between the piston and the crankshaft. Furthermore, a brief comparison between Figs. 5(*a*) and 5(*b*) reveals that the dip in the crankshaft angular velocity near TDC (firing) becomes smaller as the engine speed increases. This trend demonstrates the significant effect of the inertial forces on the overall response of the crank-slider mechanism. However, the effect of the potential energy due to the force of gravity was examined in this study and found to be insignificant. Figure 6 illustrates the predicted crankshaft angular speed during an acceleration period of 20 engine cycles. Moreover, Figs. 7 and 8 illustrate the predicted twisting of the crankshaft between the flywheel and the crank gear along with the out-of-plane transverse deformation of the crankshaft at the crank gear, respectively. It should be mentioned that the simulation is initiated from the undeformed configuration of the crank-slider mechanism. As expected, the largest deformations are obtained during the combustion period during which the energy is stored in the system in the form of strain energy. The crankshaft twisting reveals that a portion of the stored energy is released during the exhaust and intake strokes while the gas pressure buildup during the compression stroke tends to damp out the vibrations of the system (see Fig. 7).

5 Summary

A dynamic model is developed in this study to predict the rigid and flexible motions of the piston assembly/connecting rod/crankshaft mechanism of a single cylinder internal combustion engine. The model accounts for the torsional vibration and the out-of-plane transverse deformation of the crankshaft along with the out-of-plane transverse deformation of the connecting rod.

The eigenvalue problem of the crankshaft, including the counterweights, the flywheel and the crank gear, is solved to obtain the analytical expressions for the elastic modes of the crankshaft. These mode shapes along with those of the connecting rod are required for the implementation of the assumed modes method which is used herein to discretize the structural flexibility terms.

The Lagrange principle is used to derive the equations of motion. Two constraint equations are included in the formulation to avoid secondary motions of the system due to piston lateral displacements or tilting. The resulting differential-algebraic equations account for the coupling between the rigid and flexible motions of the crank-slider mechanism along with the stiffening effect of the centripetal acceleration.

The digital simulation results, generated based on the free motion of the crank-slider mechanism, reveal the superharmonic resonances in the system that are induced by the topological nonlinearities. Moreover, the combination resonances serve to demonstrate the relationships with which the rigid and flexible motions of the crank-slider mechanism would interact.

Furthermore, the digital simulation results have demonstrated the capability of the formulation in predicting, under firing conditions, the twisting of the crankshaft and the out-of-plane transverse deformation at any point on the crank-slider mechanism.

Future research work will aim at expanding the current formulation to account for the longitudinal and the in-plane transverse deformations of the crankshaft, the in-plane transverse deformation of the connecting rod, along with the secondary motions of the piston, and at validating the results with experimental data. It should be emphasized that the equations, describing the rigid and flexible motions of the crank-slider mechanism, are essential for the development of schemes that can accurately predict the instantaneous frictional losses in internal combustion engines.

Acknowledgment

The authors would like to acknowledge the technical and financial support of the Automotive Research Center (consortium of five universities directed by the University of Michigan) by the National Automotive Center, located within the US Army Tank-Automotive Research, Development, and Engineering Center (TARDEC), Warren, MI.

References

Bremer, Jr., R. C., 1979, "A Practical Treatise on Engine Crankshaft Torsional Vibration Control," SAE Paper 790763.

Carrato, P. J., and Fu, C. C., 1986, "Modal Analysis Techniques for Torsional Vibration of Diesel Crankshafts," SAE Paper 861225.

Gear, C. W., 1971, *Numerical Initial Value Problems in Ordinary Differential Equations*, Prentice-Hall, New Jersey.

Glocker, C., and Pfeiffer, F., 1992, "Dynamical Systems with Unilateral Contacts," *Nonlinear Dynamics*, Vol. 3, pp. 245–259.

Kawazoe, Y., and Zhang, S., 1991, "Small Engine Crankshaft Vibration Analysis With an Improved Transfer Matrix Method," SAE paper 911274.

Lee, D., and Rizzoni, G., 1995, "Detection of Partial Misfire in IC Engines Using a Measurement of Crankshaft Angular Velocity," SAE paper 951070.

Meirovitch, L., 1986, *Elements of Vibration Analysis*, McGraw-Hill, New York.

Morita, T., and Okamura, H., 1995, "Simple Modeling and Analysis for Crankshaft Three-Dimensional Vibrations: Part 2—Application to an Operating Engine Crankshaft," *ASME Journal of Vibration and Acoustics*, Vol. 117, No. 1, pp. 80–86.

Okamura, H., Shinno, A., Yamanaka, T., Suzuki, A., Sogabe, K., 1995, "Simple Modeling and Analysis for Crankshaft Three-Dimensional Vibrations: Part 1—Background and Application to Free Vibrations," *ASME Journal of Vibration and Acoustics*, Vol. 117, No. 1, pp. 70–79.

Priebsch, H. H., Affenzeller, J., and Gran, S., 1993, "Prediction Technique for Stress and Vibration of Nonlinear Supported, Rotating Crankshafts," ASME JOURNAL OF ENGINEERING FOR GAS TURBINES AND POWER, Vol. 115, pp. 711–720.

Rezeka, S. F., and Henein, N. A., 1984, "A New Approach to Evaluate Instantaneous Friction and its Components in Internal Combustion Engines," SAE Paper 840179.

Taraza, D., 1993, "Estimation of the Mean Indicated Pressure from Measurements of the crankshafts Angular Speed Variation," SAE Paper 932413.

Taraza, D., 1993, "Possibilities to Reconstruct Indicator Diagrams by Analysis of the Angular Motion of the Crankshaft," SAE Paper 932414.

Uras, H. M., and Patterson, D. J., 1983, "Measurements of Piston and Ring Assembly Friction-Instantaneous IMEP Method," SAE Paper 830416.

Young, D., and Felgar, R. P., 1949, "Tables of Characteristic Functions Representing Normal Modes of Vibration of a Beam," publication no. 4913, The University of Texas, Austin, TX.

APPENDIX A

The entries of the transfer function matrix for a typical Euler-Bernoulli beam element, G_i, are

$$a_{11} = a_{22} = a_{44} = a_{55} = a_i(\lambda_{w_i}^{(j)}, L_i)$$

$$a_{12} = -a_{54} = -d_i(\lambda_{w_i}^{(j)}, L_i)\lambda_{w_i}^{(j)}$$

$$a_{14} = \frac{-b_i(\lambda_{w_i}^{(j)}, L_i)}{EI_i\lambda_{w_i}^{(j)}} \quad a_{15} = -a_{24} = \frac{-c_i(\lambda_{w_i}^{(j)}, L_i)}{EI_i(\lambda_{w_i}^{(j)})^2}$$

$$a_{21} = -a_{45} = \frac{-b_i(\lambda_{w_i}^{(j)}, L_i)}{\lambda_{w_i}^{(j)}}$$

$$a_{25} = \frac{d_i(\lambda_{w_i}^{(j)}, L_i)}{EI_i(\lambda_{w_i}^{(j)})^3} \quad a_{33} = a_{66} = e_i(\lambda_{t_i}^{(j)}, L_i)$$

$$a_{36} = -\frac{f_i(\lambda_{t_i}^{(j)}, L_i)}{GJ_i\lambda_{t_i}^{(j)}}$$

$$a_{41} = -d_i(\lambda_{w_i}^{(j)}, L_i)EI_i\lambda_{w_i}^{(j)}$$

$$a_{42} = -a_{51} = c_i(\lambda_{w_i}^{(j)}, L_i)EI_i(\lambda_{w_i}^{(j)})^2$$

$$a_{52} = b_i(\lambda_{w_i}^{(j)}, L_i)EI_i(\lambda_{w_i}^{(j)})^3 \quad a_{63} = f_i(\lambda_{t_i}^{(j)}, L_i)GJ_i\lambda_{t_i}^{(j)}$$

where

$$a_i(\lambda_{w_i}^{(j)}, z_i) = 0.5\,[\cosh(\lambda_{w_i}^{(j)}z_i) + \cos(\lambda_{w_i}^{(j)}z_i)]$$

$$b_i(\lambda_{w_i}^{(j)}, z_i) = 0.5[\sinh(\lambda_{w_i}^{(j)}z_i) + \sin(\lambda_{w_i}^{(j)}z_i)]$$

$$c_i(\lambda_{w_i}^{(j)}, z_i) = 0.5[\cosh(\lambda_{w_i}^{(j)}z_i) - \cos(\lambda_{w_i}^{(j)}z_i)]$$

$$d_i(\lambda_{w_i}^{(j)}, z_i) = 0.5[\sinh(\lambda_{w_i}^{(j)}z_i) - \sin(\lambda_{w_i}^{(j)}z_i)]$$

$$e_i(\lambda_{t_i}^{(j)}, z_i) = \cos(\lambda_{t_i}^{(j)}z_i) \quad f_i(\lambda_{t_i}^{(j)}, z_i) = \sin(\lambda_{t_i}^{(j)}z_i)$$

The H_i matrices, reflecting the linear and angular momentum balance equations for the rigid body that is attached at the ith node, are given as

$$H_1 = \begin{bmatrix} -J_{x_1}^{(fl)}\dot{\theta}^2 & 0 & 0 \\ 0 & -m_{fl}\dot{\theta}^2 & 0 \\ 0 & 0 & -J_{z_1}^{(fl)}\dot{\theta}^2 \end{bmatrix}$$

$$H_2 = \begin{bmatrix} 0 & 0 & -J_{x_1}^{(cw1)}\dot{\theta}^2 \\ -m_{cw1}r\dot{\theta}^2 & m_{cw1}\dot{\theta}^2 & 0 \\ J_{z_1}^{(cw1)}\dot{\theta}^2 & 0 & 0 \end{bmatrix}$$

$$H_5 = \begin{bmatrix} 0 & 0 & -J_{z_5}^{(cw2)}\dot{\theta}^2 \\ 0 & m_{cw2}\dot{\theta}^2 & -m_{cw2}r\dot{\theta}^2 \\ J_{x_5}^{(cw2)}\dot{\theta}^2 & 0 & 0 \end{bmatrix}$$

$$H_6 = \begin{bmatrix} J_{x_5}^{(gr)}\dot{\theta}^2 & 0 & 0 \\ 0 & m_{gr}\dot{\theta}^2 & 0 \\ 0 & 0 & J_{z_5}^{(gr)}\dot{\theta}^2 \end{bmatrix}$$

ERRATUM

The paper, ''The Development of the Whittle Turbojet,'' by C. B. Meher-Homji that appeared in the April 1998 issue of this journal was published with the incorrect Figure 8. The correct figure appears below. The editor and editorial staff apologize for this error.

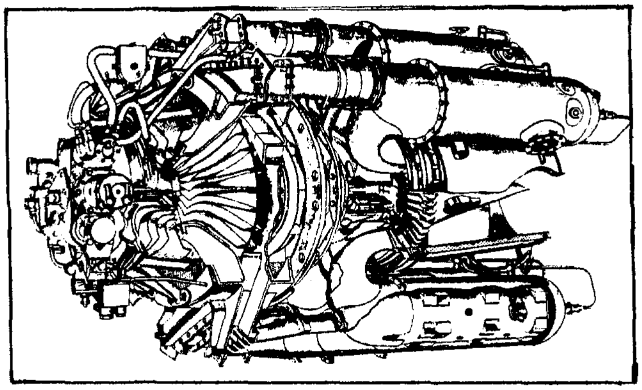

Fig. 8 The W.2/700 engine made by Power Jets Ltd. this was the last engine to be built by Power Jets. It was rated at 2500 lb thrust.